ADVANCES IN INORGANIC CHEMISTRY

Volume 55

Rudi van Eldik

Advances in

INORGANIC CHEMISTRY

———

Volume 55

ADVISORY BOARD

I. Bertini
Universitá degli Studi di Firenze
Florence, Italy

D. J. Darensbourg
Texas A&M University
College Station,
Texas, USA

J. H. Espenson
Iowa State University
Ames, Iowa, USA

L. H. Gade
Universität Heidelberg
Heidelberg, Germany

H. B. Gray
California Institute of Technology
Pasadena, California,
USA

M. L. H. Green
University of Oxford
Oxford, United Kingdom

P. A. Lay
University of Sydney
Sydney, Australia

A. E. Merbach
Institut de Chimie Moléculaire et Biologique
Ecole Polytechnique Fédérale de Lausanne
Lausanne, Switzerland

J. Reedijk
Leiden University
Leiden, The Netherlands

P. J. Sadler
University of Edinburgh
Edinburgh, Scotland

Y. Sasaki
Hokkaido University
Sapporo, Japan

K. Wieghardt
Max-Planck Institut
Mülheim, Germany

Advances in
INORGANIC CHEMISTRY
Including Bioinorganic Studies

EDITED BY

Rudi van Eldik

Institute for Inorganic Chemistry
University of Erlangen-Nürnberg
91058 Erlangen
Germany

VOLUME 55

ELSEVIER
ACADEMIC
PRESS

Amsterdam Boston Heidelberg London New York Oxford
Paris San Diego San Francisco Singapore Sydney Tokyo

ELSEVIER B.V.
Sara Burgerhartstraat 25
P.O. Box 211, 1000 AE
Amsterdam, The Netherlands

ELSEVIER Inc.
525 B Street, Suite 1900
San Diego, CA 92101-4495
USA

ELSEVIER Ltd
The Boulevard, Langford Lane
Kidlington, Oxford OX5 1GB
UK

ELSEVIER Ltd
84 Theobalds Road
London WC1X 8RR
UK

© 2004 Elsevier Inc. All rights reserved.

This work is protected under copyright by Elsevier Inc., and the following terms and conditions apply to its use:

Photocopying
Single photocopies of single chapters may be made for personal use as allowed by national copyright laws. Permission of the Publisher and payment of a fee is required for all other photocopying, including multiple or systematic copying, copying for advertising or promotional purposes, resale, and all forms of document delivery. Special rates are available for educational institutions that wish to make photocopies for non-profit educational classroom use.

Permissions may be sought directly from Elsevier's Rights Department in Oxford, UK: phone (+44) 1865 843830, fax (+44) 1865 853333, e-mail: permissions@elsevier.com. Requests may also be completed on-line via the Elsevier homepage (http://www.elsevier.com/locate/permissions).

In the USA, users may clear permissions and make payments through the Copyright Clearance Center, Inc., 222 Rosewood Drive, Danvers, MA 01923, USA; phone: (+1) (978) 7508400, fax: (+1) (978) 7504744, and in the UK through the Copyright Licensing Agency Rapid Clearance Service (CLARCS), 90 Tottenham Court Road, London W1P 0LP, UK; phone: (+44) 20 7631 5555; fax: (+44) 20 7631 5500. Other countries may have a local reprographic rights agency for payments.

Derivative Works
Tables of contents may be reproduced for internal circulation, but permission of the Publisher is required for external resale or distribution of such material. Permission of the Publisher is required for all other derivative works, including compilations and translations.

Electronic Storage or Usage
Permission of the Publisher is required to store or use electronically any material contained in this work, including any chapter or part of a chapter.

Except as outlined above, no part of this work may be reproduced, stored in a retrieval system or transmitted in any form or by any means, electronic, mechanical, photocopying, recording or otherwise, without prior written permission of the Publisher.
Address permissions requests to: Elsevier's Rights Department, at the fax and e-mail addresses noted above.

Notice
No responsibility is assumed by the Publisher for any injury and/or damage to persons or property as a matter of products liability, negligence or otherwise, or from any use or operation of any methods, products, instructions or ideas contained in the material herein. Because of rapid advances in the medical sciences, in particular, independent verification of diagnoses and drug dosages should be made.

First edition 2004

ISBN: 0-12-023655-9
ISSN: 0898-8838

♾ The paper used in this publication meets the requirements of ANSI/NISO Z39.48-1992 (Permanence of Paper).
Printed and bound in The Netherlands.

CONTENTS

PREFACE ix

Dioxygen Activation by Transition Metal Complexes. Atom Transfer and Free Radical Chemistry in Aqueous Media

ANDREJA BAKAC

I. Introduction 1
II. Preparation and Characterization 3
III. Reactivity 12
IV. Conclusions and Future Directions 50
V. Abbreviations 52
References 52

Redox Reactivity of Coordinated Ligands in Pentacyano(L)Ferrate Complexes

JOSÉ A. OLABE

I. Introduction 61
II. General Properties of the Nitroprusside ion, $[Fe(CN)_5NO]^{2-}$ (NP), and Related Nitrosyl Complexes 64
III. The Coordination Chemistry of NO. Formation and Dissociation Reactions 66
IV. The Redox Reactivity of Bound NO 75
V. The Electrophilic Reactions of Bound NO 79
VI. The Autooxidation of Hydrazine 104
VII. The Oxidation of Amines and Alcohols 106
VIII. The Disproportionation of Hydroxylamine 108
IX. Miscellaneous Reactions 110
X. Conclusions 120
References 122

Carbonato Complexes: Models for Carbonic Anhydrase

ACHYUTA N. ACHARYA, ARABINDA DAS AND ANADI C. DASH

I. Introduction 128
II. Carbonic Acid, Bicarbonate, and Carbonate 129
III. The Chemistry of Metal Carbonates 133
IV. Kinetics and Mechanism of Formation and Aquation/Decarboxylation Reactions 145
V. Discovery and Classification of Carbonic Anhydrases 159
VI. Structure of α-Class Carbonic Anhydrase from Human Erythrocytes (the High Activity form HCA II) 161
VII. Structure of β-Carbonic Anhydrase from the Red Alga, *Porphyridium purpureum* 180
VIII. Structure of γ-Class Carbonic Anhydrase of *Methanosarcina thermophila* (*Cam*) 183
IX. A δ-Class of Carbonic Anhydrase? 185
X. Model Chemistry 186
XI. Concluding Remarks 188
XII. Abbreviations 189
References 190

Transition Metal Chemistry of Glucose Oxidase, Horseradish Peroxidase, and Related Enzymes

ALEXANDER D. RYABOV

I. Introduction 201
II. Enzymes 203
III. Properties of Mediators 208
IV. Ferrocenes 210
V. Osmium and Ruthenium Compounds 239
VI. Chiral Complexes 253
VII. Cyclometalated Ruthenium(II) and Osmium(II) Mediators 257
VIII. Concluding Remarks 262
References 262

Properties of Transition Metal Complexes with Metal–Carbon Bonds in Aqueous Solutions as Studied by Pulse Radiolysis

ALEXANDRA MASARWA AND DAN MEYERSTEIN

I. Introduction 272
II. Radiolysis of Aqueous Solutions 272

III. Reaction of Aliphatic Carbon-Centered Radicals with Transition Metal Complexes in Aqueous Solutions 274
IV. Formation of Transition Metal Complexes with Metal–Carbon σ-Bonds 275
V. Properties of Complexes with Metal–Carbon σ-Bonds 278
VI. Mechanisms of Decomposition of the Transient Complexes L_mM^{n+1}–R 280
VII. Alkene Complexes 298
VIII. Complexes with Metal–Carbon σ-Bonds Formed in Redox Processes Between Transition Metal Complexes and Organic Substrates 299
IX. Elucidation of the Mechanisms of Catalytic Processes 304
References 308

Transition Metal Complexes with Bis(Hydrazone) Ligands of 2,6-Diacetylpyridine. Hepta-Coordination of 3d Metals

IVANA IVANOVIĆ-BURMAZOVIĆ AND KATARINA ANDJELKOVIĆ

I. Introduction 315
II. Aspects Studied 316
III. Concluding Discussion 350
References 356

Potential Applications for the Use of Lanthanide Complexes as Luminescent Biolabels

GRAHAM R. MOTSON, JEAN S. FLEMING AND SALLY BROOKER

I. Scope 361
II. Introduction 362
III. Properties of Lanthanide(III) Ions 363
IV. Ligand Systems Explored 369
V. Biochemical Applications 390
VI. Concluding Remarks 417
VII. Glossary 417
References 419

INDEX 433
CONTENTS OF PREVIOUS VOLUMES 443

This Page Intentionally Left Blank

PREFACE

This is my second volume as Editor of this series, and I am pleased to say that all involved in the production of this series are extremely happy with the outcome of my first Volume 54, a thematic issue devoted to Inorganic Reaction Mechanisms. More such thematic issues are in the pipeline: the next one (Volume 56) will be devoted to Redox-active Metal Complexes and dedicated to the late Dieter Sellmann, followed by Volume 57 devoted to Relaxometry of Water-Metal Ion Interactions and co-edited by Ivano Bertini.

The present volume is a non-thematic issue and includes seven contributions. The first chapter by Andreja Bakac presents a detailed account of the activation of dioxygen by transition metal complexes and the important role of atom transfer and free radical chemistry in aqueous solution. The second contribution comes from José Olabe, an expert in the field of pentacyanoferrate complexes, in which he describes the redox reactivity of coordinated ligands in such complexes. The third chapter deals with the activation of carbon dioxide and carbonato complexes as models for carbonic anhydrase, and comes from Anadi Dash and collaborators. This is followed by a contribution from Sasha Ryabov on the transition metal chemistry of glucose oxidase, horseradish peroxidase and related enzymes. In chapter five Alexandra Masarwa and Dan Meyerstein present a detailed report on the properties of transition metal complexes containing metal–carbon bonds in aqueous solution. Ivana Ivanović and Katarina Andjelković describe the importance of hepta-coordination in complexes of 3d transition metals in the subsequent contribution. The final chapter by Sally Brooker and co-workers is devoted to the application of lanthanide complexes as luminescent biolabels, an exciting new area of development.

I thoroughly believe that these contributions all cover important advances in inorganic chemistry and trust that the inorganic chemistry community will benefit from them.

Rudi van Eldik
University of Erlangen-Nürnberg
Germany
October 2003

DIOXYGEN ACTIVATION BY TRANSITION METAL COMPLEXES. ATOM TRANSFER AND FREE RADICAL CHEMISTRY IN AQUEOUS MEDIA

ANDREJA BAKAC

Ames Laboratory, Iowa State University, Ames, IA 50011, USA

I. Introduction
II. Preparation and Characterization
  A. Superoxo Complexes
  B. Hydroperoxo Complexes
  C. High-Valent Oxo Intermediates
III. Reactivity
  A. Hydrogen Atom and Hydride Abstraction by MO Complexes
  B. Reactions of Superoxo Complexes with Rh–H, O–H, and C–H Bonds
  C. Reactions of LMOO Complexes with Nitrogen Oxides and HNO_2
  D. Catalytic Oxidation of Alcohols by O_2
IV. Conclusions and Future Directions
V. Abbreviations
References

I. Introduction

This chapter is an overview of several years of our research on reactions of various forms of transition-metal-activated oxygen in aqueous solution. The term "metal-activated oxygen" refers loosely to metal complexes containing an O_2-derived ligand, such as superoxo, hydroperoxo, peroxo, or oxo. Among the metals, chromium, cobalt, and rhodium have been the most essential in our research. Their complexes exhibit a combination of reasonable persistence in the absence of added substrates and substantial reactivity toward a roster of inorganic and organic materials. The stability facilitates the handling and characterization of these compounds by a variety of techniques including, in some cases, X-ray crystallography. The reactivity toward various classes of reagents promises mechanistic variety. Indeed, electron transfer,

ADVANCES IN INORGANIC CHEMISTRY
VOLUME 55 ISSN 0898-8838 DOI 10.1016/S0898-8838(03)55001-2

© 2004 Elsevier Inc.
All rights reserved.

hydrogen atom transfer, hydride transfer, and radical coupling have all been observed.

An attempt has been made throughout to provide sufficient background information and to place our work in the proper context in this very active field, but an exhaustive coverage of the available literature is beyond the scope of this review. References (*1–43*) represent only a fraction of books and reviews published in the past five years on various aspects of dioxygen activation.

Some examples of the complexes discussed in this chapter are shown in Fig. 1. The "active site", i.e., partially reduced oxygen, appears as an end-on superoxo, hydroperoxo, or oxo group. Other ligands are mostly water, ammonia, N_4-macrocycles (cyclam and Me_6-cyclam, abbreviated as L^1 and L^2, respectively), and N_2O_2-chelates, typically salen. These ligands are chemically inert under most of the circumstances,

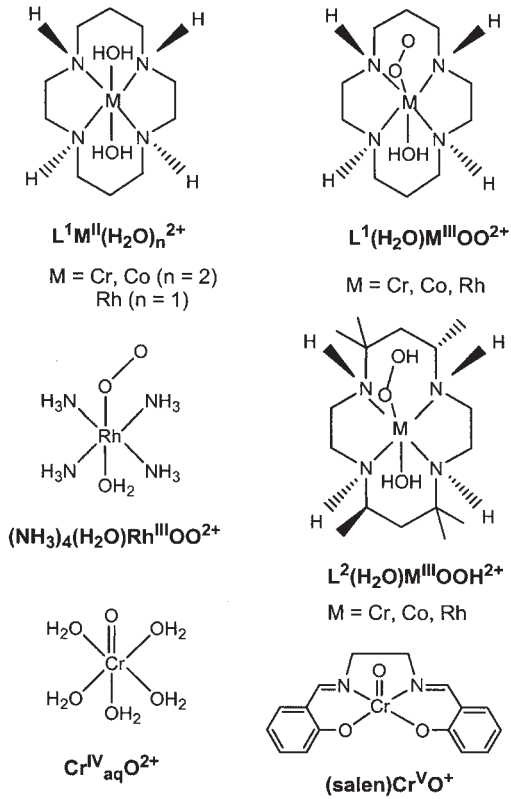

FIG. 1. Chemical structures of some of the complexes in this work.

although several cases of ligand oxidation have been observed, as discussed later.

Unless stated otherwise, the kinetic data refer to aqueous solutions at 25 °C.

II. Preparation and Characterization

A. Superoxo Complexes

These are typically prepared from low concentrations of chemically or photochemically generated low-valent metal complex (Cr^{2+}_{aq}, $L(H_2O)_2Co^{2+}$, or $L(H_2O)Rh^{2+}$) and a large excess of O_2 in slightly acidic aqueous solutions according to the chemistry in Eq. (1), where L = N_4-macrocycle, $(H_2O)_4$ or $(NH_3)_4$. The rate of formation of the superoxo complexes is mostly limited by the rate of water substitution at the metal centers, except in the case of $L(H_2O)Rh^{2+}$ ions, which are pentacoordinate in solution (*44*). Selected kinetic data are shown in Table I.

$$L(H_2O)_nM^{2+} + O_2 \underset{k_{off}}{\overset{k_{on}}{\rightleftarrows}} L(H_2O)_{n-1}MOO^{2+} + H_2O \quad n = 1 \text{ or } 2 \qquad (1)$$

The complexes in Table I have been assigned an end-on geometry on the basis of spectroscopic data, chemical behavior, and, in the case of a macrocyclic rhodium complex, X-ray crystallographic data (*53*). The O–O stretching frequencies and O–O bond lengths are useful indicators of the electronic structure of coordinated dioxygen (*54–59*),

TABLE I

Rate Constants for the Formation and Homolysis of Some Superoxometal Complexes According to Eq. (1)

Complex	$10^7\ k_{on}/M^{-1}\ s^{-1}$	k_{off}/s^{-1}	Source
$L^1(H_2O)CrOO^{2+}$	18	*a*	Ref. (*45*)
$Cr_{aq}OO^{2+}$	16	2.5×10^{-4}	Ref. (*46–48*)
$(NH_3)_4(H_2O)RhOO^{2+}$	31	*a*	Ref. (*49*)
$L^1(H_2O)RhOO^{2+}$	21	*a*	Ref. (*50*)
$L^2(H_2O)RhOO^{2+}$	8.2	*a*	Ref. (*50*)
$L^1(H_2O)CoOO^{2+}$	1.2	63	Ref. (*51,52*)
$L^2(H_2O)CoOO^{2+}$	0.50	1.66×10^4	Ref. (*51*)

[a]Not determined.

but not its geometry. The generally accepted frequency range for superoxo complexes (*60*) is 1075–1200 cm^{-1}. In addition to the more typical end-on complexes, several side-on superoxides of chromium (*61*) and copper (*62*) also exhibit bands in this range. Some side-on $Co–O_2$ trispyrazolylborates, on the other hand, feature much lower O–O stretching frequencies that lie in the peroxo region, even though the O–O distances agree well with the superoxo assignment (*63,64*).

The resonance Raman spectrum of $Cr_{aq}OO^{2+}$ (*65*) is shown in Fig. 2. The $Cr^{16}O–^{16}O$ stretch at 1166 cm^{-1} is fully consistent with the superoxo assignment, as is the 68 cm^{-1} shift to lower frequency for $Cr^{18}O–^{18}O^{2+}$. The $Cr–^{16}O^{16}O$ stretch at 503 cm^{-1} shifts to 491 cm^{-1} in the $^{18}O_2$-substituted complex.

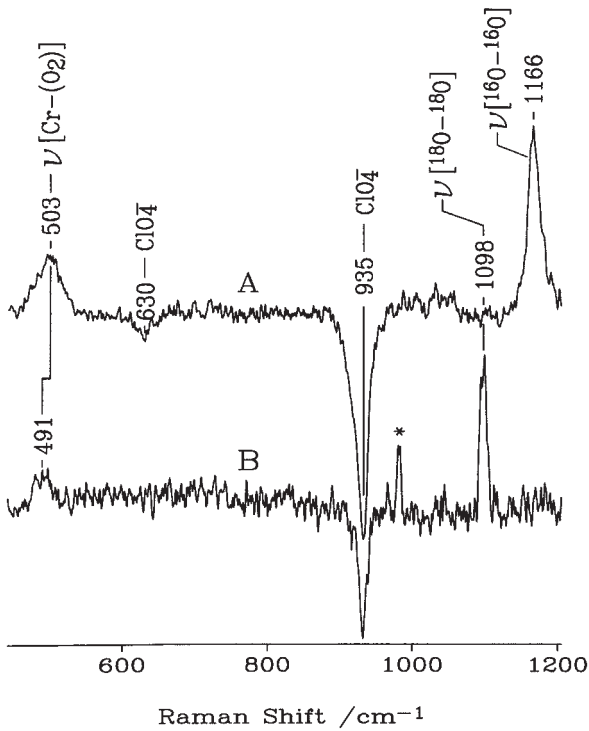

FIG. 2. 245-nm excited resonance Raman spectrum of (A) 0.225 mM $Cr_{aq}OO^{2+}$ and (B) 50 μM $Cr_{aq}{}^{18}O^{18}O^{2+}$ in 0.02 M $HClO_4$ at 0 °C. Negative peaks arise from subtraction of the intense $HClO_4$ bands at 934 and 629 cm^{-1}. The asterisk indicates a burned spot on the intensifier of the diode-array detector. Reproduced with permission from *J. Am. Chem. Soc.* **1995**, *117*, 6483–6488. Copyright 1995 American Chemical Society.

The macrocyclic analog, $L^1(H_2O)CrOO^{2+}$, exhibits bands at 1134/1145 cm^{-1} (O–O) and 489 cm^{-1} (Cr–O). The appearance of the doublet in the O–O region suggests two low-energy conformations having single and bifurcated intramolecular hydrogen bonds between the terminal oxygen and amine protons of the cyclam ligand (*65*). The recent X-ray crystal structure of a related macrocyclic superoxorhodium complex, $[L^2(CH_3CN)RhOO](CF_3SO_3)_2$, Fig. 3, supports the idea of bifurcated hydrogen bonding in this type of complexes.

In the rhodium complex (*53*), the similar N–O distances, 2.85 and 2.99 Å, suggest weak but real hydrogen bonding between oxygen and both N–H groups located on the "up" side of the macrocyclic plane. Other important features in the structure are the O–O bond length of 1.306 Å and the Rh–O(1)–O(2) angle of 115.3°, clearly identifying the coordinated oxygen as an end-on superoxide.

The ESR spectrum of another macrocyclic rhodium complex, $L^1(H_2O)RhOO^{2+}$ (*44*) in Fig. 4, exhibits three g values, $g_1 = 2.099$, $g_2 = 2.014$, $g_3 = 1.998$, characteristic of an axially asymmetric rhodium

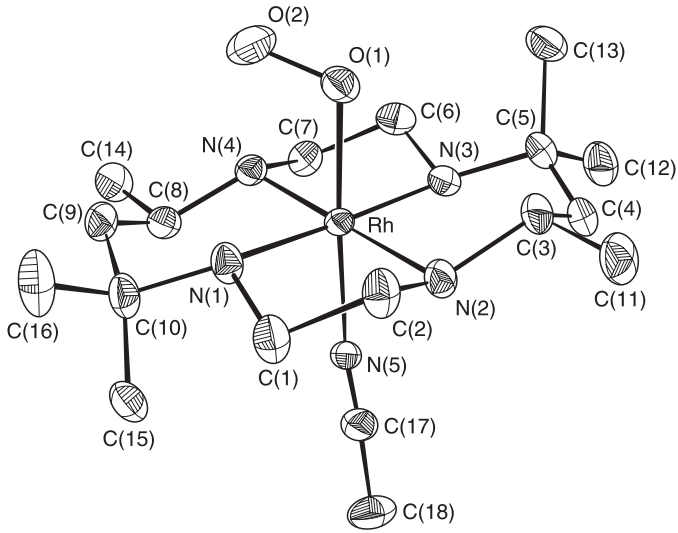

FIG. 3. Perspective view of $L^2(CH_3CN)RhOO^{2+}$ with the thermal ellipsoids at 30% probability level. Selected bond distances (Å) and angles (°): O(1)–O(2) 1.306(5), Rh–(O1) 2.005(3), Rh–(N1) 2.076(4), Rh–(N2) 2.067(4), Rh–(N3) 2.100(4), Rh–(N4) 2.062(4), Rh–(N5) 2.045(4), (O1)–Rh–(N5) 177.15(13), (O2)–(O1)–Rh 115.3(3). Reproduced with permission from *Inorg. Chem.* **2000**, *39*, 736–740. Copyright 2000 American Chemical Society.

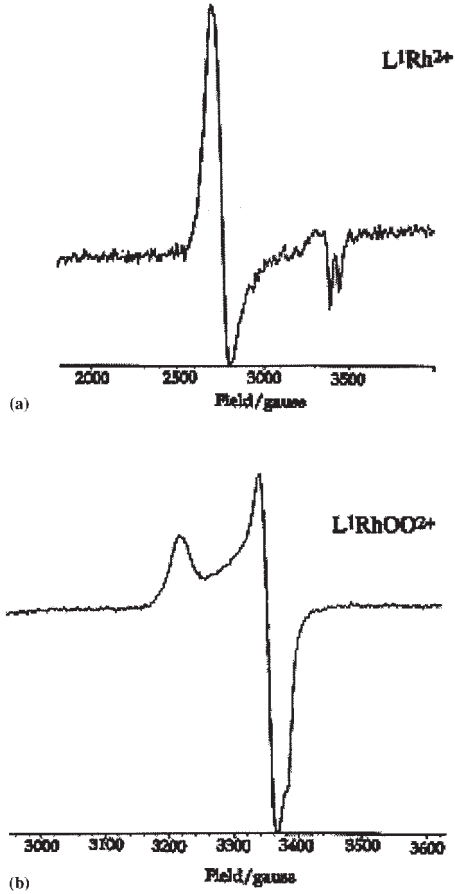

FIG. 4. ESR spectra of (a) $L^1(H_2O)Rh^{2+}$ and (b) $L^1(H_2O)RhOO^{2+}$ in 0.01 M aqueous $HClO_4$ at 120 K. Reproduced with permission from *Inorg. Chem.* **1996**, *35*, 5880–5884. Copyright 1996 American Chemical Society.

complex containing the end-on bound O_2 (*66,67*). For comparison, the $L^1(H_2O)Rh^{2+}$ precursor exhibits an axially symmetric spectrum with $g_{||} = 1.980$ ($A_{Rh} = 139$ MHz) and $g_{\perp} = 2.455$.

All the superoxo complexes absorb strongly in the UV region, Table II. The 240 nm band in the spectrum of $Cr_{aq}OO^{2+}$ has been assigned as the superoxide-centered transition on the basis of the similarity with the position and intensity of the bands for free $O_2^{\bullet -}$ (λ 245 nm, ε 2350 M^{-1} cm^{-1}) and $HO_2^{\bullet}$ (λ 225 nm, ε 1400 M^{-1} cm^{-1}) (*68*).

TABLE II

UV DATA FOR SUPEROXO ($LMOO^{2+}$) AND HYDROPEROXO ($LMOOH^{2+}$) COMPLEXES IN ACIDIC AQUEOUS SOLUTION

Complex	λ_{max} (10^{-3} ε/M^{-1} cm^{-1})		Source
LM^{2+}	$LMOO^{2+}$	$LMOOH^{2+}$	
$L^1(H_2O)Cr^{2+}$	292 (2.9)	*a*	Ref. (*69*)
Cr^{2+}_{aq}	292 (3.1); 245 (7.4)	250 (1.7)[b]	Ref. (*47,48*)
$(NH_3)_4(H_2O)Rh^{2+}$	270 (9.6)	240 (4.0)	Ref. (*49,70*)
$L^1(H_2O)Rh^{2+}$	267 (9.0)	240 (4.0)[b]	Ref. (*50*)
$L^2(H_2O)Rh^{2+}$	271 (10)	235 (3.7)[b]	Ref. (*71–73*)
	265 (11.2)[c]		Ref. (*71*)
$L^1(H_2O)Co^{2+}$	360 (2.6)[d]	225 (16)	Ref. (*51,74*)
	(2.2)[d]		Ref. (*52*)
$L^2(H_2O)Co^{2+}$	330 (4.2)[b]	240 (14)	Ref. (*51,75,76*)

[a]Not determined.
[b]Shoulder.
[c]pH 12.
[d]Not a maximum.

The corresponding bands in other superoxo complexes in Table II are obscured by ligand-based transitions.

The photochemically active 290-nm band of $Cr_{aq}OO^{2+}$ is assigned as superoxide-to-metal charge transfer. All the complexes in Table II exhibit such a band and undergo photochemically induced metal–oxygen bond cleavage, but the process is more facile for the superoxides of rhodium and cobalt which release the dioxygen even under visible light irradiation. This behavior is similar to that exhibited by the corresponding alkyl complexes, which share a number of other features with the superoxides as well (*58*).

B. HYDROPEROXO COMPLEXES

The standard route to the hydroperoxo complexes in Table II is by one-electron chemical (*77,78*) or electrochemical (*74*) reduction of the superoxides. From the practical point of view, $Ru(NH_3)_6^{2+}$ proved to be an especially useful chemical reductant (*72,77,78*) that reacts rapidly and cleanly according to Eq. (2), and often can be used even in the presence of molecular oxygen. The $Ru(NH_3)_6^{3+}$ produced in Eq. (2) is quite unreactive and absorbs only weakly in the UV region, causing

little or no interference in mechanistic studies of the hydroperoxides generated by this route.

$$L(H_2O)MOO^{2+} + H^+ + Ru(NH_3)_6^{2+} \longrightarrow L(H_2O)MOOH^{2+} + Ru(NH_3)_6^{3+} \tag{2}$$

Another general method is based on oxygen insertion into metal–hydrogen bonds (*50,72,79–81*) by any of several known mechanisms. Hydrogen abstraction by superoxo complexes followed by oxygenation of the reduced metal, as in the catalytic reaction of Eqs. (3)–(4) (*50,72*), works well but is limited by the low availability of water-soluble transition metal hydrides and slow hydrogen transfer (equivalent of reaction (3)) for sterically crowded complexes.

$$(NH_3)_4(H_2O)RhOO^{2+} + (NH_3)_4(H_2O)RhH^{2+} \longrightarrow (NH_3)_4(H_2O)RhOOH^{2+} + (NH_3)_4(H_2O)Rh^{2+} \tag{3}$$

$$(NH_3)_4(H_2O)Rh^{2+} + O_2 \xrightarrow{\text{fast}} (NH_3)_4(H_2O)RhOO^{2+} \tag{4}$$

Other hydrogen abstracting agents also have proved useful in hydroperoxide preparations. The excited uranyl ion, $^*U_{aq}O_2^{2+}$, for example, reacts rapidly with $(NH_3)_4(H_2O)RhH^{2+}$ and other rhodium(III) hydrides (*82*) to generate Rh(II) species, Eq. (5), followed by O_2 capture of Eq. (4). Finally, the $U_{aq}O_2^+$ produced in Eq. (5) reduces $(NH_3)_4(H_2O)RhOO^{2+}$ to hydroperoxide and regenerates $U_{aq}O_2^{2+}$, Eq. (6).

$$^*U_{aq}O_2^{2+} + (NH_3)_4(H_2O)RhH^{2+} \longrightarrow (NH_3)_4(H_2O)Rh^{2+} + U_{aq}O_2^+ + H^+ \tag{5}$$

$$U_{aq}O_2^+ + (NH_3)_4(H_2O)RhOO^{2+} + H^+ \longrightarrow U_{aq}O_2^{2+} + (NH_3)_4(H_2O)RhOOH^{2+} \tag{6}$$

Rhodium(III) hydrides $L(H_2O)RhH^{2+}$ ($L = L^1$, L^2, or $(NH_3)_4$) do not react with O_2 in acidic solutions, but are rapidly converted to the corresponding hydroperoxides at pH > 10 (*72*). The mechanism has not been fully elucidated, but the observed pH effect suggests deprotonation (*83*) of the hydride followed by O_2 capture and reprotonation, Eq. (7). In view of the low acidity of these hydrides (*84*),

the steps following deprotonation must have rates close to diffusion controlled to account for the rapid formation of $L(H_2O)RhOOH^{2+}$.

$$L(H_2O)RhH^{2+} \overset{-H^+}{\rightleftharpoons} L(H_2O)Rh^+ \xrightarrow{O_2} L(H_2O)RhOO^+ \xrightarrow{+H^+} L(H_2O)RhOOH^{2+} \quad (7)$$

The mechanism for the reaction of another metal hydride, $Tp^{t\text{-}Bu,Me}Co–H$ ($Tp^{t\text{-}Bu,Me}$ = *t*-butylmethyltris(pyrazolylborate), with O_2 to generate the hydroperoxide in non-aqueous solvents appears to involve migratory insertion of O_2 into the metal–H bond (*85*).

Substitutionally labile metal complexes often generate hydroperoxides by direct substitution with H_2O_2 (*86–90*) or in the reactions between O_2 and the reduced metal (*91*). These mechanisms are commonly observed in naturally occurring molecules and their mimics in the processes of activation of oxygen and hydrogen peroxide (*92–98*).

The O–O stretch for the hydroperoxo complexes (*60,86,88,90,94,95,99–103*) falls in the range 780–900 cm^{-1}. In the case of a nonheme iron complex it was found that the low-spin hydroperoxo form absorbs at a lower frequency than the high-spin peroxo complex (*89,102*). This trend also holds for some iron alkylperoxo complexes, and DFT calculations have shown the high-spin alkylperoxide form to have a larger activation energy for the O–O bond cleavage than the corresponding low-spin alkylperoxo form (*104*).

Crystal structure analysis has been carried out for several hydroperoxo complexes. The O–O bond length (1.40–1.48 Å) (*79,87,90,100,103,105*) is significantly longer than that in superoxo complexes and close to the 1.49 Å value for hydrogen peroxide (*54*).

The UV spectral data for several hydroperoxo complexes in aqueous solution are shown in Table II. Intense transitions appear for all the compounds at wavelengths that are well below the 270–290 nm maxima for the superoxo complexes. This feature is particularly useful in mechanistic studies of the complex reactions involving several forms of activated oxygen simultaneously (*58*).

C. High-Valent Oxo Intermediates

All the complexes in Table I have the ability to serve as immediate or indirect precursors to high valent species. The hydroperoxides react with one-electron reductants in Fenton-type chemistry to generate

transients that are formally metal(IV) species (*72,76,106,107*). Of those, only $Cr_{aq}O^{2+}$ has been generated and explored independently. The rest of the metal intermediates generated by one-electron reduction of the hydroperoxides decay rapidly by intramolecular ligand oxidation and aquation (*72,76*).

Dilute solutions of the ion $Cr_{aq}O^{2+}$ can be prepared from Cr^{2+}_{aq} and O_2 as previously described (*58*). The lifetime of $Cr_{aq}O^{2+}$ depends on its concentration and the acidity of the solution (*108*). The complex disproportionates to give an equivalent of $HCrO_4^-$ and two equivalents of Cr^{3+}_{aq} in a process that obeys the rate law: $-d[Cr_{aq}O^{2+}]/dt = 38.8\ [Cr_{aq}O^{2+}]^2\ [H^+]^{-1}$. At a typical concentration of 50 μM, the lifetime of $Cr_{aq}O^{2+}$ at room temperature in 0.1 M $HClO_4$ is approximately 50 s. The decay exhibits a substantial solvent kie, $k_H/k_D = 6.9$ which, combined with the kinetic data, led to a mechanistic proposal featuring hydrogen atom abstraction from a coordinated molecule of water or hydroxo group within a singly deprotonated transition state.

Another reactive aquametal(IV) species with a reasonably long lifetime in solution is the ferryl(IV) ion, $Fe_{aq}O^{2+}$, which can be prepared from Fe^{2+}_{aq} and O_3 (*109*). The ion persists for several minutes in strongly acidic solutions (pH < 1) and is characterized by a pK_a of 2.0 and an absorption maximum at 320 nm ($\varepsilon \sim 500\ M^{-1}\ cm^{-1}$) (*110*).

Metal(V) species derived from the complexes in Table I are rare. In fact, only one such species, $L^1Cr(V)$ (presumably a dioxo or hydro-oxo species), has been observed and characterized by ESR and UV–visible spectroscopies (*45,69*), Figs. 5 and 6. This Cr(V) species, which has a lifetime of several seconds at room temperature, was generated from a hydroperoxo precursor by an intramolecular transformation that closely resembles the proposed, but so far unobserved step in the chemistry of cytochrome P450, whereby the hydroperoxoiron(III) is transformed to the $Fe^{IV}(P^{\bullet+})$ form also known as "oxene" ($P^{\bullet+}$ = porphyrin radical cation). All the steps in Scheme 1 for the $L^1Cr(H_2O)_2^{2+}/O_2$ reaction have been observed directly (*45,69*).

The formation of oxenes from hydroperoxides is a rare occurrence, but especially so for simple inorganic compounds such as $L^1(H_2O)CrOOH^{2+}$. Recently, some nonheme iron(III) hydroperoxides have been proposed to generate Fe(V) as the active hydroxylating agent for alkanes (*111*), but direct observation and kinetic characterization of individual steps, such as those in Scheme 1, are still rare. In a recent example, the kinetics of formation of hydroperoxides of Fe(III)- and Mn(III)-microperoxidase-8, their transformation to

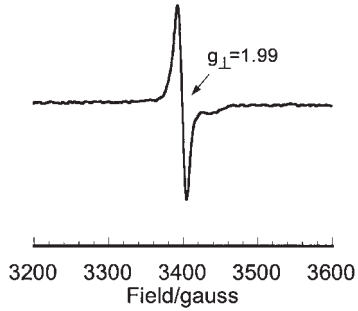

FIG. 5. First derivative ESR spectrum of $L^1Cr(V)$ ($L^1 = 14\text{-ane}N_4$) in 1:1 H_2O/propylene glycol glass at 120 K. Reproduced with permission from *J. Am. Chem. Soc.* **1996**, *118*, 10325–10326. Copyright 1996 American Chemical Society.

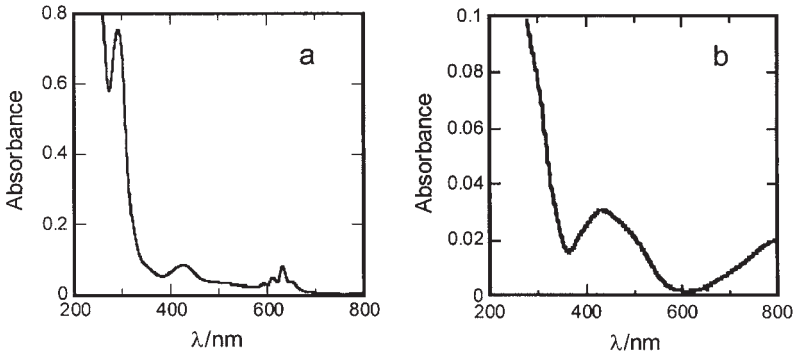

FIG. 6. UV–visible spectrum of 0.26 mM $L^1(H_2O)CrOO^{2+}$ (a) and the difference between the spectrum of $L^1Cr(V)$ and its decomposition products (b) in 0.02 M aqueous $HClO_4$. Modified from *Inorg. Chim. Acta* **2000**, *297*, 27–35, Bakac, A. and Wang, W.-D., "Generation of a macrocyclic Cr(V) complex and its reactivity toward organic and inorganic reductans and DNA", Copyright (2000) with permission from Elsevier.

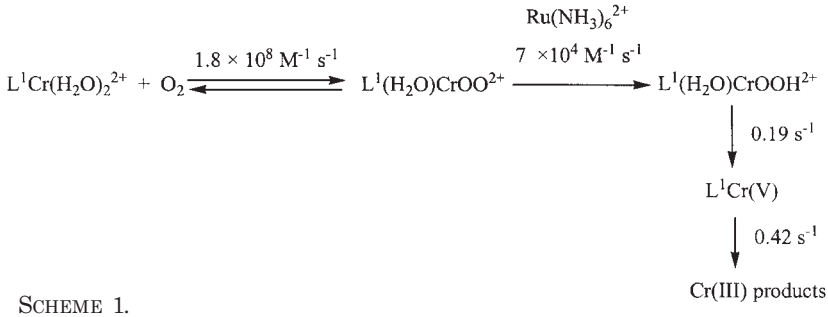

SCHEME 1.

M(IV)-peptide radicals, and decay to final products have been determined (*96*). Interestingly, the rate constants for both the formation and decay of the high-valent intermediate are much larger than the corresponding values in the chromium system in Scheme 1. Thus the lifetimes of both the hydroperoxo species and M(IV)-peptide radicals are much shorter in the enzymatic system than for the chromium macrocycles.

The chemistry shown in Scheme 1 represents a novel route to Cr(V) complexes. Such a mechanism may be important in biological environments and potentially involved in complex processes responsible for carcinogenicity of chromium compounds (*112*).

III. Reactivity

The focus of this section are the recently discovered reactions of superoxo and oxo complexes with both inorganic (metal hydrides) and organic substrates that can engage in hydrogen atom and hydride transfer. Another important class of reactions begins with radical coupling between the terminal oxygen on $LMOO^{2+}$ and an O- or N-centered radical. The complex follow-up chemistry takes advantage of the availability of several oxidation states for the metal.

The reactions of transition metal superoxides with reducing and oxidizing metal complexes have been summarized (*58*) and will not be discussed here.

A. Hydrogen Atom and Hydride Abstraction by LMO Complexes

Hydrogen atom abstraction by non-radical, metal-oxo species, once considered unlikely, has been shown in recent years to operate in a large number of reactions (*113–115*) with the kinetics responding to the thermodynamic driving force and intrinsic barriers as predicted by the Marcus cross relation (*116*).

Earlier (*58,117*) we have shown that reactions between organic materials and $Cr_{aq}O^{2+}$ can take place by either hydride or hydrogen atom transfer, the choice of the mechanism depending on the ease of formation of the organic radical. Clearly, the two pathways are energetically close, and one or the other can be enhanced by small variations in the C–H bond energy. Aliphatic alcohols, for example, react by hydride transfer, Eq. (8), but pivaldehyde undergoes hydrogen atom abstraction,

Eq. (9). As discussed earlier, $Cr_{aq}OO^{2+}$ is the fingerprint product of the two-electron (hydride transfer) path.

$$Cr_{aq}O^{2+} + CH_3OH \longrightarrow CH_2O + H_2O + Cr^{2+}_{aq} \xrightarrow{O_2,\,fast} Cr_{aq}OO^{2+} \quad (8)$$

$$Cr_{aq}O^{2+} + CMe_3CHO \longrightarrow Cr_{aq}OH^{2+} + CMe_3C^{\bullet}O \quad (9)$$

An interesting case presented itself (*53*) in a study of the oxidation of rhodium(III) hydrides, $L(H_2O)RhH^{2+}$. Here, either pathway would generate a superoxometal product, $Cr_{aq}OO^{2+}$ by hydride transfer, or $L(H_2O)RhOO^{2+}$ by hydrogen atom transfer, Scheme 2. The intense and distinct UV spectra of the two superoxides made the mechanistic assignment straightforward, and identified hydrogen atom transfer as the sole mechanism. Consistent with this conclusion, the reactions exhibit a significant H/D kinetic isotope effect. The summary of all the data is given in Table III.

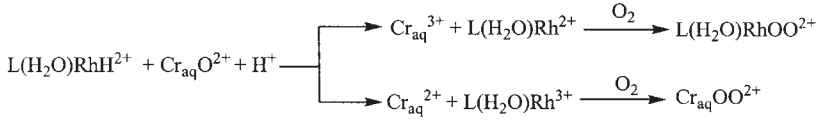

SCHEME 2.

TABLE III

RATE CONSTANTS (10^{-3} k/M^{-1} s^{-1}) FOR THE REACTIONS OF CHROMIUM(IV) AND CHROMIUM(V) COMPLEXES WITH RHODIUM HYDRIDES[a]

	$C^{IV}{}_{aq}O^{2+}$	$(salen)Cr^{V}O^{+}$
$L^1(H_2O)RhH^{2+}$ [b]	~ 10	8.8
$L^1(H_2O)RhD^{2+}$	2.7	1.6
$(NH_3)_4(H_2O)RhH^{2+}$	*d*	2.5
$L^2(H_2O)RhH^{2+}$ [c]	1.12	1.0
$L^2(H_2O)RhD^{2+}$	0.34	0.16

[a] Data from Ref. (*53*).
[b] $L^1 = [14]aneN_4$.
[c] $L^2 = Me_6$-$[14]aneN_4$.
[d] Not determined.

In contrast to $Cr_{aq}O^{2+}$, the chromium(V) complex $(salen)CrO^{+}$ reacts by hydride transfer and yields no $L(H_2O)RhOO^{2+}$. The result

should not be surprising if one considers that hydride transfer produces both metals in their most stable, 3+, oxidation state, Eq. (10).

$$(\text{salen})\text{CrO}^{+} + \text{L}(\text{H}_2\text{O})\text{RhH}^{2+} + \text{H}_2\text{O} \longrightarrow (\text{salen})\text{CrOH} + \text{L}(\text{H}_2\text{O})_2\text{Rh}^{3+} \tag{10}$$

The Fenton-type chemistry between Fe^{2+}_{aq} and several rhodium hydroperoxides yields Rh(IV) species believed to have the general formula $L(H_2O)RhO^{2+}$, Eq. (11) (*72*), although this was not established experimentally for these short-lived transients. Just like the other LMO^{2+} species generated by this route (*58*), the compounds $L(H_2O)RhO^{2+}$ ($L = (NH_3)_4$, L^1, and L^2) react rapidly with the Fe^{2+}_{aq} present in solution. The addition of substrates for $L(H_2O)RhO^{2+}$ resulted in a competition, as shown for methanol in Eqs. (12) and (13).

$$\text{L}(\text{H}_2\text{O})\text{RhOOH}^{2+} + \text{Fe}^{2+}_{aq} \longrightarrow \text{L}(\text{H}_2\text{O})\text{RhO}^{2+} + \text{Fe}_{aq}\text{OH}^{2+} \tag{11}$$

$$\text{L}(\text{H}_2\text{O})\text{RhO}^{2+} \xrightarrow{\text{CH}_3\text{OH}} {}^{\bullet}\text{CH}_2\text{OH} + \text{L}(\text{H}_2\text{O})\text{RhOH}^{2+} \qquad k_X \tag{12a}$$

$$\text{L}(\text{H}_2\text{O})\text{RhO}^{2+} \xrightarrow{\text{Fe}_{aq}^{2+},\ \text{H}^{+}} \text{Fe}_{aq}^{3+} + \text{L}(\text{H}_2\text{O})\text{Rh}^{3+} \qquad k_{Fe} \tag{12b}$$

$$\text{Fe}^{3+}_{aq} + {}^{\bullet}\text{CH}_2\text{OH} \longrightarrow \text{Fe}^{2+}_{aq} + \text{CH}_2\text{O} + \text{H}^{+} \tag{13}$$

At high initial $[Fe^{2+}_{aq}]$ in the absence of added substrates, the stoichiometric ratio $[Fe^{3+}_{aq}]_\infty/[L(H_2O)RhOOH^{2+}]_0$ approaches 2.0. At lower concentrations of Fe^{2+}_{aq}, the overall reaction produces less Fe^{3+}_{aq} because some of the newly formed $L(H_2O)RhO^{2+}$ decomposes, presumably by loss of NH_3 from the ammine complex and intramolecular ligand oxidation in the macrocyclic compounds, as observed for similar complexes of high-valent nickel, cobalt, and iron (*58,118–120*). Competition experiments were carried out at sufficiently high $[Fe^{2+}_{aq}]$ to ensure that no $L(H_2O)RhO^{2+}$ was lost in self-decay.

Added substrates changed the stoichiometry to $< 2{:}1$. The decrease is caused by both lack of formation of the full equivalent of $[Fe^{3+}_{aq}]_\infty$ because of the competition in Eq. (12), and partial reduction of already formed Fe^{3+}_{aq} by the reducing radicals, Eq. (13). From the effect of [substrate] on the yields of Fe^{3+}_{aq}, the ratio of rate constants k_{Fe}/k_X was obtained. These ratios were then used to calculate the relative rate

TABLE IV

RELATIVE REACTIVITIES OF METAL-OXO SPECIES TOWARD SUBSTRATES X IN AQUEOUS SOLUTION[a]

X	k_X/k_{EtOH}					
	$(NH_3)_4RhO^{2+}$	$Cr_{aq}O^{2+}$	$Fe_{aq}(OH)_2{}^{2+}$	$(bpy)_2(py)Ru^{IV}O^{2+}$	$Ru^{V}L^3(O)^{2+}$	$Ru^{VI}L^4(O)_2^{2+}$
CH_3OH	0.37	0.59		0.17	0.088	
C_2H_5OH	(1)	(1)	(1)	(1)	(1)	(1)
2-C_3H_7OH	1.3	0.14		32	7.9	9
$C_6H_5CH_2OH$		0.63		1160	69	134
$CH_2(OH)_2$	4.6	1.04	0.16			
C_2H_5CHO	17					
$C(CH_3)_3CHO$		0.42[b]				
HCOOH		0.13	0.066			
$HCOO^-$		75	120			
$(NH_3)_4(H_2O)RhH^{2+}$	46					
$L^1(H_2O)RhH^{2+}$	d	~100				

[a]Data from Refs. (*72,110,117,121–123*). See Fig. 7 for structures of L^3 and L^4.

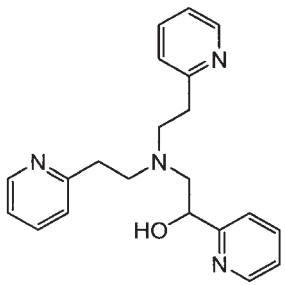

L^3

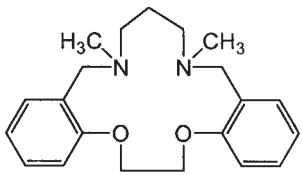

L^4

FIG. 7. Structures of ligands L^3 and L^4.

constants k_X/k_{EtOH} in Table IV. (The choice of k_{EtOH} as a standard allows literature data for $Fe_{aq}(OH)_2{}^{2+}$ to be included as well.)

All the reactions of $(NH_3)_4(H_2O)RhO^{2+}$, with the possible exception of C_2H_5CHO, appear to take place by hydrogen atom transfer as judged by a deuterium C–H kie of 5.0 for methanol and 3.2 for 2-propanol. The lack of a chain reaction in the oxidation of alcohols argues against hydride transfer for these substrates (*72*).

The clear trend in relative rate constants for the $(NH_3)_4(H_2O)RhO^{2+}$ reactions in Table IV is contrasted by the reactivity of chromyl

which oxidizes most of the substrates with similar kinetics, the only obvious exception being rhodium hydrides. The data for $Fe_{aq}(OH)_2^{2+}$, believed to react by hydrogen atom transfer (*110*), are too limited to detect a trend. The three ruthenium complexes in Table IV (*121–123*) (for ligand structures see Fig. 7) seem to be much more selective than $Cr_{aq}O^{2+}$ in their reactions with C–H bonds. The reactivity order is always $CH_3 < 1^\circ < 2^\circ < PhCH_2$ for both hydrogen atom and hydride transfer. As discussed earlier (*72*), the chromyl oxygen may get involved in hydrogen-bonded interactions with the cis waters in the transition state, and diminish the effect of other rate-controlling factors. Such an interaction is not available to other compounds in Table IV except $Fe_{aq}(OH)_2^{2+}$, for which the data are too limited to test the hypothesis.

B. Reactions of Superoxo Complexes with Rh–H, O–H, and C–H Bonds

1. Rhodium Hydrides

Prior to the work described below (*50*), hydrogen transfer to superoxometal complexes has been proposed by some (*124–126*) and questioned by others (*127*) who introduced plausible alternative mechanistic pathways. The work with rhodium hydrides (*50*) sought to establish whether hydrogen abstraction by superoxo complexes is a feasible and reasonable mechanism for thermodynamically favorable cases.

All the superoxo complexes and rhodium hydrides in this work can be handled under both aerobic and anaerobic conditions. The ability to work with superoxides in the absence of O_2 and with the hydrides in the presence of O_2 provides an exceptionally large range of reaction conditions and an opportunity to detect and identify various intermediates, and thus establish the mechanism with reasonable confidence.

A reaction between $Cr_{aq}OO^{2+}$ and $L(H_2O)RhH^{2+}$ ($L = L^1$, L^2, and $(NH_3)_4$) in the presence of O_2 produces $L(H_2O)RhOO^{2+}$ and $Cr_{aq}OOH^{2+}$, Eq. (14) and Fig. 8 (*50*).

Similarly, superoxorhodium complexes also react with the hydrides in stoichiometric (ligand systems different) or catalytic (ligand systems identical) reactions, as shown in Eq. (15) and (3)–(4), respectively (*50,70*). As can be seen from the kinetic data in Table V, steric effects play a major role as demonstrated by a large decrease in

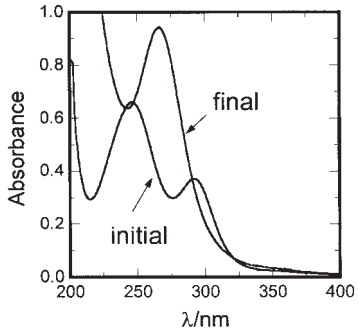

FIG. 8. Spectral transformations in the reaction between $Cr_{aq}OO^{2+}$ (9×10^{-5} M) and $L^1(H_2O)RhH^{2+}$ (2×10^{-4} M) in O_2-saturated aqueous 0.1 M $HClO_4$.

TABLE V

KINETIC DATA ($k/M^{-1}\ s^{-1}$) AT 25 °C FOR HYDROGEN ATOM TRANSFER FROM RHODIUM HYDRIDES TO SUPEROXOMETAL COMPLEXES[a]

	$Cr_{aq}OO^{2+}$	$(NH_3)_4(H_2O)RhOO^{2+}$	$L^1(H_2O)RhOO^{2+}$	$L^1(H_2O)CrOO^{2+}$
$(NH_3)_4(H_2O)RhH^{2+}$	135	32.7 93.8[b]	27.6[b]	3
$L^1(H_2O)RhH^{2+}$	129	22.8	0.4	< 1
$L(H_2O)RhD^{2+}$	17.0		0.06	
cis-$L^1(H_2O)RhH^{2+}$	123			
$L^2(H_2O)RhH^{2+}$	24			

[a]In O_2-saturated acidic aqueous solutions. $L^1 = [14]aneN_4$. $L^2 = Me_6$-$[14]aneN_4$. Data from Ref. (*50*).
[b]Argon atmosphere.

rates for the reactions where both partners are macrocyclic complexes. This behavior supports a bimolecular mechanism requiring a close approach of the two reactants in the transition state, as in hydrogen atom transfer.

$$Cr_{aq}OO^{2+} + L(H_2O)RhH^{2+} \overset{O_2}{\rightleftarrows} Cr_{aq}OOH^{2+} + L(H_2O)RhOO^{2+} \quad (14)$$

$$(NH_3)_4(H_2O)RhOO^{2+} + L^1(H_2O)RhH^{2+} \overset{O_2}{\rightleftarrows} (NH_3)_4(H_2O)RhOOH^{2+} + L^1(H_2O)RhOO^{2+} \quad (15)$$

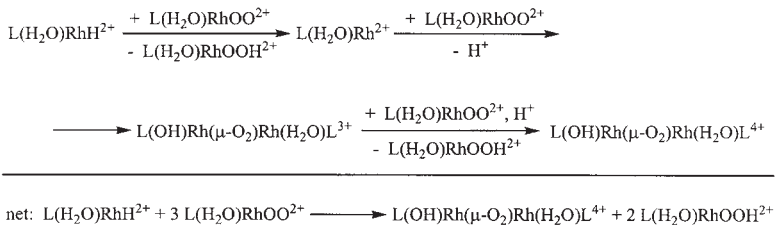

SCHEME 3.

These reactions exhibit large deuterium kie's, consistent with hydrogen atom transfer. For the reaction in Eq. (14) ($L = L^1$), $k_{RhH}/k_{RhD} = 7.6$. This ratio is much larger than the maximum of 4.2 calculated from an expression for a simple three-center model. Quantum mechanical tunneling may be involved. Although hydrogen bonding between either or both partners and the solvent (*128,129*) might be affecting the kinetics and also the observed kie, the major role for hydrogen bonding probably can be ruled out on the basis of the complete absence of a solvent kie, $k_{H2O}/k_{D2O} = 1$.

The stepwise mechanism of Eqs. (3) and (4) draws further support from the results obtained under air-free conditions. The stoichiometry now increased to 3:1, and the products changed to a mixture of the μ-superoxo dirhodium(III) complex $(NH_3)_4(OH)Rh(\mu\text{-}O_2)Rh(H_2O)(NH_3)_4^{4+}$ and $(NH_3)_4(H_2O)Rh^{3+}$. These results are easily rationalized by a scheme whereby rhodium-based oxidants take over as scavengers for $(NH_3)_4(H_2O)Rh^{2+}$ produced in the initial step, Scheme 3.

Hydrogen atom transfer from rhodium hydrides to the superoxides of chromium(III) and rhodium(III) clearly has favorable thermodynamics. On the basis of the available Rh–H bond dissociation energies (bde) in the literature, we estimate the limit for the bde of $L(H_2O)Rh\text{–}H^{2+}$ complexes at ≤ 270 kJ/mol. The energy of the $Cr_{aq}OO\text{–}H^{2+}$ bond was estimated from the thermochemical cycle in Scheme 4 using published data for the reduction potentials of $Cr_{aq}OO^{2+}$ (*130*) and $H^{\bullet}$ (*131*). The calculation yields ΔH (= bde) ~ 330 kJ/mol under the assumption that the entropies of $Cr_{aq}OOH^{2+}$ and $Cr_{aq}OO^{2+}$ are identical. The driving force for hydrogen transfer from Rh–H to $Cr_{aq}OO^{2+}$ is thus at least 60 kJ/mol. Potential data are not available for the $L(H_2O)RhOO^{2+}$ complexes, but it is reasonable to expect the overall driving force for hydride transfer to be approximately of the same order of magnitude as that estimated for the $Cr_{aq}OO^{2+}/L(H_2O)RhH^{2+}$ reaction.

$$Cr_{aq}OOH^{2+} \rightleftharpoons Cr_{aq}OO^{2+} + e^- + H^+ \qquad E_{ox} = -1.03\ V$$

$$H^+ + e^- \rightleftharpoons H^\bullet \qquad E_{red} = -2.29\ V$$

SCHEME 4.

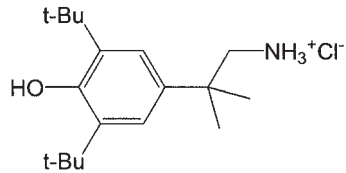

FIG. 9. Structure of $ArOH^+$.

2. Phenol

Hydrogen atom abstraction by $Cr_{aq}OO^{2+}$ from an oxygen–hydrogen bond was demonstrated in the reaction with a substituted, cationic, water-soluble phenol shown in Fig. 9 and abbreviated as $ArOH^+$ (*132*). Upon one-electron oxidation, this phenol generates a stable radical $ArO^{\bullet+}$ that absorbs strongly at 400 nm, $\varepsilon = 2.6 \times 10^3\ M^{-1}\,cm^{-1}$.

The reaction with $Cr_{aq}OO^{2+}$ has a 2:1 $[Cr_{aq}OO^{2+}]/[ArOH^+]$ stoichiometry consistent with the sequence of reactions 16–17. The kinetics of the first, rate-determining step are independent of acid concentration at a constant ionic strength, $k = 1.24\ M^{-1}\,s^{-1}$, and exhibit a kinetic isotope effect $k_{ArOH}/k_{ArOD} \sim 12$, consistent with hydrogen atom abstraction. The reaction is unaffected by the presence of Mn^{2+}_{aq}, which rules out $Cr_{aq}O^{2+}$ as an intermediate.

$$Cr_{aq}OO^{2+} + ArOH^+ \longrightarrow Cr_{aq}OOH^{2+} + ArO^{\bullet+} \qquad (16)$$

$$Cr_{aq}OO^{2+} + ArO^{\bullet+} \longrightarrow \text{products} \qquad (17)$$

An independent kinetic study of the second step, Eq. (17), yielded $k_{17} = 1.26 \times 10^4\ M^{-1}\ s^{-1}$. The combination of this large rate constant and limited solubility of $ArOH^+$ made the rate of reaction 17 (R_{17}) much larger than that of Eq. (16) (R_{16}), so that the radical $ArO^{\bullet+}$ could not be observed in the $Cr_{aq}OO^{2+}/ArOH^+$ reaction in purely aqueous solution. When the solvent was changed to mostly DMSO, the

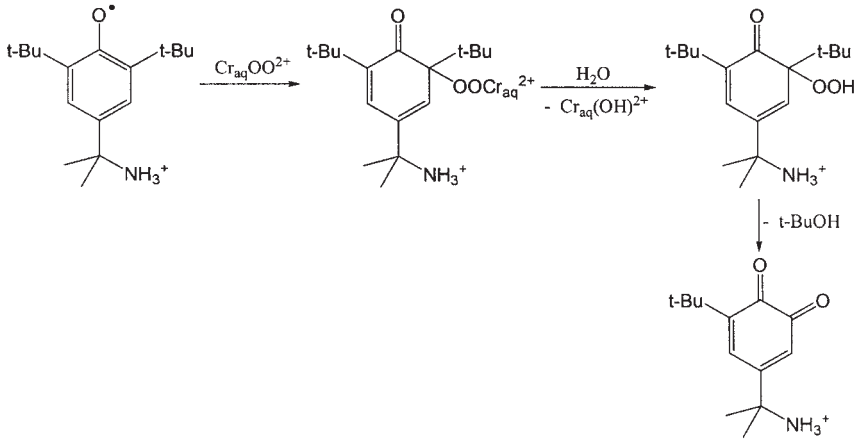

SCHEME 5.

concentration of $ArOH^+$ was increased to 0.03 M, which made the rate R_{16} larger than R_{17} at the low $[Cr_{aq}OO^{2+}]$ used (13 μM). Under these conditions the radical was detected by its visible spectrum, and the chemistry in Eq. (16) was confirmed.

The visible spectrum of the final product (λ_{max} 400 nm, ε 2.2×10^3 M^{-1} cm^{-1}) and its 1+ charge, determined by ion-exchange, are consistent with *o*-quinone, Scheme 5.

In the proposed mechanism, $Cr_{aq}OO^{2+}$ attacks the phenyl ring of $ArO^{\bullet +}$ and produces a peroxochromium intermediate I. This step is in agreement with literature precedents (*133–137*) and with the recent discussion of delocalization of electron density in phenoxyl radicals (*138*). The peroxochromium intermediate was not observed, implying that the dissociation of $Cr_{aq}OH^{2+}$ in the next step is fast. Finally, the loss of *tert*-butanol was written in analogy with the known reactions in organic solvents (*139,140*).

3. Pivaldehyde (CMe_3CHO)

In aqueous solutions pivaldehyde exists as a 4:1 mixture of CMe_3CHO and $CMe_3CH(OH)_2$ (*141*). The radicals derived from the two forms probably also exist as a rapidly equilibrating mixture of $CMe_3C^{\bullet}O$ and $CMe_3C^{\bullet}(OH)_2$, Eq. (18), similar to the parent acetyl radicals, $CH_3C^{\bullet}O$ and $CH_3C^{\bullet}(OH)_2$, for which $k_f = 2 \times 10^4$ $M^{-1}s^{-1}$ and $k_r \sim 3 \times 10^4\,s^{-1}$ (*142*). In the notation used here, the formulas CMe_3CHO

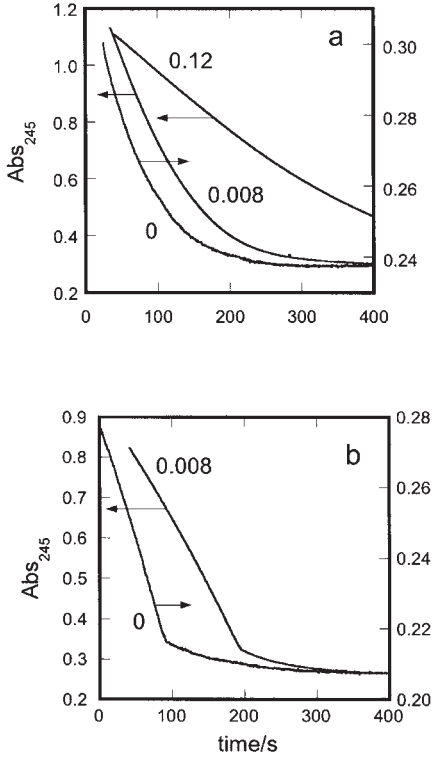

FIG. 10. Effect of methanol and O_2 on the kinetics of $Cr_{aq}OO^{2+}/CMe_3CHO$ reaction in 0.1 M $HClO_4$ at $[CMe_3CHO] = 30$ mM, λ 245 nm. (a) 0.03 mM $Cr_{aq}OO^{2+}$, 1 mM O_2 at various concentrations of methanol (0, 0.008, and 0.12 M). (b) Air-free, in the absence of methanol (right ordinate) or in 0.008 M methanol (left ordinate). Reproduced with permission from *J. Am. Chem. Soc.* **2000**, *122*, 1092–1097. Copyright 2000 American Chemical Society.

and $CMe_3C^{\bullet}O$ represent all the forms of the aldehyde and its radical, respectively.

$$CMe_3C^{\bullet}O + H_2O \underset{k_r}{\overset{k_f}{\rightleftharpoons}} CMe_3C^{\bullet}(OH)_2 \qquad (18)$$

Unlike the straightforward chemistry observed with rhodium hydrides and ArOH, the reaction with pivaldehyde is quite complex (*143,144*). The observed rate constants, and even the shape of kinetic curves, change with reaction conditions and the presence of scavengers for various intermediates. Figure 10 shows some examples.

In oxygen-saturated solutions (Fig. 10a) at low concentrations of methanol (scavenger for $Cr_{aq}O^{2+}$ by chemistry shown in Eq. (8)), the traces are almost exponential, but the rate is clearly [CH_3OH]-dependent, being lower at higher [CH_3OH]. This behavior strongly implicates $Cr_{aq}O^{2+}$ as an intermediate which regenerates $Cr_{aq}OO^{2+}$ (Eq. (8)) and thus slows the overall rate of its disappearance.

The next set of experiments was run in the presence of ≤ 5 mM Mn^{2+}_{aq}, which reduces $Cr_{aq}O^{2+}$ to the unreactive Cr^{3+}_{aq}. In O_2-saturated solutions, the kinetic traces became exponential, and the dependence on [MeOH] disappeared as expected on the basis of the large rate constant for the $Mn^{2+}_{aq}/Cr_{aq}O^{2+}$ reaction (10^5–10^6 $M^{-1}\,s^{-1}$) (*58*) which took over as the sole pathway for the removal of $Cr_{aq}O^{2+}$. The plot of the pseudo-first order rate constant against the concentration of CMe_3CHO under such conditions is linear with a slope of 0.28 $M^{-1}\,s^{-1}$.

Under air-free conditions, the traces strongly deviate from first-order kinetics, Fig. 10b, but the time required for the completion of the reaction is not grossly different from that under O_2. The shape of the traces suggests that the reaction generates Cr^{2+}_{aq} and/or organic radicals which rapidly reduce $Cr_{aq}OO^{2+}$ in a potentially autocatalytic manner. When the reaction was conducted in the presence of small amounts of $(NH_3)_5CoBr^{2+}$, which reacts rapidly with Cr^{2+}_{aq} (*145*) and with hydrated acyl radicals (*146*), the kinetic traces became exponential, Fig. 11. The data yielded a second-order rate constant of 0.16 $M^{-1}\,s^{-1}$.

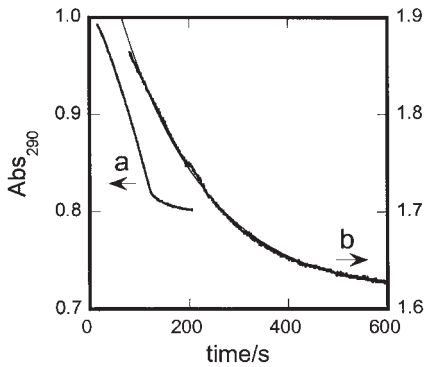

FIG. 11. Effect of $(NH_3)_5CoBr^{2+}$ on the kinetics of the reaction between $Cr_{aq}OO^{2+}$ (0.1 mM) and CMe_3CHO (49 mM) in 0.1 M $HClO_4$ under argon. (a) $[(NH_3)_5CoBr^{2+}] = 0$. (b) $[(NH_3)_5CoBr^{2+}] = 0.69$ mM. The first-order fit of data in (b) is also shown. Reproduced with permission from *J. Am. Chem. Soc.* **2000**, *122*, 1092–1097. Copyright 2000 American Chemical Society.

The overall kinetic behavior, and the effects of methanol, Mn_{aq}^{2+}, and $(NH_3)_5CoBr^{2+}$ suggest a mechanism consisting of an initial bimolecular reaction, most likely abstraction of the aldehydic hydrogen by $Cr_{aq}OO^{2+}$, to generate acyl radicals and $Cr_{aq}OOH^{2+}$. Subsequent steps generate additional intermediates ($Cr_{aq}O^{2+}$, Cr_{aq}^{2+}, acylperoxyl and alkylperoxyl radicals) which can be either removed or prevented from forming by use of various scavengers. A simplified mechanism is shown in Scheme 6. Some of the evidence for the involvement of radicals has been presented already, and some will emerge throughout the description of the individual steps of Eqs. (19)–(25).

$$Cr_{aq}OO^{2+} + CMe_3CHO \longrightarrow Cr_{aq}OOH^{2+} + CMe_3C^{\bullet}O \quad (19)$$

$$CMe_3C^{\bullet}O \longrightarrow {}^{\bullet}CMe_3 + CO \quad (20)$$

$$CMe_3C^{\bullet}O + Cr_{aq}OO^{2+} \longrightarrow \text{Products} \quad (21)$$

$$CMe_3C^{\bullet}O + O_2 \longrightarrow CMe_3C(O)OO^{\bullet} \quad (22)$$

$${}^{\bullet}CMe_3 + O_2 \longrightarrow CMe_3OO^{\bullet} \quad (23)$$

$$Cr_{aq}OO^{2+} + CMe_3C(O)OO^{\bullet} \longrightarrow \text{Products} \quad (24)$$

$$CMe_3C(O)OO^{\bullet} + CMe_3OO^{\bullet} \longrightarrow \text{Products} \quad (25)$$

SCHEME 6.

The decarbonylation of pivaloyl radicals in aqueous solution, $k \sim 2.5 \times 10^5$ s^{-1} (*147*) is somewhat slower than in most non-aqueous solvents (*148*), but sufficiently rapid to compete with the reaction with O_2 in Eq. (21) under most conditions. In the absence of O_2, most of the acyl radicals produced in Eq. (19) will dissociate CO, Eq. (20), and react with $Cr_{aq}OO^{2+}$, Eq. (21). A small fraction may disappear in bimolecular radical self-reactions.

The unusual kinetic traces under air-free conditions in Fig. 9b suggest that the chemistry in Eq. (21) produces additional equivalents of reducing intermediates resulting in an accelerated loss of $Cr_{aq}OO^{2+}$. In addition to $CMe_3C^{\bullet}O$ (presumably in its hydrated form), any Cr_{aq}^{2+}, produced either by slow homolysis of $Cr_{aq}OO^{2+}$ or in the course of the $Cr_{aq}OO^{2+}/CMe_3CHO$ reaction, will also be involved in the loss of the superoxo complex. The added $(NH_3)_5CoBr^{2+}$ in Fig. 11 removes one or both of these reducing intermediates. The reaction with Cr_{aq}^{2+} is known to be fast, $k = 6.0 \times 10^6$ M^{-1} s^{-1} (*145*), and our preliminary work has

provided an estimate of $k \sim 10^8\,M^{-1}s^{-1}$ for the reaction between $(NH_3)_5CoBr^{2+}$ and hydrated acetyl radicals. If $CMe_3C^{\bullet}O$ behaves similarly to $CH_3C^{\bullet}O$, except that the fraction of hydrated radical will be somewhat smaller, then $(NH_3)_5CoBr^{2+}$ will remove a portion of acyl radicals produced in Eq. (19) and, in the absence of O_2, simplify Scheme 6 to just two reactions, Eqs. (19)–(20). The measured rate constant in the presence of $(NH_3)_5CoBr^{2+}$ then becomes k_{19}. The dramatic effect of $(NH_3)_5CoBr^{2+}$ in Fig. 10 suggests that both Cr^{2+}_{aq} and $CMe_3C^{\bullet}O$ may be responsible for the complex behavior under air-free conditions.

In O_2-saturated solutions, a major portion of acyl radicals (60–80%) react with O_2 as in Eq. (22), the rest undergoing decarbonylation and finally formation of tert-butylperoxyl radicals, Eqs. (20) and (23). The source of $Cr_{aq}O^{2+}$, which is clearly an intermediate on the basis of the effects of methanol and Mn^{2+}_{aq}, is reaction 24. As discussed in greater detail below, $Cr_{aq}O^{2+}$ is produced by disproportionation of the initially generated $Cr_{aq}(V)$.

a. $Cr_{aq}OO^{2+}$/$CMe_3C(O)OO^{\bullet}$ cross reaction The chemistry in Eq. (24) is believed to take place by an initial radical coupling between the terminal oxygen of $Cr_{aq}OO^{2+}$ and acylperoxyl radicals. A direct study of the analogous reaction between $Cr_{aq}OO^{2+}$ and acetylperoxyl radicals was carried out recently (*149*). For the purpose of product analysis, $CH_3C(O)OO^{\bullet}$ was generated in the reaction between $Cr_{aq}OO^{2+}$ and CH_3CHO. The reaction produced large amounts of $HCrO_4^-$ (43% of total $Cr_{aq}OO^{2+}$). The yield decreased only marginally (to 35%) in the presence of added Mn^{2+}_{aq}. No CO_2 or CH_2O were observed, and the radicals $^{\bullet}CH_3$ and $CH_3OO^{\bullet}$ were shown not to be involved.

For kinetic purposes, acetylperoxyl radicals were generated by laser flash photolysis of an acetylcobalt precursor in the presence of O_2, Eq. (26). With use of $ABTS^{\bullet-}$ as a kinetic probe, the rate constant was determined for the cross-coupling reaction of Eq. (27), $k_{27} = 1.49 \times 10^8\ M^{-1}\ s^{-1}$.

$$L^1CoC(O)CH_3^{2+} \xrightarrow[-L^1Co^{2+}]{h\nu} CH_3C^{\bullet}(O) \xrightarrow[\text{fast}]{O_2} CH_3C(O)OO^{\bullet} \qquad (26)$$

$$Cr_{aq}OO^{2+} + CH_3C(O)OO^{\bullet} \longrightarrow \text{Products} \qquad (27)$$

$$Cr_{aq}OO^{2+} + CH_3C(O)OO^{\bullet} \longrightarrow [Cr_{aq}OOOOC(O)CH_3^{2+}] \longrightarrow O_2 + Cr^{V}{}_{aq}O^{3+} + CH_3COOH \quad (27a)$$

$$2Cr_{aq}O^{3+} \longrightarrow Cr_{aq}O^{2+} + HCrO_4^- + 5H^+ \quad (28)$$

$$Cr_{aq}O^{2+} + CH_3CHO \xrightarrow{O_2,\,H^+} CH_3C(O)OO^{\bullet} + Cr_{aq}^{3+} \quad (29)$$

$$Cr_{aq}O^{3+} + Cr_{aq}O^{2+} \longrightarrow HCrO_4^- + Cr_{aq}^{3+} + 3H^+ \quad (30)$$

SCHEME 7.

The mechanism in Scheme 7 takes into account all the experimental observations and known chemistry of peroxyl radicals and various chromium species in the oxidation states 3 to 6.

The dissociation of O_2 from the tetroxide in reaction 27a may initially produce a short-lived μ-peroxide (*150*), which undergoes an intramolecular electron transfer and hydrolysis to yield $Cr^{V}{}_{aq}O^{3+}$ and acetic acid. The homolytic cleavage of the μ-peroxide to $Cr^{IV}{}_{aq}O^{2+}$ and $CH_3C(O)O^{\bullet}$ is ruled out by the absence of CO_2 and $^{\bullet}CH_3$, the decarboxylation products of $CH_3C(O)O^{\bullet}$. An additional argument against $Cr_{aq}O^{2+}$ being the initial product of peroxide cleavage comes from the marginal effect of Mn_{aq}^{2+} on the yields of $HCrO_4^-$. If $Cr_{aq}O^{2+}$, rather than $Cr_{aq}O^{3+}$, were the source of chromate, then this product would be eliminated in the presence of Mn_{aq}^{2+}, contrary to the observations.

The details of reaction 24 were sorted out by utilizing either $Cr_{aq}OO^{2+}$, Eq. (19), or $Cr_{aq}O^{2+}$, Eq. (9), as hydrogen abstracting agent for the aldehyde. Solutions of $Cr_{aq}O^{2+}$ always contain significant amounts of $Cr_{aq}OO^{2+}$ and, as described in more detail later, the follow-up chemistry is the same regardless of whether reaction 9 or 19 generates the radical.

The $Cr_{aq}OO^{2+}/CMe_3CHO$ reaction yields isobutene, CO_2, Cr_{aq}^{3+}, $HCrO_4^-$ (~15%), and (presumably) carboxylic acid, $CMe_3C(O)OH$. The peracid, $CMe_3C(O)OOH$, was detected by its reaction with L^1Ni^{2+} in experiments with high initial concentrations of the aldehyde (*144*). This product arises from the secondary chemistry in Eqs. (31) and (22), which consumes some extra aldehyde and O_2, both present in large excess, but otherwise has no effect on the kinetics or products of the reaction of interest.

$$CMe_3C(O)OO^{\bullet} + CMe_3CHO \longrightarrow CMe_3C(O)OOH + CMe_3C^{\bullet}O \quad (31)$$

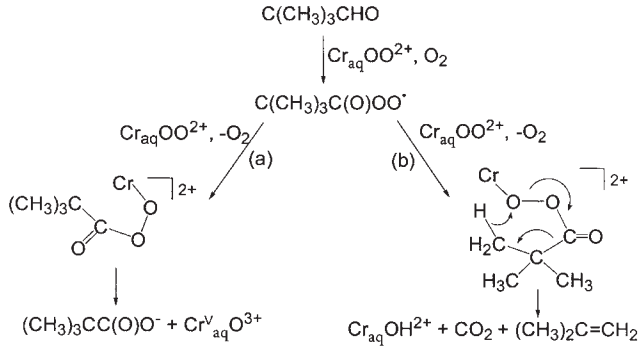

SCHEME 8.

The main chemistry generates some products ($HCrO_4^-$) reminiscent of the $Cr_{aq}OO^{2+}/CH_3CHO$ reaction, but there is clearly another path, responsible for the formation of CO_2 and isobutene. The latter was formed in comparable yields in air- and O_2-saturated solutions, which rules out the disproportionation of *tert*-butyl radicals (formed by decarbonylation) as the source of this product. It is much more likely that the initially formed intermediate branches into two sets of products, $\{Cr_{aq}O^{3+} + CMe_3C(O)OH\}$ and $\{Cr^{3+}_{aq} + CO_2 + \text{isobutene}\}$, as shown in Scheme 8.

The chemistry in path (a) is analogous to that shown for CH_3CHO in Scheme 7. Path (b) features intramolecular hydrogen transfer and elimination of O_2 and CO_2. Most likely, the product formation in step (b) also involves a μ-peroxide, which eliminates isobutene and $Cr_{aq}O^{3+}$ via a six-membered transition state. This path has no counterpart in the CH_3CHO reaction, where it would not generate stable products.

b. $CMe_3OO^•/CMe_3C(O)OO^•$ cross reaction This reaction, shown in Eq. (25), is an example of Ingold-Fischer persistent radical effect (*151,152*) and occurs with much greater probability than the homocoupling of either $CMe_3C(O)OO^•$ or $CMe_3OO^•$. As shown above, acylperoxyl radicals react readily with $Cr_{aq}OO^{2+}$, a bulk species, which keeps the steady-state concentrations of $CMe_3C(O)OO^•$ low, and the self-reaction negligible, despite its large rate constant. The self-reaction of *tert*-butylperoxyl radicals, on the other hand, has a small rate constant, $k = 5 \times 10^3$ M^{-1} s^{-1} (*153*) and no reaction was detected with $Cr_{aq}OO^{2+}$. Significant levels of $Me_3COO^•$ can thus build-up,

making the cross-reaction with $CMe_3C(O)OO^{\bullet}$ highly probable. The most decisive findings regarding this reaction came from a series of experiments utilizing mixtures of $Cr_{aq}O^{2+}$ and $Cr_{aq}OO^{2+}$, as described below.

4. Reaction of CMe_3CHO with $\{Cr_{aq}O^{2+} + Cr_{aq}OO^{2+}\}$

The kinetics of the $Cr_{aq}O^{2+}/CMe_3CHO$ reaction were determined by monitoring the absorbance decrease at 240 nm (*144*), where neither reactant absorbs. This puzzling situation arose because $Cr_{aq}OO^{2+}$, a "natural" impurity in our preparations of $Cr_{aq}O^{2+}$, absorbs strongly at 240 nm and reacts rapidly with intermediate(s) produced in the $Cr_{aq}O^{2+}/CMe_3CHO$ reaction. All the evidence, including the fact that the intermediate reacts preferentially with $Cr_{aq}OO^{2+}$ and not $Cr_{aq}O^{2+}$, identifies this intermediate as $CMe_3C(O)OO^{\bullet}$. The chemistry under such conditions is described by reactions 9, 22, and 24. In effect, $Cr_{aq}OO^{2+}$ serves as a kinetic probe for the $Cr_{aq}O^{2+}$/aldehyde reaction. The data yielded the rate constant $k_9 = 45.2\ M^{-1}\ s^{-1}$ (*143*).

The evidence for reaction 25 came from the effect of $[Cr_{aq}OO^{2+}]$ on the absorbance changes accompanying the $Cr_{aq}O^{2+}/CMe_3CHO$ reaction. As shown in Fig. 12, the traces are exponential, but the absorbance change is much smaller in trace (a) which has a proportionately lower $[Cr_{aq}OO^{2+}]$, demonstrating a competition between $Cr_{aq}OO^{2+}$ and another species for the intermediate $CMe_3C(O)OO^{\bullet}$. Moreover, even though $Cr_{aq}OO^{2+}$ was present in

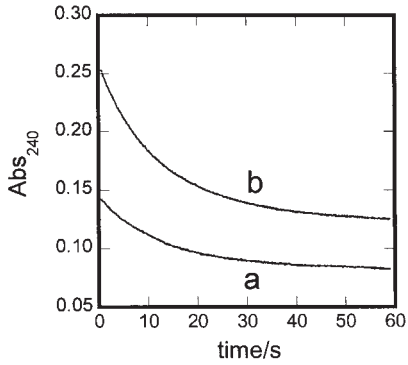

FIG. 12. Kinetic traces at 240 nm in air-saturated 0.1 M $HClO_4$ for the reaction of 1.89 mM CMe_3CHO with (a) $\{47\ \mu M\ Cr_{aq}O^{2+} + 22\ \mu M\ Cr_{aq}OO^{2+}\}$, and (b) $\{61\ \mu M\ Cr_{aq}O^{2+} + 42\ \mu M\ Cr_{aq}OO^{2+}\}$.

deficiency, some of the $Cr_{aq}OO^{2+}$ still remained unreacted after all the $Cr_{aq}O^{2+}$ had disappeared.

The obvious candidates for the two competing reactions are those shown in Eqs. (24) and (25). The mechanisms of the two reactions are probably similar, although it was not possible to show whether reaction 25 produced isobutene. The expected chemistry is shown in more detail in Eq. (32). In a less appealing possibility, the tentative peroxo intermediate would cleave homolytically to yield alkyl and alkoxyl radicals, a route that is thermodynamically much less favorable than reaction 32.

$$\begin{aligned} CMe_3C(O)OO^{\bullet} + CMe_3OO^{\bullet} &\longrightarrow [CMe_3C(O)OOOOCMe_3] \\ &\longrightarrow CH_2{=}CMe_2 + Me_3COH + O_2 + CO_2 \end{aligned} \tag{32}$$

In support of the proposed scheme, whereby $CMe_3OO^{\bullet}$ and $Cr_{aq}OO^{2+}$ compete for the intermediate $CMe_3C(O)OO^{\bullet}$, the change of aldehyde to CH_3CHO resulted in predictable changes in kinetic behavior. Because there are no persistent radicals in the CH_3CHO system, and $Cr_{aq}OO^{2+}$ is the only scavenger for peroxyacetyl radicals produced in Eq. (29), the consumption of $Cr_{aq}OO^{2+}$ is much larger than in the pivaldehyde reaction. As shown in Fig. 13, all the $Cr_{aq}OO^{2+}$ was consumed before the reaction was completed, as shown by the sudden break in the kinetic trace at $\sim$9 s. Under comparable conditions in

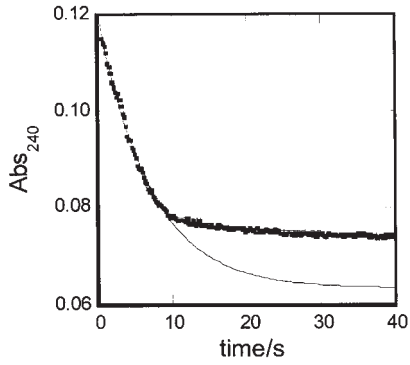

FIG. 13. Kinetic trace and exponential fit for the reaction between {47 μM $Cr_{aq}O^{2+}$ + 22 μM $Cr_{aq}OO^{2+}$} and 3.0 mM CH_3CHO in O_2 saturated aqueous 0.1 M $HClO_4$. Reproduced with permission from *J. Am. Chem. Soc.* **2002**, *124*, 9136–9144. Copyright 2002 American Chemical Society.

the CMe_3CHO reaction, about 30% of the initially present $Cr_{aq}OO^{2+}$ remained unreacted after all the $Cr_{aq}O^{2+}$ was consumed, Fig. 12a.

All the data in this and previous sections demonstrate that $Cr_{aq}OO^{2+}$ engages in complex radical chemistry and generates reactive high-valent chromium species and alkylperoxyl radicals, as shown in Schemes 6–8. Although there appear to be no other reports of such chemistry in the literature, one should expect other superoxo complexes to behave similarly. Analogs of Schemes 6–8 may be common in both aerobic biological systems and catalytic oxidations utilizing molecular oxygen and hydrogen peroxide. This is clearly a rich and widely open area for future investigations.

5. Relative Reactivities and Marcus Treatment

The rate constants for hydrogen abstraction from Rh–H, O–H, and C–H bonds by chromyl ions and $Cr_{aq}OO^{2+}$ are summarized in Table VI. Also listed in the table are selected relative rate constants for hydrogen abstraction by *tert*-butoxyl and *tert*-butylperoxyl radicals, expressed as $k_{t\text{-BuO}}/k_{t\text{-BuOO}}$. The difference between the two sets of data is striking in that alkoxyl radicals are 10^5–10^7 times more reactive than alkylperoxyl radicals, but in the chromium series the ratio k_{CrO}/k_{CrOO} is only about 10^2 for all the reactions studied. This ratio is preserved over about 10^3-fold change in absolute rate constants within each series.

TABLE VI

SUMMARY OF KINETIC DATA FOR HYDROGEN ATOM ABSTRACTION BY $Cr_{aq}O^{2+}$ (k_{CrO}) AND $Cr_{aq}OO^{2+}$ (k_{CrOO})[a]

H-donor	k_{CrO}	k_{CrOO}	k_{CrO}/k_{CrOO}	$k_{t\text{-BuO}}/k_{t\text{-BuOO}}$
L^1RhH^{2+}	$\sim 10^4$	129	78	
L^1RhD^{2+}	2.70×10^3	17	160	
$(NH_3)_4RhH^{2+}$		135		
L^2RhH^{2+}	1.12×10^3	24	47	
L^2RhD^{2+}	338			
$ArOH^{+}$ [b]	194	1.24	156	
CMe_3CHO	45.2	0.16	282	$\sim 10^7$ [c]
m- and *p*-$XC_6H_4CH_3$				$\sim 10^7$ [c]
DHA[d]				3×10^5 [c]

[a] Data from Refs. (*132*) and (*143*). L^1 = cyclam. L^2 = Me_6-cyclam.

[b] Structure shown in Fig. 9.

[c] Sources are quoted in Ref. (*143*).

[d] DHA = dihydroanthracene.

TABLE VII

THERMODYNAMIC DATA FOR $Cr_{aq}O^{2+}$, $Cr_{aq}OO^{2+}$, AND THEIR *tert*-BUTYL COUNTERPARTS

	O–H bde (kJ/mol)	Source
tert-BuOH	440	Ref. (*154*)
$Cr_{aq}OH^{2+}$	$> 373^a$	Ref. (*143*)
tert-BuOOH	369	Ref. (*155*)
$Cr_{aq}OOH^{2+}$	330^a	Ref. (*50*)

[a]Solution phase. Reproduced with permission from *J. Am. Chem. Soc.* **2000**, *122*, 1092–1097. Copyright 2000 American Chemical Society.

This, initially surprising, finding has been shown (*143*) to originate in the difference in O–H bond dissociation energies between the organic and inorganic pairs listed in Table VII. The lower limit of the value for $Cr_{aq}OH^{2+}$ (bde $\geq$ 373 kJ/mol) was estimated (*143*) from the reduction potential of the $Cr_{aq}O^{2+}/Cr_{aq}^{3+}$ couple ($\geq$ 1.6 V), K_a for Cr_{aq}^{3+} (10^{-4} M^{-1}), and the oxidation potential for $H^{\bullet}$ (2.29 V).

The observed behavior qualitatively follows the Marcus relationship for atom transfer, which predicts that the ratio of rate constants for hydrogen transfer from a common donor to two different acceptors will depend only on the relative energies of the bonds being formed, as described below.

If the rate constants of hydrogen exchange (identity reactions) for the couples $^{\bullet}CMe_3C(O)/CMe_3CHO$, $Cr_{aq}O^{2+}/Cr_{aq}OH^{2+}$, and $Cr_{aq}OO^{2+}/Cr_{aq}OOH^{2+}$ are designated k_{11}, k_{22}, and k_{33}, respectively, then the ratio of rate constants for the cross reactions (*156–159*) is given in Eq. (33), where k_{12} ($= k_{CrO}$) and k_{13} ($= k_{CrOO}$) represent the rate constants for the cross reactions, and K_{12} and K_{13} are the equilibrium constants for the same reactions. Ignoring the negligible entropy change in reaction 34, the free energy difference ΔG_{23} can be approximated as the difference in bond energies between $Cr_{aq}OO–H^{2+}$ and $Cr_{aq}O–H^{2+}$, $\geq$43 kJ/mol. Provided the rate constants for identity reactions k_{22} and k_{33} are similar, i.e., $(k_{22}/k_{33})^{0.5} \sim 1$, one obtains $k_{CrO}/k_{CrOO} \geq 6 \times 10^3$. The agreement with the observed ratio of $\sim 10^2$ is considered acceptable in view of the uncertainties and approximations made in reaching the estimated value.

$$\frac{k_{12}}{k_{13}} = \frac{(k_{11}k_{22}K_{12})^{0.5}}{(k_{11}k_{33}K_{13})^{0.5}} = \left(K_{23}\frac{k_{22}}{k_{33}}\right)^{0.5} = \left(\frac{k_{22}}{k_{33}}\right)^{0.5} e^{-0.5\,\Delta G_{23}/RT} \qquad (33)$$

$$Cr_{aq}O^{2+} + Cr_{aq}OOH^{2+} \rightleftarrows Cr_{aq}OH^{2+} + Cr_{aq}OO^{2+} \qquad (34)$$

Similar calculations for *tert*-BuO$^{\bullet}$/*tert*-BuOO$^{\bullet}$ using bond energies in Table VII and again assuming similar rate constants for the identity reactions for *tert*-BuO$^{\bullet}$/*tert*-BuOH and *tert*-BuOO$^{\bullet}$/*tert*-BuOOH yields $k_{t\text{-BuO}}/k_{t\text{-BuOO}} \sim 10^6$, close to the experimentally observed value. A large source of error in this and other calculated ratios comes from the uncertainty in the bde's, which sometimes differ widely from source to source (*160*).

The recently estimated rate constants (*116,161*) for the identity reactions $k_{t\text{-BuO}/t\text{-BuOH}}$ ($3 \times 10^4\ M^{-1}s^{-1}$) and $k_{t\text{-BuOO}/t\text{-BuOOH}}$ ($5 \times 10^2\ M^{-1}\ s^{-1}$) in non-aqueous solvents differ by a factor of ~ 60, which will cause only a modest, 8-fold increase in the estimated $k_{t\text{-BuO}}/k_{t\text{-BuOO}}$. The reasonable closeness between $k_{t\text{-BuO}/t\text{-BuOH}}$ and $k_{t\text{-BuOO}/t\text{-BuOOH}}$ strengthens the assumption made for the chromium couples, i.e., that $(k_{22}/k_{33})^{0.5} \sim 1$ is probably also correct to within an order of magnitude.

The findings in this work are very much in line with several related studies on hydrogen atom abstraction by non-radical metal-oxo species (*113,117,162*) in addition to oxygen-centered radicals. Correlations between the kinetics and thermodynamic driving force for such reactions have been reported (*113–115*). In the more recent work (*116,161*), Mayer and coworkers took the analysis to the next level and identified both the driving force and intrinsic barriers as fundamental and accessible parameters for treating the rates of hydrogen atom transfer according to Marcus cross relation in a manner previously reserved for electron transfer only. These developments are certain to reenergize the interest in hydrogen abstraction by both organic and inorganic reagents.

C. Reactions of LMOO Complexes with Nitrogen Oxides and HNO_2

The reactions of $Cr_{aq}OO^{2+}$ with acylperoxyl radicals in Eqs. (24) and (27) are not the only examples of radical coupling reactions for this superoxometal complex. As it turns out, several inorganic radicals also have been shown to react with $Cr_{aq}OO^{2+}$ and other LMOO complexes by an initial interaction at terminal oxygen. This type of reactivity is of great significance in the chemistry of nitrogen monoxide (NO) in aerobic biological systems.

Nitrogen monoxide has held the attention of scientific community from the time this small inorganic radical was discovered to play a

role, often as a cell messenger, in a number of biological processes (*163–168*). Early on, the reaction between NO and oxyglobins has been proposed to be a major pathway for the removal of NO in vivo (*169*). In analogy to free O_2^-, Eq. (35), LMOO complexes also produce nitrate, Eq. (36) (*170*), in processes that almost certainly involve intermediates, such as free and/or bound peroxynitrite, $OONO^-$, a competent oxidant and nitrating species which has been implicated in a number of pathological processes (*166,171–175*). It is still a matter of debate whether the mechanism of Eq. (35) involves the homolytic cleavage of peroxynitrite to generate hydroxyl radicals and NO_2 (*176–178*). A good portion of peroxynitrite probably reacts with carbon dioxide, which is present in most biological tissues, to generate nitrosoperoxycarbonate, $ONO_2CO_2^-$, itself an oxidant and nitrating agent (*179*).

$$NO + O_2^-/HO_2 \longrightarrow ONOO^-/HOONO \longrightarrow NO_3^- \tag{35}$$

$$NO + LMOO \longrightarrow [LMOONO] \longrightarrow \{NO_3^- + NO_2^-\} + LM \tag{36}$$

The decay of LMOONO, generated either as in Eq. (36), or by substitution of peroxynitrite into a metal complex, is usually written as a homolytic process of Scheme 9. The LMO and NO_2 so generated can then either diffuse apart or recombine within the solvent cage to either regenerate the peroxynitrito complex or form the metal-nitrato intermediate, followed by release of free nitrate by hydrolysis. At the time we initiated the work described below, there were no clear examples of LMOONO species isomerizing to a metal nitrato complex, although such reactions have been considered as a possibility (*180–182*).

A mechanistic point that is especially relevant to the design of drugs for removal/isomerization of peroxynitrite deals with the formation of

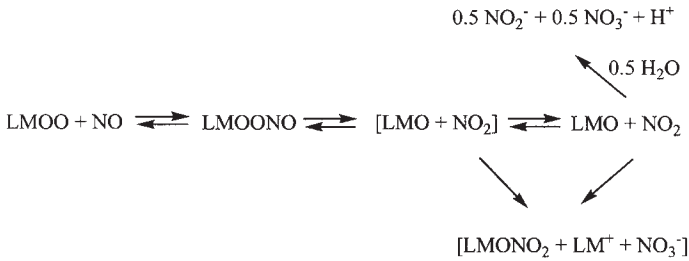

SCHEME 9.

freely diffusing NO_2 (Scheme 9), itself an undesirable species in biological environments. Good candidates for such drugs typically employ metal-porphyrin catalysts that have been shown to protect the tissue against oxidation and nitration (*182–185*), suggesting mechanisms that bypass free NO_2. Possibly, the in-cage recombination and isomerization are especially fast for such compounds. As shown below on two inorganic examples, $Cr_{aq}OONO^{2+}$ and $L^2(H_2O)RhOONO^{2+}$, the fraction of radicals that diffuse out of the solvent cage can differ dramatically between complexes that seem comparable in terms of size, charge, or expected O–O bond strength of the peroxynitrito group (*71,186*).

1. $NO/L^2(H_2O)RhOO^{2+}$ Reaction

The rapid disappearance of $L^2(H_2O)RhOO^{2+}$ takes place with a stoichiometry $[NO]/[L^2(H_2O)RhOO^{2+}] = 1$ (*71*). The reaction is believed to generate $L^2(H_2O)RhOONO^{2+}$, although this species was never observed directly. On the basis of sequential stopped-flow experiments utilizing L^1Ni^{2+} and $ABTS^{\bullet-}$ as scavengers, an upper limit of 15 μs was placed on the lifetime of $L^2(H_2O)RhOONO^{2+}$ in acidic solutions.

The evidence for NO_2 and $L^2(H_2O)RhO^{2+}$ as reaction intermediates, produced in ~40% yield, also came from experiments with L^1Ni^{2+} and $ABTS^{\bullet-}$, both of which react rapidly with NO_2 (*187,188*). This chemistry is shown in Eqs. (37)–(40).

$$L^2(H_2O)RhOO^{2+} + NO \longrightarrow [L^2(H_2O)RhOONO^{2+}] \longrightarrow L^2(H_2O)RhO^{2+} + NO_2 \tag{37}$$

$$L^2(H_2O)RhO^{2+} + ABTS^{2-} \xrightarrow{2H^+, H_2O} L^2Rh(H_2O)_2^{3+} + ABTS^{\bullet-} \tag{38}$$

$$NO_2 + ABTS^{2-} \longrightarrow NO_2^- + ABTS^{\bullet-} \tag{39}$$

$$NO_2 + L^1Ni^{2+} \longrightarrow NO_2^- + L^1Ni^{3+} \tag{40}$$

In separate experiments, the yields of $ABTS^{\bullet-}$ were twice as large as the yields of L^1Ni^{3+} consistent with NO_2 reacting with both L^1Ni^{2+} and $ABTS^{2-}$, but $L^2(H_2O)RhO^{2+}$ being scavenged only with $ABTS^{2-}$. Such an outcome was expected on the basis of the known low reactivity of macrocyclic rhodium complexes toward other macrocyclic reagents (*50*). The observed behavior supports our contention

that the fragments NO_2 and $L^2(H_2O)RhO^{2+}$ are being scavenged, rather than their precursor, $L^2(H_2O)RhOONO^{2+}$.

Another observation that supports the proposed scheme comes from the much smaller yield of $ABTS^{\bullet-}$ at pH 11 than in acidic solutions in the presence of an excess of NO. The known chemistry of NO, NO_2, and N_2O_3 is responsible for this pH effect. The rapid reaction between NO and NO_2, Eq. (41) (*189*), produces N_2O_3, which hydrolyzes, Eq. (42), much more rapidly at high pH (*190*), thus minimizing the reverse reaction and with it the amount of NO_2 available to other scavengers.

$$NO + NO_2 \rightleftharpoons N_2O_3 \tag{41}$$

$$N_2O_3 \overset{H_2O}{\rightleftharpoons} 2HNO_2 \tag{42}$$

In the absence of added scavengers, the $NO/L^2(H_2O)RhOO^{2+}$ reaction produced $\sim$10% of $L^2(H_2O)RhOOH^{2+}$ and $\sim$70% of a species assigned as the nitrato complex $L^2(H_2O)Rh(NO_3)^{2+}$ on the basis of the following observations.

On the time scale of conventional spectrophotometry, this complex is generated "instantaneously" upon the mixing of NO and $L^2(H_2O)RhOO^{2+}$. The decay exhibits a maximum absorbance change at 240 nm, as shown in Fig. 14.

The decomposition products are $L^2Rh(H_2O)_2^{3+}$ and NO_3^- throughout the pH range 1–11. Except for a small (20%) amount of NO_3^- produced initially from L^2RhO^{2+} and NO_2 in an outer-sphere process (Scheme 10), the rate of NO_3^- formation is identical, within error, to the rate of disappearance of the rhodium complex. This reaction is base-catalyzed, typical for hydrolysis of inorganic Rh(III) complexes. Finally, the complex is unreactive toward reductants such as Fe^{2+}_{aq} and $ABTS^{2-}$, and thus almost certainly not a peroxynitrito complex, which would be expected to behave as an oxidant. On the basis of these arguments, the absorbance decrease at 240 nm in Fig. 14 is assigned as hydrolysis of $L^2(H_2O)Rh(NO_3)^{2+}$. The kinetic treatment yielded the acidity constant $K_a = 1.2 \times 10^{-3}$ M^{-1} and a rate constant $k_h = 1.7 \times 10^{-3}$ s^{-1} for the hydrolysis of the conjugate base, $L^2(HO)Rh(NO_3)^+$.

All the observations on the $L^2(H_2O)RhOO^{2+}/NO$ reaction are summarized in Scheme 10. This work, and a paper from Koppenol's group (*191*), have provided first credible examples of nitrato complexes

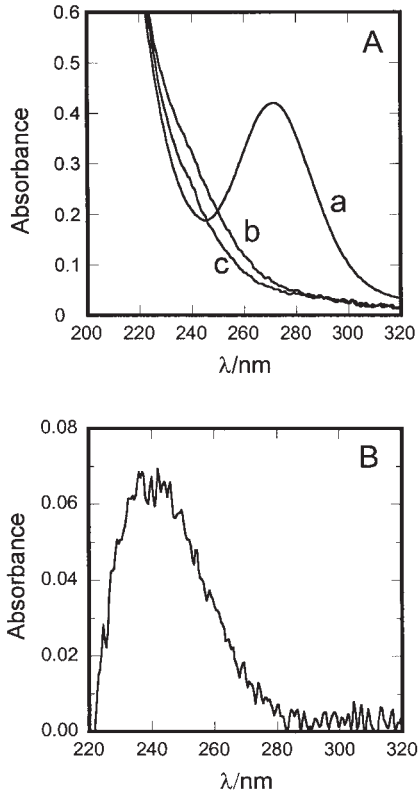

FIG. 14. (A) Spectral changes observed upon mixing 42 μM $L^2(H_2O)RhOO^{2+}$ (spectrum *a*) with 0.1 mM NO in 0.015 M $HClO_4$. Spectrum *b* was recorded immediately after mixing, and spectrum *c* 200 min later. (B) Difference spectrum (*b*–*c*) of the intermediate $L^2(H_2O)Rh(NO_3)^{2+}$. Reproduced with permission from *J. Am. Chem. Soc.* **2002**, *124*, 1698–1703. Copyright 2002 American Chemical Society.

derived from superoxo precursors and NO. As shown in Scheme 10, the precise fractions of $L^2(H_2O)Rh(NO_3)^{2+}$ produced inside the solvent cage and in bulk solution are not known, but major amounts had to be generated inside the cage to account for the total observed yield (70%) and the limited (40%) fraction of radicals escaping the cage. In the reaction of NO with another superoxo complex, $Cr_{aq}OO^{2+}$, the yield of the nitratometal product was smaller, $<30\%$ (*186*), and none of it was generated in the solvent cage, as described below.

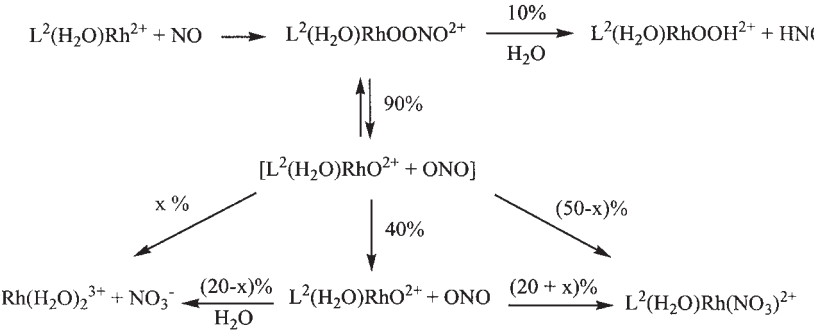

SCHEME 10. Reproduced with permission from *J. Am. Chem. Soc.* **2002**, *124*, 1698–1703. Copyright 2002 American Chemical Society.

2. *NO/$Cr_{aq}OO^{2+}$ Reaction*

Several potential intermediates in this reaction are known species, which makes this a particularly suitable case study from a mechanistic point of view.

The stoichiometry of the NO/$Cr_{aq}OO^{2+}$ reaction is a function of the absolute concentration of NO. At low [NO], the stoichiometry is 1:1, and nitrate (free and complexed) is the major product. High [NO] shifts the stoichiometry to [NO]/[$Cr_{aq}OO^{2+}$] = 3:1. Under these conditions, the reaction produces 3 moles of nitrite per mol of $Cr_{aq}OO^{2+}$. The results are consistent with Scheme 11 where all the steps are either known independently or have been verified in the course of the work on $Cr_{aq}OO^{2+}$/NO reaction (*186*), see below.

The NO/$Cr_{aq}O^{2+}$ step was found to be fast ($k > 10^4$ M^{-1} s^{-1}) (*186*) and to produce $Cr_{aq}ONO^{2+}$, a known species (*192*). Similar chemistry was reported recently for $MbFe^{IV}O$ (*193,194*). The intermediate $Cr_{aq}ONO^{2+}$ was next detected in >80% yield in the NO/$Cr_{aq}OO^{2+}$ reaction, strongly supporting the idea of $Cr_{aq}O^{2+}$ being a major intermediate.

The involvement of NO_2 was deduced from the effect of L^1Ni^{2+} in the kinetic experiments on the initial interaction of NO with $Cr_{aq}OO^{2+}$. The chemistry involved in the kinetic determinations is shown in Eqs. (43)–(45). Laser flash photolysis ($\lambda_{exc} = 266$ nm) of $Cr_{aq}NO^{2+}$ in O_2-saturated solutions generates NO and Cr^{2+}_{aq}. The rapid formation of $Cr_{aq}OO^{2+}$ in reaction 44 is followed by its reaction with NO, Eq. (45). Reactions 44 and 45 were accompanied by an absorbance increase at 290 nm (formation of $Cr_{aq}OO^{2+}$) followed by a decrease, and the rate constant k_{45} was obtained by fitting the data for the latter step to an

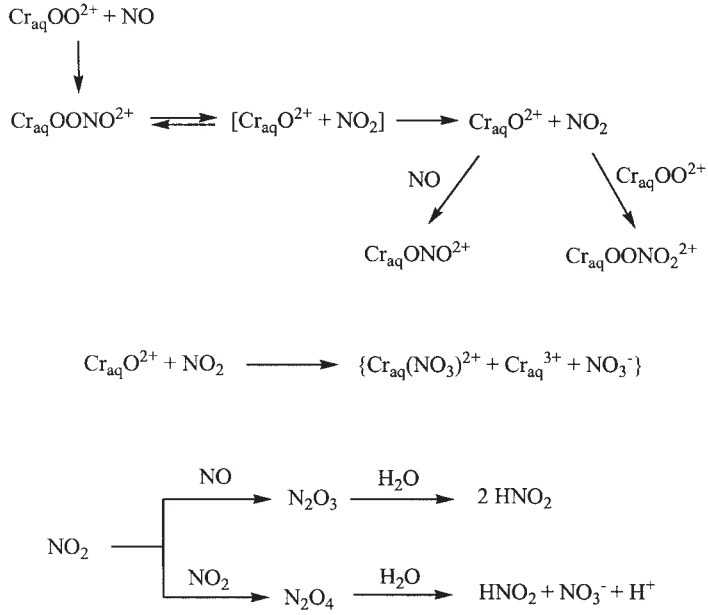

SCHEME 11.

equal-concentration second-order rate law. The value of k_{45} so obtained is $7 \times 10^8\ M^{-1}\ s^{-1}$. Under the experimental conditions, both reactions 44 and 45 are much faster than the autoxidation of NO (*195*).

$$Cr_{aq}NO^{2+} \xrightarrow{h\nu} Cr_{aq}^{2+} + NO \tag{43}$$

$$Cr_{aq}^{2+} + O_2 \longrightarrow Cr_{aq}OO^{2+} \quad k = 1.6 \times 10^8\ M^{-1}\ s^{-1} \tag{44}$$

$$NO + Cr_{aq}OO^{2+} \longrightarrow \text{products} \tag{45}$$

When the same reaction was carried out in the presence of L^1Ni^{2+}, the formation of $Cr_{aq}OO^{2+}$ in reaction 44 was followed by an absorbance increase at 360 nm, the wavelength of maximum absorption for L^1Ni^{3+}. The rate of formation of L^1Ni^{3+} and its yield exhibited little dependence on the initial concentration of L^1Ni^{2+}, showing that the formation of oxidizing intermediates is rate determining. This observation places a limit on the rate constant for the scavenging reaction with L^1Ni^{2+} at $\geq 10^8\ M^{-1}\ s^{-1}$.

Additional L^1Ni^{3+} was formed on a much slower time scale (several seconds) in the $L^1Ni^{2+}/Cr_{aq}O^{2+}$ reaction, which was examined independently and found to have a rate constant of $1 \times 10^3\ M^{-1}\ s^{-1}$.

It is highly unlikely that the initially produced $Cr_{aq}OONO^{2+}$ is the oxidant for L^1Ni^{2+} in the fast step, given that the reaction of LNi^{2+} with another peroxochromium species, $Cr_{aq}OOH^{2+}$ is at least 10^7 times slower than the scavenging step observed here, and the reaction of L^1Ni^{2+} with HOONO, which should be a better one-electron oxidant than $Cr_{aq}OONO^{2+}$, has $k = 6.5 \times 10^4\ M^{-1}\ s^{-1}$ (*196*). We therefore prefer a scenario whereby the initially produced $Cr_{aq}OONO^{2+}$ cleaves rapidly ($\tau < 0.5$ ms) to $Cr_{aq}O^{2+}$ and NO_2, and the reaction of NO_2 with L^1Ni^{2+}, $k = 1.2 \times 10^8\ M^{-1}\ s^{-1}$ (*187*), is responsible for the scavenging step observed by laser flash photolysis.

Clearly, the major portion of the two homolysis fragments, $Cr_{aq}O^{2+}$ and NO_2, had to diffuse into the bulk solution for the trapping by external reagents to take place. The highly efficient trapping of $Cr_{aq}O^{2+}$ shows that little, if any, product formation takes place inside the solvent cage. Indeed, as shown later, there is strong evidence that the cage escape approaches 100%.

The observed 3:1 $[NO]/[Cr_{aq}OO^{2+}]$ stoichiometry at high [NO] is easily explained by the combination of the known NO/NO_2 reaction (*197*) and the newly discovered $NO/Cr_{aq}O^{2+}$ reaction described above. The direct observation of $Cr_{aq}ONO^{2+}$ and the large rate constant for its formation strongly support the picture presented in Scheme 11. Other known reactions of NO with metal-oxo species are also fast, $k = 3.1 \times 10^6\ M^{-1}s^{-1}$ for $L^1Cr(ONO)(O)^+$ (*198*) and $9 \times 10^6\ M^{-1}s^{-1}$ for $MbFe^{IV}O$ (*199*).

The reaction between $Cr_{aq}O^{2+}$ and NO_2 in the absence of added NO yields $Cr_{aq}(NO_3)^{2+}$ and $\{Cr_{aq}^{3+} + NO_3^-\}$ and the stoichiometry for the overall $NO/Cr_{aq}OO^{2+}$ reaction becomes 1:1. The rate constant for the $Cr_{aq}O^{2+}/NO_2$ reaction must be large enough to compete with the self-reaction of NO_2, $k_{NO2} = 4.5 \times 10^8\ M^{-1}\ s^{-1}$ (*188*). Literature precedents include both fast [$(TMPS)Fe^{IV}O$, $k = 1.7 \times 10^7\ M^{-1}s^{-1}$ (*180*) and $MbFe^{IV}O$, $k = 1 \times 10^7\ M^{-1}\ s^{-1}$ (*182*)] and slow [$(TMPyP)Fe^{IV}O$ (*200*)] reactions of NO_2 with metal(IV) species.

The peroxynitrito complexes derived from $Cr_{aq}OO^{2+}$ and $L^2(H_2O)RhOO^{2+}$ are short lived and in that sense reminiscent of the peroxynitrites of hemoglobin (*182,201*), myoglobin (*182*), and porphyrin complexes of manganese (*183,184*) and iron (*171,180*), and different from another inorganic ion, $(CN)_5CoOONO^{3-}$, which is extremely stable (*202*).

Of the two complexes described above, the in-cage isomerization is much more efficient for the Rh complex. The success of in-cage

recombination versus cage escape is one of the crucial factors that will determine the suitability of a particular compound as catalyst for the isomerization of HOONO/$OONO^-$ in vivo. At this stage it is difficult to predict how sensitive these processes will be to the thermodynamics of the O–N bond in nitrato complexes, steric effects at the reaction center, or polarity and hydrophilicity of the catalysts, but these questions clearly need to be addressed in a rational approach to the design of isomerization catalysts. If there is a correlation with alkylmetal complexes, then the size and steric crowding would be expected to play a major role. Within a series of alkylcobalamins (alkyl = Me, Et, *n*-Pr, and adenosyl), the recombination rate varied by less than a factor of two, but the cage escape by methyl was more than five times faster than by adenosyl (*203*).

3. HNO_2 as a Source of NO and NO_2

Samples of NO almost always contain some level of HNO_2, which can either complicate the chemistry (*204*), or itself serve as a source of NO and NO_2 according to the reverse of Eqs. (41)–(42), as described below for the reaction with $L^2(H_2O)RhOO^{2+}$ (*205*).

The reaction exhibits a 3:2 stoichiometry of Eq. (46) (*205*), and kinetics that are second order in the total concentration of HNO_2, and independent of $[L^2(H_2O)RhOO^{2+}]$, consistent with the disproportionation of HNO_2 being rate determining.

$$2L^2(H_2O)RhOO^{2+} + 3HNO_2 + H_2O \longrightarrow 2L^2Rh(H_2O)_2^{3+} + 3NO_3^- + H^+ \tag{46}$$

The acid dependence, illustrated in Fig. 15, is consistent with HNO_2 participating in an acid-independent and an acid-catalyzed reaction. Additional decrease in reactivity at higher pH is caused by the deprotonation of HNO_2 which increases the proportion of the unreactive NO_2^-. The rate law is shown in Eqs. (47)–(48), where $[HNO_2]_{tot} = [HNO_2] + [NO_2^-]$, and the acidity constant for HNO_2 is $K_a = 6.3 \times 10^{-4}$ M^{-1}. The fit of the data in Fig. 15 yields $k_1 = 10.9$ M^{-1} s^{-1} and $k_2 = 175$ M^{-2} s^{-1}.

$$\frac{-d[HNO_2]}{dt} = \frac{-3\, d\left[L^2(H_2O)RhOO^{2+}\right]}{2\, dt} = 3\left(k_1 + k_2\left[H^+\right]\right)\left([HNO_2]_{tot}\,\frac{\left[H^+\right]}{K_a + \left[H^+\right]}\right)^2 \tag{47}$$

$$k_{\text{obs}} = 3\left(k_1 + k_2\left[\text{H}^+\right]\right)\left(\frac{\left[\text{H}^+\right]}{K_a + \left[\text{H}^+\right]}\right)^2 \tag{48}$$

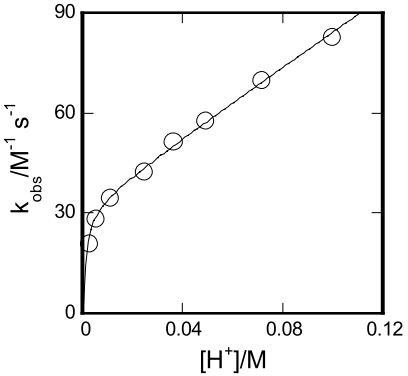

FIG. 15. Plot of k_{obs} vs. $[\text{H}^+]$ for the reaction between $L^2(H_2O)RhOO^{2+}$ and HNO_2. The solid line is the fit to Eq. (47). Reproduced with permission from *Inorg. Chem.* **2002**, *41*, 901–905. Copyright 2002 American Chemical Society.

The generally accepted mechanism for the formation of N_2O_3 in the reverse of reaction 42 involves a nucleophilic attack of NO_2^- on nitrous acidium ion $H_2NO_2^+$ (or NO^+), Eq. (49) (*206,207*). The reaction of the conjugate acid, HNO_2, with $H_2NO_2^+$, which would exhibit a first order dependence on $[\text{H}^+]$, has been considered earlier, but was difficult to detect (*208*) at unfavorable pH conditions required by other reactants (*209,210*) or in competition with other mechanistic routes (*211*). The work with $L^2(H_2O)RhOO^{2+}$ (*205*) now provides credible evidence for nitrous acid acting as a nucleophile, Eq. (50).

$$H_2NO_2^+ + NO_2^- \longrightarrow H_2O + N_2O_3 \tag{49}$$

$$H_2NO_2^+ + HNO_2 \longrightarrow H_3O^+ + N_2O_3 \tag{50}$$

The ratio of rate constants k_{49}/k_{50} is equal to the ratio $k_1/K_a k_2 \sim 1 \times 10^2$, calculated from the fit of the data to Eq. (47). As one would expect, the kinetic nucleophilicity of HNO_2 is less, but not infinitely less, than that of NO_2^-.

The reaction between HNO_2 and $L^2(H_2O)RhOO^{2+}$ generated the nitrato intermediate, $L^2(H_2O)Rh(NO_3)^{2+}$, but the yield was only half of that observed earlier in the $NO/L^2(H_2O)RhOO^{2+}$ reaction.

$$2\,HNO_2 \rightleftharpoons N_2O_3 + H_2O \qquad k_f = 10.9\ M^{-1}\ s^{-1},\ k_r = 530\ s^{-1} \qquad (42)$$

$$N_2O_3 \rightleftharpoons NO + NO_2 \qquad k_f = 8 \times 10^4\ s^{-1},\ k_r = 10^9\ M^{-1}\ s^{-1} \qquad (41)$$

$$L^2(H_2O)RhOO^{2+} + NO \rightarrow L^2(H_2O)RhOONO^{2+} \qquad k_f > 10^6\ M^{-1}\ s^{-1} \qquad (37)$$

$$L^2(H_2O)RhOONO^{2+} \rightarrow \{\, L^2(H_2O)Rh(NO_3)^{2+} + L^2Rh(H_2O)_2^{3+} + NO_3^- + L^2(H_2O)RhOOH^{2+}\} \qquad k > 10^3\ s^{-1} \qquad (51)$$

$$NO_2 + L^2(H_2O)RhOO^{2+} \rightleftharpoons L^2(H_2O)RhOONO_2^{2+} \qquad k_f > 10^3\ M^{-1}\ s^{-1} \qquad (52)$$

$$L^2(H_2O)RhOONO_2^{2+} + HNO_2 \xrightarrow{H_2O} L^2Rh(H_2O)_2^{3+} + 2\,NO_3^- + H^+ \qquad k > 500\ M^{-1}\ s^{-1} \qquad (53)$$

$$2\,NO_2 \rightleftharpoons N_2O_4 \qquad k_f = k_{NO2} = 4.5 \times 10^8\ M^{-1}\ s^{-1},\ k_r = 7 \times 10^3\ s^{-1} \qquad (54)$$

$$N_2O_4 + H_2O \rightarrow HNO_2 + NO_3^- + H^+ \qquad k = 10^3\ s^{-1} \qquad (55)$$

SCHEME 12.

The reduced yield is consistent with the proposal in Scheme 12, according to which only 50% of $L^2(H_2O)RhOO^{2+}$ reacts with NO, the other 50% being consumed by NO_2, Eqs. (52)–(53).

The reaction in Eq. (52) was written in analogy to the directly observed $NO_2/Cr_{aq}OO^{2+}$ reaction, see below. Reaction 53 draws support from the known oxidation of HNO_2 by peroxynitric acid, Eq. (56), for which two different values of rate constants have been reported, 10 $M^{-1}\,s^{-1}$ (*212*) and 50 $M^{-1}\,s^{-1}$ (*190*).

$$HOONO_2 + HNO_2 \longrightarrow 2NO_3^- + 2H^+ \qquad (56)$$

Reaction 53 needs to be much faster, $k_{53} > 500\ M^{-1}\ s^{-1}$, to account for the observed 3:2 stoichiometry. The required 50-fold rate acceleration is not unreasonable given that coordination usually causes a great increase in the reactivity of peroxides (*213*). None the less, the dimerization of NO_2 followed by hydrolysis, reactions 54–55, cannot

be ruled out as an alternative to the sequence 52–53. Both possibilities would result in the observed 3:2 stoichiometry.

4. $NO_2/CrOO^{2+}$ Reaction

Nitrogen dioxide's claim to fame comes from two major sources, environmental pollution (*214*) and the possibility that NO_2 is responsible for some of the biological damage attributed to peroxynitrite (*215,216*) from which it is formally derived by O–O bond homolysis.

Despite its significance, NO_2 has not received nearly as much attention as NO in kinetic and mechanistic studies in solution (*217*). The reason probably lies in the short lifetime of NO_2, which rapidly disproportionates to nitrite and nitrate, see Scheme 12, Eqs. (54)–(55), with an overall combined rate constant $k = 6.5 \times 10^7$ M^{-1} s^{-1}, Eq. (57). Direct kinetic studies are thus limited to rapid reactions and require the use of absorbing reactants or kinetic probes.

$$2NO_2 + H_2O \longrightarrow NO_3^- + HNO_2 + H^+ \tag{57}$$

One of the advantages of chromium complexes over those of, say, cobalt or rhodium in mechanistic studies is the much greater photoinertness of the chromium family. The superoxochromium $Cr_{aq}OO^{2+}$, for example, is almost unaffected by the >320 nm light, but the superoxides of cobalt and rhodium photohomolyze readily even when exposed to visible light, $\lambda < 500$ nm. Photochemical generation of radicals and other short-lived species is thus more easily accomplished in the presence of $Cr_{aq}OO^{2+}$. This feature facilitates kinetic studies, as illustrated by the reactions of $Cr_{aq}OO^{2+}$ with NO (Section III.C.2) and NO_2 (*218*), described below.

For kinetic purpose, NO_2 was generated (*218*) by laser-flash photolysis (λ_{exc} 355 nm) of $(NH_3)_5CoNO_2^{2+}$, Eq. (58) (*219*) in the presence of excess $Cr_{aq}OO^{2+}$. The kinetics were monitored at 290 nm, a wavelength of maximum absorption for $Cr_{aq}OO^{2+}$. The plot of k_{obs} against $[Cr_{aq}OO^{2+}]$ yielded the rate constant $k_{59} = 2.3 \times 10^8$ M^{-1} s^{-1} at pH 1 in purely aqueous solutions, and 2.6×10^8 M^{-1} s^{-1} in 40% aqueous acetonitrile (AN).

$$(NH_3)_5CoNO_2^{2+} \xrightarrow{h\nu, H^+} NO_2 + Co_{aq}^{2+} + 5NH_4^+ \tag{58}$$

$$Cr_{aq}OO^{2+} + NO_2 \longrightarrow \text{products} \quad (59)$$

The large value of k_{59}, and its similarity to the reactions of $Cr_{aq}OO^{2+}$ with two other radicals of widely different reduction and oxidation potentials, Table VIII, strongly supports radical coupling as the mechanism for reaction 59.

The same value was obtained by use of 10-methyl-9,10-dihydroacridine ($AcrH_2$) as a kinetic probe. Independent kinetic determination yielded a rate constant $k_A = 9.4 \times 10^6\ M^{-1}\ s^{-1}$ in 40% AN, Eq. (60).

$$AcrH_2 + NO_2 \xrightarrow{k_A} AcrH_2^{\bullet+} + NO_2^- \quad (60)$$

In another set of competition experiments, NO_2 was again generated by laser flash photolysis and allowed to react with a mixture of $Cr_{aq}OO^{2+}$ and $AcrH_2$. At the chosen set of concentrations, the great majority of NO_2 reacted with $Cr_{aq}OO^{2+}$ in submillisecond

TABLE VIII

KINETIC AND POTENTIAL[a] DATA FOR THE REACTIONS OF $Cr_{aq}OO^{2+}$ WITH N- AND O-CENTERED RADICALS

Radical	$10^{-8}\ k/M^{-1}\ s^{-1}$	E_{red}/V	E_{ox}/V
NO	7[b]	−0.8 ($NO/^3NO^-$)[c,d] −0.5 ($NO/^1HNO$), pH 7[e] −1.7 ($NO/^1NO$)[c]	1.21 (NO^+/NO)[f]
NO_2	2.3[g]	1.04 (NO_2/NO_2^-[f] 1.23 (NO_2/HNO_2)[f]	1.51[f], 1.6[h] (NO_2^+/NO_2)[h]
$CH_3C(O)OO^{\bullet}$[d]	1.5[i]	1.12 ($RC(O)OO^{\bullet}/RC(O)OO^-$)[j] 1.60 ($RC(O)OO^{\bullet}/RC(O)OOH$)[j]	

[a] V vs. NHE.
[b] Ref. (*186*).
[c] Ref. (*220*).
[d] Ref. (*221*).
[e] pK_a ($^1HNO/^3NO^-$) = 11.4, Ref. (*221*) or 11.6, Ref. (*220*).
[f] Ref. (*222*).
[g] Ref. (*218*).
[h] Ref. (*223*).
[i] Ref. (*149*).
[j] Ref. (*224*).

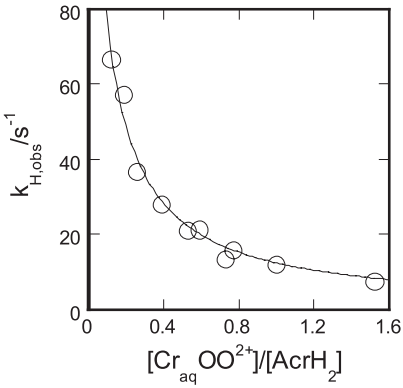

FIG. 16. Plot of $k_{H,obs}$ against the ratio $[Cr_{aq}OO^{2+}]/[AcrH_2]$ for the homolysis of $Cr_{aq}OONO_2^{2+}$ produced in the reverse of Eq. (61). Conditions: 20% aqueous acetonitrile, pH 1. Solid line is the fit to Eq. (65). Reproduced with permission from *Inorg. Chem.* **2003**, *42*, 1744–1750. Copyright 2003 American Chemical Society.

times. On much longer time scales (0.1–1 s), the absorbance increased at 417 nm, the wavelength of maximum absorption for the doubly oxidized species, $AcrH^+$. The kinetics of the absorbance increase are a function of the concentration ratio $[Cr_{aq}OO^{2+}]/[AcrH_2]$, Fig. 16, consistent with the homolysis of the initially formed $Cr_{aq}OONO_2^{2+}$ as in Scheme 13. The initial formation of $Cr_{aq}OONO_2^{2+}$ is reversed by the reaction between NO_2 and $AcrH_2$, followed by the deprotonation of $AcrH_2^{\bullet+}$ (k_d) and rapid oxidation of $AcrH^\bullet$ by either O_2 or $(NH_3)_5CoNO_2^{2+}$.

$$Cr_{aq}OONO_2^{2+} \underset{k_{Cr}}{\overset{k_H}{\rightleftharpoons}} Cr_{aq}OO^{2+} + NO_2 \qquad (61)$$

$$AcrH_2 + NO_2 \xrightarrow{k_A} AcrH_2^{\bullet+} + NO_2^- \qquad (60)$$

$$AcrH_2^{\bullet+} \underset{k_p}{\overset{k_d}{\rightleftharpoons}} AcrH^\bullet + H^+ \qquad (62)$$

$$AcrH^\bullet + Ox \xrightarrow{fast} AcrH^+ + Red \qquad (63)$$

SCHEME 13.

By treating $Cr_{aq}OONO_2^{2+}$ as a steady-state intermediate, the rate law of Eq. (64) is obtained. Rearrangement gives Eq. (65), where $k_{H,obs}$ represents the observed first-order rate constant, and k_H is the homolysis rate constant of Eq. (61). The fit of experimental data to Eq. (65), shown in Fig. 16, gives $k_H = 197\ s^{-1}$ in 40% AN.

$$\text{rate} = k_H \frac{k_A[AcrH_2]}{k_A[AcrH_2] + k_{Cr}\left[Cr_{aq}OO^{2+}\right]}\left[Cr_{aq}OONO_2^{2+}\right] \tag{64}$$

$$k_{H,\,obs} = \frac{k_H}{1 + (k_{Cr}[Cr_{aq}OO^{2+}]/k_A[AcrH_2])} \tag{65}$$

The $NO_2/CrOO^{2+}$ reaction in the absence of scavengers results in no permanent consumption of $Cr_{aq}OO^{2+}$ and yields products that do not differ significantly from those obtained in the self-reaction of NO_2. These data support a scheme whereby the homolysis of $Cr_{aq}OONO_2^{2+}$ is pulled to completion by the NO_2 self-reaction of Eqs. (54)–(55).

The reaction between $Cr_{aq}OO^{2+}$ and NO_2 appears to be the only documented study of the interaction of a superoxometal complex with NO_2. The O–O bond in the product $Cr_{aq}OONO_2^{2+}$ is weak and cleaves in the reverse process, the overall formation constant being $\sim 10^6\ M^{-1}$. In comparison, the reaction of NO_2 with HO_2 is faster in the forward direction, $k = 1.8 \times 10^9\ M^{-1}s^{-1}$ (*190*) and slower in the reverse, $k = 0.005$–$0.05\ s^{-1}$ (*225–227*), yielding a much larger equilibrium constant, $K_{66} = (3.6 \times 10^{10} - 3.6 \times 10^{11})\ M^{-1}$. The weakening of the N–O bond upon coordination of peroxynitrate can be traced to increased thermodynamic stability of the metal-superoxo fragment over HO_2.

$$HO_2 + NO_2 \rightleftarrows HOONO_2 \tag{66}$$

The rapid homolysis leaves little time for $Cr_{aq}OONO_2^{2+}$ to engage in bimolecular reactions with added substrates. In a study of the $Cr_{aq}OO^{2+}$-catalyzed cooxidation of methanol and HNO_2 described below there was no evidence for the equivalent of reaction 53. The failure of $Cr_{aq}OONO_2^{2+}$ to react casts some doubt about the involvement of $L^2(H_2O)RhOONO_2^{2+}$ in reaction 53 as well. Future work with these and other peroxynitrato complexes should explore their reactivity toward one- and two-electron reductants, and search for

longer-lived examples to make the reactions with substrates detectable above the background decomposition pathways.

D. Catalytic Oxidation of Alcohols by O_2

The reaction between NO and $Cr_{aq}OO^{2+}$ generates $Cr_{aq}O^{2+}$ quantitatively, Scheme 11. Many alcohols react with $Cr_{aq}O^{2+}$ in two-electron processes and generate $Cr_{aq}OO^{2+}$ in the presence of O_2 (*58*). The combination of these two reactions constitutes a catalytic cycle for the $Cr_{aq}OO^{2+}$-catalyzed oxidation of alcohols by O_2. The reaction requires an equivalent of a sacrificial reductant, NO, as shown in Scheme 14.

$$Cr_{aq}OO^{2+} + NO \longrightarrow Cr_{aq}O^{2+} + NO_2 \tag{67}$$

$$Cr_{aq}O^{2+} + CH_3OH \longrightarrow CH_2O + H_2O + Cr^{2+}_{aq} \xrightarrow{O_2,\ \text{fast}} Cr_{aq}OO^{2+} \tag{8}$$

Net: $CH_3OH + NO + O_2 \rightarrow CH_2O + NO_2 + H_2O$

Scheme 14.

Experimentally, Scheme 14 is unrealistic as written, because NO is itself oxidized by O_2, Eq. (68), which makes these two reagents incompatible for extended periods of time. For the scheme to work, NO should be produced in situ at low concentrations to slow the autoxidation which exhibits second-order dependence on NO (*195*), Eq. (69). The bimolecular disproportionation of HNO_2 in the reverse of Eqs. (41)–(42) turned out to be a good source of NO for this purpose. As described above, the other disproportionation product, NO_2, should not interfere except for the weak, reversible binding to a portion of the catalyst, $Cr_{aq}OO^{2+}$.

$$4NO + O_2 + 2H_2O \longrightarrow 4NO_2^- + 4H^+ \tag{68}$$

$$-d[NO]/dt = 4\, k_{NO}[NO]^2[O_2] \qquad k_{NO} = 2 \times 10^6\ M^{-2}\ s^{-1} \tag{69}$$

TABLE IX

YIELDS OF CH_2O IN $Cr_{aq}OO^{2+}$-CATALYZED OXIDATION OF HNO_2/CH_3OH[a]

[MeOH]/M	$[CH_2O]_\infty/[Cr_{aq}OO^{2+}]_0$
0.007	1
0.40	15
0.81	15
0.81	20
0.87	20
0.84	33[b]

[a]Room temperature, 0.10 M $HClO_4$, $[Cr_{aq}OO^{2+}] = 20$ μM, $[HNO_2] = (0.34–1.75)$ mM.
[b]$[Cr_{aq}OO^{2+}] = 13$ μM.

The $Cr_{aq}OO^{2+}/HNO_2/CH_3OH$ system is indeed catalytic, as shown in Table IX (*228*). Catalytic efficiencies (CE), defined as $[CH_2O]_\infty/[Cr_{aq}OO^{2+}]_0$, of up to 33 were observed.

The concentration of HNO_2 had little effect on CE, but increased concentrations of methanol up to 0.8 M increased the CE until it reached a plateau. The rate of disappearance of $Cr_{aq}OO^{2+}$ and formation of CH_2O decreased as $[CH_3OH]$ was increased in the range 0.007–2 M. This kinetic effect is caused by the formation of the inactive methyl nitrite, Eq. (70), which has $K_{RONO} = 3.5\ M^{-1}$ (*229*).

$$CH_3OH + HNO_2 \overset{K_{RONO}}{\rightleftharpoons} CH_3ONO + H_2O \qquad (70)$$

Benzyl alcohol behaves similarly, but the pronounced spectral changes that accompany the oxidation, Fig. 17, make this alcohol a much better candidate for kinetic and stoichiometric determinations. The formation constant for benzyl nitrite from benzyl alcohol has $K_{RONO} = 0.44$ (*228*).

Under the conditions of limiting HNO_2, the ratio $[PhCHO]_\infty/[HNO_2]_0$ was precisely 1.0 at $[PhCH_2OH] \geq 0.1$ M. A large portion of $Cr_{aq}OO^{2+}$ remained unreacted, consistent with its role as a catalyst. The overall reaction can thus be written as in Eq. (71). A typical CE in these experiments was around 10.

$$PhCH_2OH + O_2 + HNO_2 \xrightarrow{Cr_{aq}OO^{2+}} PhCHO + NO_3^- + H_2O \qquad (71)$$

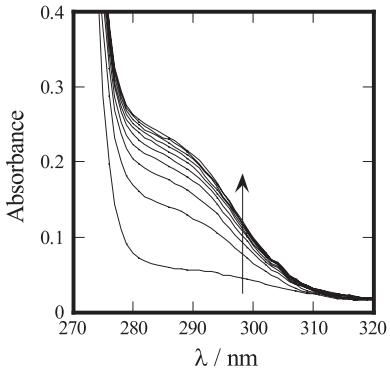

FIG. 17. Spectral changes accompanying the formation of benzaldehyde in the $Cr_{aq}OO^{2+}$-catalyzed reaction between 0.11 M $PhCH_2OH$ and 0.14 mM HNO_2 in O_2-saturated aqueous solution at pH 1. Time interval between successive spectra is 150 s. $[Cr_{aq}OO^{2+}] = 20$ μM. Modified from *J. Mol. Cat. A* **2003**, *200*, 21–29, Pestovsky, O. and Bakac, A., "Superoxometal-catalyzed co-oxidation of alcohols and nitrous acid with molecular oxygen", copyright (2003) with permission from Elsevier.

The reaction mechanism was probed by carrying out the oxidation of $PhCH_2OH$ in competition with several other alcohols, whose rate constants for the reaction with $Cr_{aq}O^{2+}$ are independently known. If, as predicted, the kinetics are determined by the rate of disproportionation of HNO_2, and $Cr_{aq}O^{2+}$ is the active oxidant, then the added alcohols should have no effect on the kinetics, but the yield of PhCHO should decrease by a predictable percentage as the oxidation products of competing alcohols grow in. In separate experiments with MeOH, EtOH, and 2-PrOH, the yield of PhCHO changed exactly as predicted, without an effect on the kinetics, confirming the role of $Cr_{aq}O^{2+}$ as the active oxidizing intermediate.

Kinetic traces exhibited rapid initial absorbance changes, identified as the conversion of a fraction of $Cr_{aq}OO^{2+}$ to $Cr_{aq}OONO_2{}^{2+}$. This step was followed by a well-behaved, second order reaction characterized by the same rate constant and same acid dependence as those obtained earlier for the disproportionation of HNO_2, Eqs. (47)–(48) (*205*). There was no dependence on $[Cr_{aq}OO^{2+}]$, $[O_2]$, or $[PhCH_2OH]$. All the data fit the mechanism in Scheme 15 and Eqs. (72) and (73).

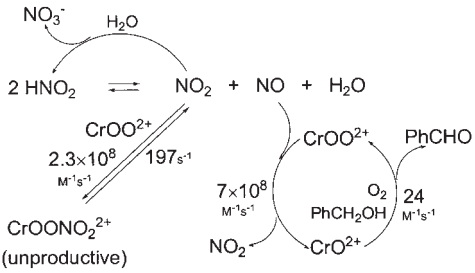

SCHEME 15. Modified from *J. Mol. Cat. A* **2003**, *200*, 21–29, Pestovsky, O. and Bakac, A., "Superoxometal-catalyzed co-oxidation of alcohols and nitrous acid with molecular oxygen", copyright (2003) with permission from Elsevier.

Most of the steps in Scheme 15 have been discussed already. The reactions in Eqs. (72) and (73) cause an irreversible loss of the catalyst and are one of the reasons for the low CE. The other, of course, is the low solubility of O_2 in water, so that about 50% of O_2 is already consumed at 20 μM $Cr_{aq}OO^{2+}$ for CE = 30.

Reaction 72 was found to proceed in one-electron steps (*228*), so that it does not regenerate $Cr_{aq}OO^{2+}$. The scavenging of Cr^{2+}_{aq} by $Cr_{aq}OO^{2+}$ in Eq. (73) (*58*) is a rapid reaction ($k_{73} = 8 \times 10^8$ M^{-1} s^{-1} at 1 M ionic strength) that generates some, but less than stoichiometric amounts of $Cr_{aq}O^{2+}$, and will therefore deplete the catalyst in Scheme 15.

$$Cr_{aq}O^{2+} + HNO_2 + H^+ \xrightarrow{k_{HONO}} Cr^{3+}_{aq} + NO_2 + H_2O \quad k_{HONO} = 950\ M^{-1}\ s^{-1} \tag{72}$$

$$Cr_{aq}OO^{2+} + Cr^{2+}_{aq} \longrightarrow Cr_{aq}O^{2+} + \text{products} \quad k = 8 \times 10^8\ M^{-1}\ s^{-1} \tag{73}$$

All of the individual steps in Scheme 15 have been observed and characterized independently, making this a particularly attractive case for kinetic simulations. This was done by use of the program Chemical Kinetics Simulator (IBM). Simulated traces reproduced the experimental data in every detail. This includes the rapid initial drop in absorbance at 290 nm and the smooth, remaining portion that obeyed second order kinetics. The rapid initial step generates the equilibrium amount of $Cr_{aq}OONO^{2+}_2$, which throughout

the reaction acts only as a storage for some $Cr_{aq}OO^{2+}$ and does not interfere with the catalytic cycle in any other way.

Somewhat surprisingly, the hydroperoxo complex $Cr_{aq}OOH^{2+}$ is just as effective as $Cr_{aq}OO^{2+}$ in catalyzing the HNO_2/MeOH oxidation. Detailed studies (*228*) showed the oxidation of $Cr_{aq}OOH^{2+}$ by NO_2 to $Cr_{aq}OO^{2+}$, the active catalyst, to be the cause for this behavior. The reaction in Eq. (74) is too slow to compete with the dimerization of NO_2 in laser flash photolysis experiments, but fast enough for a major fraction of $Cr_{aq}OOH^{2+}$ to be oxidized to $Cr_{aq}OO^{2+}$ in steady-state experiments, which places the upper limit for k_{74} at $< 10^6\ M^{-1}\ s^{-1}$.

$$Cr_{aq}OOH^{2+} + NO_2 \longrightarrow Cr_{aq}OO^{2+} + NO_2^- \qquad (74)$$

IV. Conclusions and Future Directions

The work described in this Chapter illustrates the variety of chemistry exhibited by superoxometal complexes. These compounds couple with free radicals ($RC(O)OO^{\bullet}$, NO, and NO_2) almost as fast as the parent superoxide radical, but the lifetimes of the LMOO complexes are by orders of magnitude longer than that of the transient HO_2/O_2^-. These features make the LMOO reactions not only easier for the curious to observe, but perhaps also more important in real biological and catalytic systems, where the longer lifetimes should translate into a greater chance for reactions with substrates.

The radical reactivity of $Cr_{aq}OO^{2+}$ has been especially well documented. This complex is ideal for mechanistic studies, not only because of the convenient combination of lifetime and reactivity, but also because it is nearly inert to visible-light photolysis. Photochemical generation of reactive partners in the presence of $Cr_{aq}OO^{2+}$ is thus possible, and rapid radical reactions can be observed and studied directly, as shown on the examples of acylperoxyl radicals, NO, and NO_2.

Hydrogen abstraction by $Cr_{aq}OO^{2+}$ from C–H, O–H, and Rh–H bonds is kinetically facile provided the thermodynamics are favorable (*143*). Much work remains to be done with other LMOO compounds to sort out various influences on the strength of the LMOO–H bonds, and thus, by implication, the tendency of LMOO to abstract hydrogen.

The cross-coupling with acylperoxyl radicals was shown to lead to high-valent metal species and reactive organic intermediates (*144*). The $Cr_{aq}OO^{2+}/CMe_3C(O)OO^{\bullet}$ reaction appears to be the sole example of such chemistry reported so far. Extension to other metals and types of radicals is essential before one can even begin to understand whether such reactions take place in catalytic oxidation systems and/or in aerobic organisms, and whether or how to exploit or suppress them.

$Cr_{aq}OO^{2+}$ also acts as a catalyst for oxidations with O_2 in the presence of HNO_2. Radical coupling, this time with NO, is again an essential mechanistic step. The catalysis takes advantage of the demonstrated preference for an intermediate, $Cr_{aq}O^{2+}$, to react in two-electron, hydride-transfer steps with organic materials. Reactivity studies of potential intermediates in other systems may uncover new catalytic powers of LMOO species.

Intermediates produced in O_2 reactions with the cationic, inorganic compounds such as Cr_{aq}^{2+}, $L(H_2O)_2Co^{2+}$, and $L(H_2O)Rh^{2+}$ may not seem to be ideal models for catalytic systems or in vivo reactions but, because of their simplicity, they play an essential role in illustrating the possibilities, discovering new reactions and intermediates which may be less clear cut in more complex systems, or making it possible to isolate individual steps or reaction types suggested by those complex systems.

In fact, it is both surprising and gratifying to find so much similarity and correlation between $Cr_{aq}OO^{2+}$ and, say, HbO_2 or MbO_2 in reactions with common substrates, such as NO. In all the cases, a short-lived peroxynitrato intermediate forms with similar kinetics, and ultimately produces free NO_3^- in a scheme that involves smaller or greater amounts of free NO_2 and $LM^{IV}O$ (*169,182,186,201,230*) and coordinated nitrate. The reactivity of $LM^{IV}O$ toward NO and NO_2 in subsequent reactions is again not too different for $LM = Cr_{aq}$ (*186*), $L^2(H_2O)Rh$ (*71*) Mb (Hb) (*182,199*) or iron porphyrins (*180*), although kinetic variations obviously do exist. It is indeed remarkable that a purely inorganic molecule, such as $Cr_{aq}OO^{2+}$, containing only chromium, oxygen and water, can mimic so well some of the steps exhibited by the complex, large, and fine-tuned biological molecules. Equally remarkable is the rapid conversion of another simple compound, $L^1(H_2O)CrOOH^{2+}$, to Cr(V) (*45,69*), a process that mimics a step in the catalytic action of cytochrome P450 enzymes and that might have been considered specific for these complex biological systems (which, of course, utilize iron as the central metal).

Further work with metal-activated dioxygen is bound to lead to new surprises and new exciting discoveries.

V. Abbreviations

$ABTS^{2-}$	2,2′-azinobis(3-ethylbenzothiazoline-6-sulfonate) ion
$AcrH_2$	10-methyl-9,10-dihydroacridine
bde	bond dissociation energy
bpy	2,2′-bipyridine
Bu	butyl = C_4H_9
CE	catalytic efficiency = moles of product/moles of catalyst
DMSO	dimethylsulfoxide
Et	ethyl
Hb	hemoglobin
k_f	forward rate constant
kie	kinetic isotope effect
k_r	reverse rate constant
LM	metal complex (L = ligand, M = metal)
L^1	1,4,8,11-tetraazacyclotetradecane
L^2	*meso*-Me_6-1,4,8,11-tetraazacyclotetradecane
Mb	myoglobin
Me	methyl = CH_3
Ph	phenyl
py	pyridine
salen	*N*,*N*′-ethylenebis(salicylideneiminato) ion
TMPS	*meso*-tetra(2,4,6-trimethyl-3,5-disulfonato)porphin
TMPyP	5,10,15,20-tetrakis(N-methyl-4′-pyridyl)porphyrin

Acknowledgments

The work from our group was supported by the U. S. Department of Energy, Office of Basic Energy Sciences, Division of Chemical Sciences under Contract W-7405-ENG-82 with Iowa State University, and by National Science Foundation (grants CHE-9303388, CHE-9982004 and CHE-0240409). I am grateful to all my coworkers whose efforts and dedication made it possible for us to contribute to the field. Special thanks go to Dr. Oleg Pestovsky for both his scientific contributions and help with the figures for this manuscript.

References

1. Shilov, A. E.; Shul'pin, G. B. "*Activation and Catalytic Reactions of Saturated Hydrocarbons in the Presence of Metal Complexes*". Chapters 9–11; Kluwer: Dordrecht/Boston/London, 2000.

2. Simandi, L. I., ed. "*Advances in Catalytic Activation of Dioxygen by Metal Complexes*". Catalysis by Metal Complexes, Series Eds. van Leeuven, P.; James, B. Vol. 26. Kluwer: Dordrecht, 2003.
3. Que, L. Jr.; Watanabe, Y. *Science* **2001**, *292*, 651–653.
4. Merkx, M.; Kopp, D. A.; Sazinsky, M. H.; Blazyk, J. L.; Muller, J.; Lippard, S. J. *Angew. Chem. Int. Ed.* **2001**, *40*, 2782–2807.
5. Solomon, E. I.; Chen, P.; Metz, M.; Lee, S.-K.; Palmer, A. E. *Angew. Chem. Int. Ed.* **2001**, *40*, 4570–4590.
6. Guengerich, F. P. *Biolog. Chem.* **2002**, *383*, 1553–1564.
7. Woggon, W.-D. *Top. Curr. Chem.* **1997**, *184*, 39–96.
8. Shaik, S.; de Visser, S. P.; Ogliaro, F.; Schwarz, H.; Schroeder, D. *Curr. Op. Chem. Biol.* **2002**, *6*, 556–567.
9. McLain, J. L.; Lee, J.; Groves, J. T. Biomimetic oxygenations related to cytochrome P450: metal-oxo and metal-peroxo intermediates, "*Biomimetic Oxidations Catalyzed by Transition Metal Complexes*"; Ed. Meunier, B.; Imperial College Press: London, 2000, pp. 91–169.
10. Groves, J. T.; Shalyaev, K.; Lee, J. Oxometalloporphyrins in oxidative catalysis, "*The Porphyrin Handbook. Volume 4. Biochemistry and Binding: Activation of Small Molecules*"; Eds. Kadish, K. M.; Smith, K. M.; Guilard, R.; Academic Press: San Diego, 2000, pp. 17–40.
11. Groves, J. T. *J. Porphyrins Phthalocyanines* **2000**, *4*, 350–352.
12. Schroder, D.; Schwarz, H.; Shaik, S. *Struct. Bonding (Berlin)* **2000**, *97* (Metal-Oxo and Metal-Peroxo Species in Catalytic Oxidations), 91–123.
13. Stahl, S. S.; Lippard, S. J. Dioxygen and Alkane Activation by Iron-Containing Enzymes, "*Iron Metabolism*"; Eds. Ferreira, G. C.; Moura, J. J. G.; Franco, R.; 1999, pp. 303–321.
14. Du Bois, J.; Mizoguchi, T. J.; Lippard, S. J. *Coord. Chem. Rev.* **2000**, *200–202*, 443–485.
15. Guallar, V.; Gherman, B. F.; Lippard, S. J.; Friesner, R. A. *Curr. Op. Chem. Biol.* **2002**, *6*, 236–242.
16. Kopp, D. A.; Lippard, S. J. *Curr. Op. Chem. Biol.* **2002**, *6*, 568–576.
17. Lipscomb, J. D.; Que, L. Jr. *J. Biol. Inorg. Chem.* **1998**, *3*, 331–336.
18. Shteinman, A. A. *J. Biol. Inorg. Chem.* **1998**, *3*, 325–330.
19. Que, L. Jr.; Tolman, W. B. *Angew. Chem. Int. Ed.* **2002**, *41*, 1114–1137.
20. Blackman, A. G.; Tolman, W. B. *Struct. Bonding (Berlin)* **2000**, *97* (Metal-Oxo and Metal-Peroxo Species in Catalytic Oxidations), 179–211.
21. Holland, P. L.; Tolman, W. B. *Coord. Chem. Rev.* **1999**, *190–192*, 855–869.
22. Karlin, K. D.; Zuberbuhler, A. D. Formation, structure, and reactivity of copper dioxygen complexes, "*Bioinorganic Catalysis*", 2nd edn. (Revised and Expanded); Eds. Reedijk, J.; Bouwman, E.; Marcel Dekker: New York, 1999, pp. 469–534.
23. Fukuzumi, S.; Imahori, H. Biomimetic electron-transfer chemistry of porphyrins and metalloporphyrins, "*Electron Transfer in Chemistry*", Vol. 2; Ed. Balzani, V.; Wiley-VCH Verlag GmbH: Weinheim, 2001, pp. 927–975.
24. Fukuzumi, S.; Ohtsu, H.; Ohkubo, K.; Itoh, S.; Imahori, H. *Coord. Chem. Rev.* **2002**, *226*, 71–80.
25. Musie, G.; Wei, M.; Subramaniam, B.; Busch, D. H. *Coord. Chem. Rev.* **2001**, *219–221*, 789–820.
26. Ito, M.; Fujisawa, K.; Kitajima, N.; Moro-Oka, Y. *Catalysis by Metal Complexes* **1997**, *19* (Oxygenases and Model Systems), 345–376.
27. Neumann, R. *Prog. Inorg. Chem.* **1998**, *47*, 317–370.

28. Weinstock, I. A.; Barbuzzi, E. M. G.; Sonnen, D. M.; Hill, C. L. *ACS Symposium Series* **2002**, *823* (Advancing Sustainability through Green Chemistry and Engineering), 87–100.
29. Sheldon, R. A.; Arends, I. W. C. E.; ten Brink, G.-J.; Dijksman, A. *Acc. Chem. Res.* **2002**, *35*, 774–781.
30. Van Rantwijk, F.; Sheldon, R. A. *Curr. Op. Chem. Biol.* **2000**, *11*, 554–564.
31. Kopf, M.-A.; Karlin, K. D. Models of copper enzymes and heme-copper oxidases, "*Biomimetic Oxidations Catalyzed by Transition Metal Complexes*"; Ed. Meunier, B.; Imperial College Press: London, 2000, pp. 309–362.
32. Fokin, A. A.; Schreiner, P. R. *Chem. Rev.* **2002**, *102*, 1551–1593.
33. Hu, Z.; Gorun, S. M. Methane monooxygenase models, "*Biomimetic Oxidations Catalyzed by Transition Metal Complexes*"; Ed. Meunier, B.; Imperial College Press: London, 2000, pp. 269–307.
34. Kruger, H.-J. Iron-containing models of catechol dioxygenases, "*Biomimetic Oxidations Catalyzed by Transition Metal Complexes*"; Ed. Meunier, B.; Imperial College Press: London, 2000, pp. 363–413.
35. Murahashi, S.-I.; Komiya, N. Bioinspired oxidations catalyzed by ruthenium complexes, "*Biomimetic Oxidations Catalyzed by Transition Metal Complexes*"; Ed. Meunier, B.; Imperial College Press: London, 2000, pp. 563–611.
36. Sheldon, R. A. Biocatalytic and biomimetic oxidations from an industrial perspective, "*Biomimetic Oxidations Catalyzed by Transition Metal Complexes*"; Ed. Meunier, B.; Imperial College Press: London, 2000, pp. 613–662.
37. Mansuy, D.; Battioni, P. Diversity of reactions catalyzed by heme-thiolate proteins, "*The Porphyrin Handbook. Volume 4. Biochemistry and Binding: Activation of Small Molecules*"; Eds. Kadish, K. M.; Smith, K. M.; Guilard, R.; Academic Press: San Diego, 2000, pp. 1–15.
38. Suslick, K. S. Shape-selective oxidation by metalloporphyrins, "*The Porphyrin Handbook. Volume 4. Biochemistry and Binding: Activation of Small Molecules*"; Eds. Kadish, K. M.; Smith, K. M.; Guilard, R.; Academic Press: San Diego, 2000, pp. 41–63.
39. Weiss, R.; Gold, A.; Trautwein, A. X.; Terner, J. High-valent iron and manganese complexes of porphyrins and related macrocycles, "*The Porphyrin Handbook. Volume 4. Biochemistry and Binding: Activation of Small Molecules*"; Eds. Kadish, K. M.; Smith, K. M.; Guilard, R.; Academic Press: San Diego, 2000, pp. 65–96.
40. Watanabe, Y. High-valent intermediates, "*The Porphyrin Handbook. Volume 4. Biochemistry and Binding: Activation of Small Molecules*"; Eds. Kadish, K. M.; Smith, K. M.; Guilard, R.; Academic Press: San Diego, 2000, pp. 97–117.
41. Meunier, B.; Robert, A.; Pratviel, G.; Bernadou, J. Metalloporphyrins in catalytic oxidations and oxidative DNA cleavage, "*The Porphyrin Handbook. Volume 4. Biochemistry and Binding: Activation of Small Molecules*"; Eds. Kadish, K. M.; Smith, K. M.; Guilard, R.; Academic Press: San Diego, 2000, pp. 119–187.
42. Poulos, T. L. Peroxidase and cytochrome P450 structures, "*The Porphyrin Handbook. Volume 4. Biochemistry and Binding: Activation of Small Molecules*"; Eds. Kadish, K. M.; Smith, K. M.; Guilard, R.; Academic Press: San Diego, 2000, pp. 189–218.
43. Suzuki, M.; Furutachi, H.; Okawa, H. *Coord. Chem. Rev.* **2000**, *200–202*, 105–129.
44. Bakac, A.; Thomas, L. M. *Inorg. Chem.* **1996**, *35*, 5880–5884.
45. Bakac, A.; Wang, W.-D. *Inorg. Chim. Acta* **2000**, *297*, 27–35.
46. Brynildson, M. E.; Bakac, A.; Espenson, J. H. *J. Am. Chem. Soc.* **1987**, *109*, 4579–4583.
47. Ilan, Y. A.; Czapski, G.; Ardon, M. *Isr. J. Chem.* **1975**, *13*, 15–21.
48. Sellers, R. M.; Simic, M. G. *J. Am. Chem. Soc.* **1976**, *98*, 6145–6150.

49. Lilie, J.; Simic, M. G.; Endicott, J. F. *Inorg. Chem.* **1975**, *14*, 2129–2133.
50. Bakac, A. *J. Am. Chem. Soc.* **1997**, *119*, 10726–10731.
51. Bakac, A.; Espenson, J. H. *J. Am. Chem. Soc.* **1990**, *112*, 2273–2278.
52. Wong, C.-L.; Switzer, J. A.; Balakrishnan, K. P.; Endicott, J. F. *J. Am. Chem. Soc.* **1980**, *102*, 5511–5518.
53. Bakac, A.; Guzei, I. A. *Inorg. Chem.* **2000**, *39*, 736–740.
54. Jones, R. D.; Summerville, D. A.; Basolo, F. *Chem. Rev.* **1979**, *79*, 139–179.
55. Vaska, L. *Acc. Chem. Res.* **1976**, *9*, 175–183.
56. Busch, D. H.; Alcock, N. W. *Chem. Rev.* **1994**, *94*, 585–623.
57. Momenteau, M.; Reed, C. A. *Chem. Rev.* **1994**, *94*, 659–698.
58. Bakac, A. *Prog. Inorg. Chem.* **1995**, *43*, 267–351.
59. Cheung, S. K.; Grimes, C. J.; Wong, J.; Reed, C. A. *J. Am. Chem. Soc.* **1976**, *98*, 5028–5030.
60. Nakamoto, K. *Coord. Chem. Rev.* **1990**, *100*, 363–402.
61. Qin, K.; Incarvito, C. D.; Rheingold, A. L.; Theopold, K. H. *Angew. Chem. Int. Ed.* **2002**, *41*, 2333–2335.
62. Fujisawa, K.; Tanaka, M.; Moro-oka, Y.; Kitajima, N. *J. Am. Chem. Soc.* **1994**, *116*, 12079–12080.
63. Egan, J. W. Jr.; Haggerty, B. S.; Rheingold, A. L.; Sendlinger, S. C.; Theopold, K. H. *J. Am. Chem. Soc.* **1990**, *112*, 2445–2446.
64. Reinaud, O. M.; Theopold, K. H. *J. Am. Chem. Soc.* **1994**, *116*, 6979–6980.
65. Bakac, A.; Scott, S. L.; Espenson, J. H.; Rodgers, K. L. *J. Am. Chem. Soc.* **1995**, *117*, 6483–6488.
66. Wayland, B. B.; Newman, A. R. *J. Am. Chem. Soc.* **1979**, *101*, 6472–6473.
67. Raynor, J. B.; Gillard, R. D.; Pedrosa de Jesus, J. D. *J. Chem. Soc., Dalton Trans.* **1982**, 1165–1166.
68. Bielski, B. H. *J. Photochem. Photobiol.* **1978**, *28*, 645–649.
69. Bakac, A.; Wang, W.-D. *J. Am. Chem. Soc.* **1996**, *118*, 10325–10326.
70. Endicott, J. F.; Wong, C.-L.; Inoue, T.; Natarajan, P. *Inorg. Chem.* **1979**, *18*, 450–454.
71. Pestovsky, O.; Bakac, A. *J. Am. Chem. Soc.* **2002**, *124*, 1698–1703.
72. Pestovsky, O.; Bakac, A. *Inorg. Chem.* **2002**, *41*, 3975–3982.
73. Bakac, A. *Inorg. Chem.* **1998**, *37*, 3548–3552.
74. Geiger, T.; Anson, F. C. *J. Am. Chem. Soc.* **1981**, *103*, 7489–7496.
75. Marchaj, A.; Bakac, A.; Espenson, J. H. *Inorg. Chem.* **1992**, *31*, 4164–4168.
76. Wang, W.-D.; Bakac, A.; Espenson, J. H. *Inorg. Chem.* **1995**, *34*, 4049–4056.
77. Kumar, K.; Endicott, J. F. *Inorg. Chem.* **1984**, *23*, 2447–2452.
78. Brynildson, M. E.; Bakac, A.; Espenson, J. H. *Inorg. Chem.* **1988**, *27*, 2592–2595.
79. Wick, D. D.; Goldberg, K. I. *J. Am. Chem. Soc.* **1999**, *121*, 11900–11901.
80. Roberts, H.L.; Symes, W. R. *J. Chem. Soc. A* **1968**, 1450–1453.
81. Johnston, L. E.; Page, J. A. *Can. J. Chem.* **1969**, *47*, 4241–4246.
82. Bakac, A. J. *Photochem. Photobiol., A* **2000**, *132*, 87–89.
83. Lemma, K.; Ellern, A.; Bakac, A. *Inorg. Chem.* **2003**, *42*, 3662–3669.
84. Pearson, R. G. Absolute electronegativity, hardness, and bond energies, "*Bonding Energetics in Organometallic Compounds*"; Ed. Marks, T. J.; American Chemical Society: Washington, 1990, pp. 251–262.
85. Thyagarajan, S.; Incarvito, C. D.; Rheingold, A. L.; Theopold, K. H. *Chem. Commun.* **2001**, 2198–2199.
86. Simaan, A. J.; Banse, F.; Mialane, P.; Boussac, A.; Un, S.; Kargar-Grisel, T.; Bouchoux, G.; Girerd, J. J. *Eur. J. Chem.* **1999**, 993–996.
87. Akita, M.; Miyaji, T.; Hikichi, S.; Moro-oka, Y. *Chem. Lett.* **1999**, 813–814.

88. Strukul, G.; Ros, R.; Michelin, R. A. *Inorg. Chem.* **1982**, *21*, 495–500.
89. Ho, R. Y. N.; Roelfes, G.; Hermant, R.; Hage, R.; Feringa, B. L.; Que, L. Jr. *Chem. Commun.* **1999**, 2161–2162.
90. Wada, A.; Harata, M.; Hasegawa, K.; Jitsukawa, K.; Masuda, H.; Mukai, M.; Kitagawa, T.; Einaga, H. *Angew. Chem. Int. Ed.* **1998**, *37*, 798–799.
91. Rostovtsev, V. V.; Henling, L. M.; Labinger, J. A.; Bercaw, J. E. *Inorg. Chem.* **2002**, *41*, 3608–3619.
92. Boulatov, R.; Collman, J. P.; Shiryaeva, I. M.; Sunderland, C. J. *J. Am. Chem. Soc.* **2002**, *124*, 11923–11935.
93. Sam, J. W.; Tang, X.-J.; Peisach, J. *J. Am. Chem. Soc.* **1994**, *116*, 5250–5256.
94. Mathe, C.; Mattioli, T. A.; Horner, O.; Lombard, M.; Latour, J. M.; Fontecave, M.; Niviere, V. *J. Am. Chem. Soc.* **2002**, *124.*
95. Shearer, J.; Scarrow, R. C.; Kovacs, J. A. *J. Am. Chem. Soc.* **2002**, *124*, 11709–11717.
96. Primus, J.-L.; Grunenwald, S.; Hagedoorn, P.-L.; Albrecht-Gary, A.-M.; Mandon, D.; Veeger, C. *J. Am. Chem. Soc.* **2002**, *124*, 1214–1221.
97. Burger, R. M.; Peisach, J.; Horwitz, S. B. *J. Biol. Chem.* **1981**, *256*, 11636–11644.
98. Lippard, S. J.; Berg, J. M. "*Principles of Bioinorganic Chemistry*"; Mill Valley: University Science Books, 1994.
99. Suzuki, H.; Matsuura, S.; Moro-oka, Y.; Ikawa, T. *J. Organomet. Chem.* **1985**, *286*, 247–258.
100. Carmona, D.; Lamata, M. P.; Ferrer, J.; Modrego, J.; Perales, M.; Lahoz, F. J.; Atencio, R.; Oro, L. A. *J. Chem. Soc., Chem. Comm.* **1994**, 575–576.
101. Haarman, H. F.; Bregman, F. R.; van Leeuwen, P. W. N. M.; Vrieze, K. *Organometallics* **1997**, *16*, 979–985.
102. Ho, R. Y. N.; Roelfes, G.; Feringa, B. L.; Que, L. Jr. *J. Am. Chem. Soc.* **1999**, *121*, 264–265.
103. Guzei, I. A.; Bakac, A. *Inorg. Chem.* **2001**, *40*, 2390–2393.
104. Lehnert, N.; Ho, R. Y. N.; Que, L. Jr.; Solomon, E. I. *J. Am. Chem. Soc.* **2001**, *123*, 12802–12816.
105. Takahashi, Y.; Hashimoto, M.; Hikichi, S.; Akita, M.; Moro-oka, Y. *Angew. Chem. Int. Ed.* **1999**, *38*, 3074–3077.
106. Wang, W.-D.; Bakac, A.; Espenson, J. H. *Inorg. Chem.* **1993**, *32*, 2005–2009.
107. Wang, W.-D.; Bakac, A.; Espenson, J. H. *Inorg. Chem.* **1993**, *32*, 5034–5039.
108. Nemes, A.; Bakac, A. *Inorg. Chem.* **2001**, *40*, 2720–2724.
109. Logager, T.; Holcman, J.; Sehested, K.; Pedersen, T. *Inorg. Chem.* **1992**, *31*, 3523–3529.
110. Jacobsen, F.; Holcman, J.; Sehested, K. *Int. J. Chem. Kin.* **1997**, *29*, 17–24.
111. Chen, K.; Que, L. Jr. *J. Am. Chem. Soc.* **2001**, *123*, 6327–6337.
112. Codd, R.; Dillon, C. T.; Levina, A.; Lay, P. A. *Coord. Chem. Rev.* **2001**, *216–217*, 537–582.
113. Mayer, J. M. *Acc. Chem. Res.* **1998**, *31*, 441–450.
114. Strassner, T.; Houk, K. N. *J. Am. Chem. Soc.* **2000**, *122*, 7821–7822.
115. Larsen, A. S.; Wang, K.; Lockwood, M. A.; Rice, G. L.; Won, T.-J.; Lovell, S.; Sadilek, M.; Turecek, F.; Mayer, J. M. *J. Am. Chem. Soc.* **2002**, *124*, 10112–10123.
116. Roth, J. P.; Yoder, J. C.; Won, T. J.; Mayer, J. M. *Science* **2001**, *294*, 2524–2526.
117. Scott, S. L.; Bakac, A.; Espenson, J. H. *J. Am. Chem. Soc.* **1992**, *114*, 4205–4213.
118. Barefield, E. K.; Mocella, M. T. *J. Am. Chem. Soc.* **1975**, *97*, 4238–4246.
119. McAuley, A.; Xu, C. *Inorg. Chem.* **1992**, *31*, 5549–5554.
120. Goedken, V. L.; Busch, D. H. *J. Amer. Chem. Soc.* **1972**, *94*, 7355–7363.
121. Roecker, L.; Meyer, T. J. *J. Am. Chem. Soc.* **1987**, *109*, 746–754.

122. Che, C.-M.; Tang, W.-T.; Lee, W.-O.; Wong, K.-Y.; Lau, T.-C. *J. Chem. Soc., Dalton Trans.* **1992**, 1551–1556.
123. Che, C.-M.; Ho, C.; Lau, T.-C. *J. Chem. Soc., Dalton Trans*. **1991**, 1259–1263.
124. Abel, E. W.; Pratt, J. M.; Whelan, R.; Wilkinson, P. J. *J. Am. Chem. Soc*. **1974**, *96*, 7119–7120.
125. Ghosh, S. P.; Gelerinter, E.; Pyrka, G.; Gould, E. S. *Inorg. Chem*. **1993**, *32*, 4780–4784.
126. Bear, J. L.; Yao, C.-L.; Capdevielle, F. J.; Kadish, K. M. *Inorg. Chem.* **1988**, *27*, 3782–3785.
127. Sheldon, R. A. History of Oxygen Activation, "*The Activation of Dioxygen and Homogeneous Catalytic Oxidation*"; Eds. Barton, D. H. R.; Martell, A. E.; Sawyer, D. T.; Plenum: New York and London, 1993, pp. 9–30.
128. Snelgrove, D. W.; Lusztyk, J.; Banks, J. T.; Mulder, P.; Ingold, K. U. *J. Am. Chem. Soc*. **2001**, *123*, 469–477.
129. Avila, D. V.; Ingold, K. U.; Lusztyk, J.; Green, W. H.; Procopio, D. R. *J. Am. Chem. Soc*. **1995**, *117*, 2929–2930.
130. Kang, C.; Anson, F. C. *Inorg. Chem.* **1994**, *33*, 2624–2630.
131. Wayner, D. D. M.; Parker, V. D. *Acc. Chem. Res.* **1993**, *26*, 287–294.
132. Nemes, A.; Bakac, A. *Inorg. Chem.* **2001**, *40*, 746–749.
133. Nishinaga, A.; Tomita, H.; Matsuura, T. *Tetrahedron Lett*. **1980**, *21*, 3407–3408.
134. Nishinaga, A.; Tomita, H.; Matsuura, T. *Tetrahedron Lett*. **1979**, *20*, 2893–2896.
135. Nishinaga, A.; Shimizu, T.; Matsuura, T. *Tetrahedron Lett*. **1981**, *22.*
136. Zombeck, A.; Drago, R. S.; Corden, B. B.; Gaul, J. *J. Am. Chem. Soc.* **1981**, *103*, 7580–7585.
137. Nishinaga, A.; Tomita, H.; Nishizawa, K.; Matsuura, T. *J. Chem. Soc., Dalton Trans*. **1981**, 1504–1514.
138. Ingold, K. U.; Wright, J. S. *J. Chem. Ed.* **2000**, *77*, 1062–1064.
139. Nishinaga, A.; Nakamura, K.; Matsuura, T.; Rieker, A.; Koch, D.; Griesshammer, R. *Tetrahedron* **1979**, *35*, 2493–2499.
140. Nishinaga, A.; Nishizawa, K.; Tomita, H.; Matsuura, T. *Synthesis* **1977**, 270–272.
141. Jaky, M.; Szammer, J. *J. Phys. Org. Chem.* **1997**, *10*, 420–426.
142. Schuchmann, M. N.; von Sonntag, C. *J. Am. Chem. Soc*. **1988**, *110*, 5698–5701.
143. Bakac, A. *J. Am. Chem. Soc.* **2000**, *122*, 1092–1097.
144. Bakac, A. *J. Am. Chem. Soc.* **2002**, *124*, 9136–9144.
145. Bakac, A.; Espenson, J. H. *Inorg. Chem*. **1981**, *20*, 953–954.
146. Bakac, A. Unpublished results.
147. Cabelli, D.; Bakac, A. Unpublished results.
148. Tsentalovich, Y. P.; Fischer, H. J. Chem. Soc *Perkin Trans.* **1994**, *2*, 729–733.
149. Bakac, A. *J. Am. Chem. Soc.* **2002**, *124*, 3816–3817.
150. Howard, J. A. Reactions of organic peroxyl radicals in organic solvents, "*Peroxyl Radicals*"; Ed. Alfassi, Z. B.; Wiley: Chichester, 1997, pp. 283–334.
151. MacFaul, P. A.; Arends, I. W. C. E.; Ingold, K. U.; Wayner, D. D. M. *J. Chem. Soc. Perkin Trans*. **1997**, *2*, 135–145.
152. Fischer, H. *J. Am. Chem. Soc.* **1986**, *108*, 3925–3927.
153. Neta, P.; Huie, R. E.; Ross, A. B. *J. Phys. Chem. Ref. Data* **1990**, *19*, 413–513.
154. McMillen, D. F.; Golden, D. M. *Ann. Rev. Phys. Chem.* **1982**, *33*, 493–532.
155. Das, T. N.; Dhanasekaran, T.; Alfassi, Z. B.; Neta, P. *J. Phys. Chem. A* **1998**, *102*, 280–284.
156. Marcus, R. A. *J. Chem. Phys*. **1965**, *43*, 679–701, 2654–2657.
157. Marcus, R. A.; Sutin, N. *Biochem. Biophys. Acta* **1985**, *811*, 265–322.
158. Hush, N. S. *Prog. Inorg. Chem*. **1967**, *8*, 391–444.

159. Sutin, N. *Prog. Inorg. Chem.* **1983**, *30*, 441–498.
160. Luo, Y.-R. "*Handbook of Bond Dissociation Energies in Organic Compounds*"; CRC: Boca Raton, 2003.
161. Roth, J. P.; Lovell, S.; Mayer, J. M. *J. Am. Chem. Soc.* **2000**, *122*, 5486–5498.
162. Gardner, K. A.; Mayer, J. M. *Science* **1995**, *269*, 1849–1851.
163. Schuman, E. M.; Madison, D. V. *Science* **1994**, *263*, 532–536.
164. Culotta, E.; Koshland, D. E. Jr. *Science* **1992**, *258*, 1862–1865.
165. Feldman, P. L.; Griffith, O. W.; Stuehr, D. J. *Chem. Eng. News* **1993**, 26–38.
166. Beckman, J. S.; Koppenol, W. H. *Am. J. Physiology* **1996**, *271*, C1424–C1437.
167. Garrel, C.; Fontecave, M. Nitric oxide: chemistry and biology, "*Analysis of Free Radicals in Biological Systems*"; Eds. Favier, A. E.; Cadet, J.; Kalyanaraman, B.; Fontecave, M.; Pierre, J.-L.; Birkhauser Verlag: Basel, 1995, pp. 21–35.
168. Garthwaite, J.; Boulton, C. L. *Annu. Rev. Physiol.* **1995**, *57*, 683–706.
169. Doyle, M. P.; Hoekstra, J. W. *J. Inorg. Biochem.* **1981**, *14*, 351–358.
170. Eich, R. F.; Li, T.; Lemon, D. D.; Doherty, D. H.; Curry, S. R.; Aitken, J. F.; Mathews, A. J.; Johnson, K. A.; Smith, R. D.; G. N. Phillips, J.; Olson, J. S. *Biochem.* **1996**, *35*, 6976–6983.
171. Lee, J.; Hunt, J. A.; Groves, J. T. *J. Am. Chem. Soc.* **1988**, *120*, 7493–7501.
172. Hogg, N. Pro-oxidant and antioxidant effects of nitric oxide, "*Analysis of Free Radicals in Biological Systems*"; Eds. Favier, A. E.; Cadet, J.; Kalyanaraman, B.; Fontecave, M.; Pierre, J.-L.; Birkhauser Verlag: Basel, 1995, pp. 37–49.
173. Beckman, J. S. *J. Develop. Physiol.* **1991**, *15*, 53–59.
174. Pryor, W. A.; Squadrito, G. L. *Am. J. Physiol.* **1995**, *268*, L699–L722.
175. "*Nitric Oxide. Biology and Pathobiology*"; Ed. Ignarro, L. J.; Academic: San Diego, 2000, p. 1003.
176. Koppenol, W. H.; Kissner, R. *Chem. Res. Toxicol.* **1998**, *11*, 87–90.
177. Hodges, G. R.; Ingold, K. U. *J. Am. Chem. Soc.* **1999**, *121*, 10695–10701.
178. Coddington, J. W.; Hurst, J. K.; Lymar, S. V. *J. Am. Chem. Soc.* **1999**, *121*, 2438–2443.
179. Squadrito, G. L.; Pryor, W. A. *Chem. Res. Toxicol.* **2002**, *15*, 885–895.
180. Shimanovich, R.; Groves, J. T. *Arch. Biochem. Biophys.* **2001**, *387*, 307–317.
181. Stern, M. K.; Jensen, M. P.; Kramer, K. *J. Am. Chem. Soc.* **1996**, *118*, 8735–8736.
182. Herold, S.; Exner, M.; Nauser, T. *Biochemistry* **2001**, *40*, 3385–3395.
183. Lee, J.; Hunt, J. A.; Groves, J. T. *J. Am. Chem. Soc.* **1998**, *120*, 6053–6061.
184. Shimanovich, R.; Hannah, S.; Lynch, V.; Gerasimchuk, N.; Mody, T. D.; Magda, D.; Sessler, J.; Groves, J. T. *J. Am. Chem. Soc.* **2001**, *123*, 3613–3614.
185. Herold, S.; Matsui, T.; Watanabe, Y. *J. Am. Chem. Soc.* **2001**, *123*, 4085–4086.
186. Nemes, A.; Pestovsky, O.; Bakac, A. *J. Am. Chem. Soc.* **2002**, *124*, 421–427.
187. Bakac, A. *Int. J. Chem. Kin.* **2002**, *34*, 278–281.
188. Forni, L. G.; Mora-Arellano, V. O.; Packer, J. E.; Willson, R. L. *J. Chem. Soc. Perkin Trans.* **1986**, *2*, 1–6.
189. Stedman, G. *Adv. Inorg. Chem. Radiochem.* **1979**, *22*, 113–170.
190. Loegager, T.; Sehested, K. *J. Phys. Chem.* **1993**, *97*, 10047–10052.
191. Wick, P. K.; Kissner, R.; Koppenol, W. H. *Helv. Chim. Acta* **2001**, *84*, 3057–3062.
192. Matts, T. C.; Moore, P. *J. Chem. Soc. (A)* **1969**, 1997–2001.
193. Herold, S.; Rehmann, F.-J. K. *J. Biol. Inorg. Chem.* **2001**, *6*, 543–555.
194. Herold, S.; Rehmann, F.-J. K. *Free Radical Biol. Med.* **2003**, *34*, 531–545.
195. Ford, P. C.; Wink, D. A.; Stanbury, D. M. *FEBS Lett.* **1993**, *326*, 1–3.
196. Goldstein, S.; Czapski, G. *Inorg. Chem.* **1995**, *34*, 4041–4048.
197. Graetzel, M.; Henglein, A.; Taniguchi, S. *Ber. Bunsenges. Phys. Chem.* **1970**, *74*, 292–298.

198. DeLeo, M. A.; Ford, P. C. *J. Am. Chem. Soc.* **1999**, *121*, 1980–1981.
199. Herold, S. *Nitric Oxide: Biol. and Chem.* **1999**, *3*, 36.
200. Lee, J.; Hunt, J. A.; Groves, J. T. *J. Am. Chem. Soc.* **1998**, *120*, 7493–7501.
201. Herold, S. *FEBS Lett.* **1998**, *439*, 85–88.
202. Wick, P. K.; Kissner, R.; Koppenol, W. H. *Helv. Chim. Acta* **2000**, *83*, 748–754.
203. Cole, A. G.; Yoder, L. M.; Shiang, J. J.; Anderson, N. A.; Walker, L. A. II; Holl, M. M. B.; Sension, R. J. *J. Am. Chem. Soc.* **2002**, *124*, 434–441.
204. Wolak, M.; Stochel, G.; Hamza, M.; Van Eldik, R. *Inorg. Chem.* **2000**, *39*, 2018–2019.
205. Pestovsky, O.; Bakac, A. *Inorg. Chem.* **2002**, *41*, 901–905.
206. Hughes, E. D.; Ingold, C. K.; Ridd, J. H. *J. Chem. Soc.* **1958**, 77–82.
207. Hughes, E. D.; Ingold, C. K.; Ridd, J. H. *J. Chem. Soc.* **1958**, 65–69.
208. Garley, M. S.; Stedman, G. *Inorg. Nucl. Chem.* **1981**, *43*, 2863–2867.
209. Hughes, E.D.; Ridd, J.H.*J. Chem. Soc.* **1958**, 88–98.
210. Okano, M.; Ogata, Y. *J. Am. Chem. Soc.* **1953**, *75*, 5175–5177.
211. Turney, T. A.; Wright, G. A. *Chem. Revs.* **1959**, *59*, 497–513.
212. Park, J. Y.; Lee, Y. N. *J. Phys. Chem.* **1988**, *92*, 6294–6302.
213. Strukul, G. "*Catalytic Oxidations with Hydrogen Peroxide as Oxidant*"; Kluwer Academic Publishers: Dordrecht, 1992.
214. Lerdau, M. T.; Munger, J. W.; Jacob, D. J. *Science* **2000**, *289*, 2291–2293.
215. Espey, M. G.; Xavier, S.; Thomas, D. D.; Miranda, K. M.; Wink, D. A. *Proc. Natl. Acad. Sci. USA* **2002**, *99*, 3481–3486.
216. Pfeiffer, S.; Lass, A.; Schmidt, K.; Mayer, B. *FASEB J.* **2001**, *15*, 2355–2364.
217. Huie, R. E.; Neta, P. *J. Phys. Chem.* **1986**, *90*, 1193–1198.
218. Pestovsky, O.; Bakac, A. *Inorg. Chem.* **2003**, *42*, 1744–1750.
219. Balzani, V.; Ballardini, R.; Sabbatini, N.; Moggi, L. *Inorg. Chem.* **1968**, *7*, 1398–1404.
220. Bartberger, M. D.; Liu, W.; Ford, E.; Miranda, K. M.; Switzer, C.; Fukuto, J. M.; Farmer, P. J.; Wink, D. A.; Houk, K. N. *Proc. Natl. Acad. Sci. USA* **2002**, *99*, 10958–10963.
221. Shafirovich, V.; Lymar, S. V. *Proc. Natl. Acad. Sci. USA* **2002**, *99*, 7340–7345.
222. Stanbury, D. M. *Adv. Inorg. Chem.* **1989**, *33*, 69–138.
223. Koppenol, W. H.; Moreno, J. J.; Pryor, W. A.; Ischiropoulos, H.; Beckman, J. S. *Chem. Res. Toxicol.* **1992**, *5*, 834–842.
224. Merenyi, G.; Lind, J.; Engman, L. *J. Chem. Soc. Perkin Trans.* **1994**, *2*, 2551–2553.
225. Goldstein, S.; Czapski, G. *Inorg. Chem.* **1997**, *36*, 4156–4162.
226. Lammel, G.; Perner, D.; Warneck, P. *J. Phys. Chem.* **1990**, *94*, 6141–6144.
227. Regimbal, J.-M.; Mozurkewich, M. *Journal of Physical Chemistry A* **1997**, *101*, 8822–8829.
228. Pestovsky, O.; Bakac, A. *J. Mol. Cat. A* **2003**, *200*, 21–29.
229. Casado, J.; Lorenzo, F. M.; Mosquera, M.; Prieto, M. F. R. *Can. J. Chem.* **1984**, *62*, 136–138.
230. Bourassa, J. L.; Ives, E. P.; Marqueling, A. L.; Shimanovich, R.; Groves, J. T. *J. Am. Chem. Soc.* **2001**, *123*, 5142–5143.

This Page Intentionally Left Blank

REDOX REACTIVITY OF COORDINATED LIGANDS IN PENTACYANO(L)FERRATE COMPLEXES

JOSÉ A. OLABE

Departamento de Química Inorgánica, Analítica y Química Física, and INQUIMAE, Facultad de Ciencias Exactas y Naturales, Universidad de Buenos Aires, Pabellón 2, Ciudad Universitaria, C1428EHA, Buenos Aires, Argentina

I. Introduction
II. General Properties of the Nitroprusside ion, $[Fe(CN)_5NO]^{2-}$ (NP), and Related Nitrosyl Complexes
III. The Coordination Chemistry of NO. Formation and Dissociation Reactions
IV. The Redox Reactivity of Bound NO
V. The Electrophilic Reactions of Bound NO
  A. Reactivity of Nitrosyl Complexes with OH^-
  B. Reactivity of NP with Hydrazine (Hz), MeHz, and 1,1-Me_2Hz
  C. Reactivity of NP with 1,2-Me_2Hz
  D. Reactivity of NP with other Nitrogen Hydrides: NH_2OH, NH_3, and N_3^-
  E. Reactivity of NP with Aliphatic Amines in Organic Solvents
  F. Reactivity of NP with Trioxodinitrate, $N_2O_3^{2-}$
VI. The Autooxidation of Hydrazine
VII. The Oxidation of Amines and Alcohols
VIII. The Disproportionation of Hydroxylamine
IX. Miscellaneous Reactions
  A. The Reaction of $[Fe(CN)_5H_2O]^{3-}$ with O_2 and H_2O_2
  B. The Coordination Chemistry of Sulfite
  C. The Reaction of $[Fe(CN)_5L]^{n-}$ ($L = NO^+$ and H_2O) with SH^- and Thiolates, SR^-
  D. Modification of Electron Transfer Reactivity upon Cyano-Bridge Formation
  E. Intramolecular Redox Assistance of Bimolecular Redox Reactions
X. Conclusions
References

I. Introduction

The coordination chemistry of transition metal cyanometallates has been of great and long standing concern because of the fundamental issues related to their electronic structure and reactivity. It has been

ADVANCES IN INORGANIC CHEMISTRY
VOLUME 55 ISSN 0898-8838 DOI 10.1016/S0898-8838(03)55002-4

© 2004 Elsevier Inc.
All rights reserved.

comprehensively reviewed (*1*), together with more recent developments on the solid state chemistry, comprising new synthetic and structural aspects relevant to the properties of advanced materials (*2*). Complexes containing variable relations of cyanide with other ligands in the first coordination sphere are known; however, in the present review we deal specifically with the pentacyano(L)ferrate(II) and -(III) complexes, with particular emphasis on the redox changes associated, with L. A review has been published on the basic synthetic, spectroscopic and reactivity properties of these systems (*3*). The reactivity issues comprised ligand interchange reactions (formation, dissociation, and isomerization), electron transfer and photochemical reactions, as well as some applications in dinuclear mixed-valence complexes and bioinorganics. A detailed account on the importance of high-pressure mechanistic studies for the different types of reactivity associated with the pentacyanoferrate complexes, has also been published (*4*). A more recent review reports on the advances in the chemistry of the pentacyano(L)ferrates, as well as on the ruthenium and osmium analogues, with a preliminary account of the subjects raised in this chapter (*5*). Photochemical studies have been exhaustively considered elsewhere (*4,6*), and are therefore omitted in this report. Much of the content of the present review draws heavily on the collaborative work performed by our group in recent years. This was firmly supported by the pioneering work undertaken in the 1970s by H. E. Toma, J. M. Malin and coworkers, and followed by a large number of other contributors to the field over the past two decades.

The ligands (L) binding to the $[Fe^{II}(CN)_5]^{3-}$ fragment are quite diverse (*3–5*). A key complex is $[Fe^{II}(CN)_5H_2O]^{3-}$, which can be easily prepared in solution through aquation of $Na_3[Fe(CN)_5NH_3] \cdot 3H_2O$ (*7*). The aqua-complex is an unstable species, leading to Prussian-blue type complexes as a result of the release and recombination of cyanides (*8*). It has not been isolated as a pure solid but it is an effective intermediate for binding many other L ligands, forming moderate-to-strongly stable complexes (10^3–10^6 M^{-1}) which have been well characterized in solution and generally also in the solid state ($L = NH_3$, amines, diamines, hydrazine, nitrosyl, CO, dmso, phosphines, *N*-heterocyclic ligands: py, pz and derivatives, and so forth). The complex with $L = NH_3$ can be easily prepared starting from the well known nitroprusside ion (NP), through the reaction with NH_3 (*7c,7d*), and it is currently used as a precursor for the preparation of other complexes, by simple substitution with the desired L ligand. Many of these Fe(II) complexes containing L ligands with low-energy LUMOs display intense metal-to-ligand charge-transfer (MLCT) absorptions in

the visible region, with the energies depending on the π-acceptor ability of L. An important advantage of the reviewed systems is the accessibility of Fe(III) complexes (*3–5*). Intense, visible-absorption bands are also shown by some of them (L = azide, thiocyanate, thiolates, etc.), suggesting a ligand-to-metal charge-transfer (LMCT) origin. These versatile spectroscopic features have been of crucial importance for the identification of products and/or intermediates in the kinetic and mechanistic studies. The redox potentials for the $[Fe^{III/II}(CN)_5L]^{2-/3-}$ couples span a range from ca. 0.4 up to 1.0 V (vs. NHE), depending on the ligand L (*3*).

Mixed-valence cyano complexes with diverse bridging ligands have been prepared. Particularly important are the "Creutz-Taube analogs", $[(NC)_5M^{II}–pz–M^{III}(CN)_5]^{5-}$ (pz = pyrazine; M = Fe, Ru, Os), which show remarkable changes in the electronic structure upon dissolution in different solvents (*9*). In fact, the iron mixed-valence complex appears to be a strongly localized (Class II) species in aqueous solution. It changes to a much more valence-delocalized complex in aprotic solvents such as acetonitrile, showing a borderline Class II/III behavior (*9,10*). Cyanide has also been intensively used as a bridging ligand; a vast amount of complexes of the $[(NC)_5M^{II}–CN–M^{III}(X)_5]^n$ series have been prepared with $X = CN^-$, NH_3, EDTA, polypyridines and other ancillary ligands, mainly but not exclusively with group 8 metals, showing that cyanide is a good communicating bridge for charge mediation between the metal centers. We address here only a few developments for these systems, particularly related to redox reactivity changes upon coordination of a cyano ligand through the exposed N-donor. The subject has been partially reviewed (*5*), and we suggest the interested reader to consult some specific reviews dealing with the general properties of cyano-bridged complexes, including the issue of electronic coupling and multi-electron charge transfer processes between the metal centers (*5,11*).

The present review will focus on the redox chemistry of small nitrogen-containing L ligands with bioinorganic relevance, particularly nitric oxide, NO, and its redox-interconverted forms NO^+ (nitrosyl) and NO^- (nitroside, or its protonated form, HNO, nitroxyl) (*12,13*). The ligand interchange reactions of NO will be analyzed in the context of better understanding the redox properties of the bound ligand. Both the chemically and electrochemically induced oxidation and reduction of the appropriate bound species will be considered. Comparisons between the chemistry of bound NO in NP with that found in NO–porphyrins and –chelates will be analyzed on the basis of their specific relevance to biochemical and environmental issues.

The reductive NO chemistry will cover some new developments on the electrophilic reactions of bound nitrosyl with different nucleophiles, particularly the nitrogen hydrides (hydrazine, hydroxylamine, ammonia, azide) and trioxodinitrate, along with new density functional theoretical (DFT) calculations which have allowed to better understand the detailed mechanistic features of these long-studied addition reactions, including the one with OH^-. The redox chemistry of other molecules relevant to biochemistry, such as O_2, H_2O_2 and the thiolates (SR^-) will also be presented.

The catalytic nature of some of these redox reactions will be highlighted, given the labile character of H_2O in the $[Fe^{II}(CN)_5H_2O]^{3-}$ ion. Structural and functional comparisons will be made regarding the behavior of iron-enzymes associated with the nitrogen redox cycle (*14*). Overall, the review deals mainly with the chemistry in aqueous media, with occasional mention to work in organic solvents. Cyanometallate complexes are known to display profound changes in their electronic structure and reactivity when dissolved in solvents with different acceptor capability, associated with the donor properties of the exposed electron pairs at the cyano ligands (*15*). These specific interactions are also related to the role of cationic association in the thermodynamics and kinetics of the reactions involving cyano complexes (*16*).

II. General Properties of the Nitroprusside ion, $[Fe(CN)_5NO]^{2-}$ (NP), and Related Nitrosyl Complexes

Sodium nitroprusside was first prepared and investigated in the middle of the nineteenth century, and a comprehensive summary of the earlier chemical investigations has been published (*17*). Up to 1910–1930, the addition reactions of bases to NP were explored, involving the characterization of colored intermediates (e.g., with SH^-, SR^-, and SO_3^{2-}), useful for analytical purposes. The hypotensive action of NP was first demonstrated in 1929, and a considerable research effort has attempted to establish the mode of action of NP and its metabolic fate. Questions still arise on the mechanism of NO release from NP in the biological fluids, and we refer to them below. New accounts dealing with modern structural and reactivity issues associated with the coordination of nitrosyl in NP and other complexes have appeared (*18–20*). From the bioinorganic and environmental viewpoint, nitrosyl–iron complexes have been studied with

different spectator ligands, with a recent emphasis on porphyrins (related to hemoproteins), carboxyl-binding chelates, and other biologically relevant ligands such as imidazolates and thiolates (*21,22*). According to the Enemark–Feltham notation (E–F) (*23*), the nitrosyl complexes are described as $\{MNO\}^n$, with n standing for the number of electrons associated with the metal d and π^*_{NO} orbitals. Thus, NP can be described as a member of the $\{FeNO\}^6$ class. In combination with a Walsh MO treatment, a linear FeNO structure is predicted. This electron-counting formalism considers that the {MNO} moiety is delocalized, *avoiding the use of formal oxidation numbers* for the metal or the NO ligand. For assigning the detailed electronic distribution in the {MNO} unit (on which the nature of the spectator ligands not included in the E–F description, may have an influence), diverse spectroscopic tools must be used (IR, EPR, Moessbauer, etc.) (*24*). Some ambiguity can remain, as shown below, and this is probably the reason for still assigning formal charges inside the {MNO} moieties. We refer to appropriate reviews for the discussion of the electronic structure problem (*18,23*). For NP, the idealized description as $\{Fe^{II}NO^+\}$ is generally accepted, based on its geometry, diamagnetism, IR properties (high NO stretching frequency, 1918 cm^{-1}), and short Fe–N distance (1.66 Å), consistent with a strong, multiple bond. From the reactivity viewpoint, the NO^+ ligand is attacked by nucleophiles (see below), although it is extremely inert toward thermal dissociation, which is not detectable. Similar properties arise for other classical coordination complexes where the above description is also accepted (*25,26*). However, the reversible binding studies of NO with diverse ferri-heme proteins and complexes show very fast dissociation rates in the range of 10^3–10^7 s^{-1}, which seems to be at odds with the claimed $\{Fe^{II}NO^+\}$ formulation for $n=6$ (*25*). In fact, the best limiting description of ferri-heme nitrosyls with $n=6$ is still not clearly established. Both the low-spin $\{Fe^{II}NO^+\}$ or the antiferromagnetically coupled $\{Fe^{III}NO\}$ description have been proposed, depending on the selected spectroscopic or reactivity property under consideration (*24,27*). The $\{Fe^{II}NO^+\}$ electronic distribution is usually associated with the electrophilic reactivity, and this has been certainly observed both with classical coordination complexes and with ferri-heme compounds (*25,26,28*). On the other hand, the $\{Fe^{III}NO\}$ description seems to be more adequate for explaining the high NO-dissociation rate from the iron center in the ferri-hemes. We shall come back to this important issue.

In recent years, the photoinduced linkage isomerization reactions of bound nitrosyl appearing in different complexes have been

comprehensively studied (*19*). Pioneering studies with NP and later with other $\{MNO\}^6$ complexes (M = group 8 metals, mainly ruthenium), have shown that side-bound η^2-NO and linear η^1-ON (isonitrosyls) can be generated in situ by low-temperature laser irradiation. The characterization of the linkage isomers has been done by studying the thermal decay of the photoinduced species through differential scanning calorimetry (DSC) (*29*), as well as by IR (*30*) and Raman spectroscopies (*31*). Theoretical calculations on the ground, metastable, and excited states of NP, including the end-to-end interconversion of nitrosyl and isonitrosyl in NP have been reported (*32*). The solid-state structures have been solved by modern photocrystallographic techniques (*33*). The isomers of other small molecules (N_2, NO_2^-, SO_2) have been similarly characterized (*19*). It has been proposed (*18*) that these linkage isomers could be true intermediates on the reaction coordinate for the reversible NO-binding into the $\{FeNO\}^6$ heme-protein nitrophorin 1, existing in the saliva of some blood-sucking insects (*27*). Probably this could also be the case for the chemical and photochemical reactions associated with NO coordination and further release in NP and other nitrosyl-complexes (see below).

III. The Coordination Chemistry of NO. Formation and Dissociation Reactions

The title reactions have been insufficiently investigated. Emerging studies with iron–porphyrins and –polycarboxylic chelates (*21,22*) are directed at the significance of nitrosyl in biochemically and environmentally significant issues (*20*). The use of gaseous NO as a synthetic precursor to {MNO} complexes (free of oxidizing impurities!) is contributing to discern on the fundamental properties of NO as a ligand, the preservation of its radical character upon coordination, and the redox interconversions leading to (formally) NO^+ or NO^- (HNO) bound species. With classical coordination compounds, the studies with pentacyano(L)ferrate(II) and -(III) systems have been very recently considered for L = NO (*34,35*). The mechanisms of ligand interchange with the $[Fe^{II/III}(CN)_5L]^{3-/2-}$ complexes have been studied for a broad range of ligands L, and have been comprehensively reviewed (*3–5*). It is generally accepted that dissociative mechanisms are operative, both for the formation and dissociation reactions. We show the case for L = NO and Fe^{II} (*34*) in reaction (1):

$$[Fe^{II}(CN)_5H_2O]^{3-} + NO \rightleftarrows [Fe^{II}(CN)_5NO]^{3-} + H_2O \quad k_1,\ k_{-1} \qquad (1)$$

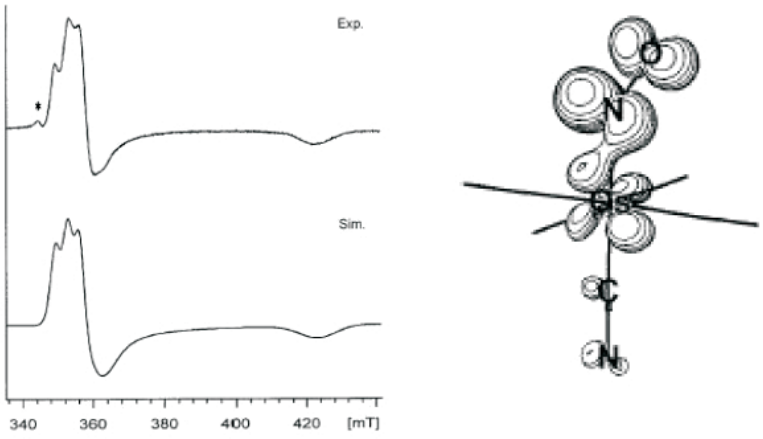

FIG. 1. (Left) Experimental and simulated EPR spectra of electrogenerated $[Os(CN)_5NO]^{3-}$ in AcN/0.1 M Bu_4NPF_6, at 3.5 K. (The asterisk denotes a low-field impurity.) (Right) Spin density distribution within $[Os(CN)_5NO]^{3-}$.

The product is a well characterized, paramagnetic $\{FeNO\}^7$ species ($S=\frac{1}{2}$) (*36*). It can be best described as a $\{Fe^{II}NO^{\bullet}\}$ unit containing a bent FeNO structure, and the EPR results and DFT calculations show that around 60% of the spin density is on the nitrosyl ligand (mainly on N), with ca. 30% remaining on iron (*37*). Figure 1 shows the experimental and simulated spectra found for the $[Os(CN)_5NO]^{3-}$ complex, together with the spin density distribution. The EPR spectral results and interpretation for the iron-derivative (*36b*) allow to propose a similar geometry and electronic distribution for the three pentacyano-complexes, which can be extended to other reduced nitrosyl-complexes containing mainly ruthenium (*26*).

The value of k_1 is 250 ± 10 M^{-1} s^{-1} (25.4 °C, $I=0.1$ M, pH 7.0), in agreement with similar values found for the entry of many other neutral ligands into $[Fe^{II}(CN)_5H_2O]^{3-}$ (*3–5*). The activation parameters are: $\Delta H^{\#} = 70 \pm 1$ kJ mol^{-1}, $\Delta S^{\#} = +34 \pm 4$ J K^{-1} mol^{-1}, $\Delta V^{\#} = +17.4 \pm 0.3$ cm^3 mol^{-1} (*34*). These results are in agreement with a rate-controlling water release step followed by a fast coordination of NO, supporting a dissociative mechanism, most probably D (*38*). It can also be inferred that no particular influence of the unpaired electron on NO exists on the formation reaction, concluding that NO behaves as other Lewis-basic diamagnetic ligands. As to the reverse reaction in Eq. (1), the interpretation of the results is complicated by the occurrence of

reaction (2), which is an example of the general instability of $\{MNO\}^7$ complexes toward the labilization or even release of a spectator *trans*-ligand (*12,20,24*). An interesting "organic analogue" of the NO^+/NO ligand redox system was found for the mpz^+/mpz pair bound to $[Fe^{II}(CN)_5]^{3-}$ (mpz^+: *N*-methylpyrazinium ion) (*39*). The mpz-centered one-electron reduction also showed the subsequent loss of cyanide, as studied by spectroelectrochemistry and EPR techniques. The mpz^+ ligand is also a weak σ-donor as well as a strong π-acceptor, although weaker than NO^+.

$$[Fe(CN)_5NO]^{3-} \rightleftarrows [Fe(CN)_4NO]^{2-} + CN^- \quad k_2, k_{-2} \tag{2}$$

From the values of $k_2 = 2.8 \times 10^2$ s^{-1} and $K_2 = 6.8 \times 10^{-5}$ M (*40*), it follows that $[Fe(CN)_5NO]^{3-}$ is the predominant species at pH 10. When cyanide was added to the mixture, the dissociation rate of NO from $[Fe(CN)_5NO]^{3-}$ could be measured without significant interference of the tetracyano complex. Besides, cyanide also acted as a scavenger of the $[Fe^{II}(CN)_5H_2O]^{3-}$ ion in the reverse process of Eq. (1), forming $[Fe(CN)_6]^{4-}$ as a final product (*34*). In this way, the pseudo-first order decay of $[Fe(CN)_5NO]^{3-}$ allowed to obtain $k_{-1} = k_{-NO} = 1.58 \times 10^{-5}$ s^{-1} (25.0 °C, $I = 0.1$ M, pH 10.0), with $\Delta H^{\#} = 106.4 \pm 0.8$ kJ mol^{-1}, $\Delta S^{\#} = +20 \pm 2$ J K^{-1} mol^{-1} and $\Delta V^{\#} = +7.1 \pm 0.2$ cm^3 mol^{-1}. The results also agree with a dissociative mechanism, although a quantitative interpretation of the magnitude of the activation volume waits for more available data on NO-dissociation processes in related systems.

Table I shows a comparative display of dissociation rate constants and activation parameters for a selected group of $[Fe^{II}(CN)_5L]^{n-}$ complexes. In agreement with a dissociative behavior, it can be seen that the values of k_d strongly depend on L. Although the activation enthalpies and positive entropies suggest a compensation effect, the overall picture supports the dissociative assignment (*3–5*). The value of k_{-NO} is significantly larger than for $L = CN^-$ and CO (ca. 10^{-7}–10^{-8} s^{-1} at 25 °C) (*41,42*). It is of the same order of magnitude as for the release of other σ–π binding ligands such as dmso (*43*), pyrazine or pyridine (*44*), and much smaller than for the σ-only binding ammonia ligand (*45*). This suggests that neutral NO is a moderate σ-donor and a π-acceptor. As expected, it behaves as a stronger σ-donor although a much weaker π-acceptor than NO^+ in NP. Given the correlation between the energies of the electronic *d–d* absorption bands and the dissociation rate constants for L in the $[M^{II}(CN)_5L]^{n-}$ series (*46*),

TABLE I

DISSOCIATION RATE CONSTANTS AND ACTIVATION PARAMETERS FOR DIFFERENT $[Fe(CN)_5L]^{n-}$ COMPLEXES

Ligand	k_d (s^{-1})	$\Delta H_d^{\#}$ (kJ mol^{-1})	$\Delta S_d^{\#}$ (J K^{-1} mol^{-1})	$\Delta V_d^{\#}$ (cm^3 mol^{-1})	Ref.
NO^+	not detected	–	–	–	
CO[b]	$< 10^{-8}$				(*41*)
CN^- [c]	ca. 4×10^{-7}				(*42*)
NO	1.58×10^{-5}	106.4 ± 0.8	$+20 \pm 2$	$+7.1 \pm 0.2$	(*34*)
dmso	7.5×10^{-5}	110.0	+46.0		(*43*)
pz	4.2×10^{-4}	110.5	58.6	13.0	(*44*)
py	1.1×10^{-3}	103.8	46.0		(*44*)
NH_3	1.75×10^{-2}	102	+68	+16.4	(*45*)

$T = 25.0\,^{\circ}C$; $I = 0.1$ M.

[b]Estimated number, measured using pz as a scavenger.

[c]Extrapolated from data reported at higher temperatures.

we are now able to include both NO and NO^+ ligands in the "spectrochemical series" (cf. Table I). The release of NO from some five-coordinate $\{FeNO\}^7$ ferro–heme proteins (*21,25*) yields values of the same order of magnitude as k_{-NO} in $[Fe(CN)_5NO]^{3-}$, although important labilizing effects have been found by introducing different substituents in the porphyrin ring (*47*). Values in the range $1–10^{-4}$ s^{-1} have been measured for the *trans*-$[Ru^{II}(NH_3)_4X(NO)]^{2+}$ complexes ($X = H_2O$, py, im–N, im–C, $P(OEt)_3$, etc.), as well as for *trans*-$[Ru(cyclam)(H_2O)(NO)]^{2+}$ (6.1×10^{-4} s^{-1}). It has been proposed that the *trans* effect and *trans* influence of the X ligand control the NO dissociation rates (*26*). How the rate of release of NO depends on the metal and/or the spectator ligands could be better understood by extending the work to other appropriate series.

The value of k_{-NO} in $[Fe(CN)_5NO]^{3-}$ has physiological significance, because it is believed that NO is released to the medium provided that the thiolates present in the biological fluids are able to reduce NP following injection in the blood stream in the hypertensive situations (*20,48*). Given the fast response to this stimulation (*20*), k_{-NO} shows a much too small value. More probably, the competing reaction (2) is operative, allowing for final NO release through the decomposition of $[Fe(CN)_4NO]^{2-}$ (*48*). We refer below to this important set of reactions, related to the electrophilic reactivity of NP toward thiolates.

The coordination of NO to the $[Fe^{III}(CN)_5H_2O]^{2-}$ ion [Eq. (3)] affords a first order rate law in each reactant, with $k_3 = 0.252 \pm 0.004$ M^{-1} s^{-1}

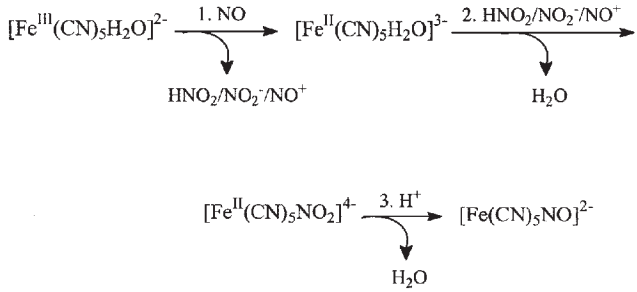

FIG. 2. Proposed mechanism involving initial reduction of $[Fe^{III}(CN)_5H_2O]^{2-}$ by NO, forming $[Fe^{II}(CN)_5H_2O]^{3-}$, with final conversion to NP.

at 25.5 °C, $I = 0.1$ M, and activation parameters: $\Delta H^{\#} = 52 \pm 1$ kJ mol^{-1}, $\Delta S^{\#} = -82 \pm 4$ J K^{-1} mol^{-1} and $\Delta V^{\#} = -13.9 \pm 0.5$ cm^3 mol^{-1} (*35*). The quantitative product is NP, and k_{-3} may be considered to be zero.

$$[Fe^{III}(CN)_5H_2O]^{2-} + NO \rightleftarrows [Fe(CN)_5NO]^{2-} + H_2O \quad k_3, k_{-3} \qquad (3)$$

For the much slower coordination reactions of several ligands L to $[Fe^{III}(CN)_5H_2O]^{2-}$ (k = ca. 10^{-4}–10^{-7} M^{-1} s^{-1}), a dissociative interchange (I_d) mechanism has been suggested (*3–5,49*). The data for reaction (3), particularly the negative values of the entropy and activation volume do not agree with the I_d mechanism, which predicts positive values in both cases. On the other hand, Fig. 2 describes the proposed mechanism.

The reaction involves a rate-determining reduction of Fe(III) to Fe(II) as a first step. Although an outer-sphere mechanism was proposed, the value of k_3, together with the redox potential of the NO^+/NO couple (1.21 V vs. NHE) (*13*), excludes this possibility. Instead, NO could behave as a reductant, following its association with cyanides in the precursor complex. After electron transfer, NO^+ is rapidly hydrolyzed to nitrite (or HNO_2, depending on pH), with further coordination of either of the latter species into the $[Fe^{II}(CN)_5H_2O]^{3-}$ ion, forming NP as the final product (*35*). Evidence for the formation of $[Fe^{II}(CN)_5H_2O]^{3-}$ as an intermediate was obtained through competition experiments in which several L ligands (pz, NCS^-, etc.) were used as trapping agents. Figure 3 shows the modified mechanistic scheme including the new experimental evidence. A complementary investigation of the reactivity of other $[Fe^{III}(CN)_5L]^{n-}$ complexes toward NO (L = py, pz, nitrite, cyanide) showed that NO also reacted in the

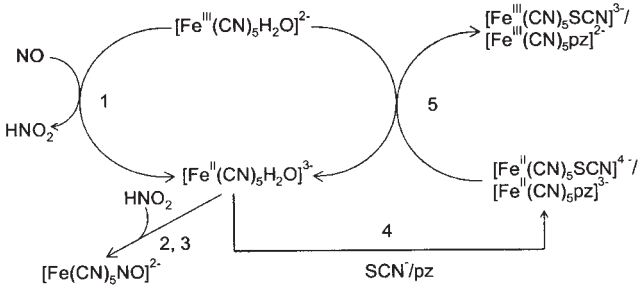

FIG. 3. Mechanistic scheme for the reaction of $[Fe^{III}(CN)_5H_2O]^{2-}$ with NO, showing the competition experiments for trapping the $[Fe^{II}(CN)_5H_2O]^{3-}$ intermediate by different ligands (pz, NCS^-).

first step through the formation of intermediate $[Fe^{II}(CN)_5L]^{(n+1)-}$ complexes (*35*).

The above mechanistic interpretation is in contrast with the one appearing in the coordination chemistry of NO on the very labile Fe(III)–porphyrins and hemoproteins, which show water substitution-controlled kinetics at the iron(III) center (*22,25*). The latter Fe(III) moieties are, however, high-spin systems, whilst the cyano-complexes are low-spin. There is strong experimental evidence to support the dissociative mechanism with the Fe(III)–porphyrins, because the rates are of the same order as the water-exchange reactions measured in these systems (*22d*). Besides, the Fe(III) centers are less oxidizing than $[Fe^{III}(CN)_5H_2O]^{2-}$ (*21,25*).

In spite of the above mechanistic insight into the initial stages of NO coordination to the ferriheme systems, the fact is that the so-called reductive nitrosylation reaction has been observed for the water-soluble ferri-heme model Fe(III)TPPS in aqueous solution (H_2TPPS^{4-} = tetraanionic form of *meso*-tetrakis(*p*-sulfonatophenyl)porphyrin), as well as for Cyt^{III}, metMb and metHb reacting with NO at various pHs, even in slightly acidic media, pH range 6–8 (*25,50*). Figure 4 describes the proposed reaction scheme for the overall reductive nitrosylation process.

Good linear plots of the pseudo-first order rate constant for the formation of Cyt^{II} from Cyt^{III} as a function of $[OH^-]$ have been found, supporting the above mechanism. Although no evidence for the N-bound nitrous acid intermediate complex was found, the k_{OH} values derived from the slopes, together with the redox potentials for nitrosyl reduction in the heme compounds are in fair agreement with the general behavior observed for the electrophilic reactions of other nitrosyl complexes, including NP (see below) (*51*).

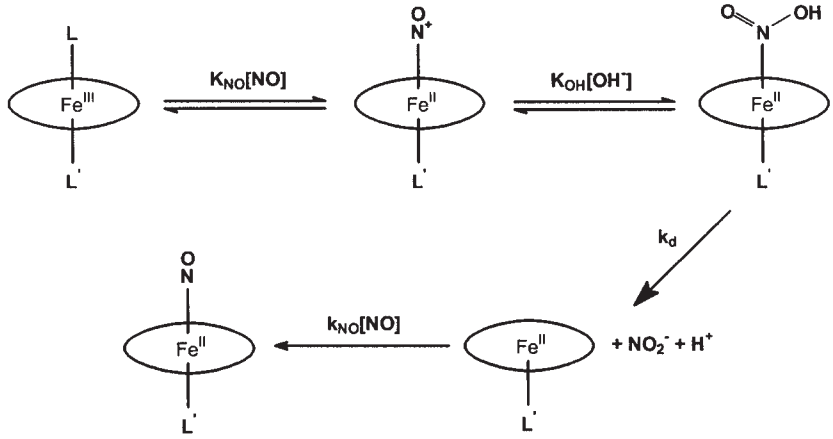

FIG. 4. Reductive nitrosylation of ferrihemes. Proposed formation of $\{Fe^{II}NO^{+}\}$ as a precursor for nucleophilic attack of OH^{-} forming the bound nitrous acid intermediate. The release of nitrite forms a labile Fe^{II} species which binds NO forming the inert $\{Fe^{II}NO\}$ complex.

As shown in Fig. 4, a $\{Fe^{II}NO^{+}\}$ species has been proposed to be formed following coordination of NO into Fe(III). This reaction appears to be related to the one in Eq. (3), associated with NP formation. However, the electron-transfer step must proceed in an inner-sphere way in the Fe(III)–porphyrin system, subsequently to the water-release. As anticipated above, the evidence on the detailed electronic structure in the ferri-hemes is still ambiguous (*24,25*). Whether the species formed in the reaction of the oxidized form of heme cd_1 nitrite reductase (NiR) with NO is best formulated as $\{Fe^{II}NO^{+}\}$ or $\{Fe^{III}NO\}$ has been qualified as a matter of semantics (*52*) (cf. the E–F formalism), although it has been recognized that substantial donation of charge from NO to Fe(III) has occurred, supporting the $\{Fe^{II}NO^{+}\}$ description. The release of NO from nitrite solutions mediated by the NiR enzyme proceeds according to Eq. (4) (*14*):

$$NO_2^- + e^- + 2H^+ \xrightarrow{NiR} NO + H_2O \qquad (4)$$

The kinetics of nitrite reduction by the heme cd_1 NiR has been studied by stopped-flow (SF) and rapid-freeze EPR spectroscopy (*53*). The first step is reported to involve very fast (out of the SF time scale) binding and proton assisted dehydration of the

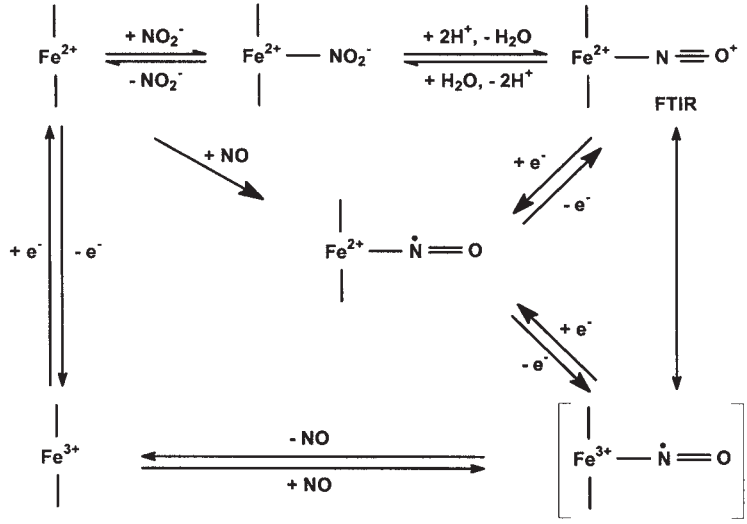

FIG. 5. Proposed mechanism for reduction of nitrite by the heme cd_1 containing nitrite reductases.

nitrite ligand to the $c^{II}d_1{}^{II}$ heme, resulting in the formation of a nitrosyl species, which is generally described as $\{Fe^{II}NO^+\}$. In Ref. (*53*), it was described as $c^{II}d_1{}^{III}NO$, suggesting it as the precursor of NO release. In the second step, an electron is transferred from the heme c^{II} to heme $d_1{}^{III}$, with a rate constant of 1 s^{-1} to form the paramagnetic $c^{III}d_1{}^{II}NO$ complex, which is rapidly reduced to $c^{II}d_1{}^{II}NO$ by an external reductant. On the basis of this and related work (particularly the evidence for the intermediacy of a Fe–nitrosyl species which is capable of undergoing nucleophilic attack by different nucleophiles such as water, azide, hydroxylamine) (*54*), Fig. 5 describes the proposed mechanism of action for the heme cd_1 NiR (*14*).

When oxidized NiR was put in contact with NO, the $\{Fe^{II}NO^+\}$ intermediate was directly observed by FTIR spectroscopy ($\nu_{NO} = 1910$ cm^{-1}) (*52*). This agrees with similar values of the stretching frequency measured for related ferri-hemes (*24*). The high values (compared to the ferro-hemes), together with the short N–O distances (1.63–1.65 Å) are consistent with a multiple bond, and indeed support the $\{Fe^{II}NO^+\}$ description, as generally accepted for NP and other classical nitrosyl complexes.

In spite of the above analysis, the remarkable fact related to the enzyme function is the ability of this $\{FeNO\}^6$ species to release NO.

The same can be said on the fast NO-release from the ferriheme compounds (*22*). It has been proposed that the heme $\{Fe^{II}NO^{+}\}$ moieties are highly reactive toward NO release, provided that they are not trapped by a nucleophile or reduced by one electron to the very stable Fe^{II}–NO species (*14*). We are now considering a comparison with the behavior of NP toward dissociation.

As shown above, the reverse reaction (3) was undetectable, in full agreement with the $\{Fe^{II}NO^{+}\}$ description. The two factors analyzed above influencing the instability of the NiR enzyme are absent for NP under normal physiological conditions. The conversion of bound NO^{+} to nitrite and further release of the latter species to the medium occur at pHs higher than 10 for NP (*55*). Besides, NP can be transformed into the moderately inert $[Fe^{II}(CN)_5NO]^{3-}$ (although more labile compared to NP, see above) under reducing conditions. Then, we can postulate that NO^{+} should be extremely inert toward dissociation in the different systems, unless some specific factor promoting labilization is present.

Another comparative issue between NP and the ferri-hemes emerges from the photochemical studies with NP, which have been early and successively investigated. The stoichiometry corresponds to the one observed in the reverse reaction of Eq. (3) (*6,56*). We may consider that the $\{Fe^{II}NO^{+}\}$ ground state in NP converts to an excited state upon irradiation, whose electronic structure is not clearly defined. It could be described as $\{Fe^{III}NO\}$, considering that the photoinduced electron transfer comprises a bonding–antibonding transition, which weakens the Fe–N bond. The fast ensuing release of NO has been quantitatively studied under different conditions, although the mechanistic details and the timing of NO release are still unknown (*6*).

The photochemical process with NP resembles the above described *thermal* one occurring in the NiR enzymes (see Eq. (4) and Fig. 5). In fact, the reduction of nitrite in the presence of $[Fe^{II}(CN)_5H_2O]^{3-}$ and the release of NO could be made photocatalytic, on the basis of the following scheme, provided that an external reductant was allowed to reduce $[Fe^{III}(CN)_5H_2O]^{2-}$ back to $[Fe^{II}(CN)_5H_2O]^{3-}$.

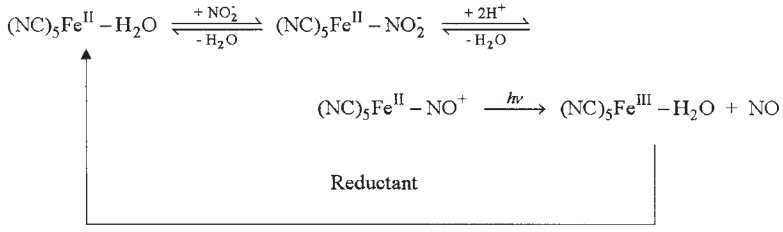

Given that a *thermal* intramolecular redox reaction converting $\{Fe^{II}NO^+\}$ to a putative redox isomer $\{Fe^{III}NO\}$ may be rejected in NP, on the basis of the not detected NO dissociation for the reverse reaction in Eq. (3), the contrast with the heme systems becomes remarkable. Why the NiR enzyme or other ferrihemes are an exception probably relates to possible labilizing factors associated with the heme structure, as commented above for the dissociative behavior of several ferro-hemes (*47*). One could suspect that the fast release of NO in the flash-photolysis experiments with the ferri-hemes in the presence of NO could be related to the relaxation of the non-steady-state system back to equilibrium comprising the decay of an excited state species. However, studies performed in parallel using either flash-photolysis or stopped-flow techniques provided the same k_{off} values (around 30–50 s^{-1} at 25 °C) for the release of NO in experiments performed with metmyoglobin–NO mixtures (*22c*). Although a limiting Fe^{II}–NO^+ description has been adopted to ascribe the above nitrosyl complex, it is probable that the electronic structure resembles an intermediate situation between the above one and Fe^{III}–NO, or that a thermally accessible state with the latter configuration is involved in the dissociation process.

For NP, not only the dissociation rate of the formally NO^+ ligand is undetectable, but neither can the coordination of NO^+ to $[Fe^{II}(CN)_5H_2O]^{3-}$ be studied, because NO^+ is very rapidly converted to nitrite in aqueous solutions (*12,13*). Similar considerations can be raised on the coordination ability of the one-electron reduced form of NO, namely NO^- or HNO. These species are also highly reactive as precursors of N_2O in aqueous media (*13*), and therefore the formation reactions, as in Eqs. (1) and (3), cannot be studied.

IV. The Redox Reactivity of Bound NO

The one-electron electrochemical reduction of NP (*57*) is a reversible process in aqueous solution, provided the measurements are performed at pH > 8 (−0.123 V vs. NHE) *(57a,57b)*. Different chemical reductants such as sodium in liquid ammonia, tetrahydroborate, ascorbic acid, quinol, dithionite, superoxide or thiolates are also known to generate the $[Fe^{II}(CN)_5NO]^{3-}$ ion (*48,57*). However, care must be taken in the products' analysis, because the negative redox potentials of some of these reductants allow for further nitrosyl reduction (*57a*). Also, the reduced product is unstable toward cyanide

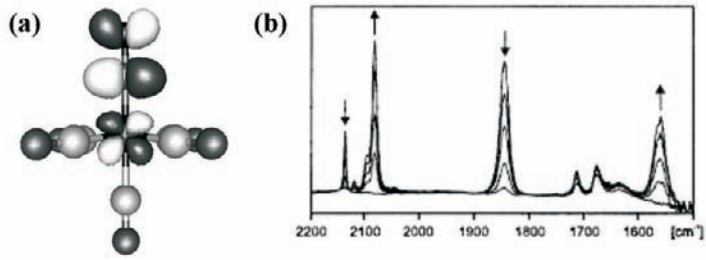

FIG. 6. (a) DFT computed LUMO of $[Fe(CN)_5NO]^{2-}$ and (b) IR–spectroelectrochemical response of $[Os(CN)_5NO]^{2-}$ on one-electron reduction in acetonitrile/0.1 M Bu_4NPF_6.

release [Eq. (2)], as demonstrated by pulse-radiolysis studies (*40*). The electrochemical evidence showed that this process can be very significant at pH < 7. A surface enhanced Raman scattering (SERS) study of the electroreduction of NP on a silver electrode in aqueous solution showed the appearance of peaks associated with the pentacyano and tetracyano reduced products (*57c*). The electrochemistry of NP in non-aqueous aprotic media (CH_2Cl_2 and AcN), showed that the first reduction is irreversible, with a fast conversion (< 10 ms) of the initial $[Fe^{II}(CN)_5NO]^{3-}$ product to the $[Fe(CN)_4NO]^{2-}$ ion (*57d*); this was identified after exhaustive electrolysis by UV–Vis and EPR spectroscopies, in agreement with the previous characterization studies (*40*).

The one-electron reduction of NP is associated with an increase in the population of the antibonding FeNO orbital. Figure 6a shows the DFT computed LUMO of NP (*58*), and Fig. 6b shows the IR electrochemical response for the $[Os^{II}(CN)_5NO]^{2-}$ ion (*59*) upon one-electron reduction in acetonitrile. The spectral characterization of the osmium–nitrosyl reduced complex could be done successfully because of the inertness of the Os–L bonds (L = NO or cyanide). In contrast, NP rapidly releases a cyanide ligand upon reduction in acetonitrile (*57b,57d*). The strong decrease of both the ν_{CN} and ν_{NO} stretching frequencies in $[Os^{II}(CN)_5NO]^{3-}$ is very noticeable, particularly ν_{NO}. This is as predicted from the LUMOs description, since the addition of electrons to $[Os^{II}(CN)_5NO]^{2-}$ must weaken the NO bond.

An alternative description of the one electron reduced product of NP was earlier associated with the protonation of nitrosyl (*20,57a*). Further electrochemical studies discarded the onset of this species in the overall electroreduction of NP (*57e*). The results of

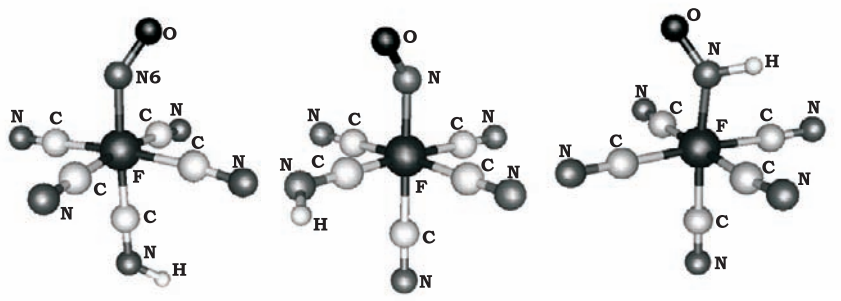

FIG. 7. Optimized geometries of the most stable cyano-protonated complexes of $[Fe(CN)_5NO]^{3-}$ and $[Fe(CN)_5HNO]^{3-}$.

the DFT calculations in Fig. 7 showed unstable structures for the nitrosyl-protonated species (*58*). In contrast, protonation of cyanides is feasible. It is now evident that both experimental and theoretical results support $[Fe^{II}(CN)_5NO]^{3-}$ as a stable form of the one electron reduction product of NP. Cyanide protonation should be operative only for pHs lower than 3, as found for related $[Fe^{II}(CN)_5L]^{3-}$ complexes (*44*).

The $[Fe^{II}(CN)_5NO]^{3-}$ ion can be oxidized back to NP in the presence of oxygen (see the reactions of NP with thiolates below) (*57,60*). Detailed kinetic studies on this important bioinorganic oxidation reaction are not available. In a more general context, the mechanism of the autoxidation reactions of NO complexes awaits a systematic study, which could in principle be afforded with the known $\{MX_5(NO^+)\}$ series (M = Fe, Ru or Os; X = amines, polypyridines, etc.), if appropriate reductants were used to generate the NO complexes.

The electrochemical processes occurring with NP at more negative potentials with respect to the first reduction wave are strongly pH-dependent, and are also influenced by the concentration ratio $[H^+]/[NP]$. The second one-electron wave has been associated with the reduction of the $[Fe(CN)_4NO]^{2-}$ ion, both in acidic and alkaline media (*57a,57e*), discarding the early proposed reduction of $[Fe(CN)_5NOH]^{3-}$ in the acidic range (*57a*). It has been proposed that $[Fe(CN)_4NO]^{2-}$ evolves in different ways upon reduction at pHs 7.6 and 3.0, according to studies by square-wave (SW) and cyclic voltammetry (CV), with the consumption of one and three electrons, respectively (*57e*). The $[Fe(CN)_4NO]^{2-}$ ion generates the Hg-adsorbed

$[Fe(CN)_4NO]^{3-}$ ion upon one-electron reduction, followed by a proton-induced disproportionation reaction to regenerate $[Fe(CN)_4NO]^{2-}$, along with the formation of $[Fe(CN)_4NH_2OH]^{2-}$. The overall reaction involves a four-electron reduction of NP to the hydroxylamine complex.

On the other hand, upon electrolysis under conditions of a two-electron reduction of NP at pH 8.8, a product has been detected with an absorption band at 445 nm, but there is no conclusive evidence on its structure (*57a*). Thus, the expected, highly elusive product HNO has not yet been adequately characterized in the pentacyanoferrate systems. However, recent DFT calculations on $[Fe^{II}(CN)_5HNO]^{3-}$ have been reported, affording a stable species with a defined geometry and spectroscopic properties (*58*). Figure 7 shows that protonation of nitrosyl at the nitrogen atom is operative for the two electron reduced product of NO, as expected for a highly nucleophilic $\{Fe^{II}NO^-\}$ moiety; on the other hand, the unprotonated species containing the nitroside (NO^-) anion was found to be unstable. The calculated values for the ν_{CN} and ν_{NO} stretching frequencies showed a decreasing trend when going successively from NP to the one-electron and two-electron reduced products. Particularly, the ν_{NO} values 1932, 1650, and ca. 1350 cm^{-1}, respectively, agree with an increasing population of the Fe–NO antibonding LUMO. A consistent increase in the NO bond length was calculated to be 1.16, 1.20, and 1.25 Å, respectively, and this is accompanied by the decrease of the FeNO angle: 177, 147, and 138 degrees, respectively. Both geometrical features agree with the predictions of the E–F formalism. The calculated values for the distance and angle for $[Fe^{II}(CN)_5HNO]^{3-}$ are in excellent agreement with experimental data reported for HNO in well characterized complexes, as revealed by structural and spectroscopic results for several inert, octahedral ruthenium and osmium centers. Different synthetic strategies for obtaining HNO complexes afforded either the selective oxidation of bound hydroxylamine, or the hydride reduction of NO complexes (*61*).

The HNO ligand in $[Fe^{II}(CN)_5HNO]^{3-}$ appears to be a very reactive species, precluding its direct spectroscopic characterization, as done for the Ru and Os complexes (*61*). However, supporting chemical evidence on the transient existence of $[Fe^{II}(CN)_5HNO]^{3-}$ has been provided during the reduction of NP with 1,2-dimethylhydrazine (*62*), as well as in the oxidation reaction of hydroxylamine to NP (*63*). This is discussed below. Although HNO should be expectedly labile toward dissociation from the iron center on the time scale of minutes (using a comparative estimation based on the dissociation rate of

NO from $[Fe^{II}(CN)_5NO]^{3-}$, see above), it seems that this time period is sufficient for HNO to survive long, before being attacked by external redox reagents, or affording a dimerization process leading to N_2O. In fact, the reactivity issues related to the bound HNO ligand have not been clearly disclosed yet, even for the well characterized Ru and Os complexes (*61*).

The irreversible electroreduction of NO^+ in NP, past the two-electron reduction stage, yields bound hydroxylamine, involving a four-electron process. Some ambiguity still exists, as to the presence of five or four cyanide spectator ligands (*51a*,*e*). On the other hand, the chemical reduction with 1,2-dimethylhydrazine affords a complete six-electron reduction to ammonia (*62*). Ammonia is also produced in the electrocatalytic reduction of nitrite with the water-soluble $[Fe^{III}(H_2O)(TPPS)]^{3-}$ ion (*64*), as well as in the reactions of some assimilatory and dissimilatory NiR enzymes (*14*). The stabilization of Fe–HNO and $Fe–NH_2OH$ intermediates on the route to NH_3 has been postulated for both the electrochemical (*64*) and the enzymatic (*65*) processes. In the latter case, the evidence comes from the crystallographic information on cytochrome *c* NiR and from DFT calculations on the detailed mechanism of the six-electron process, which also considers the initial key $NO_2^- \rightarrow NO^+$ conversion at the Fe(II) site. From the previously described and from older studies on nitrosyl reductions (*66*), we conclude that the nature of the reduction products of NO^+ strongly depends on the reductant, the nitrosyl complex and the medium conditions, making the consideration of a systematic behavior difficult. See below, however, information on the reactions of hydrazine and substituted derivatives with bound NO^+ (*62*).

V. The Electrophilic Reactions of Bound NO

The electrophilic reactions of the nitrosyl ligand constitute one of its most important reactivity modes (*12,13,25*). This has been known for a long time, and comprehensive reviews are available (*28*). A general way of describing the course of the reactions of NP with different nucleophiles is through Eqs. (5) and (6):

$$[Fe^{II}(CN)_5NO]^{2-} + B \rightleftarrows \{[Fe^{II}(CN)_5NO \cdot B\}^{n-} \quad (5)$$

$$\{[Fe^{II}(CN)_5NO \cdot B\}^{n-} + OH^- \rightleftarrows [Fe^{II}(CN)_5H_2O]^{3-} + \text{products} \quad (6)$$

Equations (5) and (6) are supported by solid evidence for the overall stoichiometries and the general way the reaction rates increase with the concentration of OH^-. This is also valid for related complexes of the $[MX_5NO]^n$ series ($M = Fe^{II}$, Ru^{II}, Os^{II}, Ir^{III}; X = amines, polypyridines, etc.). The nucleophiles B bind to the N atom of NO, and can be very diverse: OH^-, N-binding species (NH_3, amines, hydrazine, hydroxylamine, azide, trioxodinitrate), S-binding ones (SH^-, thiolates, sulfite), organic molecules, etc. The reactions occur for nitrosyl complexes bearing formal $\{M^{II}NO^+\}$ electronic distributions, for which high NO-stretching frequencies (> 1860 cm^{-1}) are usually found (*28*).

With the exception of $B = OH^-$, which relates in fact to an acid–base reaction, the other nucleophiles are potential reductants. After forming the reversible adducts [Eq. (5)], redox reactions are usually operative, leading to the reduction of nitrosyl and oxidation of the nucleophile in Eq. (6). Nevertheless, we will consider first the reaction with $B = OH^-$ for the sake of simplicity, and also because it allows for some generalizations to be made on the factors that influence the electrophilic reactivities of different nitrosyl complexes (*51*). We continue with new results for some N-binding nucleophiles (*62,67*), which throw light on the mecanisms of N_2O/N_2 production and release from the iron centers. A description of the state of the art studies on the reactions with thiolate reactants as nucleophiles will be presented later.

A. Reactivity of Nitrosyl Complexes with OH^-

The reaction scheme can be described as:

$$[Fe^{II}(CN)_5NO]^{2-} + OH^- \rightleftarrows [Fe^{II}(CN)_5NO_2H]^{3-} \quad (7)$$

$$[Fe^{II}(CN)_5NO_2H]^{3-} + OH^- \rightleftarrows [Fe^{II}(CN)_5NO_2]^{4-} + H_2O \quad (8)$$

The rate law for NP and other nitrosyl complexes approaches a first order behavior in each reactant for most of the studied systems, affording high values of $K_{eq} = K_7 \times K_8$, and sufficiently high concentrations of OH^- (*55,68*). The final product has been clearly identified as $[Fe^{II}(CN)_5NO_2]^{4-}$. No direct spectroscopic evidence on the intermediacy of $[Fe^{II}(CN)_5NO_2H]^{3-}$ has been obtained, although kinetic evidence has been provided (*55b*). A mechanistic interpretation consistent with the value of the second order rate constant and

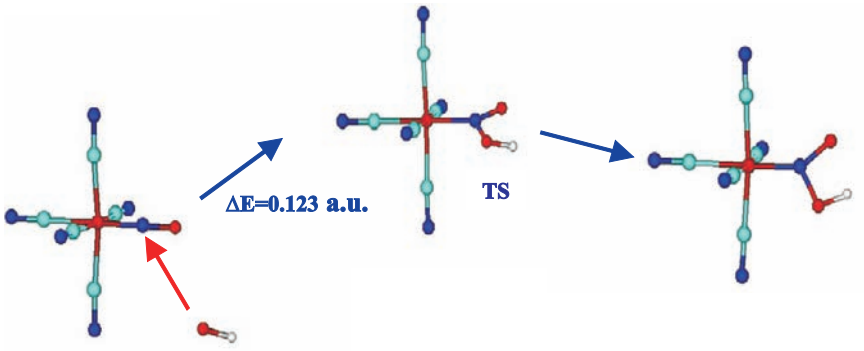

FIG. 8. Optimized geometries for the initial steps of the reaction of NP with OH^- giving the TS and the nitrous acid intermediate.

activation parameters proposes a reversible adduct formation and decay of the intermediate, with k_{OH} being the specific rate constant for OH^- addition in the first (forward) step of Eq. (7) (cf. also Eq. (5)). This mechanism has been generally accepted, and supporting evidence was obtained from DFT calculations, allowing for the structural and electronic characteristics of the different complexes along the reaction coordinate (*51*). Figure 8 shows the optimized geometries for the adduct-formation step, showing the conversion of linear FeNO into the angular Fe–NO_2H intermediate, including the description of the transition state (TS).

The energy required on going from NP to the TS is largely associated with the electronic reorganization of the N atom, while the energy involved in the evolution from the TS to the intermediate adduct is mainly associated with the change in hybridization of the O atom, from sp^3 in the OH^- ion to sp^2 in the coordinated adduct. The calculations show an increase in the bond lengths on the FeNO moiety (Fe–N and N–O) for $[Fe^{II}(CN)_5NO_2H]^{3-}$, as well as those associated with the cyano fragment, compared to NP, suggesting an increase in the electron population of the antibonding system (Table II). The angles decrease from a linear to an angular geometry, and the IR stretching frequencies decrease accordingly when going to the intermediate and final product.

In spite of the abundant work on this type of reactivity, no rate constants for the addition reactions had been obtained, with the exception of the $[M(CN)_5NO]^{2-}$ ions (M = Fe,Ru,Os) (*55,68*), until the recently published kinetic measurements for a representative set of nitrosyl complexes $\{MX_5NO\}^n$ (M = mainly ruthenium) (*51*). Table III

TABLE II

SELECTED DISTANCES (Å), ANGLES (DEGREES), AND IR STRETCHING FREQUENCIES (ν, cm^{-1}) CALCULATED FOR THE DIFFERENT STEPS OF REACTION 1, AT THE B3LYP/6-31G** LEVEL

	$[XNO]^{2-}$(exp)[a]	$[XNO]^{2-}$	TS[b]	$[XNO_2H]^{3-}$	$[XNO_2]^{4-}$
d_{FeC} ax	1.9257(9)	1.9694	1.9878	1.9888	1.987
d_{FeC} eq[c]	1.935	1.9595	1.9890	1.9880	2.011
d_{FeN}	1.6656(7)	1.6155	1.8223	1.813	2.104
d_{CN} ax	1.1591(12)	1.1683	1.1751	1.1755	1.184
d_{CN} eq[c]	1.1613	1.1691	1.1761	1.1782	1.1826
d_{NO}	1.1331(10)	1.1604	1.2255	1.2275	1.2642
d_{NO}(H)			1.4536	1.4713	1.2642
d_{OH}			0.9801	0.9784	
∡ FeNO	176.03(7)	179.96	134.69	133.11	122.48
∡ ONO			109.25	107.98	115.02
∡ CFeC eq[d]	176.63(4)	180.00		173.5	179.83
ν_{CN}(s)	2147–2177	2161–2170		2100–2120	2043
ν_{NO}(s)	1943	1907		1567, 1266, 789	1317, 1351, 802
ν_{Fe-N}(s)	658	712		575	574

Experimental values are given where available. X = $[Fe(CN)_5]$.
[a]Ref. (*33*).
[b]Transition state.
[c]The fourth digit averaged.
[d]Backward the NO_2H group.

shows the addition rate constants, together with potential indicators of NO^+ reactivity, such as the redox potential, $E_{NO^+/NO}$, and the infrared NO stretching frequency, ν_{NO}.

Figure 9 shows a linear-free-energy-relationship (LFER), revealing a very good linear correlation of the addition rate constants with the redox potentials for reactions similar to Eq. (7) with different complexes containing several MX_5 fragments (the complexes with $[Ru(py)_4X]$ fragments stand in a parallel line, with slower rates than predicted by the main line, due to possible steric constraints upon addition of OH^-). The correlation is much better than the one obtained by using the NO stretching frequencies. Figure 9 shows that the rates increase with the potential, reflecting the different bonding interactions afforded by the spectator ligands. Figure 10 shows that the increase in rate constants and redox potentials parallels an increase in *both* the activation enthalpies and entropies.

The trends in the entropies are associated with the different solvational changes related to the reactions of species carrying equal or opposite charges. The reactions of the positively charged complexes

TABLE III

ADDITION RATE CONSTANTS, ACTIVATION PARAMETERS AND CORRESPONDING ν_{NO}, $E_{NO^+/NO}$ AND K_{eq} VALUES FOR DIFFERENT $\{MX_5NO\}^n$

	Compound	k_{OH} ($M^{-1}s^{-1}$)[a]	k_3 (s^{-1})[b]	$\Delta H^{\#}$ (kJ/mol)	$\Delta S^{\#}$ (J/Kmol)	$E_{NO^+/NO}$ (V)[c]	ν_{NO} (cm^{-1})[c]	K_{eq} (M^{-2})[d]
(1)	*cis*-$[Ru(AcN)(bipy)_2NO]^{3+}$	$(5.60 \pm 0.07) \cdot 10^6$	$2.31 \cdot 10^6$			0.35	1960	
(2)	*cis*-$[Ru(bipy)(terpy)NO]^{3+}$	$(3.17 \pm 0.02) \cdot 10^5$	$1.31 \cdot 10^5$	89 ± 1	159 ± 5	0.25	1946	$2.1 \cdot 10^{23}$
(3)	*cis*-$[Ru(bipy)_2(NO_2)NO]^{2+}$	$(5.06 \pm 0.02) \cdot 10^4$	$2.75 \cdot 10^4$	83 ± 7	120 ± 20	0.18	1942	
(4)	*cis*-$[Ru(bipy)_2ClNO]^{2+}$	$(8.5 \pm 0.1) \cdot 10^3$	$4.6 \cdot 10^3$	100 ± 3	164 ± 8	0.05	1933	$1.6 \cdot 10^{15}$
(5)	*trans*-$[NCRu(py)_4CNRu(py)_4NO]^{3+}$	$(9.2 \pm 0.2) \cdot 10^3$	$3.4 \cdot 10^3$	91 ± 4	135 ± 10	0.22	1917	$3.2 \cdot 10^{15}$
(6)	*trans*-$[RuClNO(py)_4]^{2+}$	$(4.6 \pm 0.3) \cdot 10^1$	$3.1 \cdot 10^1$	62 ± 1	-6 ± 5	0.09	1910	
(7)	*trans*-$[Ru(NCS)NO(py)_4]^{2+}$	$(2.03 \pm 0.01) \cdot 10^2$	$1.36 \cdot 10^2$			0.12	1902	
(8)	*trans*-$[Ru(OH)NO(py)_4]^{2+}$	$(2.4 \pm 0.1) \cdot 10^{-1}$	$1.6 \cdot 10^{-1}$			−0.22	1866	
(9)	*trans*-$[Ru(NH_3)_4NO(pz)]^{3+}$	$(1.77 \pm 0.04) \cdot 10^2$	$9.55 \cdot 10^2$	76 ± 2	54 ± 6	−0.11	1942	$6.0 \cdot 10^8$
(10)	*trans*-$[Ru(NH_3)_4(nic)NO]^{3+}$	$(3.3 \pm 0.1) \cdot 10^1$	$1.8 \cdot 10^1$	78 ± 1	44 ± 4	−0.18	1940	$5.9 \cdot 10^7$
(11)	*trans*-$[Ru(Clpy)(NH_3)_4NO]^{3+}$	$(2.60 \pm 0.05) \cdot 10^1$	$1.40 \cdot 10^1$			−0.19	1927	$6.0 \cdot 10^6$
(12)	*trans*-$[Ru(NH_3)_4NO(py)]^{3+}$	$(1.45 \pm 0.02) \cdot 10^1$	$7.82 \cdot 10^0$			−0.22	1931	$2.2 \cdot 10^5$
(13)	*trans*-$[Ru(4\text{-}Mepy)(NH_3)_4NO]^{3+}$	$(9.54 \pm 0.06) \cdot 10^0$	$5.14 \cdot 10^0$	75 ± 1	26 ± 4	−0.25	1934	$7.7 \cdot 10^5$
(14)	*trans*-$[Ru(hist)(NH_3)_4NO]^{3+}$	$(7.6 \pm 0.4) \cdot 10^{-1}$	$4.12 \cdot 10^{-1}$			−0.39	1921	$4.6 \cdot 10^1$
(15)	$[Fe(CN)_5NO]^{2-}$	$5.5 \cdot 10^{-1}$ [8d]	$3.9 \cdot 10^0$	53 [8d]	−49 [8d]	−0.29 [15]	1945 [8d]	$1.5 \cdot 10^5$
(16)	$[Ru(CN)_5NO]^{2-}$	$9.5 \cdot 10^{-1}$ [8d]	$6.4 \cdot 10^0$	57 [8d]	−54 [8d]	−0.35 [15]	1926 [8d]	$4.4 \cdot 10^6$
(17)	$[Os(CN)_5NO]^{2-}$	$1.37 \cdot 10^{-4}$ [8d]	$8.63 \cdot 10^{-4}$	80 [8d]	−73 [8d]	−0.68 [15]	1897 [8d]	$4.2 \cdot 10^1$

[a] Derived from the rate-law.

[b] Obtained through $k_3 = k_{OH}/K_{ip}$, with K_{ip} being estimated according to an electrostatic model.

[c] Ref. (*51*).

[d] See Ref. (*51*) for the corresponding citations in the literature.

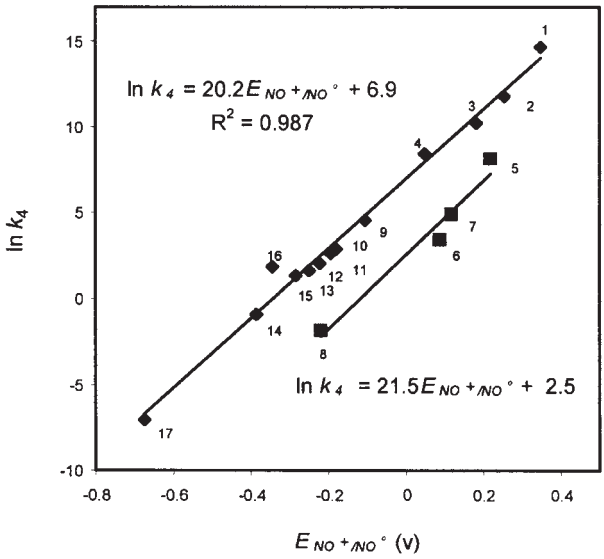

FIG. 9. LFER plot of ln k_4 (addition rate constant) vs. $E_{NO^+/NO}$ for the reactions of a series of $\{MX_5NO\}^n$ complexes with OH^-. See Table III for the assignment of numbers.

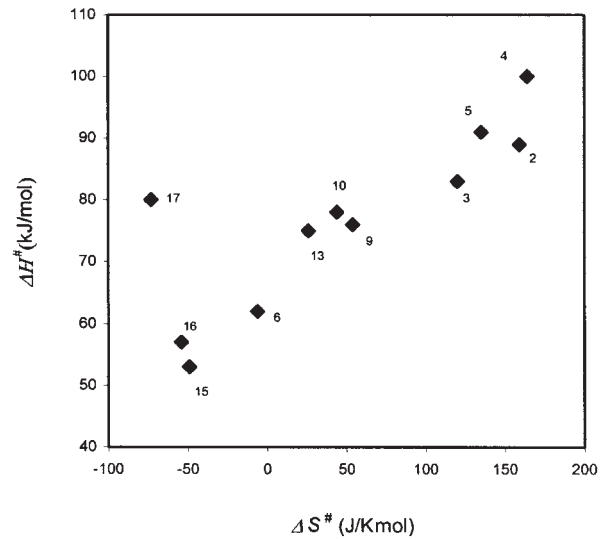

FIG. 10. Plot of the activation enthalpies versus the activation entropies for the reactions of $\{MX_5NO\}$ complexes with OH^- (see Table III).

with OH^- are expected to favor an increase in entropy because of charge neutralization, and the opposite effects are expected with the reactions of the negatively charged complexes. On the other hand, the increase in enthalpy associated with an increase in rate is not so obvious. It was proposed that the enthalpy change should be controlled mainly by the energetically costly steps involving the reorganization of the linear MNO to angular MNO_2H in the TS (see above). This cost will be maximal for the complexes at the top of Table II, associated with a larger triple bond character of the NO bond. For a selected group of complexes in Table II, other descriptors of the electrophilic reactivity have been calculated, namely the charge on the delocalized center, q_{MNO}, as well as the energy of the LUMO (*51*). The first ones are shown in Table IV. The DFT calculations also allowed for the optimized geometries of the reactants and intermediates for a selected group of complexes included in the table, as shown in Fig. 11. These also showed similar elongated bonds and smaller MNO angles for the intermediates compared to the reactants, as already discussed for NP.

Table III also shows the values of the equilibrium constants, K_{eq}, for the conversion of iron–nitrosyl complexes into the corresponding nitro derivatives. K_{eq} decreases downwards, meaning that the conversions are obtained at a lower pH for the complexes at the top of the table. Thus, NP can be fully converted into the nitro complex only at pHs greater than 10. The NO^+–NO_2^- conversion, together with the release of NO_2^- from the coordination sphere, are key features in some enzymatic reactions leading to oxidation of nitrogen hydrides to nitrite (*14*). The above conversion and release must occur under physiological conditions with the hydroxylaminoreductase enzyme (HAO), in which the substrate is seemingly oxidized through two electron paths involving HNO and NO^+ as intermediates. Evidently, the mechanistic requirements are closely related to the structure of the heme sites in HAO (*69*). No direct evidence of bound nitrite intermediates has been reported, however, and this was also the case for the reductive nitrosylation processes associated with ferri-heme chemistry (Fig. 4) (*25*).

Recently, it has been shown that NP and its ruthenium and osmium analogs engage in dinuclear complex formation with the $[Ru(NH_3)_5H_2O]^{2+}$ ion (*70*). In all cases, a new intense, broad absorption is displayed in the visible region, which is not present in either of the reacting chromophores. By proposing a $[(NH_3)_5Ru^{II}$–NC–$M(CN)_4NO]$ structure (M = Fe, Ru, Os), it was suggested that the intense band was associated with a donor–acceptor charge transfer (DACT)

TABLE IV

STRUCTURAL AND ELECTRONIC PARAMETERS DERIVED FROM CALCULATIONS USING PSEUDOPOTENTIALS FOR THE METAL CENTERS[a]

		d_{M-N}	d_{N-O}	$d_{N-O(H)}$	∠MNO	∠ONO	q_N	q_{NO}	q_{MNO}	ν_{NO}
$[Ru(AcN)(bpy)_2NO]^{3+}$	LAN	1.806	1.134		178.2		0.128	0.138	1.148	1993
	SDD	1.778	1.137		178.6		0.207	0.127	1.112	1981
$[Ru(AcN)(bpy)_2NO_2H]^{2+}$	SDD	1.994	1.203	1.389	128.0	114.2				
$[Ru(bpy)(trpy)NO]^{3+}$	LAN	1.799	1.137		175.3		0.108	0.101	1.131	1974
	SDD	1.772	1.141		176.2		0.176	0.082	1.115	1964
$[Ru(bpy)(trpy)NO_2H]^{2+}$	SDD	1.991	1.204	1.391	128.4	114.3				
$[Ru(bpy)_2ClNO]^{2+}$	LAN	1.786	1.139		172.7		0.136	0.106	0.779	1969
	SDD	1.759	1.143		175.5		0.182	0.058	0.779	1959
$[Ru(bpy)_2ClNO_2H]^{+}$	SDD	1.965	1.207	1.405		114.4				
$[RuA_4NO(py)]^{3+b}$	LAN	1.825	1.129		180.0		0.165	0.094	0.847	2005
	SDD	1.792	1.133		180.0		0.213	0.081	0.899	1983
$[RuA_4NO_2H(py)]^{2+b}$	SDD	1.952	1.209	1.394	128.6	114.7				
$[Ru(CN)_5NO]^{2-}$	LAN	1.779	1.163		180.0		0.004	−0.215	−0.067	1874
	SDD	1.758	1.164		180.0		0.105	−0.201	−0.169	1871
$[Ru(CN)_5NO_2H]^{3-}$	SDD	1.969	1.225	1.464	133.1	108.7				
$[Fe(CN)_5NO]^{2-}$	LAN	1.618	1.157		180.0		0.222	−0.026	−0.576	1906
	SDD	1.617	1.158		180.0		0.197	−0.063	−1.327	1901
$[Fe(CN)_5NO_2H]^{3-}$	SDD	1.833	1.224	1.457	132.9	108.6				

[a]Distances (d) in Å; angles in degrees; q_N: calculated charge on the N atom of the NO group; q_{NO}: calculated charge on the NO group, q_{MNO}; calculated group-charge. See Ref. (*51*) for details.

[b]A = amine.

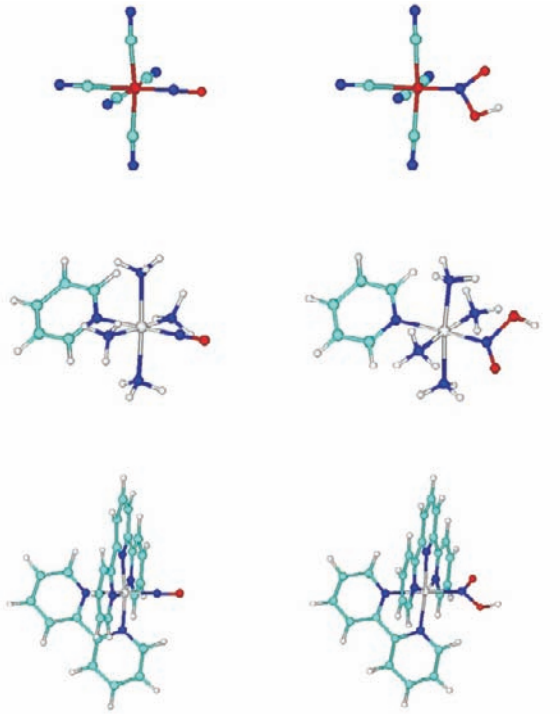

FIG. 11. Optimized geometries at the B3LYP/6-31G** level (SDD pseudopotentials on the metal centers) for representative members of the set (nitrosyls and OH^- addition products): (a) $[Fe(CN)_5NO]^{2-}$; (b) *trans*-$[Ru(NH_3)_4NO(py)]^{3+}$; (c) *cis*-$[Ru(bpy)(trpy)NO]^{3+}$.

interaction between the remote Ru(II) center and the delocalized {MNO} moiety. The absorption features resemble the properties of mixed-valence, cyano-bridged complexes with $\{M^{III}X_5\}$ acceptor fragments (X = cyanides, ammonia, etc.) (*71*), although in the new situation the acceptor is not metal-centered, but is associated with the delocalized {MNO}. Although a crystal structure was not obtained (thus, the *cis*- or *trans*-character of NO with respect to the bridging cyanide is uncertain), IR-Raman, UV–Vis and electrochemical studies were performed, showing significant changes in the relevant absorption energies upon potential-controlled redox changes leading to oxidation of the ruthenium center or reduction at the nitrosyl site. Most important from the reactivity point of view considered in this review, was the fact that the rate constant for the nucleophilic addition of OH^- to the bound nitrosyl was enhanced by ca. five orders

of magnitude when the remote Ru(II) was oxidized to Ru(III). This long distance effect is indeed associated with the good electronic communication ability of bridging cyanide (*5*). The previous kinetic study was performed in a preliminary way for M = Os, but it is likely that a similar rate increase should occur for the iron- and ruthenium analogs. A better characterized dinuclear complex, *trans*-$[NC(py)_4Ru^{II}–CN–Ru(py)_4NO]^{3+}$ was prepared later, showing similar spectroscopic and kinetic results (*72*). The latter species is attractive because of the possibility of building trinuclear (or polynuclear) species through coordination of other fragments to the exposed cyanide ligand, thus allowing for systematic studies of structure–reactivity correlations in extended linear arrays.

B. Reactivity of NP with Hydrazine (Hz), MeHz, and 1,1-Me_2Hz

Surprisingly, among the variable set of nucleophiles whose reactions had been studied with NP, the case of N_2H_4 was absent, in contrast with data available for some ruthenium–nitrosyl complexes (*28*).

Recent work describes the addition reactions of hydrazine and substituted derivatives to NP (*62*). The kinetic studies were done using UV–Vis absorption and mass spectrometric methods. Different stoichiometries were found, depending on the nucleophile. We can distinguish three different mechanistic paths, and these will be successively presented, with an effort to extract some common mechanistic features.

It was proposed that the initial step is a reversible adduct formation comprising the N-atom of the nucleophile and the N-atom of the delocalized {FeNO} moiety (which we identify as $Fe^{15}NO$), as described in Eq. (9).

$$[Fe^{II}(CN)_5^{15}NO]^{2-} + NHR_3NR_1R_2 \rightleftarrows [Fe(CN)_5^{15}N(OH)NR_3NR_1R_2]^{2-} \quad (9)$$

This reaction has been written in a generalized manner; the R_i substituents are H or Me, depending on the nucleophile under consideration. Although no details of the adduct structures can be obtained through the kinetic measurements, a deprotonation of the binding N-atom of the nucleophile is assumed. As a second key hypothesis, if another H-atom is bound to the central N ($R_3 = H$) in Eq. (9), it should be reactive toward OH^-. Further proton transfer and electronic

reorganization consummate the reaction. Thus, Eq. (9) is followed by Eq. (10):

$$[Fe(CN)_5^{15}N(OH)NR_3NR_1R_2]^{2-} + OH^- \longrightarrow [Fe(CN)_5H_2O]^{3-} + N^{15}NO + NHR_1R_2 \quad (10)$$

Equations (9) and (10) describe the reaction of Hz ($R_1 = R_2 = H$), giving NH_3 as a product. They can also be used for MeHz in one of its reactive modes, predominant at pHs below 7 ($R_1 = H$, $R_2 = Me$), rendering $MeNH_2$ as a product and, finally, for 1,1-Me_2Hz in its main reactive mode ($R_1 = R_2 = Me$), giving this time Me_2NH as a product. Equation (11) describes the overall stoichiometry for this main path, taking Hz as the nucleophile:

$$[Fe^{II}(CN)_5NO]^{2-} + N_2H_4 + OH^- \longrightarrow [Fe^{II}(CN)_5H_2O]^{3-} + NH_3 + N_2O \quad (11)$$

These reactions were studied in excess of hydrazine, and were pseudo-first order in complex. At constant pH, the plots of the rate constants (s^{-1}) against the concentration of hydrazine were linear, allowing for the calculation of the second-order rate constant, $k_{N2H4} = 0.43\ M^{-1}\ s^{-1}$ (25 °C, pH 10), with $\Delta H^{\#} = 26.8 \pm 0.2$ kJ mol^{-1}, $\Delta S^{\#} = -163 \pm 5\ J\ K^{-1}\ mol^{-1}$. The plot of k_{N2H4} against pH (Fig. 12, which includes data for the substituted hydrazines as well) showed an apparent first-order dependence with respect to OH^- in the low pH limit and zero order at high pH. The pH-dependence accounts for the role of OH^- in Eq. (10). By applying the steady-state treatment to the adduct species in Eqs. (9) and (10), an expression was derived having the same form as the experimental rate law as shown in Fig. 12.

The proposed mechanism agrees with the general picture presented in Eqs. (5) and (6). The electronic reorganization of the adduct allows the release of N_2O and NH_3, with $[Fe^{II}(CN)_5H_2O]^{3-}$ formation [Eq. (11)]. Strong evidence for the mechanism was obtained by using ^{15}N in NP, with the result that the label appeared only in $N^{15}NO$, as measured by mass spectrometry, but not in NH_3 or in the amines.

The formation of $[Fe^{II}(CN)_5H_2O]^{3-}$ as a product sets the basis for the catalytic processing of nitrite reduction by hydrazine under appropriate pH conditions. As shown in Fig. 13, nitrite binds to the aqua ion and rapidly converts to NO^+. After the attack by N_2H_4, the adduct reorganization, associated with proton migration steps, favor

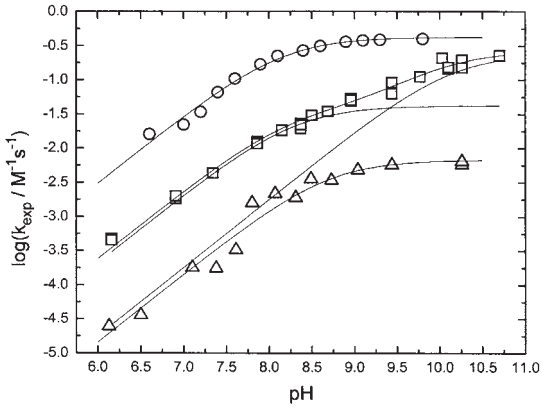

FIG. 12. Dependence of log k_{exp} on pH for the reaction of $[Fe(CN)_5NO]^{2-}$ with hydrazines. Upper curve: Hz; intermediate curve: MeHz; lower curve: 1,1-Me_2Hz. $T = 25.0\,^{\circ}C$, $I = 0.1$ M. For MeHz, the broken lines represent the individual contributions of each term in the rate equation (*62*).

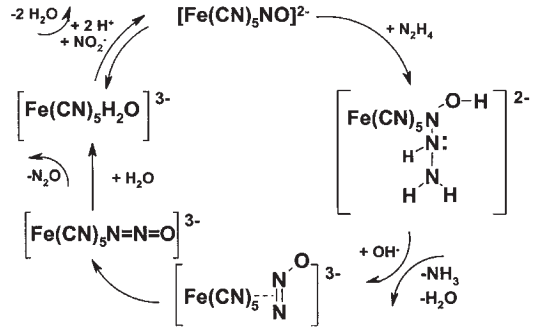

FIG. 13. Catalytic cycle showing the nucleophilic atack of hydrazine on NP, with adduct formation and reorganization. Ammonia is released, with formation of bound N_2O-linkage isomers. The release of N_2O generates the active site, $[Fe(CN)_5H_2O]^{3-}$, which coordinates nitrite, with rapid conversion to bound NO^+ in NP.

the cleavage of the N–N bond in hydrazine, with release of NH_3 and formation of bound N_2O.

Figure 13 illustrates the novel result of N_2O formation, isomerization and release, as predicted by the theoretical calculations. Figure 14a shows a DFT study (B3LYP) of the reaction profile [Eq. (11)], allowing to characterize intermediates on the potential hypersurface. It can be seen that the initially formed η^2-N_2O complex isomerizes to the linear

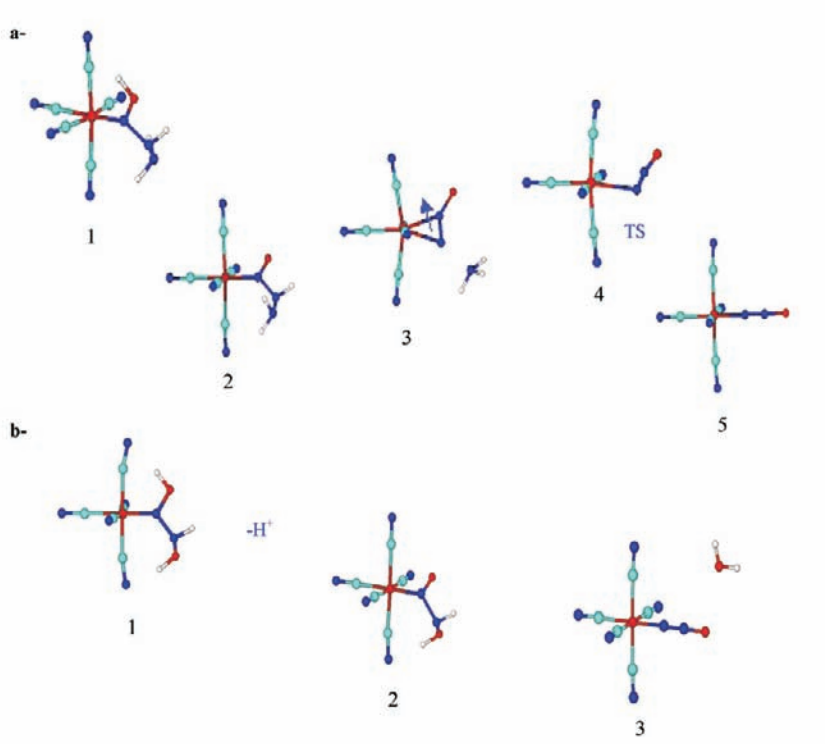

FIG. 14. (a) Schematic representation of the initial steps involved in the reaction of $[Fe(CN)_5NO]^{2-}$ with hydrazine, rendering the N_2O-bound intermediates. The structures correspond to single points on the potential hypersurface, calculated at the B3LYP/6-31G** level. Relative energies (y-coordinate) are not drawn to scale. Arrows indicate changes in the molecule that lead to the next step. From left to right: 1: $[(NC)_5FeN(OH)NHNH_2]^{2-}$; 2: $[(NC)_5FeN(O)NHNH_2]^{3-}$; 3: $[(NC)_5Fe\text{-}\eta^2\text{-}N_2O]^{3-}$; 4: TS structure; 5: $[(NC)_5Fe\text{-}\eta^1\text{-}N_2O]^{3-}$; (b) The same for hydroxylamine. From left to right: 1: $[(NC)_5FeN(OH)NHOH]^{2-}$; 2: $[(NC)_5FeN(O)NHOH]^{3-}$; 3: $[(NC)_5Fe\text{-}\eta^1\text{-}N_2O]^{3-}$.

η^1-N_2O complex, followed by release of N_2O to the medium. The mechanism of hydrazine addition in the first steps of the addition process are entirely similar as previously described for OH^- as a nucleophile, referring to the geometrical and bond distance changes, as shown in Table V.

Besides the remarkable results associated with the N_2O-isomers (*62*), the mechanism of reaction (11) has several additional interesting features: (1) The products are different, compared to the reactions

TABLE V

CALCULATED DISTANCES (Å), ANGLES (deg), AND SELECTED IR FREQUENCIES (cm^{-1}) FOR THE REACTANT, $[Fe(CN)_5NO]^{2-}$ (NP), AND THE DEPROTONATED ADDUCT INTERMEDIATES, $\{Fe(CN)_5NO \cdot B\}^{n-}$, FORMED BY REACTION WITH NUCLEOPHILE B, for $B = N_2H_4$, NH_2OH, NH_3, AND N_3^-

	FeNO (NP)	$FeNO–N_2H_4$	$FeNO–NH_2OH$	$FeNO–NH_3$	$FeNO–N_3^-$
Fe–N	1.615	1.785	1.787	1.789	1.825
N–O	1.160	1.376	1.377	1.367	1.443
$N–N_1$[a]	–	1.365	1.385	1.354	1.310
$N_1–N_2$[b,c]		1.405	1.403	–	1.342
Fe–C *cis*	1.959	1.962	1.955	1.960	1.983
trans	1.965	1.972	1.958	1.960	1.971
C–N *cis*	1.169	1.172	1.175	1.173	1.175
trans	1.168	1.172	1.170	1.169	1.175
∡ FeNO	179.9	123.0	124.8	125.6	121.3
∡ $FeNN_1$		133.0	130.8	129.0	133.9
∡ NN_1N_2[c]		115.8	114.5	–	109.7
ν_{NOH}[d]		1008, 1041	1006, 1487	989	906
ν_{NNH}[d]		1021, 1160, 1310	751, 1414	819, 1188	1090
ν_{CN}	2160	2127–2172	2125–2176	2122–2172	2130–2143

[a] N_1: N atom binding to nitrosyl.
[b] N_2: N atom binding to N_1.
[c] N_2 is O for the case of NH_2OH.
[d] H must be replaced by N for the cyclic azide intermediate.

of hydrazine with other nitrosyl complexes, $[Ru^{II}(NH_3)_5NO]^{3+}$ and $[M^{II}(pdma)_2Cl(NO)]^{2+}$ (M = Ru, Os; pdma: *o*-phenylenebis(dimethylarsine)), which lead to $HN_3 + H_2O$, as apparent precursors of N_2O and N_2 (although not NH_3) (*28*). Evidently, the adduct decomposition modes depend on the nature of the MX_5 fragment in the original nitrosyl-complexes, and this is an issue which merits further study. (2) It shows a rare example of N_2O formation (it has been also found in the related electrophilic reactions of HNO_2) as a product of hydrazine oxidations, which generally lead to N_2 (*73*). (3) The formation of NH_3 as a product generated by a two-electron oxidant is also a novel feature in the mechanistic redox chemistry of hydrazine (*73*). (4) The catalytic cycle for nitrite reduction shows some similarities with the above described chemistry of dissimilatory NiR enzymes (*14*), in the sense that the latter are also able to process nucleophiles such as hydrazine (*54*); however, a crucial difference is that N_2O, but not NO is released as a reduction

product of nitrite bound as NP, with the interesting detail that neither NO nor NO^- (or HNO) are detectable intermediates. The direct production of N_2O has also been observed for some fungal denitrifications (*14*).

An alternative reaction path was found for MeHz, as shown in Eq. (12).

$$2[Fe^{II}(CN)_5{}^{15}NO]^{2-} + MeHNNH_2 + 2OH^- \longrightarrow 2[Fe^{II}(CN)_5H_2O]^{3-} + N^{15}N + N^{15}NO + MeOH \quad (12)$$

$$[Fe^{II}(CN)_5{}^{15}NO]^{2-} + MeHNNH_2 + OH^- \longrightarrow [Fe^{II}(CN)_5H_2O]^{3-} + MeNH_2 + N^{15}NO \quad (11')$$

The different distribution of products in Eq. (12) compared to the main path [Eq. (11′)] was evident at pHs greater than 8. The mass balance accounted for 0.7 mol of N_2O and 0.3 mol of N_2 and MeOH, per mole of initial NP, and the labeling experiments showed that ^{15}N was distributed among $N^{15}N$ and $N^{15}NO$, of molar masses 29 and 45, respectively, supporting the simultaneous occurrence of Eqs. (12) and (11′), which is equivalent to Eq. (11) previously used for Hz. Therefore, MeHz is able to attack the nitrosyl group by two parallel paths, either using the N atom close to the Me group or the other one. The spectral results showed that a shoulder developed at ca. 480 nm (in addition to the characteristic maximum of $[Fe^{II}(CN)_5MeHz]^{3-}$ at 400 nm), suggesting a mixture of complexes. The intensity of this shoulder increased with the progress of the reaction, with no further decay after 80–90% of initial NP was transformed into $[Fe^{II}(CN)_5MeHz]^{3-}$. The new path in Eq. (12) was traced to adduct formation through the methylated N-atom of MeHz. As the adduct intermediate has no reactive H at the central N-atom, OH^- may then react as in Eq. (13):

$$[Fe(CN)_5{}^{15}N(OH)NMeNH_2]^{2-} + OH^- \longrightarrow [Fe(CN)_5N(OH)NMeNH]^{3-} + H_2O \quad (13)$$

The product of Eq. (13) is probably responsible for the persistent absorbance at 480 nm. The deprotonated adduct may react as a nucleophile toward another NP, giving a dimer which, induced

by OH^- attack, may further rearrange by cleavage at the unlabeled N–N bond and displacement of the Me group, Eq. (14).

$$[Fe(CN)_5{}^{15}N(OH)NMeN^{15}N(OH)Fe(CN)_5]^{5-} + OH^- + H_2O \longrightarrow 2[Fe^{II}(CN)_5H_2O]^{3-} + N^{15}N + N^{15}NO + MeOH \quad (14)$$

The reaction with 1,1-Me_2Hz showed a similar alternative path; however, the existence of two methyl groups on the nucleophilic N-atom made this contribution negligibly slow. On the other hand, 1,2-Me_2Hz showed a completely different mechanism, which is described below (*62*).

C. Reactivity of NP with 1,2-Me_2Hz

The new stoichiometry was as follows:

$$[Fe^{II}(CN)_5{}^{15}NO]^{2-} + 3MeHNNHMe + OH^- \longrightarrow [Fe^{II}(CN)_5H_2O]^{3-} + {}^{15}NH_3 + 3MeNNMe + H_2O \quad (15)$$

The formation of azomethane as a two-electron oxidation product of 1,2-Me_2Hz, and the exclusive label on $^{15}NH_3$ suggest that the full six-electron reduction of NO^+ to NH_3 is accomplished through three successive two-electron processes. The plausible intermediates must be $[Fe^{II}(CN)_5{}^{15}HNO]^{3-}$ and $[Fe^{II}(CN)_5{}^{15}NH_2OH]^{3-}$. The proposed mechanism involves an initial adduct formation, similar as for other hydrazines (the DFT calculations show that the adduct formation is not sterically hindered), as shown by Eq. (16), followed by a two-electron transfer from 1,2-Me_2Hz to the N-atom in nitrosyl, Eq. (17).

$$[Fe(CN)_5{}^{15}NO]^{2-} + MeHNNHMe \rightleftarrows [Fe(CN)_5{}^{15}N(OH)NMeNHMe]^{2-} \quad (16)$$

$$[Fe(CN)_5{}^{15}N(OH)NMeNHMe]^{2-} + OH^- \longrightarrow [Fe^{II}(CN)_5H^{15}NO]^{3-} + MeNNMe + H_2O \quad (17)$$

It can be seen that the formation of N_2O through the cleavage of the N–N bond, as occurring for other hydrazines, is avoided. The nucleophile is able to form a very stable product, azomethane, by transferring two electrons and protons. Thus, the nitroxyl species, $[Fe^{II}(CN)_5H^{15}NO]^{3-}$, can be formed in Eq. (17) and survive enough to react with

another 1,2-Me_2Hz, forming another intermediate, $[Fe^{II}(CN)_5{}^{15}NH_2OH]^{3-}$ [Eq. (18)] which has been described in the literature, although its identity could be questioned (*74*). Its transient existence is however very likely, as suggested in the electrochemical reduction process of iron–nitrosyl-porphyrins (*64*). The final two-electron reduction in Eq. (19) leads to $[Fe^{II}(CN)_5NH_3]^{3-}$, which rapidly releases NH_3 to the medium.

$$[Fe^{II}(CN)_5H^{15}NO]^{3-} + MeHNNHMe \longrightarrow [Fe^{II}(CN)_5{}^{15}NH_2OH]^{3-} + MeNNMe \quad (18)$$

$$[Fe^{II}(CN)_5{}^{15}NH_2OH]^{3-} + MeHNNHMe \longrightarrow [Fe^{II}(CN)_5{}^{15}NH_3]^{3-} + MeNNMe + H_2O \quad (19)$$

If the analyzed mechanistic possibilities were not considered as diverse and (interestingly) complicated, showing the influence of the hydrazine substituents on the reaction path, the last reaction of NP with 1,2-Me_2Hz also showed an alternative reaction mode, leading to the same products as in Eq. (15), although with formation of the intermediate complex $[Fe^{II}(CN)_5NO]^{3-}$. This was detected by EPR. It was proposed that 1,2-Me_2Hz added to two NP reactants, thus transferring one electron to each NP (*62*).

Figure 15 shows a mechanistic description of the addition of 1,2-Me_2Hz to NP, leading to a catalytic behavior in the presence of excess nitrite. The new feature of the catalytic reaction, compared to the stoichiometric process described by Eq. (15), is that no NH_3 is produced but, instead, N_2O is evolved (azomethane is the other product in both cases, however). The left-hand cycle describes this behavior. It was assumed that nitrite traps the $[Fe^{II}(CN)_5NH_2OH]^{3-}$ intermediate forming N_2O, as already studied independently in the reaction of NP with NH_2OH (*75*, see below). The right hand cycle shows the participation of the radical $[Fe^{II}(CN)_5NO]^{3-}$ ion in the alternative route which finally leads to the same products as in the main reaction path. Under stoichiometric conditions, when no excess of nitrite is present in the medium, the $[Fe^{II}(CN)_5NH_2OH]^{3-}$ intermediate can be further reduced to $[Fe^{II}(CN)_5NH_3]^{3-}$ [Eq. (19)].

We refer to the original work (*62*) in order to further analyze the above results. Summarizing, the key mechanistic requirements in the addition behavior of hydrazine and its substituted derivatives are the presence of two protons in an adjacent position to the reacting N atom for the evolution of fast addition processes leading to cleavage

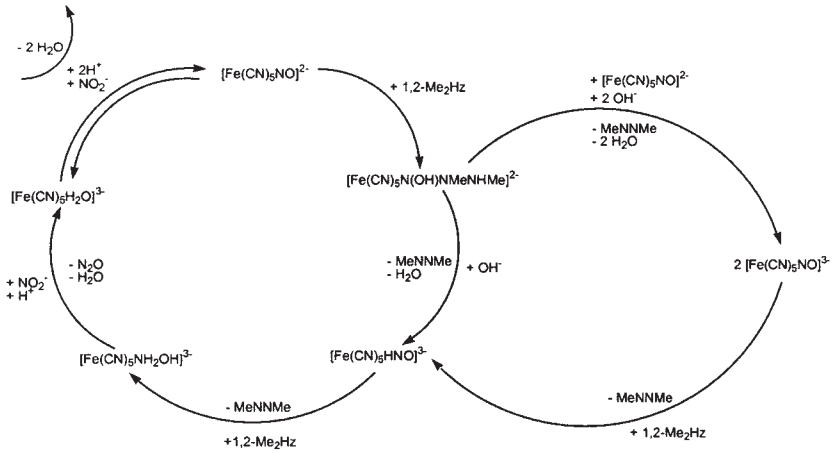

FIG. 15. Catalytic mechanism for the addition of 1,2–Me_2Hz to $[Fe(CN)_5NO]^{2-}$ in excess of nitrite, showing the participation of $[Fe(CN)_5NO]^{3-}$ in an alternative path.

of the N–N bond, as described in Eq. (11). If one Me substituent is present at the attacking position in place of H, an alternative route is developed through dimer formation and evolution of mixtures of N_2/N_2O, together with the production of MeOH (see above, Eq. (12)). With 1,1-Me_2Hz, the addition through the bis-methylated N-atom is disfavored with respect to the main path; some adduct is formed, however, but no gaseous products are released. The case of 1,2-Me_2Hz in Eq. (15) is a peculiar situation related to the specific structure of the reactant; thus, the N–N cleavage is avoided, and, instead, a stable N=N bond is formed in azomethane. As a brief conclusion of the pattern of reactions obtained with NP reacting with the structurally related hydrazine-derivatives as nucleophiles, $1e^-$, $2e^-$, and $6e^-$ paths have been found, depending on the reductant, with intermediates appearing at the $2e^-$ and $4e^-$ stages for the full $6e^-$ process. In each case, kinetic control is revealed for the corresponding reaction profiles and the different intermediates and products consequently formed.

D. Reactivity of NP with other Nitrogen Hydrides: NH_2OH, NH_3, and N_3^-

These reactions have been comprehensively studied in the literature (*75,76*). Given the mechanistic similarities with the addition

reactions of other nucleophiles, and the success of the DFT methodology in establishing the geometries of the reactants, intermediates and products for the above discussed reactions with OH^- and N_2H_4, a similar study was afforded for reactions (20–22) (*67*). The stoichiometries of the relevant reactions are as follows:

$$[Fe^{II}(CN)_5NO]^{2-} + NH_2OH + OH^- \longrightarrow [Fe^{II}(CN)_5H_2O]^{3-} + N_2O + H_2O \quad (20)$$

$$[Fe^{II}(CN)_5NO]^{2-} + NH_3 + OH^- \longrightarrow [Fe^{II}(CN)_5H_2O]^{3-} + N_2 + H_2O \quad (21)$$

$$[Fe^{II}(CN)_5NO]^{2-} + N_3^- + H_2O \longrightarrow [Fe^{II}(CN)_5H_2O]^{3-} + N_2 + N_2O \quad (22)$$

All of these reactions are assumed to proceed through the general pattern described by Eqs. (5) and (6). Experimental results and mechanistic analysis led to the following values for the forward nucleophilic rate constants in Eq. (5), associated with reactions (20–22): $k_{NH2OH} = 4.6$ (pH 9, 26 °C, $I = 1$ M) (*75*), $k_{N_3^-} = 0.2$ (23 °C, $I = 1$ M) (*75*). Ammonia is a poor nucleophile toward NP in aqueous alkaline solutions (*76*). An estimation of $k_{NH3,}$ ca. 10^{-4}–10^{-5} M^{-1} s^{-1} (50 °C) *(76b)* showed it to be much lower than the one for OH^-, $k = 0.55$ M^{-1} s^{-1} (25 °C, $I = 1$ M) (*55*). Significantly higher values of k_5 have been measured for the more polarizable sulfur binding nucleophiles, ca. 10^2–10^4 M^{-1} s^{-1} (*77*). The differences in the values of k_5 still allow to include most of the studied electrophilic reactions of nitrosyl in a common mechanistic framework, as described by Eqs. (5) and (6).

Figure 14b shows the calculated geometries for the hydroxylamine-adduct, rendering the η^1-N_2O complex.

Table V summarizes the relevant calculated distances, angles, and IR frequencies for the different adducts, including the one with hydrazine. Again, the linear-to-bent transformation of the FeNO moiety can be observed, as with OH^-, and an elongation of the Fe–N and N–O distances occurs, showing the decrease in bond order. The bending agrees with the E–F rules, in the sense that the addition process involves a two-electron transfer to the antibonding LUMO, forming a $\{FeNO\}^8$ species. The LUMO is highly delocalized in the FeNO moiety, with mainly π^*_{NO} character (*18,23*).

By displaying the η^1-N_2O complex, Fig. 14b shows a significant contrast with Fig. 14a, where the η^2-N_2O isomer was formed first, with ensuing conversion to η^1-N_2O. In Fig. 14a, linear η^1-N_2O is not easily

attained in a single step from the initial hydrazine-adduct, since it is η^2-N_2O that only needs angular reorganization after release of NH_3. Also, the TS for the conversion lies higher in energy, as expected. The η^1-isomer is the more stable form, and this is understandable, given the existence of the well characterized $[Ru(NH_3)_5(\eta^1\text{-}N_2O)]^{2+}$ (*78*). The structure and reactivity of the pentaammine-L and pentacyano-L complexes show close similarities (*79*), although the greater lability of L in the latter ones is well recognized (*3,5*).

It is a remarkable fact that the mechanisms of adduct decompositions differ significantly for the hydrazine and hydroxylamine complexes. In the hydrazine-adduct, the oxygen atom of the resulting N_2O is obviously the one previously existing in NP [Eq. (9)]. With hydroxylamine, however, the labeling experiments have demonstrated that the O-atom in N_2O comes from this reactant (*75*). The O atom belonging to NO is released as water, leaving the linear intermediate, after angular reorganization, in a single step. The main structures involved, shown in Fig. 14, are true minima in the potential hypersurface. In this case, the proposed mechanism is substantially supported by the experimental evidence. The different kinetic stabilization of the intermediates offers an explanation for this crucial mechanistic feature that differentiates nucleophiles that are structurally as similar as hydrazine and hydroxylamine.

Figure 16 shows the DFT results for reaction (21). Figure 16a shows the structure of the calculated adduct-intermediate and of the η^1-N_2 isomer that is attained by its further conversion.

The formation of N_2 can be described as a comproportionation reaction, with a three-electron interchange between the reactants and further proton and OH^- loss. The end-on linear coordination mode, η^1-N_2, is well known to be a stable form for N_2 bound to transition metal centers (*80*).

In addition, Fig. 16b shows that a stable energy minimum can also be obtained for the η^2-N_2 intermediate. The η^1-N_2 isomer was calculated to be more stable by 1.06 eV than the η^2-N_2 one. For the reaction shown in Fig. 16b, the energy of the adduct is lower than that of η^2-N_2, and therefore the intermediate is not expected to occur. Note however that the η^2-N_2 mode has been observed in low-temperature irradiated samples of $[Os(NH_3)_5(\eta^1\text{-}N_2)][PF_6]_2$ (*81*). The DFT calculated distances, angles, and IR frequencies for the η^1-N_2 linkage isomer are in agreement with reported values for related N_2-complexes, and the values for the η^2-N_2 isomer also agree with those measured for the osmium complex analogue, as shown in Table VI. As to the calculated values for the $[Fe(CN)_5N_2O]^{3-}$ isomers, given that they have not

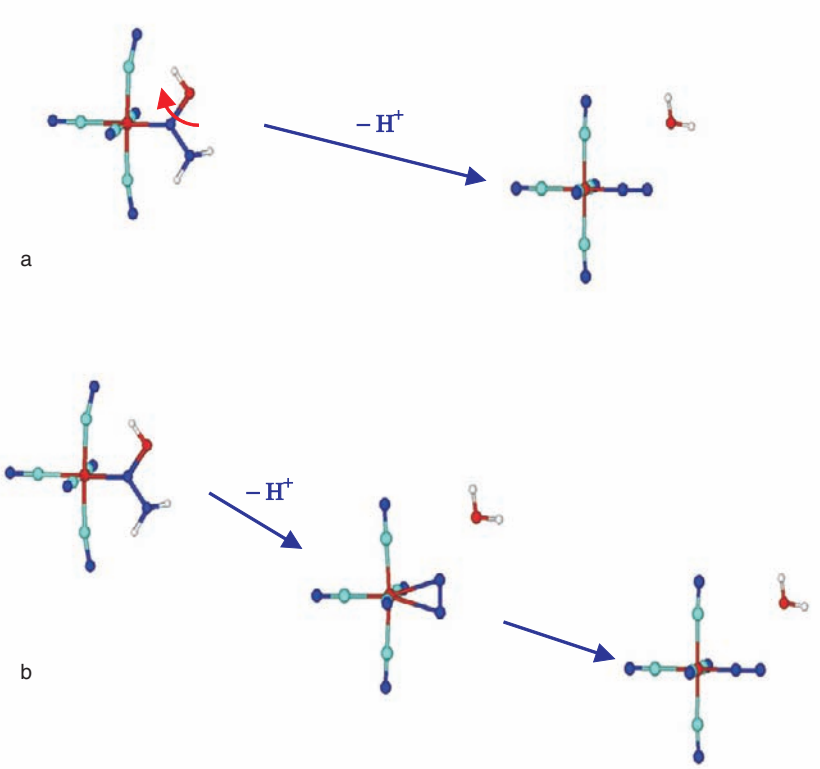

FIG. 16. Structures involved in the decomposition of the adduct intermediate resulting from the reaction of $[Fe(CN)_5NO]^{2-}$ with NH_3. (a) Only the formation of the linear, η^1-N_2 complex is considered. (b) The formation of η^2-N_2 as an intermediate step is also included. The structures correspond to single points on the potential hypersurface, calculated at the B3LYP/6-31G** level. Relative energies are not drawn to scale. Arrows indicate changes in the molecule that lead to the next step.

been described in the literature, we have compared them with IR data for the $[Ru(NH_3)_5(\eta^1\text{-}N_2O)]^{2+}$ ion and with the bond distances in free N_2O (*78*). No structural data exists for any type of N_2O coordination compounds.

Finally, Fig. 17 shows the geometry of the cyclic adduct formed by azide with NP, together with the calculated decomposition paths, with different possible intermediates (see Eq. (22)). Although the cyclic structure has been predicted for related metallonitrosyl adducts (*82*), this was not the case for the reaction with NP, where a

TABLE VI

CALCULATED DISTANCES (Å), ANGLES (deg) AND RELEVANT IR FREQUENCIES (cm^{-1}) FOR THE STABLE INTERMEDIATES FORMED WITH N_2O AND N_2 LIGANDS AFTER THE DECOMPOSITION OF THE DIFFERENT ADDUCTS DESCRIBED IN THE TEXT

	η^2-$N_2O^{a,b}$	η^1-$N_2O^{a,b}$	η^2-$N_2^{c,d}$	η^1-$N_2^{c,d}$
Fe–N	2.075, 1.992	1.820	2.226, 2.226	1.793
N–O	1.254	1.242	–	–
N–N	1.191	1.138	1.133	1.128
Fe–C *cis*	1.975	1.990	1.988	1.989
trans	1.949	1.962	1.928	1.976
C–N *cis*	1.175	1.176	1.177	1.176
trans	1.175	1.176	1.177	1.176
∡ FeNO	142.5	–	–	–
∡ FeNN	76.8	179.8	75.3	180.0
∡ NNO	140.6	179.8		
ν_{NNO}	1159, 659	2287, 1120	–	–
ν_{NN}	1812		2100	2167
ν_{CN}	2127–2147	2114–2131	2106–2116	2115–2126

[a]Distances in free N_2O: N–N, 1.1282 Å; N–O, 1.1842 Å.

[b]Fundamental IR wavenumbers in free N_2O: ν_1 (asymmetric stretch), 1285 cm^{-1}; ν_2 (bending), 589 cm^{-1}; ν_3 (symmetric stretch), 2224 cm^{-1}.

[c]N–N distance in free N_2, 1.10 Å; N–N distance in $[Ru(NH_3)_5(\eta^1\text{-}N_2)]^{2+}$, 1.12 Å.

[d]See text for comparisons with η^1- and η^2-complexes of $[Os(NH_3)_5N_2]^{2+}$. Data related to *a–d* were taken from Refs. (*78,80,81*).

linear addition mode was proposed (*75*). Interestingly, the cyclic adduct geometry was compatible with the labeling experiments, but it was rejected without further consideration. Our calculations do not render a stable species for the linear adduct of NP with azide. As to the alternative decomposition paths, Fig. 17(a,b) show two possible modes differing in the different cleavage paths of the bound cyclic adduct. On the other hand, Fig. 17(c) describes an OH^- substitution-promoted azide dissociation, which further decomposes to N_2 and N_2O products. A detailed theoretical analysis considering solvent effects on the energetics of each of the different paths has been considered (*67*).

E. REACTIVITY OF NP WITH ALIPHATIC AMINES IN ORGANIC SOLVENTS

The reactions of NP with different aliphatic amines (ethyl-, *n*-propyl-, *n*-butyl-, cyclohexyl-, and benzylamines) and amino acids have

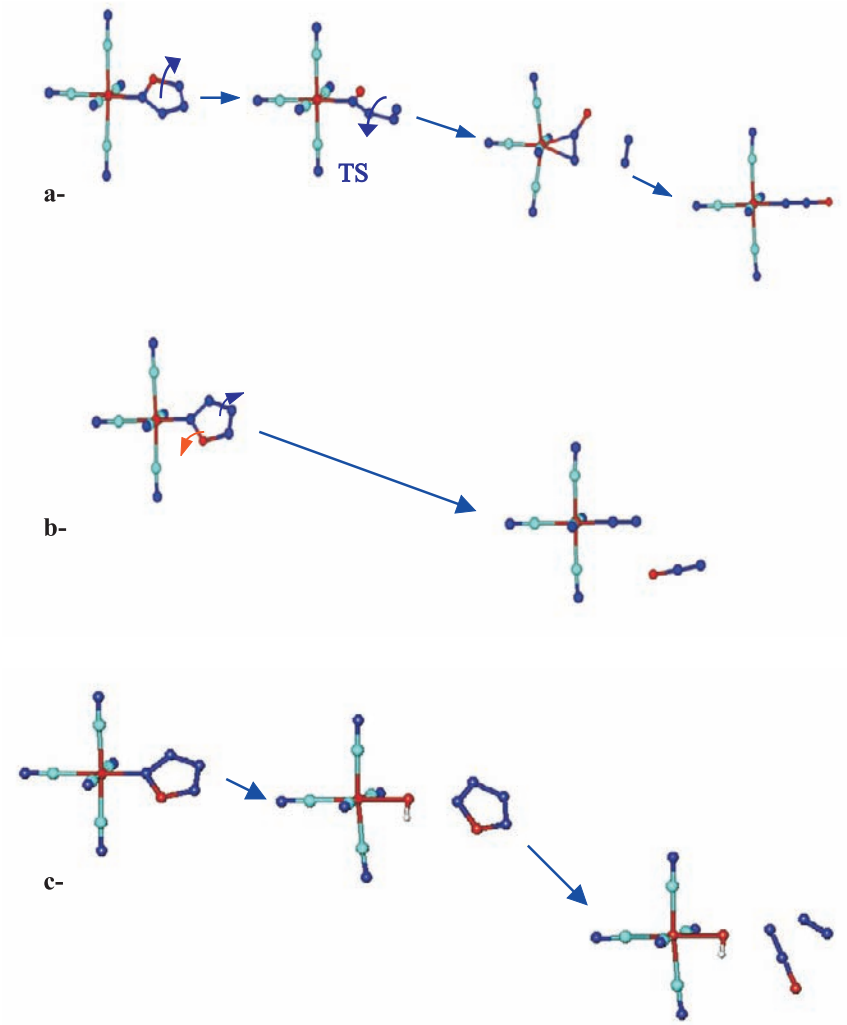

FIG. 17. Possible decomposition paths of the cyclic adduct formed by reaction of $[Fe(CN)_5NO]^{2-}$ with azide. (a) N_2 release and stabilization of the N_2O-bound intermediates. (b) N_2O release and stabilization of the N_2-bound intermediate. (c) N_4O release promoted by OH^- substitution. The cyclic species decomposes to give N_2O and N_2 in a reaction that is exothermic by 60 kcal mol^{-1}. The structures correspond to single points on the potential hypersurface, calculated at the B3LYP/6-31G** level. Relative energies are not drawn to scale. Arrows indicate changes in the molecule that lead to the next step.

been studied in aqueous solution (*83*). The stoichiometry of the reactions is:

$$[Fe(CN)_5NO]^{2-} + RNH_2 + OH^- \longrightarrow [Fe(CN)_5H_2O]^{3-} + N_2 + ROH \quad (23)$$

Nitrosation, diazotation, and deamination processes take place in the reactions resulting in alcohols and N_2 gas as final products. From the studies on the pH-dependence of the rate constants at different temperatures, a mechanism was proposed involving diazonium ions as intermediates. With the prediction that coordination to the metal could stabilize the otherwise extremely reactive diazonium species, the mechanism of these reactions are being studied in organic media.

The reactions of $[M(CN)_5NO]^{2-}$ (M = Fe, Ru, Os) with lithium *n*-butylamide were recently reported (*84*). Free (*E*)-*n*-butyldiazoate was found as the only product arising from the amide. The intermediate diazoate complex is labile and therefore it is rapidly replaced by other ligands present in the reaction medium. This result provides a strong indication that diazoates (and/or diazoic acids) are intermediates in the reactions of amines with these nitrosyl complexes. This is consistent with a mechanism described in Fig. 18, in which one equivalent of amide adds nucleophilically to the nitrosyl, while a second equivalent rapidly abstracts a proton from the diazoic acid before it decomposes producing a diazonium ion.

When the same reaction was carried out with $(tba)_2[Ru(CN)_5NO]$ and $(tba)_2[Os(CN)_5NO]$, signals attributable to *n*-butyldiazoate were observed again by ^{13}C NMR. Indirect UV–Vis evidence indicates that the diazoate complex is labile enough as to be substituted by

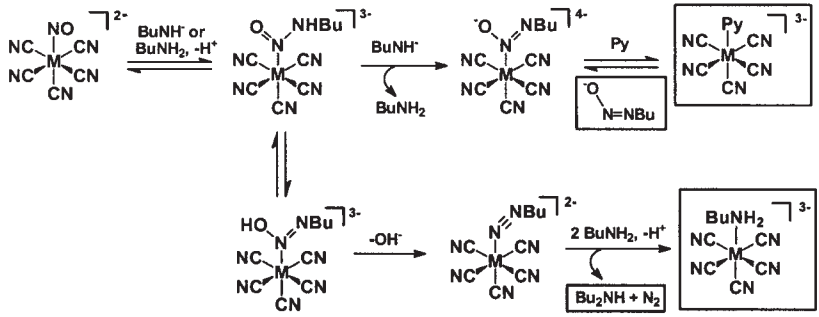

FIG. 18. Proposed mechanism for the reactions of lithium *n*-butylamide and *n*-butylamine with $[M(CN)_5NO]^{2-}$ (M = Fe, Ru, Os).

other ligands present in the reaction medium (such as pyridine used as a co-solvent) even in the case of the inert osmium complex.

The formation of *n*-butyldiazoate by reaction of $[Fe(CN)_5(NO)]^{2-}$ with lithium *n*-butylamide contrasts with the formation of dibutylamine as the main product in the reaction of the same complex with *n*-butylamine (*85*). This can be explained if the diazoic/diazoate equilibrium shown in Fig. 18 is shifted to the left far enough to form of a diazenido by loss of hydroxide. Attack of *n*-butylamine on the α-carbon of the diazenido species, produces dibutylamine. DFT computed results suggest that the stabilization by complexation of the intermediate diazonium ion (see Fig. 18) is large for the iron-pentacyano complex, in agreement with the fact that no rearrangement products were observed in the reaction of this species with *n*-butylamine (*86*). The reaction has been proposed as a good route for the preparation of symmetrical, unsymmetrical, and cyclic secondary amines (*85*).

On the other hand, $[Fe(CN)_5NO]^{2-}$ reacts with benzylamine, $PhCH_2NH_2$, to produce mainly *N*-benzylphenyl-methanimine and PhCN as oxidation products (the latter one only in the presence of oxygen). $(PhCH_2)_2NH$, $PhCH_2Cl$, and $PhCH_2OH$ are produced as diazotization products. Products derived from the benzyl radical $PhCH_2^{\bullet}$ (such as PhMe), are also formed, a fact that suggests that the benzyl radical is an intermediate. Since oxidation products are generated even in the absence of oxygen, a mechanism in which the nitrosyl ligand acts as an oxidant has been proposed (*87*).

F. Reactivity of NP with Trioxodinitrate, $N_2O_3^{2-}$

A kinetic study of the reaction of NP with $N_2O_3^{2-}$ (the anion of Angeli's salt (*13*)) has been performed in the pH range 5–11, at different relative concentrations of the reactants (*88a*). UV–Vis and mass-spectrometric techniques have been used, including ^{15}N labeling at the N-1 position of trioxodinitrate, $^{-}ON^1=N^2O_2^-$. A fast production of nitrite was observed and Eq. (24) was proposed:

$$[Fe(CN)_5NO]^{2-} + HN_2O_3^- \longrightarrow NO_2^- + \text{products} \qquad (24)$$

The initial product was described as $[Fe^{II}(CN)_5(NO^+NO^-)]^{2-}$ (I), formed after the nucleophilic addition of the N-1 atom of $HN_2O_3^-$ to the bound nitrosyl, with further cleavage of the N=N bond in $HN_2O_3^-$. The evolution of NO and N_2O was observed at the early stages of the

reaction, together with the formation and decay of complex I. Complex I was proposed to be the precursor of NO release, with formation of an intermediate complex II, absorbing at 410 nm, which was identified as $[Fe(CN)_5NO]^{3-}$. It was suggested that II decomposed to $[Fe^{III}(CN)_5 H_2O]^{2-}$ and NO^-, with the nitroside ion acting as the precursor of N_2O.

In spite of the detailed mechanistic study, the nature of intermediates I and II seems not to be clearly defined. The maximum at 410 nm should not be ascribed to the $[Fe(CN)_5NO]^{3-}$ ion, which, on the other hand, shows a main absorption at 345 nm and a lower intensity one at 440 nm (*40*). Furthermore, the $[Fe(CN)_5NO]^{3-}$ ion is not expected to decompose intramolecularly leading to NO^-; instead, it is known to release NO very slowly (see above). Certainly, $[Fe(CN)_5NO]^{3-}$ could be converted to other products under oxidative or reductive conditions, and this is an issue that merits further investigation. As a conclusion, the mechanistic scheme, and the crucial issue dealing with the characterization and mechanism of formation of the NO^- or HNO species as precursors to N_2O still remain uncertain.

A related kinetic and mechanistic study was performed for the same nucleophile reacting with the $[Ru(NH_3)_5NO]^{3+}$ cation (*88b*). The initial stages suggested a similar route as described before, but a significant difference was shown through the different splitting mode of $N_2O_3^{2-}$, leading this time to free NO and bound nitrite. These reactions, together with the previously studied one of trioxodinitrate with nitrous acid (*88c*), offer an interesting set for valuable comparisons on the influence of the fragments bound to NO^+ in the stoichiometry and mechanistic features of the corresponding nitrosation processes. However, to make this possible, they should be revisited.

VI. The Autooxidation of Hydrazine

The redox reactions of hydrazine toward main-group and transition metal oxidants have been reviewed (*73*). Different stoichiometries have been found, with N_2 appearing as the N-containing oxidized product, sometimes accompanied by the formation of NH_3 and/or HN_3. The mechanisms have been analyzed in terms of the one- or two-electron nature of the oxidants, and imply both outer- and inner-sphere routes, depending on the oxidant. The very reactive, key intermediate, diazene (diimide), N_2H_2, has been proposed in most of these reactions.

The reaction with O_2 is absent from these studies. It turns out that the autoxidation reaction should be a very slow process because of

kinetic barriers. It has been known for a long time that traces of aqueous metal ions (Cu, Fe) catalyze the oxidation of hydrazine to dinitrogen by dissolved oxygen (*89*). Assuming that coordination is involved, no mechanistic studies are available, however, probably because of the difficulties associated with intermediate detection in such labile systems. Pentacyanoferrates(II) are known to form stable, well characterized complexes with hydrazine (*90a*), and the ligand interchange kinetic properties have been described (*90b*). Traces of the labile pentacyano(L)ferrate(II) ions (L = H_2O, NH_3, N_2H_4, etc.) are able to decompose large quantities of hydrazine upon O_2 exposure in a catalytic way, with release of N_2 (*91*). Mixtures prepared in approximately equimolar conditions of $[Fe^{II}(CN)_5NH_3]^{3-}$, O_2, and N_2H_4 developed orange-to-red colors, which decayed if more O_2 was introduced in the medium, showing N_2 release. Experiments performed under different conditions enabled to detect two intermediates absorbing at 440 and 515 nm. Although the first one was assigned to the $[Fe^{III}(CN)_5N_2H_4]^{2-}$ ion, complementary experiments performed later suggest that the 440 nm band, which is a precursor of the one at 515 nm, should be related to the mononuclear $[Fe(CN)_5N_2H_2]^{3-}$ ion. The second absorption at 515 nm was proposed to be associated with the diazene-bridged complex, $[(NC)_5Fe^{II}HN{=}NHFe^{II}(CN)_5]^{6-}$ (*91*). Although the molar absorptivity of the 515 nm band could not be measured because of its transient character, the order of magnitude is certainly around 10^3 M^{-1} cm^{-1}, suggesting an MLCT transition from Fe(II) to the vacant diazene orbital. More conclusively, the Resonance Raman spectrum obtained with argon ion laser irradiation showed an absorption at 1440 cm^{-1}, assignable to the N=N stretching vibration. Figure 19 describes a simplified mechanism for the catalytic process.

The high lability of bound N_2 in $[Fe^{II}(CN)_5N_2]^{3-}$ regenerates the active site, namely the $[Fe^{II}(CN)_5H_2O]^{3-}$ ion, which is able to further bind and process hydrazine. A more detailed kinetic study could be warranted for this interesting set of reactions. Some uncertainties still remain as to the nature of the intramolecular electron-transfer rate processes (*91*). At the employed concentration levels of the complex, the participation of mixtures of mononuclear and dinuclear complexes complicate the spectral evolution. Even the nature of the dinuclear intermediates (cyano- or hydrazino-bridged) could be put into question (probably both are involved, due to the labile interconversion equilibria). The participation of Fe(III) species, either in the mononuclear or dinuclear species, as reactive intermediate precursors of the formation of diazene and N_2

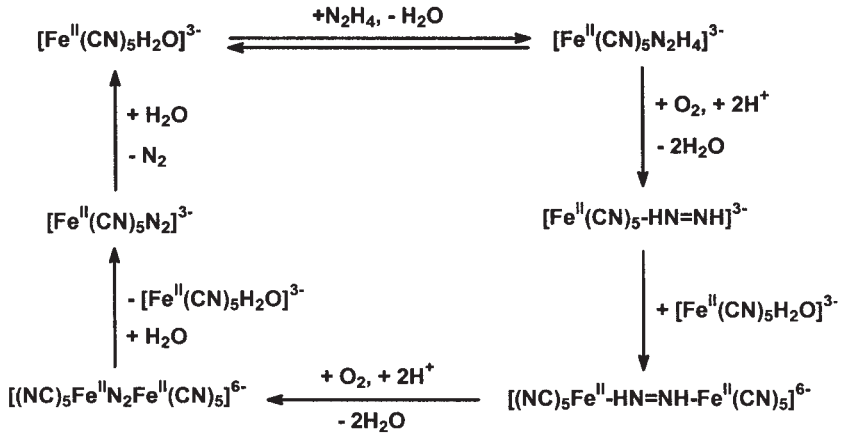

FIG. 19. Catalytic cycle promoted by the $[Fe(CN)_5H_2O]^{3-}$ ion, for the reaction of hydrazine with O_2, giving N_2, with the intermediate formation of bound diazene as mononuclear and dinuclear complexes.

complexes, is highly feasible, but has not been proved. Certainly true, however, are the gross stoichiometric features of the catalytic process, involving the oxidation of hydrazine through two successive $2e^-$ steps, and the participation of bound diazene complexes as intermediates. Recent spectroscopic evidence on related systems is available for sustaining the latter point (*92*). The successive two-electron transfers are highly feasible for O_2 and transiently formed H_2O_2 acting as oxidants in the overall reaction process, most probably through a mechanistic path involving association of the reactants (cf. the autoxidation of $[Fe^{II}(CN)_5H_2O]^{3-}$ to $[Fe^{III}(CN)_5H_2O]^{2-}$, see below).

VII. The Oxidation of Amines and Alcohols

Oxidative dehydrogenation reactions of alcohols and amines are widespread in enzymatic biochemistry, and are of potential importance with regard to the operation of fuel cells based on simple alcohols such as methanol. The nature of products, and their rates of formation, may vary depending on the reaction conditions, and a role of metal ions has been recognized. The oxidation of amines may lead to a variety of products (nitriles, nitro species, etc.) although dehydrogenated diimine products are obtained quantitatively when the oxidation of the amine occurs via coordination to metal centers. A review is available on the mechanisms of oxidative dehydrogenations of coordinated amines and alcohols (*93*).

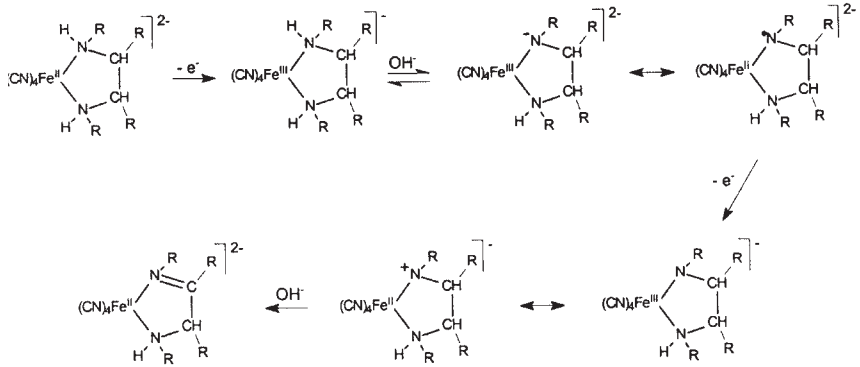

FIG. 20. Proposed mechanism for the oxidation of chelating diamine ligands bound to $[Fe^{II}(CN)_4]^{2-}$, with formation of different intermediates involving Fe^{II}, Fe^{III} species, and final formation of the $[Fe^{II}(CN)_4(\text{diimine})]^{2-}$ complexes.

A large amount of work has been devoted to N-binding macrocyclic complexes of Ni, Cu and Fe, which yield imine ligand products. Bidentate amine ligands, mainly ethylenediamine (en), have been used with Ru and Os complexes. The oxidation of coordinated ethylenediamine and related ligands stops at the diimine stage and does not continue to the dinitrile. The α,α′-diimine entity –N=C–C=N– formed in the four-electron oxidation is particularly stable (*93*).

Ligand oxidations have been studied within a series of complexes of the type $[Fe^{III}(CN)_4(1,2\text{-diamine})]^-$ {1,2-diamine = ethylenediamine, (*R*)-1,2-diaminopropane, (*R*,*R*)-1,2-diaminocyclopentane, (*R*,*R*)-1,2-diaminocyclohexane, *N*,*N*′-dimethylethylenediamine} and $[Fe^{III}(CN)_4$ {2-(aminomethyl)pyridine}$]^-$. The results have been interpreted in a similar manner to the macrocyclic complexes (*94–96*). Related autoxidation processes have been published, particularly with the $[Fe^{II}(CN)_4(en)]^{2-}$ complex, leading to deep-red ethylenediimine derivatives (*97*). The Fe(II) species undergo oxidative dehydrogenation induced by a variety of oxidants, such as O_2, H_2O_2, and $[Fe(CN)_6]^{3-}$. Figure 20 shows the proposed mechanism for the dehydrogenation reactions of the above mentioned diamines. The initial Fe(II) species is oxidized to Fe(III), and a base-assisted deprotonation occurs. Deuterium isotope effect studies confirmed the site as the N–H rather than the α-CH bond. Intramolecular electron transfer from the deprotonated nitrogen atom to the Fe(III) center allows the formation of a Fe(II) radical species, which is subsequently oxidized to an Fe(III) radical analogue. A further intramolecular electron transfer from the nitrogen radical

to Fe(III) generates a putative Fe(II) cationic species. Proton release may then occur to form the imine product.

Alternatively, the effective role of the ruthenium and osmium centers in promoting the oxidative dehydrogenation of amine and alcohol ligands has been traced to their ability to attain an oxidation state two units greater than the final state, using a non-radical mechanistic route. As shown in Fig. 20 for the iron derivatives, the proposed intramolecular one-electron oxidation steps involve ligand-radical species, but the possibility of a similar mechanism for iron through the formation of Fe(IV) intermediates has been raised. The question remains ambiguous (*93*).

Given the characterization of mononuclear $[Fe(CN)_5(en)]^{3-}$ (*98*), as well as of other bound diamines (*99*), their ability toward reactive dehydrogenation could be expected, probably in a more effective way if dinuclear complex formation is allowed for. Some precedent exists for the autoxidation of bound 4-aminomethylpyridine to 4-cyanopyridine in $[Fe(CN)_5]^{3-}$ (*100*). The preparation of these putative dinuclear complexes, bridged by unsaturated diimine ligands could be an interesting issue, reinforced by the possibility of preparing new mixed-valence species, and stimulated by the renaissance experienced in this field, related to the diverse electronic delocalization patterns (*9,10*).

The reaction between $Na_2[Fe^{III}(CN)_5NH_3] \cdot H_2O$ and various aromatic amines and nitrogen heterocycles was originally investigated as a color reaction for the determination of the organic compounds (*101*). Amino compounds such as *p*-phenylenediamine generate coordinated quinoneimine complexes bound to pentacyanoferrate(II) (*102*). By extending the work to the reactions of the Fe(III) compound with *p*-aminophenol, it has been shown that the oxidized *p*-aminophenoxyl radical can be stabilized in the $[Fe^{II}(CN)_5]^{3-}$ fragment. The complex has been isolated as a zinc salt and evidence for the bound radical has been provided through IR, EPR, and Moessbauer measurements (*103*).

VIII. The Disproportionation of Hydroxylamine

Disproportionation reactions of "free" NH_2OH have earlier been reported to produce N_2, N_2O, and NH_3 (*104*). Given that these processes are very slow, it has been proposed that they should have originated from metal ion impurities, suggesting that previous coordination of NH_2OH is a prerequisite to disproportionation (*105*). Unfortunately, the redox properties of coordinated

NH_2OH as compared to the uncoordinated ligand have not been studied in great detail (*104*). Coordination of NH_2OH to the metal and further attack by another NH_2OH have been proposed for the initial step in the disproportionation of NH_2OH to N_2 and NH_3 by the labile $[Ni(CN)_4]^{2-}$ ion in anaerobic medium. The participation of $[Ni(CN)_3(NO)]^{2-}$, containing the nitroside anion, has been proposed as an intermediate precursor for the formation of products (*106*). Other evidences have been reported in the literature on the role of iron complexes catalyzing the disproportionation reactions. This is the case for NP (*75*), as well as for soluble iron–nitrosyl porphyrins reacting with NH_2OH (*107*). However, neither detailed kinetic studies nor even a rigorous stoichiometric picture have been provided.

The NH_2OH disproportionation reaction catalyzed by NP (*75*) was considered in a detailed kinetic study, performed spectrophotometrically and gas volumetrically (*108*). The found products were N_2, N_2O, and NH_3, and a mechanistic interpretation identified a fast route, probably effected by radicals derived from a bridged hydroxylamine dinuclear complex. The slow route was associated with the intermediacy of a nitroside complex.

The above results and interpretation show no conclusive evidence for the proposed paths, given the complexity of the product distribution and its dependence on different medium conditions. The reaction process is currently being revisited (*63*), using $[Fe(CN)_5NH_3]^{3-}$ in place of NP as a starting reagent and as a controlled source for the expected active catalyst, $[Fe(CN)_5H_2O]^{3-}$. Ongoing investigations confirm the nature of the above reaction products, establishing the required conditions for obtaining mixtures of N_2/N_2O in different proportions, as well as exclusively N_2. Most remarkably, the studies demonstrate that NP is also an important oxidation product of NH_2OH in particular conditions. It can be shown that small amounts of $[Fe(CN)_5NH_3]^{3-}$ are able to process much larger amounts of NH_2OH, with reproducible cycling. The participation of mononuclear and cyano-bridged dinuclear intermediates can be described, as well as of Fe(II)–Fe(III) intermediates. The mechanistic proposal has an impressive resemblance with the reduction and oxidation reactions of NH_2OH carried out by the relevant enzymes acting in the natural systems, which effect, on the one hand, the reduction of NH_2OH to NH_3 (*109*), and, on the other hand, the oxidation to nitrite (*69*). The latter process apparently involves successive two-electron oxidation steps leading to Fe^{II}–HNO and Fe^{II}–NO^+ intermediates, with final conversion to nitrite and release to the medium.

IX. Miscellaneous Reactions

A. The Reaction of $[Fe(CN)_5H_2O]^{3-}$ with O_2 and H_2O_2

The stoichiometry of the autoxidation reaction was earlier established (*7a,7c*) as:

$$4[Fe^{II}(CN)_5H_2O]^{3-} + 4H^+ + O_2 \longrightarrow 4[Fe^{III}(CN)_5H_2O]^{2-} + 2H_2O \quad (25)$$

Reaction (25) is remarkable, because the aqua complex ion has a very similar redox potential as the hexacyano-complex (ca. 0.40 V), and the latter is known to be unreactive toward oxygen (*1*). The mechanism of reaction (25), comprising the one-electron reduction of O_2 to O_2^- as an initial step through an outer-sphere route, appears to be endergonic, and therefore other mechanistic paths should be considered. Toma demonstrated elegantly in 1975 (*6a*) that the rate of reaction (25) was very slow, and was influenced by the presence of spurious ferrous ions, which are always present in aged solutions of $[Fe(CN)_5H_2O]^{3-}$. By performing systematic studies with added ferrous ions, as well as using chelating species as inhibitors, he provided strong evidence that a catalytic mechanism was underway, based on the rate law: $-d[Fe(CN)_5H_2O^{3-}] = k_3\ [Fe(CN)_5H_2O^{3-}]\ [O_2]\ [Fe^{2+}_{aq}]$, with $k_3 = 5.6 \times 10^6\ M^{-2}\ s^{-1}$, at 25 °C, $I = 0.1$ M, pH 4.5. Kinetically indistinguishable structures for the activated complexes were proposed, involving either end-on or bridged O_2 structures between the associated pentacyano and Fe^{2+}_{aq} species. A similar picture appears for the oxidation of pentacyano and hexacyano complexes with hydrogen peroxide (*110*). Reaction (25) was studied in very diluted complex solutions, ca. 10^{-5} M, where the mononuclear aqua ion is highly predominant. Our own preliminary results show that the oxidation also develops in more concentrated solutions, with a significant presence of the cyano-bridged mixed-valence dinuclear complex, as revealed by the appearance of NIR absorptions, in addition to the absorptions in the near UV region (*111*).

B. The Coordination Chemistry of Sulfite

The electrophilic reaction of NP with sulfite (the Boedeker reaction) has been studied, and follows a similar reaction pattern as with other reactants [Eqs. (5) and (6)]. The red color shows up at 475 nm, and this decays in an unknown way with formation of $[Fe(CN)_5SO_3]^{5-}$ as the

final product. A strong influence of the type of alkaline countercations has been observed on the spectroscopic and reactivity properties, consistent with the highly negative charges afforded by the reactants (*28*). A related adduct has been prepared by the reaction of sulfite with *cis*-$[RuCl(bpy)_2NO]^{2+}$ allowing for the determination of the crystal structure of the adduct, *cis*-$[RuCl(bpy)_2\{N(O)SO_3\}]$. This is the first adduct for which structural data exists, demonstrating the addition of the nucleophile to the N atom of nitrosyl (*28*).

The $[Fe(CN)_5SO_3]^{5-}$ ion has been prepared and characterized as a sodium salt (*112*). By reacting with one equivalent of the oxidizing agents $[Ir^{IV}Cl_6]^{2-}$and $[Fe^{III}(CN)_6]^{3-}$, it can be oxidized to the Fe(III) analogue (*113*), as also observed with excess $S_2O_8^{2-}$ (*114*). An exploration of the reactions of the Fe(III) complex with excess oxidant leads to free sulfate, with the intermediacy of ill-characterized colored intermediates (*113*).

The reactivity of $[Fe(CN)_5SO_3]^{5-}$ toward reduction has not been investigated. However, a report on the closely related $[Ru^{II}(NH_3)_5(SO_2)]^{2+}$ ion described its electrochemical reduction to $[Ru^{II}(NH_3)_5(H_2S)]^{2+}$ (*115*), where the sulfur ligand remains bound through the net six-electron change. The $[Fe^{III}(TPPS)(H_2O)_n]^{3-}$ complex ($n=1$ or 2), which was shown above to mimic the action of a NiR enzyme in its ability to reduce NO_2^- to NH_3 catalytically (*64*), is also an effective electrocatalyst for the reduction of HSO_3^- to H_2S (*116*), a process that occurs in nature via a stepwise process that is carried out by the sulfite reductase enzymes (*117*). Given the commented analogies between the pentaammineruthenium and pentacyanoferrate chemistry (*79*), as well as the previously described catalytic nitrite reduction processes associated with the pentacyanoferrates(II), it seems that the issue of sulfite reduction in the latter system could be an attractive challenge.

C. The Reaction of $[Fe(CN)_5L]^{n-}$ ($L=NO^+$ and H_2O) with SH^- and Thiolates, SR^-

The electrophilic reactions of NP with SH^- and several SR^- have been studied and reviewed (*28*). The nature of the reversible addition reactions [Eq. (5)] are reasonably well understood for the thiolates. A kinetic study including some bioinorganically relevant nucleophiles (cysteine, glutathione) was performed by using stopped-flow and T-jump techniques (*77*). The rate constants for the forward and reverse processes in Eq. (5) were in the range 10^3–10^4 M^{-1} s^{-1} and 10^1–10^3 s^{-1} at 25 °C, respectively.

The typical red colors (absorptions at ca. 522–526 nm, with $\varepsilon = 10^3$–10^4 M^{-1} cm^{-1} (*118*), for different structurally related thiols and thiolates) strongly suggest that the binding of the nucleophile occurs through the sulfur atom and the N atom of nitrosyl, and are most probably associated with MLCT transitions. The intensities of these absorptions are larger in alkaline media, suggesting that previous deprotonation of sulfur is occurring. Although no crystal structures of the adduct species are available, a recent IR study of the reaction of NP with EtSH (*119*) demonstrated that the $\{Fe^{II}$–NO(SEt)$\}$ moiety is present, on the basis of ν_{NO} found at 1380 cm^{-1}, which is consistent with a double N=O bond and also with a similar electronic distribution to the one previously discussed for the addition of OH^- and N-binding nucleophiles to NP.

The addition reactions of thiolates to NP are generally followed by the decomposition of the red adducts. A survey on the persistence of the red colors showed that the adduct with thiosuccinic acid was extremely stable over days (*118*). Some rationalization on the different adduct stabilities has been advanced; thus, the presence of electron-rich or electron-withdrawing groups on the thiolate anion destabilize or stabilize the adducts, respectively. The great stability of the thiosuccinic acid adduct with NP has shown to be valuable for the quantitative determination of the nitrosyl complex (*34,35*).

The decomposition mode of the adducts has early been noticed to be associated with redox reactions (*60,77*), and is currently under scrutiny because of its great bioinorganic relevance. It has been shown that the reduction of NP to the EPR-active $[Fe(CN)_5NO]^{3-}$ ion occurs in the reaction with cysteine, which is oxidized to cystine (*60*). In this reaction, NP showed to behave catalytically with respect to the autoxidation of cysteine to cystine, provided enough oxygen was present. A recent kinetic and mechanistic study has thrown more light on the complex mechanistic details comprising the decompositions of the red adducts formed by NP with cysteine, *N*-acetylcysteine, ethyl cysteinate, and glutathione (*120*). Under conditions of excess of NP, in anaerobic medium, the reversible adduct formation step is shown by Eq. (26):

$$[Fe(CN)_5NO]^{2-} + RS^{n-} \rightleftarrows [Fe(CN)_5N(O)SR]^{(n+2)-} \qquad (26)$$

Reaction (26) is followed by a first order process, which has been interpreted as an homolytic splitting of the N–S bond, Eq. (27), with formation of the one-electron reduction product of NP, $[Fe(CN)_5NO]^{3-}$,

and thiyl radicals that are the precursors of disulfide formation, RSSR. In the related reaction of NP with SEt^-, the decay of the IR absorption at 1380 cm^{-1}, corresponding to the red $[Fe(CN)_5N(O)SEt]^{3-}$ adduct (*119*), correlates with the increase at 1648 cm^{-1} for $[Fe(CN)_5NO]^{3-}$, as predicted by Eq. (27):

$$[Fe(CN)_5N(O)SR]^{(n+2)-} \longrightarrow [Fe(CN)_5NO]^{3-} + RS^{(n-1)-} \qquad (27)$$

The rates depend on the thiol structure, and correlate well with inductive effects. Thus, the $-NH_2$ and COO^- groups destabilize and stabilize the red adduct, respectively. When the groups are blocked by acetylation or esterification, their influence is suppressed, as shown by *N*-acetylcysteine, which forms the most stable adduct in the series because of the unprotected COO^- and the acetylated amino group.

Figure 21 shows a reaction scheme for the above reactions. The scheme also includes the distinct behavior under excess thiolate conditions, which reveals a faster adduct decomposition. The kinetics are complicated, showing induction periods that are indicative of autocatalysis through a chain reaction initiated by the $RS^{(n-1)-}$ radicals, Eq. (28):

$$RS^{(n-1)-} + RS^{n-} \rightleftarrows RSSR^{(2n-1)-} \qquad (28)$$

These radicals can be scavenged by both complexes in Eq. (26). Chain propagation is proposed to occur through Eq. (29), forming a dithiolato transient species that reacts according to Eq. (30).

$$[Fe(CN)_5N(O)SR]^{(n+2)-} + RSSR^{(2n-1)-} \longrightarrow [Fe(CN)_5N(O)(SR)_2]^{(2n+2)-} + RS^{(n-1)-} \qquad (29)$$

$$[Fe(CN)_5N(O)(SR)_2]^{(2n+2)-} \longrightarrow [Fe(CN)_5NO]^{3-} + RSSR^{(2n-1)-} \qquad (30)$$

Reactions (28–30) generate additional quantities of the $RSSR^{(2n-1)-}$ radicals, leading to the catalysed redox decomposition of the $[Fe(CN)_5N(O)SR]^{(n+2)-}$ complex. Finally, the reaction between NP and $RSSR^{(2n-1)-}$ terminates the chain mechanism, Eq. (31).

$$[Fe(CN)_5NO]^{2-} + RSSR^{(2n-1)-} \longrightarrow [Fe(CN)_5NO]^{3-} + RSSR \qquad (31)$$

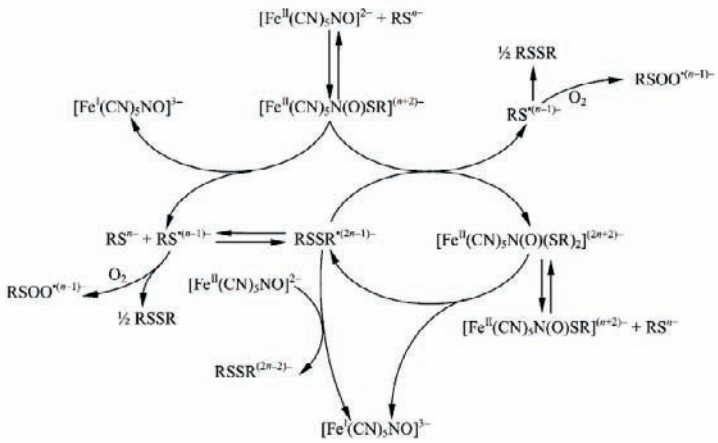

FIG. 21. Proposed scheme for the reactions of NP with thiolates, RS^{n-}, showing the formation and spontaneous homolytic splitting of the adduct, $[Fe(CN)_5N(O)SR]^{(n+2)-}$, followed by autocatalytic redox reactions proceeding with thiolate excess, in anaerobic medium. The influence of oxygen is also included for some of the reactions.

Reactions (32–33) may also contribute to the termination of the catalytic cycle.

$$RS^{(n-1)-} + RS^{(n-1)-} \rightleftarrows RSSR \tag{32}$$

$$[Fe(CN)_5N(O)(SR)_2]^{(2n+2)-} \rightleftarrows [Fe(CN)_5N(O)SR]^{(n+2)-} + RS^{n-} \tag{33}$$

The proposed radical mechanism presented in Eqs. (27)–(33) and Fig. 21 was also modeled with the aid of DFT calculations.

In the proposed description, the one-electron reduced product of NP, $[Fe(CN)_5NO]^{3-}$, is described as a Fe(I) species, which formally implies a NO^+ ligand. As shown above (Section III), even considering the delocalized nature of the FeNO moiety (*23*), there is enough spectroscopic evidence, particularly IR (*36a,119*), EPR *(36b,37)*, as well as kinetic evidence (*34*), to support that $[Fe(CN)_5NO]^{3-}$ is best described as containing a $\{Fe^{II}NO^{\bullet}\}$ unit, with a low-spin d^6 iron species bound to a NO radical.

The overall mechanistic study shows a significant contribution to the bioinorganically relevant reactions of NP with thiolates. Although the route shown in Eqs. (26)–(33) is operative under anaerobic conditions, the study also comprised some experiments to disclose the

influence of oxygen on some of these reactions, as shown in Fig. 21, which are not discussed in detail here. As concluded by the authors, the studied systems are eventually more complex for a detailed mechanistic interpretation, because other additional equilibria comprising thiol protonations, ion pair effects and the type and concentration of countercations could be important. Moreover, the studies were performed at pH 10, where no perturbations associated with cyanide release from $[Fe(CN)_5NO]^{3-}$ are expected (see above). However, at physiological pH the latter process, involving the formation of $[Fe(CN)_4NO]^{2-}$ intermediates, has been shown to be significant. The latter species is presumably the precursor of NO release to the medium following the reduction of NP after injection (*48*). Further mechanistic studies on this process would be desirable.

An earlier report on the reaction of NP with SH^- suggests that a similar route as previously indicated for the thiolates is operative (*121*). However, the ill-defined nature of the intermediates and products has prompted a reinvestigation of this reaction. Ongoing results (*111*) show that $[Fe(CN)_5NO]^{3-}$ and sulfur are produced as primary products of the decomposition of the initially formed, red adduct. pH and other reaction conditions are shown to influence the course of the overall reaction in a still unraveled way.

The coordination chemistry of several SR^- (although not SH^-) to $[Fe^{II}(CN)_5H_2O]^{3-}$ has been studied (*122*). The complexes are not very stable (K_{st} ca. 10^3 M^{-1}) compared to other $[Fe^{II}(CN)_5L]^{3-}$ because of the high dissociation rates of the SR^- ligands (ca. 10^{-1}–10^{-2} s^{-1}). Thiolate coordination to $[Fe^{III}(CN)_5H_2O]^{2-}$ leads to fast reduction to Fe(II), with a transient appearance of blue colors, probably associated with LMCT transitions in the unstable $[Fe^{III}(CN)_5(SR)]^{3-}$ species (*111*). An independent kinetic study of the coordination and redox reactions of thiolates on Fe-aqua catalytic sites seems to be as important as the need to study the reactions with nitrosyl, given the presence of oxygen in the physiological media.

D. Modification of Electron Transfer Reactivity upon Cyano-Bridge Formation

As anticipated above, the reactivity of the cyano complexes of transition metals are strongly influenced by the structure of the medium, namely the nature of the solvent (specific cyano-donor interactions), or the type and concentration of the counterions (*15*). Both of these factors have a profound influence in the electronic structure, and determine the observed changes in reactivity, particularly in

the electron transfer reactions, where a catalytic role of alkaline cations has been proposed (*5,16*).

When the above factors are put under control, the possibility of changing the ligand L in the pentacyano(L)ferrate complexes adds a further dimension for studying systematic reactivity changes, brought out by the controlled modification of the redox potentials of the Fe(II)–Fe(III) redox couples. In this way, the rates of electron transfer reactions between a series of $[Fe^{II}(CN)_5L]^{n-}$ complexes toward a common oxidant like $[Co^{III}(NH_3)_5(dmso)]^{3+}$ showed a variation in agreement with Marcus predictions for outer-sphere electron transfer processes, as demonstrated by linear plots of the rate constants versus the redox potentials (*123*).

Another crucial factor influencing the redox reactivity of cyano complexes is the possibility of bridging one (or more) cyano ligands to an acceptor moiety. As anticipated before, we are not attempting to discuss here the broad subject of mixed-valence chemistry, related to the intermetallic electronic coupling between metal centers, favored by the conjugated nature of cyanide or other bridging ligands like pyrazine. However, we believe that the current studies showing the ability of cyano complexes to bind on nanocrystalline and colloidal TiO_2 surfaces merits a specific comment, because of the general importance of affording a molecular approach for the conversion of light into electricity. Sensitization of these n-type semiconductors to visible light with metal cyano coordination compounds has been early recognized (*124*). Coordination of $[Fe(CN)_6]^{4-}$ to the TiO_2 surface results in the appearance of a broad absorption band around 420 nm, assigned to an $Fe(II) \rightarrow TiO_2$ metal-to-particle charge-transfer (MPCT) band (*125a*). Surface-enhanced Raman scattering techniques have been used to estimate the vibrational reorganization energy for the MPCT intervalence transition, thus enabling the identification of the relevant internal modes associated with the interfacial charge transfer. Together with the main stretching of the cyano bridge, a number of other vibrations were found to contribute to the activation barrier, including some surface modes associated with Ti–O and Ti–N stretching (*125b*). Most important was the finding of a fast, inverted, interfacial electron-transfer behavior associated with the reverse reaction in Eq. (34).

$$[Fe^{II}(CN)_5L^{n-}]\text{–}TiO_2 \rightleftarrows [Fe^{III}(CN)_5L^{(n-1)-}]\text{–}TiO_2\ (e) \qquad (34)$$

By photochemically pumping the tail of the MPCT transition, the recovery kinetics was measured in the nanosecond time scale (*125c*).

The measurements were performed with a series of $Fe^{II}(CN)_5L$ complexes (L = cyanide, py, and py-substituted derivatives) affording different redox potentials. The plot of log k_{et}, the interfacial electron transfer rate constant, versus the reduction potentials showed a negative slope, with a decreasing trend of k_{et} as the relative driving force increases, in agreement with the behavior expected for a process operating in the inverted region. Electroabsorption (Stark) spectroscopy has been used to better understand the nature of the acceptor state involved in the MPCT transition (*125d*). The average charge transfer distance determined from the Stark spectra is 5.3 Å, which is similar to the estimated distance between the Fe(II) center of the complex and the Ti^{IV} surface site, as described by $(NC)_5Fe^{II}$–CN–Ti^{IV} (particle). It has been suggested that the electron injection is to either an individual titanium surface site or to a small number of Ti centers localized around the site of hexacyanoferrate coordination to the particle and not into a conduction band orbital delocalized over the nanoparticle.

E. Intramolecular Redox Assistance of Bimolecular Redox Reactions

In spite of the abundant work on synthetic, thermodynamic, structural, and spectroscopic aspects of mixed-valence compounds, the dynamic solution behavior toward external redox reagents has not been much addressed. When such compounds are unsymmetrical and valence-localized, several problems arise when a fully reduced dinuclear complex reacts with an oxidant. Haim pioneered a systematic study performed with different systems reacting with a common two-electron oxidant, peroxydisulfate (*126*). A relevant example is given by reaction (35):

$$[(NC)_5Fe^{II}pyCNRu^{II}(NH_3)_5]^- + S_2O_8^{2-} \longrightarrow [(NC)_5Fe^{III}pyCNRu^{III}(NH_3)_5]^+ + 2SO_4^{2-} \quad (35)$$

In most of the reactions studied, the appearance of biphasic kinetics showed that the full oxidation process is achieved through the stepwise oxidation of one of the metal centers, rendering a mixed-valence species which is further oxidized to the final product. The question arises in Eq. (35) as to the alternative first oxidation of iron or ruthenium. The stoichiometry of the first oxidation step with bridging 4- and 3-cyanopyridines (with the N-atom of py binding to

iron and the N-atom of the nitrile group binding to ruthenium) was found to be (*127*):

$$[(NC)_5Fe^{II}pyCNRu^{II}(NH_3)_5]^- + S_2O_8^{2-} \longrightarrow [(NC)_5Fe^{III}pyCNRu^{II}(NH_3)_5] + SO_4^{2-} + SO_4^- \quad (36)$$

That the above redox isomer is formed instead of the $\{Fe^{II}Ru^{III}\}$ one, can be demonstrated by careful analysis of the MLCT band of the product, as well as by the properties of the intervalence (IV) band. However, it is well known that the $[Ru^{II}(NH_3)_5L]^{n+}$ ions are generally much more reactive that the $[Fe^{II}(CN)_5L]^{n-}$ analogues toward oxidation by peroxydisulfate (*126,128*), as required by the lower redox potential at the ruthenium center. A careful mechanistic analysis showed that, although the $\{Fe^{III}Ru^{II}\}$ isomer is the thermodynamically stable product, it is not the kinetically accessible one. Then, the reaction evolves as follows:

$$[(NC)_5Fe^{II}pyCNRu^{II}(NH_3)_5]^- + S_2O_8^{2-} \longrightarrow [(NC)_5Fe^{II}pyCNRu^{III}(NH_3)_5] + SO_4^{2-} + SO_4^- \quad (37)$$

$$[(NC)_5Fe^{II}pyCNRu^{III}(NH_3)_5] \rightleftarrows [(NC)_5Fe^{III}pyCNRu^{II}(NH_3)_5] \quad (38)$$

$$[(NC)_5Fe^{III}pyCNRu^{II}(NH_3)_5] + S_2O_8^{2-} \longrightarrow [(NC)_5Fe^{III}pyCNRu^{III}(NH_3)_5]^+ + SO_4^{2-} + SO_4^- \quad (39)$$

The mechanism can be described by using a $R \rightarrow M' = M \rightarrow Ox$ scheme. The fully reduced complex R is oxidized by a one-electron process to the thermodynamically unstable electronic isomer, M′, which is formed by attack on the Ru^{II} center, in a kinetically controlled reaction. Then, M′ rapidly isomerizes via intramolecular electron transfer to M, the thermodynamically stable isomer. As the latter species has again a very reactive Ru^{II} site, the complete oxidation to Ox is consumed. A similar mechanism has been described for the related oxidations of the $[(edta)Ru^{II}pzRu^{II}(NH_3)_5]$ complex (*129*).

A variation to the above situation is found with other complexes. By consideration of spectral results, electrochemical measurements and kinetic analysis, it has been shown that the alternative scheme $R \rightarrow M = M' \rightarrow Ox$ is operative. We illustrate this behavior for $R = [(NC)_5Fe^{II}ImRu^{II}(NH_3)_5]^{2-}$, with $Im^- =$ imidazolate ion (*130*).

$$[(NC)_5Fe^{II}ImRu^{II}(NH_3)_5]^{2-} + S_2O_8^{2-} \longrightarrow [(NC)_5Fe^{II}ImRu^{III}(NH_3)_5]^{-} + SO_4^{2-} + SO_4^{-} \quad (40)$$

$$[(NC)_5Fe^{II}ImRu^{III}(NH_3)_5]^{-} \rightleftarrows [(NC)_5Fe^{III}ImRu^{II}(NH_3)_5]^{-} \quad (41)$$

$$[(NC)_5Fe^{III}ImRu^{II}(NH_3)_5]^{-} + S_2O_8^{2-} \longrightarrow [(NC)_5Fe^{III}ImRu^{III}(NH_3)_5] + SO_4^{2-} + SO_4^{-} \quad (42)$$

In this alternative route, the first one-electron oxidized product in Eq. (40) is the kinetically favored as well as the thermodynamically stable electronic isomer, M. The evolution of the oxidation process, is now facilitated by the rapid isomerization to the unstable electronic isomer M′ in Eq. (41), which has again an available Ru^{II} site for the reaction proceeding to Ox as in Eq. (42). This route has been also found for $R = [(NC)_5Fe^{II}bpaRu^{II}(NH_3)_5]^{-}$, containing the non-communicating ligand bpa = μ-1,2-bis(4-pyridyl)ethane (*131*), and for $[(NC)_5Fe^{II}pzRu^{II}(NH_3)_5]^{-}$ (*132*).

By putting together the rate constants measured (or estimated according to the proposed models) for the relevant electron transfer steps in a broad variety of systems, including the rates found for the mononuclear $[Ru^{II}(NH_3)_5L]^{n+}$ ions, a LFER relationship was found by plotting ln k_{et} vs. E_{Ru} for the "intramolecular" electron transfer in the ion pairs $[X_5M–L–Ru^{II}(NH_3)_5]^{n+}//S_2O_8^{2-}$. The slope shown in Fig. 22 agrees with the theoretical value predicted by Marcus theory, assuming that the reorganization energies for the pentaammine–Ru(II) and –Ru(III) exchanges are insensitive to the identity of X_5ML (*133*).

A conclusion from these studies is that the slowly reacting X_5M fragments, such as $(NC)_5Fe^{II}$ and $(edta)Ru^{II}$, can be oxidized much faster when a rapidly reacting moiety is attached, such as $(NH_3)_5Ru^{II}$.

The discussed mechanisms represent a form of intramolecular "catalysis" of the oxidation of the $Fe^{II}(CN)_5$ or $Ru^{II}(edta)$ centers by the $Ru^{II}(NH_3)_5$ moiety. The first two moieties react sluggisly and, on the other hand, the electron in $Ru^{II}(NH_3)_5$ is readily accessible to the external oxidant and is given up. The rapid electronic isomerization processes aid in the consumption of the full oxidation process. This is not truly catalytic because the "catalyst" is the reactant itself, which, of course, is consumed in the reaction. A better description involves a net oxidation of the $Fe^{II}(CN)_5$ or $Ru^{II}(edta)$ sites through activation by the facile intramolecular electron transfer between the metal centers. The mechanism is described in Fig. 23, bearing some resemblance to the classical chemical mechanism for inner sphere electron

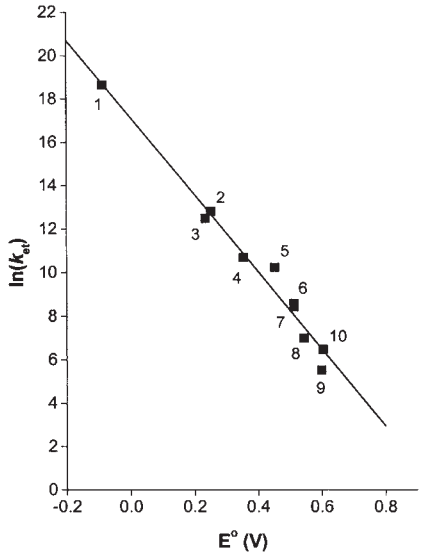

FIG. 22. Plot of $\ln(k_{et})$ vs. E°_{Ru} for "intramolecular" electron transfer in the ion pairs $[X_5M–L–Ru^{II}(NH_3)_5]^{n+}//S_2O_8^{2-}$. The $X_5M–L$ moieties are: (1) $(NC)_5Fe^{III}–Im^{3-}$; (2) $(NC)_5Fe^{II}–bpa^{3-}$; (3) $(NC)_5Fe^{III}–bpa^{2-}$; (4) $(edta)Ru^{II}–pz^{2-}$; (5) $(NC)_5Fe^{II}–pz^{3-}$; (6) $(NC)_5Fe^{II}–3pyCN^{3-}$; (7) $(NC)_5Fe^{II}–4pyCN^{3-}$; (8) $(NC)_5Fe^{III}–3pyCN^{2-}$; (9) $(NC)_5Co^{III}–pz^{2-}$; (10) $(NC)_5Fe^{III}–4pyCN^{2-}$.

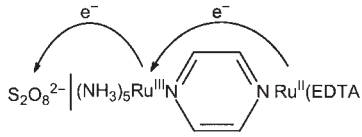

FIG. 23. Oxidation of a Ru^{II}(edta) site by $S_2O_8^{2-}$, assisted by intramolecular electron-transfer mediated by the $Ru(NH_3)_5$ moiety. A similar mechanism operated for $Fe^{II}(CN)_5^{3-}$ as donor.

transfer (*126*). It is interesting to point out that the bridging ligand should not necessarily be electronic communication (cf. the bpa case), but should only favor the fast electron transfer in an appropriate geometric environment (Fig. 23).

X. Conclusions

The chemistry of redox-active ligands L in the pentacyano(L) ferrate(II) and -(III) complexes is of fundamental concern for disclosing

the mechanistic features which are operative in stoichiometric and catalytic processes associated with oxidation, reduction, and disproportionation of L. The possibility of good spectroscopic and kinetic characterization of reactants, intermediates, and products is particularly important, because these results can be obtained on a time-scale of minutes, in contrast with the difficulties found for the identification of related species associated with the much more reactive hexaaqua ions. For the Fe(II)-cyano complexes, the back-bonding ability of the metal center aids in the stabilization and eventual spectroscopic characterization of otherwise elusive intermediates, while still maintaining a sufficient lability of L in order to provide for the regeneration of Fe(II)-aqua ion as a catalytic site. This is particularly important for small molecules displaying a versatile coordination behavior, such as the *N*-binding species associated with the nitrogen redox cycle, which display complex, multi-electronic paths for oxidation or reduction in most cases, generally under kinetic rather than thermodynamic control. In addition, the relevance of the cyanometallate systems for studying the coordination and reactivity of biologically relevant S- and O-binding species has been emphasized.

The accessibility of $Fe^{II/III}$ redox states sets the basis for redox cycling, providing a possible mechanism for ligand oxidation or reduction mediated by intramolecular electron transfer between the metal and the ligand. A crucial favorable feature for the catalytic requirements is the moderate lability of water in the easily generated $[Fe^{II}(CN)_5H_2O]^{3-}$ ion, and the robust nature of the pentacyano moiety in the overall processes, with interesting exceptions such as the $[Fe^{II}(CN)_5NO]^{3-}$ ion. The lability of some L ligands may preclude however their adequate characterization in the iron systems, as shown for some intermediates such as HNO. In that case, the possibility of studying the same reactions in the more inert ruthenium and particularly in the osmium analogues should be considered, and this is also a great advantage of the systems under consideration.

By using modern DFT methodologies, the prediction and identification of reactants and intermediates in the potential energy surfaces associated with the addition reactions of different nucleophiles with nitrosyl complexes has shown to be most revealing. Although some of these intermediates (viz. the linkage isomers of N_2O) have not been detected experimentally because of the lability at the iron centers, their existence is feasible on the basis of related results obtained for other linkage isomers (NO, N_2) in low-temperature photoinduced reactions, as well as considering the reasonable results obtained for the optimized geometries and spectroscopic calculations.

Acknowledgments

The author thanks his collaborators, as detailed in the corresponding references, for making this review possible. We appreciate the financial support of the Argentine agencies, CONICET and FONCYT, as well as of the Volkswagenstiftung.

References

1. Sharpe, A. G. "*The Chemistry of Cyano Complexes of the Transition Metals*"; Academic Press: New York, 1976.
2. Dunbar, K. R.; Heintz, R. A. *Prog. Inorg. Chem.* **1997**, *45*, 283–391.
3. Macartney, D. H. *Rev. Inorg. Chem.* **1988**, *9*, 101–151.
4. Stochel, G. *Coord. Chem. Rev.* **1992**, *114*, 269–295.
5. Baraldo, L. M.; Forlano, P.; Parise, A. R.; Slep, L. D.; Olabe, J. A. *Coord. Chem. Rev.* **2001**, *219–221*, 881–921.
6. (a) Balzani, V.; Carassiti, V. "*Photochemistry of Coordination Compounds*"; Academic Press, 1970, Chap. 5; (b) Stasicka, Z.; Wasielewska, E. *Coord. Chem. Rev.* **1997**, *159*, 271–294; (c) Szacilowski, K.; Macyk, W.; Stochel, G.; Stasicka, Z.; Sostero, S.; Traverso, O. *Coord. Chem. Rev.* **2000**, *208*, 277–297.
7. (a) Toma, H. E. *Inorg. Chim. Acta* **1975**, *15*, 205–211; (b) Toma, H. E.; Malin, J. M. *Inorg. Chem.* **1974**, *12*, 1772–1774; (c) Kenney, D. J.; Flynn, T. P.; Gallini, J. B. *J. Inorg. Nucl. Chem.* **1961**, *20*, 75; (d) Brauer, G. "*Handbook of Preparative Inorganic Chemistry*", Vol. 2, 2nd edn.; Academic Press: New York, NY, 1965, p. 1511.
8. Zerga, H. O.; Olabe, J. A. *Inorg. Chem.* **1983**, *22*, 4156–4158.
9. Kaim, W.; Klein, A.; Gloeckle, M. *Acc. Chem. Res.* **2000**, *33*, 755–763.
10. (a) Demadis, K. D.; Hartshorn, C. M.; Meyer, T. J. *Chem. Rev.* **2001**, *101*, 2655; (b) Brunschwig, B. S.; Creutz, C.; Sutin, N. *Chem. Soc. Rev.* **2002**, *31*, 168–184.
11. (a) Vahrenkamp, H.; GeiS, A.; Richardson, G.N. *J. Chem. Soc. Dalton Trans.* **1997**, 3643–3651; (b) Scandola, F.; Argazzi, R.; Bignozzi, C.; Chiorboli, C.; Indelli, M. T.; Rampi, M. A. *Coord. Chem. Rev.* **1993**, *125*, 283–292; (c) Scandola, F.; Bignozzi, C. A. "*Supramolecular Photochemistry*"; D. Reidel Publishing Company, 1987, pp. 121–133; (d) Vogler, A.; Osman, A. H.; Kunkely, H. *Coord. Chem. Rev.* **1985**, *64*, 159–173; (e) Watson, D. F.; Bocarsly, A. B. *Coord. Chem. Rev.* **2001**, *211*, 177–194; (f) Chang, C. C.; Pfennig, B.; Bocarsly, A. B. *Coord. Chem. Rev.* **2000**, *208*, 33–45; (g) Wu, Y.; Pfennig, B. F.; Sharp, S. L.; Ludwig, D. R.; Warren, C. J.; Vicenzi, E. P.; Bocarsly, A. B. *Coord. Chem. Rev.* **1997**, *159*, 245–255.
12. Richter-Addo, G. B.; Legzdins, P. "*Metal Nitrosyls*"; Oxford University Press: New York, 1992.
13. "*Methods in Nitric Oxide Research*"; Eds. Feelisch, M.; Stamler, J. S.; Wiley, 1996.
14. Averill, B. A. *Chem. Rev.* **1996**, *96*, 2951–2964.
15. Chen, P.; Meyer, T. J. *Chem. Rev.* **1998**, *98*, 1439.
16. Metelski, P. D.; Swaddle, T. W. *Inorg. Chem.* **1999**, *38*, 301–307.
17. Swinehart, J. H. *Coord. Chem. Rev.* **1967**, *2*, 385–402.
18. Westcott, B. L.; Enemark, J. L. "*Inorganic Electronic Structure and Spectroscopy, Vol. II: Applications and Case Studies*"; Eds. Solomon, E. I.; Lever, A. B. P.; J. Wiley & Sons, Inc., 1999, pp. 403–450.
19. Coppens, P.; Novozhilova, I.; Kovalevsky, A. *Chem. Rev.* **2002**, *102*, 861–884.

20. (a) Clarke, M. J.; Gaul, J. B. *Struct. Bonding (Berlin)* **1993**, *81*, 147–181; (b) Butler, A. R.; Glidewell, C. *Chem. Soc. Rev.* **1987**, *16*, 361–380; (c) Butler, A. R.; Megson, I. L. *Chem. Rev.* **2002**, *102*, 1155–1165.

21. Hoshino, M.; Laverman, L.; Ford, P. C. *Coord. Chem. Rev.* **1999**, *187*, 75–102.

22. (a) Wolak, M.; van Eldik, R. *Coord. Chem. Rev.* **2002**, *230*, 263–282; (b) Wanat, A.; Wolak, M.; Orzel, L.; Brindell, M.; van Eldik, R.; Stochel, G. *Coord. Chem. Rev.* **2002**, *229*, 37–49; (c) Laverman, L. E.; Wanat, A.; Oszajca, J.; Stochel, G.; Ford, P. C.; van Eldik, R. *J. Am. Chem. Soc.* **2001**, *121*, 285–293; (d) Schneppensieper, T.; Zahl, A.; van Eldik, R. *Angew. Chem. Int. Ed.* **2001**, *40*, 1678–1680.

23. Enemark, J. H.; Feltham, R. D. *Coord. Chem. Rev.* **1974**, *13*, 339–406.

24. Scheidt, W. R.; Ellison, M. K. *Acc. Chem. Res.* **1999**, *32*, 359–359.

25. Ford, P. C.; Lorkovic, I. M. *Chem. Rev.* **2002**, *102*, 993–1018.

26. Tfouni, E.; Krieger, M.; Mc Garvey, B. R.; Franco, D. W. *Coord. Chem. Rev.* **2003**, *236*, 57–69.

27. Ding, X. D.; Weichsel, Q.; Andersen, J. F.; Shokhireva, T. K.; Balfour, C.; Pierik, A. J.; Averill, B. A.; Montfort, W. R.; Walker, F. A. *J. Am. Chem. Soc.* **1999**, *121*, 128–138.

28. (a) Bottomley, F. "*Reactions of Coordinated Ligands*", Vol. II; Ed. Braterman, P. S. Plenum: New York, 1985, pp. 115–222; (b) Mc Cleverty, J. *Chem. Rev.* **1979**, *79*, 53–76.

29. Zollner, H.; Woike, Th.; Krasser, W.; Haussuehl, S. *Z. Kristallogr.* **1989**, *188*, 139.

30. (a) Chacón Villalba, M. E.; Guida, J. A.; Varetti, E. L.; Aymonino, P. J. *Spectrochim. Acta* **2001**, *A57*, 367–373; (b) Chacón Villalba, M. E.; Guida, J. A.; Varetti, E. L.; Aymonino, P. J. *Inorg. Chem.* **2003**, *42*, 2622–2627.

31. Morioka, Y.; Takeda, S.; Tomizawa, H.; Miki, E. *Chem. Phys. Lett.* **1998**, *292*, 625–630.

32. (a) Delley, B.; Schefer, J.; Woike, Th. *J. Chem. Phys.* **1997**, *107*, 10067–10074; (b) Gorelsky, S. I.; Lever, A. B. P. *Int. J. Quantum Chem.* **2000**, *80*, 636–645; (c) Boulet, P.; Buchs, M.; Chermette, H.; Daul, C.; Gilardoni, F.; Rogemond, F.; Schlapfer, C. W.; Weber, J. *J. Phys. Chem. A* **2001**, *105*, 8991–8998; (d) Boulet, P.; Buchs, M.; Chermette, H.; Daul, C.; Furet, E.; Gilardoni, F.; Rogemond, F.; Schlapfer, C. W.; Weber, J. *J. Phys. Chem. A* **2001**, *105*, 8999–9003.

33. Carducci, M. D.; Pressprich, M. R.; Coppens, P. *J. Am. Chem. Soc.* **1997**, *119*, 2669–2678.

34. Roncaroli, F.; Olabe, J. A.; van Eldik, R. *Inorg. Chem.* **2003**, *42*, 4179–4189.

35. Roncaroli, F.; Olabe, J. A.; van Eldik, R. *Inorg. Chem.* **2002**, *42*, 5417–5425.

36. (a) Nast, R.; Schmidt, J. *Angew. Chem. internat. Edit.* **1969**, *8*, 383; (b) van Voorst, J. D. W.; Hemmerich, P. *J. Chem. Phys.* **1966**, *45*, 3914–3918.

37. Wanner, M.; Scheiring, T.; Kaim, W.; Slep, L. D.; Baraldo, L. M.; Olabe, J. A.; Zalis, S.; Baerends, E. J. *Inorg. Chem.* **2001**, *40*, 5704–5707.

38. Langford, C. H.; Gray, H. B. "*Ligand Substitution Processes*"; W. A. Benjamin, Inc., 1965.

39. Waldhoer, E.; Kaim, W.; Olabe, J. A.; Slep, L. D.; Fiedler, J. *Inorg. Chem.* **1997**, *36*, 2969–2974.

40. (a) Cheney, R. P.; Simic, M. G.; Hoffman, M. Z.; Taub, I. A.; Asmus, K. D. *Inorg. Chem.* **1977**, *16*, 2187–2192; (b) Hankiewicz, E.; Stradowski, Cz.; Wolszczak, M. J. *Radioanal. Nucl. Chem. Lett.* **1986**, *105*, 291–302.

41. Toma, H. E.; Moroi, N. M.; Iha, N. Y. M. *An. Acad. brasil. Cienc.* **1982**, *54*, 315–323.

42. Legros, J. *J. Chim. Phys. Phys.-Chim. Biol.* **1964**, *61*, 909.

43. Toma, H. E.; Malin, J. M.; Giesbrecht, E. *Inorg. Chem.* **1973**, *12*, 2084.

44. Toma, H. E.; Malin, J. M. *Inorg. Chem.* **1973**, *12*, 2080.

45. Toma, H. E.; Batista, A. A.; Gray, H. B. *J. Am. Chem. Soc.* **1982**, *104*, 7509–7515.

46. (a) Toma, H. E.; Giesbrecht, E.; Malin, J. M.; Fluck, E. *Inorg. Chim. Acta* **1975**, *14*, 11; (b) Olabe, J. A.; Zerga, H. O.; Gentil, L. A. *J. Chem. Soc. Dalton Trans.* **1987**, 1267–1269.
47. (a) Bohle, D. S.; Hung, C. H. *J. Am. Chem. Soc.* **1995**, *117*, 9584–9585; (b) Bohle, D. S.; Debrunner, P.; Fitzgerald, J. P.; Hansert, B.; Hung, C. H.; Thomson, A. *J. Chem. Commun.* **1997**, 91–92.
48. (a) Butler, A. R.; Calsy-Harrison, A. M.; Glidewell, C. *Polyhedron* **1988**, *7*, 1197–1202; (b) Oszajca, J.; Stochel, G.; Wasiliewska, E.; Stasicka, Z.; Gryglewski, R. J.; Jakubowski, A.; Cieslik, K. *J. Inorg. Biochem.* **1998**, *69*, 121–127.
49. (a) Stochel, G.; van Eldik, R. *Inorg. Chim. Acta* **1991**, *190*, 55–59; (b) James, A. D.; Murray, R. S.; Higginson, W. C. E. *J. Chem. Soc. Dalton Trans.* **1974**, 1273–1278.
50. Hoshino, M.; Maeda, M.; Konishi, R.; Seki, H.; Ford, P. C. *J. Am. Chem. Soc.* **1996**, *118*, 5702–5707.
51. Roncaroli, F.; Ruggiero, M. E.; Franco, D. W.; Estiú, G. L.; Olabe, J. A. *Inorg. Chem.* **2002**, *41*, 5760–5769.
52. Wang, Y.; Averill, B. A. *J. Am. Chem. Soc.* **1996**, *118*, 3972–3973.
53. Silvestrini, M. C.; Tordi, M. G.; Musci, G.; Brunori, M. *J. Biol. Chem.* **1990**, *265*, 11783–11787.
54. Kim, C. H.; Hollocher, T. C. *J. Biol. Chem.* **1984**, *259*, 2092–2099.
55. (a) Swinehart, J. H.; Rock, P. A. *Inorg. Chem.* **1966**, *5*, 573–576; (b) Masek, J.; Wendt, H. *Inorg. Chim. Acta* **1969**, *3*, 455–458.
56. Wolfe, S. K.; Swinehart, J. H. *Inorg. Chem.* **1975**, *14*, 1049–1053.
57. (a) Masek, J.; Maslova, E. *Collection Czechoslov. Chem. Commun.* **1974**, *39*, 2141–2160; (b) Fiedler, J. *Collection Czechoslov. Chem. Commun.* **1993**, *58*, 461–473; (c) Bertolino, J. R.; Della Védova, C. O.; Sala, O. *Polyhedron* **1989**, *8*, 361–365; (d) Bowden, W. L.; Bonnar, P.; Brown, D. B.; Geiger, W. E. Jr. *Inorg. Chem.* **1977**, *16*, 41–43; (e) Carapuca, H. M.; Simao, J. E. J.; Fogg, A. G. *J. Electroanal. Chem.* **1998**, *455*, 93–105.
58. González Lebrero, M. C.; Scherlis, D. A.; Estiú, G. L.; Olabe, J. A.; Estrin, D. A. *Inorg. Chem.* **2001**, *40*, 4127–4133.
59. Baumann, F.; Kaim, W.; Baraldo, L. M.; Slep, L. D.; Olabe, J. A.; Fiedler, J. *Inorg. Chim. Acta* **1999**, *285*, 129–133.
60. Morando, P. J.; Borghi, E. B.; Schteingart, L. M.; Blesa, M. A. *J. Chem. Soc. Dalton Trans.* **1981**, 435–440.
61. (a) Wilson, R. D.; Ibers, J. A. *Inorg. Chem.* **1979**, *18*, 336–343; (b) Southern, J. S.; Hillhouse, G. L. *J. Am. Chem. Soc.* **1997**, *119*, 12406–12407; (c) Sellmann, D.; Gottschalk-Gaudig, T.; Hausinger, D.; Heinemann, F. W.; Hess, B. A. *Chem Eur. J.* **2001**, *7*, 2099–2103.
62. Gutiérrez, M. M.; Amorebieta, V. T.; Estiú, G. L.; Olabe, J. A. *J. Am. Chem. Soc.* **2002**, *124*, 10307–10319.
63. Alluisetti, G.; Almaraz, A. E.; Amorebieta, V. T.; Doctorovich, F. D.; Olabe, J. A. Work in progress.
64. Barley, M. H.; Takeuchi, K. J.; Meyer, T. J. *J. Am. Chem. Soc.* **1986**, *108*, 5876–5885.
65. Einsle, O.; Messerschmidt, A.; Huber, R.; Kroneck, P. M. H.; Neese, F. *J. Am. Chem. Soc.* **2002**, *124*, 11737–11745.
66. (a) Armor, J. N.; Hoffman, M. Z. *Inorg. Chem.* **1975**, *14*, 444–446; (b) Cheney, R. P.; Armor, J. N. *Inorg. Chem.* **1977**, *16*, 3338.
67. Olabe, J. A.; Estiú, G. L. *Inorg. Chem.* **2003**, *42*, 4873–4880.
68. Baraldo, L. M.; Bessega, M. S.; Rigotti, G. E.; Olabe, J. A. *Inorg. Chem.* **1994**, *33*, 5890–5896.

69. (a) Hendrich, M. P.; Logan, M.; Andersson, K. K.; Arciero, D. M.; Lipscomb, J. D.; Hooper, A. B. *J. Am. Chem. Soc.* **1994**, *116*, 11961–11968; (b) Hendrich, M. P.; Petasis, D.; Arciero, D. M.; Hooper, A. B. *J. Am. Chem. Soc.* **2001**, *123*, 2997–3005.
70. Forlano, P.; Parise, A. R.; Olabe, J. A. *Inorg. Chem.* **1998**, *37*, 6406–6407.
71. Burewicz, A.; Haim, A. *Inorg. Chem.* **1988**, *27*, 1611.
72. Roncaroli, F.; Baraldo, L. M.; Slep, L. D.; Olabe, J. A. *Inorg. Chem.* **2002**, *41*, 1930–1939.
73. Stanbury, D. M. *Adv. Inorg. Chem.* **1989**, *33*, 69–138.
74. Lunak, S.; Veprek-Siska, J. *Collection Czechoslov. Chem. Commun.* **1974**, *39*, 2719–2723.
75. Wolfe, S. K.; Andrade, C.; Swinehart, J. H. *Inorg. Chem.* **1974**, *13*, 2567–2572.
76. (a) Katz, N. E.; Blesa, M. A.; Aymonino, P. J. *J. Inorg. Nucl. Chem.* **1980**, *42*, 581–585; (b) Maciejowska, I.; Stasicka, Z.; Stochel, G.; van Eldik, R. *J. Chem. Soc. Dalton Trans.* **1999**, 3643–3649.
77. Johnson, M. D.; Wilkins, R. G. *Inorg. Chem.* **1984**, *23*, 231–235.
78. (a) Trogler, W. C. *Coord. Chem. Rev.* **1999**, *187*, 303–327; (b) Armor, J. N.; Taube, H. *J. Am. Chem. Soc.* **1969**, *91*, 6874–6876; (c) Bottomley, F.; Brooks, W. V. F. *Inorg. Chem.* **1977**, *16*, 501–502; (d) Tuan, D. F.; Hoffmann, R. *Inorg. Chem.* **1985**, *24*, 871–876.
79. Taube, H. *Pure Appl. Chem.* **1979**, *51*, 901–912.
80. Hidai, M.; Mizobe, Y. "*Reactions of Coordinated Ligands*", Vol. II; Ed. Braterman, P. S. Plenum Publ. Corp: New York, 1989, pp. 53–114.
81. Fomitchev, D. V.; Bagley, K. A.; Coppens, P. *J. Am. Chem. Soc.* **2000**, *122*, 532–533.
82. Douglas, P. G.; Feltham, R. D. *J. Am. Chem. Soc.* **1972**, *94*, 5254–5258.
83. (a) Dozsa, L.; Kormos, V.; Beck, M. T. *Inorg. Chimica Acta* **1984**, *82*, 69; (b) Butler, A. R.; Glidewell, C.; Reglinski, J.; Waddon, A. *J. Chem. Res. Synop.* **1984**, *9*, 279; (c) Casado, J.; Mosquera, M.; Rodríguez Prieto, M.F.; Vázquez Tato, J. *Ber. Bunsenges. Phys. Chem.* **1985**, *89*, 735; (d) Beck, M. T.; Kathó, A.; Dozsa, L. *Inorg. Chim. Acta* **1981**, *55*, L55.
84. Trápani, C.; Escola, N.; Doctorovich, F. *Organometallics* **2002**, *21*, 2021–2023.
85. Doctorovich, F.; Trápani, C. *Tetrahedron Lett.* **1999**, *40*, 4635–4638.
86. Doctorovich, F.; Escola, N.; Trápani, C.; Estrin, D. A.; González Lebrero, M. C.; Turjanski, A. G. *Organometallics* **2000**, *19*, 3810–3817.
87. Doctorovich, F.; Granara, M.; Di Salvo, F. *Transition Met. Chemistry* **2001**, *26*, 505–509.
88. (a) Akhtar, M. J.; Bonner, F. T.; Borer, A.; Cooke, I.; Hughes, M. N. *Inorg. Chem.* **1987**, *26*, 4379–4382; (b) Akhtar, M. J.; Bonner, F. T.; Hughes, M. N.; Lu, C. S.; Wallis, H. L.; Wimbledon, P. E. *Inorg. Chem.* **1987**, *26*, 2437; (c) Hughes, M. N.; Wimbledon, P. E. *J. Chem. Soc. Dalton Trans.* **1976**, 703.
89. Audrieth, L. F.; Ogg, B. A. "*The Chemistry of Hydrazine*"; J. Wiley & Sons: New York, 1951.
90. (a) Katz, N. E.; Olabe, J. A.; Aymonino, P. J. *J. Inorg. Nucl. Chem.* **1977**, *39*, 908–910; (b) Olabe, J. A.; Gentil, L. A. *Transition Metal Chem.* **1983**, *8*, 65–69.
91. Funai, I. A.; Blesa, M. A.; Olabe, J. A. *Polyhedron* **1989**, *8*, 419–426.
92. (a) Lehnert, N.; Wiesler, B. E.; Tuczek, F.; Hennige, A.; Sellmann, D. *J. Am. Chem. Soc.* **1997**, *119*, 8869–8878; (b) *ibid.* 1997, 119, 8879–8888, and refs. therein.
93. Keene, F. R. *Coord. Chem. Rev.* **1999**, *187*, 121–149.
94. da Costa Ferreira, A. M.; Toma, H. E. *J. Chem. Soc. Dalton Trans.* **1983**, 2051–2055.
95. Goto, M.; Takeshita, M.; Kanda, N.; Sakai, T.; Goedken, V. L. *Inorg. Chem.* **1985**, *24*, 582–587.
96. Toma, H. E.; da Costa Ferreira, A. M.; Murakami Iha, N. Y. *Nouv. J. Chim.* **1985**, *9*, 473–478.
97. Goedken, V. L. *J. Chem. Soc. Chem. Commun.* **1972**, 207.

98. (a) Olabe, J. A.; Aymonino, P. J. *J. Inorg. Nucl. Chem.* **1974**, *36*, 1221–1226; (b) Blesa, M. A.; Olabe, J. A.; Aymonino, P. J. *J. Chem. Soc. Dalton Trans.* **1976**, 1196–1199.
99. Katz, N. E.; Blesa, M. A.; Olabe, J. A.; Aymonino, P. J. *J. Chem. Soc. Dalton Trans.* **1978**, 1603–1606.
100. Williams, P. A. M.; Aymonino, P. J. *Inorg. Chim. Acta* **1986**, *113*, 37–41.
101. Herington, E. F. G. *J. Chem. Soc.* **1959**, *3633*, 72.
102. Felix, F.; Ludi, A. *Inorg. Chim. Acta* **1977**, *24*, L-11.
103. Bott, P. A.; Lott, K. A. K. *Inorg. Chim. Acta* **1986**, *111*, L33–L34.
104. Wieghardt, K. *Adv. Inorg. Bioinorg. Mech.* **1984**, *3*, 213–274.
105. Lunak, S.; Veprek-Siska, J. *Collection Czechoslov. Chem. Commun.* **1974**, *39*, 391–395.
106. Lunak, S.; Veprek-Siska, J. *Collection Czechoslov. Chem. Commun.* **1974**, *39*, 41–48.
107. Choi, I. K.; Liu, Y.; Wei, Z.; Ryan, M. D. *Inorg. Chem.* **1997**, *36*, 3113–3118.
108. Banyai, I.; Dozsa, L.; Beck, M. T.; Gyemant, G. *J. Coord. Chem.* **1996**, *37*, 257–270.
109. (a) Singh, J. *Biochimica et Biophysica Acta* **1973**, *333*, 28–36; (b) Allen, J. W. A.; Watmough, N. J.; Ferguson, S. J. *Nature Struct. Biol.* **2000**, *7*, 885–888.
110. (a) Davies, G.; Garafalo, A. R. *Inorg. Chem.* **1976**, *15*, 1101–1106; (b) Bray, D. G.; Thompson, R. C. *Inorg. Chem.* **1994**, *33*, 905–909.
111. Olabe, J. A. *et al.* Unpublished work.
112. (a) Gmelins Handbuch der anorganischen Chemie, **1932**, *B59*, 903; (b) Baran, E. J.; Muller, A. *Z. Anorg. Allg. Chemie* **1969**, *B368*, 144–154.
113. James, A. D.; Murray, R. S. *J. Chem. Soc. Dalton Trans.* **1977**, 319–321.
114. Sulfab, Y. *Inorg. Chim. Acta* **1977**, *22*, 35–38.
115. Kuehn, C. G.; Taube, H. *J. Am. Chem. Soc.* **1976**, *98*, 689–702.
116. Kline, M. A.; Barley, M. H.; Meyer, T. J. *Inorg. Chem.* **1987**, *26*, 2197–2198.
117. Lui, A. M.; Liang, W.; Soriano, A.; Cowan, J. A. *J. Am. Chem. Soc.* **1994**, *116*, 4531–4536.
118. Szacilowski, K.; Stochel, G.; Stasicka, Z.; Kisch, H. *New J. Chem.* **1997**, *21*, 893–902.
119. Schwane, J. D.; Ashby, M. T. *J. Am. Chem. Soc.* **2002**, *124*, 6822–6823.
120. Szacilowski, K.; Wanat, A.; Barbieri, A.; Wasiliewska, E.; Witko, M.; Stochel, G.; Stasicka, Z. *New J. Chem.* **2002**, *26*, 1495–1502.
121. Rock, P. A.; Swinehart, J. H. *Inorg. Chem.* **1966**, *5*, 1078–1079.
122. Macartney, D. H.; McAuley, A. *J. Chem. Soc. Dalton Trans.* **1981**, 1780–1787.
123. Oliveira, L. A. A.; Giesbrecht, E.; Toma, H. E. *J. Chem. Soc. Dalton Trans.* **1979**, 236–239.
124. Vrachnou, E.; Gratzel, M.; McEvoy, A. J. *J. Electroanal. Chem.* **1989**, *258*, 193.
125. (a) Yang, M.; Thompson, D. M.; Meyer, G. *J. Inorg. Chem.* **2002**, *41*, 1254–1262; (b) Blackbourn, R. L.; Johnson, C. S.; Hupp, J. T. *J. Am. Chem. Soc.* **1991**, *113*, 1060–1062; (c) Lu, H.; Proeskorn, J. N.; Hupp, J. T. *J. Am. Chem. Soc.* **1993**, *115*, 4927–4928; (d) Khoudiakov, M.; Parise, A. R.; Brunschwig, B. C. *J. Am. Chem. Soc.* **2003**, *125*, 4637–4642.
126. Haim, A. ''*Adv. Chem. Ser.*''; American Chemical Society: Washington, USA, 1997, pp. 239–254, Chapter 14.
127. Almaraz, A. E.; Gentil, L. A.; Baraldo, L. M.; Olabe, J. A. *Inorg. Chem.* **1996**, *35*, 7718–7727.
128. Chen, M. H.; Lee, S.; Liu, S.; Yeh, A. *Inorg. Chem.* **1996**, *35*, 2627–2629.
129. Ram, M. S.; Haim, A. *Inorg. Chem.* **1991**, *30*, 1319.
130. Parise, A. R.; Baraldo, L. M.; Olabe, J. A. *Inorg. Chem.* **1996**, *35*, 5080–5086.
131. Olabe, J. A.; Haim, A. *Inorg. Chem.* **1989**, *28*, 3277.
132. Yeh, A.; Haim, A. *J. Am. Chem. Soc.* **1985**, *107*, 369.
133. Nordmeyer, F.; Taube, H. *J. Am. Chem. Soc.* **1968**, *90*, 1162.

CARBONATO COMPLEXES: MODELS FOR CARBONIC ANHYDRASE

ACHYUTA N. ACHARYA[1,2], ARABINDA DAS[3] and ANADI C. DASH[1]

[1]Department of Chemistry, Utkal University, Bhubaneswar 751 004, India
[2]Present Address: Institute of Textile Technology, Choudwar 754 025, Orissa, India
[3]Department of Neurology, Medical University of South Carolina, 96 Jonathan Lucas Str., Charleston, SC 29425, USA

I. Introduction
II. Carbonic Acid, Bicarbonate, and Carbonate
  A. Solubility and Equilibria of CO_2 in Solution
  B. Kinetics of CO_2 Hydration and Carbonic Acid Dehydration
III. The Chemistry of Metal Carbonates
  A. Solution Equilibria and Solid State Studies
IV. Kinetics and Mechanism of Formation and Aquation/Decarboxylation Reactions
  A. Formation of Carbonato Complexes
  B. Aquation/Decarboxylation Reaction
V. Discovery and Classification of Carbonic Anhydrases
VI. Structure of α-Class Carbonic Anhydrase from Human Erythrocytes (the High Activity form HCA II)
  A. The pK_a of Zinc-bound H_2O
  B. Catalytic Mechanism
  C. Interconversion Between CO_2 and HCO_3^-
  D. The H_2O Splitting Step
  E. Electronic Mechanism for Catalysis of HCA II
  F. Mechanistic Insight for the Catalyzed Reaction
  G. Mechanism of Inhibition
  H. Activators
VII. Structure of β-Carbonic Anhydrase from the Red Alga, *Porphyridium purpureum*
  A. Proposed CO_2 Hydration Mechanism
VIII. Structure of γ-Class Carbonic Anhydrase of *Methanosarcina thermophila* (*Cam*)
  A. Proposed CO_2 Hydration Mechanism for γ-Class Carbonic Anhydrase
IX. A δ-Class of Carbonic Anhydrase?
X. Model Chemistry
  A. Recognition of Anionic Inhibitors by the Model Complexes
XI. Concluding Remarks
XII. Abbreviations
References

ADVANCES IN INORGANIC CHEMISTRY
VOLUME 55 ISSN 0898-8838 DOI 10.1016/S0898-8838(03)55003-6

© 2004 Elsevier Inc.
All rights reserved.

I. Introduction

The general chemistry of carbonato complexes of metals was reviewed by Maccoll (*1*) and Harris *et al.* (*2*) during 1969 and 1970. This was then followed by an extensive and detailed review in 1983 by Palmer and van Eldik (*3*) covering, synthesis, structure, spectroscopy, solid state, and solution state kinetic studies in addition to the thermodynamic and kinetic properties of carbon dioxide dissolved in aqueous medium. They also discussed the chemistry of metal–carbon dioxide complexes including insertion of CO_2 in the M–H, M–C, M–N, and M–O bonds, and geochemical aspects of carbonato complexes (*3*). Subsequently further details on the organometallic chemistry of carbon dioxide with group six (M = Cr, Mo, W) metal atoms, the structure and bonding modes of CO_2, and the photo-isomerization of coordinated CO_2 was discussed in a review by Gibbson (*4*). A spectroscopic and theoretical study of the reactions of group six metal atoms (Cr, Mo, W) with CO_2 was reported by Souter and Andrews (*5*). It was shown by them that the group 6 metal atoms generated by laser ablation react with CO_2 to give the insertion products, OMCO and $OM(CO)_2$; these were isolated in argon matrices and identified by the effects of isotopic substitution on their infrared spectra. The CO_2 complex $Cr(\eta^1\text{-OCO})$ upon irradiation with UV-light undergoes photo-isomerisation to give OCrCO, an interesting example of photo-activation of CO_2. The chemical fixation of CO_2, methods of recycling CO_2 generated in industrial emissions and also replacing petroleum by CO_2 as the starting material for the synthesis of fine chemicals presents exciting and potential fields of research on CO_2 which is considered as not environmental friendly due to the "green house" effect. Accordingly, CO_2 reduction, activation and insertion have been actively pursued and review literature on this subject is quite extensive (*6–9*). As a result of chemical, photochemical, and electrochemical transformations of CO_2, a wide variety of products such as carbonates, methanol, formate, oxalate, alkanes have been generated and a wide range of insertion reactions involving CO_2 continue to be reported, enriching the chemistry of CO_2 and metal carbonate. The growing interest in the metal ion speciation in the aquatic environment in the presence of carbonate, structural, and coordination modes of CO_3^{2-}, has resulted in the synthesis and structural characterization of mononuclear and bridged carbonato complexes with varying degree of nuclearity (*10*). The interaction of CO_2 with transition metal substituted heteropoly anions in non-polar solvents has been reported (*11*). This is of great importance in terms of CO_2 fixation and its

conversion to desirable products by electrochemical reduction under mild conditions.

The importance of the biochemistry of hydration of CO_2 and dehydration of HCO_3^- in an aqueous environment has led to extensive and invigorating research on the enzyme carbonic anhydrase pertaining to its structural details, metal ion cofactor, its coordination environment (*12*) and kinetic activity. Model studies, both theoretical and experimental, have been undertaken using primarily the complexes of Zn(II), Mn(II), and Co(II), the latter one being its closest equivalent (*13*).

It is the intention of the authors to present a brief account on metal carbonato complexes which have a direct bearing on the reversible hydration of CO_2 by the enzyme carbonic anhydrase. Emphasis is placed on the integration of the kinetic and mechanistic concepts derived from the studies on model systems with the available kinetic, chemical and structural information on the enzyme carbonic anhydrase. To start, the kinetics and equilibria of dissolved CO_2, relevant to the present context, are presented.

II. Carbonic Acid, Bicarbonate, and Carbonate

A. Solubility and Equilibria of CO_2 in Solution

Carbon dioxide is a symmetric linear molecule with zero dipole moment. Hence its interaction with a dipolar molecule like H_2O is weak. However, it is moderately soluble in water and in many other organic solvents. The solubility equilibrium can be described by Eq. (1):

$$CO_2(g) \overset{K_s}{\rightleftharpoons} CO_2(s) \tag{1}$$

where the abbreviations "g" and "s" denote gas and solution phases, respectively, and $CO_2(s)$ is the total dissolved carbon dioxide. The solubility of CO_2 in water, D_2O and various organic solvents and their aqueous binaries has been reported (*14*). For water the mole fraction of dissolved CO_2 (X) at 1 atmosphere partial pressure is expressed as $R \ln X = A + B/T\ C \ln(T/K) + D\ T$ at $273 < T/K < 358$ with $A = -1327.8\,J\,K^{-1}\,mol^{-1}$, $B = 72{,}611.6\,J\,mol^{-1}$, $C = 179.99\,J\,K^{-1}\,mol^{-1}$, $D = -0.009159\,J\,K^{-1}\,mol^{-1}$. The corresponding values for D_2O (298–358°K) are −1256.2, 71,256.6, and 167.75 for A, B, and C, respectively (*15*).

The equilibrium constant K_s^0 (molality scale) and ΔH_s^0 at 25.0 °C (1 atmosphere pressure = 101.325 kPa) from the available data for aqueous medium are 0.03416 ± 0.00015 mol Kg^{-1} $atom^{-1}$ and -19.74 ± 0.17 kJ mol^{-1}, respectively (*16*). Patterson and co-workers (*17*) determined the dissociation constant of carbonic acid, H_2CO_3 [Eq. (2)], $K_0 = (1.72 \pm 0.05) \times 10^{-4}$ mol Kg^{-1}) the species believed to be formed by hydration of CO_2,

$$H_2CO_3 \overset{K_0}{\rightleftharpoons} H^+ + HCO_3^- \tag{2}$$

by high field conductivity measurements. Available data from pressure jump (1.6×10^{-4} mol Kg^{-1}, 25.0 °C, $I = 0.01$ M) and flow thermoelectric methods (*18*) ($2.5 \pm 0.3 \times 10^{-4}$ mol Kg^{-1}) are in good agreement. The majority of studies report the ionization of dissolved CO_2 as

$$CO_2(aq) + H_2O \overset{K_1}{\rightleftharpoons} H^+ + HCO_3^- \tag{3}$$

$$HCO_3^- \overset{K_2}{\rightleftharpoons} H^+ + CO_3^{2-} \tag{4}$$

and only 2–3% dissolved CO_2 constitute H_2CO_3. The hydration equilibrium of CO_2 is given by

$$CO_2 + H_2O \overset{K_{hyd}}{\rightleftharpoons} H_2CO_3 \tag{5}$$

for which the equilibrium constant, K_{hyd}^0, $(= K_1^0/K_0^0)$, based on $K_1^0 = 4.48 \times 10^{-7}$ and $K_0^0 = 1.72 \times 10^{-4}$, is 2.6×10^{-3} (*19*), indicating that the hydrolysis equilibrium of CO_2 is far removed to the left. The thermodynamic data for ionization of CO_2(aq) at 25.0 °C (1 atmosphere pressure) may be cited as $pK_1^0 = 6.356$, $\Delta H_1^0 = 9.156 \pm 0.063$ kJ mol^{-1}, $\Delta S_1^0 = -90.9 \pm 0.3$ J K^{-1} mol^{-1}; $pK_2^0 = 10.329$, $\Delta H_2^0 = 14.84$ kJ mol^{-1} and $\Delta S_2^0 = -148$ J K^{-1} mol^{-1}. For further details Ref. (*3*) may be consulted. The isotopic exchange equilibria [see Eqs. (6)–(8)]

$$H_2O + D_2O \rightleftharpoons 2HDO \quad K_3 \tag{6}$$

$$HCO_3^- + D_2O \rightleftharpoons DCO_3^- + HDO \quad K_4 \tag{7}$$

$$HCO_3^- + HDO \rightleftharpoons DCO_3^- + H_2O \quad K_5 \tag{8}$$

have been reported by Oliver and Davies (*20*). Using $K_3 = 3.8$ (25.0 °C), the values of K_4 and K_5 were calculated as 1.9 ± 0.2 and 0.5 ± 0.05, respectively, for 1 M $NaHCO_3$.

B. Kinetics of CO_2 Hydration and Carbonic Acid Dehydration

The rate of reversible hydration of carbon dioxide has been studied extensively and a critical evaluation of different techniques used has been documented by Kern (*21*). In the absence of an externally added catalyst the hydration reaction can be described as follows:

$$CO_2(aq) + H_2O \underset{k_{-1}}{\overset{k_1}{\rightleftharpoons}} H_2CO_3 \overset{K_0}{\rightleftharpoons} H^+ + HCO_3^- \tag{9}$$

$$CO_2(aq) + OH^- \underset{k_{-2}}{\overset{k_2}{\rightleftharpoons}} HCO_3^- \overset{K_2}{\rightleftharpoons} CO_3^{2-} + H^+ \tag{10}$$

$$CO_2(aq) + CO_3^{2-} + H_2O \underset{k_{-3}}{\overset{k_3}{\rightleftharpoons}} 2HCO_3^- \tag{11}$$

Below pH 7.4 (i.e., the pH of blood), Eq. (9) predominates and H_2CO_3 is an intermediate existing less than 2% of the total dissolved CO_2. The diffusion controlled rate constant for the protonation of HCO_3^- based on the coulombic concept is ca. 6.5×10^{10} M^{-1} s^{-1} in agreement with the experimental value reported by Eigen (*22*) as 4.7×10^{10} M^{-1} s^{-1} and this coupled with the equilibrium constant K_0 further yield the dissociation rate constant for H_2CO_3 as 1.1×10^7 s^{-1}. The dehydration rate constant (k_{-1}) from different sources has been tabulated by Palmer and van Eldik (*3*). An average value of k_{-1} (25.0 °C) is 23.7 s^{-1} and the associated activation parameters are: $\Delta H^{\neq} = 60.7 \pm 1.8$ kJ mol^{-1}, $\Delta S^{\neq} = -15.6$ J K^{-1} mol^{-1}. A study of the effect of pressure on k_{-1} by van Eldik and Palmer (*23*) yielded $\Delta V^{\neq} = +6.4 \pm 0.4$ cm^3 mol^{-1} (25.0 °C, $I = 0.5$ M), giving the mechanistic insight for a predominantly dissociative transition state. k_{-1} is insensitive to the ionic strength. The uncatalyzed hydration rate constant is generally calculated from k_{-1} and K_H ($k_1 = k_{-1}K_H$). Typical values of K_H (25.0 °C, $I = 0$) $= 2.6 \times 10^{-3}$ and with $k_{-1} = 23.7$ s^{-1} yield $k_1 = 6.16 \times 10^{-2}$ s^{-1} at 25.0 °C ($I = 0$). Contrastingly, the hydration rate constant (k_1) is significantly influenced by ionic strength $\{k_1$ (s^{-1}) $= -(8 \pm 3) \times 10^{-3} I + (3.9 \pm 0.5) \times 10^{-2}$; $0.005 \leq I$ (M) $\leq 3.0\}$ (*24,25*) despite the fact that the reaction involves neutral species. The currently proposed mechanism for hydration/dehydration

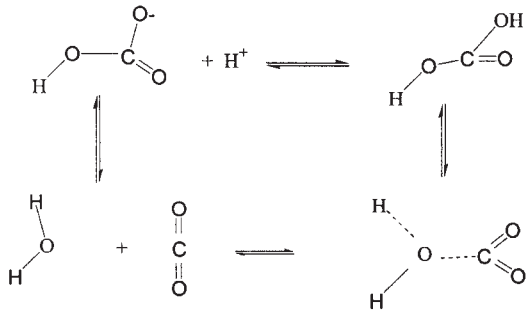

SCHEME 1. Uncatalyzed hydration/dehydration mechanism of CO_2.

is presented by Scheme 1 (*26a*). However, this mechanism still remains ambiguous.

Paneth and O'Leary (*26a*) investigated the ^{13}C isotope effects on the dehydration of HCO_3^- in water and D_2O at 1, 22, and 24 °C. The values for (k^{12}/k^{13}) reported by them are 1.0171 ± 0.0006 (1 °C, H_2O), 1.0151 ± 0.0008 (22 °C, H_2O), and 1.0178 ± 0.0005 (24 °C, D_2O) {earlier reported value: 1.0147 ± 0.0007 at 24 °C, H_2O} (*26b*). Model calculations were also made by them. They concluded that the mechanism of HCO_3^- dehydration is stepwise [see Eq. (12)]. The first step involves the protonation of bicarbonate by hydronium ion to the zwitterionic intermediate, H_2O^+–CO_2^-, which then decomposes to yield the products (CO_2 and H_2O); the rates of protonation and decomposition are similar.

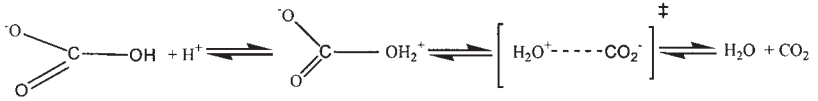

(12)

Whether the formation of the zwitterionic intermediate occurs by way of carbonic acid (H_2CO_3) or directly by the reaction of the hydronium ion with HCO_3^- still remains uncertain from the kinetic considerations.

The base hydrolysis of CO_2 [see Eq. (10)] has been extensively studied and a comparative account of the rate constant k_2 has been presented by Palmer and van Eldik (*3*). k_2 is 10^5 times higher than k_1 under comparable conditions despite the fact that CO_2 is a symmetrical and uncharged molecule with zero dipole moment. The values of $k_{2(av)}$ (M^{-1} s^{-1}), $\Delta H^{\neq}_{(av)}$ (kJ mol^{-1}) and $\Delta S^{\neq}_{(av)}$ (J K^{-1} mol^{-1}) at 25.0 °C and $I = 0$ are $(8.0 \pm 0.6) \times 10^3$, 54.4 ± 2.4, and 12 ± 8, respectively. k_2 also shows a minor ionic strength dependence ($\log k_2 = 3.772 + (0.213 \pm 0.013)$

I–$(0.0214 \pm 0.0028)I^2$) (*27*). The reverse rate constant k_{-2} calculated from the equilibrium constant $k_2/k_{-2} = 2.66 \times 10^7$ M^{-1} and $k_{2(av)} = 8.0 \times 10^3$ M^{-1} s^{-1} is 3.0×10^{-4} s^{-1} (25 °C) which is in good agreement with the value ($k_{-2} = 2.25 \times 10^{-4}$ s^{-1}, 25.0 °C) reported by Welch *et al.* (*28*).

Excess CO_3^{2-} catalyzes hydration of CO_2 {see Eq. (11); $k_{3(av)} = 1.2$ M^{-1} s^{-1} at 25 °C, $I = 0.5$, 1.5, and 2.5 M NaCl} (*25*). A general relationship [Eq. (13)] for the observed rate constant of hydration of CO_2 in terms of acid/base catalysis has been proposed and its experimental validity tested (*29,30*).

$$k_{obs} = k_1 + k_2[OH^-] + k_{HB}[HB] + k_B[B] \tag{13}$$

For $HB = H_2PO_4^-$, $k_{HPO_4^{2-}} = 0.3$ M^{-1} s^{-1}, and $k_{H_2PO_4^-} = 0$ ($I = 0$, 25 °C), where HPO_4^{2-} is considered as a weak base (*29*). Dennard and Williams (*29*) have also laid down criteria for oxoanions (on the basis of basicity) which behave as good catalysts. Two more reactions proposed for the catalyzed hydrolysis of CO_2 are

$$CO_2(aq) + CO_3^{2-} + OH^- \underset{k_{-4}}{\overset{k_4}{\rightleftharpoons}} HCO_3^- + CO_3^{2-} \tag{14}$$

$$CO_2(aq) + HCO_3^- + H_2O \underset{k_{-5}}{\overset{k_5}{\rightleftharpoons}} HCO_3^- + H_2CO_3 \tag{15}$$

for which $k_4 = 1.4 \times 10^5$ M^{-2} s^{-1}, $k_5 = 4.7 \times 10^{-2}$ M^{-1} s^{-1} (25.0 °C, $I = 0.5$–2.5) (*25*). The study of the intermolecular exchange reaction between CO_2(aq) and CO_3^{2-} in mild alkaline medium by Silverman *et al.* (*31,32*) using both ^{18}O label and ^{13}C enriched CO_3^{2-} has brought into focus the labile dimeric carbonato species ($-O_2C-O-CO_2^-$) which acts as a possible intermediate in the exchange process for which the rate constant is 114 ± 11 M^{-1} s^{-1}, $\Delta H^{\neq} = 63$ kJ mol^{-1} at 25.0 °C. Albeit bicarbonate does not enter into the exchange process. It still undergoes oxygen exchange with water (*33*).

III. The Chemistry of Metal Carbonates

A. Solution Equilibria and Solid State Studies

The stability constants of several carbonato complexes of metal ions in solution has been compiled (*3*). Several recent publications have dealt with the isolation and characterization of carbonato complexes

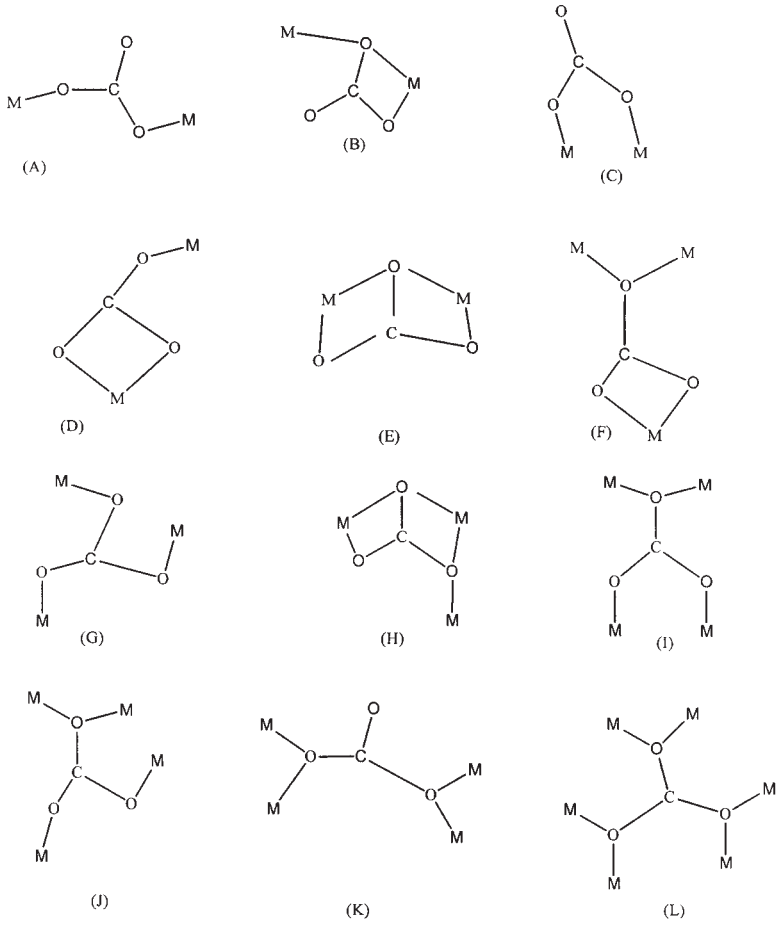

CHART 1. Different coordination modes of carbonate in metal carbonates.

in the solid state (*33*). A significant advancement has been made in understanding the hydration/dehydration reactions of CO_2 using Zinc(II) complexes which mimic the behavior of carbonic anhydrase (*34*). The novelty of the carbonate ligand is that it is capable of binding metal ions at the oxygen sites in a variety of ways generating mononuclear monodentate, bidentate, and poly nuclear complexes as depicted in Chart 1.

Martell *et al.* (*33g*) while studying the complex equilibria of a new octaaza macrobicyclic cryptand, $(MX)_3(tren)_2$ (containing two tren moieties and three *m*-xylyl groups) reported the synthesis and

X-ray structure of a carbonate bridged dicopper(II) cryptate, $[Cu_2(\mu\text{-}CO_3)((MX)_3\text{-}(tren)_2)H_3O)]Br_3 \cdot 3H_2O$. The cation consists of two five-coordinate copper(II) atoms separated by 5.850 Å; the copper atoms are simultaneously bridged by the binucleating ligand $(MX)_3(tren)_2$ and oxygen atoms of the carbonate which monodentately binds both the metal centers. The coordination geometry about each copper atom is trigonal bipyramidal; the carbonate oxygen atoms and tertiary nitrogen atoms of $(MX)_3(tren)_2$ occupy the axial sites and the secondary nitrogens of the cryptand occupy the equatorial sites. The crystallographic data for the dinuclear copper(II) cryptate shows a disordered carbonate bridge, the uncoordinated carbonate oxygen is hydrogen bonded to a hydronium ion. It was also pointed out that the Cu–O bond lengths for the bridging carbonate ($Cu^{II}O$–C(O)–OCu^{II}) is much shorter (Cu_1–$O_1 = 1.884$ Å, Cu_2–$O_2 = 1.821$ Å for the major component and Cu–$O_1 = 1.960$ Å, Cu_2–$O_2 = 2.046$ Å for the minor component of the cryptate, respectively) than Cu–O bond lengths observed for any other small complexes with ligands such as nitrate, carbonate, acetate, and formate, thereby suggesting the compression of the bonds of the bridging carbonate which may be responsible for the disorder.

Carbonate is a strong ligand for complexing *f*-group elements and plays important role in sequestering the lanthanides and actinides in the environment (*35*). Depending on the CO_2 partial pressure, pH, and ionic strength, $MOHCO_3$ (*36*), $M_2(CO_3)_3 \cdot nH_2O$, (*35–37*) and $NaM(CO_3)_2 \cdot nH_2O$ (*38*) (M = lanthanide and actinide) have been precipitated from carbonate containing solutions. The few single crystal structures recently reported for trivalent lanthanide carbonates consist of extended arrays of $La_2(CO_3)_2 \cdot 8H_2O$ (*39*), $(La/Ce)_2(CO_3)_3 \cdot 8H_2O$ (*40*) and $CsPr(CO_3)_2$ (*41*). The powder X-ray diffraction technique was used to study most solid carbonates of lanthanides. Lanthanide/actinide complexes, $M(CO_3)_2^{3-2n}$ ($n = 1$–3) have been identified spectroscopically in the solution phase (*37,42*). The first characterization of a mononuclear carbonato complex of Nd^{3+}, $[C(NH_2)_3]_5[Nd(CO_3)_4(OH_2)] \cdot H_2O$, by a single crystal X-ray structure determination and its solution structure by UV–vis–near-IR absorbance measurements have been reported by Runde and coworkers (*33d*). Nd in the anion $[Nd(CO_3)_4(OH_2)]^{5-}$ retains nine-coordination in a distorted monocapped antiprism with a twist angle of 23.2°. The central Nd atom is bound to nine O atoms of four bidentate carbonates and one coordinated H_2O capping the top. The Nd–O bond distances for the bidentate carbonates range between 2.452(3) and 2.544(3) Å; the longest distance 2.649(4) Å is to the oxygen atom of the

coordinated H_2O. The visible spectral shift from 574.1 to 583.6 nm for Nd^{3+} aqua cation due to carbonate coordination in saturated carbonate solution matched with the diffuse reflectance spectra of $[C(NH_2)_3]_5[Nd(CO_3)_4(OH_2)] \cdot H_2O$ crystal (λ_{max} 582.3 nm). Runde *et al.* (*33d*) also pointed out that in solution lower carbonato complexes of Nd^{3+} are formed even in the presence of high concentration of the carbonate ligand. Similar studies have been reported on the Plutonium(IV) carbonato complexes, and the solid and solution state structure of $[Pu(CO_3)_5]^{6-}$ has been elucidated (*33f*). In the anion $[Pu(CO_3)_5]^{6-}$, the central Pu atom is 10-coordinate, each carbonate being linked to the metal through its two O atoms as a bidentate ligand. This structural unit is very similar to that of $[Th(CO_3)_5]^{6-}$ (*43*). The carbonato complexes of lanthanides and actinides are of importance with regard to the metal ion speciation in the environment. These are, however, not linked with the enzyme models for carbon dioxide hydration and hence are not dealt with in further detail.

The pH dependent complexation of copper(II) with ^{13}C labeled carbonate in aqueous medium was investigated by optical spectroscopy and continuous wave and pulse EPR by Schossler and co-workers (*33c*). They demonstrated the presence of different copper(II) carbonato complexes, in which carbonate is bound as monodentate (pH = 5.5) and bidentate ligand (*p*H 6.5 and 8). The proposed structures of the Cu(II)–carbonato complexes are shown in Fig. 1. The weakness of the monodentate coordination of carbonate is reflected by a small interaction of the unpaired electron of Cu^{2+} with ^{13}C of the carbonate. The bidentate coordination of carbonate in the equatorial plane is believed to result in a much larger coupling between the unpaired electron and ^{13}C which was explained in terms of a higher covalency of the bonding and delocalization of spin density through the π system of the carbonate ligand. Bidentate coordination of carbonate is a dominant feature at ambient temperature. The current research interest on atmospheric CO_2 fixation using Cu^{2+} has led to the synthesis and characterization of four new μ-CO_3^{2-} bridged copper(II) complexes with different coordination modes for the carbonato bridge: $\{(\mu_3\text{-}CO_3)[Cu_3(ClO_4)_3(Et_3dien)_3]\}(ClO_4)$ (**1**), $\{(\mu\text{-}CO_3)[Cu_2(OH_2)(Et_4dien)_2]\}(ClO_4)_2 \cdot H_2O$ (**2**); $\{(\mu\text{-}CO_3)[Cu_2(H_2O)_2)(EtMe_4dien)_2]\}(ClO_4)_2 \cdot 2H_2O$ (**3**); and $\{(\mu\text{-}CO_3)[Cu_2(H_2O)(Me_5dien)_2]\}(ClO_4)_2 \cdot H_2O$ (**4**) have been reported (*33e*) and the crystal structure of (**2**) has been solved. The structure of (**2**) consists of strongly asymmetric dinuclear unit $\{(\mu\text{-}CO_3)[Cu_2(OH_2)(Et_4dien)_2]\}^{2+}$, two ClO_4^- counter ions and one H_2O connected by hydrogen bonds. Susceptibility measurements indicated ferromagnetic behavior of the tri-nuclear compound (**1**),

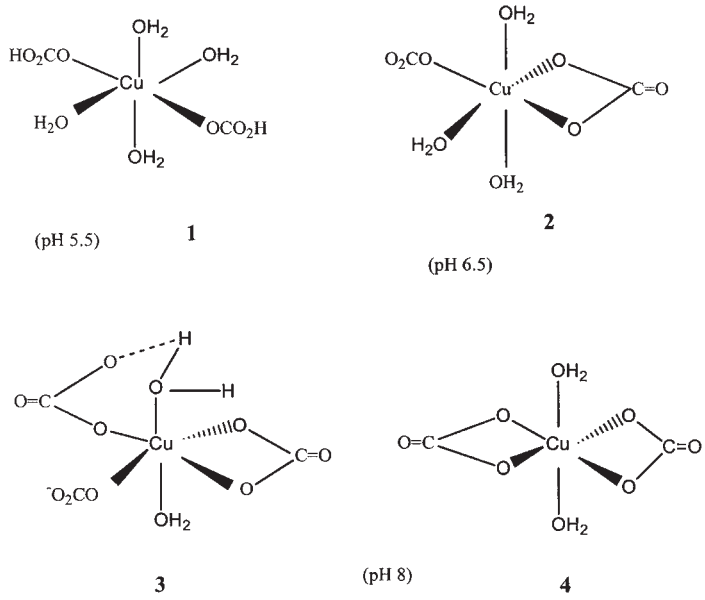

FIG. 1. Proposed structures of Cu(II)–carbonato complexes (*33e*).

while **2**–**4** are anti-ferromagnetically coupled [for further details see Ref. (*33e*)].

Two stable bicarbonato complexes of bis(1,10-phenanthroline) copper(II) were reported for the first time by Mao *et al.* (*44*). These are akin to the Lipscomb and Lindskog structures of human carbonic anhydrase (HCA) (*45*). In the Lipscomb structure the bicarbonate acts as a bidentate ligand while in the Lindskog structure it is essentially coordinated to the metal center in unidentate fashion (Fig. 2).

In the study of model systems, however, bicarbonato complexes of the type $L_mM^{II}(OCO_2H)$ (M = Zn, Cu, Co, Ni) were always considered to be unstable towards elimination of CO_2 and so far could not be fully structurally characterized (*10c,46*). It is important to note that these two structural motifs have been suggested to be part of the catalytic mechanism, possibly involving intramolecular proton transfer in the hydration/dehydration of CO_2 by HCA I and II (*45,47*). A few other structurally characterized chelated bicarbonato complexes reported so far are, $[Rh(H)_2(P(i\text{-}Pr)_3)_2(O_2COH)]$ (*48*) and $[Co(tepa)(O_2COH)](ClO_4)_2 \cdot 3H_2O$ (*49*). A chelated carbonato complex of cobalt(III) with macrocyclic tetradentate amine ligand, 9-(3-amino-propyl)-1,5,9-triazacyclododecane (L_1), $[Co(L_1)(O_2CO)](ClO_4)$ has been recently synthesized and structurally characterized (*50*). Knowledge

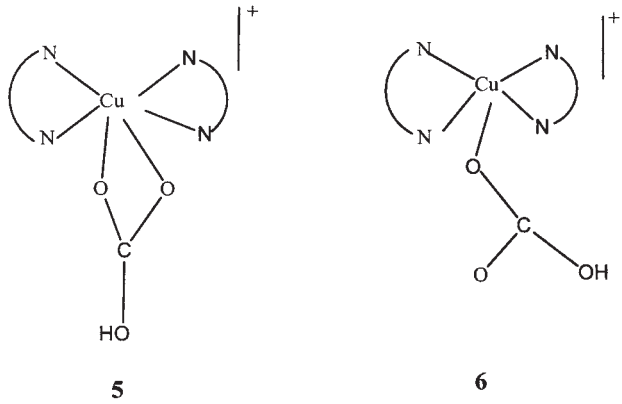

FIG. 2. $[Cu(phen)_2(OCO_2H)]^+$: N–N = 1,10-phenanthroline. **5** – Lipscomb structure; **6** – Lindskog structure.

of the structural features of carbonato and bicarbonato complexes of metal ions, Zn(II) in particular, is essential to fully understand the catalytic action of human carbonic anhydrase HCA. This requirement has accelerated the experimental and theoretical investigations of the carbonato complexes. The structural informations on some mononuclear carbonato and bicarbonato (monodentate/chelated) complexes are collected in Table I.

The X-ray structures of HCO_3^-–HCA I and a mutant intermediate of HCO_3^-–HCA II (Thr-200→His) (*52,53*) supports the Lindskog structure in which bicarbonate is bound to the metal ion Zn^{2+} in the active site of the enzyme as a unidentate ligand. On the other hand, the structure of bicarbonate bound to Co^{2+} in the Co^{II}-substituted carbonic anhydrase closely resembles the Lipscomb structure in which HCO_3^- is coordinated to the metal center as a bidentate ligand (with the two oxygen atoms of the coordinated bicarbonate at 2.3–2.5 Å from Co^{II}) (*54*). The bicarbonato complexes of Zn^{2+} have eluded structural characterization due to their instability to facile CO_2 elimination. Attempted synthesis and isolation of $[Zn(phen)_2(O_2COH]ClO_4$ in the solid state by van Hanauer *et al.* (*34m*) proved unsuccessful while it led to the isolation of the corresponding carbonato complex, $[Zn(phen)_2(O_2CO)]$, which was fully structurally characterized. However, they have used density functional theory (DFT) (*34m*) to calculate the structure and stabilities of the two possible bicarbonato complexes, $[Zn(phen)_2(OCO_2H)]^+$ and $[Zn(phen)_2(O_2C–OH)]^+$ in which bicarbonate is monodentate and bidentate, respectively, mimicking the Lindskog and Lipscomb structures (*45*) (Fig. 3).

TABLE I

METAL–OXYGEN BOND LENGTHS ($M–O_1$ AND $M–O_2$) AND THE BONDING MODES OF CARBONATE/BICARBONATE IN SOME MONONUCLEAR COMPLEXES

Complex	$M–O_1$/Å	$M–O_2$/ Å	HCO_3^-/CO_3^{2-}	Ref.
		Bonding mode		
$[RhH_2(P(i\text{-}Pr)_3)(O_2COH]$	2.306(3)	2.279(2)	bidentate	(*48*)
$[PPN]\{W(CO_5)(O_2COH)\}$	2.19	3.4	monodentate	*a*
$[Co(tepa)(O_2COH)](ClO_4)_2$	1.926(4)	1.932	bidentate	(*49*)
$[Co(L_1)(O_2CO)]ClO_4$	1.924(3)	1.923(3)	bidentate	*b*
$[Co(NH_3)_5(OCO_2)]Br,H_2O$	1.93		monodentate	*c*
$[Co(NH_3)_4(O_2CO)]Br$	1.93	1.94	bidentate	*c*
$[Co(en)_2(O_2CO)]I \cdot 2H_2O$	1.91	1.96	bidentate	*c*
$[Co(tn)_2(O_2CO)]ClO_4$	1.92	1.96	bidentate	*c*
$[Co(tren)(O_2CO)]Cl \cdot 3H_2O$	1.91(t), 1.93(p)	1.96	bidentate	*c*
$[Co(cyclen)(O_2CO)]ClO_4 \cdot H_2O$	1.91	1.96	bidentate	*c*
$[Co(3,8\text{-}Me_2trien)(O_2CO)]ClO_4$	1.92	1.96	bidentate	*c*
$[Co(Py)_4(O_2CO)]ClO_4$	1.89	1.98	bidentate	*c*
$[Co(phen)_2(O_2CO)]Br \cdot 4H_2O$	1.89	1.93	bidentate	*c*
$[Co(bipy)_2(O_2CO)]\ NO_3 \cdot 5H_2O$	1.89	1.92	bidentate	*c*
$[Co(tet\text{-}b)(O_2CO)]ClO_4$	1.91	2.02	bidentate	*c*
$[Cu(phen)_2(O_2COH)]ClO_4$	2.359(3)	2.359(7)	bidentate	(*34l*)
$[Cu(phen)_2(OCO_2H)]ClO_4$	2.23	2.54	monodentate	(*34l*)
$[Cu(phen)_2(O_2CO)] \cdot 7H_2O$	1.972	2.421	bidentate	(*34k*)
$[Cu(phen)_2(OCO_2)] \cdot 11H_2O$	1.964		monodentate	(*34k*)
$[Zn(phen)_2(O_2CO)] \cdot 7H_2O$	2.130	2.092	bidentate	(*34m*)
HCO_3^-–HCAII	2.23	2.54	monodentate	(*52*)
HCO_3^-–HCAI	1.8	3.5	monodentate	(*53*)

[a] Darensburg, D. J.; Jones, M. L. M.; Ribenspies, J. H. *Inorg. Chem.* **1993**, *32*, 4675.
[b] L_1 = 9(3-aminopropyl)-1,5,9-triazacyclododecane: Ref. (*50*).
[c] See Table 4 of Ref. (*51*).

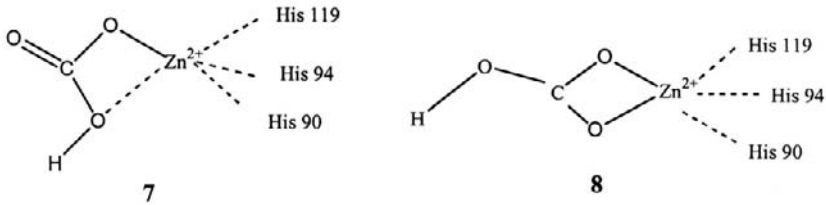

FIG. 3. **7** – Lindskog structure; **8** – Lipscomb structure.

From the DFT calculations the $Zn–O_1$ and $Zn–O_2$ distances for the gas phase structure of $[Zn(phen)_2(O_2CO)]$ (bidentate mode of binding of CO_3^{2-}) were calculated by them as 2.027Å in comparison to 2.130 and 2.092 obtained from X-ray structure. The structure and stability data for the two bicarbonato complexes of Zn^{II} obtained by DFT calculations were sensitive to the different basis sets and the polarization functions used. For example, the bidentate bicarbonate complex, $[Zn(phen)_2(O_2C–OH)]^+$ was found to be 34.3 kJ mol^{-1} (SHA svp), 26.8 k.J mol^{-1} (Ahlrichs triple zeta with polarization function) and 14.6 kJ mol^{-1} (Ahlrichs triple zeta) more stable than the quasi-monodentatate bicarbonato complex $[Zn(phen)_2(OCO_2H)]^+$. For the chelated bicarbonate complex (Fig. 4: **A**), the $Zn–O_1$ and $Zn–O_2$ bond lengths (calculated values) are 2.156 and 2.228 Å, respectively. The former is ~0.2 Å and the latter 0.13 Å shorter than in the related Cu^{II} complex (*34k*) and 0.129 and 0.201 Å longer than in the corresponding Zn^{II}–carbonate complex. The C–O(3) distance is elongated to 1.350 Å, and C–O(1) and C–O(2) distances are shortened to 1.267 and 1.260 Å, respectively. The influence of protonation of O(3) on the structure of phenanthroline is small and Zn–N bond lengths are 2.159, 2.169, 2.158, and 2.166 Å. The coordination sphere of the metal ion is best described as distorted octahedral (Fig. 4: **B**).

In the calculated stucture of **B** $[Zn(phen)_2(OCO_2H)]$ (monodentate coordination of bicarbonate), a strong Zn–O(2) bond of 1.972 Å and a weak binding of O(1) to Zn^{II} (Zn–O(1) bond length 2.698 Å) were reported, consistent with the corresponding Cu^{II} complex. It appears that the binding mode of bicarbonate in the Zn complex (**B**), assumes relatively more bidentate character than the same for the corresponding Cu^{II} complex which clearly shows monodentate coordination of bicarbonate (*34k*).

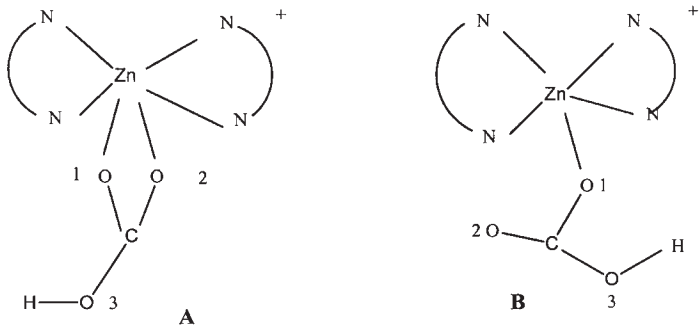

FIG. 4. $[(phen)_2ZnHCO_3]^+$. **A** – chelated; **B** – monodentate bicarbonate.

Based on the optimized structures, the ^{13}C NMR shielding factors for the carbonate/bicarbonate ligands in $[Zn(phen)_2(CO_3/HCO_3)]^{0/+}$ were also calculated. It appears that protonation of the chelated carbonate does not lead to any significant change in ^{13}C chemical shift, in contrast with the ring-opened protonated species. A comparison further showed that in the latter case the ^{13}C chemical shift is very close to that of the uncoordinated bicarbonate, suggesting thereby that the bicarbonate ligand is only weakly coordinated to the Zn^{II} center.

A series of binuclear bicarbonato and trinuclear carbonato complexes have been isolated (*34j*) when $[M(tren)(OH_2)](ClO_4)_2$ (M = Cu(II), Zn(II)) was allowed to react with $NaHCO_3$ at pH 6.5 and 8.5, respectively. Increasing the pH of the reaction mixture to 10 resulted in the formation of hydroxo bridged binuclear complexes. X-ray structures of these carbonato complexes are reported (*34j*).

1. $\{[Cu(tren)]_3(\mu_3\text{-}CO_3)\}(ClO_4)_4 \cdot H_2O$

The μ_3-bridged carbonato complex posseses a pseudo-3-fold molecular symmetry. Each of the Cu atoms is five coordinate with the four nitrogen atoms of tren and one oxygen atom of the carbonate ligand (**C**). The coordination polyhedron of the Cu atom can be described as almost (TBP), the copper ions being slightly out of the plane (0.15 Å) of the three primary amine groups (Fig. 5).

The carbonate group retains planarity and the three copper ions deviate from this plane by 0.05 Å. The Cu–O bond lengths in the complex are typical of five coordinate metal complexes

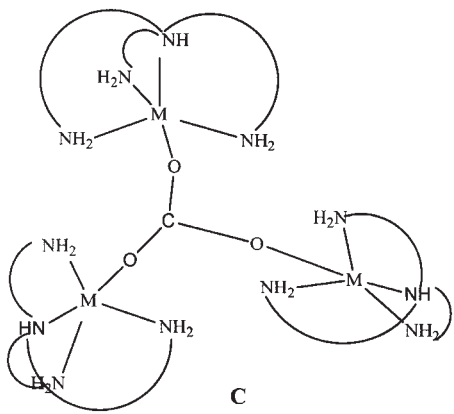

C

FIG. 5. **C** – $\{[M(tren)]_3(\mu_3\text{-}CO_3)\}$: M = Cu^{2+}, Zn^{2+}.

(Cu_1–O_1 = 1.922(8), Cu_2–O_2 = 1.922(9), Cu_3–O_3 = 1.933(6)). The CO_3^{2-} ion coordinates to the copper ions along the axis of the trigonal pyramidal structure. This differs from other cases in which CO_3^{2-} coordinates to copper ions along the basal plane of the SQPY (*33a,33b,55–58*).

2. {[Zn(tren)]$_3$(μ_3-CO$_3$)](ClO$_4$)$_4$ · H$_2$O

The structure of this complex is very similar to that of its copper(II) analogue. The coordination polyhedron of the zinc atom is essentially TBP with zinc ions slightly out of plane (±0.06 Å) of the three primary amine groups of *tren*. The three zinc atoms deviate from the plane of the carbonate group by ±0.05 Å. The bond lengths of Zn_1–O_1, Zn_2–O_2, and Zn_3–O_3 are 1.998(6), 2.007(7), and 1.998(7) Å, respectively. These are slightly longer than the corresponding Cu–O bond lengths in the analogous Cu complex. The structures of a few reported μ_3-carbonate bridged trinuclear complexes are summarized in Table II. It is worth noting that the tripodal tren and tmpa ligands favor the TBP structure in contrast with the tetragonal pyramidal coordination environment around the metal ion offered by the cyclic N_4 chelating ligand such as cyclen.

The three carbonato bridged polynuclear complexes of Cu(II) and Zn(II) with 1,10-phenanthroline and bipyridyl as the primary ligands

TABLE II

COORDINATION GEOMETRY AROUND THE METAL ION IN REPORTED μ_3-CO_3^{2-} BRIDGED COMPLEXES

Complex	Metal geometry	CO_3^{2-} position	Ref.
{[Cu(pip)(H_2O)]$_3$(μ_3-CO_3)}(ClO_4)$_4$	TP	Basal plane	(*56*)
{[Zn(dpt)]$_3$(μ_3-CO_3)}(ClO_4)$_4$	Tetrahedral	Apical	(*59*)
{[Cu(medpt)]$_3$(μ_3-CO_3)}(ClO_4)$_4$	TP	Basal plane	(*33a*)
{[Ni(medpt)]$_3$(μ_3-CO_3)(NCS)$_4$}	Octahedral	Apical	(*33b*)
{[Zn_3(bpy)$_6$(μ_3-CO_3)(H_2O)$_2$](ClO_4)$_4$	Octahedral and TBP	Apical and equatorial plane	(*57*)
{[Cu_6(bpy)$_{10}$(μ_3-CO_3)$_2$(μ_2-OH)$_2$]}(ClO_4)$_6$	TP	Basal plane and axial position	(*58*)
{[Zn(cyclen)]$_3$(μ_3-CO_3)}(ClO_4)$_4$	TP	Apical	(*34d*)
{[Cu([15]aneN_3O_2)]$_3$(μ_3-CO_3)}(ClO_4)$_4$	TP	Basal plane	(*55*)
{[Zn([15]aneN_3O_2)]$_3$(μ_3-CO_3)}(ClO_4)$_4$	TBP	Equatorial plane	(*55*)
{[Zn(tmpa)]$_3$(μ_3-CO_3)}(ClO_4)$_4$	TBP	Apical	(*60*)
{[Cu(tren)]$_3$(μ_3-CO_3)}(ClO_4)$_4$	TBP	Apical	(*34j*)
{[Zn(tren)]$_3$(μ_3-CO_3)}(ClO_4)$_4$	TBP	Apical	(*34j*)

reported by Mao *et al.* (*34l*) are $\{[Cu(phen)_2]_2(\mu_2\text{-}CO_3)\}$ $(ClO_4)_2 \cdot 4.25H_2O$ (**D_1**,**D_2**), $\{[Cu(phen)_2]_2(\mu_2\text{-}CO_3)\}$ $(ClO_4)_3 \cdot DMF \cdot H_2O$ (**E**), and $[(bpy)_2(H_2O)(\mu_2\text{-}CO_3)Zn(bpy)_2](NO_3)_2 \cdot 7H_2O$ (**F**). These compounds have been structurally characterized by X-ray. In the crystal of **D** they reported that there were two molecular units of identical composition but distinctly different structures with reference to the Cu–O bond distances. The structural data showed that the two N_4 bound Cu(1) and Cu(2) ions are bridged by carbonate approximately bidentately and unidentately, respectively. In one of the molecules the complex **D** shows a distortion between modes **D_1** and **D_2**, approaching **D_2**, a typical mode of carbonate binding not reported earlier as claimed by the authors (Fig. 6).

The coordination environment of the two copper atoms is tetragonal pyramidal and the carbonate coordinates along the basal plane. In the molecule both the N_4 coordinated Cu^{2+} ions are bridged by carbonate in a bidentate fashion (see **E**). The $Cu \cdots Cu$ distances in the molecules **D_1** and **D_2** are 4.303 and 4.548 Å, respectively, and the phen ligands show strong stacking interaction in the crystal.

In $\{[Cu(phen)_2]_2(\mu_2\text{-}CO_3)\}(ClO_4)_2 \cdot DMF \cdot H_2O$ (**E**), however, carbonate acts as a monodentate bridge between the two N_4Cu units which are in *anti–anti* modes. The structure of the complex is very similar to that of $\{[Cu(bpy)_2]_2(\mu_2\text{-}CO_3)\}(ClO_4)_2$ (*58*). The coordination polyhedron around the copper atoms is approximately tetragonal pyramidal and carbonate coordinates to the atoms along the basal plane with Cu–Cu distance of 5.296 Å (Cu_1–O_1 = 1.938 Å and Cu_2–O_2 = 2.693 Å for the terminal O of bound carbonate). Variable temperature magnetic moment measurements show weak ferromagnetic coupling of the copper(II) centers in both these complexes which is believed to occur intramolecularly via the carbonate bridge. The magnetic data in the temperature range 5–300 K of both the complexes fitted the relationship

$$\chi_m = (2N\beta^2 g^2/kT)[3 + \exp(-J/kT)]^{-1}(1 - \rho) + (N\beta^2 g^2/2kT)\rho + 0.000120$$

$$J = 13.0 \text{ cm}^{-1}, g = 2.00, \rho = 0.01 \text{ for complex } \mathbf{D};$$

$$J = 0.013 \text{ cm}^{-1}, g = 2.21, \rho = 0.001 \text{ for complex } \mathbf{E}$$

in which the second term accounts for a small proportion ρ of uncoupled copper(II); J is the singlet–triplet (S–T) energy gap, and the other parameters have their usual meaning. The difference in the values of

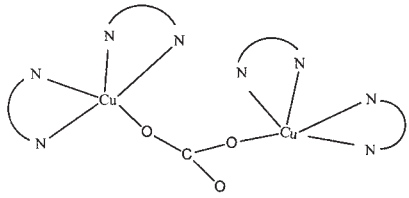

D1

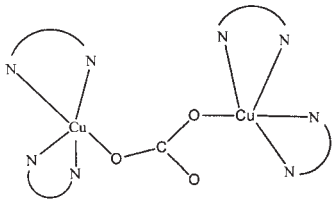

D2

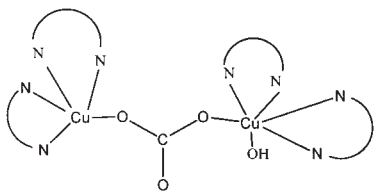

E

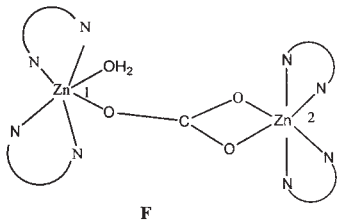

F

FIG. 6. Binuclear carbonato bridged complexes. N–N = phen (**D** and **E**); N–N = bpy (**F**).

J was attributed to the difference in the Cu–Cu distance and the simultaneous effect of the carbonate bridging mode for the two complexes.

In the binuclear complex, $[(bpy)_2(OH_2)Zn(\mu_2\text{-}CO_3)Zn(bpy)_2](NO_3)_2 \cdot 7H_2O$ (**F**), the two N_4-bound Zn_1 and Zn_2 ions are bridged by carbonate in monodentate and bidentate modes, the Zn_1 being coordinated to one H_2O. Both the zinc ions are octahedrally coordinated with a relatively greater degree of distortion at Zn_2 due to the chelating mode of the carbonate bridge. In these binuclear carbonate complexes of Zn(II) and Cu(II) an unexpected behavior, viz. Zn–O distances < Cu–O distances for carbonate coordination, was reported (*34l*).

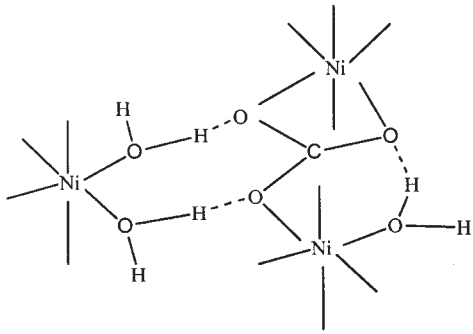

FIG. 7. Hydrogen bonding for $Ni_2(\mu\text{-}CO_3)(dmpd)_4(H_2O)]$ $[Ni(dmpd)_2(H_2O)_2](ClO_4)\cdot H_2O$.

A novel tridentate coordination mode for the carbonato–nickel(II) system was reported by Escuer and co-workers (*61*). The trinuclear compound $[Ni_2(\mu\text{-}CO_3)(dmpd)_4(H_2O)][Ni(dmpd)_2(H_2O)_2](ClO_4)_4\cdot H_2O$ was obtained from the reaction of basic solutions of nickel(II) perchlorate and 2,2-dimethylpropane-1,3-diamine (dmpd) with atmospheric CO_2. The three nickel atoms show octahedral coordination with three different environments, $Ni(CO_3\text{–}O,O')(dmpd)_2$, $Ni(CO_3\text{–}O')(dmpd)_2(H_2O)$ and $Ni(dmpd)_2(H_2O)_2$. The carbonate anion acts as a bridge between two nickel ions whereas the $[Ni(dmpd)_2(H_2O)_2]^{2+}$ subunit is linked by hydrogen bonds to the dinuclear group (Fig. 7). The dinuclear $[Ni_2(\mu\text{-}CO_3)(dmpd)_4(H_2O)]^{2+}$ subunit shows a moderately weak antiferromagnetic coupling with a J value of -7.8 cm^{-1}.

The syntheses and the crystal structures of the new tetranuclear μ_4-CO_3 complexes of copper(II), $[(\mu_4\text{-}CO_3)(\mu\text{-}Br)_2\{Cu_4(bapa)_4\}]Br_4$ and $[(\mu_4\text{-}CO_3)(\mu\text{-}Cl)_2\{Cu_4(bapma)_4\}]Cl_4\cdot 12H_2O$, were also reported by Escuer and co-workers (*62*) to elucidate the multiple bridging mode of CO_3^{2-}. The analogous compound $[(\mu\text{-}CO_3)(\mu_4\text{-}Cl)_2\{Cu_4(bapa)_4\}]Cl_4$ was also synthesized by them for comparative purposes. All these carbonato complexes showed very strong antiferromagnetic coupling.

IV. Kinetics and Mechanism of Formation and Aquation/Decarboxylation Reactions

The different types of coordination modes of carbonate in metal carbonato complexes offer challenges to investigate intimate mechanisms of their formation. The study of the kinetics and mechanisms of the formation and decomposition of such complexes, therefore, continue to be an interesting area of activity as it has a direct bearing on

the hydration of CO_2 and dehydration of bicarbonate by the enzyme carbonic anhydrase. This section is devoted to a general survey of the kinetics and mechanism of formation and aquation/substitution of metal carbonato complexes.

A. Formation of Carbonato Complexes

CO_2 dissolved in aqueous medium is an equilibrium mixture of CO_2/H_2CO_3, HCO_3^-, and CO_3^{2-} as denoted by Eq. (16).

$$CO_2(aq) + H_2O \rightleftharpoons (H_2CO_3) \rightleftharpoons \begin{matrix} HCO_3^- \\ \Big\uparrow\!\Big\downarrow K_2 \\ CO_3^{2-} \end{matrix} + H^+ \quad : K_1 \qquad (16)$$

The hydration rate constant of CO_2, the dehydration rate constant of carbonic acid (H_2CO_3), and pK_1, pK_2 values (p$K_1 = 6.03$, p$K_2 = 9.8$ at 25 °C, $I = 0.5$ M) (*63*) are such that nearly 99% of dissolved carbon dioxide in water at pH < 4 exists as CO_2. However, these four different species may be considered as the reactive species under different pH conditions which can react with aqua metal ions or their hydroxide analogues to generate the metal carbonato complexes. The metal bound aqua ligand is a substantially stronger acid than bulk H_2O (p$K = 15.7$). Typical value of the pK of H_2O bound to a metal ion may be taken to be ~7. Hence the substantial fraction of such an aqua metal ion will exist as M–OH(aq)$^{(n-1)+}$ species at nearly neutral pH in aqueous medium. A major reaction for the formation of carbonato complex, therefore, will involve pH controlled CO_2 uptake by the M–OH$^{(n-1)+}$ as given in Eq. (17).

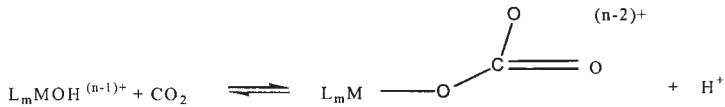

(17)

The monodentate carbonato complex may undergo ring closure to the chelated carbonato complex [see Eq. (18)].

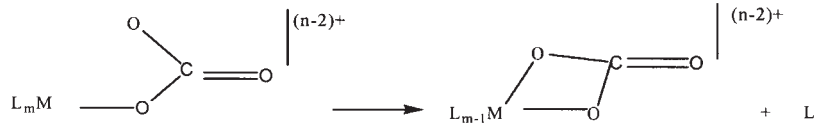

(18)

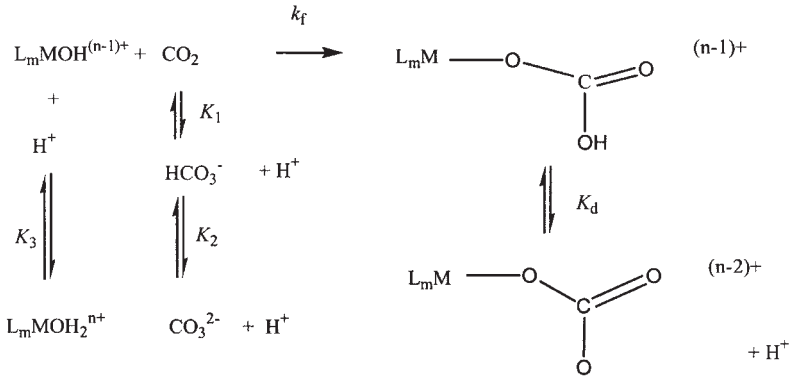

SCHEME 2. CO_2 uptake reaction of $[L_mMOH]^{(n-1)+}$ species.

The kinetics of the formation of carbonato complexes by CO_2 uptake reaction has been extensively investigated (*3*). The two methods of study, the "equilibrium method" and "acidification method", genuinely devised by Harris and co-workers were adapted to the stopped-flow kinetics measurement (*63*). The following general reaction scheme was proposed by them for the formation of monodentate carbonato/bicarbonato complexes by the CO_2 uptake reaction of $M–OH^{(n-1)+}$ species (Scheme 2).

Accordingly the pseudo-first order rate constant (k_{obs}) is given by

$$k_{obs} = k_f\{K_3/(K_3 + [H^+])\}\,[CO_2] \tag{19}$$

and $[CO_2] = [H^+]^2[\text{total carbonate}]/([H^+]^2 + K_1[H^+] + K_1K_2)$, [total carbonate] $= [CO_3^{2-}] + [HCO_3^-] + [CO_2]$. A summary of the CO_2 uptake rate constant (k_f), associated activation parameters, pK_3 data of the aqua metal ions has been presented by Palmer and van Eldik (*3*), which shows that the trend in the reactivities of the metal-hydroxo species parallel their basicities. The linearity of the plot of log k_f vs. pK_3 (slope $= 0.15 \pm 0.04$, intercept $= 1.3 \pm 0.3$), irrespective of the nature of the metal ions and their ligand environments (*3*), envisages the nucleophilic activity of the M–OH species. Extrapolation of the plot to p$K_3 = 15.7$ (i.e., pK of H_2O) yielded a value of log $k_f = 3.7$ for the CO_2/OH^- reaction in reasonable agreement with the reported value for the same (log $k_f = 3.9$ at 25 °C) (*34e,64,65*). The activation volumes $\Delta V^{\neq}$ for CO_2 uptake reactions of $[(NH_3)_5MOH]^{2+}$ ($M = Co^{III}$, Rh^{III}, Ir^{III}) ($\Delta V^{\neq} = -10.1 \pm 0.6$ (Co^{III}), -4.7 ± 0.8 (Rh^{III}), -4.0 ± 1.0 (Ir^{III}) $cm^3\ mol^{-1}$ at

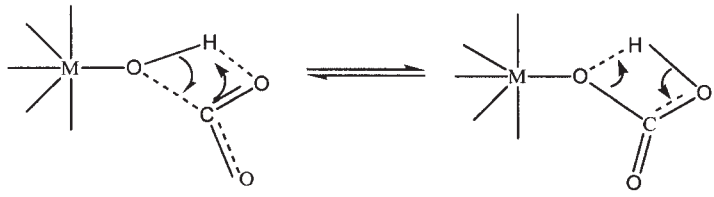

FIG. 8. Rearrangement of metal bicarbonate complexes.

25 °C, $I = 0.5$ M) (*66*) confirm the associative mechanism in which the retention of M–O bond in the activation process is invoked (Fig. 8).

For the aqua metal ions having pK_a around 7, this mechanism is virtually unperturbed by the nature of the metal ion and steric and electronic factors of its ligand envelope as evident from a linear isokinetic plot ($\Delta H^{\neq} = \Delta G_0^{\neq} + \beta_0 \Delta S^{\neq}$, β_0 is the isokinetic temperature) (*3*). The kinetics of CO_2 uptake by *cis*-$[Co(en)_2(im)OH]^{2+}$ (im = imidazole) was studied by Acharya and Dash (*67*). The activation parameters ($\Delta H^{\neq} = 41 \pm 1$ kJ mol^{-1}; $\Delta S^{\neq} = -60 \pm 4$ J K^{-1} mol^{-1}) for this reaction is substantially low ($\Delta H^{\neq} > 60$ kJ mol^{-1}, $\Delta S^{\neq} > -8$ J K^{-1} mol^{-1} in general for the CO_2 uptake reaction of M–OH species as cited in Table 31 of Ref. (*3*)), while the k_f value (324 ± 82 M^{-1} s^{-1} (25 °C, $I = 0.5$ M)) is comparable to those for analogous cobalt(III) and related complexes. This difference was ascribed to the relatively greater degree of ordering in the transition state enforced by the specific solvation of the coordinated imidazole (*T.S.*). The hydration/hydrogen bonding of imidazole in aqueous medium has been dealt with by Del Bene and Cohen (*68*). The lowering of the activation entropy consequently lowers the activation enthalpy such that the isokinetic relationship is obeyed (Fig. 9).

The CO_2 uptake reaction of M–OH species has a direct bearing on the hydration reaction of CO_2 by the enzyme carbonic anhydrase (*69*). In order to resolve the nature of the active site of the enzyme, model complexes of Co(III)/Co(II), Cu(II), and the most important Zn(II) (*34a,e,70–72*) have been designed. Four such structurally well defined tetramine macrocyclic complexes of Zn(II) (M_1–M_4, see below), generate the active L–$Zn^{II}OH$ species in the physiological pH range {pK(H_2O) values are 8.7, 8.0, 8.3, and 7.3 for M_1, M_2, M_3, and M_4, respectively (*72*)} and are considered to be suitable models for carbonic anhydrase. The [12]aneN_3 complex (M_4) is the ideal mimic of CA considering its low pK_a (= 7.3) for the coordinated water and the distorted tridentate *N*-donor ligand. The pH dependence of CO_2 hydration by the Zn^{II}-[12]aneN_3 complex (M_4) has been interpreted in terms of a mechanism involving the formation of the corresponding

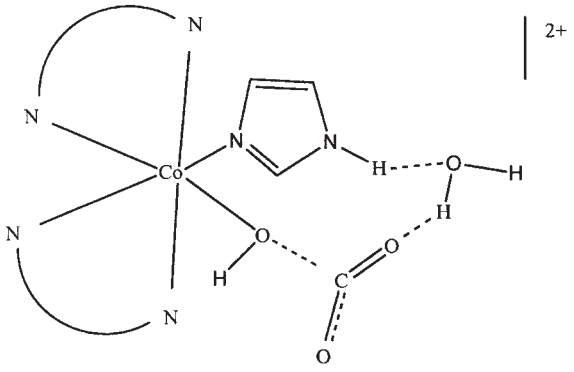

FIG. 9. Solvation of the Co(III) coordinated imidazole (*T.S.*).

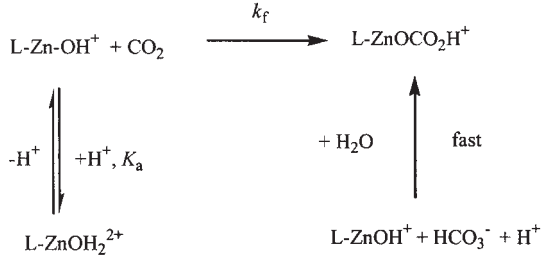

SCHEME 3. CO_2 uptake reaction of $[LZnOH]^{(n-1)+}$ species; L = [12]aneN_3.

bicarbonate complex via CO_2 uptake by L-Zn^{II}OH (*34f*) as delineated in Scheme 3 (Fig. 10).

The $(k^h_{cat})_{obs}$ vs. pH ($6 \le pH \le 9$) plot was sigmoid in keeping with Eq. (20)

$$(k^h_{cat})_{obs} = k^h_{cat} K_a / ([H^+] + K_a) \tag{20}$$

and the values of $k^h_{cat} = 581 \pm 64$ M^{-1} s^{-1} and $K_a = (3.5 \pm 0.4) \times 10^{-8}$ M ($pK_a = 7.45 \pm 0.10$) (25.0 °C) has been reported by Zhang *et al.* (*34f*).

The bicarbonato complex is a transient intermediate and rapidly aquates to HCO_3^- and the aqua complex due to the high substitutional lability of the monodentate ligand bound to Zn^{II} (*73*). The aqua complex [L–ZnOH_2]$^{2+}$, however, then undergoes a fast aqua-hydroxo equilibration. A similar study extended to the cyclen complex, Zn^{II}–[12]aneN_4(M_4), has provided the highest value of the hydration rate constant ($k^h_{cat} = (3.5 \pm 0.1) \times 10^3$ M^{-1} s^{-1}), which is one-third of

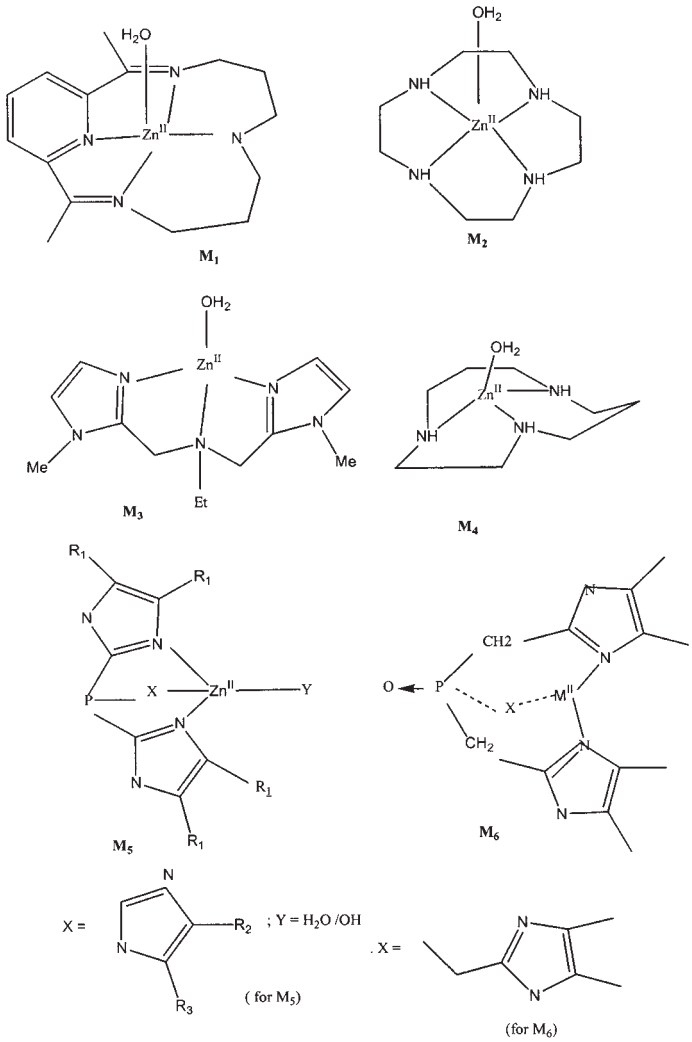

FIG. 10. Zinc complexes as models for CAs.

the hydration rate constant of HCA III, $pK_a = 8.1$ at 25 °C, $I = 0.1$ M $NaClO_4$; $pK_a = 7.8$ from equilibrium measurements (*34a*); the corresponding hydroxo complex $[L–ZnOH]^+$ being the active Zn species. The bicarbonato complex in this case also serves as an unstable intermediate.

A value of 590 ± 30 M^{-1} s^{-1} was reported for the CO_2 uptake reaction of [Cu(gly)OH], but the higher rate is proportional to a

higher value of pK_a (=9.4) of the corresponding aqua complex (*74*). However, the complex M_4 is more reactive than $[ZnCROH]^+$ for which the CO_2 uptake rate constant was reported to be 225 ± 23 M^{-1} s^{-1} (*75*). For another series of tris(imidazole) complexes (M_5 and M_6) the maximum value of the rate constant of 900 (M_5, $R_1 = R_2 = R_3 = CH(CH_3)_2$), 1500 ($R_1 = CH(CH_3)_2$, $R_2 = R_3 = H$), and 2700 M^{-1} s^{-1} ($R_1 = R_2 = R_3 = CH(CH_2CH_3)$) were reported (*72i*). The high catalytic activity of these complexes was attributed to the hydrophobic environment of the metal center, which possibly is responsible for effective pre-association of CO_2 close to the reaction site.

The stopped-flow and T-jump techniques were used by Mao and co-workers (*34j*) to investigate the kinetics of complex formation of $[Cu(tren)(OH_2)]^{2+}$ by HCO_3^-. In large excess of HCO_3^- and pH = 6–9, the formation of the mononuclear bicarbonato/carbonato complex was too fast to be studied kinetically. The kinetically observed reaction was the reversible formation of the binuclear complex, $[(Cu(tren))_2(O_2CO)]^{2+}$ and this occurred as shown below:

$$[Cu(tren)(OH_2)]^{2+} + HCO_3^- \rightleftharpoons [Cu(tren)(OCO_2H)]^+ + H_2O \quad \text{fast} \tag{21}$$

$$[Cu(tren)(OCO_2H)]^+ \rightleftharpoons [Cu(tren)(OCO_2)] + H^+ \quad \text{fast} \tag{22}$$

$$[Cu(tren)(OCO_2)] + [Cu(tren)(H_2O)]^{2+} \underset{k_{-4}}{\overset{k_4}{\rightleftharpoons}} [(Cu(tren))_2(O_2CO)]^{2+} + H_2O \tag{23}$$

for which

$$k_{obs} = \tau^{-1} = k_4[Cu(tren)(H_2O)^{2+}] + k_{-4}. \tag{24}$$

The second-order rate constant k_4 for the formation of the binuclear complex is 494 ± 10 M^{-1} s^{-1} at 25.0 °C and $I = 0.25$ M and k_{-4} is too small (ca. < 0.1 s^{-1}) to be estimated (*34j*). The corresponding Zn^{II} complex was not amenable to the rate measurements although the binuclear complex $\{[Zn(tren)]_2(\mu\text{-}CO_3H)\}(ClO_4)_3$ could be isolated and characterized (*34j*).

In another recent study, Mao *et al.* (*34k*) have used the Cu^{II} complexes of 2,2′-bypridine and 1,10-phenanthroline to identify the different carbonate coordination modes which may be kinetically significant. Stopped-flow and T-jump techniques were used. The

concentrations of HCO_3^-, $[Cu(L_2)H_2O]^{2+}$ (L = bipyridine, 1,10-phenanthroline) and pH (= 6–10) were varied. Due to the high lability of the coordinated water in $[Cu(bpy)_2(OH_2)]^{2+}$ and $[Cu(phen)_2(OH_2)]^{2+}$ and the high pK_a values of the aqua complexes (p$K_a \geq 10.3 \pm 0.1$ and $\geq 11.3 \pm 0.3$ at 25 °C for $[Cu(bpy)_2OH_2]^{2+}$ and $[Cu(phen)_2OH_2]^{2+}$, respectively), the formation of the monodentate bicarbonato complexes (five-coordinate) is equilibrium controlled. This is then followed by the rate-limiting ring closure of the bicarbonato complex to generate the chelated carbonato complex (distorted octahedral) with ionization of a proton. The chelated carbonato complexes further undergo a rapid equilibrium with the aqua complex, $[Cu(L)_2OH_2]^{2+}$ leading to the formation of the binuclear species, $[(Cu(L)_2)_2(\mu\text{-}CO_3)]^{2+}$ [see Eqs. (25)–(27)]:

$$[Cu(L)_2(OH_2)]^{2+} + HCO_3^- \rightleftharpoons [Cu(L)_2(OCO_2H]^+ + H_2O \quad \text{fast} \qquad (25)$$

$$[Cu(L)_2OCO_2H]^+(\text{5-coord.}) \longrightarrow [Cu(L)_2O_2CO](\text{6-coord.}) + H^+ \quad k \qquad (26)$$

$$[Cu(L)_2O_2CO] + [Cu(L)_2OH_2)]^{2+} \rightleftharpoons [(Cu(L)_2)_2(\mu\text{-}CO_3)]^{2+} + H_2O \quad \text{fast} \qquad (27)$$

The pressure and temperature dependence of the ring closure rate constant, k, are also reported. At 25.0 °C, the values of k (s^{-1}), $\Delta H^{\neq}$ (kJ mol^{-1}), $\Delta S^{\neq}$ (J K^{-1} mol^{-1}), and $\Delta V^{\neq}$ (cm^3 mol^{-1}) are: 20.7 ± 0.8 (20.5 ± 0.8), 41.2 ± 0.9 (53.7 ± 0.8), -82.0 ± 2.5 (-39.6 ± 2.5), -16.9 ± 0.4 (-26.6 ± 1.0), respectively, for $[Cu(bpy)_2OH_2]^{2+}$ ($[Cu(phen)_2OH_2]^{2+}$). Substantially negative values of $\Delta S^{\neq}$ and $\Delta V^{\neq}$ were believed to be due to bond formation and relatively higher solvation demands of the transition state and the release of H^+ (*76*) in line with the suggested rate-limiting step [see Eq. (26)].

It is evident from such studies that the formation of the bicarbonato complex via CO_2 uptake reaction of M–OH is not favorable for the aqua metal complexes with high pK_a value and high lability of the coordinated water. The alternative path is the direct substitution of the aqua ligand by HCO_3^-. This is also true for the labile square-planar complexes of Pd^{II}, which undergo reversible aqua ligand substitution by HCO_3^- (*77*). Although a vast majority of data for the formation of the carbonato complexes of Co^{III} and Rh^{III} established that CO_2 uptake by M^{III}–OH is the predominant reaction, the other modes of reaction i.e., anation via HCO_3^-/CO_3^{2-} was also shown to be valid for aquapentamine–rhodium(III) (*78*) and (diaqua)

(tren)cobalt(III) (*79*) at pH > 10 where the concentration of CO_2 is vanishingly low. The rate constants of anation of $[(tren)Co(OH)_2]^+$ by HCO_3^- and CO_3^{2-} at 50 °C and $I = 0.5$ M are $(4.7 \pm 0.1) \times 10^{-2}$ M^{-1} s^{-1} and $(4.0 \pm 1.5) \times 10^{-4}$ M^{-1} s^{-1}, respectively, which are at least 10^4 times smaller than the rate constant for the CO_2 uptake reaction of the dihydroxo species (*3*). $k(HCO_3^-) \gg k(CO_3^{2-})$ was attributed to the importance of proton transfer between the dihydroxo complex and bicarbonate (*79*) prior to the rate limiting process: $[(tren)Co(OH)_2,HCO_3^-] \rightleftharpoons [(tren)Co(OH)(OH_2),CO_3^{2-}]$. The mechanism was believed to be dissociative interchange (I_d). The ring-closure of the hydroxo–carbonato complex, $[(tren)Co(OH)(OCO_2)]$ to the corresponding chelated carbonato complex is slow ($k = 8 \times 10^{-3}$ s^{-1} at 50 °C and pH 10.3).

The kinetic effects of CO_3^{2-} in the base catalyzed hydrolysis of some carboxylato amine cobalt(III) complexes have been reported (*80–82*). In the base catalyzed hydrolysis of oxalatopentaammine-cobalt(III) (*80*), CO_3^{2-} retarded the reaction due to the formation of a virtually unreactive ion-pair, $[(NH_3)_5CoO_2C–CO_2^+ \cdot CO_3^{2-}]$. The equilibrium constant for formation of carbonate ion-pairs with (glycinato-*O*) (tetraethylene-pentamine)cobalt(III), (*81*) and (*o*-methoxybenzoato) (tetraethylenepentamine)cobalt(III) (*82*) were, however, much smaller than for the oxalatopentamminecobat(III) and a very weak rate retardation and virtually no effect was observed in the base catalyzed hydrolysis of the latter two complexes.

B. Aquation/Decarboxylation Reaction

1. Monodentate Carbonato Complexes

The carbonato complexes undergo aquation to the corresponding aqua complexes by various paths depending on the nature of the complex. This aspect will be discussed briefly for complexes in which carbonate acts as a monodentate and bidentate ligand. The monodentate carbonato complexes of Co^{III}, Cr^{III}, Rh^{III}, and Ir^{III}, undergo acid-catalyzed decarboxylation. This can be represented by Eq. (28).

$$L_nM^{III}(OCO_2) + H^+ \overset{K_d}{\rightleftharpoons} L_nM^{III}(OCO_2H) \xrightarrow{k_H} \begin{matrix} L_nM^{III}OH \\ {\scriptstyle +H^+}\uparrow\downarrow \\ L_nM^{III}OH_2 \end{matrix} + CO_2 \quad (28)$$

$$k_{obs} = k_H[H^+]/([H^+] + K_d) \quad (29)$$

Rapid scan spectrophotometry (*83*) provided direct spectral evidence of protonation of the carbonato complex, $[(NH_3)_5CoOCO_2]^+$ (λ_{max}, nm; ε, M^{-1} cm^{-1}): 505(94) for $[(NH_3)_5CoOCO_2]^+$; 485(65) for $[(NH_3)_5CoOCO_2H]^{2+}$). k_{obs} exhibits the expected sigmoid pH dependence. The values of pK_d for the bicarbonato complexes closely correspond to that for the first dissociation constant of CO_2; the nature of the metal ion and its ligand envelope have only minor perturbing influence on both k_H and pK_d (*3*). The values of k_H and pK_d for a representative complex, $[(tetren)CoOCO_2]^+$, are 0.28 ± 0.03 s^{-1} and 6.4, respectively (25.0 °C, $I = 0.5$ M) (*84*). Also $\Delta H^{\neq}$ and $\Delta S^{\neq}$ display mutually compensatory changes with respect to changes in M^{III} and its ligand environment in line with the consistancy of the intimate mechanism. The values of k_H (M^{-1} s^{-1}), $\Delta H^{\neq}$ (kJ mol^{-1}) and $\Delta S^{\neq}$ (J K^{-1} mol^{-1}) for some closely related cobalt(III) complexes, *cis*-$[(en)_2CoL(OCO_2H)]^{2+}$ (L = H_2O, NH_3, and imidazole) are: 0.81 ± 0.04, 60 ± 3, -46 ± 12 (L = H_2O) (*3*); 0.60 ± 0.02, 68 ± 2, -17 ± 3 (L = NH_3) (*3*); and 1.43 ± 0.04, 75.0 ± 0.2, 8 ± 0.6 (L = imidazole) (*67*), respectively. The rate accelerating effect of imidazole, though small, is worth noting. The $\Delta S^{\neq}$ data indicate that the bound imidazole favors the decarboxylation by influencing the solvation demand of the transition state.

The decarboxylation of HCO_3^- by the Zn^{II} complexes of [12]aneN_3 (*34e*) and [12]aneN_4 (*34a*) (L–Zn–OH_2^{2+}) around pH ~ 7 and in excess of HCO_3^- was interpreted in terms of the reactivities of the corresponding mononuclear bicarbonato complexes. The bicarbonato complexes were presumed to be formed by reversible anation of the aqua complexes by HCO_3^- and catalyzed the decarboxylation process as delineated in Scheme 4.

Non Michaelis–Menten behavior (i.e., no saturation kinetics in presence of excess HCO_3^-) was observed and the second-order rate constants for the catalyzed decarboxylation ($k_{cat}^d = k_1k_2/(k_{-1} + k_2)$ for

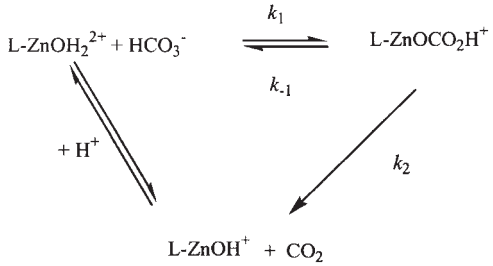

SCHEME 4. Anation of the aqua complexes by HCO_3^-.

$k_1[HCO_3^-] \ll (k_{-1} + k_2)$ were 4.8 ± 0.7 and 51 ± 8 M^{-1} s^{-1} (25.0 °C, $I = 0.1$ M) for the [12]aneN_3 and [12]aneN_4 complexes, respectively. The relatively higher stability of $[[12]aneN_3–Zn–OCO_2H]^+$ (for which chelation of the Zn^{II} center by the coordinated bicarbonate is possible: Lipscomb structure) was attributed to its reduced reactivity.

It is pertinent to discuss further the mechanism of decarboxylation of monodentate carbonato complexes in the light of the recent report on the mechanism of the spontaneous dehydration of bicarbonate [Eq. (12)] reported by Paneth and O'Leary (*26a*). The important aspect is the zwitterionic intermediuate due to protonation of HCO_3^-. Such type of zwitterionic intermediate was not considered to be important in the acid-catalyzed decarboxylation of monodentate carbonato complexes (*3,84–86*). However, such a possibility cannot be completely excluded. An exhaustive study of the decarboxylation of bicarbonatopentaamminecobalt(III) (*87*) in aqueous-organic solvents (0–70 wt% organic co-solvents (methanol, propane-2-ol, *tert*-butanol, ethylene glycol, acetone, acetonitrile, dimethyl sulfoxide, and ethylene carbonate) at $15 \leq t/°C \leq 40$) revealed that the reaction is catalyzed by co-solvents, the effect being relatively more pronounced for the dipolar aprotic solvents. The catalysis is enhanced by increasing hydrophobicity of the medium. This is in keeping with the destabilization of the zwitterionic form of the bicarbonato complex (see Scheme 5) with increasing co-solvent component. The zwitterionic

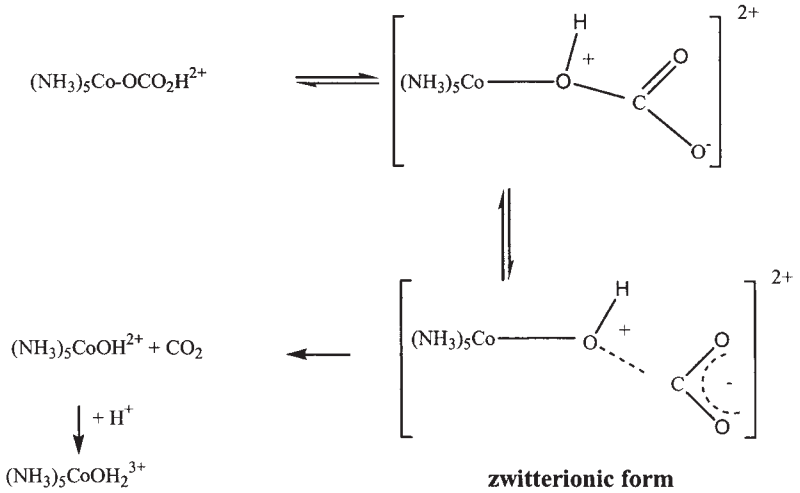

SCHEME 5. Decarboxylation of $[(NH_3)_5CoOCO_2H]^{2+}$ through its zwitterionic form.

form is likely to be stabilized by hydrogen bonding interaction with the hydroxylic solvent component of the solvent mixtures. The activation parameters ($\Delta H^{\neq}$ and $\Delta S^{\neq}$) were sensitive to the solvent structure. However, the variations of $\Delta H^{\neq}$ and $\Delta S^{\neq}$ with solvent compositions are mutually compensatory as expected for no significant change in the mechanism of the reaction. There was a negligible solvent isotope effect on rate and activation parameters ($k_{H_2O}/k_{D_2O} = 0.998 \pm 0.013$ at 15–40 °C; $\Delta H^{\neq} = 77.7 \pm 1.0$, 77.8 ± 0.9 kJ mol^{-1} and $\Delta S^{\neq} = 16 \pm 3$, 16 ± 3 J K^{-1} mol^{-1} for H_2O and 99% D_2O media, respectively, $I = 0.02$ M) also in conform with the mechanism shown in Scheme 5.

2. Chelated Carbonato Complexes

The acid catalyzed aquation of the chelated carbonato complexes involves three steps: (i) the initial rapid protonation pre-equilibrium of the exocyclic oxygen, (ii) carbonate ring opening, and (iii) decarboxylation of the resulting bicarbonato complex [see Eq. (30)].

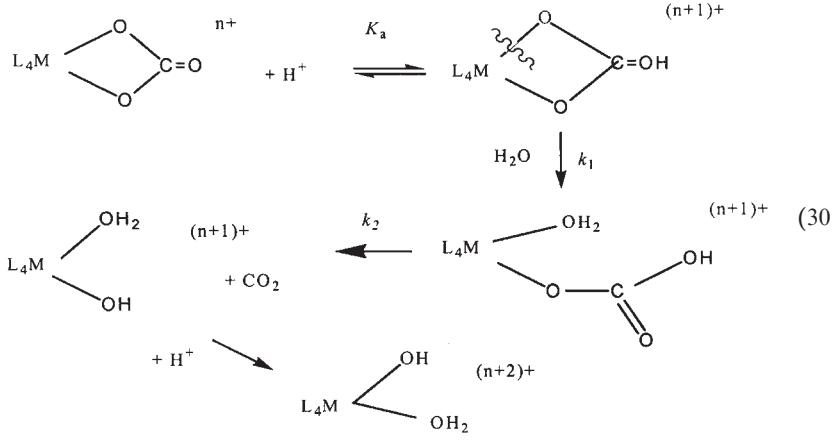

(30)

The latter two processes are slow as a result of which the detection of the protonated carbonato complex, and determination of its protonation constant by stopped-flow, rapid scan spectrophotometry were possible in some cases. van Eldik *et al.* (*83*) interpreted the initial spectral changes (shift of absorption maxima and the isosbestic points) of β-*cis*-$[Co(edda)CO_3]^-$ and $[Co(nta)CO_3]^-$ at $[H^+] = 0.05$ M due to the formation of the protonated carbonato complexes, β-*cis*-$[Co(edda)CO_3H]$ and $[Co(nta)CO_3H]$. Repetitive rapid scan spectral measurements at $[H^+] = 2.0$ M, however, led them to the identification

of the ring-opened bicarbonato complex, β-*cis*-[Co(edda)(OH_2)(OCO_2H)], as was observed in the case of the *cis*-$[Co(en)_2CO_3]^+$ (*88*). Their studies indicate that the spectra of the ring opened bicarbonato complexes, β-*cis*-[Co(edda)(OH_2)(OCO_2H)] and *cis*-$[Co(en)_2(OH_2)(OCO_2H)]^{2+}$, are similar to that of $[(NH_3)_5CoOCO_2H]^{2+}$ and the protonation constant of the chelated carbonate is small.

Buckingham and Clark (*89*) re-examined the acid catalyzed decarboxylation/aquation of the chelated carbonato complexes, $[(NH_3)_4(O_2CO)]^+$, α- and β-$[Co(trien)(O_2CO)]^+$, $[Co(tren)(O_2CO)]^+$, $[Co(nta)(O_2CO)]^{2-}$, *cis*-$[Co(gly)(O_2CO)]^-$, $[Co(cyclen)(O_2CO)]^+$, and $[Co(N\text{-mecyclen})(O_2CO)]^+$. The acid dissociation constants of the protonated carbonato complexes, $[Co(gly)(O_2COH)]$, $[Co(cyclen)(O_2COH)]^{2+}$ and $[Co(nta)(O_2COH)]^-$ were determined spectrophotometrically (553, 522, and 560 nm, respectively) following stopped-flow mixing of the complex with $HClO_4$ and then collecting the absorbance data at zero time by extrapolation. The zero-time absorbance data (A_0) at different $[H^+]$ were used to compute the protonation constant, K_a, by Eq. (31),

$$\Delta A = (A_2 - A_1)[H^+]/([H^+] + K_a^{-1}) \tag{31}$$

where $\Delta A = A_1 - A_0$, and A_1 and A_2 are the absorbances of the unprotonated and protonated carbonato complexes, respectively, for the same concentration of the carbonato complex as for A_0. However, full protonation of the complexes could not be achieved and as such A_2 and K_a^{-1} were used as the variables for data fitting. Values of K_a^{-1} thus obtained by them are ca. 0.66, 1.15 ± 0.28 ($I = 1.0$ M) and 0.42 ± 0.06 ($I = 2.7$ M) for $[Co(gly)(O_2CO)]^-$, $[Co(nta)(O_2CO)]^{2-}$ and $[Co(cyclen)(O_2CO)]^+$ (25 °C), respectively. The proton affinity of the chelated carbonato group decreases with a decrease in the overall negative charge of the complex.

The acid catalyzed decarboxylation/aquation was essentially biphasic [Eq. (32)]

$$A \xrightarrow{k_{fast}} B \xrightarrow{k_{slow}} C \tag{32}$$

where

$$k_{fast} = k_1 K_a[H^+]/(1 + K_a[H^+]) \tag{33}$$

$$k_{slow} = k_2 \tag{34}$$

TABLE III

VALUES OF THE ACID DISSOCIATION CONSTANT (K) AND RING-OPENING RATE CONSTANT (k_1) OF $[L_4Co(O_2COH)]^{2+}$ AND THE DECARBOXYLATION RATE CONSTANT (k_2) OF THE CORRESPONDING MONODENTATE BICARBONATO COMPLEXES (AT 25.0 °C, $I = 1.0$ M)

Complex	K/M	k_1/s^{-1}	k_2/s^{-1}	Ref.
$[Co(en)_2(O_2COH)]^{2+}$	1.0	0.85	0.93	*a*
$[Co(nta)(O_2COH)]^{-}$	0.85(1.1)	85.0	2.0	*b*
α-$[Co(trien)(O_2COH)]^{2+}$	1.4	9.7	0.62	*b*
$[Co(tren)(O_2COH)]^{2+}$	1.6	4.25	0.31	*b*
$[Co(gly)_2(O_2COH)]$	0.73(0.66)	4.1	4.1	*b*
$[Co(NH_3)_4(O_2COH)]^{2+}$	1.0	1.68	1.50	*b*
β-$[Co(trien)(O_2COH)]^{2+}$	1.25	0.285	0.45	*b*
$[Co(cyclen)(O_2COH)]^{2+}$	0.70	0.0102		
$[Co(N\text{-mecyclen})(O_2COH)]^{2+}$	2.3	0.0076		

[a]Kinetically determined.

[b]Buckingham, D. A.; Clark, C. R. *Inorg. Chem.* **1993**, *32*, 5405. Values in parentheses were determined directly from zero-time absorbance data.

These equations are in line with Eq. (30), such that k_1 denotes the ring-opening rate constant of the protonated carbonato complex and k_2 is the decarboxylation rate constant of the ring-opened bicarbonato complex. Values of these rate constants and the acid dissociation constants of some protonated carbonato complexes of cobalt(III) (see Table III) reflect the ligand dependence with respect to charge variations, steric constraint, and donor properties of the non-labile ligands.

For all these systems the spontaneous ring-opening path was, however, non-existent. Such a path may be of minor importance (*3,90–92*).

The H^+-catalyzed ring-opening [see Eq. (30)] occurs with Co–O bond cleavage (dechelation process). This was shown by Posey and Taube (*93*) for $[(NH_3)_4Co(O_2CO)]^+$ and then by Francis and Jordan (94) for $[Co(en)_2(O_2CO)]^+$, $[Co(phen)_2(O_2CO)]^+$ and $[Co(bipy)_2(O_2CO)]^+$. Subsequent loss of CO_2 (decarboxylation) from the ring-opened bicarbonato species occurs with C–O bond cleavage. This is the currently accepted mechanism established by the extent of $^{18}OH_2$ incorporation into the final aqua product and non-incorporation of the solvent label into the released CO_2 (*95,96*). The protonated carbonato complex $[Co(tepa)(O_2COH)](ClO_4)_2 \cdot H_2O$ has been characterized in the solid state by X-ray (*49*). The site of protonation is the *exo*-oxygen of the chelated carbonate which has been

made further clear in $[Rh(H)_2(P(i\text{-}Pr)_3)_2(O_2COH)]$ (*48*). This mode of protonation is also consistent with the very little change in the pK of the protonated carbonate (see Table III) with the variation of the non-labile ligands.

The decarboxylation rate constant (k_2) is virtually insensitive to the nature of the complex and is close to $\sim 1\ s^{-1}$ (25 °C), in line with expectations that C–O bond breaking is involved and the ligand effects are not transmitted to the site of the bond breaking. The decarboxylation of $[Co(cyclen)(OH_2)(OCO_2H)]^{2+}$ and $[Co(mecyclen)(OH_2)(OCO_2H)]^{2+}$ could not be observed by Buckingham and Clark (*89*) as this is preceded by very slow H^+-catalyzed ring opening. However, they suggested $k_2 \sim 1\ s^{-1}$ (25 °C) for these complexes. The wide variation of k_1 (see Table III) due to the variation of the non-labile ligand envelope is a consequence of the steric effect on the strained four-membered chelate ring of the coordinated bicarbonate as well as the transmission of electronic effects of the ligands to the Co–O bond, influencing its breakage. The possibility of differing degrees of protonation of the *endo* (ring) oxygen and *exo*-oxygen in the transition state for the Co–O breaking process (as a consequence of the difference in basicity of the two oxygen atom sites) cannot be overlooked which ultimately could contribute to the variation in k_1 (*89*).

V. Discovery and Classification of Carbonic Anhydrases

The existence of erythrocyte carbonic anhydrase as a distinct enzyme was first discovered by Meldrum and Roughten (*97*) some 70 years ago. Keilin and Mann (*98,99*) discovered that carbonic anhydrase from mammalian erythrocyte contained ~0.2% zinc (corresponds to 1 g/mol of enzyme; MW = 30,000) and concluded that zinc might play a unique role in enzyme catalysis. During the last 40 years, carbonic anhydrase has played a significant role in the elucidation of the principles underlying enzyme activities. In addition to its intrinsic physiological importance, CAs are rigorously studied (*69*) because the isolable zinc enzyme is stable in solution and during storage and robust in constitution in the pH range 5.5 to 12. In general, the carbonic anhydrases (CA, EC 4.2.1.1) catalyze an important simple and reversible reaction (*100*), $CO_2 + H_2O = HCO_3^- + H^+$. This chapter describes the integrated information on structure, catalytic mechanism (kinetics of reaction) and inhibition kinetics

of the enzyme, and comparison of the kinetics of catalyzed reactions with uncatalyzed reactions is also made to explore the model systems, which can mimic CA.

Several carbonic anhydrases are also reported to catalyze the hydration of cyanamide to urea (*101*). Urea or the ureate anion thus formed after the hydrolytic reaction is blocked within the enzyme active-site where it is directly coordinated to the Zn^{2+} through a protonated nitrogen atom and also forms eight hydrogen bonds with the residues Thr-199 and Thr-200 and three water molecules. Thus, cynamide is reported to act as the first potent suicide substrate of these enzymes (*102*). The three-dimensional crystal structure determined by cryogenic X-ray diffraction techniques, shows that two different adducts are formed under experimental conditions: (i) the high occupancy form consists of a binary HCA II–cyanamide complex where the substrate has replaced the zinc-bound hydroxide anion present in the native enzyme maintaining the tetrahedral geometry around the metal ion; and (ii) the low occupancy form consists of a HCA II–cyanamide–water ternary complex where the catalytic zinc ion bound to cyanamide, is approached by a water molecule in a five-coordinate adduct. Guerri *et al.* (*102*) reported that a transient five-coordinate adduct of HCA II with cyanamide, that is hydrated to form urea, provides direct evidence about the possible operation of different hydration reactions of CAs depending on the electronic and stereochemical properties of substrates.

Since discovery of cabonic anhydrase by Meldrum and Roughten (*97*), 14 different carbonic anhydrase isoenzymes or carbonic anhydrase-related proteins (CA-RP) are identified in higher vertebrates including humans (*103*), which are involved in critical physiological functions including respiration and transport of CO_2 and bicarbonate between metabolizing tissues and the lungs, pH homeostasis, and electrolyte secretion in a variety of tissues and organs, as well as biosynthetic reactions, such as gluconeogenesis and ureagenesis (*104,105*). Based on sequence homologies, carbonic anhydrases are classified into three evolutionarily distinct groups, designated as α-, β-, and γ-CAs. The α-class CAs are mostly identified and characterized from mammalian species and includes at least 14 mammalian isoenzymes, along with two isoenzymes from *Chlamydomonas reinhardtii*, and two prokaryotic isoenzymes (*103*). The β-class has been discovered in phototropic organisms, including higher plants and certain algae and bacteria. The prototype for the γ-class of carbonic anhydrase has been identified and characterized in archaea, including methanoarchaeon *Methanosarcina thermophila* (Cam) (*106*).

There are several types of α-class CAs i.e., α-CA I–VII, reported in the literature, out of which the human carbonic anhydrase II (HCA II), the most extensively studied carbonic anhydrase, has an exceptionally high CO_2 hydration rate and a wide tissue distribution (*107*). The HCA II comprises a single polypeptide chain with a molecular mass of ~29.3 kDa and contains one catalytic zinc ion, coordinated to three histidine residues, His 94, His 96, and His 119. A tetrahedral coordination geometry around the metal center is completed with a water molecule, which forms a hydroxide ion with a pK_a value of 7.0 (*108*). Quigley and co-workers (*109,110*) reported that the inhibition of the synthesis of HCO_3^- from CO_2 and OH^- reduces aqueous humor formation and lowers intra-ocular pressure, which is a major risk factor for primary open-angle glaucoma.

VI. Structure of α-Class Carbonic Anhydrase from Human Erythrocytes (the High Activity form HCA II)

The high-resolution crystallographic structure of CA II, the high activity form of human erythrocytes has been refined at 0.154 nm resolution (*111–113*). X-ray crystal structure data of HCA II indicated that the active site is located in the central region of a 10-stranded, twisted β-sheet and composed of a cone-shaped cleft, 15 Å deep with a tetrahedral Zn^{2+} at the bottom of the cleft. Analysis of the structural evidences reveals a hierarchy of three conserved features that control the properties of the metal binding site. First, three histidine residues from the protein, at positions 94, 96, and 119 known as His 94, His 96, and His 119 respectively, and a water molecule (or hydroxide ion) are directly coordinated to the Zn^{2+}. Mutation of any of these histidine residues leads to a much larger zinc dissociation constant and around a 1000-fold decrease in catalytic power (*114*) indicating thereby that these residues exhibit major biological importance of the enzyme i.e., to constrain the Zn^{2+} ion in the active site. It has also been reported that a transient five-fold coordination involving a second water molecule can also occur (*115*). Second, these histidine residues form hydrogen bonds to indirect ligands (or "second-shell" ligands) Gln 92, Asn 244, and Glu 117, respectively, (see Fig. 11) with the exception that Asn 244 is hydrogen bonded to His 96 through its main chain carbonyl oxygen atom and the zinc-bound hydroxide ion forms hydrogen bond to Thr 199. These second-shell interactions enhance the basicity of the direct histidine residues and optimize the direct ligands for optimal metal coordination (*69b*,*116–119*).

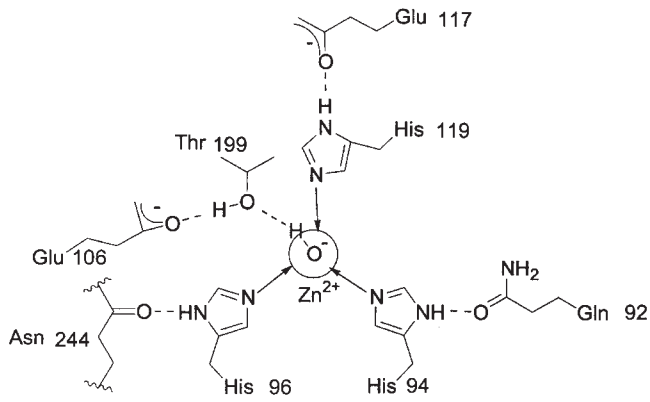

FIG. 11. Schematic drawing of the direct and indirect metal ligands in the HCA II.

Mutation of these second shell residues leads to lowering of catalytic activities, revealing the fact that the active site ligands have been optimally selected by a natural process of selection (*117–120*). Third, aromatic residues Phe 93, Phe 95, and Trp 97 form the hydrophobic core, anchor the β-strand containing direct ligands His 94 and His 96 in the hydrophobic core of the enzyme and stabilize its conformation. These aromatic core residues help to pre-orient direct and second-shell ligands to optimize zinc binding geometry and destabilize alternate geometries (*121*). These aromatic amino acids also contribute to the high zinc affinity and slow zinc dissociation rate constant of CA II (*122*). In different catalytic active CAs, Trp is conserved at position 97, while any one of the hydrophobic amino acids (Phe, Leu, Ile, Met) is retained at positions 93 and 95. It has been proposed that these "hydrophobic shell" residues enhance protein-metal affinity by establishing a metal site environment with a reduced dielectric constant (*123*). The direct and indirect ligands are invariant in all sequenced and catalytically active α-CAs (*103a*).

Three binding sites have been identified in the cavity of carbonic anhydrase (*12*,*69d*,*125*). The Zn^{2+} ion is located at the bottom of the conical cavity where it is coordinated by the N-atoms of His 94, His 96, and His 119 and by a water molecule/hydroxide ion (Wat 263) in a slightly distorted tetrahedral geometry (*69d*,*113*,*126*,*127*). The hydroxide binding site that provides a tetrahedral structure around the metal ion is designated as site A. Thr-199 orients the incoming ligands through hydrogen bonding. Thr-199 and Thr-200 along with their protein backbone (–NH–CO–) identify a hydrophilic environment,

which plays a pivotal role in the energetic balance of ligand binding. Back of this region, Val 143, Leu 198, and Trp 209 residues form a hydrophobic cavity (one part of the cavity is dominated by hydrophobic amino acid side chains and the other part is hydrophilic in nature). It has been proposed that the hydrophobic part of the cavity hosts the substrate CO_2 (*128*). More than one CO_2 molecules are located within the active site region, one bound to Zn^{2+} and other molecules are adjacent to the hydrophobic part of the cavity (*129,130*). It has also been proposed that two water molecules participate in the turnover reaction (*131*). The presence of a water molecule in the X-ray structure reveals that this is H-bonded to the Zn^{2+}-coordinated water. Ligands with hydrophobic end could easily be placed in this binding position, known as site B. X-ray structure data of the thiocyanate adduct of HCA II indicated that the coordinated water molecule would change its position in order to make appropriate angles between the coordinated groups to stabilize it; this site is called C. In this case the geometry of the five-coordinate derivative can be roughly described as a distorted SQPY with His 94 in the apical position. In case of aromatic sulfonamides, which bind as anions, the NH^- binds zinc in the site A and forms a hydrogen bond with Thr-199 (*124,125*). The sulfonamide oxygens do not bind to the metal and one of them is located in the hydrophobic region, i.e., in site B. In case of ^-OCN binding, tetrahedral derivatives are reported (*132*). It is interesting to note that cyanide is the only ligand that may bind in a 2:1 ratio, possibly through formation of a bis-cyanide adduct which has the same arrangement as the NCS^-–H_2O derivative (*133*).

The importance of maintaining the active site water network in CA II for efficient proton transfer was investigated by substituting different amino acids of varying size at position 65 and measuring the rate constants for proton transfer in the variant carbonic anhydrases (*134*). These results revealed that intramolecular proton transfer between zinc-bound water and His 64 is significantly inhibited by the introduction of bulky amino acids at position 65; consequently intermolecular proton transfer between protonated His 64 and external buffer was also inhibited. The active solvent bridge between zinc-bound water and His 64 is disrupted by substitutions at position 65, indicating thereby that the active site solvent structure is likely to be an important determinant in proton transfer via the alternate proton pathway that is operative in the absence of a functional intramolecular proton shuttle group. The inhibition of proton transfer reactions in corroboration with the crystallographic data suggested that the solvent network, including water molecules 292, 264, and 369,

or a structurally related network, forms the proton transfer pathway in CA II for both intramolecular proton transfer (*133,134*).

The most efficient pathway for proton transfer in CA II appears to be the His 64 residue which acts as a proton acceptor. Mutation of His 64 with other residues has revealed that the proton transfer from the zinc-bound water to His 64 is the pathway, which leads to high catalytic activity. It has been proposed that two water molecules between Zn-bound water and His 64 may, most likely, serve as a bridge which could allow the proton transfer to proceed through a shuttle mechanism (*69c*), although the possibility of a single water molecule bridge between Zn-bound water and His 64 cannot be ruled out. Nair and Christianson (*135*) proposed that His 64 indeed has flexible conformations, i.e., conformations depend upon changing pH and mutation of some residues around the active site (possibly Thr-200) (*117*). At high pH ($\sim$8.5), His 64 is located in the active-site cavity with its imidazole ring in the "inward" conformation, whereas at low pH ($\sim$5.7) it prefers to stay in an "outward" position. Most strikingly, the His 64 conformation is also sensitive to the involvement of water molecules, protonation state of other residues, and involvement of an electrolyte medium. Nair and Christianson (*135*) suggested that the conformational change of His 64 upon changing the protonation state implies its biological significance, i.e., such a change makes it easier for delivery of a proton to the solvent. The catalytic activity of His-64 Ala variant of HCA II is decreased 10 times in comparison to wild type HCA II but loss of catalytic activity of this variant is rescued in the presence of 4-methylimidazole (4-meim), an exogenous proton donor (*136*). 4-Methylimidazole binds in the active-site cavity of His-64 Ala HCA II near the position of His-64 in the "outward" conformation in the wild-type enzyme structure. The proton transfer capability of 4-meim is observed to be very similar to that of His-64 in wild-type HCA II suggesting thereby that His-64 in the "outward" position is a significant contributor to proton transfer catalysis. Furthermore, the crystal structure of His-64 Ala HCA II showed that the exogeneous acceptor/donor 4-meim forms a π-stacking complex with Trp 5 and binds in a location close to that of His 64 in the "outward" conformation in the wild-type HCA II structure, where the histidine side chain points away from the zinc ion in the active-site cavity and out into solution. This result strongly suggests that the "outward" conformation of His 64 is effective for the transfer of a proton between the zinc-bound solvent molecule and solution (*136*).

The cobalt-substituted carbonic anhydrase has been extensively studied as it offers easily measurable pH-dependent electronic spectra

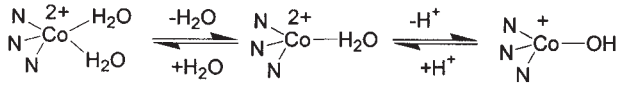

FIG. 12. Three different Co^{II} species of Co HCA I (or Co BCA II).

to elucidate structures and reactivities of these enzymes. The CoHCA I exists almost entirely in the low-pH form at pH 5.7 and five-coordinate species has been proposed for HCA I at low pH values (*132*). The acid–base equilibrium of Co-substituted carbonic anhydrase is proposed in terms of three species as in Fig. 12, where the first equilibrium has never been accurately determined. Experimental data indicated that CoHCA I would have a pK_a of ~8, CoBCA II (B denotes for bovine) and CoHCA II a pK_a of ~6.5, and CoBCA III a pK_a ~ 5.5. The pH-dependence of the electronic spectra of CoHCA I and CoHCA II indicated that these CAs contain at least another histidine in the cavity which has a pK_a of ~6.5 in the free state. The interaction between the acidic group of this histidine and metal coordinated water, possibly, via the network of hydrogen bonds may influence the dissociation constants. Hence these are called apparent acid dissociation constants at the microscopic level. The three-dimensional structure of a complex between catalytically active CoHCA II and bicarbonate revealed that one water molecule and two bicarbonate oxygen atoms are located at distances between 2.3 and 2.5 Å from the cobalt ion in addition to three histidyl residues contributed by the protein chain. This also suggested the presence of a water–bicarbonate exchange state where two unprotonated oxygen atoms of the bicarbonate are bound in a carboxylate binding site and the hydroxyl group is free to move closer to the metal thereby replacing the metal-bound water molecule. The geometry around the metal center is difficult to classify but might best be described as distorted octahedral (*113b*).

^{1}H NMR data of copper–carbonic anhydrase (CuCA) complexes in the presence of different anions indicated that water is present in the coordination sphere along with the anions (*137*). The three histidines, the anion, and the coordinated water molecule arrange themselves to maintain essentially a SQPY. His-94 would be in the apical position of the SQPY and two other histidine residues (His-96 and His-119) along with the anion and the coordinated water are positioned in the basal plane. Most likely the anion is present in the hydrophobic pocket or in the B site and the coordinated water molecule is present in the C site or the hydrophilic binding site.

The EPR spectral data indicated that two cyanide anions bind to copper at low temperature where two cyanide anions and two histidines are present in the basal plane and the third histidine residue is present in the axial position. It has been proposed that the second cyanide anion displaces the coordinated water. Similarly, it has been proposed that the oxalate anion coordinated in a bidentate fashion and displaced the coordinated water. In case of sulfonamides, the coordination geometry is reported to be the same as that of ZnCa. ^{13}C NMR spectroscopy was used to explore the location of CO_2 and HCO_3^- with respect to metal ion in CuCa (*129,130,138*). It indicated that HCO_3^- is bound directly to Cu (*137*). The affinity constant of CO_2 for CuCa is <1 M^{-1} but the paramagnetic effect is paradoxically high (*130*). These results indicated that CO_2 does not bind to a specific site but probably is attracted by the cavity either by hydrophobic interactions or by the metal ion or by both.

MnCA is not completely inactive; the $CO_2 \rightleftharpoons HCO_3^-$ interconversion at pH 8.5 is about 4% of that of native enzyme (*139*). ^{13}C NMR data indicated that in MnCA–HCO_3^-, bicarbonate might be ligated in a bidentate fashion in the catalytic cycle (*139*). Data from ^{113}Cd NMR studies on CdBCA II and CdHCA I indicated that the cadmium derivative could be five-coordinate with two water molecules. ^{113}Cd NMR studies of CdBCA II in the presence of benzene sulfonamides provided direct evidence of cadmium–nitrogen bonding in sulfonamides (*140*), which has also been confirmed by X-ray crystal structure determination (*124*).

Keifer and co-workers reported the three-dimensional structure of the His 94→Asp variant of CA II, which contains tetrahedral zinc coordination polyhedron of composition $His_2Asp–Zn^{2+}$ (*141*). The structural studies of His-94→Asp CA II demonstrate that: (i) the hydrogen bond network involving zinc-bound H_2O is decisive for catalytic reactions; (ii) the chemical nature of the ligands at the zinc center influences the pK_a of the zinc-bound solvent without any dramatic effect on its reactivity; (iii) the protein structure of the enzyme around the zinc center is sufficiently flexible to allow subtle rearrangements to accommodate metal binding with optimal stereochemistry. X-ray crystal structures of zinc-bound Phe93Ile/Phe95Met/Trp97Val and Phe93Ser/Phe95Leu/Trp97Met CA IIs reveal introduction of new cavities in the hydrophobic core and the enzyme maintains tetrahedral zinc coordination geometry. The cobalt-bound variant, Phe93Ile/Phe95Met/Trp97Val CA II, maintains tetrahedral metal coordination geometry whereas for other cobalt-bound variant, Phe93Ser/Phe95Leu/Trp97Met CA II, TBP geometry is reported. However, these

copper-bound variants exhibit either SQPY or TBP metal-coordination geometry due to the addition of a second solvent molecule to the metal coordination polyhedron (*121*).

A. The pK_a of Zinc-bound H_2O

The pK_a of Zn–H_2O in the isoenzymes are determined from the pH dependence of 4-nitrophenyl acetate esterase activity and spectroscopic properties of the metal substituted (essentially Co^{II}) enzyme (*142–146*). In bovine isoenzyme II, the titration behavior of zinc–H_2O and His-64 are interdependent and both have similar pK_a values. Similar behavior has been reported for human isoenzyme II (*147*).

In isoenzyme I, the titration behavior of zinc–H_2O is complicated due to the presence of three titratable active-site histidines as described in Section VI.D. Lindskog reports a value of 7.1 for the pK_a of zinc–H_2O (*142*), but higher values were obtained by other authors. The pH-rate profile for 4-nitrophenyl acetate esterase activity yields p$K_a = 7.45$ (*142*).

The CO_2 hydration activity of cat isoenzyme III is independent of pH in the range of $5.0 \leq \text{pH} \leq 8.5$ (*148*). The pK_a value of zinc–H_2O is outside this pH range and probably quite low due to electrostatic effects from positively charged active-site groups such as Lys-64 and Arg-67 (*143*).

B. Catalytic Mechanism

1. Transfer of H^+ Between Active Site and Reaction Medium

Lindskog *et al.* (*142*) first reported that the catalytic activities of CA I and II are controlled by an ionizing active-site group with a p$K_a \sim 7$ under experimental conditions. The hydration of CO_2 with turnover number of 1×10^6 s^{-1} (pH 9, 25 °C) (*149,150*), $\sim 2 \times 10^5$ s^{-1} (pH 9, 25 °C) (*149*), and 4×10^3 s^{-1} (pH 7.5, 25 °C) (*151*) has been reported for high activity isoenzyme CAII, less active isoenzyme CAI, and very low active isoenzyme CAIII, respectively (see Table IV).

For every turnover cycle of CO_2 hydration, an H^+ ion must be transferred from the active site to the reaction medium. In this case, H^+ ion donor is the enzyme activity-linked group and the acceptor is H_2O and according to Eigen and Hammes (*152*) the rate of H^+ ion transfer to the reaction medium, H_2O, is the rate of CO_2 hydration (10^3–10^4 s^{-1} at pH 7). However, the observed higher rate of CO_2 hydration for isoenzymes CA I and II than the rate of H^+ ion transfer under identical experimental conditions indicate that H^+ transfer must

TABLE IV

k_{cat} VALUES FOR THE HYDRATION OF CO_2 CATALYZED BY CA

Species	k_{cat}, s^{-1}	k_{cat}/K_m, $M^{-1}\,s^{-1}$	Ref.
Isozyme I (human)	2×10^5	5×10^7	*a*
Isozyme II (human)	1.4×10^6	1.5×10^8	*a*
Isozyme III (feline)	1×10^4	3×10^5	*b*

[a]Khalifah, R. G. *J. Biol. Chem.* **1971**, *246*, 2561.
[b]Karali, T.; Silverman, D. N. *J. Biol. Chem.* **1985**, *260*, 3434.

proceed by an alternative mechanism. Several authors (*144,153,154*) proposed that a sufficiently rapid H^+ transfer could occur between the activity-linked group and buffer molecules,

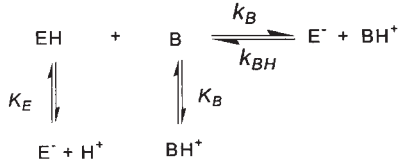

(35)

where EH and B denote the activity-linked enzyme and exogenous proton acceptors in solution or a residue of the enzyme itself, respectively; K_E and K_B are the acid-dissociation constants of enzyme and buffer, respectively. Rowlett and Silverman (*155*) reported that buffer activation is unspecific for a large number of buffer systems and k_B essentially depends on the pK_B of the buffer. k_B was expressed as in Eq. (36)

$$k_B = k_B^o \cdot K_E/(K_E + K_B) \tag{36}$$

where k_B^o is the limiting value of k_B when $K_B \ll K_E$. For isoenzyme CA II, a k_B^o value of $\sim 1 \times 10^9$ $M^{-1}\,s^{-1}$ was obtained, suggesting thereby that the H^+ transfer is nearly diffusion controlled. Lindskog *et al.* (*144*) suggested that the catalytic mechanism can be composed of two consecutive half-reactions, (i) a CO_2–HCO_3^- interconversion reaction and (ii) a buffer mediated H^+ transfer reaction. Similarly, a k_B^o value of $\sim 2 \times 10^7$ M^{-1} s^{-1} was estimated for isoenzyme CA I and this indicated that the buffer-mediated H^+ transfer is considerably slower in isoenzyme I than in isoenzyme II. At very low buffer concentrations, the CO_2 hydration rates catalyzed by isoenzyme CA I becomes buffer independent. Lindskog (*156*) also reported that the buffer-mediated

pathway is ineffective in isoenzyme CA III for which H^+ transfer to H_2O limits the rate of hydration. However, an intramolecular H^+ transfer mechanism has also been proposed (*142*) (see Section VI.D).

C. Interconversion Between CO_2 and HCO_3^-

The ^{13}C-NMR line broadening experiments indicated that rates of CO_2–HCO_3^- exchange at chemical equilibrium is rapid in the presence and absence of buffers for both isoenzymes I and II and this also confirmed the hypothesis that CO_2–HCO_3^- interconversion and buffer-mediated H^+ transfer are separate half-reactions in the catalytic cycle (*157a,b*). This rapid exchange rate is independent of both H_2O and D_2O, indicating that the rate of exchange is not limited by an H^+ transfer process. These results are commensurate with a simple kinetic model given in Eq. (37)

$$E^- + CO_2 \underset{k_{-1}}{\overset{k_1}{\rightleftharpoons}} E^- - CO_2 + H_2O \underset{k_{-2}}{\overset{k_2}{\rightleftharpoons}} EH - HCO_3^- \underset{k_{-3}}{\overset{k_3}{\rightleftharpoons}} EH + HCO_3^- \tag{37}$$

For HCA II, the larger value of the exchange catalyzed rate constant (k_{cat}^{ex}) than the observed maximal values of the turnover parameters, $k_{cat}^{CO_2}$ and $k_{cat}^{HCO_3^-}$ suggests that the turnover rates are not limited by steps in the CO_2–HCO_3^- exchange pathway. The k_{cat}^{ex} for HCA II is ~ 50 times larger than for HCA I. Thus, the most striking differences in kinetic properties of these two isoenzymes is associated with CO_2–HCO_3^- interconversion. For isoenzyme I, the maximal value of $k_{cat}^{CO_2}$ and $k_{cat}^{HCO_3^-}$ are reported to be $\sim 2 \times 10^5$ and 3.6×10^4 s^{-1}, respectively (*157c*). Based on this result for isoenzyme I, a common rate-limiting step for dehydration turnover and CO_2–HCO_3^- exchange is postulated. Assuming that the small, neutral CO_2 molecule exchanges rapidly with the active site (large k_{-1}), k_{-2} is considered to be rate-limiting step. The observed isotope effect of 1 for k_{cat}^{ex} discounted the possibility of involvement of H^+ transfer but supported the transfer of an OH^- moiety from HCO_3^- to Zn^{2+}.

D. The H_2O Splitting Step

For each turnover cycle of CO_2 hydration, an O–H bond in H_2O must be broken and in the dehydration step H_2O must be formed.

For isoenzymes I and II, the CO_2 hydration rates are independent of buffer at high buffer concentrations, indicating thereby that a reaction step other than the buffer-dependent step becomes rate limiting. Studies of both hydration and dehydration reactions at high concentrations of buffers in H_2O and D_2O indicated that the kinetic parameter, k_{cat}, for isoenzyme II has large isotope effect ($k_H/k_D \sim 3$–4) (*45b*). This is consistent with involvement of H^+ transfer in the rate-limiting step. The H^+ transfer half-reaction is composed of at least two steps,

$$EH \rightleftharpoons HE \tag{38}$$

$$HE + B \rightleftharpoons E^- + BH^+ \tag{39}$$

where "EH" and "HE" denote the enzyme in its native form and after intramolecular H^+ transfer, respectively and E^- denotes deprotonated enzyme. Venkatsubban and Silverman (*158*) have reported that the rate-limiting step involves the transfer of two or more H^+ ions. The crystal structure studies of HCA II indicate an ordered water structure in the active site.

The ^{18}O-exchange studies (*159*) show that ^{18}O in labeled HCO_3^- transiently appears as $Zn–^{18}OH^-$ without exchanging with bulk H_2O. The release of ^{18}O from the active site in the rate-limiting step corroborates with the intramolecular H^+-transfer that results in the protonation of zinc-bound $^{18}OH^-$ to form zinc-bound H_2O which rapidly dissociates. Tu *et al.* (*160*) reported that the release of $H_2{}^{18}O$ from $HC^{18}O_3^-$ is inhibited by Hg^{2+} or Cu^{2+}, while the rate of CO_2–HCO_3^- exchange is unaffected. Hence a specific Hg^{2+}-binding site at His-64, which influenced the proton shuttle in isoenzyme II, was inferred.

Similar isotope effects for human isoenzyme I (*157c*) on k_{cat} and K_m for CO_2 hydration are ~1.7. Silverman and Tu (*161*) report an isotope effect of ~2.5 for $H_2{}^{18}O$ release and suggest that the intrinsic isotope effect of intramolecular H^+ transfer might be significantly smaller in isoenzyme I than in isoenzyme II. Hence, the H_2O-splitting step might also limit the rate of CO_2 hydration in isoenzyme I. Human isoenzyme I has three titratable active-site histidines with pK_a values 4.7, 6.0, and 6.1 for His-64, His-67, and His-200, respectively (*162*). The low pK_a value of His-64 discounts it as a sufficiently good H^+ acceptor. The His-200 being closest to the metal ion is the best candidate for proton-transfer and His-67 may also play a role.

An isotope effect of ~2.4 for $H_2{}^{18}O$ release from the active site of cat isoenzyme III is reported (*148*). There is no efficient pathway

for the transfer of H^+ between the metal site and the reaction medium because of lack of titratable active-site histidines in this isoenzyme. Thus, the H_2O-splitting step, plausibly limits the rate of CO_2 hydration in isoenzyme III.

E. Electronic Mechanism for the Catalysis of HCA II

Metal-substituted CAs and their pH-dependent studies indicated that both HCA I and II have two acidic groups, the zinc-coordinated water and a free histidine. The catalytic cycle for HCA II is presented (*69i*) in Scheme 6.

The Zn–OH (**A**), the enzyme is essentially present in this form at the physiological pH, is a relatively good nucleophile and poised for nucleophilic attack on carbon dioxide. Structural studies indicated

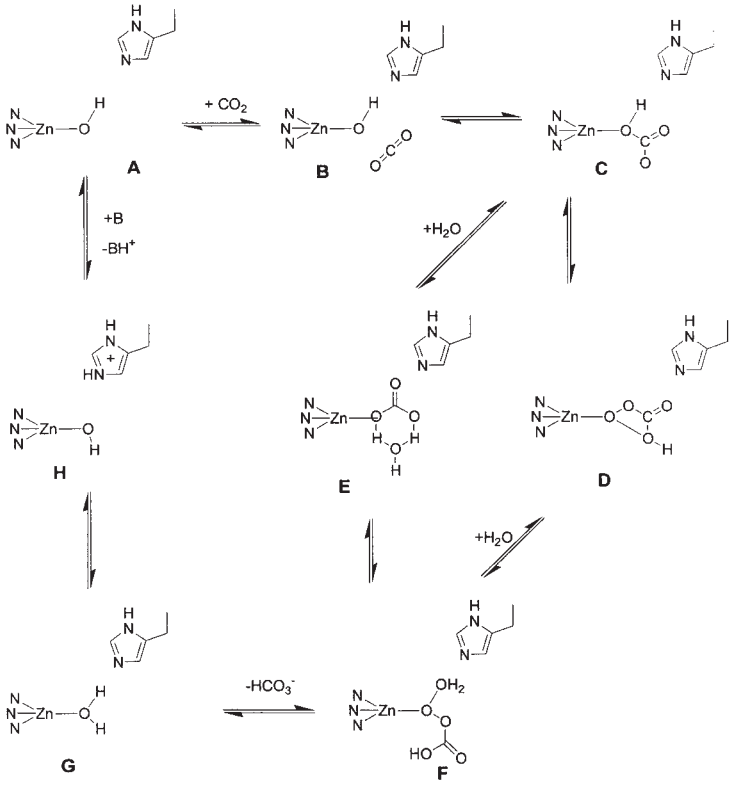

Scheme 6. Proposed CO_2 hydration mechanism for HCA II (α-CA).

that Thr-199 orients the hydroxide for attack on the substrate CO_2 and the concentration of CO_2 in the cavity is higher than in bulk solution (**B**). It has been reported that there are either three (*163*) or two (*164*) potential wells for CO_2 in the hydrophobic pocket. Site-directed mutagenesis results indicated that when Val-143 is replaced by the much larger Phe, the activity decreases by a factor of 10^3 (*128b*). This is rationalized in terms of less space available within the cavity to accommodate CO_2 because of the relatively larger Phe residue. It has also been reported that CO_2's interactions with positive charges around zinc activate the carbon for nucleophilic attack (*165*). Merz reported that the positioning of CO_2 between zinc and the peptide NH of Thr-199 would be ideal for neucleophilic attack by hydroxide (*164*).

It has been reported that a proton is transferred from the Zn-bound water (pK_a for HCA II ~ 7) to a residue, thought to be His-64, thus generating zinc-bound hydroxide (**A**). This proton is subsequently transferred to a buffer or solvent. It was postulated that once bicarbonate is formed (**C**), the proton has to transfer to a terminal oxygen atom, either via an intermediate in which bicarbonate is bidentate (**D**) or via a hydrogen-bond network (**E**). Additional hydrogen bonds with one or more water molecules in the active site that coordinate His-64 will link the bicarbonate proton to the exocarboxylate oxygen (*166*). The crystal structure of the bicarbonate complex with Co(II) substituted HCA II shows that the coordination of two oxygens of the bicarbonate and the oxygen of a water molecule is within 2.3–2.5 Å from cobalt. Håkansson and Wehnert (*113b*) described this residue of Thr-200-His variant of HCA II as "pseudo bidentate" coordination of bicarbonate to the metal. However, Tu *et al.* (*167*) pointed out from ^{18}O-exchange experiments that the bicarbonate bound to the metal is monodentate allowing proton transfer to the metal bound hydroxide (see Fig. 13).

Lipscomb *et al.* (*168*) suggested the proton transfer path and Lindskog and co-workers (*142*) described rotation along the bond between the carbon and zinc-bound oxygen as depicted in Fig. 14.

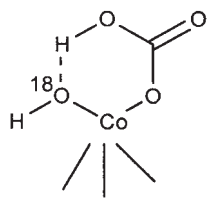

FIG. 13. Proposed structure of Co^{II}–HCO_3^- adduct of Co^{II}-substituted HCA II.

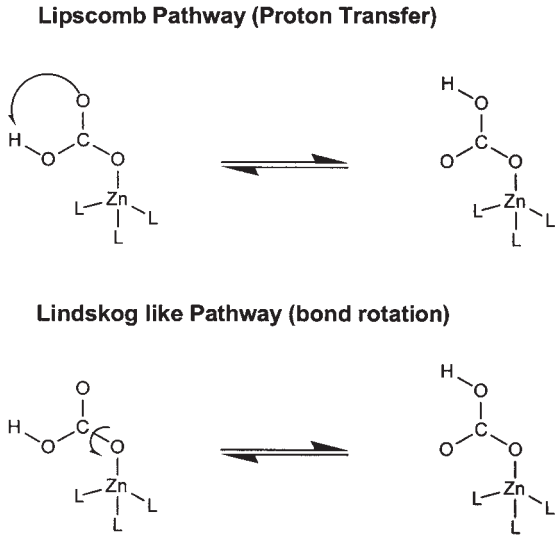

FIG. 14. Proposed rearrangement of bicarbonate during CO_2 hydration in HCA II.

The bicarbonate derivative is in equilibrium between four- (**G**) and five-coordinate species (**F**), as indicated from the electronic spectra of the cobalt derivative (*169*). This five-coordinate bicarbonate species would locate in the **B** site and water in the **C** site. Some anionic and neutral inhibitors are competitive with bicarbonate, possibly because they also bind at the B site. The proton (H^+) has to be released from G as the second substrate to yield (**H**). It is reasonable to believe that the proton is transferred to a group inside the cavity, i.e., His-64, and subsequently to solvent or buffer. This is also discussed in Section VI.F. In the absence of buffers, transfer of proton to the solvent is the rate-limiting step for HCA II. In the presence of buffers, which can assist proton transfer, the rate-limiting step becomes the internal proton transfer. The crucial role of the water chain connecting the zinc hydroxyl to His-64 and the role of buffer at this step is also reported. The rate for this reaction cycle will be influenced by (i) cooperative effects of His-64, (ii) multiple pathways for proton loss through the hydrogen-bonded network, and (iii) buffer or solvent that accepts a proton. Pocker and Deits (*170*) also confirmed the proton transfer in this step. A proton from the zinc-bound water will transfer through Thr-199 to Glu-106 regenerating zinc-bound hydroxide.

Koenig and Brown (*171*) also proposed a "ping-ping-pong" mechanism for catalysis. The first "ping" is reported to be the catalytic generation

of enzyme-bound bicarbonate from CO_2 using enzyme-bound hydroxyl as the nucleophile. The second "ping" is the combination of a non-substrate water molecule with zinc-bound bicarbonate to form free bicarbonate and enzyme-bound water. The third "pong" is release of H^+ from the Zn–H_2O generating catalytic species, Zn–OH.

F. Mechanistic Insight for the Catalyzed Reaction

van Eldik and co-workers (*23,172*) proposed a reaction mechanism for reversible CO_2 uptake by HCA II and the corresponding spontaneous reactions based on the principle that bond formation and breakage for both reactions may proceed in a parallel way. The mechanisms for the catalyzed and spontaneous reactions are presented in Schemes 7 and 8, respectively. It has been proposed that two water molecules participate in the spontaneous reaction (Scheme 8) (*172*), which is comparable to the catalyzed reaction (Scheme 7) i.e., one water molecule is the reactant and the second is equivalent to the enzyme $E{\equiv}Zn^{2+}{-}OH^-$.

The volume profile analysis (*172*) indicate that the nucleophilic attack of $E{\equiv}Zn^{2+}{-}OH^-$ on CO_2 proceeds via an outer-sphere mechanism and is associative. During this the oxygen of $E{\equiv}Zn^{2+}{-}OH^-$ (for reaction: $1{\rightarrow}2$) directly attacks the carbon of CO_2. Two mechanisms [Lipscomb (*45a*) and Lindskog mechanism (*45c,159*)] have been proposed for formation of the bicarbonate intermediate $E{\equiv}Zn(OH)CO_2^+ {\rightarrow} E{\equiv}ZnOCO_2H^+$ ($2{\rightarrow}3$). Lipscomb proposed that there is a proton transfer between two oxygen atoms following the nucleophilic attack (*45a,173*) and Lindskog proposed direct coordination of oxygen atom to Zn^{2+} center without any proton transfer (*45c,174*). The rate-determining step for the decarboxylation reaction, however, is the proton transfer from the uncoordinated oxygen atom to the coordinated oxygen atom of the carbonate ligand: $E{\equiv}ZnOCO_2H^+ {\rightarrow} E{\equiv}Zn(OH)CO_2^+$. The volume profile studies (*172*) have shown that the product $E{\equiv}ZnOCO_2H^+$ is not necessarily formed as a stable species during the forward reaction but a relatively stable species may be a hydrogen bridging intermediate between $E{\equiv}Zn(OH)CO_2^+$ and $E{\equiv}ZnOCO_2H^+$. The bridging proton labilizes the Zn–O bond ($E{\equiv}Zn\cdots OHCO_2^+$) during substitution of HCO_3^- by H_2O and this step is reported to be a substitution reaction. During the decarboxylation reaction the bridging proton weakens the O–C bond ($E{\equiv}ZnHO\cdots CO_2^+$) and the CO_2 is released. The CO_2 release and a proton transfer are concerted steps during the dehydration reaction. The CO_2 release and the substitution of H_2O by HCO_3^- on

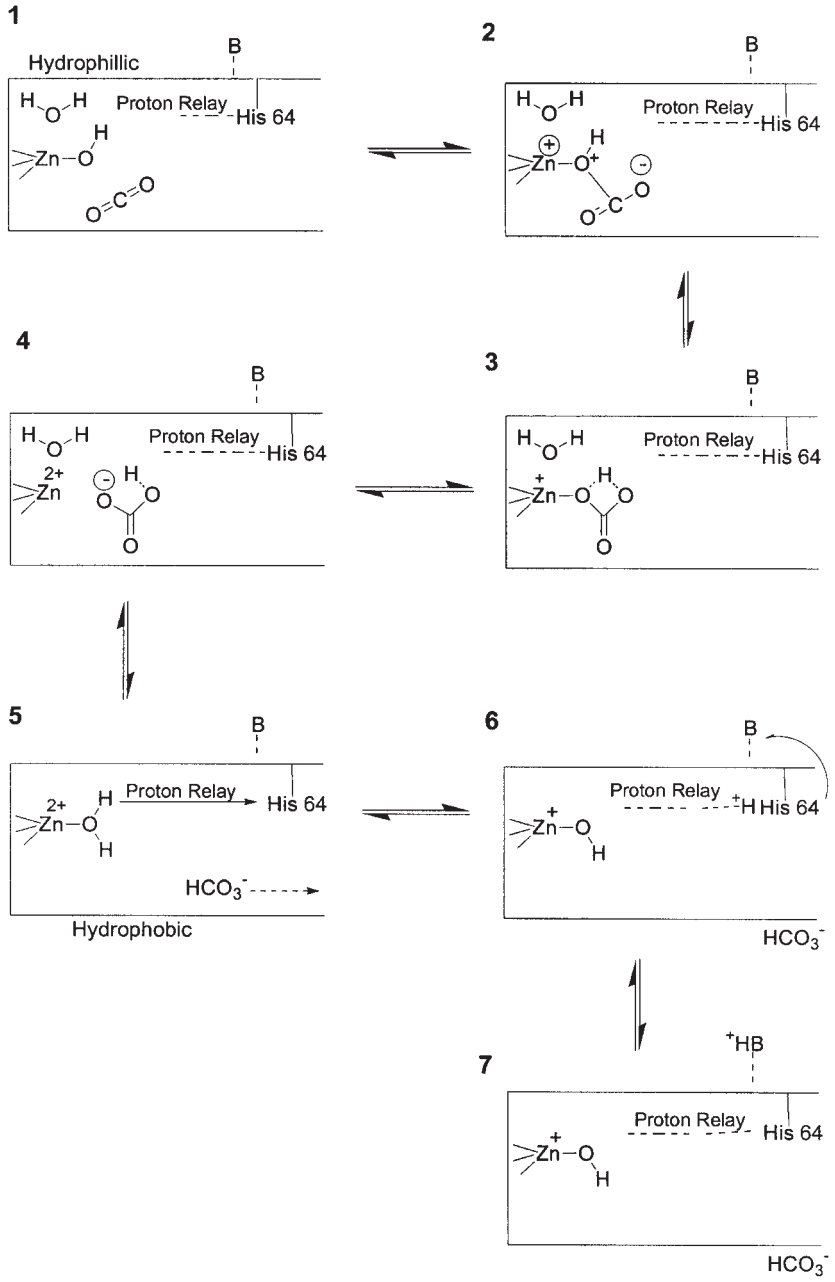

SCHEME 7. CO_2 catalyzed hydration and dehydration reaction by HCA II based on volume profile analysis.

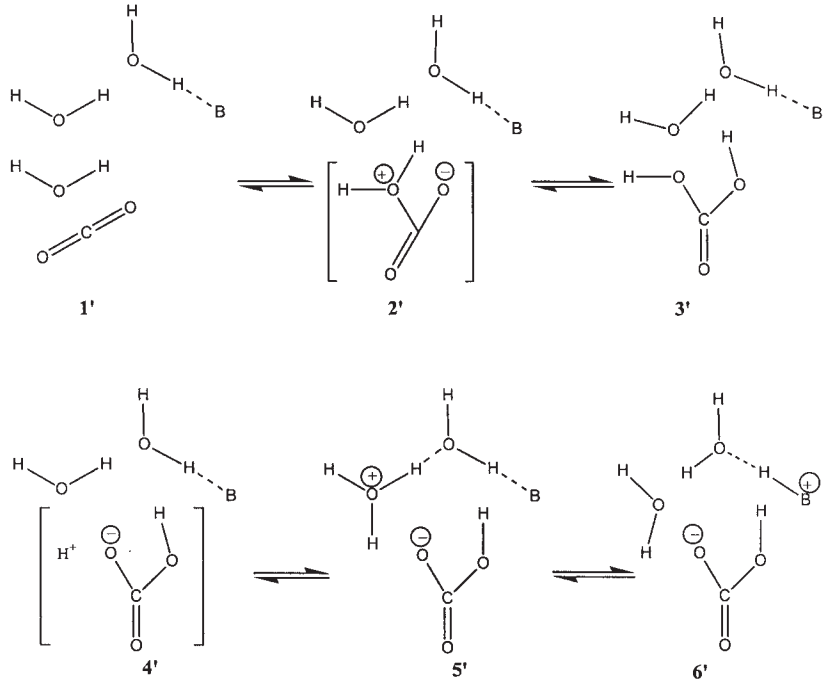

SCHEME 8. Spontaneous CO_2 uptake and dehydration reaction.

the zinc center follow a dissociative mechanism (most likely a limiting D mechanism). It has been suggested that when neither hydration of CO_2 nor dehydration of HCO_3^- are necessitated physiologically, the hydrogen bridging bicarbonate intermediate is at equilibrium: $E{\equiv}Zn(OH)CO_2^+ \rightleftharpoons E{\equiv}ZnOCO_2H^+$. This is recognized as the novel characteristics of the enzyme. The spontaneous reactions and the model catalyzed reactions proceed slowly, possibly, due to lack of these environments.

G. MECHANISM OF INHIBITION

In higher vertebrates this enzyme is quite abundant in the brain mainly as the cytosolic isoenzymes CA II, CA IV, and the membrane-bound isoform CA XIV (*104,175–179*). The inhibition of the brain CA's causes a selective increase of the cerebral blood flow with concomitant rise of carbon dioxide partial pressure (*104,175–179*). As a result CA inhibitors are recognized as potent candidates for treatment of

conditions associated with increased intracranial pressure (*180*), as well as different neurological/neuromuscular pathologies such as epilepsy (*181*), genetic hemiplegic migraine and ataxia (*182*), tardive dyskinesia (*183*), hypokalemic periodic paralysis (*184,185*), essential tremor and Parkinson's disease (*186*), and mountain sickness (*187,188*).

The inhibitors are generally monoanions or neutral molecules capable of deprotonation to yield anionic species. These neutral inhibitors (mostly sulfonamides) (*189*) bind to the active site Zn–H_2O. Monovalent anions like I^-, CN^-, SCN^-, N_3^-, NCO^-, SH^- etc. (*190,191*), inhibit the catalyzed reaction of CA enzyme by binding directly to the metal ion either by displacing H_2O to yield a tetra-coordinate metal ion or by adding to the coordination sphere to yield a penta-coordinate metal ion with H_2O as the fifth ligand (see Table V). In some cases an equilibrium between these two coordination geometries is also reported.

In general, anion inhibition is non-competitive below pH 7 and uncompetitive at pH 9 towards CO_2 hydration, whereas it is competitive towards HCO_3^- dehydration at low and neutral pH (*169,157c*). Other inhibitors such as alkylcarbonates, acetates, alkoxides, alcohols (*192a*) and divalent metal ions like Cu(II), Hg(II) are also reported (*160, 190,192b*).

The Zn–H_2O form of the enzyme, EH, is the only one which interacts with anions (X^-),

$$EH + X^- \rightleftharpoons EHX^- \tag{40}$$

where EHX^- denotes a mixed-complex. Under equilibrium conditions [Eq. (40)], HCO_3^- will efficiently displace the bound anion from the active site. The E^- form of CA enzyme does not bind anions strongly and there is little inhibition.

Lindskog reported that Cl^- is a competitive inhibitor of the CO_2–HCO_3^- exchange reaction for isoenzyme I (*157c*). ^1H NMR experiments (*142,157c*) and pH dependence of the SCN^- inhibition of the 4-nitrophenyl acetate esterase activity have shown that the affinity constants of SCN^- for various free enzyme forms follow the order HEH > EH > HE > E (*142*). The estimated values of the affinity constants are found to be $\sim 5 \times 10^4$ M^{-1} and < 2 for HEH and E, respectively. Under inhibitory conditions the CA has a finite residual activity (k_{cat} value) which is large for I^-, intermediate for N_3^- and SCN^-, and very small for NCO^-. This has been explained on the basis of the relative binding affinities of these anions for the enzyme (*190*).

TABLE V

COORDINATION PATTERN OF DIFFERENT INHIBITORS WITH Zn–CA II (WILD TYPE) AND Co–CA II AND THEIR ASSOCIATION CONSTANTS (*190,191c*)

Species	pH[a]	Inhibitor	Metal coordination:		Zn–CA	Co	CA
			Metal ligand	Log K_{app}	Coordination type[b]	Log K_{app}	Coordination type[c]
Wild type	6.0		H_2O		4		
Wild type	7.8		OH^-		4		
Wild type	7.8	SH^-	SH^-	5.7	4	5.8	4
Wild type	7.3	HSO_3^-	$HOSOO^-$	1.5	4	> 5	5
Wild type	6.0	Br^-	Br^-	1.2	4	2.1	4–5
Wild type	7.8	N_3^-	NNN^-	3.2	4	3.6	4–5
Wild type	6.0	1,2,4-triazole	N_4	2.7	4	–	–
Wild type	8.5	OCN^-	H_2O	4.2	4	5.2	4
Wild type	8.5	CN^-	H_2O	5.5	4	> 5	4
Wild type	6.0	NO_3^-	H_2O	1.3	4	3.5	5
Wild type	7.6	$HCOO^-$	H_2O	1.7	5	2.7	5
Wild type	8.5	SCN^-	H_2O	4.0	5	3.8	5
Wild type	6.0	CH_3COO^-	CH_3COO^-	1.1	4–5	2.1	5
T200H[d]	7.8	HCO_3^-	$HOCOO^-$	0.9	5	1.6	4–5

[a]pH is related to metal–ligand coordination to Zn–CA II.
[b]Determined from X-ray crystallography.
[c]Determined from spectroscopy.
[d]Mutant Thr-200-His.
[e]Investigated crystallographically and found to be octahedrally coordinated.

Phenol binds to the hydrophobic pocket; it is a competitive inhibitor for CO_2 hydration and mixed non-competitive inhibitor of HCO_3^- dehydration reaction (*192a*,*193*). In contrast, 2-nitrophenol is shown to be uncompetitive with respect to CO_2 hydration at high pH. 1,2,4-Triazole is a non-competitive inhibitor towards both CO_2 hydration and HCO_3^- dehydration (*194*). In contrast, tetrazole as an inhibitor is uncompetitive for CO_2 hydration and competitive for HCO_3^- dehydration at neutral and alkaline pH (*194*). Different inhibitors showing metal coordination with native enzyme and that of the Co-variant are presented in Table V.

Both imidazole and triazole show inhibitory activities over a large range of pH (*194*) because both the neutral and anionic species can bind the aqua form of the enzyme with essentially the same affinity. Notably, the reaction of imidazole with the Zn–OH species cannot be distinguished thermodynamically from the reaction of the imidazolate with the aqua forms. It is postulated that the non-coordinated nitrogen of these inhibitors can interact with a group in the protein via a hydrogen bond. This could be the NH group of His-200 in HCA I or the hydroxyl group of Thr-200 in HCA II.

H. Activators

Compounds which enhance the catalytic activities of the CAs are known as activators. Activators of carbonic anhydrases are less studied because CA is one of the most efficient enzymes known. Carbonic anhydrase II activation by phosphorylation in the presence of protein kinase and cAMP has been reported (*195,196*). Also some anions are activators for CA III (*197,198*); the catalytic effect is due to the proton shuttling capacities of such activators. Histamine, a well known activator, for native and Co(II)-substituted isoenzymes I and II CA is reported by Briganti *et al.* (*199*). Amines [Ar–CH(R^3)CH(R^2)NH(R^1); Ar = Aromatic/heterocyclic group; $R^1 = R^2 = H$, Me; $R^3 = H$, OH, COOH] and amino acids are efficient activators for CA I–III (*200–207*). These amines possess a bulky aromatic/heterocyclic moiety in their molecular structure and act as proton acceptor (*204–207*).

According to Supuran and co-workers (*199,204*), an enzyme-activator complex may be formed in which the activator facilitates the proton transfer. A general reaction scheme is presented in Scheme 9.

Scozzafava and Supuran (*207*) reported that activators might be used for development of new drugs/diagnostic tools for treatment associated with memory therapy, i.e., Alzhemier's disease and enhancement of synaptic efficacy, spatial learning, and memory.

SCHEME 9. Reaction scheme in the presence of activators ("A" denotes activators).

VII. Structure of β-Carbonic Anhydrase from the Red Alga, *Porphyridium purpureum*

β-CA has been widely studied in higher plants due to its pivotal role in the physiology of photosynthesis. This enzyme is thought to minimize the resistance to the diffusion of CO_2 from the stomatal air spaces to the chloroplast stroma where CO_2 is fixed by the enzyme RuBisCO (*208*). This enzyme plays a prominent role in the CO_2 concentrating mechanism in C_4 plants by converting CO_2 to HCO_3^-, and provides substrate for phosphoenolpyruvate carboxylase. In more common C_3 plants, this enzyme is present as a major component in leaf protein, and is localized primarily in the stroma of the chloroplast, where it plays a critical role in the cytoplasm of photosynthetic cells (*209*). The alkaline pH stabilizes bicarbonate relative to CO_2 in the stroma, where the enzyme helps in promoting efficient photosynthesis by providing a CO_2 source in close proximity to the CO_2 sink (*210*).

Mitsuhashi *et al.* (*211*) reported the crystal structure of β-CA from the red alga, *Porphyridium purpureum*, at 2.2 Å resolution. The β-CA monomer is composed of two internally repeating structures folded as a pair of fundamentally equivalent motifs of an α/β domain and three projecting α-helices (*211*). The two motifs are related to each other by a two-fold axis perpendicular to the pseudo two-fold axis in the monomer. The two halves are known as N-terminal half (residues 86–309) and C-terminal half (residues 340–563). Six main chain hydrogen bonds are reported to exist between the N- and C-terminal halves of a monomer indicating thereby that these two halves are in intimate contact with each other and unable to divide into two independent structural domains. The CA monomer has a molecular mass of ~55 kDa (~25–30 kDa per zinc ion) and contains two zinc atoms per monomer. This dimeric nature of the β-carbonic anhydrase has evolved through gene duplication and fusion of an ancestral CA monomer. Similarly, octameric β-CA from pea is also reported with a monomer of ~27 kDa (*212*). This homodimeric carbonic anhydrase behaves like a tetramer with pseudo 222 symmetry. The X-ray absorption fine structure data suggest that the coordination sphere of zinc

in β-CAs of higher plants should have one or more sulfur ligands (*213*). The two zinc-binding sites of the β-CA of *Porphyridium purpureum* reside in two clefts on both sides of a monomer. One of the catalytic zinc atoms maintain tetrahedral coordination geometry with the S-γ atom of Cys-149, the O-δ_2 of Asp-151, the N-ε_2 of His-205, and the S-γ of Cys-208 in the N-terminal half and the other is with equivalent atoms of Cys-403, Asp-405, His-459, and Cys-462 in the C-terminal half. Hence zinc coordinated by the former tetrad is reported as Zn–N and that by the latter as Zn–C. Most remarkably, no water or hydroxide participates in zinc coordination. This is considered to be most striking difference from the structures of both α- and γ-CAs in which a hydroxide or water molecule occupies the fourth coordination site of Zn.

It has been postulated that there are two distinct groups of β-CAs, differing in their pattern of sequence conservation, active site design, and possibly in their mechanism. The three zinc-bound ligands and the Asp/Arg pair are conserved in every β-CA sequence known. Two sets of sequences are observed for active site residues, viz. in higher plants (Gln-151, Ser-161, Ser-163, Phe-179, Val-184, and Tyr-205) and in *M. thermoautotrophicum*, *Mycobacterium tuberculosis*, and *Bacillus subtilis* and others (Pro-151, Met-161, Thr/Ala-163, Lys-179, Ala-184, and Val-205) (*214*). Kimber and Pai (*208*) designated, for convenience, the group as "plant" type for plant sequences and those with the altered site as the "Cab" type after the *M. thermoautotrophicum* enzyme. The results of the kinetic studies of β-CAs of higher plants revealed that a basic form of the enzyme is the active species and the pK_a for the activity linked group is approximately 8.5 (*215*). The extended X-ray fine structure data indicate that one of the nitrogen/oxygen atoms of the Asp residue coordinate to the zinc atom but not a water molecule. The results of site-directed mutagenesis analysis indicated that only one of the two carboxyl oxygen atoms of Asp-152 is necessary for zinc binding and the other carboxyl oxygen or its negative charge is essential for catalytic activity.

The residues in the active site clefts are classified into two groups. Group I includes residues located around Zn–C and reside in the C-terminal half; group II includes residues that surround Zn–C and are present in the N-terminal half. Group I residues include Ser-406, Arg-407, Gly-463, Tyr-543, and 4-zinc ligands (Cys-403, Asp-405, His-459, and Cys-462), while group II residues are Gln-140, Pro-142, Gly-165, Phe-168, Tyr-190, and Leu-195. These 4-zinc ligands are associated with a number of hydrogen bonds with residues in the immediate vicinity of the active site cleft (Fig. 15).

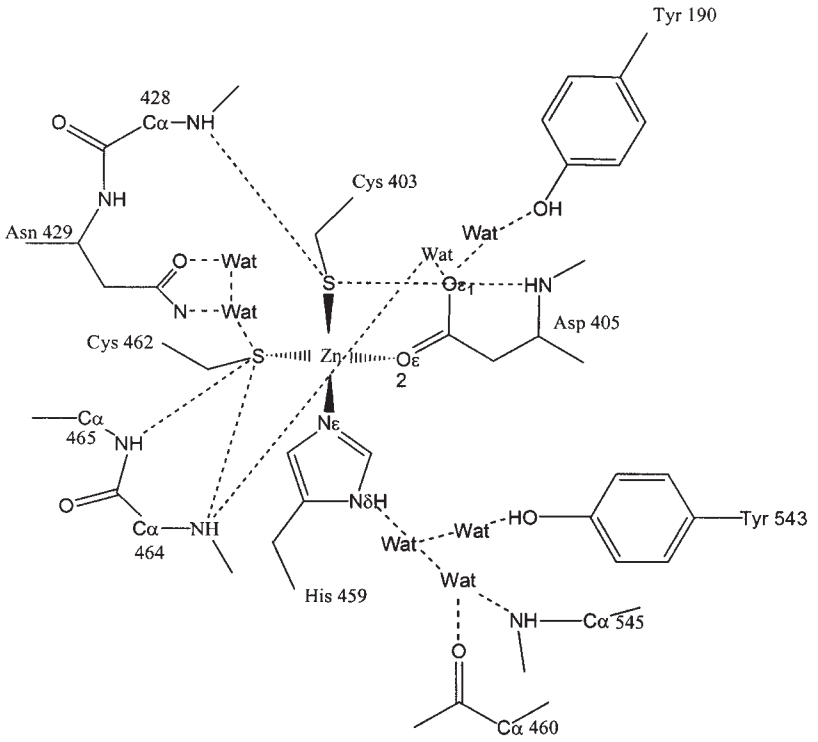

FIG. 15. Proposed hydrogen bonding at the active site of β-CA (*P. Purpureum*).

Each zinc-ligating cysteine residues form two NH–S hydrogen bonds. Also Tyr-190 (group II) and Tyr-543 (group I) are hydrogen-bonded to Asp-405 and His-459, respectively, through water molecule(s). These hydrogen bonds were proposed to be providing a possible proton shuttle pathway between activated water and the bulk solvent.

A. PROPOSED CO_2 HYDRATION MECHANISM

The results of site-directed mutagenesis analysis of zinc ligands of higher plant β-carbonic anhydrase and of *P. purpureum* carbonic anhydrase have confirmed that zinc is essential for catalysis. X-ray fine structure data indicated that a water molecule is hydrogen bonded to the zinc-ligated Asp-151 and Asp-405. The water molecule is not directly coordinated to the zinc atom. A possible catalytic mechanism of CO_2 hydration cycle (*211*) has been proposed as given in Scheme 10.

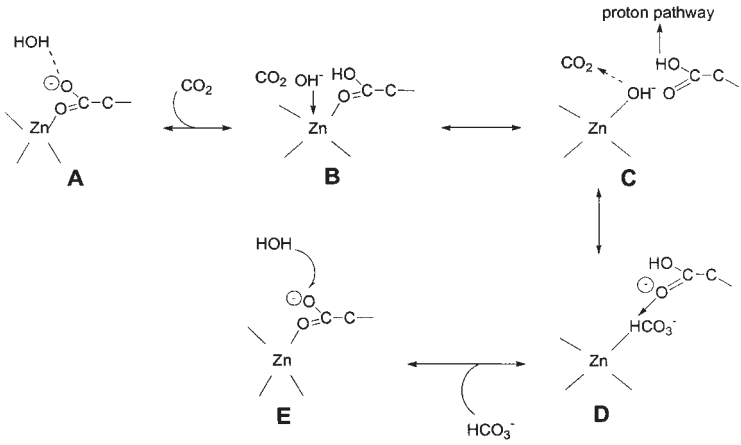

SCHEME 10. Proposed CO_2 hydration mechanism for β-CA (*P. Purpureum*).

The hydrophobic pockets formed by Pro-142, Phe-168, Leu-195 (around Zn–C) and Pro-396, Phe-422, Leu-449 (around Zn–N) are termed as active site for CO_2 association. The zinc-bound aspartate behaves as a base to accept a proton from its hydrogen-bonded water and forms a nucleophilic hydroxide (step A). The zinc-bound aspartate on protonation is released and the nucleophilic hydroxide coordinates to zinc (step B). The zinc-bound hydroxide attacks the CO_2 molecule to generate zinc-bound HCO_3^-. In the next step, the proton is transferred from the protonated aspartate to the bulk solvent or buffer through one of the hydrogen-bonded pathways immediately surrounding the zinc ligands (step C). HCO_3^- is a better leaving group and the zinc-bound HCO_3^- is replaced with a deprotonated Asp yielding a zinc-bound Asp (step D). Finally, a water molecule binds the zinc-bound Asp to regenerate the A (step E). The absence of a water molecule in the zinc coordination sphere suggests that the mechanism of the CO_2 hydration cycle in α-CAs and γ-CAs is different from that of β-CAs. Kimber and Pai also reported a similar mechanism of catalysis for β-CA from *Pisum sativum* (*208*).

VIII. Structure of γ-Class Carbonic Anhydrase of *Methanosarcina thermophila* (*Cam*)

The γ-class is expected to have evolved between 3 and 4.5 billion years ago (*216*) and precedes evolution of the α-class at 200–300 million years ago (*217*). Kisker *et al.* (*218*) reported the crystal structures of

zinc-containing and cobalt-substituted γ-class CAs from *M. thermophila* between 1.46 and 1.95 Å resolution in the unbound form or co-crystallized with either SO_4^{2-} or HCO_3^-. X-ray crystal structure data of the native enzyme, Zn-Cam, indicated that the overall fold of Zn-Cam is a left handed β-helix and no significant overall structural change occurs upon metal substitution (Zn by Co). The Cam forms a trimer in the crystal (*218*). The active site coordination geometry is sensitive to the nature of the divalent metal ion and the presence or absence of additional ligands.

Crystallographic studies indicated that in the active-site of Zn-Cam, Zn^{2+} has three residues of the protein and two solvent ligands arranged in a TBP geometry (*219*). The zinc ion is bound by three histidines (protein residues) of two monomers; His-81 and His-122 are contributed by one monomer and His-117 is contributed by an adjacent monomer. The active-site of γ-class carbonic anhydrase in Cam is located at the base of the cleft between two monomers. The proposed hydrophobic pocket consisting of Met-135b (where b denotes that the residue belongs to the adjacent monomer), Phe-138, Phe-140, Il2-157, and Val-172 residues serve as a binding site for CO_2 in the active site. EXAFS data conform to penta-coordination of Zn (*218*); discrete conformations of Glu-84 are observed for Zn-Cam (one of which points toward the active-site and lies within hydrogen-bonding distance of the side chain of Glu-62). Both these residues (Glu-62 and Glu-84) are located at the base of the active-site in a negatively charged tunnel which may favor protein-solvent proton transfer. Alber and co-workers (*220a*) suggest that Arg-59 contributes to the thermodynamic stability and structural integrity of both native trimer and active site of Cam. Arg 59 is important for catalysis of the interconversion of CO_2 and HCO_3^-, product release, or both and replacement of this residue results in substantial decrease in both k_{cat} and k_{cat}/K_m (*220b*).

Cobalt(II) in Co-Cam is hexa-coordinate in a distorted octahedral arrangement with three histidine residues and three water molecules (*219*). Zn-Cam co-crystallized with bicarbonate indicated that the latter binds zinc ion in a bidentate fashion (*219*). HCO_3^- is stabilized by coordination of one oxygen (O_3) directly to the active-site zinc and by a hydrogen bond contact of the same oxygen (O_3) to the side chain of Glu-62; the second HCO_3^- oxygen (O_1) makes a long contact with the zinc ion. The third oxygen (O_2) of the HCO_3^- is within hydrogen-bonding distance of both carboxylate oxygens of the Glu-62 side chain. Thus, Glu-62 could partially fulfill a "gatekeeper" function. Furthermore, multiple binding modes for HCO_3^- in the active site of

Cam suggest the availability of a continuum binding mode to the substrate, and perhaps isomerization of HCO_3^- could occur before its release. Kinetic studies also indicated that bicarbonate acts as a proton donor to the zinc-bound hydroxide during catalysis (*219*). Co-Cam co-crystallized with bicarbonate indicated that HCO_3^- binds monodentately to cobalt(II).

A. Proposed CO_2 Hydration Mechanism for γ-Class Carbonic Anhydrase

Based on these structural features and biochemical evidences, a possible reaction mechanism (see Scheme 11) has been proposed (*219*) which is similar to that for HCA II.

In the native enzyme, Zn^{2+} is coordinated to one water molecule and one hydroxide ion at the beginning of the reaction (**A**). The CO_2 binds adjacent to the zinc-bound hydroxyl, the exact position is still unknown (**B**). The Zn-bound hydroxyl attacks CO_2 (**C**), leading to a transition state in which the protonated oxygen of the bicarbonate is ligated to the metal, most likely stabilized by either Gln-75 or Asn-202. The bicarbonate exhibit several binding modes, most favorably it proceeds via bidentate binding mode with loss of the metal-bound water molecule in this case (**D**). The bicarbonate may isomerize (**C** and **D**) before replacement by a water molecule (**E**). Deprotonation of zinc-bound water occurred by shuttling a proton from one of the metal-bound water molecules to Glu-62 (**F**) and the side chain of Glu-84 pre-orient itself to accept the proton. The proton is finally transferred from Glu-62 to Glu-84 (**G**), and with transfer of a proton to the solvent, the active zinc-bound hydroxyl (**A**) is regenerated.

IX. A δ-Class of Carbonic Anhydrase?

Roberts *et al.* reported a 27 kDa monomeric carbonic anhydrase, TWCA1, from the marine diatom *Thalassiosira weissflogii* (*221*). X-ray absorption spectroscopy indicated that the catalytic zinc is coordinated by three histidines and a water molecule, similar to the active sites of the α- and γ-CAs (*222*). Also, the active site geometry is similar to that of α-CAs. Based on these results the catalytic mechanism is expected to be similar to that of the α-class carbonic anhydrases. Tripp *et al.* (*223*) proposed that this TWCA1 is the prototype of a fourth class carbonic anhydrase designated as δ-class CAs. In the

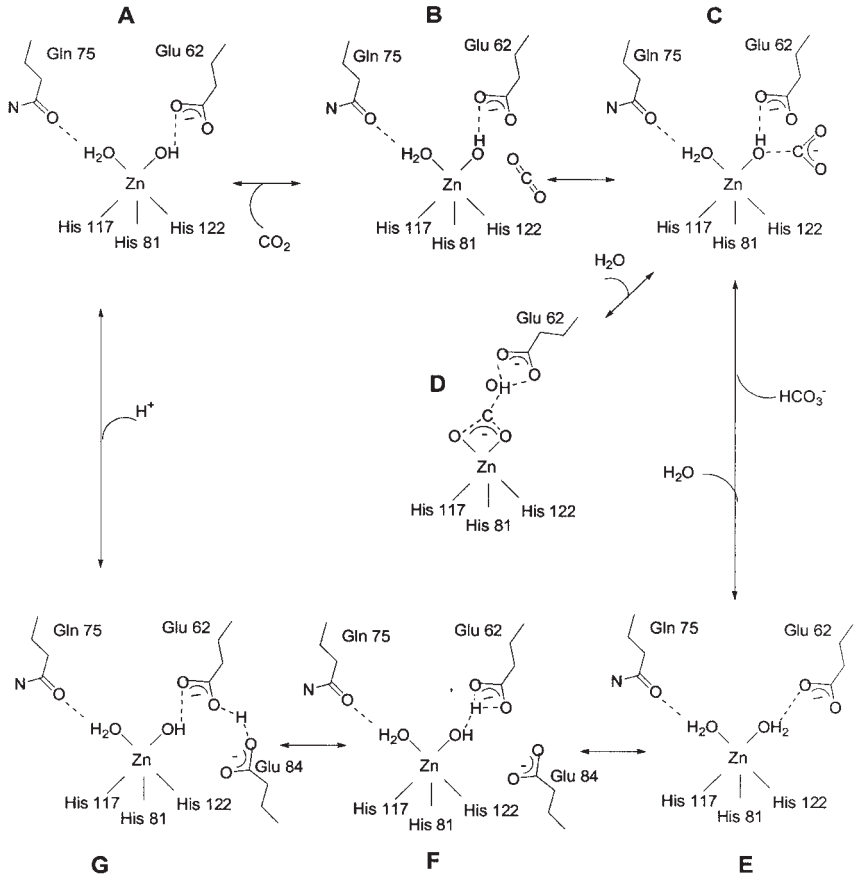

SCHEME 11. Proposed reaction scheme for γ-carbonic anhydrase (*Cam*).

absence of gene encoding data for this CA it is not known whether this represents a new class or belongs to a pre-existing class.

X. Model Chemistry

A number of papers on some transition-metal model complexes have been reported in the literature to mimic the activity of CA and explore further information on the catalytic mechanism of CA. This aspect has been dealt with in Section IV on formation and aquation/decarboxylation of carbonato complexes. A few more relevant

informations are included here. The complex $[Co(TPyMA)OH_2]^{2+}$ provides a five-coordinate adduct with a weakly bound axial nitrogen (*224*). The interconversion between $[Co(TPyMA)OH_2]^{2+}$ and $[Co(TPyMA)OH]^{+}$ was studied and the high- and low-pH forms of this complex resembles CoCA (*224*).

Kimura (*225*) studied a potentially attractive model Zn-complex of [12]aneN$_3$. It confirms to a tetrahedral geometry with a H_2O at the fourth coordination site $[LZn^{II}OH_2]$ and pK_a of Zn-bound water is 7.3 (25 °C, $I = 0.1$ M $NaClO_4$) (*34g*). X-ray crystal structure analysis revealed that a trimer of the hydroxide forms of the complex was formed but retained the tetrahedral coordination around zinc center. In aqueous solution, two basic hydroxide form of the complex, and one neutral species are produced. Similarly, a square pyramidal complex of Zn^{II} with cyclen ($LZn^{II}OH_2$) forms its hydroxo species, Zn^{II}–OH, on deprotonation (pK_a of $[Zn(cyclen)OH_2]^{2+} = 7.9$, 25 °C) (*72c*), which behaves as a strong nucleophile. These findings interestingly demonstrate that simple zinc complexes can mimic CAs if appropriately chosen. The kinetic results for the Zn complex of [12]aneN$_3$ for hydration of CO_2 demonstrated the catalytic nature of the zinc complex at various pH values, and the hydroxide form of the Zn complex was observed to be the active species. In HCA II, the rate-determining step is believed to involve proton transfer from the product Zn–OH_2 species to solvent through His-64 as a proton shuttle to produce catalytically active Zn–OH species. In the absence of a proton shuttle residue in the model system, aquation of the bicarbonate product complex [ZnL–OCO_2H] releases HCO_3^- and the Zn-complex of [12]aneN$_3$; the latter then deprotonates relatively fast under the reaction conditions. The HCO_3^- dehydration is catalyzed by the model system and the reactive species is the Zn–OH_2 complex which undergoes aqua ligand substitution by HCO_3^-, followed by decarboxylation as shown in Scheme 4. Thus the model complex Zn-complex of [12]aneN$_3$ exhibited the same essential zinc functions and similar pH-dependent hydration and dehydration reactions catalyzed by CAs. Similar kinetic patterns were also observed for the model Zn-cyclen complex also.

A. Recognition of Anionic Inhibitors by the Model Complexes

X-ray crystal structure of Zn^{2+}–[12]aneN$_3$–$(NCS)_2$ revealed a five-coordinate TBP which mimics the structure of the NCS^- adduct of CA (*225*). Kinetic results demonstrated that NCS^- and N_3^- inhibit competitively the catalytic activity of 4-nitrophenyl acetate (NA) hydrolysis by Zn^{2+}–[12]aneN$_3$ (*46b*). These results lend support to

the competitive inhibition by NCS^- and N_3^- in the analogous reaction of CA.

The neutral inhibitors of CA like sulfonamide, such as acetozolamide, bind to Zn^{2+}–[12]aneN_3 in a 1:1 stoichiometry as determined from 4-NA hydrolysis and isolation of Zn–sulfonamide–pendant [12]aneN_3 complex. UV-spectral data indicated coordination of sulfonamide anion to Zn^{2+}–[12]aneN_3. The X-ray crystal structure of the Zn–imidazole–pendant [12]aneN_3 complex revealed a five-coordinate TBP structure with imidazole N at an equatorial position and a Cl^- counter ion at an apical position. Neither this complex nor its deprotonated imidazolate form ($pK_a \sim 10.3$) hydrolyzes 4-NA in aqueous solution, indicating the inhibitory action of imidazole similar to that for CA.

Crystallographic data for a Zn–phenol–pendant [12]aneN_3 (*226*) revealed its TBP structure with extremely short equatorial phenolate–Zn^{2+} bond distance; a water molecule is present at the apical position (*227*). It was observed that the deprotonation of phenol was promoted by coordination {pK_a shifting from 9.2 (without zinc) to 6.8 with zinc} and this has a direct bearing on the acidity of the CA–phenol complex.

Some model Zn^{2+} complexes of the ethanol–pendant [12]aneN_3 *(34i)* and ethanol–pendant cyclen (*228*) were reported. The former formed a dimeric alkoxide complex, while the latter ($pK_a \sim 7.6$) yielded a mononuclear hydroxide species. Some model Zn^{2+} complexes of carboxymethyl and carboxyethyl– and carboxypropyl–pendant cyclen were prepared. All these zinc complexes exist in equilibrium between the CO_2-bound and CO_2-unbound forms in acidic aqueous solution. Herr *et al.* (*229*) synthesized some zinc(II) complexes with tripodal peptide ligands with histidine side chains to mimic the zinc(II)-coordination sphere of CA.

XI. Concluding Remarks

Carbonate has proved to be a versatile ligand. Its coordination mode expands from 1 to 6, the last one is visualized when each O atom binds two metal ions simultaneously. In recent years, significant progress has been made in the synthesis, structure, and magnetic properties of polynuclear carbonato complexes of transition metal ions. Such studies have also been extended to lanthanides and actinides. The speciation studies of these metal ions in aquatic environments in the presence of carbonate have resulted in significant

and useful data applicable to take care of environmental pollution problems. The use of heteropoly anions to trap CO_2, and convert it to metal carbonates and related products is of recent origin. This broadens the carbonate chemistry. Research on the novel polynuclear carbonato complexes with reference to structure, magnetism, the kinetics and mechanism of formation and CO_2 fixation, appears to be of renewed interest. It is beyond doubt that some model carbonato complexes in the past have been very useful to understand the mechanism of action of carbonic anhydrase (CA). However, it is far from true that research in this respect has reached its final goals.

The structures of different CAs are well characterized, but precatalytic association of CO_2 in the hydrophobic pocket is not clear. Substitution of the metal ion at the active site of the native CAs reduces catalytic activity significantly; but "what distinguishes active from inactive metals" is still unanswered. Although both four- and five-coordination geometries at the metal center of the native α-class CA are reported, the catalytic mechanism is centered on four-coordinate tetrahedral zinc-bound hydroxide/water and hydrophobic pocket around the reaction site. This is the area of future studies for the CAs to elucidate the catalytic mechanism. For γ-CA, CO_2 binds adjacent to the zinc bound hydroxyl, the position of which is unknown. Many active site residues (Glu-62, Glu-84, and Asn-202) are poorly conserved between Cam and homologues, but none of these homologous proteins have yet been shown to exhibit carbonic anhydrase activity. It is not clearly demonstrated how well these residues (Arg-59, Asp-61, and Gln-75) are conserved near the active site in Cam and in homologues and influence the catalytic mechanism. The residues that potentially function in proton transport have been identified, but the residues with potential to function in CO_2 hydration have not yet been classified. A number of biological questions remain unanswered. Future studies on different mutants will have to be launched for better understanding of the structural differences in different isoenzymes and their correlations with catalytic activity. The search for new forms of the isoenzyme may continue.

XII. Abbreviations

bapa	bis(3-aminopropyl)amine
bapma	bis(3-aminopropyl)methylamine
bipy	bipyridine
Cam	*Methanosarcina thermophila*

CA RP	Carbonic anhydrase related proteins
CR	Me_2pyO[14]triene N_4
cyclen	tetraazacyclododecane
dien	diethylenetriamine
dmpd	2,2-dimethylpropane-1,3 diamine
dpt	bis(3-amino propyl)amine
edda	ethylenediamin,*N*,*N*′-diacetate
EXAFS	extended X-ray absorption fine structure
gly	glycinate
HCA	Human carbonic anhydrase
medpt	bis(3-aminopropyl)methylamine
4-meim	4-methyl imidazole
4-NA	4-nitrophenyl acetate
nta	nitrilotriacetate
phen	1,10-orthophenanthroline
pip	2-(2-(2-pyridyl)ethyliminoethyl)pyridine
py	pyridine
RuBisCO	ribulose biphosphate carboxylase/oxygenase
SHA svp	Schäffer Horn Aldrich split valence polarization constant
TBP	trigonal bipyramid
tet-b	5,7,7,12,14,14-hexamethyl-1,4,8,11-tetraazacyclotetradecane (b-isomer)
tetren	tetraethylenepentamine (1,11-diamino-3,6,9-triaza undecane)
tepa	tris 2-(2-pyridylethyl)amine
tn	1,3-diamino propane
TP	tetragonal pyramid
tmpa	tris(2-pyridyl)methylamine
TpyMA	tris-(3,5-dimethyl-1-pyrazolylmethyl)amine
tren	tris-(2 amino ethylamine)
trien	triethylene tetramine (1,8-diamino, 3,6-diaza octane)
[15]ane N_3 O_2	1,4-dioxa-7,10,13-tetraazacyclopentadecane
[12]aneN_3	1,5,9-triazacyclododecane
[12]ane N_4	1,4,7,10-tetraazacyclododecane

References

1. Piriz Maccoll, C. R. *Coord. Chem. Rev.* **1969**, *4*, 147.
2. Krishnamurthy, K. V.; Harris, G. M.; Sastri, V. S. *Chem. Rev.* **1970**, *70*, 171.
3. Palmer, D. A.; van Eldik, R. *Chem. Rev.* **1983**, *83*, 651.
4. Gibson, D. H. *Chem. Rev.* **1996**, *96*, 2063.

5. Souter, P. F.; Andrews, L. *J. Am. Chem. Soc.* **1997**, *119*, 7350.

6. (a) Halman, M. M. "*Chemical Fixation of Carbon Dioxide*"; CRC Press: Boca Raton, FL, 1993; (b) "*Catalytic Activation of Carbon Dioxide*"; Ed. Ayers, W. M.; ACS Symposium Series 363; American Chemical Society: Washington DC, 1988; (c) "*Carbon Dioxide as a Source of Carbon*"; Eds. Aresta, M.; Forti, G.; D. Reidel: Dordrecht, 1987; (d) "*Organic and Bio-organic Chemistry of Carbon Dioxide*"; Eds. Inoue, S.; Yamazaki, N.; John Wiley: New York, 1982; (e) Darensbourg, D. J.; Holtcamp, M. W. *Coord. Chem. Rev.* **1996**, *153*, 155; (f) Leitner, W. *Coord. Chem. Rev.* **1996**, *155*, 247; (g) Gibson, D. H. *Chem. Rev.* **1996**, *96*, 2063; (h) Jessop, P. G.; Ikariya, T.; Noyori, R. *Chem. Rev.* **1995**, *95*, 259; (i) Leitner, W. *Angew. Chem. Int. Ed. Engl.* **1995**, *34*, 2207; (j) Aresta, M.; Quaranta, E.; Tommasi, I. *New. J. Chem.* **1994**, *18*, 133; (k) Willner, I.; Willner, B. *Top. Curr. Chem.* **1991**, *159*, 157; (l) Collin, J. P.; Sauvage, J. P. *Coord. Chem. Rev.* **1989**, *93*, 245; (m) Braunstein, P.; Matt, D.; Nobel, D. *Chem. Rev.* **1988**, *88*, 747; (n) Behr, A. *Angew. Chem., Int. Ed. Engl.* **1988**, *27*, 661; (o) Walther, D. *Coord. Chem. Rev.* **1987**, *79*, 135; (p) Darensbourgh, D. J.; Kudaroski, R. A. *Adv. Organomet. Chem.* **1983**, *22*, 129; (q) Sneeden, R. P. A. "*Comprehensive Organometallic Chemistry*"; Eds. Wilkinson, G.; Stone, F. G. A.; Abel, E. W.; Pergamon Press: New York, 1982, Chapter 50.4; (r) Eisenberg, R.; Hendriksen, D. E. *Adv. Catal.* **1979**, *28*, 79.

7. (a) Evans, W. J.; Seibel, C. A.; Ziller, J. W. *Inorg. Chem.* **1998**, *37*, 770; (b) Min, D.; Lee, S. W. *Inorg. Chem. Commun.* **2002**, *5*, 978; (c) Paul, P.; Tyagi, B.; Bilakhiya, A. K.; Bhadbhade, M. M.; Erugathodi, S.; Ramachandraiah, G. *Inorg. Chem.* **1998**, *37*, 5733; (d) Hutschka, F.; Dedieu, A.; Eichberger, M.; Furnika, R.; Leitner, W. *J. Am. Chem. Soc.* **1997**, *119*, 4437; (e) Gennaro, A.; Isse, A. A.; Saveant, J. M.; Severin, M.-G.; Vianello, E. *J. Am. Chem. Soc.* **1996**, *118*, 7190; (f) Bhugun, I.; Lexa, D.; Saveant, J.-M. *J. Am. Chem. Soc.* **1996**, *118*, 1769; (g) Gassner, F.; Dinjus, E.; Gorls, H.; Leitner, W. *Organometallics* **1996**, *15*, 2078; (h) Nagao, H.; Mizukawa, T.; Tanaka, K. *Inorg. Chem.* **1994**, *33*, 3415; (i) Tsai, J. C.; Nicholas, K. M. *J. Am. Chem. Soc.* **1992**, *114*, 5117; (j) Hori, Y.; Murata, A.; Takahashi, R.; Suzuki, S. *J. Chem. Soc. Chem. Commun.* **1988,** *17*; (k) Grant, J. I.; Goswami, K.; Spreer, I. O.; Otvos, J. W.; Calvin, M. *J. Chem. Soc. Dalton Trans.* **1987**, 1377; (l) Ogura, K.; Uchida, H. *J. Chem. Soc., Dalton Trans.* **1987**, 1377.

8. (a) Bhugun, I.; Lexa, D.; Saveant, J.-M. *J. Phys. Chem.* **1996**, *100*, 19981; (b) Gennaro, A.; Isse, A. A.; Severin, M.-G.; Vianello, E.; Bhugun, I.; Saveant, J.-M. *J. Chem. Soc. Faraday Trans.* **1996**, *92*, 3963; (c) Kushi, Y.; Nagao, H.; Nishioka, T.; Isobe, K.; Tanaka, K. *J. Chem. Soc. Chem. Commun.* **1995**, 1223; (d) Kumeda, N.; Nagao, H.; Matsui, T.; Adachi, G.; Tanaka, K. *J. Am. Chem. Soc.* **1992**, *114*, 3625; (e) Hammaouche, M.; Lexa, D.; Momenteau, M.; Saveant, J.-M. *J. Am. Chem. Soc.* **1991**, *113*, 8455.

9. (a) Field, L. D.; Lawrenz, E. T.; Shaw, W. J.; Turner, P. *Inorg. Chem.* **2000**, *39*, 5632; (b) Kushi, Y.; Nagao, H.; Nishioka, T.; Isobe, K.; Tanaka, K. *Chem. Lett.* **1994**, 2175; (c) Becker, J. Y.; Vainas, B.; Eger, R.; Kaufman, I. *J. Chem. Soc. Chem. Commun.* **1985**, 1171.

10. (a) Runde, W.; Neu, M. P.; Pelt, C. V.; Scott, B. L. *Inorg. Chem.* **2000**, *39*, 1050; (b) Escuer, A.; Mautner, F. A.; Penalba, E.; Vicente, R. *Inorg. Chem.* **1998**, *37*, 4190; (c) Schosseler, P. M.; Wehrli, B.; Schweiger, A. *Inorg. Chem.* **1997**, *36*, 4490; (d) Schrodt, A.; Neubrand, A.; van Eldik, R. *Inorg. Chem.* **1997**, *36*, 4579; (e) Clark, D. L.; Conradson, S. D.; Keogh, D. W.; Palmer, P. D.; Scott, B. L.; Tait, C. D. *Inorg. Chem.* **1998**, *37*, 2983.

11. Szepankiewicz, S. H.; Ippolito, C. M.; Santro, B. P.; Van de ven, T. J.; Ippolito, G. A.; Fronckowiak, L.; Wiatrowski, F.; Power, T.; Kuzik, M. *Inorg. Chem.* **1998**, *37*, 4344.
12. Dunn, M. F. "*Struct. Bonding*", Vol. 23; Spring-Ver: New York, 1975, p. 61.
13. Coleman, J. E. *Progr. Bioorg. Chem.* **1971**, *1*, 160.
14. Cargill, R. W.; Macphee, D. E. *J. Chem. Res.* **1981**, 232; Takahashi, M.; Kobayashi, Y.; Takeuchi, H. *J. Chem. Engg. Data* **1982**, *27*, 328; Reddy, M. M.; Gaillard, W. D. *J. Colloid Interface Sci.* **1981**, *80*, 171; Ladha, S. S.; Diaz, J. M.; Danckwerts, P. V. *Chem. Eng. Sci.* **1981**, *80*, 171; Annesini, M. C.; Fumasoni, S.; Pochetti, F. *Chim. Ind. (Milan)* **1979**, *61*, 898; Chai, C.-P.; Paulitis, M. E. *J. Chem. Eng. Data* **1981**, *26*, 277.
15. Wilhelmy, E.; Battino, R.; Wilcox, R. *Chem. Rev.* **1977**, *77*, 219.
16. Berg, R. L.; Vanderjee, C. E. *J. Chem. Thermodynamics* **1978**, *10*, 1113.
17. Washburn, K. F.; French, D. M.; Patterson, A. Jr. *J. Phys. Chem.* **1954**, *58*, 693; Berg, D.; Patterson, A. Jr. *J. Am. Chem. Soc.* **1953**, *75*, 5197.
18. Roughton, F. J. W. *J. Am. Chem. Soc.* **1941**, *63*, 2930.
19. Patterson, C. S.; Slocum, G. H.; Busey, R. H.; Mesmer, R. E. *Geochim. Cosmochim. Acta* **1982**, *46*, 1653.
20. Oliver, B. G.; Davies, A. R. *Can. J. Chem.* **1973**, *51*, 698.
21. Kern, D. M. *J. Chem. Ed.* **1960**, *37*, 14.
22. Eigen, M. *Angew. Chem.* **1963**, *75*, 489.
23. van Eldik, R.; Palmer, D. A. *J. Soln. Chem.* **1982**, *11*, 339.
24. Patel, R. C.; Boe, R. J.; Atkinson, G. *J. Soln. Chem.* **1973**, *2*, 357.
25. Poultonm, D. J.; Baldwin, H. W. *Can. J. Chem.* **1967**, *45*, 1045.
26. (a) Paneth, P.; O'Leary, M. H. *J. Am. Chem. Soc.* **1985**, *107*, 7381; (b) Marlier, J. F.; O'Leary, M. H. *J. Am. Chem. Soc.* **1984**, *106*, 5054.
27. Pinsent, B. R. W.; Rouhghton, F. J. W. *Trans. Faraday Soc.* **1951**, *47*, 263.
28. Welch, M. J.; Lifton, J. F.; Seek, J. A. *J. Phys. Chem.* **1969**, *73*, 3351.
29. Dennard, A. E.; Williams, R. J. P. *J. Chem. Soc.* **1966**, 812.
30. Pocker, Y.; Bjorkquist, D. W. *J. Am. Chem. Soc.* **1977**, *99*, 6537.
31. Tu, C. K.; Silverman, D. N. *J. Phys. Chem.* **1975**, *79*, 1647.
32. Gerster, R. H.; Maren, M. H.; Silverman, D. N. *Proc. Int. Conf. Stable Isot. Chem. Biol. Med., 1st* **1973**, 219.
33. (a) Escuer, A.; Vicente, R.; Pealba, E.; Sloan, X.; Font-Bardia, M. *Inorg. Chem.* **1996**, *35*, 248; (b) Escuer, A.; Vicente, R.; Kumar, B. S.; Sloan, X.; Font-Bardia, M.; Canesschi, A. *Inorg. Chem.* **1996**, *35*, 3094; (c) Schossler, P. W.; Wehrli, B.; Schweiger, A. *Inorg. Chem.* **1997**, *36*, 4490; (d) Runde, W.; Neu, P. M.; Pelt, C. V.; Scott, B. L. *Inorg. Chem.* **2000**, *39*, 1051; (e) Escuer, A.; Mautner, F. A.; Penalba, E.; Vicente, R. *Inorg. Chem.* **1998**, *57*, 4190; (f) Clark, D. L.; Conradson, S. D.; Keog, D. W.; Palmer, P. D.; Scott, B. L.; Tait, C. D. *Inorg. Chem.* **1998**, *37*, 2893; (g) Menif, R.; Reibenspies, R.; Martell, A. E. *Inorg. Chem.* **1991**, *30*, 3446.
34. (a) Zhang, X.; van Eldik, R. *Inorg. Chem.* **1995**, *34*, 5606; (b) Hartman, M.; Clark, T.; van Eldik, R. *J. Mol. Model* **1996**, *2*, 358; (c) Hartman, M.; Merz, K. M. Jr.; van Eldik, R.; Clark, T. *J. Mol. Model* **1998**, *4*, 355; (d) Schrodt, A.; Neubrand, A.; van Eldik, R. *Inorg. Chem.* **1997**, *36*, 4579; (e) Herr, U.; Spahl, W.; Steglich, W.; Thaler, F.; van Eldik, R. *Bioorg. Medic. Chem.* **1999**, *7*, 699; (f) Zhang, X.; van Eldik, R.; Koike, T.; Kimura, E. *Inorg. Chem.* **1993**, *32*, 5749; (g) Kimura, E.; Nakamura, I.; Koike, T.; Kodama, Y. *J. Chem. Soc.* **1990**, *112*, 5805; (h) Kimura, E.; Koike, T. *Comments Inorg. Chem.* **1991**, *11*, 285; (i) Kimura, E.; Nakamura, I.; Koike, T.; Shiokoya, M.; Kodama, Y.; Ikeda, T.; Shiro, M. *J. Am. Chem. Soc.* **1994**, *116*, 4764; (j) Mao, Z.-W.; Liehr, G.; van Eldik, R. *J. Chem. Soc. Dalton Trans.* **2001**, 1593; (k) Mao, Z.-W.; Hieneman, F. W.; Liehr, G.; van Eldik, R. *J. Chem. Soc. Dalton Trans.* **2001**, 3652;

(l) Mao, Z.-W.; Liehr, G.; van Eldik, R. *J. Am. Chem. Soc*. **2000**, *122*, 4839; (m) Eras-Hanauer, H.; Mao, Z.-W.; Liehr, G.; Clark, T.; van Eldik, R. *Eur. J. Inorg. Chem*. **2003**, 1562; (n) Lipscomb, W. N.; Strater, N. *Chem. Rev*. **1996**, *96*, 2375.

35. Fuger, K. Jr. *Radiochim. Acta*. **1992**, *59*, 813; Kim, J. I. *Mater. Res. Soc. Sympo. Proc*. **1993**, *294*, 3.

36. Runde, W.; Meinrath, G.; Kim, J. I. *Radiochim. Acta* **1992**, *58*/*59*, 93; Vitorage, P. *Radiochim. Acta* **1992**, *58*/*59*, 105.

37. Meinrath, G.; Kim, J. I. *Radiochim. Acta* **1991**, *52*/*53*, 29.

38. Rao, L. F.; Rai, D.; Felmy, A. R.; Filtop, R. W.; Novak, C. F. *Radiochim. Acta* **1996**, *75*, 141; Mochizuki, A.; Nagashima, K.; Wakita, H. *Bull. Chem. Soc. Jpn*. **1974**, *47*, 755.

39. Sahin, D. B.; Eick, H. A. *Inorg. Chem*. **1968**, *7*, 1340.

40. Dal Negro, A.; Rossi, G.; Tazzoli, V. *Am. Mineral* **1997**, *62*, 1142.

41. Lessin, A.; Meyer, G. Z. Z. *Anorg. Allgem. Chem*. **1993**, *619*, 2031.

42. Kim, J. I.; Klinze, R.; Weiner, H.; Runde, W.; Hauser, W. *J. Alloys Compd*. **1994**, *217*, 333.

43. Voliotis, P. S.; Rimsky, E. A. *Acta Crystallogr*. **1975**, *B31*, 2615; Marsh, R. E.; Herbstein, F. H. *Acta Crystallogr*. **1988**, *B44*, 77.

44. Mao, Z.-W.; Liehr, G.; van Eldik, R. *J. Am. Chem. Soc*. **2000**, *122*, 4839.

45. (a) Lipscomb, W. N. *Annu. Rev. Biochemistry* **1983**, *52*, 17; (b) Liang, J.-Y.; Lipscomb, W. N. *Biochemistry* **1987**, *26*, 5293; (c) Lindskog, S. ''*Zinc Enzymes*''; Ed. Sapiro, G.; Wiley: New York, 1983, p. 77.

46. (a) Alsfasser, R.; Trofimenko, S.; Looney, A.; Parkin, G.; Vahrenkamp, H. *Inorg. Chem*. **1991**, *30*, 4098; (b) Koike, T.; Kimura, E.; Nakamura, I.; Hashimoto, Y.; Shiro, M. *J. Am. Chem. Soc*. **1992**, *114*, 7338; (c) Looney, A.; Parkin, G. *Inorg. Chem*. **1994**, *33*, 1234.

47. Kimura, E.; Koike, K.; Shinoya, M. *Struct. Bonding* **1997**, *89*, 1.

48. Yoshida, T.; Thorn, D. L.; Okano, T.; Ibers, J. A.; Otsuka, S. *J. Am. Chem. Soc*. **1979**, *101*, 4212.

49. Baxter, K. E.; Hanton, L. R.; Simpson, J.; Vincent, B. R.; Blackman, A. G. *Inorg. Chem*. **1995**, *34*, 2795.

50. Massoud, S. S.; Mautner, F. A.; Abu-Youssef, M. A. M. *Cryst. Res. Technol*. **2000**, *35*, 1229.

51. Buckingham, D. A.; Clark, C. R. *Inorg. Chem*. **1994**, *33*, 6121.

52. Xue, Y.; Vidgren, J.; Svensson, L. A.; Liljas, A.; Jonsson, B. H.; Lindskog, S. *Proteins* **1993**, *15*, 80.

53. Kumar, V.; Kannan, K. K. *J. Mol. Biol*. **1994**, *241*, 220.

54. Bertini, I.; Luchinat, C.; Scozzafava, A. *Struct. Bonding* **1982**, *48*, 45.

55. Bazzicalupi, C.; Bencini, A.; Bianchi, A.; Corana, F.; Fusi, V.; Giorgi, P.; Paoli, P.; Paoletti, P.; Valtancoli, B.; Zanchini, C. *Inorg. Chem*. **1996**, *35*, 5540.

56. Kolks, G.; Lippard, S. J.; Waszczak, J. V. *J. Am. Chem. Soc*. **1980**, *102*, 4832.

57. Chen, X.-M.; Deng, Q.-Y.; Wang, G.; Xu, Y.-J. *Polyhedron* **1994**, *13*, 3085.

58. Kruger, P. E.; Fallon, G. D.; Moubaraki, B.; Berry, K. J.; Murray, K. S. *Inorg. Chem*. **1995**, *33*, 4808.

59. Itoh, T.; Fujii, Y.; Tada, T.; Yoshikawa, Y.; Hisada, H. *Bull. Chem. Soc. Jpn*. **1997**, *36*, 2594.

60. (a) Altomare, A.; Cascarano, G.; Giacovazzo, C.; Guagliardi, A.; Burla, M. C.; Polidori, G.; Camalli, M. SIR-92, A package for solving crystal structures by Direct methods. *J. Appl. Crystallogr*. **1992**, *22*, 389.; (b) Sheldrick, G. M. ''*SHELXL-93, A System for Crystal Structure Refinement*''; University of Gottingen: Germany, 1993.

61. Escuer, A.; Vicente, R.; Kumar, S. B.; Solans, X.; Bardia, M. F. *J. Chem. Soc. Dalton Trans*. **1997**, 403.

62. Escuer, A.; Penalba, E.; Vicente, R.; Solans, X.; Font-Bardia, M. *J. Chem. Soc. Dalton Trans.* **1997**, 2315.
63. Chaffee, E.; Dasgupta, T. P.; Harris, G. M. *J. Am. Chem. Soc.* **1973**, *95*, 4169.
64. Harris, G. M.; Dasgupta, T. P. *J. Indian Chem. Soc.* **1977**, *54*, 62.
65. Zhang, X.; van Eldik, R.; Koike, T.; Kimura, E. *Inorg. Chem.* **1993**, *32*, 5749.
66. Sirs, A. Jr. *Trans Faraday Soc.* **1958**, *54*, 201.
67. Acharya, A. N.; Dash, A. C. *Proc. Indian Acad. Sci. (Chem. Sci.)* **1993**, *105*, 275.
68. Del Bene, J.; Cohen, I. *J. Am. Chem. Soc.* **1978**, *100*, 5285.
69. For extensive review of carbonic anhydrase see: (a) Dodgson, S. J.; Tashman, R. E.; Gros, G.; Carter, N. D. "*The Carbonic Anhydrases*"; Plenum Press: New York, 1991; (b) Christianson, D. W. *Adv. Protein Chem.* **1991**, *41*, 281; (c) Silverman, D. N.; Lindskog, S. *Acc. Chem. Res.* **1988**, *21*, 30; (d) Coleman, J. E. "*Zinc Enzymes*"; Eds. Bertin, I.; Luchinat, C.; Maret, W.; Zeppezsuer, M.; Birkhauser: Boston, 1986, p. 317; (e) Botre, F.; Gros, G.; Screy, B. T. "*Carbonic Anhydrase*"; VCH: Weinheim, Germany, 1991; (f) Bertini, I.; Mangani, S.; Pierartelli, R. "*International Conference on Carbon Dioxide Utilisation; Lectures and Posters*"; University of Bari: Italy, 1993, p. 223; (g) Kumar, V.; Kannan, K. K. *Ind. J. Biochem. Biophys.* **1994**, *31*, 377; (h) Liljas, A.; Laurberg, M. *EMBO Reports* **2000**, *1*, 17; Christianson, D. W.; Fierke, C. A. *Acc. Chem. Res.* **1996**, *29*, 331.
70. (a) Groves, J. T.; Baron, L. A. *J. Am. Chem. Soc.* **1989**, *111*, 5442; (b) Chin, J.; Banaszczyk, M. *J. Am. Chem. Soc.* **1989**, *111*, 2724.
71. (a) Hay, R. W.; Basak, A. K.; Pujari, M. P. *J. Chem. Soc. Dalton Trans.* **1989**, 197; (b) Chin, J.; Jubian, V. *J. Chem. Soc. Chem. Commun.* **1989**, 839.
72. (a) Gellman, S. H.; Petter, R.; Breslow, R. *J. Am. Chem. Soc.* **1986**, *108*, 2388; (b) Iversion, B. L.; Lerner, R. A. *Science* **1989**, *243*, 1185; (c) Koike, T.; Kimura, E. *J. Am. Chem. Soc.* **1991**, *113*, 8935; (d) Kimura, E.; Koike, T. *Comments Inorg. Chem.* **1991**, *11*, 285; (e) Norman, P. R. *Inorg. Chim. Acta* **1987**, *130*, 1; (f) Norman, P. R.; Tate, A.; Rich, P. *Inorg. Chim. Acta* **1988**, *145*, 211; (g) Marcel, L. M. P.; David, N. R. *J. Am. Chem. Soc.* **1980**, *102*, 7571; (h) Brown, R. S.; Salmon, D.; Curtis, N. J.; Kusuma, S. *J. Am. Chem. Soc.* **1982**, *104*, 3188; (i) Slebocks-Tilk, H.; Cocho, J. L.; Prakman, Z.; Brown, R. S. *J. Am. Chem. Soc.* **1984**, *106*, 2421.
73. Margerum, D. W.; Cayley, G. R.; Weatherburn, D. C.; Pagenkopf, G. K. "*Coordination Chemistry*", vol. 2; Eds. Martell, A. E.; ACS monogr. 174, American Chemical Society: Washington, D.C., 1978, p. 9.
74. Dasgupta, T. P.; Harris, G. M. *J. Am. Chem. Soc.* **1977**, *99*, 2490.
75. Wooley, P. *Nature* **1975**, *258*, 677.
76. (a) van Eldik, R.; Asano, T.; leNoble, W. J. *Chem. Rev.* **1989**, *89*, 549; (b) Drljaca, A.; Hubbard, C. D.; van Eldik, R.; Asano, T.; Basilevsky, M. V.; le Noble, W. J. *Chem. Rev.* **1998**, *98*, 2167.
77. Mahal, G.; van Eldik, R. *Inorg. Chem.* **1985**, *24*, 4165.
78. Cloete, E.; Breet, E.; van Eldik, R. *J. Chem. Soc. Dalton Trans.* **1995**, 3591.
79. van Eldik, R.; Harris, G. M. *Inorg. Chem.* **1980**, *19*, 3684.
80. Dash, A. C.; Nanda, R. K. *J. Indian Chem. Soc.* **1975**, *52*, 298.
81. Dash, A. C.; Das, S. *Indian J. Chem. (Sec. A)* **1994**, *33*, 1013.
82. Acharya, A. N.; Dash, A. C. *Int. J. Chem. Kinet.* **1994**, *26*, 681.
83. van Eldik, R.; Spitzer, U.; Kelm, H. *Inorg. Chim Acta* **1983**, *74*, 149.
84. Dasgupta, T. P.; Harris, G. M. *Inorg. Chem.* **1978**, *17*, 3304.
85. van Eldik, R. *Coord. Chem. Revs.* **1999**, *182*, 373.
86. (a) Erikson, J.; Mønsted, L.; Mønsted, O. *Acta Chem. Scand.* **1992**, *46*, 521; (b) Hay, R. W.; Basak, A. K. *Inorg. Chim. Acta* **1983**, *73*, 179.

87. Dash, A. C.; Dash, N.; Das, P. K.; Pradhan, J. *J. Chem. Soc. Faraday Trans.* **1991**, *87*, 3753.
88. van Eldik, R.; Harris, G. M. *Inorg. Chim. Acta* **1983**, *70*, 147.
89. Buckingham, D. A.; Clark, C. R. *Inorg. Chem.* **1994**, *33*, 6171.
90. Pederson, K. J. *J. Am. Chem. Soc.* **1931**, *53*, 181.
91. Francis, D. J.; Searle, G. H. *Aust. J. Chem.* **1974**, *27*, 269.
92. Coddington, P. M.; Hyde, K. E. *Inorg. Chem.* **1983**, *22*, 2211.
93. Posey, F. A.; Taube, H. *J. Am. Chem. Soc.* **1953**, *75*, 4099.
94. Francis, D. J.; Jordan, R. B. *Inorg. Chem.* **1972**, *11*, 461.
95. Hunt, J. P.; Rutenburg, A. C.; Taube, H. *J. Am. Chem. Soc.* **1952**, *74*, 268.
96. Bunton, C. A.; Llewellyn, D. R. *J. Chem. Soc.* **1953**, 1692.
97. Meldrum, N. U.; Roughten, F. J. W. *J. Physiol. (London)* **1934**, *80*, 113.
98. Keilin, D.; Mann, T. *Biochem. J.* **1940**, *34*, 1163.
99. Keilin, D.; Mann, T. *Nature* **1944**, *153*, 107.
100. Lindskog, S. *Pharmacol. Ther.* **1997**, *74*, 1.
101. Briganti, F.; Mangani, S.; Scozzafava, A.; Vernaglione, G.; Supuran, C. T. *J. Biol. Inorg. Chem.* **1999**, *4*, 528.
102. Guerri, A.; Briganti, F.; Scozzafava, A.; Supuran, C. T.; Mangani, S. *Biochemistry* **2000**, *39*, 12391.
103. (a) Hewett-Emmett, D.; Tashian, R. E. *Mol. Phylogenet. Evol.* **1996**, *5*, 50; (b) Soltes-Rak, E.; Mulligan, M. E.; Coleman, J. R. *J. Bacteriol.* **1997**, *179*, 769.
104. Supuran, C. T. ''*Carbonic Anhydrase and Modulation of Physiologic and Pathologic Processes in the Organism*''; Ed. Puscas, I.; Helicon, Timisoara, Romania, 1994, pp. 29–111.
105. Scozzafava, A.; Menabuoni, L.; Mincione, F.; Briganti, F.; Mincione, G.; Supuran, C. T. *J. Med. Chem.* **1999**, *42*, 2641.
106. Alber, B. E.; Ferry, J. G. *Proc. Natl. Acad. Sci. USA* **1994**, *91*, 6909.
107. Sly, W. S.; Hu, P. Y. *Annu. Rev. Biochem.* **1995**, *64*, 375.
108. Recacha, R.; Costanzo, M. J.; Maryanoff, B. E.; Chattopadhyay, D. *Biochem. J.* **2002**, *361*, 437.
109. Quigley, H. A. *N. Engl. J. Med.* **1993**, *328*, 1097.
110. Tielsch, J. M.; Katz, J.; Sommer, A.; Quigley, H. A.; Javitt, J. C. *Arch. Opththamol.* **1994**, *112*, 69.
111. (a) Forsman, C.; Behraven, G.; Osterman, A.; Jonsson, B.-H. *Acta. Chem. Scand.* **1988**, *B42*, 314; (b) Eriksson, E. A.; Jones, T. A.; Liljas, A. *Proteins* **1988**, *4*, 274.
112. Liljas, A.; Kannan, K. K.; Bergsten, P.-C.; Warra, I.; Fridborg, K.; Strandberg, B.; Carlbom, U.; Jarup, L.; Lovgren, S.; Petef, M. *Nature (London) New Biol.* **1972**, *235*, 131.
113. (a) Håkansson, K.; Carlsson, M.; Svensson, L. A.; Liljas, A. *J. Mol. Biol.* **1992**, *227*, 1192; (b) Håkansson, K.; Wehnert, A. *J. Mol. Biol.* **1992**, *228*, 1212.
114. Keifer, L. L.; Fierke, C. A. *Biochemistry* **1994**, *33*, 15233.
115. Lu, D.; Voth, G. A. *Proteins: Structure, Function, and Genetics* **1998**, *33*, 119.
116. Christianson, D. W.; Alexander, R. S. *J. Am. Chem. Soc.* **1989**, *111*, 6412.
117. Keifer, L. L.; Paterno, S. A.; Fierke, C. A. *J. Am. Chem. Soc.* **1995**, *117*, 6831.
118. Lesburg, C. A.; Christianson, D. W. *J. Am. Chem. Soc.* **1995**, *117*, 6838.
119. Huang, C.-C.; Lesburg, C. A.; Kiefer, L. L.; Fierke, C. A.; Christianson, D. W. *Biochemistry* **1996**, *35*, 3439.
120. Krebs, J. F.; Fierke, C. A.; Alexander, R. S.; Christianson, D. W. *Biochemistry* **1991**, *30*, 9153.

121. Cox, J. D.; Hunt, J. A.; Compher, K. M.; Fierke, C. A.; Christianson, D. W. *Biochemistry* **2000**, *39*, 13687.
122. Hunt, J. A.; Fierke, C. A. *J. Biol. Chem.* **1997**, *272*, 20364.
123. Yamashita, M. M.; Wesson, L.; Eisenman, G.; Eisenberg, D. *Proc. Natl. Acad. Sci. USA* **1990**, *87*, 5648.
124. Eriksson, A. E.; Jones, A. T.; Liljas, A. *Proteins* **1983**, *4*, 274.
125. Eriksson, A. E., *et al. Proteins* **1983**, *4*, 289.
126. Kannan, K. K.; Petef, M.; Fridborg, K.; Lövgren, S.; Ohlsson, A. *Proc. Natl. Acad. Sci. USA* **1975**, *72*, 51.
127. Kannan, K. K.; Petef, M.; Fridborg, K.; Cid-Dresdner, H.; Lövgren, S. *FEBS Lett.* **1977**, *73*, 115.
128. (a) Nair, S. K.; Calderone, T. L.; Christianso, D. W.; Fierke, C. A. *J. Biol. Chem.* **1991**, *266*, 17320; (b) Fierke, C. A.; Calderone, T. L.; Krebs, J. F. *Biochemistry* **1991**, *30*, 11054.
129. Bertini, I.; Canti, G.; Luchinat, C.; Borghi, E. *J. Inorg. Biochem.* **1983**, *18*, 221.
130. Bertini, I.; Luchinat, C. M.; Monnanni, R.; Rodens, S.; Moratal, J. M. *J. Am. Chem. Soc.* **1987**, *109*, 7855.
131. Pocker, Y.; Janjic, N. *J. Am. Chem. Soc.* **1989**, *111*, 731.
132. Bertini, I.; Luchinat, C. *Acc. Chem. Res.* **1983**, *16*, 272.
133. Haffner, P. H.; Coleman, J. E. *J. Biol. Chem.* **1973**, *248*, 6630.
134. Jackman, J. E.; Merz, K. M. Jr.; Fierke, C. A. *Biochemistry* **1996**, *35*, 16421.
135. Nair, S. K.; Christianson, D. W. *J. Am. Chem. Soc.* **1991**, *113*, 9455.
136. Duda, D.; Tu, C.; Qian, M.; Laipis, P.; Agbandje-McKenna, M.; Silverman, D. N.; McKenna, R. *Biochemistry* **2001**, *40*, 1741.
137. Bertini, I.; Luchinat, C. "*Biological and Inorganic Chemistry*", Vol. 1; Eds. Karlin, K. D.; Zubieta, J.; Academic Press, 1986.
138. Bertini, I.; Borghi, E.; Luchinat, C. *J. Am. Chem. Soc.* **1979**, *102*, 7069.
139. Led, J. J.; Neesgard, E. *Biochemistry* **1987**, *26*, 183.
140. Evelhoch, J. L.; Bocian, D. F.; Sudmeier, J. L. *Biochemistry* **1981**, *20*, 4951.
141. Keifer, L. L.; Ippolito, J. A.; Fierke, C. A.; Christainson, D. W. *J. Am. Chem. Soc.* **1993**, *115*, 12 581.
142. Lindskog, S.; Engberg, P.; Forsman, C.; Ibrahim, S. A.; Jonsson, B.-H.; Simonsson, I.; Tibell, L. "*Annals New York Academy of Science*", Vol. 429; Eds. Tashian, R. E.; Hewett-Emmett, D.; The New York Academy of Science: New York, 1984, p. 61.
143. Lindskog, S. "*Advances in Inorganic Biochemistry*", Vol. 4; Eds. Eichhorn, G. L.; Marzilli, L. G.; Elsevier Biomedical: New York, 1982, p. 115.
144. Lindskog, S.; Coleman, J. E. *Proc. Natl. Acad. Sci.* **1973**, *70*, 2505.
145. Bertini, I.; Canti, G.; Luchinat, C.; Scozzafava, A. *Biochem. Biophys. Res. Commun.* **1977**, *78*, 158.
146. Koneig, S. H.; Brown, R. D.; Jacob, G. S. "*Biophysics and Physiology of Carbon Dioxide*"; Eds. Bauer, C.; Gros, G.; Bartels, H.; Springer: Berlin, 1980, p. 238.
147. Lindskog, S.; Ibrahim, S. A.; Jonsson, B.-H.; Simonsson, I. "*The Coordination Chemistry of Metalloenzymes*"; Eds. Bertini, I.; Drago, R. S.; Luchinat, C.; D. Reidel: Dordrecht, 1983, p. 49.
148. Tu, C. K.; Sanyal, G.; Wynns, G. C.; Silverman, D. N. *J. Biol. Chem.* **1983**, *258*, 8867.
149. Khalifah, R. G. *J. Biol. Chem.* **1971**, *246*, 2561.
150. Steiner, H.; Jonsson, B.-H.; Lindskog, S. *Eur. J. Biochem.* **1975**, *59*, 253.
151. Sanyal, G.; Swenson, E. R.; Pessah, N. I.; Maren, T. H. *Mol. Pharmacol.* **1982**, *22*, 211.
152. Eigen, M.; Hammes, G. G. *Adv. Enzymol.* **1963**, *25*, 1.
153. Khalifah, R. G. *Proc. Natl. Acad. Sci. USA* **1973**, *70*, 1986.

154. Prince, R. H.; Wooley, P. R. *Bioorg. Chem.* **1973**, *2*, 337.
155. Rowlett, R. S.; Silverman, D. N. *J. Am. Chem. Soc.* **1982**, *104*, 6737.
156. Lindskog, S. *J. Mol. Catalysis* **1984**, *23*, 357.
157. (a) Koenig, S. H.; Brown, R. D.; Needham, T. E.; Matwiyoff, N. A. *Biochem. Biophys. Res. Commun.* **1973**, *53*, 624; (b) Koenig, S. H.; Brown, R. D.; London, R. E.; Needham, T. E.; Matwiyoff, N. A. *Pure Appl. Chem. Commun.* **1974**, *40*, 103; (c) Simonsson, I. B.-H.; Honsson, B.-H.; Lindskog, S. *Eur. J. Biochem.* **1982**, *129*, 165.
158. Venkatsubban, K. S.; Silverman, D. N. *Biochemistry* **1980**, *19*, 4984.
159. Pullman, A. *Ann. N. Y. Acad. Sci.* **1981**, *367*, 340, and references therein.
160. Tu, C. K.; Wynns, G. C.; Silverman, D. N. *J. Biol. Chem.* **1981**, *256*, 9466.
161. Silverman, D. N.; Tu, C. K. *Inorg. Chim. Acta* **1983**, *79*, 38.
162. Campbell, I. D.; Lindskog, S.; White, A. I. *J. Mol. Biol.* **1974**, *90*, 469.
163. Liang, J.-Y.; Lipscomb, W. N. *Proc. Natl. Acad. Sci. USA* **1990**, *87*, 3675.
164. Merz, K. M. *J. Mol. Biol.* **1990**, *214*, 799.
165. "*Enzymatic and Model Carboxylation and Reduction Reactions for Carbon Dioxide Utilization*"; Eds. Aresta, M.; Schloss, J. V.; Kluwer, 1990.
166. Coleman, J. E. *Ann. N. Y. Acad. Sci.* **1984**, *429*, 26.
167. Tu, C.; Tripp, B. C.; Ferry, J. G.; Silverman, D. N. *J. Am. Chem. Soc.* **2001**, *123*, 5861.
168. Liang, J.-Y.; Lipscomb, W. N. *Int. J. Quantum Chem.* **1989**, *36*, 299.
169. Bertini, I.; Canti, G.; Luchinat, C.; Scozzafava, A. *J. Am. Chem. Soc.* **1978**, *100*, 4873.
170. (a) Pocker, Y.; Deits, T. L. "*Annals New York Academy of Science*", Vol. 429; Eds. Tashian, R. E.; Hewett-Emmett, D.; The New York Academy of Science: New York, 1984, p. 76; (b) Pocker, Y.; Deits, T. L. *J. Am. Chem. Soc.* **1982**, *104*, 2424.
171. Koenig, S. H.; Brown, R. D. III. "*Annals New York Academy of Science*", Vol. 429; Eds. Tashian, R. E.; Hewett-Emmett, D.; The New York Academy of Science: New York, 1984, p. 99.
172. Zhang, X.; Hubbard, C. D.; van Eldik, R. *J. Phys. Chem.* **1996**, *100*, 9161.
173. Eriksen, J.; Mønsted, L.; Mønsted, O. *Acta. Chem. Scand.* **1992**, *46*, 52.
174. Sola, M.; Leidos, A.; Duran, M.; Bertran, J. *J. Am. Chem. Soc.* **1992**, *114*, 869 and references therein.
175. (a) Jabusch, J. R.; Bray, R. P.; Deutsch, H. F. *J. Biol. Chem.* **1980**, *255*, 9196; (b) Forsman, C.; Jonsson, B.-H.; Lindskog, S. *Biochim. Biophys. Acta* **1983**, *748*, 300.
176. Supuran, C. T.; Scozzafava, A. *Expert Opin. Ther. Pat.* **2000**, *10*, 575.
177. Supuran, C. T.; Scozzafava, A. *Curr. Med. Chem. Immunol. Endoc. Metab. Agents* **2001**, *1*, 61.
178. "*The Carbonic Anhydrases-New Horizons*"; Eds. Chegwidden, W. R.; Edwards, Y.; Carter, N.; Birkhauser Verlag: Besel, Switzerland, 2000 (and references therein).
179. Masereel, B.; Rolin, S.; Abbate, F.; Scozzafava, A.; Supuran, C. T. *J. Med. Chem.* **2002**, *45*, 312.
180. Scarrow, A. M.; Segal, R.; Medsger, T. A.; Wasko, M. C. *Neurosurgery* **1998**, *43*, 1470.
181. Reiss, W. G.; Oles, K. S. *Ann. Pharmacother.* **1996**, *30*, 514.
182. Batlistini, S.; Stenirri, S.; Piatti, M.; Gelfi, C.; Righetti, P. G.; Rocchi, R. *Neurology* **1999**, *13*, 38.
183. Cowen, M. A.; Green, M.; Bertollo, D. N.; Abbott, K. *J. Clin. Psychopharmacol.* **1997**, *17*, 190.
184. Griggs, R. C.; Moxley, R. T.; Riggs, J. E.; Engel, W. K. *Ann. Neurol.* **1978**, *3*, 531.
185. Links, T. P.; Smit, A. J.; Molenaar, W. M.; Zwarts, M. J.; Oosterhuis, H. J. *J. Neuro. Sci.* **1994**, *122*, 33.
186. Uitti, R. J. *Geriatrics* **1998**, *53*, 46.

187. Bernhard, W. N.; Schalik, L. M.; Delaney, P. A.; Bernhard, T. M.; Barnas, G. M. *Aviat. Space Environ. Med.* **1989**, *69*, 883.
188. Bradwell, A. R.; Wright, A. D.; Winterborn, M.; Imray, C. *Int. J. Sports Med.* **1992**, *13*(1), 63.
189. (a) Hartman, G. D.; Halczenko, W.; Smith, R. L.; Sugrue, M. F.; Mallorga, P. J.; Michelson, S. R.; Randall, W. C.; Schwam, H.; Sondey, J. M. *J. Med. Chem.* **1992**, *35*, 3822; (b) Scozzafava, A.; Briganti, F.; Mincione, G.; Menabuni, L.; Mincione, F.; Supuran, C. T. *J. Med. Chem.* **1999**, *42*, 3690; (c) Svedhem, S.; Enander, K.; Karlsson, M.; Sjobom, H.; Liedberg, B.; Lofas, S.; Martensson, L.-G.; Sjostrand, S. E.; Svensson, S.; Carlsson, U.; Lundstrom, I. *Anal. Biochem.* **2001**, *296*, 188; (d) Kim, C.-Y.; Chandra, P. P.; Jain, A.; Christianson, D. W. *J. Am. Chem. Soc.* **2001**, *123*, 9620; (e) Vidgren, J.; Svensson, A.; Liljas, A. *Int. J. Biol. Macromol.* **1993**, *15*, 97.
190. Liljas, A.; Hånkansson, K.; Jonsson, B. H.; Xue, Y. *Eur. J. Biochem.* **1994**, *229*, 1 and references therein.
191. (a) Bertini, I.; Luchinat, C.; Scozzafava, A. *Bioinorg. Chem.* **1978**, *9*, 93; (b) Peng, Z.; Merz, K. M.; Banci, L. *Proteins: Structure, Function, and Genetics* **1993**, *17*, 203; (c) Bertini, I.; Luchinat, C.; Scozzafava, A. *Struct. Bonding* **1982**, *48*, 45.
192. (a) Bertini, I.; Luchinat, C. *Acc. Chem. Res.* **1983**, *16*, 272; (b) Garmer, D. R.; Krauss, M. *J. Am. Chem. Soc.* **1992**, *114*, 6487; (c) J. D.; Hunt, J. A.; Compher, K. M.; Fierke, C. A.; Christianson, D. W. *Biochemistry* **2000**, *39*, 13687.; (d) Hunt, J. A.; Ahmed, M.; Fierke, C. A. *Biochemistry* **1999**, *38*, 9054.
193. (a) Nair, S. K.; Ludig, P. A.; Christianson, D. W. *J. Am. Chem. Soc.* **1994**, *116*, 3659; (b) Tibell, L.; Forsman, C.; Simonsson, I.; Lindskog, S. *Biochim. Biophys. Acta* **1985**, *829*, 202; (c) Rogers, J. I.; Mukherjee, J.; Khalifah, R. G. *Biochemistry* **1987**, *26*, 5672.
194. (a) Tibell, I.; Forsman, C.; Simonsson, I.; Lindskog, S. *Biochim. Biophys. Acta* **1985**, *829*, 202; (b) Mangani, S.; Liljas, A. *J. Mol. Biol.* **1993**, *232*, 9; (c) Khalifah, R. G.; Zhang, F.; Parr, J. S.; Rowe, E. S. *Biochemistry* **1993**, *32*, 3058.
195. Narumi, S.; Miyamoto, E. *Biochim. Biophys. Acta* **1974**, *350*, 215.
196. Igbo, I. N. A.; Reigel, C. E. Jr.; Greene, I. M.; Kenny, A. D. *Pharmacology* **1994**, *49*, 112.
197. Shelton, J. B.; Chegwidden, W. R. *Biochem. Soc. Trans.* **1988**, *16*, 853.
198. Rowlett, R. S.; Gargiulo, N. J. III; Santoli, F. A.; Jackson, J. M.; Corbett, A. H. *J. Biol. Chem.* **1991**, *266*, 933.
199. Briganti, F.; Mangani, S.; Orioli, P.; Scozzafava, A.; Vernaglione, G.; Supuran, C. T. *Biochemistry* **1997**, *36*, 10384.
200. (a) Supuran, C. T. *Rev. Roum. Chim.* **1992**, *37*, 411; (b) Supuran, C. T.; Barboiu, M.; Luca, C.; Pop, E.; Brewster, M. E.; Dinculescu, A. *Eur. J. Med. Chem.* **1996**, *31*, 597.
201. Supuran, C. T.; Claramunt, R. M.; Lavandera, J. L.; Elguero. *J. Biol. Pharam. Bull. Japan* **1996**, *19*, 1417.
202. Supuran, C. T.; Balaban, A. T. *Rev. Roum. Chim.* **1994**, *39*, 107.
203. (a) Puscas, I.; Supuran, C. T.; Manole, G. *Rev. Roum. Chim.* **1990**, *35*, 683; (b) Puscas, I.; Supuran, C. T.; Coltau, M.; Chis, F.; Puscas, I. C. *Rev. Roum. Biochim.* **1994**, *31*, 171.
204. Supuran, C. T.; Puscas, I. "*Carbonic Anhydrase and Modulation of Physiologic and Pathologic Processes in the Organism*"; Ed. Puscas, I.; Helicon: Timisoara, 1994, p. 119.
205. (a) Supuran, C. T. *Rev. Roum. Chim.* **1992**, *37*, 411; (b) Supuran, C. T.; Barboiu, M.; Luca, C.; Pop, E.; Brewster, M. E.; Dinculescu, A. *Eur. J. Med. Chem.* **1996**, *31*, 597.
206. Clare, B. W.; Supuran, C. T. *J. Pharm. Sci.* **1994**, *83*, 768.
207. Scozzafava, A.; Supuran, C. T. *J. Med. Chem.* **2002**, *45*, 284.

208. Kimber, M. S.; Pai, E. F. *EMBO J.* **2000**, *19*, 1407.
209. Badger, M. R.; Price, G. D. *Annu. Rev. Plant Physiol. Plant Mol. Biol.* **1994**, *45*, 369.
210. Jebanathirajah, J. A.; Coleman, J. R. *Planta* **1998**, *204*, 177.
211. (a) Mitsuhashi, S.; Miyachi, S. *J. Biol. Chem.* **1996**, *271*, 28703; (b) Mitsuhashi, S.; Mizushima, T.; Yamashita, E.; Yamamoto, M.; Kumasaka, T.; Moriyama, H.; Ueki, T.; Miyachi, S.; Tsukihara, T. *J. Biol. Chem.* **2000**, *275*, 5521.
212. Johansson, I. M.; Forsman, C. *Eur. J. Biochem.* **1993**, *218*, 439.
213. Bracey, M. H.; Christiansen, J.; Tovar, P.; Cramer, S. P.; Barlett, S. G. *Biochemistry* **1996**, *33*, 13126.
214. Smith, K. S.; Ferry, J. G. *J. Bacteriol.* **1999**, *181*, 6247.
215. Rowlett, R. S.; Chance, M. R.; Wirt, M. D.; Sidelinger, D. E.; Royal, J. R.; Woodroffe, M.; Wang, Y. F.; Saha, R. P.; Lam, M. G. *Biochemistry* **1994**, *33*, 13967.
216. Smith, K. S.; Jakubzick, C.; Whittam, T. S.; Ferry, J. G. *Proc. Natl. Acad. Sci. USA* **1999**, *96*, 15184.
217. Jiang, W.; Gupta, D. *Biochem. J.* **1999**, *344*, 385.
218. Kisker, C.; Schindelin, H.; Alber, B. E.; Ferry, J. G.; Rees, D. *EMBO J.* **1996**, *15*, 2323.
219. Iverson, T. M.; Alber, B. E.; Kisker, C.; Ferry, J. G.; Rees, D. C. *Biochemistry* **2000**, *39*, 9222.
220. (a) Alber, B. E.; Colangelo, C. M.; Dong, J.; Stålhandske, C. M. V.; Baird, T. T.; Tu, C.; Fierke, C. A.; Silverman, D. N.; Scott, R. A.; Ferry, J. G. *Biochemistry* **1999**, *38*, 13119; (b) Tripp, B. C.; Tu, C.; Ferry, J. G. *Biochemistry* **2002**, *41*, 669.
221. Roberts, S. B.; Lane, T. W.; Morel, F. M. M. *J. Phycol.* **1997**, *33*, 845.
222. Cox, E. H.; McLendon, G. L.; Morel, F. M. M.; Lane, T. W.; Prince, R. C.; Pickering, I. J.; George, G. N. *Biochemistry* **2000**, *39*, 12128.
223. Tripp, B. C.; Smith, K.; Ferry, J. G. *J. Biol. Chem.* **2001**, *276*, 48625.
224. Bertini, I.; Canti, G.; Luchinat, C.; Mani, F. *Inorg. Chem.* **1981**, *20*, 1670.
225. Kimura, E. *Acc. Chem. Res.* **2001**, *34*, 171.
226. Kimura, E.; Yamaoke, M.; Morioka, M.; Koike, T. *Inorg. Chem.* **1986**, *25*, 3883.
227. Kimura, E.; Koike, T.; Torium, K. *Inorg. Chem.* **1988**, *27*, 3687.
228. Koike, T.; Kajitani, S.; Kimura, E.; Shiro, M. I. *J. Am. Chem. Soc.* **1995**, *117*, 1210.
229. Herr, U.; Spahl, W.; Trojandt, G.; Steglich, W.; Thaler, F.; van Eldik, R. *Bioorg. Med. Chem.* **1999**, *7*, 699.

This Page Intentionally Left Blank

TRANSITION METAL CHEMISTRY OF GLUCOSE OXIDASE, HORSERADISH PEROXIDASE, AND RELATED ENZYMES

ALEXANDER D. RYABOV

Department of Chemistry, Carnegie Mellon University, 4400 Fifth Avenue, Pittsburgh, PA 15213, USA

I. Introduction
II. Enzymes
  A. Glucose Oxidase from *Aspergillus niger*
  B. Horseradish Peroxidase (HRP)
  C. PQQ-Dependent Dehydrogenases (PQQ, Pyrroloquinoline Quinone)
III. Properties of Mediators
IV. Ferrocenes
  A. Glucose Oxidase from *Aspergillus niger*
  B. Horseradish Peroxidase
V. Osmium and Ruthenium Compounds
  A. Glucose Oxidase and PQQ-Dependent Oxidoreductases
  B. Horseradish Peroxidase
VI. Chiral Complexes
VII. Cyclometalated Ruthenium(II) and Osmium(II) Mediators
VIII. Concluding Remarks
  References

I. Introduction

The goal of this review is to highlight a progress in the transition-metal chemistry of some enzymes that catalyze oxidative and reductive reactions. These enzymes are referred to as *oxidoreductases* (*1,2*) and transition metals are usually found in their active sites. However, the discussion will not be devoted to these metals, which are absolutely essential for biocatalysis. Such information is brilliantly summarized in several recent fundamental reviews and monographs (*3–9*).

ADVANCES IN INORGANIC CHEMISTRY
VOLUME 55 ISSN 0898-8838 DOI 10.1016/S0898-8838(03)55004-8

© 2004 Elsevier Inc.
All rights reserved.

This account deals with the electron transfer between either reduced or oxidized active sites of both metal-free and metal-containing enzymes and transition metal complexes. The latter, "external" metal complexes, capable of moving electrons between reduced or oxidized enzyme active sites and transferring them at an electrode, constitute a skeleton of the entire discussion. The importance of a deep understanding of the electron transfer, which has been emphasized by Kulys and Čenas in the early eighties (*10*), is due to the fact that this type of electron travel is one of the key features of modern bioanalytical amperometric instruments (biosensors), the functioning of which is based on the *mediated electron transfer* (MET). Biosensors are unique analytical tools in terms of specificity and sensitivity (*11–16*) due to a phenomenal capability of enzymes to catalyze a particular reaction of a particular compound. For example, the glucose oxidase (GO) enzyme oxidizes effectively β-D-glucopyranose, Eq. (1). The corresponding α anomer, L-glucose, or other pyranoses are significantly less reactive (*17,18*). Glucose oxidase recognizes this particular molecule and converts it into

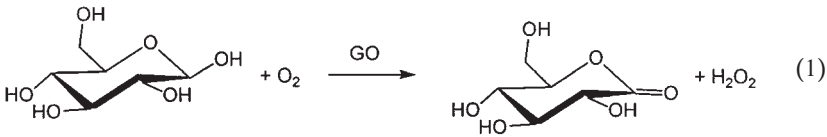

(1)

δ-D-gluconolactone acquiring two electrons and two protons. For the reasons discussed in more detail below, these two electrons cannot be readily transferred at an anode. Otherwise amperometric biosensors could function as shown in Scheme 1A. In nature, the abstraction of the two electrons from reduced GO is usually performed by dioxygen, which is reduced into hydrogen peroxide. The work of dioxygen can be performed by a variety of transition metal complexes, which are then oxidized at an electrode as demonstrated in Scheme 1B. The overall effect is such that electrons move from a substrate to an enzyme, then to a transition metal complex, and finally to an electrode. The electrode is thus able to "diagnose" the enzymatic redox reaction and "report" adequately on a substrate concentration in a sample. Scheme 1B is actually a simplified illustration of the principle of action of MET-based biosensors which are intelligent assemblies consisting of (i) an oxidoreductase that catalyzes a redox reaction, (ii) a low-molecular-weight compound (mediator) that moves electrons between an oxidoreductase active site and an electrode, (iii) and a polymeric network designed to keep together an oxidoreductase and a mediator at the

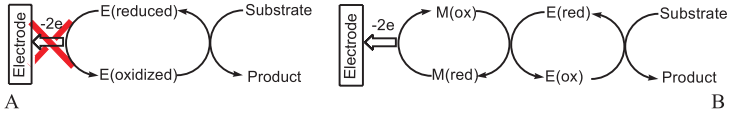

SCHEME 1. Schematic presentation of direct (non-mediated) electron transfer (**A**) and mediated electron transfer (**B**) from enzyme to electrode.

electrode surface. The network ensures also the most facile electron exchange, eliminates leakage of any biosensor element, and sets up high operational stability of biomaterials (*11,12,15,16,19*). Components (i)–(iii) are equally important and current research is aimed at improving the performance of oxidoreductases, mediators, and polymeric networks. The scope of this account is limited to interactions between E(ox) and M(red), or E(red) and M(ox), which are essential attributes of the mediated biosensors (*16*). Scheme 1B shows the interaction of E(red) with M(ox), but the case E(ox) + M(red) is also considered in much detail. A particular goal of this account is to highlight the principles of mediator design and main directions of research in this multidisciplinary field.

II. Enzymes

It is essential to understand basic principles of structural organization and mechanisms of action of the key enzymes used in amperometric biosensors. These are glucose oxidase from *Aspergillus niger*, horseradish peroxidase (HRP), and a group of pyrroloquinoline quinone (PQQ)-dependent enzymes such as alcohol and glucose dehydrogenases. These oxidoreductases can be referred to as model enzymes, although each of them is particularly important. They are available, rather inexpensive, and stable. Many studies on mediator design have been performed with these enzymes. Furthermore, testing a new compound as a potential mediator should be started with GO and/or HPR. If the mediator performance is promising, the investigation could be extended to less available and more expensive enzymes. As a rule, a good metal-incorporating mediator of GO is also good for HRP and *vice versa*.

A. GLUCOSE OXIDASE FROM *ASPERGILLUS NIGER*

This is a metal-free glycoprotein (*17*). It catalyzes the oxidation of β-D-glucopyranose into δ-D-gluconolactone by dioxygen, which is

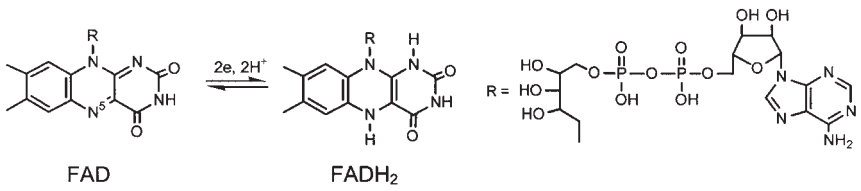

SCHEME 2. Structures of oxidized (FAD) and reduced ($FADH_2$) forms of flavin adenine dinucleotide.

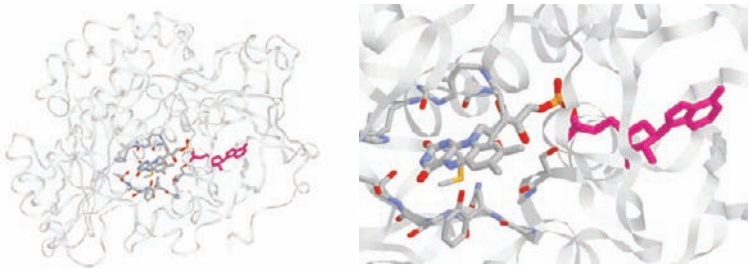

FIG. 1. Subunit of GO from *Aspergillus niger* with FAD hidden inside the protein globule (left) and a FAD area of GO with amino acid residues in a 8.0 Å vicinity from the N5 atom of FAD (right) (*21*).

reduced to H_2O_2, Eq. (1). The 160 kDa enzyme consists of two identical subunits which have 120 contact points. Each subunit has one prosthetic group tightly, non-covalently bound flavin adenine dinucleotide (FAD), Scheme 2. The separation between two FAD molecules in the dimer equals ca. 40 Å. FAD is deeply buried in the protein globule; the distance from N^5 to the protein surface equals 13–18 Å (Fig. 1). The polypeptide and saccharide shells are thus FAD insulators. The active site is a deep, funnel-shaped pocket. The entrance diameter is 10 Å. FAD is close to Asn514, His516, and His559. Highly reliable structural information on GO is based on the X-ray crystallographic investigation of the enzyme, which has been carried out with a 2.3 (*20*) and 1.9 Å resolution (*21*).

Glucose oxidase obeys a classical "ping-pong" mechanism of catalysis, i.e., involves two consecutive half-reactions (*22*). The native form of the enzyme, FAD-containing GO(ox), oxidizes β-D-glucose into the lactone forming the $FADH_2$-containing reduced enzyme GO(red), Eq. (2). GO(red) is then reoxidized by dioxygen, Eq. (3).

$$\beta\text{-D-glucose} + \text{GO(ox)} \longrightarrow \delta\text{-D-gluconolactone} + \text{GO(red)} \qquad (2)$$

$$GO(red) + O_2 \longrightarrow GO(ox) + H_2O_2 \quad (k_3) \tag{3}$$

Step 3 is very fast, especially at pH 5, when the enzymatic activity of GO is the highest. The second-order rate constant k_3 equals 1.6×10^6 M^{-1} s^{-1} (*23,24*) but decreases more than 100-fold at pH›8 (*24*). Similar pH effect has been reported for GO from *Penicillium vitale* (*25*). The oxidation of $FADH_2$ occurs in two 1e steps. At pH 5.3 the corresponding directly obtained redox potentials for the *Aspergillus niger* enzyme equal –0.048 and –0.050 V vs. NHE (*26*). The rate constant k_3 is a very important characteristic of GO because a good mediator must oxidize the reduced enzyme not slower than dioxygen.

B. Horseradish Peroxidase (HRP)

The reader will find extensive information about this and related peroxidases in the excellent monograph by Dunford (*8*). More recent findings are reported elsewhere (*27*). HRP catalyzes the oxidation of a variety of organic compounds (H_2A) by hydrogen peroxide as schematically shown in Eq. (4) The "variety" usually implies a low

$$H_2O_2 + 2\,H_2A \xrightarrow{HRP} 2\,HA^{\bullet} + 2\,H_2O \quad \text{(Further transformations)} \tag{4}$$

level of specificity for the enzyme. This is in fact true, if applied to H_2A electron donors of HRP. The specificity and high reactivity of HRP is manifested toward H_2O_2 as a carrier of oxidation equivalents. The corresponding second-order rate constant equals 1.7×10^7 M^{-1} s^{-1} for the most common HRP isoenzyme *C*, a hemin-containing glycoprotein (*28*). Hemin (Scheme 3) is coordinatively bound to the apo-enzyme via imidazole nitrogen of His170 and iron(III) is five-coordinate in the resting state. HRP has a single polypeptide chain of molecular mass 33,890 Da; the total mass of HRP equals 44 kDa. Likewise GO from *A. niger*, the structure of HRP has been established by X-ray crystallography (*29,30*). Most of the hemin is immersed into the protein globule. Only its edge is exposed to the surface (Scheme 3).

The mechanism of catalysis by HRP [Eqs. (5)–(7)] is generally well understood (*8*). The enzyme in its iron(III) resting state reacts initially with hydrogen peroxide to afford the so-called Compound I of HRP, which is two oxidation equivalents above the resting state. Compound I is involved in two one-electron oxidations. Transfer of the first electron at Compound I generates Compound II, which is one

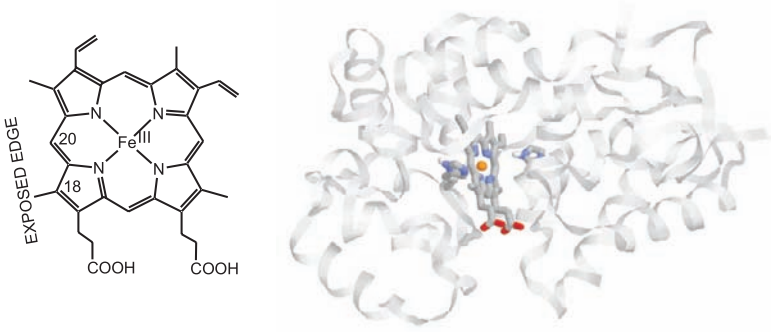

SCHEME 3. Structures of hemin, the iron(III) complex of protoporphyrin IX, and recombinant HRP isoenzyme *C* (*29*).

$$E(Fe^{III}, por) + H_2O_2 \longrightarrow E(Fe^{IV}, por^{+\bullet}) + H_2O \quad (k_5) \tag{5}$$

Compound I

$$E(Fe^{IV}, por^{+\bullet}) + H_2A \longrightarrow E(Fe^{IV}, por) + HA^{\bullet} \quad (k_6) \tag{6}$$

Compound II

$$E(Fe^{IV}, por) + H_2A \longrightarrow E(Fe^{III}, por) + HA^{\bullet} \quad (k_7) \tag{7}$$

$$HA^{\bullet} \longrightarrow \longrightarrow \longrightarrow \text{various products} \tag{8}$$

oxidation equivalent above the resting state. Structurally Compound I is an oxo derivative of iron(IV). The second oxidation equivalent is localized at the porphyrin ring in a form of a cation-radical. Compound II is the oxoiron(IV) complex. Both Compounds I and II are very strong oxidants: $E^{\circ\prime}$(C-I/C-II) $\sim E^{\circ\prime}$(C-II/HRP) $\sim$0.9 V (vs. NHE). Nevertheless, the reactivity of Compound I is usually a factor of 100 of Compound II. This effect is accounted for in terms of the inability of electron donor H_2A to approach the oxoferryl(IV) oxygen of Compound II. In contrast, H_2A does approach the exposed edge of the hemin of Compound I. The distance of the electron transfer is higher for Compound II and the reactivity is correspondingly lower (*27*). Natural substrates of HRP are aromatic amines, phenols, indoles, sulfonates, which are usually oxidized into oligomers or polymers. Mediators as electron donors act instead of H_2A in the peroxidase

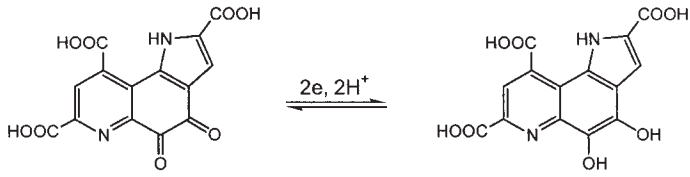

SCHEME 4. Oxidized and reduced states of the PQQ prosthetic group.

catalysis. Their role is to rapidly reduce Compounds I and II into the resting state.

C. PQQ-DEPENDENT DEHYDROGENASES (PQQ, PYRROLOQUINOLINE QUINONE)

This is the youngest group of oxidoreductases. Their PQQ cofactor (Scheme 4) has been discovered about two decades ago (*31*). The enormous popularity of this family of oxidizing enzymes is due to fact that electron acceptors other than dioxygen perform their reoxidation. Cytochromes *c*, small blue-copper proteins, or an internal heme *c* group can function as natural electron acceptors for the dehydrogenases (*31–35*). Therefore, artificial transition metal acceptors are expected substitutes of the natural ones in electrocatalysis by PQQ-dependent enzymes. Enzymes using quinone cofactors are quinoproteins, copper-quinoproteins, or quinohemoproteins. They are mainly involved in the direct oxidation of alcohols, sugars, and amines. The behavior of quinoproteins and quinohemoproteins varies sometime. In particular, the alcohol dehydrogenase (ADH) quinohemoprotein from *Gluconobacter sp. 33* adsorbed on carbon electrodes is involved in nonmediated electron exchange with an electrode in the presence of ethanol (*36,37*). The electron exchange mechanism as in Scheme 1A is realized for ADH due to its structural features (*35,38*). There are heme moieties in ADH, which act as bridges for the electron transfer from PQQ to the electrode surface. The shortest distance between PQQ and heme *c* in alcohol dehydrogenase from *Comamonas testosteron* equals 12.9 Å only (*39*). Heme-free protein glucose dehydrogenase (GDH) has a significantly lower tendency to exchange electrons with an electrode. It should however be mentioned that the involvement of an enzyme in direct electron exchange (Scheme 1A) does not underestimate the importance of its studies in MET (Scheme 1B). Sufficient current density may not be reached via direct electron exchange and switching to MET could be a right way to accomplish this goal.

Detailed discussion of the above-mentioned and other oxidoreductases involved in MET is beyond the scope of this account. Limited information on structural and catalytic features of GO, HRP, and PQQ dehydrogenases is however essential for better understanding mechanisms of interactions of inorganic and organometallic mediators with these and related enzymes.

III. Properties of Mediators

A good mediator needs (i) to be sufficiently small to be able to reach usually buried enzyme active sites, (ii) to have proper redox potential, and (iii) a medium-independent Nerstian electrode behavior, and (iv) to have high electron exchange rate between oxidized or reduced enzyme active sites (*11*). These requirements are encountered in many general accounts dealing with principles of the biosensor design and functioning. Mononuclear transition metal complexes with non-bulky ligands are in fact sufficiently small. A right choice of a particular metal and a particular set of ligands tunes the redox potential correspondingly using, for example, the Lever additivity concept (*40*). The mediator redox potential is medium-independent, if a transition metal complex is free from labile ligands susceptible to hydrolysis or substitution. Thus, requirements (i)–(iii) are readily fulfilled, but the designed transition metal complex might show no tendency to exchange electrons with enzyme active sites. For example, the redox potentials of the complexes $[Fe(CN)_6]^{4-}$, $[Co(bpy)_3]^{2+}$, and $[Cu(bpy)_2]^{2+}$ equal 396, 302, and 59 mV vs. NHE, respectively, but none of them is a good mediator of GO from *Aspergillus niger* (*41*). Remarkably, the redox potentials are almost ideal for this enzyme; the complexes are small and coordinatively saturated. But their performance with GO is unsatisfactory. The result with $[Fe(CN)_6]^{4-}$ is, however, slightly confusing in view of several reports on biosensors involving the $[Fe(CN)_6]^{3-/4-}$–GO couple (*42–52*). There is an extra feature in addition to (i)–(iii) mentioned above and this is the mediator self-exchange rate (*53,54*) that must be rather high for good mediator performance (*41,55*). High electron exchange rate between a mediator and an oxidized or reduced enzyme active site will then be achieved. The self-exchange rate constants k_{SE} for inorganic and organometallic molecules frequently used as mediators are summarized in Table I. The highest k_{SE} values are observed for osmium, ruthenium, and iron complexes with diimine ligands such as 2,2′-bipyridine (bpy) and 1,10-phenanthroline (phen). They are close to diffusion-controlled for osmium and ruthenium (Entries 1, 2, and 11).

TABLE I

REDOX POTENTIALS (VS. SCE) AND SELF-EXCHANGE RATE CONSTANTS k_{SE} FOR THE PROCESS $M^{n+} + {}^*M^{(n+1)+} \rightarrow M^{(n+1)+} + {}^*M^{n+}$ INVOLVING REPRESENTATIVE INORGANIC AND ORGANOMETALLIC COMPLEXES FREQUENTLY USED AS MEDIATORS IN AQUEOUS MEDIUM AT 25 °C

Entry	Complex	Redox potential/mV	$k_{SE}/M^{-1}\,s^{-1}$	Conditions	Ref.
1	$[Ru(bpy)_3]^{3+/2+}$	1025	1.2×10^9	1.0 M $HClO_4$	(*60*)
2	$[Ru(phen)_3]^{3+/2+}$	1025	1.2×10^9	1.0 M $HClO_4$	(*60*)
3	$[Ru(CN)_6]^{3-/4-}$	685	8.3×10^3	0.1 M NaClO4	(*61*)
4	$[Ru(NH_3)_6]^{3+/2+}$	−345	8.2×10^2	μ 0.013, D_2O	(*62*)
5	$[Ru(en)_3]^{3+/2+}$	−455	$< 2 \times 10^2$	μ 0.1 M	(*62*)
6	$[Fe(phen)_3]^{3+/2+}$	825	$1.3 \times 10^{7\,a}$	D_2O/D_2SO_4, μ ∼ 0.4 M	(*63*)
7	$[Fe(CN)_6]^{3-/4-}$	185	$2.4 \times 10^{2\,b}$	μ 0.2 M	(*56*)
8	$[Fe(CN)_6]^{3-/4-}$		1.5×10^4		(*64*)
9	Ferrocene/ ferricenium	270	5.7×10^6	1:1 v/v *n*-PrOH/H_2O 0.05 M $Ba(ClO_4)_2$	(*65*)
10	$[FcCH_2N^+Me_3]^{0/+}$	385	1.2×10^7	pD 5, 0.1 M $NaBF_4$	(*66*)
11	$[Os(bpy)_3]^{3+/2+}$	600	$> 10^9$	μ > 0.9 M	(*67*)
12	$[Co(phen)_3]^{3+/2+}$	175	40	0.1 M KNO_3	(*68*)
13	$[Co(phen)_3]^{3+/2+}$		0.35	μ 0.11 M	(*69*)
14	$[Co(bpy)_3]^{3+/2+}$	125	17	0.1 M KNO_3	(*68*)
15	$[Co(en)_3]^{3+/2+}$	−425	3.4×10^{-5}	0.2 M KCl	(*68*)
16	$[Co(NH_3)_6]^{3+/2+}$	−185	$\sim 10^{-7}$	–	(*68*)
17	$[Co(sep)]^{3+/2+c}$	−524	5	0.2 M NaCl	(*68*)
18	$[Co([9]aneS_3)_2]^{3+/2+c}$	−655[d]	9.5×10^4	μ 0.1 M	(*69*)

Redox potentials of common mediators are compiled from Ref. (*59*).

[a] at 3 °C.

[b] 100 times lower than usually reported due to the K^+ effect.

[c] sep = sepulhrate (1,3,6,8,10,13,16,19-octaazabicyclo[6.6.6]eicosane); ([9]aneS$_3$) = 1,4,7-trithiacyclononane.

[d] From Ref. (*70*).

The k_{SE} rate constants decrease extensively for complexes with CN^-, NH_3, and amine ligands. This trend is seen for Ru (Entries 1–5) and Co complexes (Entries 12–16) although the reactivity of Ru and Co species is separated by a huge gap. The k_{SE} constants are high for ferrocenes (Entries 9 and 10). The exchange rates increase substantially with increasing the rigidity of the ligand shell (Entries 14 and 17). The frequently used k_{SE} values for the $[Fe(CN)_6]^{3-/4-}$ couple have been recently questioned by Zahl *et al.* (*56*). A true value seems to be 100 times lower than that commonly used in theoretical calculations based on the Marcus formalism (*54*). The rate constants k_{SE} might be very useful for predicting the mediating performance of metal species in electron

exchange reactions with GO and HRP. As it will be seen below, the rate constant $k_{SE} \sim 10^3$ M^{-1} s^{-1} is critical for a complex to show a good performance with GO or HRP. But it should be remembered that this criterion is not applicable to all oxidoreductases. For example, the rate constants for the oxidation of reduced sulfite oxidase by cobalt(III) diimine type complexes are around 5×10^4 M^{-1} s^{-1} and higher (*57,58*) whereas these species have low self-exchange rates and are unreactive toward GO from *Aspergillus niger*.

IV. Ferrocenes

A. Glucose Oxidase from *Aspergillus niger*

1. Intermolecular Interactions

In 1984, Cass *et al.* have reported on the ability of ferrocene and its derivatives to reoxidize GO in the course of catalytic oxidation of D-glucose (*71*).[1] The effect has been monitored by cyclic voltammetry and the principal result is shown in Fig. 2. The current increased dramatically on addition of the enzyme demonstrating a perfect mediating performance of ferrocene carboxylic acid according to the mechanism in Scheme 1B. Cass and co-workers have tested several ferrocene derivatives (Table II) (*71*) and enzymes including PQQ-dependent alcohol dehydrogenase from *Pseudomonas extorquens* (*72*). The second-order rate constants for the oxidation of reduced GO and other enzymes by electrochemically generated ferricenium cations have been estimated assuming the formalism [Eq. (9)]:

$$Fc - e^- \rightleftharpoons Fc^+; \quad GO(red) + Fc^+ \xrightarrow{k_f} GO(ox) \tag{9}$$

The first reaction of oxidation of ferrocene occurs at an electrode followed by oxidation of GO(red) in solution with the pesudo-first-order rate constant $k_f = k[GO(red)]$. The values k_f/a ($a = nF\nu/RT$; ν is a scan rate) estimated from the experimentally measured i_p/i_p^0 ratios (Fig. 2) using the Nicholson and Shain approach (*73*) have been

[1]The impact of this publication in *Anal. Chem.* is phenomenal. Its citation rate is extremely high (807 citations by 22.01.04). During a visit to Imperial College (London) several years ago Tony Cass told an interesting story about this work. The manuscript was originally submitted to *J. Am. Chem. Soc.* where it was rejected for the lack of general interest and novelty. Indeed, scientific refereeing is questionable!

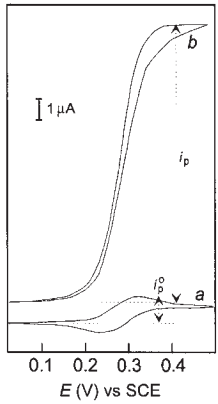

FIG. 2. (a) Cyclic voltammogram of ferrocene carboxylic acid (5×10^{-4} M) at pH 7 and 25 °C, in the presence of D-glucose (0.05 M) at a scan rate of 1 mV s^{-1}. (b) As for (a) but with the addition of GO (1.09×10^{-5} M). From Ref. (*71*).

TABLE II

REDOX POTENTIALS TRANSITION METAL MEDIATORS AND THE SECOND-ORDER RATE CONSTANTS FOR THE OXIDATION OF GO(red) BY ELECTROCHEMICALLY GENERATED OXIDIZED FORM OF A MEDIATOR (pH 7, 25 °C)

Mediator	Redox potential/mV vs. SCE	Rate constant/M^{-1} s^{-1}	Ref.
1,1′-Me_2Fc	100	0.77×10^5	(*71*)
Ferrocene (HFc)	165	0.26×10^5	(*71*)
$HOCH_2Fc$	190	60×10^5	(*74*)
H_2C=CHFc	250	0.30×10^5	(*71*)
HOOCFc	275	2.01×10^5	(*71*)
HOOCFc	290	1.5×10^5	(*74*)
HOOCFc		2.2×10^5	(*75*)
1,1′-$(HOOC)_2$Fc	285	0.26×10^5	(*71*)
Me_2NCH_2Fc	400	5.25×10^5	(*71*)
Me_2NCH_2Fc	370	100×10^5	(*74*)
Me_2NCH_2Fc	315	5.2×10^5	(*76*)

plotted against the inverse scan rate. The rate constants have been calculated from the slopes of linear plots. This description of the procedure for calculating the rate constants is essential. The numerical values reported by different authors vary and sometime appreciably (Table II). This might be due to the fact that (i) estimation of k_f/a using the method of Nicholson and Shain is to a certain extent arbitrary, (ii) the activity of GO may vary, although using pure commercial

preparations with the highest activity is a good warranty of the consistency of the data, (iii) the pseudo-first order approximation (9) do not often reflect a real situation, and (iv) modified or alternative routines for obtaining the rate constants are used (*77,78*). Therefore, Bourdillon and co-workers have analyzed in detail the electrochemical behavior of the ferrocene–GO–glucose system in terms of the following scheme (*74*):

$$\mathrm{GO(ox)} + \mathrm{Glucose} \rightleftharpoons \{\mathrm{GO(ox)}, \mathrm{Glucose}\} \quad (k_{10};\, k_{-10}) \tag{10}$$

$$\{\mathrm{GO(ox)}, \mathrm{Glucose}\} \longrightarrow \mathrm{GO(red)} + \mathrm{Gluconolactone} \quad (k_{11}) \tag{11}$$

$$\mathrm{GO(red)} + 2\mathrm{Fc}^{+} \longrightarrow \mathrm{GO(ox)} + 2\mathrm{Fc} \quad (k_{12}) \tag{12}$$

Here, Eq. (12) is a "global" reaction, since the glucose/gluconolactone and $FADH_2$/FAD couples are ($2e^- + 2H^+$) systems. k_{12} is a second-order rate constant. Step (12) involves two consecutive one electron-oxidations driven by k'_{12} and k''_{12} and therefore $\left[(1/k_{12}) = (1/k'_{12}) + (1/k''_{12})\right]$. The k_{12} rate constants has been suggested to be calculated using Eq. (13)

$$\frac{i_p}{i_p^0} = 3.16\left(\frac{k_{12}[\mathrm{GO}]}{\nu}\frac{RT}{F}\right)^{1/2} \tag{13}$$

from the slope of a linear plot of i_p/i_p^0 vs. $([\mathrm{GO}]/\nu)^{1/2}$ (υ is the scan rate). Equation (13) holds for a high concentration of D-glucose and very low concentration of ferrocene, but the latter must still be higher than that of GO to ensure the pseudo-first-order conditions. Bourdillon and co-workers have disclosed some features of the re-oxidation of reduced GO overlooked by Cass *et al.* (*71*). Cass and co-workers have reported that step (9) or (12) is pH-independent. But the electron transfer is actually speeded up as pH is raised from 4.2 to 8.2 (*74*). The pH effect is ascribed to the deprotonation of both $FADH_2$ and $FADH^{\bullet}$, the pK_a for both processes being around 7. The reduction of deprotonated species must obviously be more favorable.

The mechanism of reoxidation of reduced GO by ferricenium cations suggested by Bourdillon and co-workers (*74*) involves intermediate complex-formation between GO(red) (designated as $FADH_2$ in Scheme 5) and ferricenium cation (designated as Q which transforms into ferrocene designated as P). Although no evidence for this has been obtained from the electrochemical data, the formation of the GO–ferricenium intermediate has been kinetically proven in later

$FADH_2 + Q \rightleftharpoons \{FADH_2,Q\}$	(k_{14}, k_{-14})	(14)
$\{FADH_2,Q\} \rightarrow FADH_2^{\bullet+} + P$	(k_{15})	(15)
$FADH_2^{\bullet+} \rightleftharpoons FADH^{\bullet} + H^+$	($pK_{a,16} = 2$)	(16)
$FADH_2 \rightleftharpoons FADH^- + H^+$	($pK_{a,17} = 7$)	(17)
$FADH^- + Q \rightleftharpoons \{FADH^-,Q\}$	(k_{18}, k_{-18})	(18)
$\{FADH^-,Q\} \rightarrow FADH^{\bullet} + P$	(k_{19})	(19)
$FADH^{\bullet} + Q \rightleftharpoons \{FADH^{\bullet},Q\}$	(k_{20}, k_{-20})	(20)
$\{FADH^{\bullet},Q\} \rightarrow FADH^+ + P$	(k_{21})	(21)
$FADH^+ \rightleftharpoons FAD + H^+$	($pK_{a,22} = 0$)	(22)
$FADH^{\bullet} \rightleftharpoons FAD^{\bullet-} + H^+$	($pK_{a,23} = 7$)	(23)
$FAD^{\bullet-} + Q \rightleftharpoons \{FAD^{\bullet-},Q\}$	(k_{24}, k_{-24})	(24)
$\{FAD^{\bullet-},Q\} \rightarrow FAD + P$	(k_{25})	(25)

SCHEME 5. The electrochemical mechanism of oxidation of GO(red) by ferricenium salts (*74*).

studies (*79*). The mediator removes electrons from the reduced and semi-reduced prosthetic group of GO, Eqs. (15), (19) and (21), (25), respectively. Nature takes care about subsequent deprotonations by making the pK_a values of the reduced species significantly lower than physiological pH, Eqs. (16) and (22). Steps (17) and (23) account for the pH profile of the mediator activity. Shifted pH profiles for the oxidation of GO(red) by dioxygen and ferricenium mediators deserve a comment. It has been mentioned in Section II.A that k_{0_2} equals 1.6×10^6 M^{-1} s^{-1} at pH 5, but it is ca. 1×10^4 M^{-1} s^{-1} at pH 7. The solubility of O_2 in water in the presence of D-glucose is approximately 1×10^{-3} M (*80*). The pathway for oxidation of GO(red) by O_2 in the presence of 1×10^{-4} M mediator will be negligible when

$$10 \times k_{0_2}[O_2] \sim k_M[M] \tag{26}$$

Substitution of the numerical values into Eq. (26) gives $k_M = 1 \times 10^6$ M^{-1} s^{-1} for an ideal mediator performance at pH 7 in solution. But since the solubility of O_2 in saline solutions is lower than in pure water, a satisfactory mediator performance is often observed when k_M is lower.

Independent evidence supporting Scheme 5 has been obtained in the spectrophotometric steady-state study of reaction (27) (*79*).

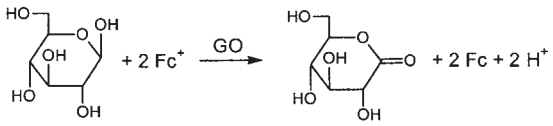

(27)

Deep blue ferricenium ions are rapidly reduced by GO(red) when introduced to the GO–glucose solution (*81–83*). Typical spectral changes that accompany the reduction of the ferricenium dye [Eq. (27)] are shown in Fig. 3 (*79*). The steady-state kinetics of reaction 27 has been investigated at different concentrations of ferricenium and D-glucose. The Michaelis-Menten kinetics holds with respect to both reagents. An approximate constancy of the ratio $V_{m,app}/K_{M,app}$ in a wide concentration range of D-glucose supports the "ping-pong" mechanism (*84–86*) involving two glucose [Eqs. (10) and (11)] and two ferricenium half-reactions [Eqs. (28) and (29)].

$$\mathrm{GO(red)} + \mathrm{HFc^+} \rightleftharpoons \{\mathrm{GO(red)}, \mathrm{HFc^+}\} \quad (k_{28}, k_{-28}) \tag{28}$$

$$\{\mathrm{GO(red)}, \mathrm{HFc^+}\} \longrightarrow \mathrm{GO(ox)} + \mathrm{HFc} \quad (k_{29}) \tag{29}$$

Here GO(ox) and GO(red) are the oxidized (native) and reduced forms of the enzyme, respectively. The effect of dioxygen is neglected and the transfer of the first electron from reduced $FADH_2$ at ferricenium ion is considered as the rate-limiting step for simplicity. Equation (30) describes the steady-state rate of the enzymatic ferricenium fading.

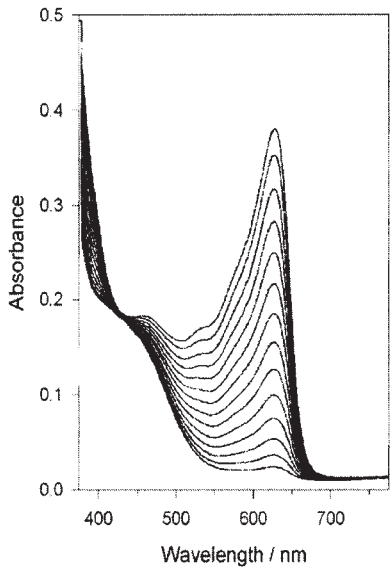

FIG. 3. Fading of $Fc^+PF_6^-$ in the presence of GO (2.7×10^{-7} M) and D-glucose (0.1 M) at 25 °C, pH 6.7. Spectra were recorded with 1 min interval. From Ref. (*79*).

It is generated applying the steady-state approximation to all intermediates involved in Eqs. (10), (11), (28) and (29) and using the mass balance equation to all coexisting forms of GO.

$$\nu = \frac{k_{11}k_{29}[\mathrm{E}]_t[\mathrm{Gl}]_t\left[\mathrm{HFc}^+\right]_t}{k_{29}K_M^{Gl}\left[\mathrm{HFc}^+\right]_t + k_{11}K_M^{Fc}[\mathrm{Gl}]_t + (k_{11}+k_{29})[\mathrm{Gl}]_t\left[\mathrm{HFc}^+\right]_t} \qquad (30)$$

Here $K_M^{Fc} = (k_{29} + k_{-28})/k_{28}$ and $K_M^{Gl} = (k_{11} + k_{-10})/k_{10}$; $[\mathrm{E}]_t$, $[\mathrm{Gl}]_t$ and $[\mathrm{HFc}^+]_t$ are the total concentrations of GO, D-glucose, and ferricenium ion, respectively. Fitting the experimental data to Eq. (30) allowed estimating the values of K_M^{Fc} (0.17 M), K_M^{Gl} (0.27 M), k_{11} (570 s^{-1}), and k_{29} (1.6×10^4 s^{-1}) that are worth comparing with the parameters obtained in electrochemical studies (*74*). The data for the glucose half-reaction summarized in Table III reveal an amazing coincidence. The values for k_{11} reported for the ferrocene systems (Table III, Entries 1–3) agree also with the data of Weibel and Bright (Entry 4) obtained using an essentially different technique (*23*).

The data for the ferricenium half-reaction deserve several comments. The Michaelis-Menten kinetics obtained in the UV–vis experiment supports the formation of the GO–ferricenium intermediates postulated in Scheme 5. The ratio k_{29}/K_M^{Fc}, which corresponds to the bimolecular interaction of GO(red) with the ferricenium ion, equals ca. 1×10^5 M^{-1} s^{-1} (*79*) and this must be compared with the observed rate constants of 1.4×10^5 M^{-1} s^{-1} found for ferrocene using the electrochemical technique under similar conditions (*87*).

The pH-dependence of the ferrocene half-reaction has been convincingly demonstrated by using a more illustrative spectrophotometric technique (*79*). The rate of reaction (29) increases sharply in the pH range 3–7 (Fig. 4). The maximal rate is around pH 7.5–8. The pH profile in Fig. 4 classifies ferricenium salts as Group II electron

TABLE III

KINETIC PARAMETERS FOR THE GLUCOSE HALF-REACTION OF GO AT pH ~7, 25 °C, Eqs. (10)–(11)

Entry	$[k_{10}k_{11}/(k_{11}+k_{-10})]/M^{-1}\,s^{-1}$	k_{11}/s^{-1}	Ref.
1	1.32×10^4	780	(*74*)
2	2.1×10^4	570	(*79*)
3	–	540	(*75*)
4	–	800	(*23*)

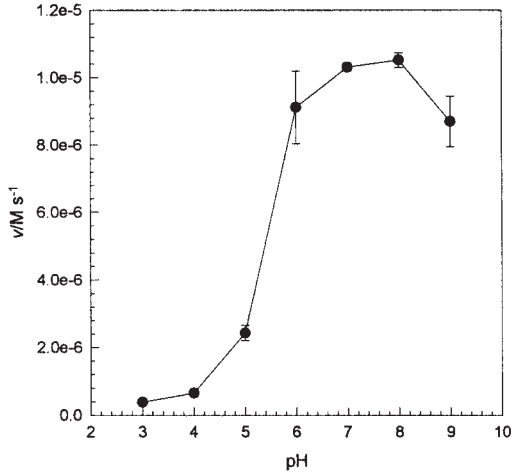

FIG. 4. pH profile for the steady-state rate of GO-catalyzed reduction of $Fc^+PF_6^-$ at [Fc^+] 0.002 M, [D-glucose] 0.05 M, [GO] 2×10^{-7} M, 25 °C, phosphate buffer, [Triton X-100] 2% (v/v); from Ref. (*79*).

acceptors of GO. This group of acceptors includes organic molecules such as methylene blue, toluidine blue, tetrathiafulvalene, tetracyanoquinodimethane, and benzylviologen (*17*).

The kinetic evidence for the formation of the intermediate GO–ferricenium complex and the structural similarity of RFc^+ and RFc suggest that the latter may inhibit the GO activity. In fact, ferrocene carboxylic acid is a competitive inhibitor of the oxidation of GO(red) by the ferricenium ion (*79*). The choice of HOOCFc is dictated by a higher redox potential of the acid ($\Delta E = 0.11$ V) precluding rapid electron exchange between the ferricenium cation HFc^+ and HOOCFc. The inhibition constant K_i of 3×10^{-3} M is by an order of magnitude higher than the apparent Michaelis constant for the ferricenium ion. The inhibiting capacity of ferrocenes is hence marginal and they do not play a role in reaction (27).

Attempts to correlate the activity of ferricenium ions toward GO(red) with their redox potentials are disappointing. Clear-cut dependencies have been established neither in the earlier (*72*), nor in the recent studies (*76*). The investigation of over 50 substituted ferrocene derivatives has confirmed that the rate of mediation with GO depends on a number of conflicting factors (*76*). The redox potentials varied in the range from –0.20 (HOFc) to +0.39 V ($Me_3NCH_2Fc^+ClO_4^-$) vs. SCE; the rate constants calculated as

suggested by Bartlett *et al.* (*77*), varied in the range from 0.3×10^5 (HOFc and $HOOC(CH_2)_nFc$, $n = 3$ and 4) to 8.2×10^5 M^{-1} s^{-1} ($HOCH_2Fc$) at pH 7. Redox potentials of ferricenium cations vary with changes in the size and geometry of the oxidants. The size increase prevents closer approach to $FADH_2$ of reduced GO. This enhances the electron transfer distance and lowers the rate constants. The data included in Table II and those reported by Forrow and coworkers (*76*) suggest the rate constant of 10^6 M^{-1} s^{-1} as a realistic upper limit for the oxidation of GO(red) by a ferricenium ion. The rate constant of 10^7 M^{-1} s^{-1} reported for $Me_2NCH_2Fc^+$ (*74*) has never been confirmed in other studies (Table II).

Ferrocene substituents may decrease the solubility of the mediators in water precluding reproducible electrochemical measurements. This impediment has been overcome in part by showing that the electrocatalytic activity of ferrocenes toward GO stays high in the presence of neutral, positively, and negatively charged surfactants (*87,88*). These studies followed the report of Fraser *et al.* (*89*) on a ferrocene-derivatized detergent, 11-(ferrocenylundecyl)trimethylammonium bromide. It is an electron acceptor for GO(red) when electrochemically oxidized to the corresponding ferricenium ion. Commercially available detergents sodium dodecylsulfate (SDS), cetyltrimethylammonium bromide (CTAB), and Triton X-100 have been used for solubilization of ferrocene and its substituted derivatives (*87,90*). A series of *n*-alkylferrocenes $H(CH_2)_nFc$ ($n = 3$–8, 12) have been prepared by the Friedel–Crafts acylation of ferrocene followed by the reduction of ketones formed by Zn/Hg (*91*). Electrochemical properties of $H(CH_2)_nFc$ in micellar solutions and the corresponding cations $H(CH_2)_nFc^+$ in micelle-free media are rather curious. The measured redox potentials of ferrocenes increase linearly with the number of methylene groups up to $n = 8$. The $E^{\circ\prime} = \alpha + \beta \times n$ equation holds in the presence and in the absence of micelles and uniformly β equals ca. 29 mV. This is unusual because the electron-donating power of the alkyl substituents is similar (*92*) and comparable values of the redox potentials are rather to be expected.

The increase in redox potentials should at least formally increase the driving force of reaction (12) and the rate constants k_{12}. An opposite effect is however observed and the rate constants decrease gradually with increasing redox potentials of *n*-alkylferrocenes (Fig. 5) (*90*). *n*-Octylferrocene is rather unreactive ($k_{12} = 8.4 \times 10^3$ $M^{-1}s^{-1}$) (*90*) and no coupling is found for *n*-dodecylferrocene (*87*). Low-potential decamethylferrocene and pentamethylferrocenes [(η^5-Me_5C_5)(η^5-XC_5H_4)Fe] (X = H, COOH, CH_2NMe_2) are also unreactive.

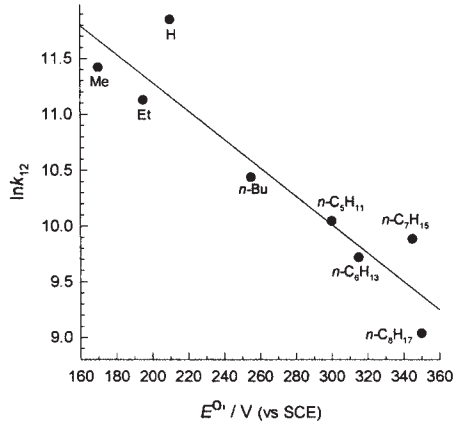

FIG. 5. Lowering of the rate constant for oxidation of reduced GO by ferricenium ions k_{12} with elongation of the alkyl radical of $H(CH_2)_nFc^+$ (pH 7.0; 0.1 M phosphate; 25 °C). From Ref. (*90*).

Consequently, the oxidation of GO(red) by ferricenium ions is very sensitive to their bulkiness.

Most of the data for poor-water ferrocenes is obtained in the presence of surfactants which affect the reactivity in a peculiar way. Figure 6 shows how the length of alkyl radical affects the reactivity of alkylferricenium cations toward GO(red) in the presence of the positively charged micelles of CTAB, negatively charged of SDS, and neutral of Triton X-100 (*90*). The relative rate constants $k_{surf}/k_{X\text{-}100}$, where k_{surf} and $k_{X\text{-}100}$ are the rate constants for the oxidation of GO(red) by RFc^+ in CTAB or SDS media and Triton X-100 micelles, respectively, are plotted against the number of methylene carbons in the ferrocene alkyl chain (n). The ratio $k_{surf}/k_{X\text{-}100}$ is close to unity when $n = 0$, viz. for HFc in both CTAB and SDS media. A noticeable divergence starts with $n = 2$. The upper CTAB curve reaches a maximum at $n = 4$ and then declines. The SDS curve decreases monotonically and the rate constant k_{12} is too low to be measured for *n*-hexylferrocene. Thus, a given *n*-alkylferrocene acquires different reactivity if incorporated into micelles of different charge. The maximal 14-fold increase relative to the Triton X-100 medium is observed for *n*-BuFc in the positive CTAB micelles. The negative SDS micelles bring about 3000-fold retardation in the case of *n*-pentylferrocene.

The simplest rationalization of the effect in Fig. 6 invokes an electrostatic model. The isoelectric point of GO from *A. niger* equals 4 (*17*) and its total charge is –60 at pH 7 (*93*). It could be hypothesized that the

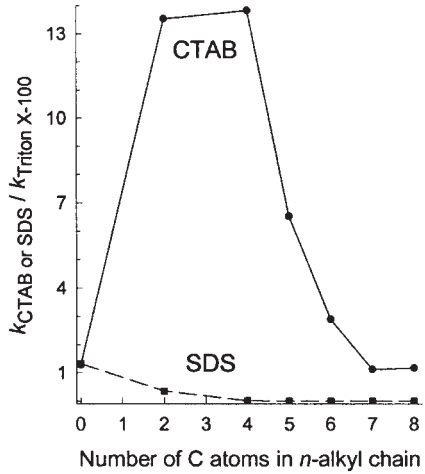

FIG. 6. Recognition by reduced glucose oxidase of the charge of micelle with solubilized electrochemically generated *n*-alkylferricenium ions. From Ref. (*90*).

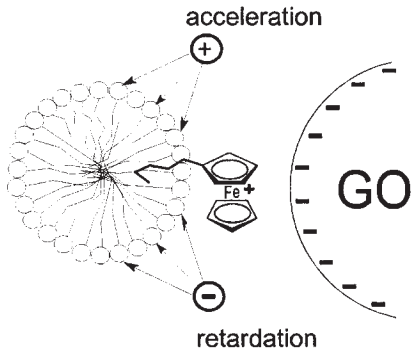

FIG. 7. A plausible mechanism of tuning the activity of reduced glucose oxidase by micelle charge toward solubilized *n*-alkylferricenium cations.

alkyl group "anchors" the electrochemically generated alkylferricenium ion to the micelle and the electron transfer from GO(red) is tuned by the micelle charge (Fig. 7). The highest and the lowest reactivities are anticipated for positively charged CTAB and negatively charged SDS micelles, respectively, as seen in Fig. 6. The same conclusions have been reached in the UV–vis study (*94*). For *n*-BuFc$^+$, the reaction rate is maximal in the cationic CTAB micelles, the anionic SDS micelles exhibit almost no activity, and the intermediate activity is in neutral micelles of Triton X-100.

2. Intramolecular Interactions

Proteins can be modified chemically by a myriad of ways using their surface functional groups (*95,96*). The advanced ferrocene chemistry has virtually no limits for their derivatization (*97*). It has been rapidly understood that a covalent binding of ferrocene derivatives to the GO surface could afford enzyme preparations capable of exchanging electrons with an electrode without a freely diffusing mediator. Such an electron transfer referred to as *pseudo-mediatorless* is a sort of mechanistic changeover from B to A in Scheme 1. Degani and Heller have selected a carbodiimide strategy for a covalent binding of HOOCFc to amino groups of glucose oxidase as shown in Scheme 6 (*98*). Ferrocene carboxylic acid has been treated with 1-(dimethylaminopropyl)-3-ethylcarbodiimide hydrochloride (EDC) and then reacted with GO in the presence of 3 M urea. After gel filtration, the preparation contained 14 ferrocene units (Fc_{14}–GO) and retained 50–66% of the initial enzymatic activity.

The cyclic voltammogram of Fc_{14}–GO has a feature from covalently bound ferrocenes at ca. 0.5 V vs. SCE. The current increased strongly in the presence of D-glucose indicative of direct electrochemical communication between the modified enzyme and an electrode. Bartlett *et al.* have reported on using ferrocene carboxylic, -acetic, or -butanoic acids. The best electrochemical performance is achieved on modification of GO by ferrocene acetic acid (*99*). Comparing the latter preparation with native GO in oxidation of D-glucose, D-mannose, 2-deoxy-D-glucose, D-xylose, and D-galactose suggests that the modification has little effect on the selectivity of the enzyme (*100*). Ryabov *et al.* have used a reverse-micelle micro-reactor for the carbodiimide modification of GO by ferrocene carboxylic acid (*101*). This less laborious procedure is carried out without urea and only five surface amino groups are therefore modified. Importantly, there are no limitations on solubility of a ferrocene derivative in the aqueous medium because the

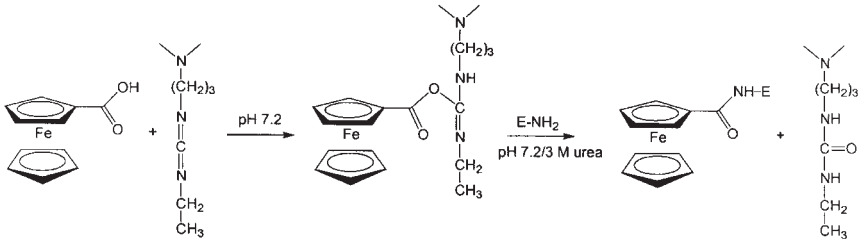

SCHEME 6. Steps involved in attaching ferrocene units to GO (*98*).

carboxylic group activation is performed in acetonitrile. High-pressure technique has been applied for the modification of GO by ferrocenes (*102*). Multi-labeling of ferrocenes to a glucose oxidase–digoxin conjugate has been used for the development of a homogeneous electroenzymatic immunoassay (*103*). In all above-mentioned studies, as well as in the work of Badia *et al.* (*104*), free amino groups of 32 of GO (*105*) have been converted into amido linkages. Schuhmann and co-workers have modified a saccharide part of GO (*106*). The enzyme has been first oxidized by sodium periodate to develop formyl groups on its surface (Scheme 7A). Amino derivatives of ferrocenes have been prepared from ferrocene carboxaldehyde and a variety of di- ($H_2N(CH_2)_nNH_2$) and triamines ($H_2NCH_2NH(CH_2)_nNH_2$). Ferrocene amines have been reacted with the periodate-oxidized GO to form the Schiff bases followed by reduction of the latter by $NaBH_4$ into the secondary amines (Scheme 7B).

The bioelectrochemical performance of the conjugates GO–$CH_2NH(CH_2)_nNHCH_2$–Fc ($n = 2$, 3, 6, 8, and 10) in terms of the current density is the highest for $n = 8$, i.e., when a 13 bond chain separates GO and the ferrocene moiety. The current density is seven times lower when $n = 2$ (7 bond chain). By using partly denatured conjugates, the authors have concluded that the intermolecular electron transfer plays an insignificant role when $n = 8$. The same conclusion has not been reached for a short chain conjugate ($n = 2$). The intermolecular process could not be ruled out in this case. This is surprising

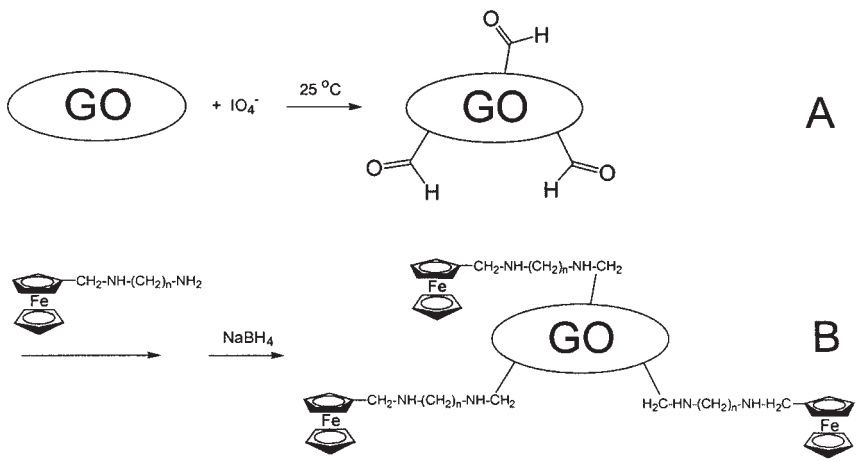

SCHEME 7. Preparation of GO modified by peripherally bound ferrocenes. From Ref. (*106*).

because common sense suggests that the intermolecular interaction might be easier for long chain conjugates with freely hanging ferrocene units. In this respect, the report of Muzutani and Asai on the electrochemical intermolecular coupling between GO and bovine serum albumin modified by ferrocene units should be mentioned (*107*).

The intramolecular electron flow from reduced $FADH_2$ to covalently linked ferricenium can be quantified by a first-order rate constant k_{intra}, which is an intramolecular analog of the intermolecular rate constant k_{12}, Eq. (12). Badia and co-workers have suggested an algorithm for estimating k_{intra} based on Eqs. (31)–(35). The notations here are as in Scheme 5. The mechanism is operative at saturating concentrations of D-glucose, i.e., when all GO is virtually in the reduced form $FADH_2$ (*104*).

$$FADH_2\text{–}Q \rightleftharpoons FADH_2\text{–}Q^+ + e^- \quad \text{(electrode)} \tag{31}$$

$$FADH_2\text{–}Q^+ \longrightarrow FADH^{\bullet}\text{–}Q + H^+ \quad (k_{32}) \tag{32}$$

$$FADH^{\bullet}\text{–}Q \rightleftharpoons FADH^{\bullet}\text{–}Q^+ \quad \text{(electrode)} \tag{33}$$

$$FADH^{\bullet}\text{–}Q^+ \longrightarrow FAD\text{–}Q + H^+ \quad (k_{34}) \tag{34}$$

$$FAD\text{–}Q \xrightarrow{\text{D-glucose}} FADH_2\text{–}Q \quad (k_{35}) \tag{35}$$

The limiting anodic current i_{max} is related to the intramolecular rate constant k_{intra}:

$$i_{max} = 2FA(D_{GO}k_{intra})^{1/2}[Fc\text{–}GO] \tag{36}$$

where F is the Faraday constant (96,500 C mol^{-1}), A is the electrode area (cm^2), D_{GO} is the diffusion coefficient for GO (4×10^{-7} cm^2 s^{-1}), and $k_{intra} = k_{32}k_{34}/(k_{32}^{1/2} + k_{34}^{1/2})^2$. The electron-hoping from one ferrocene unit to another in GO modified by several ferrocene residues is neglected here. Equation (36) has been applied to GO modified with HOOCFc using the carbodiimide technique such as to obtain the enzyme preparations Fc_n–GO with different loading of ferrocene units. The measured rate constants k_{intra} vary insignificantly in the range of n 3.6–25, the rate constants being 0.16 or 0.28 s^{-1} for these boundary cases, respectively, at 25 °C and pH 7.2 (0.085 M phosphate). This observation has lead to the conclusion about a few key ferrocene

groups with respect to FAD, which are critical for the electrocatalytic activity, rather than the number of ferrocene units loaded onto the enzyme. The shortest through space distance between the N^5 atom of FAD and a lysine N_ε atom is 23.6 Å (Lys152). Six other contacts fall within the 25 ± 1 Å range. This suggests that the distance of electron transfer is in fact very large in accord with the low values of the rate constants k_{intra} for intramolecular electron transfer (on assumption that the intermolecular process is not involved). Thus, the random modification of the surface functional groups of GO by ferrocene residues has obvious limitations.

A targeted modification of GO and D-aminoacid oxidase from pig kidney by a ferrocene residue has been performed by Riklin *et al.* (*108*). Ferrocene carboxylic acid has been wired to the adenine ring of FAD and the Fc–FAD conjugate has been loaded into the GO apoenzyme (Scheme 8). The generation of apo-GO at pH below 2 and the reconstitution of apo-GO by an excess of Fc–FAD are not difficult tasks. Much more tricky and laborious is the synthesis of the Fc–FAD precursor, i.e., N^6-(2-aminoethyl)–FAD ($H_2NCH_2CH_2$–FAD) (*109*). The Willner group has successfully used this key building block in several instances (*12,110,111*). The cyclic voltammogram of Fc–FAD adsorbed on a gold electrode at pH 7.3 exhibits two reversible waves at –50 and 0.35 V vs. SCE due to a two-electron redox process of FAD and a

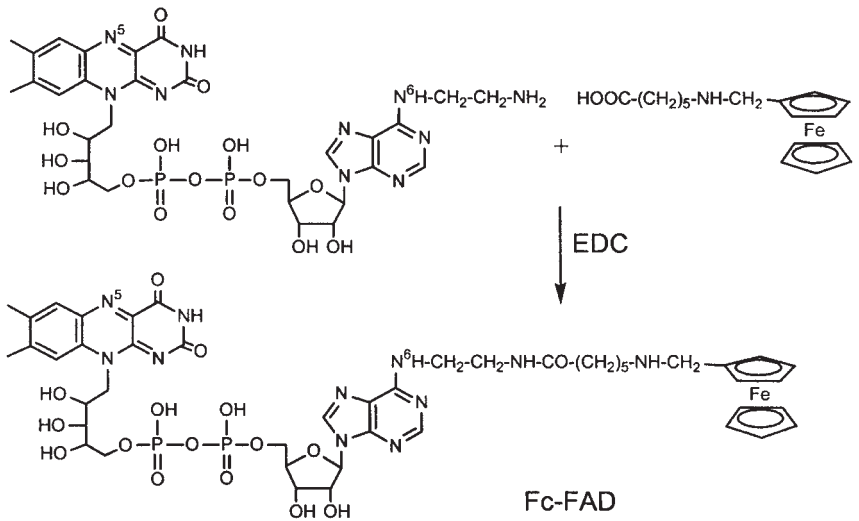

SCHEME 8. The Bückmann N^6-(2-aminoethyl)–FAD ($H_2NCH_2CH_2$–FAD) (*109*) and its ferrocene derivative Fc–FAD loaded into apo-GO (*108*).

one-electron reaction of the ferrocene unit. The GO enzyme reconstituted by Fc–FAD in solution has the ferrocene feature only indicative of the embedding of Fc–FAD into the apo-enzyme and communication of the ferrocene residue with an electrode. The enzymatic activity of the reconstituted GO (Fc–GO) was approximately 60% of the native enzyme (40% in a full report (*112*)). Studies of Fc–GO in the presence of D-glucose using a gold foil working electrode precoated with a cystamine monolayer have in fact demonstrated that the electrocatalytic anodic current is enhanced as the glucose concentration is increased, and reaches a saturation value. The Michaelis–Menten type of dependence has been revealed with $I_{max} = 4$ μA and $K_M = 2.9$ mM (*108*). Additional information about this Fc–GO preparation has been reported elsewhere (*112*). The intramolecular electron transfer rate constant k_{intra} calculated using Eq. (36) equals 40 s^{-1} and is by a factor of 50 higher than that for the randomly modified GO (*104*). The distance separating the ferrocene unit and FAD in Fc–GO is believed to be ca. 19 Å, by 2 Å shorter than in the most effective electrically contacted enzyme generated by the random modification of GO by ferrocene units. This information supports the hypothesis about the key locations of ferrocene groups that play the dominant role in the electrocatalysis (*104*).

B. Horseradish Peroxidase

Horseradish peroxidase catalyzes the *oxidation* of ferrocenes into ferricenium cations by hydrogen peroxide according the stoichiometric Eq. (37) (*113*).

$$2Fc + H_2O_2 + 2H^+ \xrightarrow{HRP} 2Fc^+ + 2H_2O \qquad (37)$$

Thus, HRP and GO are a kind of "twin" enzymes involved in oxidation of ferrocene and reduction of ferricenium, Eq. (27). When reaction (37) is followed spectrophotometrcially, the observed spectral changes are as in Fig. 3, but the absorbance grows now due to the generation of ferricenium ion. First studies involving reaction (37) have been performed in the seventies (*114–117*). Its importance has been realized after finding that reaction (37) can be monitored amperometrically (*118*). A variety of amperometric biosensors incorporating HRP and ferrocenes have been designed because the system responds to H_2O_2.

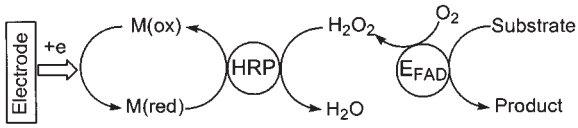

SCHEME 9. Principle of action a bienzyme biosensor incorporating HRP, an oxidase (E_{FAD}), and a an electron shuttle.

Hydrogen peroxide is produced by numerous dioxygen-dependent oxidases according to Eq. (38).

$$\text{Substrate} + O_2 \xrightarrow{\text{OXIDASE}} \text{Product} + H_2O_2 \tag{38}$$

Thus, an oxidase converts a particular target substrate into a matching product and H_2O_2, the latter oxidizes ferrocene in the HRP-catalyzed process, and ferricenium formed is finally reduced at an electrode. As a result, a catalytic ensemble such as in Scheme 9 represents the reaction details for a particular substrate.

1. Intermolecular Interactions

HRP-catalyzed steady-state oxidation of ferrocenes by H_2O_2 is fun to study by UV–vis spectroscopy because ferricenium ions generated are the only absorbing species at 500–700 nm (Fig. 3). A problem, actually solved by using micellar solutions, is the limited solubility of ferrocenes in water. The kinetics of oxidation of *n*-alkylferrocenes (alkyl = H, Me, Et, Bu and C_5H_{11}) (*119*) and later of larger variety of ferrocenes shown in Chart 1 (*120*) via Eq. (37) has been studied in detail in micellar systems of Triton X-100, CTAB, and SDS, mostly at pH 6.0 and 25 °C. Ferrocenes with longer alkyl radicals are oxidized immeasurably slow.

The rate of oxidation is a function of $[H_2O_2]$. A broad plato persists at a H_2O_2 concentration around 2×10^{-4} M at different concentrations of ferrocene and *n*-BuFc. The gradual rate decrease at higher H_2O_2 concentrations has been recently rationalized by the conversion of the catalytically active forms of HRP into the inactive oxyperoxidase (*121*) (Section V.B). The measurements have been performed at $[H_2O_2] = 2 \times 10^{-4}$ M, i.e., under the most favorable conditions. Reaction (37) is strictly first-order in both HRP and RFc in the concentration ranges 10–160 pM and $(0.2–65) \times 10^{-4}$ M, respectively. The observed second-order rate constants k_{39} decrease with the elongation of the alkyl substituent R. Increasing the surfactant concentration lowers the rate constants k_{39} for ferrocenes with uncharged groups R

R = H (**1**)
Me (**2**)
Et (**3**)
n-Bu (**4**)
CO_2H (**5**)
CH_2CO_2H (**6**)
CH_2NMe_2 (**7**)
$CO(CH_2)_2CO_2H$ (**8**)
$CO(CH_2)_3CO_2H$ (**9**)
CHOHMe (**10**)
C(Me)=NOH (**11**)

R = R' = CO_2H (**12**)
R = Et, R' = $CO(CH_2)_2CO_2H$ (**13**)
R = n-Bu, R' = CO_2H (**14**)

R = H (**15**)
CO_2H (**16**)
CH_2NMe_2 (**17**)

(**18**)

CHART 1. Ferrocenes studied as substrates of HRP (*120*).

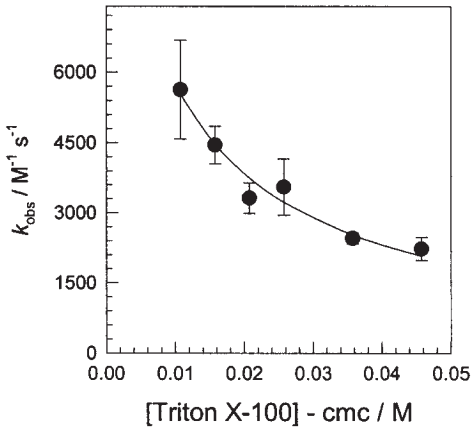

FIG. 8. Steady-state rate of HRP-catalyzed oxidation of 1,2,4,1′,2′,4′-hexamethylferrocene (**18**) by H_2O_2 as a function of [Triton X-100]; [H_2O_2] 2×10^{-4} M; [HRP] 10^{-7} M, [**18**] 10^{-3} M, pH 7.0, 25 °C. From Ref. (*90*).

as shown in Fig. 8. The oxidation of ferrocenes with charged arms R is usually surfactant-independent. The retardation arises from the binding of RFc to micelles, rather than due to the enzyme inactivation. The micellar effects are accounted for in terms of the Berezin pseudophase model of micellar catalysis (*122,123*). The observed second-order rate constant k_{39} for the interaction between HRP and RFc in the most general case is given by Eq. (39) .

$$k_{39} = \frac{k_m P_{HRP} P_{RFc} CV + k_w(1 - CV)}{\{1 + (P_{HRP} - 1)CV\}\{1 + (P_{RFc} - 1)CV\}} \qquad (39)$$

Here k_m and k_w are the second-order rate constants in the "micellar" pseudo-phase and the aqueous phase, respectively, P_{HRP} and P_{RFc} are the partition coefficients for HRP and RFc, respectively, between the micellar and aqueous phases ($P_A = [A]_m/[A]_w$, A = HRP or RFc), C is the total surfactant concentration without cmc ($C = [\text{surfactant}]_t$-cmc), and V is the molar volume of micelles. Equation (39) simplifies assuming $P_{HRP} \ll 1$ and $P_{RFc} \gg 1$. In fact, the hydrophilic enzyme molecule is expected to be in the aqueous phase, while hydrophobic, water-insoluble ferrocenes have a higher affinity to the micellar pseudo-phase. Taking also into account that relatively low surfactant concentrations are used, i.e., $CV \ll 1$, Eq. (39) transforms into Eq. (40).

$$k_{39} = \frac{k_m P_{HRP} P_{RFc} CV + k_w}{1 + P_{RFc} CV} \tag{40}$$

Data such as in Fig. 8 indicate that $k_w > k_m P_{HRP} P_{RFc} CV$ as suggested by a decrease in k_{39} with increasing the surfactant concentration. The fitting of the data such as in Fig. 8 to Eq. (40) has shown insignificance of the micellar term k_m into the overall rate; thus Eq. (40) transforms into (41) manifesting that the HRP-catalyzed oxidation of occurs predominantly in the aqueous phase.

$$k_{39} = \frac{k_w}{1 + P_{RFc} CV} \tag{41}$$

Equation (41) allows obtaining the intrinsic rate constants k_w which do not depend on the nature of surfactant used (CTAB, Triton X-100, or SDS). As it will be shown below, they correspond to the electron transfer from ferrocenes at Compound II (k_7 in Eq. (7)). Data for ferrocenes in Chart 1 as ln k_7 against $E^{\circ\prime}$ are presented in Fig. 9. As seen, all ferrocenes studied fall into two groups. Group I is comprised by mono- and 1,1′-disubstituted ferrocenes, whereas Group II consists of $Cp^*FeC_5H_4X$ molecules ($Cp^* = C_5Me_5$) and 1,2,4,1′,2′,4′-hexamethylferrocene, the redox potentials of which are shifted cathodically by 200–400 mV compared to Group I ferrocenes. There is a linear dependence between ln k_7 and $E^{\circ\prime}$ within Groups I and II and the corresponding slopes equal −0.010 and −0.042 mV^{-1}, respectively. The objective was to document enhanced reactivity for Group II ferrocenes, the reaction driving force which is significantly higher. This could be the case if the kinetic behavior of Groups I and II ferrocenes follows

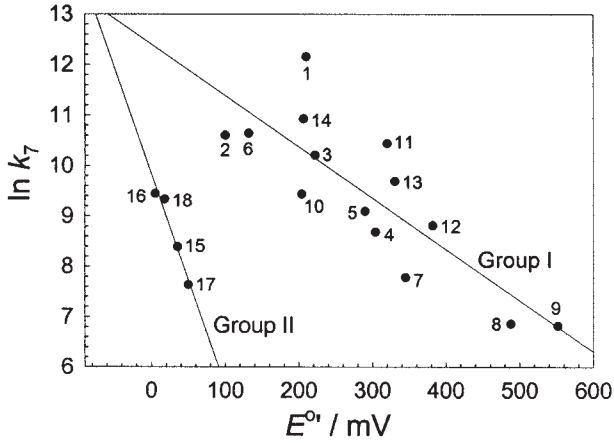

FIG. 9. LFER plot for ln k_7 (pH 7, 25 °C) vs. $E^{o\prime}$ using the data from Refs. (*119,120,130*). Numbers correspond to ferrocenes shown in Chart 1.

the same linear free energy relationship (LFER). This, however, does not occur.

The first order in ferrocenes is indicative of kinetic insignificance of the enzyme-substrate binding. This points to an intermolecular electron transfer from ferrocenes to HRP Compound II in the rate-limiting step. The fact that LFER holds for Group I suggests that, within the series, the HRP-catalyzed oxidation of ferrocenes is an electronically driven process with an approximately similar distance of electron transfer. Introduction of the steric bulk gives rise to a new set of ferrocenes (Group II) without the expected rate increase. There are two possible rationalizations for this effect. The first invokes the postulate that electron transfer has features typical of an outer-sphere process and the ferrocenes approach partly exposed the hemin edge which is ca. 8–11 Å from the iron (Fig. 10). Figure 10 has been created on the basis of X-ray structural data for horseradish peroxidase isoenzyme C (*29*) and using a Sculpt 2.6.0. program for optimization of the structures of ferrocene and pentamethylferrocene. Pentamethylated ferrocenes are much bulkier compared to Group I molecules and therefore they cannot approach the heme edge as close as Group I molecules (cf. Fig. 10A and 10B). The electron should overcome longer distance for Group II molecules in order to reach the heme edge. The increase in the reaction driving force is thus neutralized by elongating the electron transfer distance (*124*).

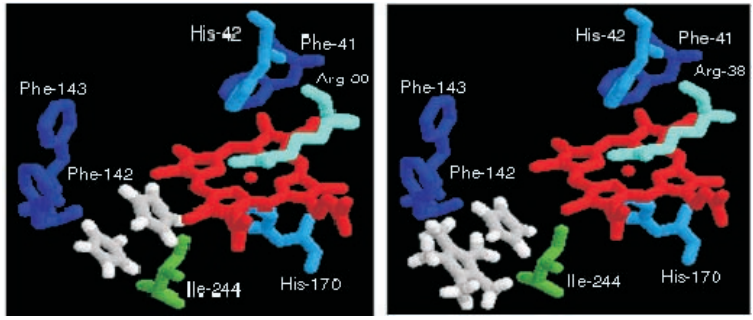

FIG. 10. Graphical visualization of the steric requirements during the approach of ferrocene (left) and pentamethylferrocene (right) to the heme edge of HRP. For details, see text.

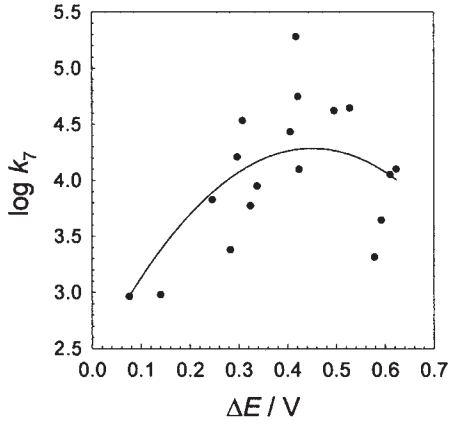

FIG. 11. Treatment of the kinetic data shown in Fig. 9 in terms of Eq. (42).

The origin of Groups I and II is otherwise rationalized in terms of the Marcus formalism (*54*) as in the case of HRP-catalyzed oxidation of phenols (*125,126*). The data in Fig. 11 are plotted to highlight the inverted Marcus region in reaction (37). The following standard assumptions have been made in the calculations (*53,54*):

$$k_7 = k_{ET} K_{OS}, \quad k_{ET} = k_o e^{-(\Delta G^{\neq}/RT)}, \quad \Delta G^{\neq} = \frac{\lambda}{4}\left(1 + \frac{\Delta G^0}{\lambda}\right)^2$$

Here, k_{ET} is the electron-transfer rate constants within an outer-sphere enzyme-substrate intermediate the stability of which is

determined by K_{OS}; k_o is the rate constant for activationless electron transfer; and λ is the reorganization parameter. A combination of these equations results in Eq. (42) on condition that $\Delta G^\circ = -nF\Delta E$, F is expressed in eV/V and $E^{\circ\prime} = 0.869$ V for the Compound II/HRP couple (vs. NHE) (*127*).

$$\log k_7 = \log(k_o K_{OS}) - \frac{\lambda}{4}\left(1 + \frac{\Delta E}{\lambda}\right)^2 \tag{42}$$

The data in Fig. 11 were fitted to Eq. (42), and the best-fit values for ($k_o K_{OS}$) and the reorganization parameter λ equal $(1.9 \pm 0.4) \times 10^4$ M^{-1} s^{-1} and 0.45 ± 0.04 eV, respectively. The latter is close to that found in HRP-catalyzed oxidation of phenols (*125*). Group II ferrocenes underscore the inverted region which was not clearly observed in the case of HRP-catalyzed oxidation of phenols (*125*).

Data in Fig. 9 show that ferrocene is the most reactive in this family of HRP substrates. The rate constant k_7 of 2×10^5 M^{-1} s^{-1} at pH 7 and 25 °C indicates that its reactivity is comparable with the frequently used electron donors of HRP. Ferrocene follows first-order kinetics and k_7 should be compared with the ratio k_{cat}/K_M, where k_{cat} and K_M are the catalytic and the Michaelis constants for substrates obeying the Michaelis–Menten kinetics, respectively. Such are iodide, guaiacol, and ABTS (2,2′-azino-bis(3-ethylbenzothiazoline-6-sulfonic acid) (*128*). The available ratios of 0.15×10^5, 1.3×10^5, and 34×10^5 M^{-1} s^{-1}, respectively (*129*), indicate that ferrocene is more reactive than iodide and comparable with guaiacol. High reactivity of ferrocene makes it a convenient analytical reagent for routine assays of H_2O_2 in the presence of HRP by monitoring the enzymically produced ferricenium dye at 617 nm (*113*).

The rate-limiting step under the steady-state is the oxidation of ferrocenes by HRP Compound II. This has been proved by performing steady-state and stopped-flow single turnover studies using water-soluble ferrocene carboxylic acid (**5**) and dimethylaminomethylferrocene (**7**) (*130*). The pseudo-first-order rate constants for the oxidation of **5** and **7** by Compounds I and II depend linearly on ferrocene concentrations for all four pairs. The second-order rate constants obtained by the stopped-flow technique (k_7) and under steady state (k_7') are similar for both **5** and **7** (Table IV). This proves the nature of the rate-limiting step. The reactivity of Compound I toward HOOCFc and Me_2NCH_2Fc is by a factor of 100 higher compared to that of Compound II. The behavior of HRP toward common organic substrates,

TABLE IV

SECOND-ORDER RATE CONSTANTS FOR THE OXIDATION OF FERROCENES AND FERROCYANIDE BY COMPOUNDS I (k_6) AND II (k_7) AND FOR THE HRP-CATALYZED STEADY-STATE OXIDATION (k'_7) AT [H_2O_2] 2.4×10^{-4} M (pH 6, 25 °C)

Substrate	Stopped-flow		Steady-state	Ref.
	k_6 (M^{-1} s^{-1})	k_7 (M^{-1} s^{-1})	k'_7 (M^{-1} s^{-1})	
HOOCFc	10.0×10^5	1.12×10^4	0.89×10^4	(*130*)
HOOCFc[a]			0.73×10^4	(*131*)
Me_2NCH_2Fc	2.7×10^5	0.25×10^4	0.24×10^4	(*130*)
$[Fe(CN)_6]^{4-}$	18×10^5	3.3×10^4		(*132*)

[a]From electrochemical data.

ferrocenes, and osmium(II) species (see Section V.B) is similar in this respect.

The solubility limitation does not allow direct measuring k_6 for ferrocene and Compound I. However, it is worth estimating k_6 for this most reactive electron donor among ferrocenes. Using the observed ratio $k_6 \approx 100 \times k_7$ for substituted ferrocenes (Table IV) and the steady-state rate constant k'_7 for ferrocene of 2×10^5 M^{-1} s^{-1} (*119*), the k_6 should be around 2×10^7 M^{-1} s^{-1}. Thus, ferrocene reacts very rapidly with Compound I, 10-fold as fast as $[Fe(CN)_6]^{4-}$.

Cyclic voltammetry has been also used for estimation of the rate constants for oxidation of water-soluble ferrocenes in the presence of HRP (*131*). There is a perfect match between the data obtained spectrophotometrically and electrochemically (Table IV), which proves that the cyclic voltammetry reveals information on the oxidation of ferrocenes by Compound II. It is interesting to note that an enzyme similar to HRP, viz. cytochrome *c* peroxidase, which catalyzes the reduction of H_2O_2 to water using two equivalents of ferrocytochrome *c* (*133–136*), is ca. 100 times more reactive than HRP (*131,137*). The second-order rate constant equals 1.4×10^6 M^{-1} s^{-1} for HOOCFc at pH 6.5 (*131*). There is no such rate difference in oxidation of $[Fe(CN)_6]^{4-}$ by cytochrome *c* peroxidase and HRP (*8*). These comparisons should not however create an impression that the enzymatic oxidation of ferrocenes is always fast. The active-R_2 subunit of *Escherichia coli* ribonucleotide reductase, which has dinuclear non-heme iron center in the active site, oxidizes ferrocene carboxylic acid and other water-soluble ferrocenes with a rate constant of 0.20 M^{-1} s^{-1} at pH 6.5–8.5 (*138*). The rate constants for the oxidation

of ferrocenes by ribonucleotide reductase are similar to those of a variety of Co^{II} complexes (*139*).

2. Intramolecular Interactions

Random modification of the HRP surface by ferrocene units and using this preparation for the detection of hydrogen peroxide and linoleic hydroperoxide have been described by Tsai and Cass (*140*). Similar to the random modification of GO, the location of ferrocenes on the protein surface is difficult to define. The direct X-ray crystallographic assignment has been applied to cytochrome P 450_{cam} from *Pseudomonas putida* after its modification by an electroactive sulfhydryl-specific reagent, *N*-(2-ferrocenylethyl)maleimide, as a redox-active reporter group (*141*). The crystal structure of the modified enzyme has been determined at 2.2 Å resolution and compared to the structure of the native enzyme complexed with its natural substrate (*142*). Two electroactive untis were attached to the protein. One of the ferrocenes was linked to Cys85 and occupied the camphor-binding site in the substrate pocket. The other ferrocene was linked to Cys136 on the surface of the protein. The electrochemical study of the labeled enzyme showed clear signals originating both from the heme and from the covalently linked ferrocenes. Interestingly, the heme redox potential of the ferrocene-containing P 450_{cam} was shifted from −380 mV for the camphor-bound wild-type protein to −280 mV for the modified protein. Random modification is actually "half-targeted" when, for example, sulfhydryl specific reagents are used. In addition to *N*-(2-ferrocenylethyl)maleimide, such a case is *N*-(ferrocenyl)iodoacetamide with a reversible Fc^{+}/Fc couple at 0.345 V (SCE) in acetonitrile (*143*). The latter has been coupled to sulfhydryl-modified oligonucleotide, cysteine, glutathione, and sulfhydryl-modified bovine serum albumin. A location of ferrocene redox labels is unquestionable when a total number of sulfhydryl groups in a biomolecule corresponds to the amount of ferrocene units introduced.

Carboxylic groups of the protoporphyrin IX ligand (Scheme 10) are phenomenal candidates for the targeted active-site modification of HRP and other heme-containing proteins. There is a clear parallel with the active site modification of GO (Section IV.A.2). The modification of hemin chloride by H_2NCH_2Fc in the presence of EDC and *N*-hydroxysuccinimide in DMF affording mono- and bis-amidated propionic acid residues is shown in Scheme 10 (*144*). The Fc–Heme is actually a mixture of two diastereomers. Apo-HRP has been prepared according to an acidic "methyl ethyl ketone" procedure of Teale (*145*)

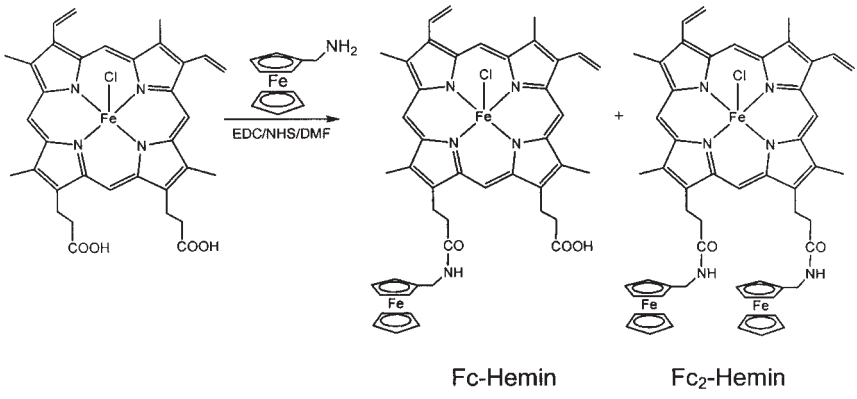

SCHEME 10. Modification of hemin by aminomethylferrocene. Fc–Hemin is a mixture of two diastereomers. From ref. (*144*).

and purified by gel-filtration. The degree of heme removal was better than 98%. The reconstitution of HRP using Fc–Hemin to afford Fc–HRP has been carried out by adding a solution of Fc–Hemin in dimethyl sulfoxide to apo-HRP dissolved in the Tris buffer (pH 8) and keeping the mixture at 0 °C for 0.5 h followed by gel-filtration. The reconstitution of apo-HRP by Fc_2–Hemin was made in the same way but the preparation was enzymatically silent.

The catalytically active Fc–HRP preparation has the R/Z ratio of 1.3. The relatively low value is attributed to the absorption of the ferrocene fragment at 280 nm. The isoelectrofocusing of Fc–HPR confirmed its homogeneity with the expectedly shifted isoelectric point to a more basic pH (cf. 8.1 and 8.5 for HRP and Fc–HRP, respectively). Cyclic voltammetry experiments indicated the ferrocene moiety in Fc–HRP (Fig. 12). New anodic and cathodic peaks are around 360 and 300 mV, respectively (Fig. 12b). The redox potential of 327 mV for Fc–HRP is shifted anodically compared with that for Fc–Hemin in water (264 mV). This may indicate that the ferrocene unit is shielded by amino acid residues located in the vicinity of the active site.

The Fc–HRP activity was quantified using two different substrates of HRP, i.e., ABTS and water-soluble ferrocene derivatives. Rate laws and kinetic parameters for native HRP and Fc–HRP have been compared. The native and the reconstituted enzymes catalyze the oxidation of ABTS in accordance with the Michaelis–Menten kinetics; the inverse rate versus $[ABTS]^{-1}$ plots are linear and the values of the maximum rates V_m and the Michaelis constant K_M are summarized

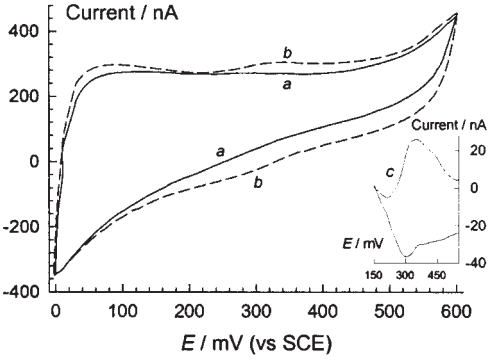

FIG. 12. Cyclic voltammograms of HRP (*a*), Fc–HRP (*b*), and the difference (*a*–*b*) trace (*c*) in aqueous solution ([Fc–HRP] 1.3×10^{-5} M, scan rate 160 mV s^{-1}, 25 °C, pH 7). From Ref. (*144*).

TABLE V

KINETIC CHARACTERISTICS FOR NATIVE HRP AND RECONSTITUTED Fc–HRP OBTAINED AT 25 °C

Enzyme	Substrate	V_m/M s^{-1}	$k_{cat} = V_m/[E]/s^{-1}$	$k_{cat}/K_M/M^{-1}\,s^{-1}$	K_M/M
HRP (native)	ABTS	226×10^{-10}	226	51×10^4	4.4×10^{-4}
	HOOCFc	–	–	0.89×10^4 [a]	–
	Me_2NCH_2Fc	–	–	0.24×10^4 [a]	–
Fc–HRP	ABTS	71×10^{-10}	71	17×10^4	4.2×10^{-4}
	HOOCFc	26×10^{-7}	26	2.4×10^4	11×10^{-4}
	Me_2NCH_2Fc	4.0×10^{-7}	4.03	2.7×10^4	1.4×10^{-4}

ABTS: pH 6.0, [HRP] 1×10^{-10} M, [H_2O_2] 7×10^{-4} M; Ferrocenes: pH 7.0, [HRP] 1×10^{-7} M, [H_2O_2] 2×10^{-4} M.

[a] The second-order rate constant k_7 (rate $= k_7$[HRP][RFc]).

in Table V. K_M does not change, but V_m decreases by a factor of 3 on going from HRP to Fc–HRP. The overall loss in reactivity toward ABTS is as low as a factor of 3.

In contrast to ABTS, the kinetic behavior of native HRP and Fc–HRP toward water-soluble ferrocenes HOOCFc and Me_2NCH_2Fc is remarkably different. Instead of first-order kinetics observed for native HRP, the reaction rate levels off on increasing the ferrocene concentration for Fc–HRP, Fig. 13. The Michaelis–Menten kinetics holds for both ferrocene substrates, and the inverse rate vs. [ferrocene]$^{-1}$ plots are linear. The values of V_m for HOOCFc and

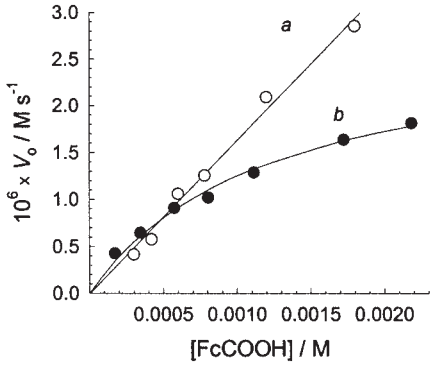

FIG. 13. Steady-state rate of HRP: (*a*) and Fc–HRP-catalyzed (*b*) oxidation of HOOCFc by hydrogen peroxide. For conditions, see legend to Table V.

Me_2NCH_2Fc, which are also summarized in Table V together with the corresponding values of K_M, differ by a factor of 6.4. Such a difference rules out trivial rationalization of the Michaelis–Menten kinetics in catalysis by peroxidase and related enzymes due to the rate-limiting interaction between the resting ferric state of the enzyme and hydrogen peroxide. It should be noted that the reactivity of HOOCFc toward HRP and Fc–HRP is very close at low substrate concentrations (Fig. 13). The comparison of the second-order rate constant k_7 and the k_{cat}/K_M ratio in the case of HRP and Fc–HRP, respectively (Table V), indicates that the reactivity of the reconstituted enzyme toward artificial organometallic substrates (ferrocenes) is higher compared with that of the native enzyme in terms of the k_7 vs. k_{cat}/K_M formalism!

The rate law changeover has been rationalized using the computer modeling of Fc–HRP. The X-ray structural study of HRP revealed a pretty loosened arrangement of its active site (*29*). Therefore, a Fc–Hemin diastereomer could be embedded into the active site, Gln176 being the only amino acid residue subjected to a more or less significant alteration of its position. The ferrocene core is almost on the protein surface (Fig. 14) in accordance with the observed electron exchange between the redox label and the electrode. Similar results of structural modeling were obtained for other diastereomers. Both diastereomers could be incorporated into apo-HRP and the ferrocenyl fragment is at the surface of HRP, but the loading of the positional isomer shown in Scheme 10 is however less sterically demanding. As seen in Fig. 14, there is a triangle, the apexes of which are the ferrocenyl fragment and the phenyl rings of Phe68 and Phe179.

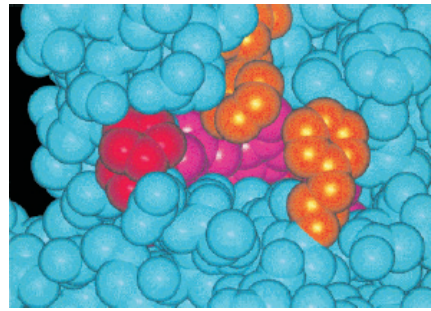

FIG. 14. View of the Fc–HRP model showing (i) that the ferrocene frame (in red) is located on the protein surface and (ii) new artificial cavity within the triangle in the apexes of which are ferrocene and shown in orange Phe 179 (top) and 68 (right). Hemin atoms are purple.

The importance of the latter two for the binding of aromatic substrates of HRP has been emphasized on the basis of site-directed mutagenesis and the ^{1}H NMR studies (*146*). All three apexes, viz. ferrocenyl and two phenyl groups, are hydrophobic especially the Phe68 residue. The three groups presumably generate a novel hydrophobic binding center for non-planar aromatic substrates such as ferrocenes on the enzyme surface close to hemin. The distances between the η^5-C_5H_5 ring of ferrocene and phenyl groups of Phe 179 and 68, fall in the range 4.6–6 and 6–8 Å, respectively, and might be favorable for the ferrocene binding. Therefore, the kinetic and mechanistic changeover is likely due to the artificially created ferrocene-binding site.

3. Design of Ferrocene-Containing Reactive Mediators

The results described in Section IV leave no doubts that ferrocenes are reactive electron carriers for the HRP and GO oxidoreductases. An advantage of ferrocenes as HRP substrates is that the products of enzymatic reaction, i.e., ferricenium ions, are more soluble in water than the starting materials. These substrates are enzyme-friendly and the products do not inactivate HRP due to "sticking" to its surface. However, some natural organic molecules display higher reactivity toward HRP, suggesting an approach to novel artificial substrates of oxidoreductases. It is based on bringing in one molecule a ferrocenyl fragment and a traditional organic substrate of HRP as shown in Scheme 11 (*147*).

Anilines and phenols as traditional substrates of HRP (*148*) have been first conjugated with ferrocene to obtain enzyme-friendly, reactive organometallic substrates. Both *p*-ferrocenylaniline and -phenol are

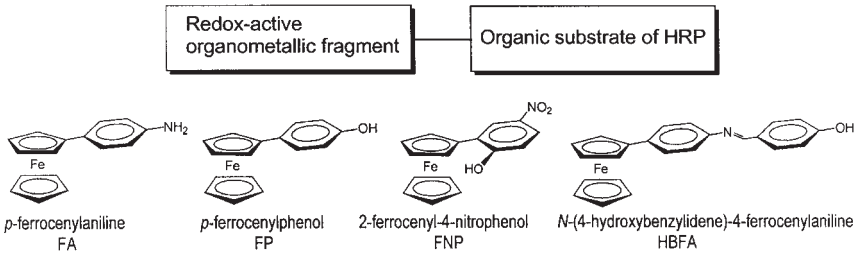

SCHEME 11. The bioorganometallic concept of mediator design (top) and some examples of ferrocene-containing substrates (bottom).

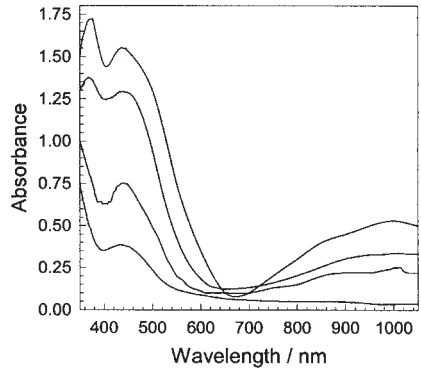

FIG. 15. Spectral changes of FA in the presence of HRP (3.25×10^{-8} M) and H_2O_2 (2×10^{-4} M) after ca. 2 min; [Triton X-100] 4.6×10^{-3} M, pH 5 (0.07 M citrate-phosphate), 25 °C. From Ref. (*147*).

rapidly oxidized by peroxidase and laccase (*147*). The spectra of FA and FP are unaffected by either H_2O_2 or HRP, whereas the absorbance grows rapidly at 439 and 1013 (FA, Fig. 15) or 436 and 851 nm (FP) in the presence of both followed by a slower fading. The primary enzymatic products are unstable in water. The spectra in Fig. 15 suggest that, in contrast to the HRP-catalyzed oxidation of ferrocenes, the primary products are not ferricenium cations but rather fulvenoid structures (*147*) which are readily produced from ferrocene derivatives bearing α-carbenium ion (*149,150*). The formation of such in the case of FA can be envisaged as shown in Scheme 12. The enzymatic electron transfer affords the unstable α-carbenium ion, which transforms rapidly into intermediate fulvene.

Kinetic measurements in micellar solutions have shown that the HRP-catalyzed oxidation of FA and FP by H_2O_2 is much faster

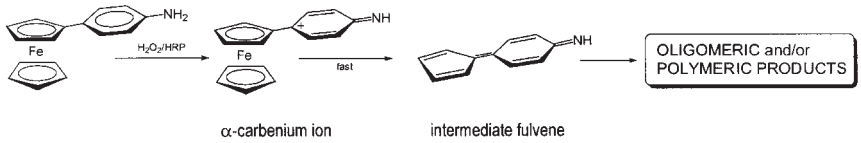

SCHEME 12. Tentative mechanism of oxidative degradation of *p*-ferrocenylaniline (*147*).

TABLE VI

RATE CONSTANTS k'_7 FOR THE HRP-CATALYZED OXIDATION OF FA AND FP (SCHEME 11) AND SOME REFERENCE COMPOUNDS BY H_2O_2 IN THE AQUEOUS PSEUDO-PHASE AT pH 5, 25 °C, $[H_2O_2]$ 2.4×10^{-4} M

Substrate	$k'_7/M^{-1}\,s^{-1}$	Ref.
FA	2.4×10^7	(*147*)
FP	1.7×10^7	(*147*)
Aniline	2.4×10^5	(*148*)
Phenol	2.8×10^6	(*148*)
Ferrocene	1.9×10^5	(*119*)
ABTS (k_{cat}/K_M)	3.4×10^6	(*129*)

than that of alkylferrocenes. The intrinsic, surfactant-independent rate constants (Table VI) have been extracted using Eq. (41) as described in Section IV.B.1. The rate constants show that the conjugation of two good peroxidase substrates of different nature does generate a much more reactive species. The "bifunctional" substrates are 10–100 times as reactive as their precursor building blocks and more reactive than ABTS. The increase in reactivity is not due to a decrease in the redox potential of FA or FP. It equals 0.245 V for FA to be compared with 0.210 V for ferrocene (vs. SCE). The conjugated substrates are presumably capable of selecting the most favorable mode of the rate-limiting interaction with the HRP Compound II.

Mediators made by the approach shown in Scheme 11 couple readily with laccase (*147*) and PQQ-dependent dehydrogenases (*151*). Ferrocene derivatives such as FNP and HBFA (Scheme 11) are perfect mediators of the PQQ-dependent glucose and alcohol dehydrogenases on screen-printed carbon electrodes used for D-glucose and ethanol monitoring (*152*). These molecules contain electropolymerizable anilinic and phenolic moieties and the electrochemical polymerization affors conducting films on electrode surfaces (*147,153–155*).

Immobilization of redox enzymes onto the films is a technology for easy-to-make reagentless biosensors. The HRP–poly(*m*-aminoanilinomethylferrocene)-modified glassy carbon electrode has, for example, been used for measuring hydrogen peroxide and other organic peroxides in both aqueous and organic medium at a low applied potential of −0.05 V (vs. Ag/AgCl) without interference from dioxygen. When modified with GO, the bienzyme electrode is sensitive and selective with respect to D-glucose (*155*).

V. Osmium and Ruthenium Compounds

Early reports on interactions between redox *enzymes* and ruthenium or osmium compounds prior to the biosensor burst are hidden in a bulk of chemical and biochemical literature. This does not apply to the ruthenium biochemistry of cytochromes where complexes $[Ru(NH_3)_5L]^{2+}$, $[Ru(bpy)_2L_2]^{2+}$, and structurally related ruthenium compounds, which have been widely used in studies of intramolecular (long-range) electron transfer in proteins (*124,156–158*) and biomimetic models for the photosynthetic reaction centers (*159*). Applications of these compounds in biosensors are rather limited. The complex $[Ru(NH_3)_6]^{2+}$ has the correct redox potential but its reactivity toward oxidoreductases is low reflecting a low self-exchange rate constant (see Tables I and VII). The redox potentials of complexes $[Ru(bpy)_3]^{2+}$ and $[Ru(phen)_3]^{2+}$ are way too much anodic (1.25 V vs. NHE) ruling out applications in MET. The complex $[Ru(bpy)_3]^{3+}$ is such a powerful oxidant that it oxidizes HRP into Compounds II and I (*160*). The electron-transfer from the resting state of HRP at $pH < 10$ when the hemin iron(III) is five-coordinate generates a π-cation radical intermediate with the rate constant $2.5 \times 10^7\ M^{-1}\ s^{-1}$ (pH 10.3) followed by a slower water ligation ($4.1\ s^{-1}$) and a fast formation of Compound II (Scheme 13). The oxidation of Compound II into Compound I occurs with a rate constant of $11 \times 10^7\ M^{-1}\ s^{-1}$, i.e., faster than the formation of the π-cation radical.

The oxidation such as in Scheme 13 is inapplicable for biosensor design because $[Ru(bpy)_3]^{3+}$, likewise $[IrCl_6]^{2-}$ (*127,161*), is an overwhelmingly strong oxidant. It is capable of oxidizing reduced GO (*162*), but a potential of the biosensor working electrode cannot be set up that high. Complexes of interest should be oxidized by Compounds I and II producing the resting state of HRP, i.e., Scheme 13 should formally be read from right to left. Such low potential ruthenium and osmium species are also capable of oxidizing reduced active sites of FAD-oxidases and PQQ-dehydrogenases.

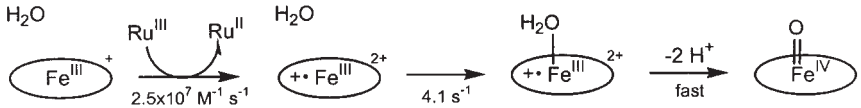

SCHEME 13. Mechanism of oxidation of the five-coordinate form of HRP by $[Ru(bpy)_3]^{3+}$ via the formation of π-cation radical intermediate (*160*).

A. GLUCOSE OXIDASE AND PQQ-DEPENDENT OXIDOREDUCTASES

1. Intermolecular Interactions

The ammino and cyano ruthenium(II) complexes $[Ru(NH_3)_5py]^{2+}$ and $[Ru(CN)_6]^{4-}$ are the first compounds reported as mediators of glucose oxidase (*163*). This event has had however little impact compared to the report of Degani and Heller on "macromolecular wires" (*164*). The wires are electrostatically or covalently bound to GO and mediate effectively electron transfer. The wires consist of polycationic redox polymers with (i) a potential that is oxidizing with respect to the potential of the $FAD/FADH_2$ centers and (ii) fast redox kinetics. A particularly effective wire is the polycationic copolymer of poly(N-methylvinylpyridinium chloride) and poly[vinylpyridine-$Os(bpy)_2Cl$] that forms, at moderate ionic strength (0.15 M NaCl), an electrostatic complex with the polyanionic enzyme. It looks as if the osmium complex is only mentioned between the lines, but nevertheless this report has launched a new race in developing amperometric biosensors, the key role in which belongs to osmium (and ruthenium) mediators. The macromolecular wires have been extensively investigated in the early nineties (*165–169*) and early results are summarized in two accounts by Heller (*170,171*). Further studies have revealed that poly(1-vinylimidazole) is more advantageous because it is easier to make (*172,173*) but high current density is achieved using PQQ-dependent glucose dehydrogenase instead of glucose oxidase (*174*). Use of poly(allylamine) has also been reported (*175*).

The key inorganic mediating species is *cis*-$[OsCl_2(bpy)_2]$. Its redox potential in aqueous buffered solution at pH 7 equals –36 mV (SCE), suggesting that chloro ligands might be hydrolyzed and the rate constant for the oxidation of GO(red) by the electrochemically generated osmium(III) is high, viz. 4.5×10^5 M^{-1} s^{-1} (*176*). Thus, the low potential does not compromise the reactivity at all. The redox potential of the related ruthenium complex *cis*-$[RuCl_2(bpy)_2]$, the hydrolysis of which in water is well documented (*177–179*), equals 300 mV under the same conditions. The difference of 300 mV is typical of compositionally

similar ruthenium and osmium compounds (see Tables VII and IX, for example) suggesting the hydrolysis of *cis*-$[OsCl_2(bpy)_2]$. Although the redox potential of the Ru^{II} complex is significantly higher, the rate of its oxidation of GO(red) is lower (*179*). In the macromolecular wires, osmium(II) is bound either to pyridine or imidazole nitrogens depending on whether polyvinylpyridine or polyvinylimidazole is used. The binding to an aromatic nitrogen donor increases the redox potential of the "$(R\text{-}py)Os(bpy)_2Cl$" fragment and therefore the working potentials of osmium wired biosensors are around 100 mV. Redox potentials of osmium and ruthenium mediators can be tuned or, alternatively, a mediator speciation can be predicted from its redox potential. The concept known as *electrochemical parametrization of metal complex redox potentials* has been introduced by Lever (*40*) by the example of $Ru^{II/III}$ couples. It is very helpful in studies of mediating features of ruthenium complexes (*180*) and applicable to osmium compounds.

Osmium(II) and ruthenium(II) complexes are strongly absorbing species. Their extinction coefficients are in the range $(5-11) \times 10^3$ M^{-1} cm^{-1} around 500 nm. The corresponding complexes in the oxidation state 3+ absorb visible light much weaker and therefore the GO-catalyzed oxidation of D-glucose by Os^{III} complexes, which obeys stoichiometric Eq. (43), can be monitored spectrophotometrically as in the case of ferricenium salts.

$$\text{D-glucose} + 2M^{III} \xrightarrow{GO} \text{D-}\delta\text{-gluconolactone} + 2M^{II} + 2H^+ \qquad (43)$$

An example is shown in Fig. 16 (*181*). It has been found that reaction 43 follows first-order kinetics in Os^{III} and pseudo-first-order rate constants k_{obs} can be calculated. The second-order rate constant for the oxidation of reduced glucose oxidase by $[OsCl_2(phen)_2]^+$ in air equals 1.2×10^5 M^{-1} s^{-1} at pH 6.7, [D-glucose] 0.05 M (saturating concentration) and 25 °C which is ca. 20% less than that when the reaction solutions are purged with argon. This value agrees with that found electrochemically for $[OsCl_2(bpy)_2]$.

The pH profile of k_{obs} shown in Fig. 17 has two sets of data, obtained in buffered and buffer-free solutions (*181*). Both pH profiles are bell-shaped with a sharp maximum around 7 indicative of the involvement of the histidine residues located in the vicinity of FAD (Fig. 1). The rate constants are somewhat higher in unbuffered solutions especially at pH below 7. The difference disappears at higher pH. This is qualitatively rationalized by a specific effect of phosphate on the

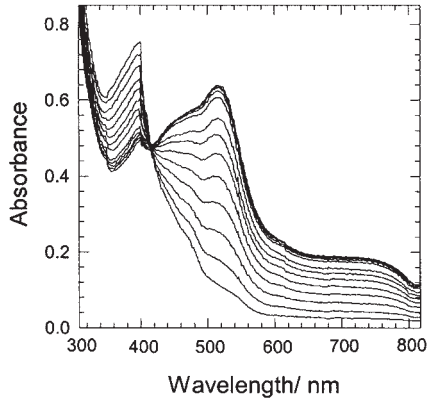

FIG. 16. GO-catalyzed reduction of Os^{III} into Os^{II} by D-glucose accompanied by a strong absorbance change; [GO] 1.7×10^{-8} M, [D-glucose] 0.05 M, $[OsCl_2(phen)_2^+]$ 1×10^{-4} M, 0.01 M phosphate, pH 6.7, 25 °C, time intervals 2 min. From Ref. (*181*).

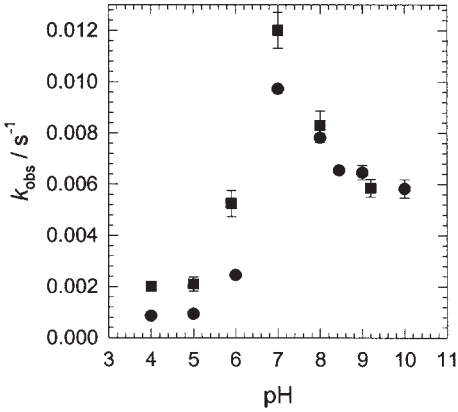

FIG. 17. pH-dependence of k_{obs} for the GO-catalyzed oxidation of $[Os(phen)_2Cl_2]^+$ by D-glucose in 0.01 M $NaClO_4$ (■) and 0.01 M phosphate (●); 25 °C, [Triton X-100] 2%, [GO] 1.5×10^{-7} M, [D-glucose] 0.05 M. From Ref. (*181*).

catalytic activity of GO, rather than by a change in a coordinative environment of the Os^{III} complex. The electrochemically investigated pH profile using the osmium complex $[Os(R_1\text{-bpy})_3]^{2+}$ revealed a broader maximum in the pH range 7.5–9.5 (*182*).

Ways of changing the coordination sphere and properties of osmium and ruthenium complexes (see, for example, Ref. (*183*)) are much broader

compared to ferrocenes. It is therefore not surprising that many osmium and ruthenium complexes have been tested as mediators of GO from *A. niger*. Table VII is a compilation of the rate constants k_{12} obtained electrochemically using the approaches of Nicholson (*73*) and Bourdillon (*74*), which give consistent rate constants according to Danilowicz *et al.* (*184*). Comments follow.

(i) As could be anticipated, there is no clear correlation between the rate constants and the redox potentials. The plot of log k_{12} against E (not shown) reminds of a cloud. The "averaged" mediator with $E = 336$ mV will oxidize GO(red) with a rate constant of 2.8×10^6 M^{-1} s^{-1}. This non-scientific averaging gives however a correct estimate of the reactivity of a good mediator!

(ii) Rate constants for the same mediator reported by different authors may vary 10-fold (Entries 2–4). However, all data give a true impression of the mediator activity.

(iii) A more critical analysis of the rate constants in Table VII reveals some inconsistencies. For example, alkylation of bpy or phen complexes normally decreases the performance, the reaction driving force decreases and the mediator size increases. Both factors are unfavorable for the oxidation of GO(red). Hence, the comparison of Entries 5 and 6 suggests that the reactivity of $[Os(4,7\text{-}Me_2phen)_3]^{2+}$ is most likely overestimated.

(iv) Some mediators are by the order of magnitude more reactive than the "average" one (Entries 13 and 14) (*186*). The rate enhancement is due to an optimal positive charge on a mediator ($+5$), which facilitates the interaction with the negatively charged GO. Noticeably, mediators bearing charges > 5 are less reactive. The rate constants slightly above 1×10^7 M^{-1} s^{-1} seem to be the upper limit. It should be mentioned however that the ligands of osmium complexes in Entries 13 and 14 are not easy to make. The same level of reactivity has been reached for the complex $[OsCl(4,4'\text{-bpy})(bpy)_2]^+$ with commercially available ligands (*176*). Its reactivity is rationalized in terms of the antenna effect as recently introduced by the Gray group (*190,191*). A mediator must contain a "wire" made of phenyl–ethynyl units coordinated monodentately to a central metal. This long, highly conjugated ligand acts as a probe capable of reaching buried active sites of redox proteins. The 4,4′-bpy ligand of $[OsCl(bpy)_2(4,4'\text{-bpy})]^+$ presumably acts as an antenna that finds the reduced flavin adenine dinucleotide buried inside the enzyme.

TABLE VII

REDOX POTENTIALS AND RATE CONSTANTS FOR THE OXIDATION OF REDUCED GO FROM *ASPERGILLUS NIGER* BY OSMIUM AND RUTHENIUM COMPLEXES AT 25 °C AND pH 7. COMPLEXES ARE SHOWN AS INTRODUCED NEGLECTING HYDROLYSIS IN WATER. SEE FOOTNOTE FOR THE KEY

Entry	Compound	Potential/mV (SCE)	$10^{-5} \times k_{12}/M^{-1}\,s^{-1}$	Ref.
1	*cis*-$[OsCl_2(bpy)_2]$	−36	4.5	(*176*)
2	$[Os(bpy)_3]^{2+}$	610	21	(*182*)
3	”	614	50 (pH 7.4)	(*162*)
4	”	585	7.9	(*41*)
5	$[Os(phen)_3]^{2+}$	629	51 (pH 7.4)	(*162*)
6	$[Os(4,7\text{-}Me_2phen)_3]^{2+}$	439	169 (pH 7.4)	(*162*)
7	$[Os(R_1\text{-}bpy)_3]^{2+}$	225	25	(*182,185*)
8	$[Os(R_2\text{-}bpy)_3]^{2+}$	−230	0.0022	(*182*)
9	$[Os(R_3\text{-}bpy)_3]^{2+}$	425	3.2	(*182*)
10	”	399	18.6	(*41*)
11	$[Os(R_1\text{-}bpy)(R_3\text{-}bpy)_2]^{2+}$	400	60	(*182*)
12	$[Os(R_2\text{-}bpy)_2(R_3\text{-}bpy)]^{2+}$	−60	67	(*182*)
13	$[Os(R_2\text{-}bpy)_2(Z_1\text{-}bpy)]^{4+}$	50	150	(*186*)
14	$[Os(R_2\text{-}bpy)_2(Z_2\text{-}bpy)]^{4+}$	−50	140	(*186*)
15	$[Os(Z_1\text{-}bpy)_3]^{8+}$	610	1.0	(*186*)
16	$[Os(imidazole)_2(bpy)_2]^{2+}$	245	41	(*41*)
17	$[OsCl(imidazole)(bpy)_2]^{+}$	88	2.8	(*41*)
18	$[OsCl(4,4'\text{-}bpy)(bpy)_2]^{+}$	250	108	(*176*)
19	$[OsCl(pyrazine)(bpy)_2]^{+}$	225	21	(*176*)
20	$[OsCl(py\text{-}3\text{-}COOH)(bpy)_2]^{+}$	210	0.42	(*184*)
21	$[OsCl(py\text{-}4\text{-}CHO)(bpy)_2]^{+}$	240	4.0	(*184*)
22	$[Cl(bpy)_2Os(4,4'\text{-}bpy)OsCl(bpy)_2]^{2+}$	270	64	(*176*)
23	$[Cl(bpy)_2Os(4,4'\text{-}bpy)RuCl(bpy)_2]^{2+}$	280, 510	38	(*176*)
24	$[Cl(bpy)_2Ru(4,4'\text{-}bpy)RuCl(bpy)_2]^{2+}$	515	5	(*176*)
25	*cis*-$[RuCl_2(bpy)_2]$	300	0.54	(*179*)
26	$[RuCl(py)(bpy)_2]^{+}$	490	4.1	(*179*)
27	$[RuCl(imidazole)(bpy)_2]^{+}$	415	4.4	(*179*)
28	$[Ru(CN)_6]^{4-}$	685	0.1	(*163*)
29	$[Ru(NH_3)_6]^{2+}$	∼ −200	0.024 (pH 7.4)	(*187*)
30	”		∼ 0.001	(*188*)
31	$[Ru(NH_3)_5py]^{2+}$	50	1.0	(*163*)
32	$[Ru(NH_3)_5(pyrazine)]^{2+}$	∼ 200	1.9	(*189*)
33	$[Ru(R_1\text{-}bpy)_3]^{2+}$	700	5.5	(*182*)
34	$[Ru(R_2\text{-}bpy)_3]^{2+}$	275	16	(*182*)
35	$[Ru(R_3\text{-}bpy)_3]^{2+}$	260	2.2	(*182*)
36	$[Ru(R_2\text{-}bpy)_2(Z_1\text{-}bpy)]^{4+}$	530	30	(*186*)

(*Continued*)

TABLE VII
CONTINUED

Entry	Compound	Potential/mV (SCE)	$10^{-5} \times k_{12}/M^{-1} s^{-1}$	Ref.
37	$[Ru(R_2\text{-bpy})_2(Z_2\text{-bpy})]^{4+}$	530	37	(*186*)
38	$[Ru(bpy)_3]^{2+}$	1044	2.1 (pH 7.4)	(*162*)
39	$[Ru(phen)_3]^{2+}$	1110	1.1 (pH 7.4)	(*162*)
40	$[RuCl(4,4'\text{-bpy})(bpy)_2]^{+}$	470	5	(*176*)
41	$[Fe(R_1\text{-bpy})_3]^{2+}$	510	2.2	(*182*)
42	$[Fe(R_2\text{-bpy})_3]^{2+}$	100	1.4	(*182*)

Key:

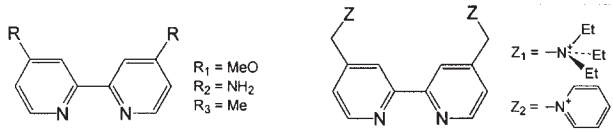

(v) Redox potentials of compositionally similar ruthenium complexes are by 300–400 mV higher than those of their osmium counterparts. The osmium compounds are nevertheless ca. 10 times more reactive.

(vi) The reactivity of dinuclear osmium and/or ruthenium complexes is normally lower than that of their mononuclear counterparts (Entries 22–24).

(vii) Mediator activity drops sharply when the redox potential of a mediator becomes close to –200 mV presumably due to a too low driving force.

(viii) Not all data reported in the literature for Os and Ru mediators are included in Table VII. Nevertheless, it gives a general perception of oxidative features of GO mediators and predictions of properties of new complexes can also be made.

2. Intramolecular Interactions

In contrast to ferrocenes, osmium and ruthenium complexes are capable of forming coordinative bonds with donor centers of GO including histidine imidazoles. There are therefore two ways of bringing coordinated transition metals onto enzyme surfaces, i.e., via natural and artificial donor sites. Artificial centers are commonly made of functionalized pyridines or imidazoles, which must be covalently attached to GO followed by the complexation of an osmium or

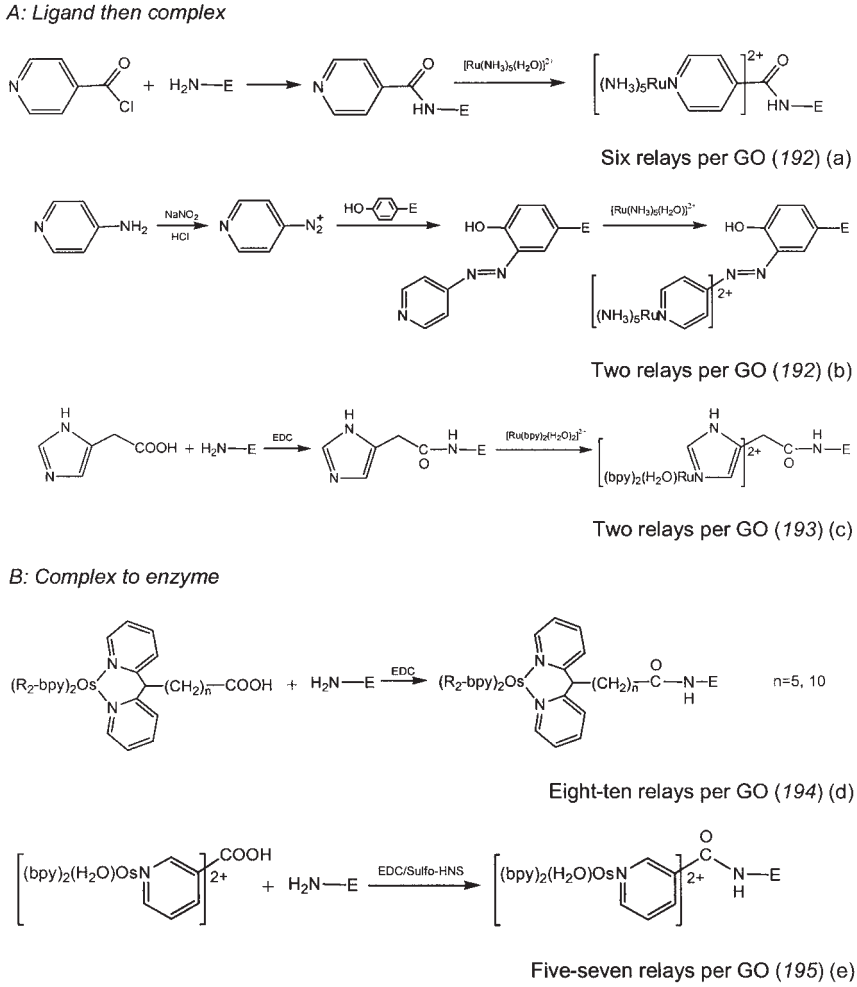

SCHEME 14. Two ways of attaching ruthenium or osmium complexes onto GO surface via artificial and natural donor centers. For explanations, see text.

ruthenium complex. Alternatively, a complex itself must have proper peripheral functional groups for covalent binding to the enzyme. Examples of the modifications involving artificial donor centers and natural sites are shown in Scheme 14.

The coordinative modification is carried out using complexes in the oxidation state 2+, not 3+, for facilitating the ligand substitution reactions leading to the binding (*192,196*). The reason is that the

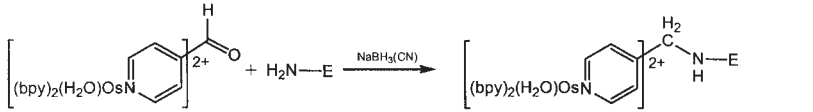

Five relays per GO (*195*) (f)

NATURAL SITES

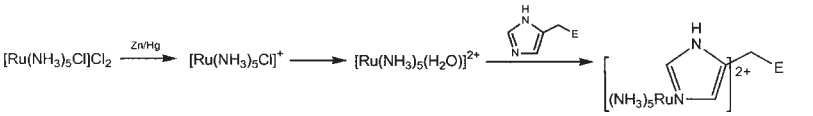

Fourteen relays per GO (*192*) (g)

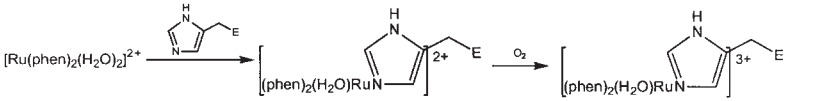

Three relays per GO (*196*) (h)

SCHEME 14. Continued.

ligand substitution on complexes of metals in higher oxidation states, occurs slower (*197*). Correspondingly, the coordinative conjugates display higher stability when the metal is in a higher oxidation state (*192*). The electrochemical coupling between osmium or ruthenium centers and the active site of GO has been observed for all systems in Scheme 14, the electron exchange efficacy being different. Less significant catalytic currents have been reported for GO modified with the $[Ru(NH_3)_5]^{2+}$ moiety particularly when bound via the pyridyl azo function (*192*). This could be due to the rigidity of the azo ligand chain and generally weaker mediator performance of the $[Ru(NH_3)_5]^{2+}$ unit (see Table VII). Better results have been obtained for $[Ru(bpy)_2]^{2+}$ as a mediator unit attached to GO via the imidazole bridge (Fig. 18) (*193*). The rate constant $k_{intra} = 2\ s^{-1}$ (22 °C, pH 7) for the conjugate in Scheme 14c has been evaluated by the computer simulation (*198*) of cyclic voltammograms in Fig. 18. The mechanism shown by Eqs. (31)–(35) with the assumption that $k_{32} = k_{34}$ has been applied. It is very close to $k_{intra} = 3.6\ s^{-1}$ for the GO randomly modified with 13 ferrocene carboxylic acid residues (*104*). Much higher values of k_{intra} have been observed for the modification of natural donor sites of GO by $[Ru(phen)_2]^{2+}$ and $[Ru(bpy)_2]^{2+}$ units (Scheme 14h) (*196*). The simulation of cyclic voltammograms such as in Fig. 19 gives the rate

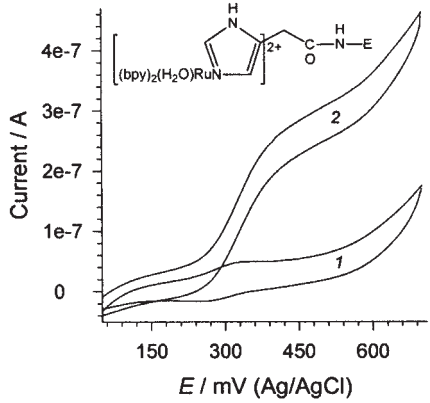

FIG. 18. Cyclic voltammograms of the conjugate in Scheme 14c in the absence (*1*) and in the presence (*2*) of D-glucose (0.033 M), [conjugate] 10 mg mL^{-1}, pH 7, scan rate 2 mV s^{-1}, 22 °C. From Ref. (*193*).

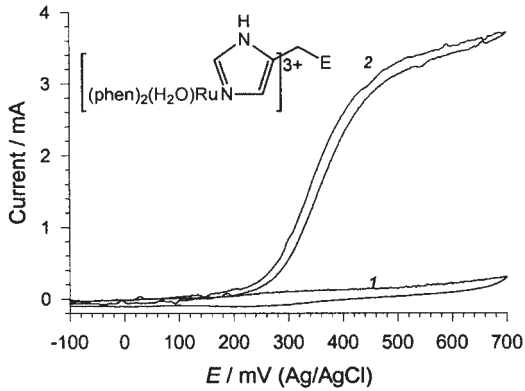

FIG. 19. Cyclic voltammograms of the conjugate in Scheme 14g in the absence (*1*) and in the presence (*2*) of D-glucose (0.033 M), [conjugate] 17.1 mg mL^{-1}, pH 7, scan rate 10 mV s^{-1}, 22 °C. From Ref. (*196*).

constants of 70 and 12 s^{-1} for $[Ru(phen)_2]^{2+}$ and $[Ru(bpy)_2]^{2+}$, respectively, which are comparable to that reported for the reconstituted GO preparation with FAD modified with a ferrocene unit (40 s^{-1}) (*112*). The coordinative modification is a mild procedure, it affords preparations characterized by a rapid intramolecular electron transfer, and the catalytic activity of GO (*192,196,199*), D-amino acid oxidase (*192*), and PQQ-dependent glucose dehydrogenase (*199*) declines insignificantly. It should however be remembered that the catalytic activity

can significantly decrease, if the modification involves the active site histidine residues which are essential for catalysis (*199*).

B. Horseradish Peroxidase

As extra evidence for the rule "good for GO–good for HRP", the enzyme-osmium wiring technology has been successively applied for HRP containing systems (*200*). This stimulated spectral and electrochemical kinetic studies of the HRP-catalyzed oxidation of osmium(II) and ruthenium(II) complexes. Similar to ferrocenes [Eq. (37)], the oxidation follows Eq. (44).

$$2M^{II} + H_2O_2 + 2H^+ \xrightarrow{HRP} 2M^{III} + 2H_2O \qquad (44)$$

As in the ferrocene case, the reaction is first order in both HRP and a metal electron donor suggesting kinetic insignificance of the enzyme–electron donor intermediate (*181*). It should be mentioned that the first order in M^{II} is observed for complexes of moderate reactivity. Very reactive complexes such as $[Os(bpy)_2(py)(H_2O)]^+$ in Table VIII obey the Michaelis–Menten kinetics because the formation of Compound I [Eq. (5)] starts to slow down the rate (see below). The dependence of the rate of reaction 44 on the H_2O_2 concentration shown in Fig. 20 resembles the ferrocene case (*119*). The decline in rate after reaching a maximum has routinely been rationalized in terms of an "inactivation" of HRP. The true nature of this phenomenon has recently been underscored in the course of detailed spectroscopic and electrochemical studies of the HRP-catalyzed oxidation of $[OsCl(bpy)_2(py)]^+$ (*121*). Thus, transition metal electron donors are convenient probes for solving fundamental problems of enzymology.

Second-order rate constants for the oxidation of Ru^{II} and Os^{II} complexes obtained under steady-state at $[H_2O_2]$ optimal for catalysis (when the oxidation by Compound II is rate-limiting), are summarized in Table VIII. They are in the range 10^4–10^5 M^{-1} s^{-1} for the majority of ruthenium complexes. The highest reactivity has been found for $[Ru(4,4'\text{-}Me_2bpy)_2(H_2O)_2]^{2+}$, the redox potential which is the lowest among ruthenium(II) diimine complexes. The complexes with potentials higher than 0.5 V vs. SCE react very slow. The reactivity decreases on binding ligands that increase redox potentials of complexes. For example, addition of pyridine to $[Ru(bpy)_2(H_2O)_2]^{2+}$ retards its HRP-catalyzed oxidation due to equilibrium (45). Analysis of the rate versus [py] profile gives the same equilibrium constant K_{45} as

TABLE VIII

REDOX POTENTIALS AND SECOND-ORDER RATE CONSTANTS FOR HRP-CATALYZED OXIDATION OF COMPLEXES $[M^{II}(N^{\cap}N)XY]$ (M = Ru, Os) BY H_2O_2 OBTAINED BY UV–VIS SPECTROSCOPY UNDER THE STEADY STATE (25 °C, pH 6.7)

M or Complex	N∩N	X/Y	Tentative structure of complexes in solution	Rate constant/$M^{-1}\,s^{-1}$	Redox potential/mV (SCE)	Ref.
Ru	bpy	Cl/Cl	$[Ru(bpy)_2(H_2O)_2]^{2+}$	1.54×10^4	300	(*201*)
Ru	bpy	Cl/py	$[Ru(bpy)_2(py)(H_2O)_2]^{2+}$	0.2×10^4	465	(*201*)
Ru	4,4′-Me_2bpy	Cl/Cl	$[Ru(Me_2bpy)_2(H_2O)_2]^{2+}$	72×10^4	229	(*201*)
Ru	phen	Cl/Cl	$[Ru(phen)_2(H_2O)_2]^{+}$	15×10^4	382	(*201*)
Ru	bpy	Br/Br	$[Ru(bpy)_2(H_2O)_2]^{2+}$	2.2×10^4	292	(*201*)
Ru	bpy	SCN/SCN	$[Ru(bpy)_2(NCS)_2]$	0.93×10^4	276	(*201*)
Ru	bpy	CO_3	$[Ru(bpy)_2(CO_3)]$	1.26×10^4	270	(*201*)
Ru	bpy	Cl/NO	$[Ru(bpy)_2Cl(NO)]^{+}$	0.088×10^4	542	(*201*)
Ru	bpy	dmso/dmso	$[Ru(bpy)_2(dmso)_2]^{2+}$	~ 0	522	(*201*)
Os	bpy	Cl/py	$[Os(bpy)_2(py)(H_2O)]^{2+}$	800×10^4 [a]	210	(*121*)
$[Ru(NH_3)_5py]^{2+}$			$[Ru(NH_3)_5py]^{2+}$	1.2×10^4 [b]	28	(*118*)
Ferrocene				20×10^4		(*119*)

[a] pH 7.4, $1 \times 10^7\ M^{-1}\,s^{-1}$ by stopped-flow, $1.4 \times 10^7\ M^{-1}\,s^{-1}$ by cyclic voltammetry.

[b] pH 6.2, by cyclic voltammetry, $3.6 \times 10^6\ M^{-1}\,s^{-1}$ for cytochrome *c* peroxidase.

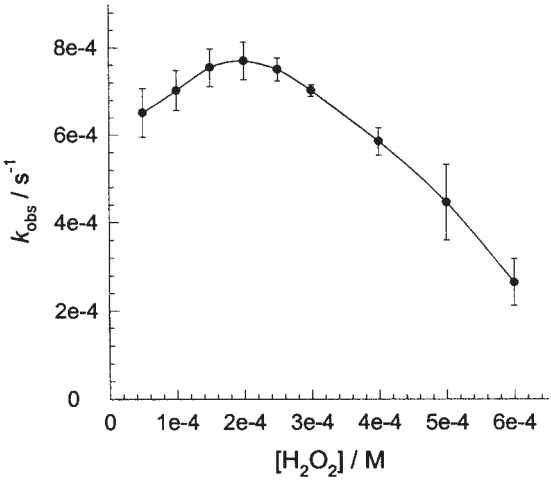

FIG. 20. Dependence of k_{obs} on H_2O_2 concentration for the HRP-catalyzed oxidation of $[Ru(bpy)_2(H_2O)_2]^{2+}$ at 25 °C, pH 6.7. From Ref. (*181*).

obtained from UV–vis and electrochemical data (*181*). It should be noted that equilibrium (45) was favorable in the electrocatalysis by GO because it increased the reaction driving force (*179*). The coordination of pyridine increases the redox potential by 165 mV, accounting for almost a 10-fold rate retardation of the HRP-catalyzed oxidation of $[Ru(bpy)_2(py)(H_2O)]^{2+}$.

$$[Ru(bpy)_2(H_2O)_2]^{2+} + py \rightleftharpoons [Ru(bpy)_2(H_2O)(py)]^{2+} \quad (K_{45}) \qquad (45)$$

The systematic analysis of the system HRP–H_2O_2–$[OsCl(bpy)_2(py)]^{2+}$ by cyclic voltammetry complemented by steady-state and stopped-flow experiments allowed a precise determination of the mechanism of catalysis and inhibition involved in the reaction of HRP with H_2O_2 and an outer-sphere single electron donor (Scheme 15) (*121*). There are numerous interesting findings and their solutions in this work. In particular, the electrochemical response increases for very small concentrations of H_2O_2, as expected, then a maximum and a descending dependence are observed at high concentration (cf. with data in Fig. 20). This behavior is caused by the reaction of the HRP Compound II with H_2O_2, forming oxyperoxidase (HRP Compound III), which inhibits the catalysis. However, Compound III is not a dead end in the catalytic process, since not only does it decompose slowly into

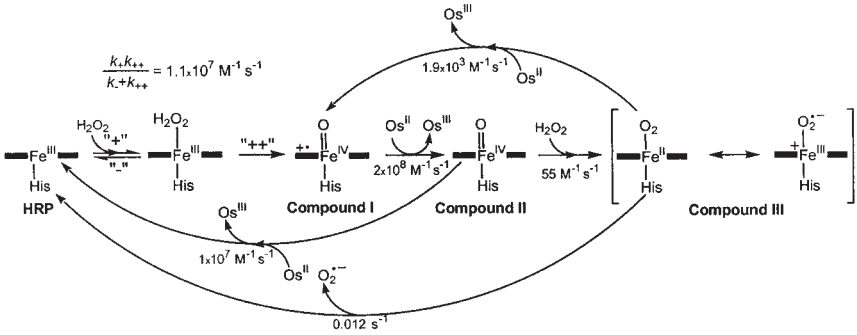

SCHEME 15. Detailed mechanism of HRP catalysis in the system HRP–H_2O_2–$[Os(bpy)_2(py)(H_2O)_2]^{2+}$ at pH 7.4 and 20 °C (*121*).

native HRP and superoxide ion ($k = 0.012\ s^{-1}$), it also reacts with Os^{II} to regenerate Compound I ($k = 1.9 \times 10^3\ M^{-1}\ s^{-1}$), thus starting again the primary catalytic cycle. In the framework of the mechanism in Scheme 15, conditions have been defined (low H_2O_2 concentrations, rapid recording of the voltammogram) which render inhibition insignificant.

The reductions of Compounds I and II by $[OsCl(bpy)_2py]^+$ are remarkably fast (2×10^8 and $1 \times 10^7\ M^{-1}\ s^{-1}$, respectively) compared to other electron donors, up to 10-fold faster than the fastest natural phenolic co-substrates, making this osmium(II) complex one of the most reactive co-substrates to HRP. Higher rates have only been observed for cyclometalated ruthenium(II) complexes described in Section VII. Consistent values for the reactivity of Compound II ($k \sim 1 \times 10^7\ M^{-1}\ s^{-1}$) have been obtained in the transient experiment, under steady-state, and from the electrochemical data. Stopped-flow studies have confirmed significantly higher reactivity of Compound I as compared to Compound II for this group of HRP electron donors. Michaelis–Menten kinetics has been found in the steady-state experiments. Its origin is discussed in some detail below. Intriguing hysteresis observed on cyclic voltammograms of the HRP–H_2O_2–$[OsCl(bpy)_2(py)]^{2+}$ systems and trace crossing behaviors have also been quantitatively explained (*121*). Hysteresis results from the delay time required for the various forms of the enzyme to reach a steady state. Trace crossing results from the additional interference of cosubstrate diffusion in the control of the current.

Two procedures have been used to reassemble apo-HRP employing the heme 1-(3-aminopropyl)imidazole conjugate (*201*). The first, targeted modification, included the complexation of *cis*-$[Ru(phen)_2$

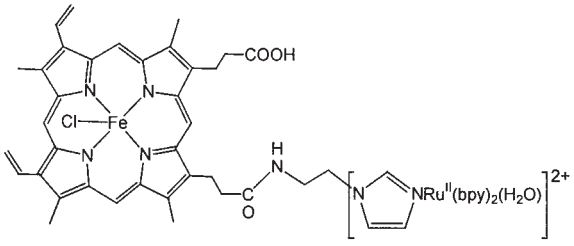

SCHEME 16. The ruthenium complex of the hemin and 1-(3-aminopropyl)-imidazole conjugate used for reconstitution of apo-HRP. From Ref. (*201*).

$(H_2O)_2]^{2+}$ with the imidazole residue of the conjugate followed by the loading of the resulting complex (Scheme 16) into the apo enzyme. The second procedure involved the reconstitution of apo-HRP with the conjugate followed by the complexation with *cis*-$[Ru(phen)_2(H_2O)_2]^{2+}$. Both approaches gave similar Ru-containing catalytically active (72 and 83% relative to native HRP with respect to ABTS) but electrochemically silent preparations capable of intramolecular oxidation by H_2O_2 of ruthenium(II) coordinated to an imidazole arm of the conjugate.

VI. Chiral Complexes

The principal question addressed, is there any kind of chiral recognition in electron transfer reactions involving GO or HRP and enantiomerically pure metal complexes. The chirality of optically active metal complexes may be different. Examples include central carbon chirality, when a complex has a side chain with an asymmetric sp^3 carbon (Chart 2A), planar chirality as in the case of asymmetrically 1,2-substituted ferrocenes (Chart 2B,C), and central metal chirality when an octahedral central metal itself generates Λ and Δ enantiomers (Chart 2D) (*202*). These three types are discussed in this section.

The very first two reports dealing with the central carbon chirality set up a fog of scientific intrigue. Electrochemical studies of Marx-Tibbon *et al.*, have suggested that (*S*)-*N*,*N*-dimethyl-1-ferrocenylethylamine (Chart 2A) reacts with reduced GO twice as fast as the corresponding *R* enantiomer (*203*). Less than a year later, Alzari and co-workers could not reproduce the results and the enantioselectivity has not been observed for this pair of enantiomers (*204*). Careful reading of the both publications raises some questions. The study of the effect of *N*,*N*-dimethyl-1-ferrocenylethylamine

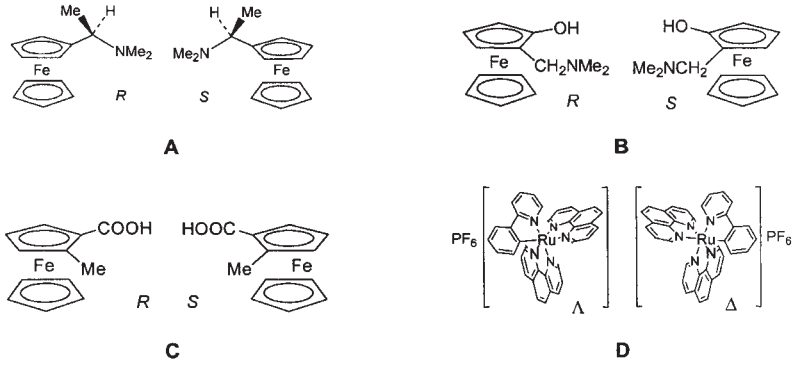

CHART 2. Examples of chiral complexes studied in redox reactions with GO, HRP, and cytochrome *c* peroxidase.

concentration on the electrocatalytic anodic current has revealed the Michaelis–Menten dependence with $I_{max} = 25$ μA for both enantiomers and $K_M = 0.04$ and 0.11 mM for *S* and *R* forms, respectively (*203*). This implies that the stereoselectivity should be observed when the mediator concentration is lower, preferably much lower, than the Michaelis constant K_M. Electrochemical measurements reported by Alzari *et al.*, have been performed at the ferrocene concentration of 0.24 mM (*204*). If the data of Marx-Tibbon were correct, the current ratio for the *S* and *R* enantiomers should be as low as 1.25 at this concentration. The ratio is too close to unity for any constructive conclusion on enantioselectivity. (*S*)- and (*R*)-*N*,*N*-Dimethyl-1-ferrocenylethylamines have again been tested with GO but even at higher mediator concentrations (0.5–1.0 mM) (*76*). Practically identical rate constants have been documented for both enantiomers, as anticipated. The reports from three different groups suggest that if the central carbon chirality plays any role in electrocatalysis by GO, this might occur under a very narrow set of conditions.

Planar chirality is a valuable feature of the ferrocene chemistry (Chart 2B,C) (*205*). This "unnatural" chirality type has attracted attention of several groups. Sadeghi and co-workers have demonstrated that the planar chiral ferrocenes **B** are recognized by cytochrome *c* peroxidase (*206*). The rate constants for the oxidation of *R* and *S* enantiomers by the wild type enzyme equal 2.9×10^6 and 1.6×10^6 M^{-1} s^{-1}, respectively. Interestingly, the enantioselectivity inverts for the aspartate 34 for lysine mutant and the rate constants become equal to 5.9×10^6 and 14.8×10^6 M^{-1} s^{-1}, respectively. The discrimination of planar chiral ferrocenes is the case, but the stereoselectivity factors are lower than 3.

Recognition of the planar chirality by HRP has been investigated using enantiomers **C** in Chart 2 (*207*). There is a first-order kinetics in 2-methylferrocene carboxylic acid and HRP. The corresponding observed second-order rate constants equal 4.6×10^4 and 2.5×10^4 M^{-1} s^{-1} for *R* and *S* enantiomers, respectively, at $[H_2O_2] = 2 \times 10^{-4}$ M, pH 7, 25 °C. The enantioselectivity is strongly pH dependent and the pH profile is bell-shaped with a maximum at pH 7. The enantioselectivity almost vanishes at pH 5. Curiously, the oxidative activity of HRP is higher at lower pH. The highest enzymatic activity *is not* thus required for achieving the highest enantioselectivity. No discriminating ability has been found for heme-containing chloroperoxidase from *Caldariomyces fumago* (*207*). The steady-state kinetics of oxidation of the 2-methylferrocene carboxylic acids has been investigated under conditions when the enzyme displays the peroxidase activity, i.e., in the presence of H_2O_2 only. No enantioselectivity could principally be observed, if the catalysis is performed as oxidative *halogenation*, i.e., in the presence of hydrogen peroxide and chloride or bromide (*208*). The pH optimum for chloroperoxidase is around 3 and the enzyme is inactive toward ferrocenes at pH 5. The steady-state rate of generation of the ferricenium cations follows the Michaelis–Menten dependence at pH 2.75, showing no enantioselectivity. Two rationalizations are possible. It could be because of using a "wrong" pH as suggested by the pH-dependence of enantioselectivity for HRP and due to the fact that the electron transfer from ferrocene is not a rate-limiting step under the steady-state conditions, but rather the formation of Compound I.

HRP-generated cations of *S* and *R* enantiomers of 2-methylferrocene carboxylic acid have been used to demonstrate by UV–vis spectroscopy that their enzymatic *reduction* by reduced GO is also enantioselective, the *S* enantiomer being by a factor of 1.54 more reactive than *R*. The planar chiral enantioselectivity in the GO catalysis has also been confirmed by the cyclic voltammetry study of the 2-methylferrocene carboxylic acids in the presence of GO and D-glucose at glassy carbon and pyrolytic graphite electrodes at 25 °C and pH 7. The corresponding enantioselectivity factors k_S/k_R equal 1.7 and 1.6, respectively, matching the results of spectrophotometric measurements (*207*). The evidence described confirms that the electron transfer between oxidoreductases and planar chiral organometallics can be stereoselective, as well as their other synthetically important biotransformations (*209,210*). The enantioselective electron transfer cannot be observed in the case of (i) the "incorrect" rate-limiting step, (ii) unfavorable mediator concentration and pH, and

(iii) the deficit of charged groups attached to ferrocenes that eliminates coulombic interaction.

Moderate enantioselectivity factors have also been found for electron transfer reactions between HRP or GO and resolved octahedral ruthenium or osmium complexes, respectively. In particular, the rate constants for the oxidation of GO(red) by electrochemically generated Λ and Δ enantiomers of $[Os(4,4'\text{-}Me_2bpy)_3]^{3+}$ equal 1.68×10^6 and 2.34×10^6 M^{-1} s^{-1}, respectively (25 °C, pH 7) (*41*). The spectral kinetic study of the HRP-catalyzed oxidation of Λ and Δ isomers of the cycloruthenated complex $[Ru(phpy)(phen)_2]PF_6$ (Fig. 21) by hydrogen peroxide has revealed similarities with the oxidation of planar chiral 2-methylferrocene carboxlic acid (*211*). In both cases the stereoselecivity factor is pH dependent and the highest factors are not observed at the highest rates. The k_Λ/k_Δ ratio for $[Ru(phpy)(phen)_2]PF_6$ is close to 1 at pH 5–6.5 but increases to 2.5 at pH around 8 (*211*).

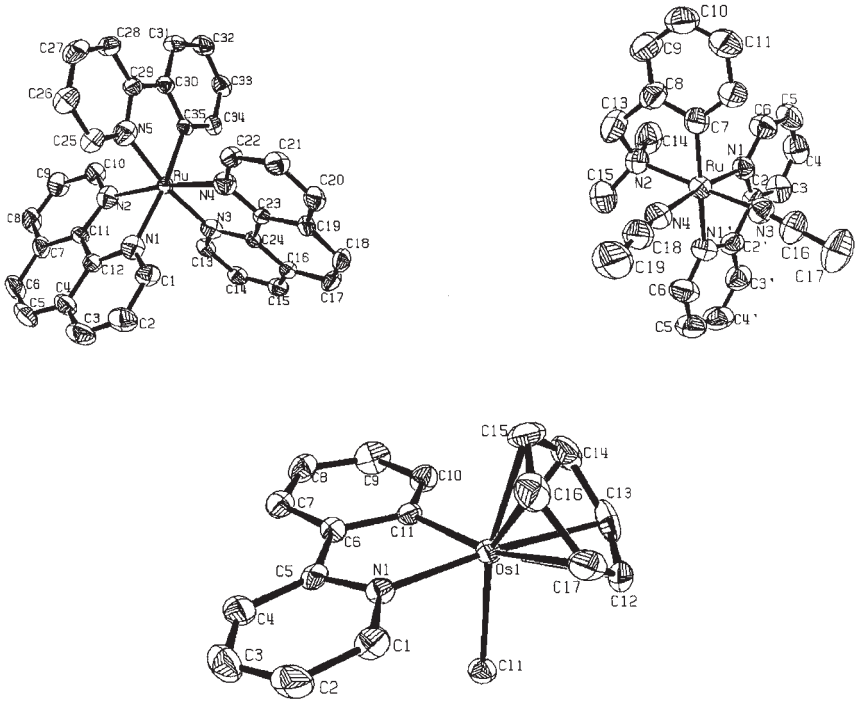

FIG. 21. Crystal structures of cyclometalated Ru^{II} and Os^{II} complexes $[Ru(phpy)(phen)_2]PF_6$, $[Ru(dmba)(bpy)(MeCN)_2]PF_6$ (*55*) and $[(\eta^6\text{-}C_6H_6)Os(phpy)Cl]$ (*235*). Counter ions of Ru^{II} complexes are not shown for clarity.

VII. Cyclometalated Ruthenium(II) and Osmium(II) Mediators

As already mentioned, tris-diimine complexes of ruthenium(II) and osmium(II) $[M(LL)_3]^{2+}$ (LL = bpy or phen) could be ideal mediators for GO and HRP due to their inertness to substitution and almost diffusion-controlled self-exchange rates (Section IV) providing high reactivity with GO (Table VII). But the $M^{II/III}$ redox potentials of the complexes in water are too high, excluding their applications in MET-based biosensors. There is however an elegant technique for eliminating the "high-potential" limitation. It preserves the structural motif and the reactivity of the complexes but decreases substantially the $M^{II/III}$ redox potentials. A metal–nitrogen bond should simply be replaced by a metal–carbon bond (Scheme 17) (*55*). The redox potentials of such compounds decrease profoundly due to a combination of two effects; lowering the overall complex charge and introducing a strong σ-donor ligand. Compounds with the σ-M–C bonds, which are stabilized by chelation, are known as cyclometalated complexes or metalacycles (*212,213*). First reported in 1965 (*214*), cyclometalated complexes of the platinum metals have been shown to be promising in various fields of chemistry including fine organic synthesis (*215–218*), catalysis (*219,220*), bioinorganic chemistry (*207,221–224*), and material science (*225–227*). An easy synthesis of cyclometalated Ru^{II} mediators involves cyclometalation of 2-phenylpyridine (2-phpy), 2-(4-tolyl)pyridine (2-topy), *N,N*-dimethylbenzylamine (dmbaH) (*55*), or 2-phenylimidazole (2-phim) (*228*) by $[(\eta^6\text{-}C_6H_6)Ru(\mu\text{-}Cl)Cl]_2$ (*229*), followed by treating ruthena (II)cycles formed with 2,2′-bipyridine or 1,10-phenanthroline type ligands to give a variety of target compounds (Scheme 18). These syntheses are more feasible than previous, where the complexes *cis*-$[RuCl_2(bpy)_2]$ or $[RuCl_3(tpy)]$ have been used to cyclometalate 2-phenylpyridine and its derivatives (*230–233*). A bunch of diverse compounds have been prepared in good yields. Crystal structures of some of them are shown in Fig. 21 and their useful properties are summarized in Table IX.

Steady-state rates of the HRP-catalyzed oxidation of Ru^{II} into Ru^{III} by H_2O_2 have been measured spectrophotometrically (*55*). In contrast

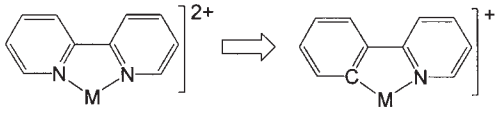

SCHEME 17. Designing cyclometalated Ru^{II} and Os^{II} mediators (*55*).

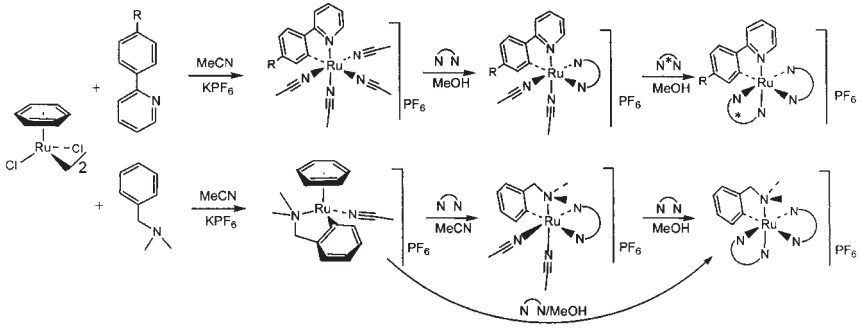

SCHEME 18. Synthetic routes to cyclometalated Ru^{II} mediators (*55*). 2-Phenylimidazole reacts similar to 2-phenylpyridine (*228*).

TABLE IX

REDOX POTENTIALS CYCLOMETALATED Ru^{II} AND Os^{II} COMPLEXES AND RATE CONSTANTS FOR THE ELECTRON EXCHANGE BETWEEN M^{II}/M^{III} SPECIES AND HRP/GO, RESPECTIVELY (pH 6.7, 0.01 M PHOSPHATE, 25 °C)

Complex	Redox potentials/mV (vs. SCE)	HRP: $10^{-8} \times k_7$/ $M^{-1}s^{-1}$	GO: $10^{-7} \times k_{12}$/ $M^{-1}s^{-1}$	Ref.
$[Ru(phpy)(bpy)_2]PF_6$	280	0.3	0.35	(*55*)
$[Ru(phpy)(phen)_2]PF_6$	280	1.7	0.75	(*55*)
$[Ru(phpy)(5,6\text{-}Me_2phen)_2]PF_6$	340	0.38	1.8	(*55*)
$[Ru(phpy)(bpy)(5,6\text{-}Me_2phen)]PF_6$	295	0.8	0.85	(*55*)
$[Ru(topy)(phen)_2]PF_6$	265	1.1	0.93	(*55*)
$[Ru(phim)(phen)_2]PF_6$	250	0.93	0.81	(*228*)
$[Ru(phim)(bpy)_2]PF_6$	205	0.23	0.48	(*228*)
$[Ru(phim)(4,4'\text{-}Me_2bpy)_2]PF_6$	130	0.65	0.52	(*228*)
$[Ru(dmba)(bpy)_2]PF_6$	190	0.30	1.0	(*55*)
$[Ru(phpy)(acac)(bpy)_2]^+$	−210	–	No coupling	Unpublished
$[Os(phpy)(phen)_2]PF_6$	30	–	1.1	(*235*)
$[Os(phpy)(4,4'\text{-}Me_2bpy)_2]PF_6$	−100	–	0.1	(*235*)

to the *N,N*-diimine complexes $[Ru^{II}(LL)_2X_2]$ (*201*), a first-order kinetics in $[Ru^{II}]$ does not hold and the reaction rate levels off at $[Ru^{II}] > 1 \times 10^{-5}$ M, Fig. 22, as for $[Os(bpy)_2(py)(H_2O)]^{2+}$ (*121*). This indicates that the rate constant k_1 for the formation of Compound I of HRP contributes to the overall rate. Fitting the data in Fig. 22 to Eq. (46), which holds

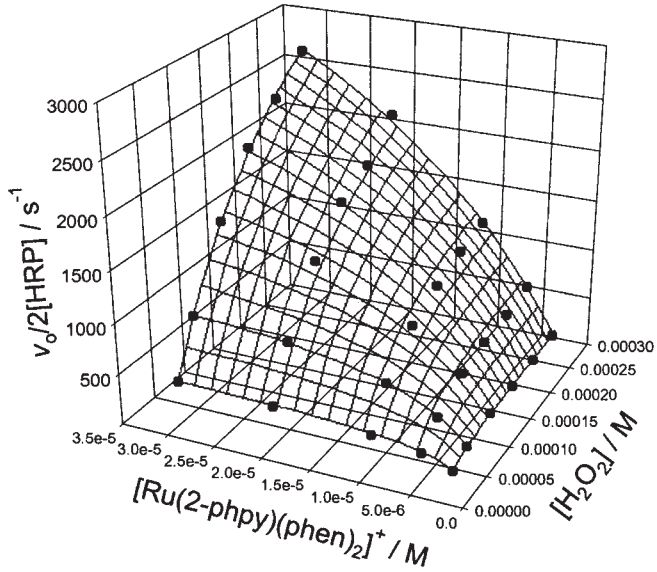

FIG. 22. 3D plot showing steady-state rate of the HRP-catalyzed oxidation of $[Ru(phpy)(phen)_2]^+$ by H_2O_2 against $[H_2O_2]$ and $[Ru^{II}]$ at [HRP] 5×10^{-11}, pH 6.7, 2% MeOH, 25 °C. From Ref. (*55*).

when $k_6 > k_7$ [Eqs. (5)–(7)], affords the rate constants k_5 and k_7 of 2.4×10^7 and 1.7×10^8 M^{-1} s^{-1}, respectively.

$$v_o = 2k_5k_7[H_2O_2[Ru^{II}][HRP]/(k_5[H_2O_2] + k_7[Ru^{II}]) \quad (46)$$

Thus, the $[Ru(phpy)(phen)_2]^+$ ruthenacycle is a strikingly reactive electron donor for HRP. High rate constants for other complexes are summarized in Table IX. Plant peroxidases from sources other than horseradish also show a high reactivity to cyclometalated ruthenium(II) complexes listed in Table IX (*234*).

The cyclometalated Ru^{III} species generated electrochemically are very reactive in oxidation of reduced flavin adenine dinucleotide of GO. The excellent coupling between GO reduced by D-glucose and the Ru^{III} species is illustrated by the rate constant for the complex $[Ru(phpy)(Me_2phen)_2]PF_6$, which equals 1.8×10^7 M^{-1} s^{-1} at pH 6.7 and 25 °C. There are no complexes of higher reactivity in Table VII! Other cycloruthenated complexes are very reactive as well (Table IX). Variation of the nature of cycloruthenated and diimine

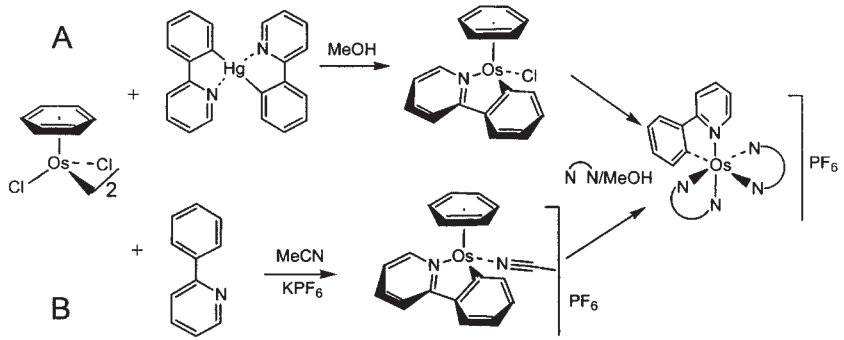

SCHEME 19. Synthetic routes to cyclometalated Os^{II} mediators.

ligands allows lowering of the redox potentials of the complexes practically without compromising the reactivity.

The performance of osmium mediators is higher than that of ruthenium ones (Table VII). Therefore, structurally similar cyclometalated Os^{II} compounds have been prepared and tested with GO. There are two synthetic pathways to osma(II)cycles $[Os(phpy)(LL)_2]PF_6$ (LL = phen and 4,4′-Me_2-2,2′-bpy) (*235*). Better yields are obtained in the reaction of $[(\eta^6\text{-}C_6H_6)Os(\mu\text{-}Cl)Cl]_2$ with the symmetric organomercurial $[Hg(phpy)_2]$ in MeOH. This transmetalation reaction affords $[(\eta^6\text{-}C_6H_6)Os(phpy)Cl]$ in a 65% yield (Scheme 19A). Its X-ray crystal structure is shown in Fig. 21. The reaction of $[(\eta^6\text{-}C_6H_6)Os(\mu\text{-}Cl)Cl]_2$ with 2-phenylpyridine in MeCN affords $[(\eta^6\text{-}C_6H_6)Os(phpy)(MeCN)]PF_6$ via sp^2-C–H bond cleavage in a low yield (16%) (Scheme 19B). Both the complexes react cleanly with diimine ligands LL to afford the cyclometalated compounds $[Os(phpy)(LL)_2]PF_6$. Their redox potentials (Table IX) are appreciably lower as compared with the cyclometalated ruthenium counterparts, as expected.

The electrochemically generated Os^{III} derivatives of $[Os^{II}(phpy)(LL)_2]^+$, oxidize reduced GO with second-order rate constants of 1.1×10^7 and 0.1×10^7 M^{-1} s^{-1} for LL = phen and 4,4′-Me_2-2,2′-bpy, respectively (25 °C, pH 7). The low-potential cyclometalated osmium(II) complexes are very reactive toward the enzyme even when electron transfer may be an up-hill process as in the case of $[Os^{II}(phpy)(4,4'\text{-}Me_2bpy)_2]^+$. The rate constant k_{12} for $[Os^{II}(phpy)(phen)_2]^+$ (1.1×10^7 M^{-1} s^{-1}) is in the range typical of the most reactive mediators of GO. Further "cathodic" tuning of the redox potential of osma(II)cycles has been achieved by using 4,4′-Me_2bpy as a diimine ligand. The mediator $[Os^{II}(phpy)(4,4'\text{-}Me_2bpy)_2]^+$ has in fact a very low potential (–100 mV),

but this compromises the activity. The rate constant k_{12} decreases more than 10-fold compared to $[Os^{II}(phpy)(phen)_2]^+$. It should be pointed out that such a potential decrease due to the use of an electron-rich diimine ligand does not decrease the reactivity of ruthenacyclic mediators with $k_{12} \sim 10^7$ M^{-1} s^{-1} (Table IX). The redox potential of even $[Ru(phim)(4,4'\text{-}Me_2bpy)_2]^+$ is however still appreciably higher than that of flavin adenine dinucleotide in GO. This suggests that high rates of the electron exchange with GO are difficult to achieve when the redox potential of a mediator becomes closer to that of $FADH_2$/$FADH_2^{\bullet+}$ and $FADH^{\bullet}/FADH^+$ couples of GO. The latter statement is supported by the fact that ruthenacycles with very low potentials do not exchange electrons with GO at all (Table IX).

Up to now the mediator properties have been discussed focusing on MET. There is however an additional aspect of the entire mediator concept. Mediators are also molecules that facilitate enzymatic oxidation of other substrates, the oxidation of which by enzymes only is slow (*236,237*). They are *oxidative mediators* that speed up the oxidation of poor substrates. They are oxidized by enzymes first and then, using their oxidative potential, react with substrate molecules to form product(s). Equations (47) and (48) illustrate the mechanism of action of oxidative mediators in catalysis by HRP.

$$\text{Compound I/II} + M_{red} \longrightarrow HRP + M_{ox} \tag{47}$$

$$M_{ox} + AH_2 \longrightarrow M_{red} + AH^{\bullet} \quad (k_{48}) \tag{48}$$

Here a mediator is an electron shuttle between the enzyme active site and a target molecule rather than between the active site and an electrode as in MET. Cyclometalated ruthenium(II) complexes are also promising as oxidative mediators in co-oxidation with plant peroxidases (*234*). The mediating efficacy of $[Ru(phpy)(bpy)_2]PF_6$ has been evaluated for catechol as a poor substrate of peroxidase from sweet potato (*238*). The pseudo-first-order rate constant for the enzymatic oxidation of catechol increases by more than 4 orders of magnitude on addition of 0.1 mM $[Ru(phpy)(bpy)_2]^+$. Using the property of $Ru^{II/III}$ complexes to change color in redox reactions, a routine for calculating the second-order rate constant k_{48} for the oxidation of catechol by the Ru^{III} complex generated enzymatically from $[Ru^{II}(phpy)(bpy)_2]^+$ has been put forward. The $k_{48} = 0.75$ M^{-1} s^{-1} has been obtained from UV–vis measurements of the limiting Ru^{II} concentrations at different [catechol] (pH 4.5, 25 °C).

VIII. Concluding Remarks

This review consolidates more then 15 years of interest of the author in this field which is at the interface of inorganic, organometallic, analytical, physical chemistry, enzymology, and biochemistry. Interactions of organometallic compounds with enzymes as functioning biological motors have been always particularly appealing and fascinating. It is now a recognized discipline (*239*) referred to as bioorganometallic chemistry or organometallic biochemistry that has been highlighted a decade ago (*209,210,240*).

Glucose oxidase from *A. niger* and horseradish peroxidase are the enzymes that catalyze absolutely different reactions. They have different prosthetic groups and there is nothing similar in mechanisms of their action. But they have common electron transfer mediators! If good for one of the enzymes, the mediator appears to be good for the other. Several examples show that this rule does not hold for other redox enzymes. Explanations will probably be given in future studies. The second order rate constants of 10^8 and 10^7 M^{-1} s^{-1} are the highest values achieved so far for HRP and GO, respectively, using designed transition metal mediators. Such speed of electron movement guarantees successful applications of various devices involving **M**ediated **E**lectron **T**ransfer.

References

1. "*Methods of Enzymic Analysis, Vol. 3: Enzymes 1: Oxidoreductases, Transferases*"; Ed. Moss, D. W.; Verlag Chemie: Weinheim, 1983.
2. "*Enzyme Handbook: Volume 10: Class 1.1.: Oxidoreductases*"; Eds. Schomburg, D.; Stephan, D.; Springer: Berlin, Germany, 1995.
3. Poulos, T. L. *Adv. Inorg. Biochem.* **1988**, *7*, 1.
4. Bertini, I.; Gray, H. B.; Lippard, S. J.; Valentine, J. S. "*Bioinorganic Chemistry*"; Univ. Sci. Books: Mill Valley, California, 1994.
5. "*Bioinorganic Chemistry*"; Eds. Lippard, S. J.; Berg, J. M.; Univ. Sci. Books: Mill Valley, California, 1994.
6. English, A. M.; Tsaprailis, G. *Adv. Inorg. Chem.* **1995**, *43*, 79.
7. Sono, M.; Roach, M. P.; Coulter, E. D.; Dawson, J. H. *Chem. Rev.* **1996**, *96*, 2841.
8. Dunford, H. B. "*Heme Peroxidases*"; Wiley-VCH: New York, Chichester, Weinheim, 1999.
9. Solomon, E. I.; Brunold, T. C.; Davis, M. I.; Kemsley, J. N.; Lee, S.-K.; Lehnert, N.; Neese, F.; Skulan, A. J.; Yang, Y.-S.; Zhou, J. *Chem. Rev.* **2000**, *100*, 235.
10. Kulys, J. J.; Čenas, N. K. *Biochim. Biophys. Acta* **1983**, *744*, 57.
11. Turner, A. P. F.; Karube, I.; Wilson, G. S. "*Biosensors. Fundamentals and Applications*"; Oxford University Press: Oxford, New York, Tokyo, 1987.

12. Willner, I.; Katz, E. *Angew. Chem., Int. Ed. Engl.* **2000**, *39*, 1180.
13. O'Connell, P. J.; Guilbault, G. G. *Anal. Lett.* **2001**, *34*, 1063.
14. Schuhmann, W. *Rev. Molec. Biotech.* **2002**, *82*, 425.
15. Gáspár, S.; Bontidean, I.; Collins, A.; Niculescu, M.; Nistor, C.; Sukharev, V.; Ryabov, A. D.; Csöregi, E. "*Recent Res. Dev. Anal. Chem*", Vol. 2; Ed. Pandalai, S. G.; Transworld Research Network: Kerala, India, 2002, p. 33.
16. Chaubey, A.; Malhotra, B. D. *Biosens. Bioelectron.* **2002**, *17*, 441.
17. Wilson, R.; Turner, A. P. F. *Biosens. Bioelectron.* **1992**, *7*, 165.
18. Raba, J.; Mottola, H. A. *Crit. Rev. Anal. Chem.* **1995**, *25*, 1.
19. Schuhmann, W. *Biosens. Biolectron.* **1995**, *10*, 181.
20. Hecht, H. J.; Kalisz, H. M.; Hendle, J.; Schmid, R. D.; Schomburg, D. *J. Mol. Biol.* **1993**, *229*, 153.
21. Wohlfahrt, G.; Witt, S.; Hendle, J.; Schomburg, D.; Kalisz, H. M.; Hecht, H.-J. *Acta Crystallograph., Sect. D: Biol. Crystallograp.* **1999**, *D55*, 969.
22. Gibson, Q. H.; Swoboda, B. E. P.; Massey, V. *J. Biol. Chem.* **1964**, *239*, 3927.
23. Weibel, M. K.; Bright, H. J. *J. Biol. Chem.* **1971**, *246*, 2734.
24. Su, Q.; Klinman, J. P. *Biochemistry* **1999**, *38*, 8572.
25. Aleksandrovskii, Y. A.; Bezhikina, L. V.; Rodionov, Y. V. *Biokhimiya (Moscow)* **1981**, *46*, 708.
26. Stankovich, M. T. *Anal. Biochem.* **1980**, *109*, 295.
27. Veitch, N. C.; Smith, A. T. *Adv. Inorg. Chem.* **2000**, *51*, 107.
28. Dolman, D.; Newell, G. A.; Thurlow, M. D.; Dunford, H. B. *Can. J. Biochem.* **1975**, *53*, 495.
29. Gajhede, M.; Schuller, D. J.; Henriksen, A.; Smith, A. T.; Poulos, T. L. *Nature Struct. Biol.* **1997**, *4*, 1032.
30. Henriksen, A.; Smith, A. T.; Gajhede, M. *J. Biol. Chem.* **1999**, *274*, 35 005.
31. Duine, J. A. *J. Biosci. Bioeng.* **1999**, *88*, 231.
32. Mcintire, W. S. *Ann. Rev. Nutrition* **1998**, *18*, 145.
33. Anthony, C.; Ghosh, M. *Prog. Biophys. Mol. Biol.* **1998**, *69*, 1.
34. Duine, J. A. "*Bioinorganic Catalysis*"; Eds. Reedijk, J.; Bouwman, E.; Marcel Dekker, Inc: New York, 1999, p. 563.
35. Anthony, C. *Antioxidants & Redox Signaling* **2001**, *3*, 757.
36. Ikeda, T. "*Frontiers in Biosensorics. Fundamental Aspects*", Vol. 1; Eds. Scheller, F. W.; Schubert, F.; Fedrowitz, J.; Birkhauser verlag: Basel, 1997, p. 243.
37. Razumiene, J.; Niculescu, M.; Ramanavicius, A.; Laurinavicius, V.; Csöregi, E. *Electroanalysis* **2002**, *14*, 43.
38. Mathews, F. S. *Meth. Enzymol.* **1995**, *258*, 191.
39. Oubrie, A.; Rozeboom, H. J.; Kalk, K. H.; Huizinga, E. G.; Dijkstra, B. W. *J. Biol. Chem.* **2002**, *277*, 3727.
40. Lever, A. B. V. *Inorg. Chem.* **1990**, *29*, 1271.
41. Nakabayashi, Y.; Nakamura, K.; Kawachi, M.; Motoyama, T.; Yamauchi, O. *J. Biol. Inorg. Chem.* **2003**, *8*, 45.
42. Hall, J. W.; Tucker, D. M. *Anal. Biochem.* **1968**, *26*, 12.
43. Afanas'eva, G. A.; Shcherbukhin, V. D. *Prikl. Biokhim. Mikrobiol.* **1975**, *11*, 460.
44. Kawaguri, M.; Yoshioka, T.; Nankai, S. *Denki Kagaku oyobi Kogyo Butsuri Kagaku* **1990**, *58*, 1119.
45. Bartlett, P. N.; Ali, Z.; Eastwick-Field, V. *J. Chem. Soc., Faraday Trans.* **1992**, *88*, 2677.
46. Du, G.; Lin, C.; Bocarsly, A. B. "*Proceedings of the Fifth International Symposium on Redox Mechanisms and Interfacial Properties of Molecules of Biological Importance*", 1993, p. 197.

47. Taliene, V. R.; Ruzgas, T.; Razumas, V.; Kulys, J. *J. Electroanal. Chem.* **1994**, *372*, 85.
48. Shul'ga, A. A.; Koudelka-Hep, M.; de Rooij, N. F. *Sens. Actua. B: Chem.* **1995**, *B27*, 432.
49. Ikeda, S.; Yoshioka, T.; Nankai, S. *Denki Kagaku oyobi Kogyo Butsuri Kagaku* **1995**, *63*, 1145.
50. Dou, X.; Ozaki, Y. *Appl. Spectrosc.* **1998**, *52*, 815.
51. Ge, F.; Zhang, X.-E.; Zhang, Z.-P.; Zhang, X.-M. *Anal. Lett.* **1998**, *31*, 383.
52. Chailapakul, O.; Promnil, J.; Somasundrum, M.; Tanticharoen, M. *J. Sci. Res. Chulalongkorn Univ.* **2000**, *25*, 157.
53. Marcus, R. A.; Sutin, N. *Biochim. Biophys. Acta* **1985**, *811*, 265.
54. Marcus, R. A. *Angew. Chem. Int. Ed. Engl.* **1993**, *32*, 1111.
55. Ryabov, A. D.; Sukharev, V. S.; Alexandrova, L.; Le Lagadec, R.; Pfeffer, M. *Inorg. Chem.* **2001**, *30*, 6529.
56. Zahl, A.; van Eldik, R.; Swaddle, T. W. *Inorg. Chem.* **2002**, *41*, 757.
57. Coury, L. A. Jr.; Oliver, B. N.; Egekeze, J. O.; Sosnoff, C. S.; Brumfield, J. C.; Buck, R. P.; Murray, R. W. *Anal. Chem.* **1990**, *62*, 452.
58. Yang, L.; Coury, L. A. Jr.; Murray, R. W. *J. Phys. Chem.* **1993**, *97*, 1694.
59. Fultz, M. L.; Durst, R. A. *Anal. Chim. Acta* **1982**, *140*, 1.
60. Young, R. C.; Keene, F. R.; Meyer, T. J. *J. Am. Chem. Soc.* **1977**, *99*, 2468.
61. Hoddenbagh, J. M. A.; Macartney, D. H. *Inorg. Chem.* **1990**, *29*, 245.
62. Meyer, T. J.; Taube, H. *Inorg. Chem.* **1968**, *7*, 2369.
63. Doine, H.; Swaddle, T. W. *Can. J. Chem.* **1988**, *66*, 2763.
64. Cheung, E.; English, A. M. *Can. J. Chem.* **1995**, *73*, 1181.
65. Pladziewicz, J. R.; Espenson, J. H. *J. Phys. Chem.* **1971**, *75*, 3381.
66. Nielson, R. M.; Hupp, J. T. *Inorg. Chem.* **1996**, *35*, 1402.
67. Holzwarth, J.; Juergensen, H. *Berichte Bunsen Gesellschaft Phys. Chem.* **1974**, *78*, 526.
68. Creaser, I. I.; Sargeson, A. M.; Zanella, A. W. *Inorg. Chem.* **1983**, *22*, 4022.
69. Grace, M. R.; Swaddle, T. W. *Inorg. Chem.* **1993**, *32*, 5597.
70. Küppers, H. J.; Neves, A.; Pomp, C.; Ventur, D.; Wieghardt, K.; Nuber, B.; Weiss, J. *Inorg. Chem.* **1986**, *25*, 2400.
71. Cass, A. E. G.; Davis, G.; Francis, G. D.; Hill, H. A. O.; Aston, W. J.; Higgins, I. J.; Plotkin, E. O.; Scott, L. D. L.; Turner, A. P. F. *Anal. Chem.* **1984**, *56*, 667.
72. Cass, A. E. G.; Davis, G.; Green, M. J.; Hill, H. A. O. *J. Electroanal. Chem.* **1985**, *190*, 117.
73. Nicholson, R. S.; Shain, I. *Anal. Chem.* **1964**, *36*, 706.
74. Bourdillon, C.; Demaille, C.; Moiroux, J.; Savéant, J.-M. *J. Am. Chem. Soc.* **1993**, *115*, 2.
75. Bartlett, P. N.; Pratt, K. F. E. *J. Electroanal. Chem.* **1995**, *397*, 53.
76. Forrow, N. J.; Sanghera, G. S.; Walters, S. J. *J. Chem. Soc., Dalton Trans.* **2002**, 3187.
77. Bartlett, P. N.; Tebbutt, P.; Whitaker, R. G. *Progr. React. Kinet.* **1991**, *16*, 55.
78. Antiochia, R.; Lavagnini, I.; Magno, F. *Electroanalysis* **2001**, *13*, 601.
79. Ryabov, A. D.; Firsova, Y. N.; Nelen', M. I. *Appl. Biochem. Biotechnol.* **1996**, *61*, 25.
80. Vaastroebiezen, S. A. M.; Janssen, A. P. M.; Janssen, L. J. *J. Anal. Chim. Acta* **1993**, *280*, 217.
81. Tegoulia, V.; Gnedenko, B. B.; Ryabov, A. D. *Biochem. Molec. Biol. Intern.* **1993**, *31*, 769.
82. Luong, J. H. T.; Male, K. B.; Zhao, S. *Anal. Biochem.* **1993**, *212*, 269.
83. Male, K. B.; Luong, J. H. T.; Trani, M. *Appl. Biochem. Biotechnol.* **1994**, *44*, 91.
84. Fersht, A. ''*Enzyme Structure and Mechanism*''; Freeman: New York, 1985.
85. Keleti, T. ''*Basic Enzymic Kinetics*''; Mir: Moscow, 1990.
86. Fersht, A. ''*Structure and Mechanism in Protein Science: A Guide to Enzyme Catalysis and Protein Folding*''; Freeman: New York, 1999.

87. Ryabov, A. D.; Amon, A.; Gorbatova, R. K.; Ryabova, E. S.; Gnedenko, B. B. *J. Phys. Chem.* **1995**, *99*, 14 072.
88. Deshaies, C.; Chopineau, J.; Moiroux, J.; Bourdillon, C. *J. Phys. Chem.* **1996**, *100*, 5063.
89. Fraser, D. M.; Zakeeruddin, S. M.; Graetzel, M. *Biochim. Biophys. Acta* **1992**, *1099*, 91.
90. Ryabov, A. D.; Ryabova, E. S.; Reshetova, M. D. *J. Organomet. Chem.* **2001**, *637–639*, 469.
91. Bazhenova, M. A.; Bogoush, S. S.; Herbst, A. G.; Demeschik, T. V.; Komarovskya, Y. G.; Kurova, V. S.; Reshetova, M. D.; Ryabov, A. D.; Ryabova, E. S.; Firsova, Y. N. *Izv. RAN, Ser. Khim.* **1996**, 2575.
92. Hansch, C.; Leo, A.; Taft, R. W. *Chem. Rev.* **1991**, *91*, 165.
93. Voet, J. G.; Coe, J.; Epstein, J.; Matossian, V.; Shipley, T. *Biochemistry* **1981**, *20*, 7182.
94. Firsova, Y. N.; Ryabov, A. D. *Izv RAN, ser. Khim.* **1997**, 1795.
95. "*Chemical Modification of Enzymes*"; Eds. Kurganov, B. I.; Nagradova, N. K.; Lavrik, O. I.; Nova Sci. Publ: New York, 1996.
96. Qi, D.; Tann, C.-M.; Haring, D.; Distefano, M. D. *Chem. Rev.* **2001**, *101*, 3081.
97. Perevalova, E. G.; Reshetova, M. D.; Grandberg, K. I. "*Methods of Elementoorganic Chemistry. Organoiron Compounds. Ferrocene*"; Nauka: Moscow, 1983.
98. Degani, Y.; Heller, A. *J. Phys. Chem.* **1987**, *91*, 1285.
99. Bartlett, P. N.; Whitaker, R. G.; Green, M. J.; Frew, J. *J. Chem. Soc., Chem. Commun.* **1987**, 1603.
100. Bartlett, P. N.; Bradford, V. Q.; Whitaker, R. G. *Talanta* **1991**, *38*, 57.
101. Ryabov, A. D.; Trushkin, A. M.; Baksheeva, L. I.; Gorbatova, R. K.; Kubrakova, I. V.; Mozhaev, V. V.; Gnedenko, B. B.; Levashov, A. V. *Angew. Chem., Int. Ed. Engl.* **1992**, *31*, 789.
102. Kunugi, S.; Murakami, Y.; Ikeda, K.; Itoh, N. *Int. J. Biol. Macromol.* **1992**, *14*, 210.
103. Suzawa, T.; Ikariyama, Y.; Aizawa, M. *Anal. Chem.* **1994**, *66*, 3889.
104. Badia, A.; Carlini, R.; Fernandez, A.; Battaglini, F.; Mikkelsen, S. R.; English, A. M. *J. Am. Chem. Soc.* **1993**, *115*, 7053.
105. Wolowacz, S. E.; Yon Hin, B. F. Y.; Lowe, C. R. *Anal. Chem.* **1992**, *64*, 1541.
106. Schuhmann, W.; Ohara, T. J.; Schmidt, H. L.; Heller, A. *J. Am. Chem. Soc.* **1991**, *113*, 1394.
107. Muzutani, F.; Asai, M. *Denki Kagaku* **1988**, *56*, 1100.
108. Riklin, A.; Katz, E.; Willner, I.; Stocker, A.; Bückmann, A. F. *Nature* **1995**, *376*, 672.
109. Bückmann, A.F.; Wray, V.; Stocker, A. *Meth. Enzymol.* **1997**, 360.
110. Willner, I.; Willner, B. *Trends Biotechnol.* **2001**, *19*, 222.
111. Willner, I.; Willner, B. *Pure Appl. Chem.* **2002**, *74*, 1773.
112. Katz, E.; Riklin, A.; Heleg-Shabtai, V.; Willner, I.; Buckmann, A. F. *Anal. Chim. Acta* **1999**, *385*, 45.
113. Goral, V. N.; Nelen', M. I.; Ryabov, A. D. *Anal. Lett.* **1995**, *28*, 2139.
114. Micheel, B.; Bierwolf, D.; Randt, A.; Franz, H.; Mohr, J. "*Antigen-Antibody React., Contrib. Symp. Immunol., 4th*"; Ed. Ambrosius, H.; Fischer, Jena, Ger. Dem. Rep., 1971, p. 72.
115. Epton, R.; Hobson, M. E.; Marr, G. *J. Organomet. Chem.* **1977**, *134*, C23.
116. Epton, R.; Hobson, M. E.; Marr, G. *J. Organomet. Chem.* **1978**, *149*, 231.
117. Epton, R.; Hobson, M. E.; Marr, G. *Enzyme Microb. Technol.* **1979**, *1*, 37.
118. Frew, J. E.; Harmer, M. A.; Hill, H. A. O.; Libor, S. I. *J. Electroanal. Chem.* **1986**, *201*, 1.
119. Ryabov, A. D.; Goral, V. N. *J. Biol. Inorg. Chem.* **1997**, *2*, 182.
120. Ryabov, A. D.; Goral, V. N.; Ivanova, E. V.; Reshetova, M. D.; Hradsky, A.; Bildstein, B. *J. Organomet. Chem.* **1999**, *589*, 85.

121. Dequaire, M.; Limoges, B.; Moiroux, J.; Saveant, J.-M. *J. Am. Chem. Soc.* **2002**, *124*, 240.
122. Berezin, I. V.; Martinek, K.; Yatsimirskii, A. K. *Usp. Khim.* **1973**, *42*, 1729.
123. Martinek, K.; Yatsimirsky, A. K.; Levashov, A. V.; Berezin, I. V. "*Micellization, Solubilization, and Microemulsions*", Vol. 2; Ed. Mittal, K. L.; Plenum Press: New York, London, 1977, p. 489.
124. Gray, H.; Winkler, J. R. *Ann. Rev. Biochem.* **1996**, *65*, 537.
125. Folkes, L. K.; Candeias, L. P. *FEBS Lett.* **1997**, *412*, 305.
126. Candeias, L. P.; Folkes, L. K.; Wardman, P. *Biochemistry* **1997**, *36*, 7081.
127. Farhangrazi, Z. S.; Fosset, M. E.; Powers, L. S.; Ellins, W. R. *Biochemistry* **1995**, *34*, 2866.
128. Childs, R. E.; Bardsley, W. G. *Biochem. J.* **1975**, *145*, 93.
129. Ozaki, S.-i.; Ortiz de Montellano, P. R. *J. Am. Chem. Soc.* **1995**, *117*, 7056.
130. Goral, V. N.; Ryabov, A. D. *Biochem. Mol. Biol. Int.* **1998**, *45*, 61.
131. Sadeghi, S. J.; Gilardi, G.; Cass, A. E. G. *Biosens. Bioelectron.* **1997**, *12*, 1191.
132. Hasinoff, B. B.; Dunford, H. B. *Biochemistry* **1970**, *9*, 4930.
133. Erman, J. E.; Vitello, L. B. *Biochim. Biophys. Acta* **2002**, *1597*, 193.
134. Tollin, G. *Elect. Trans. Chem.* **2001**, *4*, 202.
135. Erman, J. E.; Vitello, L. B. *J. Biochem. Molec. Biol.* **1998**, *31*, 307.
136. Erman, J. E.; Satterlee, J. D. *Adv. Biophys. Chem.* **1995**, *5*, 141.
137. Cooper, J. M.; Bannister, J. V.; McNeil, C. J. *J. Electroanal. Chem.* **1991**, *312*, 155.
138. Liu, A.; Leese, D. N.; Swarts, J. C.; Sykes, A. G. *Inorg. Chim. Acta* **2002**, *337*, 83.
139. Swarts, J. C.; Sykes, A. G. *Inorg. Chim. Acta* **1996**, *242*, 165.
140. Tsai, W.-C.; Cass, A. E. G. *Analyst* **1995**, *120*, 2249.
141. Di Gleria, K.; Hill, H. A. O.; Wong, L. L. *FEBS Lett.* **1996**, *390*, 142.
142. Di Gleria, K.; Nickerson, D. P.; Hill, H. A. O.; Wong, L.-L.; Fülöp, V. *J. Am. Chem. Soc.* **1998**, *120*, 46.
143. Lo, K. K.-W.; Lau, J. S.-Y.; Ng, D. C.-M.; Zhu, N. *J. Chem. Soc., Dalton Trans.* **2002**, 1753.
144. Ryabov, A. D.; Goral, V. N.; Gorton, L.; Csöregi, E. *Chem. Eur. J.* **1999**, *5*, 961.
145. Teale, F. W. J. *Biochim. Biophys. Acta* **1959**, *35*, 543.
146. Veitch, N. C.; Gao, Y.; Smith, A.; White, C. G. *Biochemistry* **1997**, *36*, 14 751.
147. Ryabov, A. D.; Kurova, V. S.; Goral, V. N.; Reshetova, M. D.; Razumiene, J.; Simkus, R.; Laurinavicius, V. *Chem. Mater.* **1999**, *11*, 600.
148. Job, D.; Dunford, H. B. *Eur. J. Biochem.* **1976**, *66*, 607.
149. Nesmeyanov, A. N.; Sazonova, V. A.; Romanenko, V. I. *Dokl. Akad. Nauk SSSR* **1963**, *152*, 1358.
150. Nesmeyanov, A. N.; Sazonova, V. A.; Drozd, V. N. *Dokl. Akad. Nauk SSSR* **1964**, *154*, 1393.
151. Razumiene, J.; Meskys, R.; Gureviciene, V.; Laurinavicius, V.; Reshetova, M. D.; Ryabov, A. D. *Electrochem. Commun.* **2000**, *2*, 307.
152. Razumiene, J.; Vilkanauskyte, A.; Gureviciene, V.; Laurinavicius, V.; Roznyatovskaya, N. V.; Ageeva, Y. V.; Reshetova, M. D.; Ryabov, A. D. *J. Organomet. Chem.* **2003**, *668*, 83.
153. Wang, C.-L.; Mulchandani, A. *Anal. Chem.* **1995**, *67*, 1109.
154. Mulchandani, A.; Wang, C.-L.; Weetall, H. H. *Anal. Chem.* **1995**, *67*, 94.
155. Mulchandani, A.; Pan, S. *Anal. Biochem.* **1999**, *267*, 141.
156. Bjerrum, M. J.; Casimiro, D. R.; Chan, I.-J.; Di Bilio, A. J.; Gray, H. B.; Hill, M.; Langen, R.; Mines, G. A.; Skov, L. K.; Winkler, J. R.; Wuttke, D. S. *J. Bioenerg. Biomembrane* **1995**, *27*, 295.

157. Gray, H. B.; Winkler, J. R. *Elect. Trans. Chem.* **2001**, *3*, 3.
158. Millett, F.; Durham, B. *Biochemistry* **2002**, *41*, 11315.
159. Dürr, H.; Bossmann, S. *Acc. Chem. Res.* **2001**, *34*, 905.
160. Berglund, J.; Pascher, T.; Winkler, J. R.; Gray, H. B. *J. Amer. Chem. Soc.* **1997**, *119*, 2464.
161. Yamada, H.; Yamazaki, I. *Arch. Biochem. Biophys.* **1974**, 728.
162. Zhang, C.; Haruyama, T.; Kobatake, E.; Aizawa, M. *Anal. Chim. Acta* **2000**, *408*, 225.
163. Crumbliss, A. L.; Hill, H. A. O.; Page, D. J. *J. Electroanal. Chem.* **1986**, *206*, 327.
164. Degani, Y.; Heller, A. *J. Am. Chem. Soc.* **1989**, *111*, 2357.
165. Gregg, B. A.; Heller, A. *J. Phys. Chem.* **1991**, *95*, 5970.
166. Gregg, B. A.; Heller, A. *Anal. Chem.* **1990**, *62*, 258.
167. Pishko, M. V.; Katakis, I.; Lindquist, S. E.; Ye, L.; Gregg, B. A.; Heller, A. *Angew. Chem.* **1990**, *102*, 109.
168. Gregg, B. A.; Heller, A. *J. Phys. Chem.* **1991**, *95*, 5976.
169. Pishko, M. V.; Michael, A. C.; Heller, A. *Anal. Chem.* **1991**, *63*, 2268.
170. Heller, A. *Acc. Chem. Res.* **1990**, *23*, 128.
171. Heller, A. *J. Phys. Chem.* **1992**, *96*, 3579.
172. Ohara, T. J.; Rajagopalan, R.; Heller, A. *Polym. Mater. Sci. Eng.* **1993**, *70*, 182.
173. Ohara, T. J.; Rajagopalan, R.; Heller, A. *Anal. Chem.* **1994**, *66*, 2451.
174. Ye, L.; Hämmerle, M.; Olsthoorn, A. J. J.; Schuhmann, W.; Schmidt, H.-L.; Duine, J. A.; Heller, A. *Anal. Chem.* **1993**, *65*, 238.
175. Corton, E.; Battaglini, F. *J. Electroanal. Chem.* **2001**, *511*, 8.
176. Ryabov, A. D.; Roznyatovskaya, N. V.; Suwinska, K.; Revenco, M.; Ershov, A. Y. *J. Biol. Inorg. Chem.* **2003**, *8*, 815.
177. Davies, N. R.; Mullins, T. L. *Aust. J. Chem.* **1967**, *20*, 657.
178. Allen, L. R.; Craft, P. P.; Durham, B.; Walsh, *J. Inorg. Chem.* **1987**, 26, 53.
179. Ryabova, E. S.; Csöregi, E.; Ryabov, A. D. *J. Mol. Catal. B: Enzymatic* **2000**, *11*, 139.
180. Kurova, V. S.; Ershov, A. Y.; Ryabov, A. D.Izv. RAN *Ser. Khim.* **2001**, *50*, 1766.
181. Ryabov, A. D.; Firsova, Y. N.; Ershov, A. Y.; Dementiev, I. A. *J. Biol. Inorg. Chem.* **1999**, *4*, 175.
182. Zakeeruddin, S. M.; Fraser, D. M.; Nazeeruddin, M.-K.; Grätzel, M. *J. Electroanal. Chem.* **1992**, *337*, 253.
183. Seddon, E. A.; Seddon, K. R. "*The Chemistry of Ruthenium*"; Elsevier: Amsterdam–Oxford–New York–Tokyo, 1984.
184. Danilowicz, C.; Corton, E.; Battaglini, F. *J. Electroanal. Chem.* **1998**, *445*, 89.
185. Shklover, V.; Zakeeruddin, S. M.; Nesper, R.; Fraser, D.; Grätzel, M. *Inorg. Chim. Acta* **1998**, *274*, 64.
186. Fraser, D. M.; Zakeeruddin, S. M.; Grätzel, M. *J. Electroanal. Chem.* **1993**, *359*, 125.
187. Chen, L.; Gorski, W. *Anal. Chem.* **2001**, *73*, 2862.
188. Morris, N. A.; Cardosi, M. F.; Birch, B. J.; Turner, A. P. F. *Electroanalysis* **1992**, *4*, 1.
189. Battaglini, F.; Calvo, E. J. *J. Chem. Soc. Faraday Trans.* **1994**, *90*, 987.
190. Villahermosa, R. M.; Kuciauskas, D.; Mayo, E. I.; Lewis, N. S.; Winkler, J. R.; Gray, H. B. *"Abstr. Pap.-Am. Chem. Soc.*", Vol. 221; 2001, p. INOR.
191. Hess, C. R.; Winkler, J. R.; Hill, M. G.; Dooley, D. M.; Gray, H. B. *"Abstr. Pap.-Am. Chem. Soc.*", Vol. 221st; 2001, p. INOR.
192. Degani, Y.; Heller, A. *J. Am. Chem. Soc.* **1988**, *110*, 2615.
193. Goral, V. N.; Csöregi, E.; Mattiasson, B.; Ryabov, A. D. *Mendeleev Commun.* **1999**, 173.
194. Zakeeruddin, S. M.; Graetzel, M.; Fraser, D. M. *Biosens. Bioelectron.* **1996**, *11*, 305.
195. Battaglini, F.; Bartlett, P. N.; Wang, J. H. *Anal. Biochem.* **2000**, *72*, 502.

196. Ryabova, E. S.; Goral, V. N.; Csoregi, E.; Mattiasson, B.; Ryabov, A. D. *Angew. Chem., Int. Ed. Engl.* **1999**, *38*, 804.
197. Cusanelli, A.; Frey, U.; Richens, D. T.; Merbach, A. E. *J. Am. Chem. Soc.* **1996**, *118*, 5265.
198. Gosser, D. K. Jr. "*Cyclic Voltammetry. Simulation and Analysis of Reaction Mechanisms*"; VCH: New York, Weinheim, Cambridge, 1993.
199. Reiter, S.; Eckhard, K.; Blochl, A.; Schuhmann, W. *Analyst* **2001**, *126*, 1912.
200. Ohara, T. J.; Vreeke, M. S.; Battaglini, F.; Heller, A. *Electroanalysis* **1993**, *5*, 825.
201. Ryabov, A. D.; Firsova, Y. N.; Goral, V. N.; Sukharev, V. S.; Ershov, A. Y.; Lejbolle, C.; Bjerrum, M. J.; Eliseev, A. V. *Inorg. React. Mech.* **2000**, *2*, 343.
202. von Zelewsky, A. "*Stereochemistry of Coordination Compounds*"; John Wiley & Sons: Chichester, New York, 1996.
203. Marx-Tibbon, S.; Katz, E.; Willner, I. *J. Amer. Chem. Soc.* **1995**, *117*, 9925.
204. Alzari, P.; Anicet, N.; Bourdillon, C.; Moiroux, J.; Savéant, J.-M. *J. Amer. Chem. Soc.* **1996**, *118*, 6788.
205. Sokolov, V. I. *J. Organomet. Chem.* **1995**, *500*, 299.
206. Sadeghi, S. J.; Gilardi, G.; Nicolosi, G.; Cass, A. E. G. *J. Chem. Soc., Chem Commun.* **1997**, 517.
207. Ryabov, A. D.; Firsova, Y. N.; Goral, V. N.; Ryabova, E. S.; Shevelkova, A. N.; Troitskaya, L. L.; Demeschik, T. V.; Sokolov, V. I. *Chem. Eur. J.* **1998**, *4*, 806.
208. Shevelkova, A. N.; Sal'nikov, Y. I.; Kuz'mina, N. L.; Ryabov, A. D. *FEBS Lett.* **1996**, *383*, 259.
209. Ryabov, A. D. *Angew. Chem. Int. Ed. Engl.* **1991**, *30*, 931.
210. Ryabov, A.D. *Ross. Khim. Zh.* **1995**, 139.
211. Ivanova, E. V.; Ryabov, A. D.Vestnik MGU *ser. Khim.* **2002**, *43*, 424.
212. Omae, I. "*Organometallic Intramolecular-Coordination Compounds*"; Elsevier Science Publishers: Amsterdam, New York, 1986.
213. Ryabov, A. D. *Chem. Rev.* **1990**, *90*, 403.
214. Cope, A. C.; Siekman, R. W. *J. Am. Chem. Soc.* **1965**, *87*, 7272.
215. Ryabov, A.D. *Synthesis* **1985**, 233.
216. Pfeffer, M. *Recl. Trav. Chim. Pays-Bas* **1990**, *109*, 567.
217. Spencer, J.; Pfeffer, M. *Adv. Metal-Organic Chem.* **1998**, *6*, 103.
218. Ritleng, V.; Sirlin, C.; Pfeffer, M. *Chem. Rev.* **2002**, *102*, 1731.
219. van Koten, G.; van Leeuwen, P. W. N. M. *Stud. Surf. Sci. Catal.* **1999**, *123*, 289.
220. Herrmann, W. A.; Böhm, V. P. W.; Reisinger, C.-P. *J. Organomet. Chem.* **1999**, *576*, 23.
221. Krooglyak, E. V.; Kazankov, G. M.; Kurzeev, S. A.; Polyakov, V. A.; Semenov, A. N.; Ryabov, A. D. *Inorg. Chem.* **1996**, *35*, 4804.
222. Kurzeev, S. A.; Kazankov, G. M.; Ryabov, A. D. *Inorg. Chim. Acta* **2000**, *305*, 1.
223. Alexandrova, L.; D'yachenko, O. G.; Kazankov, G. M.; Polyakov, V. A.; Samuleev, P. V.; Sansores, E.; Ryabov, A. D. *J. Am. Chem. Soc.* **2000**, *122*, 5189.
224. Kazankov, G. M.; Sergeeva, V. S.; Efremenko, E. N.; Alexandrova, L.; Varfolomeev, S. D.; Ryabov, A. D. *Angew. Chem., Int. Ed. Engl.* **2000**, *39*, 3117.
225. Hudson, S. A.; Maitlis, P. M. *Chem. Rev.* **1993**, *93*, 861.
226. "*Metallomesogens, Synthesis, Properties, and Applications*"; Ed. Serrano, J. L.; VCH, Weinheim: New York, Basel, Cambridge, Tokyo, 1996.
227. Albrecht, M.; Lutz, M.; Spek, A. L.; van Koten, G. *Nature* **2000**, *406*, 970.
228. Soukharev, V. S.; Ryabov, A. D.; Csöregi, E. *J. Organomet. Chem.* **2003**, *668*, 75.
229. Fernandez, S.; Pfeffer, M.; Ritleng, V.; Sirlin, C. *Organometallics* **1999**, *18*, 2390.
230. Reveco, P.; Medley, J. H.; Garber, A. R.; Bhacca, N. S.; Selbin, J. *Inorg. Chem.* **1985**, *24*, 1096.

231. Reveco, P.; Schmehl, R. H.; Cherry, W. R.; Fronczek, F. R.; Selbin, J. *Inorg. Chem.* **1985**, *24*, 4078.
232. Constable, E. C.; Holmes, J. M. *J. Organomet. Chem.* **1986**, *301*, 203.
233. Constable, E. C.; Hannon, M. J. *Inorg. Chim. Acta* **1993**, *211*, 101.
234. Alpeeva, I. S.; Soukharev, V. S.; Alexandrova, L.; Shilova, N. V.; Bovin, N. V.; Csöregi, E.; Ryabov, A. D.; Sakharov, I. Y. *J. Biol. Inorg. Chem.* **2003**, *8*, 363.
235. Ryabov, A. D.; Soukharev, V. S.; Alexandrova, L.; Le Lagadec, R.; Pfeffer, M. *Inorg. Chem.*, **2003**, *42*, 6598.
236. Bourbonnais, R.; Rochefort, D.; Paice, M. G.; Renaud, S.; Leech, D. *Tappi J.* **2000**, *83*, 68.
237. Rochefort, D.; Bourbonnais, R.; Leech, D.; Paice, M. G. *J. Chem. Soc., Chem. Commun.* **2002**, 1182.
238. Castillo, L. J.; Alpeeva, I. S.; Chubar, T. A.; Galaev, I. Y.; Csöregi, E.; Sakharov, I. Y. *Plant Sci.* **2002**, *163*, 1011.
239. Jaouen, G.; Fish, R. H. *J. Organomet. Chem.* **2003**, *668*, 1.
240. Jaouen, G.; Vessières, A.; Butler, I. S. *Acc. Chem. Res.* **1993**, *26*, 361.

This Page Intentionally Left Blank

PROPERTIES OF TRANSITION METAL COMPLEXES WITH METAL–CARBON BONDS IN AQUEOUS SOLUTIONS AS STUDIED BY PULSE RADIOLYSIS

ALEXANDRA MASARWA[1] and DAN MEYERSTEIN[1,2]

[1]Department of Chemistry, Ben-Gurion University of the Negev, Beer-Sheva, Israel
[2]Department of Biological Chemistry, The College of Judea and Samaria, Ariel, Israel

I. Introduction
II. Radiolysis of Aqueous Solutions
III. Reaction of Aliphatic Carbon-Centered Radicals with Transition Metal Complexes in Aqueous Solutions
IV. Formation of Transition Metal Complexes with Metal–Carbon σ-Bonds
V. Properties of Complexes with Metal–Carbon σ-Bonds
  A. Spectra of the Complexes
  B. Acid Dissociation Constants for Transient α-Hydroxyalkyl Complexes
VI. Mechanisms of Decomposition of the Transient Complexes L_mM^{n+1}–R
  A. Heterolysis of the Metal–Carbon σ-Bond
  B. Homolysis of the Metal–Carbon σ-Bond
  C. Oxidation of $L_{m-1}M^{n+1}$–R Followed by Homolysis
  D. β-Hydride Shift Reactions
  E. β-Elimination Reactions
  F. β-Elimination of Carboxylates
  G. CO Insertion/Methyl Migration
  H. Bimolecular Decomposition of the Transient Complexes
  I. Methyl Transfer Reactions
  J. Rearrangement of the Carbon-Skeleton of R
  K. $(H_2O)_5CrCHO^{2+}$ as a Hydride Transfer Reducing Agent
VII. Alkene Complexes
VIII. Complexes with Metal–carbon σ-Bonds Formed in Redox Processes Between Transition Metal Complexes and Organic Substrates
  A. Reduction of Halo–Alkanes
  B. Decomposition of Cu(III)Peptide Complexes
  C. Participation of Complexes with Metal–Carbon σ-Bonds in the Reduction of Alkenes
IX. Elucidation of the Mechanisms of Catalytic Processes
References

ADVANCES IN INORGANIC CHEMISTRY
VOLUME 55 ISSN 0898-8838 DOI 10.1016/S0898-8838(03)55005-X

© 2004 Elsevier Inc.
All rights reserved.

I. Introduction

Transition metal complexes with metal–carbon σ-bonds are key intermediates in many important industrial processes, in biochemical reactions, organic synthesis, and processes involving aliphatic radicals. Of special interest are those complexes, which are short-lived intermediates in catalytic processes. However due to the high reactivity of the latter complexes, the study of their properties is difficult as their steady state concentration is in most cases far below the detection limit.

It has been shown that Pulse Radiolysis is a powerful tool for the study of the properties of such short lived intermediates (*1,2*). The application of this technique is based on the capability of producing a large variety of aliphatic radicals (vide infra) within less than 1 μs in physically observable concentrations. Thus one can follow by different techniques the kinetics of disappearance of the initially formed radicals and the properties of unstable intermediates, if formed, in these reactions. The most common detection technique is the spectrophotometric one, but changes in specific conductivity, EPR, resonance Raman, etc., can be applied and are often helpful in elucidating the nature of the short lived intermediate observed.

II. Radiolysis of Aqueous Solutions

The radiolysis of dilute aqueous solutions can be summed up by the equation (*3–5*):

$$H_2O \xrightarrow{\gamma,e^-} e^-_{aq}(2.65); {}^{\bullet}OH(2.65); H^{\bullet}(0.60); H_2(0.45); H_2O_2(0.75); H_3O^+(2.65) \quad (1)$$

where the values in parentheses are the number of molecules of a given product formed by the absorption of 100 eV in the medium. The radicals thus formed are powerful redox reagents, i.e., e^-_{aq} ($E^\circ = -2.87$ V); $H^{\bullet}$ ($E^\circ = \pm 2.31$ V); and ${}^{\bullet}OH$ ($E^\circ = +2.73$ V) (*6*).

Thus a mixture of strong single electron oxidizing- and reducing-agents is formed. However the hydrated electrons can be transformed into hydroxyl radicals via (*7*):

$$e^-_{aq} + N_2O \xrightarrow{H_2O} {}^{\bullet}OH + N_2 + OH^- \quad (2)$$

and into hydrogen atoms via (*7*):

$$e^-_{aq} + H_3O^+ \longrightarrow {}^\bullet H + H_2O \qquad (3)$$

In pulse radiolysis experiments these radicals are formed by a short pulse, 10^{-12}–10^{-6} s depending on the experimental set up, in concentrations enabling their physical observation. The linear electron accelerator of the Hebrew University of Jerusalem, which is used, forms up to 2×10^{-5} M of radicals within $< 1.5 \times 10^{-6}$ s. The reactions of the radicals thus formed, or their reaction products, can be followed by a variety of physical techniques including spectrophotomety (this technique is used most commonly), EPR, electrical conductivity, polarography, resonance Raman, NMR etc. (*3–5*). The primary radicals formed can be transformed via the addition of different solutes into a variety of secondary inorganic radicals (e.g., $O_2^{\bullet-}$; $HO_2^\bullet$; $O_3^{\bullet-}$; $CO_2^{\bullet-}$; $CO_3^{\bullet-}$; $CN^\bullet$; $N_3^\bullet$; ${}^\bullet NH_2$; ${}^\bullet NO$; ${}^\bullet NO_2$; ${}^\bullet NO_3$; $NCO^\bullet$; $PO_3^{2-\bullet}$; $PO_4^{2-\bullet}$; $HS^\bullet$; $RSSR^\bullet$; $SO_2^{\bullet-}$; $SO_3^{\bullet-}$; $SO_4^{\bullet-}$; $SO_5^{\bullet-}$; $(SCN)_2^{\bullet-}$; $SeO_3^{\bullet-}$; $HSeO_4^{2-\bullet}$; $(SeCN)_2^{\bullet-}$; $Cl_2^{\bullet-}$; $Br_2^{\bullet-}$; $I_2^{\bullet-}$; $ClO_2^\bullet$; $BrO_2^\bullet$; $IO_2^\bullet$; etc.) (*8*) and organic radicals (e.g.,${}^\bullet CH_3$; ${}^\bullet CH_2CH_3$; ${}^\bullet CH_2CH_2CH_3$; ${}^\bullet CH(CH_3)_2$; ${}^\bullet C(CH_3)_3$; *c*-${}^\bullet C_5H_9$; ${}^\bullet CH_2Cl$; ${}^\bullet CH_2Br$; ${}^\bullet CF_3$; ${}^\bullet CCl_3$; ${}^\bullet CBr_3$; ${}^\bullet CH_2OH$; ${}^\bullet CH(CH_3)OH$; ${}^\bullet C(CH_3)_2OH$; ${}^\bullet CH_2CH_2OH$; ${}^\bullet CH_2C(CH_3)_2OH$; ${}^\bullet CH_2OCH_3$; ${}^\bullet CH(CH_3)OC_2H_5$; ${}^\bullet CH(OH)CH_2OH$; ${}^\bullet CH_2CHO$; ${}^\bullet CH_2CO_2H$; ${}^\bullet CH(CH_3)CO_2H$; ${}^\bullet CH(OH)CO_2H$; ${}^\bullet C(OH)(CH_3)CO_2H$; ${}^\bullet CH(CH_2NH_3^+)CO_2^-$; ${}^\bullet CH(CH_3)NH_2$; ${}^\bullet CH_2C(CH_3)_2NH_3^+$; ${}^\bullet CH_2CN$; ${}^\bullet CH_2C_6H_5$; ${}^\bullet SC_2H_5$; $CH_3OO^\bullet$; $CCl_3OO^\bullet$; $NCCH_2OO^\bullet$; $HO_2CCH_2OO^\bullet$; etc.) (*9,10*) with desired redox potentials (*6–11*).

The organic radicals are produced essentially by one of the following methods: Aliphatic carbon-centered radicals are formed mainly from saturated aliphatic compounds via hydrogen atom abstraction by ${}^\bullet OH$ and ${}^\bullet H$ radicals (${}^\bullet H$ radicals react with solutes to produce the same radicals as ${}^\bullet OH$ radicals, but the rate constants are usually considerably smaller (*7*)):

$${}^\bullet OH/{}^\bullet H + RH \longrightarrow {}^\bullet R + H_2O/H_2 \qquad (4)$$

These reactions are fast for α-hydrogens to –OH, –OR, or $–NH_2$ substituents and considerably slower for α-hydrogens to $–CO_2^-$ and $–NH_3^+$ substituents (*7*). A small part of the primary radicals react with hydrogens at the β-position. ${}^\bullet OH/{}^\bullet H$ radicals react very fast with aliphatic unsaturated compounds and aromatic compounds via addition to a double bond:

$${}^\bullet OH/{}^\bullet H + R^1R^2C = {}^\bullet CR^3R^4 \longrightarrow CR^1R^2C(OH/H)R^3R^4 \qquad (5)$$

Several radicals are formed by special routes. Methyl radicals for example are formed from $(CH_3)_2SO$ according to the following equations (*12*):

$$^{\bullet}OH + (CH_3)_2SO \longrightarrow (CH_3)_2S^{\bullet}(O)OH \quad (6)$$

$$(CH_3)_2S^{\bullet}(O)OH \longrightarrow CH_3S(O)OH + {}^{\bullet}CH_3 \quad (7)$$

All the organic radicals are relatively strong single electron oxidizing and reducing agents. The redox properties of aliphatic carbon-centered radicals depend on the substituents on the α-carbon. Thus for example radicals of the type $^{\bullet}CR^1R^2(OH)$ are relatively strong reducing agents (*6*); however they do oxidize low-valent transition metal complexes, e.g., $Cr(H_2O)_6^{2+}$ (*13*) and $V(H_2O)_6^{2+}$ (*14*). On the other hand $^{\bullet}CCl_3$ and $^{\bullet}CH_2CO_2H$ are relatively strong oxidizing agents (*6*). The known redox potentials of many radicals are summed up in two reviews (*6,11*).

III. Reaction of Aliphatic Carbon-Centered Radicals with Transition Metal Complexes in Aqueous Solutions

The reactions of the appropriate radicals with $M(H_2O)_m^{n+}$ ions or with M^nL_m complexes enable the formation of complexes with metal–carbon σ-bonds among a variety of possible reactions as detailed in the following.

The kinetics and mechanisms of reaction of many carbon-centered radicals with a large variety of transition metal complexes were studied. The specific rates of most of these reactions are summed up in Ref. (*10*). In principle these reactions might proceed via one of the following mechanisms:

$$\longrightarrow M^{n\pm1}L_m + R^{-/+} \quad (8)$$

$$\longrightarrow L_mM^{n+1}\text{–}R \text{ or } L_{m-1}M^{n+1}\text{–}R + L \quad (9)$$

$$M^nL_m + R^{\bullet} \longrightarrow M^{n-1}L_{m-1} + L\text{–}R \text{ or } L^{\pm} + R^{-/+} \quad (10)$$

$$\longrightarrow L_{m-1}M^n\text{–}LR^{\bullet} \longrightarrow M^{n\pm1}L_{m-1} + L\text{–}R^{-/+} \text{ or } + L^{\pm} + R^{-/+} \quad (11)$$

$$\longrightarrow L_{m-1}M^n(L^{\pm}) + R^{-/+} \longrightarrow M^{n\pm1}L_m + R^{-/+} \quad (12)$$

Equation (8) describes outer-sphere redox processes. As the self exchange rates for the $R^{\bullet/-}$ and $R^{+/\bullet}$ couples are usually slow these

reactions are not abundant. However outer-sphere reductions of transition metal complexes by $^{\bullet}CR^1R^2OH$ or $^{\bullet}CR^1R^2O^-$ radicals (*15–23*) were observed. This is reasonable as these radicals are powerful reducing agents and as the oxidation of these radicals does not require major bond rearrangements. Thus the self exchange rate for the couple $C(CH_3)_2OH^{+/0}$ has been estimated to be $\sim 10^3\ M^{-1}s^{-1}$ (*21*). It should be noted that $CO_2^{\bullet -}$ is also a powerful reducing agent (*6,24*) but as it is bent and CO_2 is linear most of its reactions proceed via the inner-sphere mechanism (*25*).

Processes following the mechanism described in Eq. (10) are mainly observed for halide, and analogous complexes as the oxidizing species, e.g. (*15,19,23,26*):

$$M(NH_3)_5X^{2+} + R^{\bullet} \longrightarrow RX + M_{aq}^{2+} + 5NH_4^+ \qquad (13)$$

In principle also the reactions [see for example Refs. (*27,28*)]:

$$L_mM^{n+1} - R + R'^{\bullet} \longrightarrow M^nL_m + RR' \text{ or } RH + R'_{-H} \text{ or } R'_H + R_{-H} \qquad (14)$$

which are discussed below in detail for R=R′, follow an analogous mechanism.

Processes following the mechanism described in Eq. (11) are observed for the addition of alkyl (*29*) and substituted alkyl (*26*) radicals to aromatic ligands followed by the reduction of the central cation and proton loss from the aromatic ring. In principle the central cation could also be oxidized by its radical-ligand. However, such reactions are not known.

Processes following the mechanism described in Eq. (12) are abundant, though only processes in which the ligand is reduced are known (*30–40*); an example to this is the formation of $\{(NH_3)_5Co^{III}-^{-}O_2CC_6H_4NO_2^{\bullet -}\text{-p}\}^+$ followed by reaction (15):

$$\{(NH_3)_5Co^{III} -^{-} O_2CC_6H_4NO_2^{\bullet -}\text{-p}\}^+ \longrightarrow \{(NH_3)_5Co^{II-} - O_2CC_6H_4NO_2\text{-p}\}^+ \qquad (15)$$

IV. Formation of Transition Metal Complexes with Metal–Carbon σ-Bonds

Processes following the mechanism described in Eq. (9) are the common mechanism of reaction for “low valent” complexes with ligand

exchange rates, and/or steric structures, which enable bond formation between the central metal cation and the attacking radical. The products of these reactions are transient or stable complexes with metal–carbon σ-bonds.

The identification of the intermediate is usually based on the following arguments:

(1) It is formed in a reaction between the metal complex and the radical $^{\bullet}R$, as verified by the first order dependence of its formation on $[M^nL_m]$ and $[^{\bullet}R]$.
(2) Its spectrum is similar to those of related compounds containing metal–carbon σ-bonds and it is noticeably different from that of other possible reaction products, e.g., $M^{n+1}L_m$, $M^{n-1}L_m$.
(3) Its kinetics of decomposition differs from those of other possible intermediates.
(4) Analysis of the final products formed.

The question whether the mechanism of formation of the transient complex with the metal–carbon σ-bond involves ligand exchange, or is accompanied by an increase in the coordination number is often not clear. In some cases the results indeed suggest that an increase in the coordination number occurs at least initially (*41–43*), whereas in other cases the reaction seems to require a loss of one of the ligands L (*44*). Recently measurements of the volumes of activation of several of these reactions pointed out that the rate determining step in most of these reactions is the ligand interchange step, i.e., that the number of ligands is not increased in these processes (*45*). An I_d mechanism was indicated for $M^n = Co^{II}$, Ni^{II}, Cr^{II}, Cu^{II}, an I mechanism for Fe^{II}, and an I_a mechanism for Mn^{II} (*46*).

The specific rates of reactions proceeding via this mechanism were measured for first row transition metal complexes with different ligands for which M^n = Ti(III) (*19,42,47*) (though the transient complexes with a Ti^{IV}–C bond were not observed), V(II) (*11,48*) (though the transient complexes with a V^{III}–C bond were not observed), Cr(II) (*13,49–58*), Cr(III) (*58*), Mn(II) (*59,60*), Mn(III) (*60*) (though the transient complexes with a Mn^{IV}–C bond were not observed), Fe(II) (*59,61–67*), Fe(III) (*65,67,68*), Co(II) (*2,27,28,54,59,69–79*), Ni(I) (*61,80–82*), Ni(II) (*43,61,80, 83,84*), Cu(I) (*85–94*), and Cu(II) (*87,94–102*).

Rate constants of such reactions which result in the formation of complexes with metal–carbon σ-bonds are summed up in reference (*10*). It should be noted that the rates of these reactions in general follow the rate of ligand exchange for the specific metal complex in accord with the above mechanism. Thus for a given metal complex the

rates of formation with a series of different radicals are usually similar. Fast rates of formation are reported for e.g., the reaction of Cu(I) systems (without sterical hindrance), which react nearly diffusion controlled ($k_9 > 10^9$ M^{-1} s^{-1}) (*85*). The rates of Cu(II) systems are usually considerably slower ($8 \times 10^5 - 8 \times 10^8$ M^{-1} s^{-1}) (*97*). For Cr(II) systems rate constants of $3 \times 10^7 - 4 \times 10^8$ M^{-1} s^{-1} are observed (*13,44*).

It was established that steric hindrance due to the ligands L and/or the $^{\bullet}R$ radical has a pronounced effect on the rate constants of these reactions. Thus comparing rates of formation for LCu^{II}–R systems with $L^1 = H_2O$ ligands to that with $L^2 =$ 2,5,8,11-tetramethyl-2,5,8,11-tetraazadodecane and a series of aliphatic R groups (*92*) shows:

(1) that the non-participating ligand L has a marked effect on the rates of formation of the intermediate containing the metal–carbon σ-bond. The rates of formation with several aliphatic radicals are nearly diffusion controlled for the system containing aquo ligands ($> 3 \times 10^9$ M^{-1} s^{-1}) but considerably lower ($6 \times 10^6 - 1 \times 10^8$ M^{-1} s^{-1}) for the L^2 ligand due to the steric hindrance imposed by it (*92*).

(2) Steric hindrance on the R group affects the rate constants of the formation of these intermediates as well. Thus in the above study the reaction of the $^{\bullet}R = {}^{\bullet}CH(CH_3)CO_2^-$ with $(Cu^{I}L^2)^+$ is too slow to be measured, whereas a rate constant of 6.3×10^6 M^{-1} s^{-1} was derived for the similar radical $^{\bullet}R = {}^{\bullet}CH_2CH_2CO_2^-$ (and even higher rates for less sterically hindered radicals) in the L^2 system (*92*).

Basically the strength of the formed metal–carbon σ-bond depends on the following factors:

(1) The nature of the central metal ion. In principle the redox potential of the $M^{n+1/n}$ couple and the stabilization of the M^{n+1} ion by the ligand R^- affect the metal–carbon bond strength. The stability of the transient complex is also affected by the rate of ligand exchange of the L_mM^{n+1}–R complex.

(2) The equatorial ligands, which influence the redox properties of the central metal ion, depending on their σ-donor character. Thus structure and identity of the equatorial ligands affect the properties of the transient complex, i.e., the stability of the M–C bond.

(3) The nature of the axial ligand in the trans position to the R group. For a series of cobalt–methyl complexes it was shown, that ligands in the trans position affect the cobalt–carbon bond

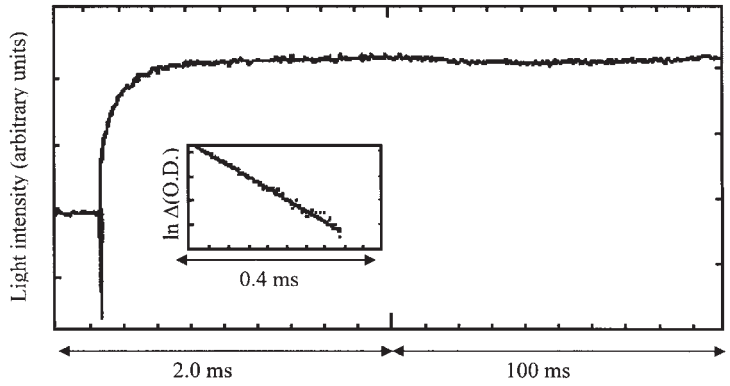

FIG. 1. Computer trace of the time-dependence of the formation of $[(NH_3)_5Co^{III}–CH_2CO_2^-]^+$ followed at 300 nm and first order plot (insert). (1 M CH_3CO_2Na, 1×10^{-3} M $CoSO_4$, ~20% NH_3, N_2O saturated aqueous solution irradiated with a maximum pulse.)

length considerably and thus the UV/Vis absorption spectra of the complexes in agreement with the spectroscopic series $H_2O < NH_3 < CN^- \sim NO_2^-$ (*103*).

(4) The nature of the substituents on the aliphatic residue R.

(5) Steric hindrance caused by the equatorial ligand structure and/or from the substituents on •R.

Figure 1 shows a typical time trace of formation of a transient complex as observed in the linear accelerator setup.

V. Properties of Complexes with Metal–Carbon σ-Bonds

A. Spectra of the Complexes

The spectra of the complexes L_mM^{n+1}–R, containing a metal–carbon σ-bond, usually consist of several distinguishable bands: the major bands with high extinction coefficients in the UV region are LMCT bands, followed sometimes by bands with mixed characters and the d–d bands in the visible region with low extinction coefficients. The location of the maximum of the LMCT transition is naturally strongly affected by the nature of the substituents R and by the redox potential of the central $M^{(n+1)}$ ions.

The spectra of chromium compounds $(H_2O)_5Cr^{III}–CR^1R^2R^3$ were studied intensively and the following conclusion were derived (*104*).

The dominant band in the far UV shows a maximum between 210–260 nm with absorption coefficients 2500–7000 M^{-1} cm^{-1}. This absorption was assigned to the σ-t_{2g} LMCT transition. The second band, observed only for substituents containing non-bonding electron pairs, appears in the region 260–310 nm ($\varepsilon = 1500$–3300 M^{-1} cm^{-1}). It was suggested that this transition originates from a non-bonding electron pair on a substituent R^i (e.g., $R = CH_2OH$), or from a π-bond in R^i (e.g., $R = CH_2CN$), to the central chromium cation. Electron withdrawing substituents on the aliphatic group cause a blue shift, whereas electron donating substituents cause a red shift of the location of these two bands. The difference in energy between the high-energy transitions indicates a dependence of ΔE on the nature of the lone pair or π-donor. The maximum of the third, much weaker band, is hardly affected by the nature of the organic σ-donor ($\lambda_{max} = 385$–410 nm, $\varepsilon = 50$–560 M^{-1} cm^{-1}) in accord with its assignment to a d–d transition mixed with some charge-transfer character. The band due to d–d-transitions is observed in the visible region around 500 nm. Analogous bands are observed for L^iCu^{II}–R and $(nta)H_2O)Co^{III}$–R complexes, though here the LMCT bands are clearly σ-e_g transitions (*28,92*).

B. Acid Dissociation Constants for Transient α-Hydroxyalkyl Complexes

α-Hydroxyalkyl complexes of the type $(nta)Co^{III}CR^1R^2OH$ were the first for which a pK_a of the alcoholic group has been observed (*28*):

$$(nta)(H_2O)Co^{III}CR^1R^2OH^- \rightleftarrows (nta)(H_2O)Co^{III}CR^1R^2O^{2-} + H^+ \quad (16)$$

Depending on the pH of the solution spectra composite of the relative amounts of acid and base form of the transient complex are observed after its formation and equilibration due to Eq. (16) and K_{16} can thus be derived.

The values of K_{16} (0.22–1.2×10^{-4} M) are at least 12 orders of magnitude larger than those for the corresponding alcohols, thus the $(nta)(H_2O)Co^{III}$- moiety exerts a large inductive effect on the alcoholic residue. K_{16} of $(nta)(H_2O)Co^{III}CH_2OH^-$ (2.2×10^{-5} M) is also 4 orders of magnitude larger compared to the corresponding $(hedta)Co^{III}$–CH_2OH^- complex (1.0×10^{-9} M), suggesting that K_{16} depends strongly on the degree of covalency of the metal–carbon

bond (the higher the ionic nature of the bond, the higher the pK_a for the alcoholic group) (*28*).

No analogous pK values for other α-hydroxyalkyl complexes were observed so far. Similar chromium(III) complexes (e.g., $(nta)(H_2O)Cr^{III}–CR^1R^2OH^-$ and $(H_2O)_5Cr^{III}–CR^1R^2OH^{2+}$) (*13,44*) show no such pH effect, i.e., one spectral form of the transient complex is observed over the whole pH-range studied. The chromium–carbon bond in these complexes clearly has a more ionic character than that of the cobalt–carbon bonds in the above study, as the corresponding Cr(II) complexes are considerably stronger reducing agents. Thus it is expected that the pK_a for chromium–α-hydroxyalkyl complexes will only be observed at higher pH values.

α-Hydroxyalkyl complexes containing other metal centers may have to be reinvestigated thoroughly, bearing the possibility of the acid–base equilibrium in mind.

VI. Mechanisms of Decomposition of the Transient Complexes $L_mM^{n+1}–R$

The mechanisms and kinetics of decomposition of the transient complexes $L_mM^{n+1}–R$ in aqueous solutions depend on the nature of the central cation, of the ligands, L, of the substituents on the aliphatic residue, R, on the pH and on the presence and nature of various substrates, S, in the medium, e.g., O_2. In the following section the major mechanisms observed are discussed.

A. Heterolysis of the Metal–Carbon σ-Bond

The major mechanism of decomposition observed in aqueous solution is the heterolysis of the metal–carbon σ-bond. In aqueous solutions the hydrolysis of the metal–carbon σ-bond can proceed according to the following two pathways:

$$\longrightarrow M^{n+1}L_m + RH + OH^- \tag{17}$$

$$L_mM^{n+1} - R + H_2O— \longrightarrow M^{n-1}L_m + ROH/R_{-H} + H_3O^+ \tag{18}$$

The oxidative (in reference to the starting complex) heterolysis, Eq. (17), is observed mainly for complexes M^nL_m which are relatively strong reducing agents and which are not expected to be reduced, for example,

complexes of Cr(II) (*13,50,53,56–58,105*), Mn(II) (*60,61*), Fe(II) (*42,62*), Co(II) (*29*), Ni(I) (*61,81,82,106*), and Cu(I) (*85,86,92*). This reaction is usually acid (*11,50,53,57,92*) and general base catalyzed (*53,105,107*). For an acid catalyzed reaction the rate of decomposition obeys the rate law:

$$-\mathrm{d}[\mathrm{LM}^{n+1}\text{–R}]/\mathrm{d}t = \{k_1 + k_2[\mathrm{H}^+]\}[\mathrm{LM}^{n+1}\mathrm{R}] \qquad (19)$$

where k_1 represents the spontaneous and k_2 the acid-catalyzed pathways, respectively.

Studies of the heterolysis reaction for a series of Cr–α-hydroxyalkyl complexes established that the presence or absence of a *cis*-aqua ligand has a negligible effect on the specific rate of the heterolytic decomposition (*44,107*). Thus it was suggested that the electrophilic attack of a solvent water molecule at the carbon center of the chromium–carbon σ-bond is the rate determining step in the heterolysis process (*44,107*).

Measurements of the volumes of activation (*108*) and solvent H/D isotope effect (*50*) of some of the heterolytic decomposition reactions suggest that they proceed via a transition state of the type (*108*):

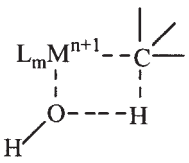

It was found that $\Delta V^{\#}$ for both the acid-independent and acid-catalyzed pathways are approximately zero (*109*). Thus it was interpreted that Eq. (17) can be considered a substitution reaction of the Cr(III) central cation which proceeds through an interchange, I, mechanism (*109*). The large H/D isotope effect (*50*) points out that the O–H bond dissociates in the transition state.

Furthermore, the heterolysis reaction is catalyzed by the addition of anions (organic and inorganic oxy anions, e.g., acetate) (*44,107, 110,111*). Comparing the acetate effect in the presence of different chelating ligands ([15]aneN_4 and nta) to those of the aquated system led to the conclusion that the oxy anions have to occupy the trans position to the R group in order to labilize the M–R bond (trans labilization effect) and thus catalyze the heterolytic decomposition (*44,107,110,111*).

Thus for $\mathrm{M}^{n+1} = \mathrm{Cr}^{\mathrm{III}}$ reaction (17) was shown to proceed according to Scheme 1 (*105*).

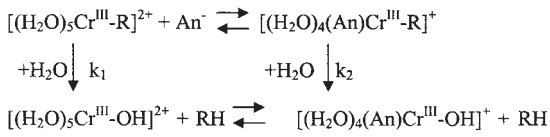

SCHEME 1.

Measuring the volumes of activation for several reactions of this type indicates that the An^- ligand, usually in the trans position to R, weakens the Cr–C bond, thus shifting the mechanism from a pure I to an I_d mechanism (*105,109*). For a large variety of anions $\Delta V^{\#}(k_2) = 10\ cm^3\ mol^{-1}$ was measured.

The reductive heterolysis, Eq. (18), is mainly observed for complexes M^nL_m which can be reduced and are difficult to oxidize, e.g., Fe(III) (*68*), Cu(II) (*97*), and with proper ligands for Co(II) (*70,78*). Measurements of the volumes of activation of some of these reactions (*108*) suggest that they proceed via a transition state of the type:

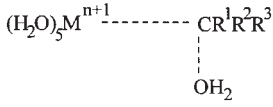

i.e., the water molecule binds to the carbon atom and shifts the M–C σ-bond electrons towards the metal center, thus causing its reduction. For this type of reaction no solvent H/D isotope effect is observed (*108*). In general the kinetics of decomposition of the metal–carbon bond following a heterolytic decomposition pathway show a first order dependence on the L^iM^{n+1}–$CR^1R^2R^3$ complexes and are independent of the concentration of the initial M^nL_m complexes.

It is of interest to note the ligand effect on the mechanisms of decomposition of several copper complexes of the type LCu^{III}–CH_3:

$$Cu^{III}–CH_3^{2+}aq \longrightarrow Cu_{aq}^{+} + CH_3OH \ (112) \qquad (20)$$

$$(H_2NCH_2CO_2^-)_2Cu^{III}–CH_3 \longrightarrow Cu^{III}(H_2NCH_2CO_2^-)_2^+ + CH_4 \ (100) \qquad (21)$$

$$\text{(glycylglycylglycine)}Cu^{III}–CH_3^+ \longrightarrow Cu^{I}\text{(glycylglycylglycine)} + CH_3OH \ (113) \qquad (22)$$

The shift in mechanism from reductive to oxidative heterolysis caused by the glycine ($H_2NCH_2CO_2^-$) ligands was attributed (*100*) to their effect on the redox potential of the $Cu^{III/II}$ couple. However, the glycylglycylglycine ligand stabilizes the Cu^{III} oxidation state even more than the glycines. Thus it seems that the choice of the mechanism of decomposition of the transient complexes depends on the activation energies of the different plausible mechanisms and not on the total free energy gain. This is plausible as the $^{\bullet}CH_3$ radicals are both powerful oxidizing and reducing agents (*6,69*), and therefore both the reaction mechanisms are highly exothermic. The relatively long life time of (glycylglycylglycine)Cu^{III}–CH_3^+ ($k_{22} = 0.0035\ s^{-1}$) (*113*) suggests that complexes of this type might play an important role in radical induced biological processes.

B. Homolysis of the Metal–Carbon σ-Bond

In many systems studied the results point out that Eq. (9) is an equilibrium process and that the mechanism of decomposition of the transient complex L_mM^{n+1}–R involves radical processes.

The homolytic mechanism of decomposition has been observed for a large variety of complexes of Cr(III) (*50,57*), Mn(III) (*59*), Fe(III) (*59,61*), Fe(IV) (*68*), Co(III) (*28,72,73*), Ni(III) (*43,83,84*), and Cu(II) (*87,114–117*). In most systems studied the observed reaction is

$$L_{m-1}M^{n+1} - R + L \longrightarrow M^nL_m + {}^{\bullet}R \qquad (-9)$$

i.e., the coordination number is not changed during the reaction. According to the principle of microscopic reversibility (*2*) the mechanism of reaction (–9) proceeds via the same transition state as the forward reaction (9), which proceeds usually via a mechanism involving a ligand interchange (*28,45,73*), vide supra. Thus the measurement of $\Delta H^{\#}$ of reaction (–9) does not yield the M–C bond strength as was proposed (*118–122*), but the difference between this energy and the metal–ligand bond dissociation energy, though the determination of the bond strengths by this method were performed mainly in aprotic solvents which do not behave as ligands.

The homolysis equilibrium constants (K_{-9}) can be determined by the following two approaches:

(a) For systems with a relatively large equilibrium constant of homolysis (small formation equilibrium constant) the dependence of the observed rate of formation of $L_{m-1}M^{n+1}$–R on $[M^nL_m]$ is determined (under pseudo first order conditions of

excess $[M^nL_m]$). The slope of the straight line obtained equals k_9 and the intercept yields k_{-9} (*123*). Alternatively the dependence of the yield of $L_{m-1}M^{n+1}$–R on $[M^nL_m]$ is measured according to the absorption due to $L_{m-1}M^{n+1}$–R and K_9 is calculated (*123*).

(b) For systems with small equilibrium constants of homolysis (large formation equilibrium constants) method (a) is inapplicable, as the intercept is too small to be determined accurately, and nearly a full yield of $L_{m-1}M^{n+1}$–R is obtained even in solutions containing the lowest possible concentration of M^nL_m. In such systems the addition of a scavenger, S, for the free radicals $^\bullet$R is required. The kinetics of the decomposition of $L_{m-1}M^{n+1}$–R in the presence of S are:

$$^\bullet R + S \longrightarrow \text{products} \tag{23}$$

$$-d[L_{m-1}M^{n+1}\text{–R}]/dt = \frac{k_{23}k_{-9}[L_{m-1}M^{n+1}\text{–R}][S]}{k_9[M^nL_m] + k_{23}[S]} \tag{24}$$

$$\text{i.e.,}\quad 1/k_{obs} = \frac{[M^nL_m]}{K_{(-9)}k_{23}[S]} + \frac{1}{k_{-9}} \tag{25}$$

Therefore by plotting $1/k_{obs}$ vs. $[M^nL_m]$ or vs. 1/[S], K_9 (K_{-9}), and k_{-9} can be determined and k_9 calculated as well.

Table I shows an overview of equilibrium constants of homolysis (K_{-9}) for selected systems M^nL_m, $[N(CH_2CO_2)_3Co^{II}(H_2O)_2]^-$ (*28*) and $Cr(H_2O)_6^{2+}$ (*124,125*), for which a systematic study with a number of aliphatic residues was performed. For the $[N(CH_2CO_2)_3Co^{II}(H_2O)_2]^-$ system K_{-9} decreases along the series R = $^\bullet CH_3$, $^\bullet CH_2OH$, $^\bullet CH(CH_3)_2$ OH, $^\bullet C(CH_3)_2OH$, and $^\bullet CH(CH_3)OC_2H_5$ (*28*). A similar trend is observed

TABLE I

EFFECT OF RESIDUES $^\bullet$R ON THE EQUILIBRIUM CONSTANTS OF HOMOLYSIS FOR TWO SELECTED SYSTEMS $L_{m-1}M^{n+1}$–R + $H_2O \rightleftarrows M^nL(H_2O)$ + $^\bullet$R

	K (M)	
$^\bullet$R\M^nL_m	$Cr(H_2O)_6^{2+}$ (*50,124*)	$[\{N(CH_2CO_2)_3\}Co^{II}(H_2O)_2]^-$ (*28,72*)
$^\bullet CH_3$	–	3.7×10^{-7}
$^\bullet CH_2OH$	2.3×10^{-13}	2.0×10^{-4}
$^\bullet CH(CH_3)OH$	1.1×10^{-11}	9.1×10^{-4}
$^\bullet C(CH_3)_2OH$	2.5×10^{-9}	2.0×10^{-3}
$^\bullet CH(CH_3)OC_2H_5$	5.9×10^{-11}	9.1×10^{-3}

in the $Cr(H_2O)_6^{2+}$ system though with the exception of $R = {}^{\bullet}CH(CH_3)OC_2H_5$ (*124,125*). Thus the results show that the dependence of the substituents on the alkyl residue on the homolysis equilibrium constant is slightly different in the two systems. Consequently, K_{-9} is not directly related to the redox potential of $^{\bullet}R$ (*124,125*), steric factors have to be taken into consideration as well. The effect of steric hindrance on the formation constants of the transient complex with a metal–carbon σ-bond was established, vide supra. Clearly the stabilization of the $L_{m-1}M^{n+1}$ oxidation state by the $-R^-$ ligand affects the homolysis equilibrium constant.

Table II shows a comparison of the homolysis equilibrium constants for a system containing three different metal centers (Fe, Mn, Co) in a $[N(CH_2CO_2)_3(H_2O)M^{III}–CH_3]^-$ complex. The values indicate that for these complexes ΔG° depends only slightly on the nature of the central cation (*28,59,72*). This is somewhat surprising as it is normally claimed, that $L^iCo^{III}–CR^1R^2R^3$ are stabilized by the d^6 electronic configuration. It should be noted, that for the corresponding complexes with M = Cr (*44*), Ni (*126*), and Cu (*99*) different mechanisms of decomposition are observed.

Table III summarizes a recent study comparing equilibrium constants of homolysis and volumes of activation and reaction for the formation and homolysis reaction of transient complexes with metal–carbon σ-bonds containing different metal centers (*46*). Previously the large volumes of activation for the homolysis reaction that were measured for Cr^{III} (*56*), Co^{III} (*73*), Ni^{III} (*43*) (15–26 $cm^3\ mol^{-1}$) were interpreted as indication for an S_H1 mechanism (i.e., due to bond breakage and to the breakup of the solvent cage due to the separation of the aliphatic radicals from the $L_{m-1}M^n$ center) (*127*). But as an I mechanism for the forward (formation)

TABLE II

EFFECT OF METAL CENTER ON THE EQUILIBRIUM CONSTANTS OF HOMOLYSIS FOR $\{N(CH_2CO_2^-)_3\}(H_2O)M^{III}–CH_3^- + H_2O \rightleftarrows M^{II}\{N(CH_2CO_2^-)_3\}(H_2O)_2^- + {}^{\bullet}CH_3$

M	K (M)	Ref.
Mn	8.3×10^{-4}	(*59*)
Fe	4.3×10^{-4}	(*59*)
Co	3.7×10^{-7}	(*72*)

TABLE III

VOLUMES OF ACTIVATION AND REACTION FOR THE FORMATION AND HOMOLYSIS OF TRANSIENT COMPLEXES WITH METAL–CARBON σ-BONDS

Complex	$\Delta V^{\ddagger}(k_9)$ ($cm^3\ mol^{-1}$)	$\Delta V^{\ddagger}(k_{-9})$ ($cm^3\ mol^{-1}$)	$\Delta V^{\circ}(K_9)$ ($cm^3\ mol^{-1}$)	K_9 (M^{-1})	Ref.
$(hedta)Fe^{III}–CO_2^{2-}$	+2.0	+7.0	−5.0	2.5×10^5	(*46*)
$(hedta)Fe^{III}–CH_3^-$	+3.8	+2.7	+1.1	7.0×10^2	(*46*)
$(H_2O)_5Cr^{III}–C(CH_3)_2OH^{2+}$	+5.7	+15.1	−9.4	4.0×10^8	(*56*)
$(nta)(H_2O)Co^{III}–CH_3^-$	+6.0	+18.6	−12.6	2.7×10^6	(*73*)
$(cyclam)Ni^{III}–CH_3^{2+}$	+4.0	+24.4	−20.4	1.1×10^7	(*43*)

reaction and an S_H1 mechanism for the homolysis reaction are incompatible due to the microscopic reversibility principle, vide supra, the explanation for the large volume of activation for the homolysis reaction of the above complexes has to be due to special properties of the central metal cations (*46*). Indeed, comparing the results of the previous studies with those for an $M^nL_m = Fe^{II}(hedta)(H_2O)^-$ and $^{\bullet}R = {}^{\bullet}CH_3$ and $CO_2^{\bullet-}$ system, where the electronic configuration of both $Fe^{II}(hedta)(H_2O)^-$ and $(hedta)Fe^{III}–R$ is high spin, proved this hypothesis. As can be seen in Table III, the smallest volumes of activation for the homolysis reaction were found for the above Fe systems (*46*).

The increase in volume change for the Cr system is explained by the electronic change in the inner coordination sphere from the Jahn-Teller distorted coordination sphere of Cr^{II} to an octahedral one in $Cr^{III}–R$ (*56*). Further increase for the Co system is due to change of the electronic configuration of high spin d^7 for Co^{II} to low spin d^6 for $Co^{III}–R$ in this system (*73*). The largest volume of activation found in the Ni system is attributed to the change in coordination number of the central Ni ion from planar low spin d^8 $(Nicyclam)^{2+}$ to octahedral d^7 for the Ni–R complex (*43*).

The charge on the R group also has a pronounced effect on the equilibrium constant of homolysis of complexes with metal–carbon σ-bonds. Comparing the stability constants of homolysis for $(hedta)Fe^{III}–R$ for $R = {}^-CH_3$ and CO_2^{2-}, Table III (*46*), shows that the complexes for $R = CO_2^{2-}$ are considerably more stable, than those formed with $R = {}^-CH_3$ (*46*). This difference is attributed to the stronger electrostatic interaction between the central cation and the CO_2^{2-} ligand and probably due to some d–π* interaction (*46*).

TABLE IV

OVERVIEW OF RATE CONSTANTS FOR THE REACTION OF METHYL RADICALS WITH LM^{n+1}–CH_3 FOR SEVERAL SYSTEMS

$M^{n+1}L_m$–CH_3	2k (M^{-1} s^{-1})	Ref.
$[(NH_3)_5Co–CH_3]^{2+}$	$(6 \pm 3) \times 10^8$	(*27*)
$[\{N(CH_2CO_2)_3\}(H_2O)Co–CH_3]^-$	$(7.5 \pm 2.0) \times 10^7$	(*72*)
$[\{N(CH_2CO_2)_3\}(H_2O)Fe–CH_3]^-$	$(1.1 \pm 0.3) \times 10^9$	(*59*)
$[\{N(CH_2CO_2)_3\}(H_2O)Mn–CH_3]^-$	$(3.2 \pm 0.6) \times 10^9$	(*59*)
$[cyclam(H_2O)Ni–CH_3]^{2+}$	$(8.0 \pm 2) \times 10^7$	(*84*)
$[(hedta)Fe–CH_3]^{2+}$	$(2.7 \pm 0.2) \times 10^7$	(*46*)

Homolysis of the M^{n+1}–C bond can be followed by a variety of possible radical processes, e.g.,

(1) The bimolecular reaction of the radicals leads to dimers or their disproportionation products:

$$2R^{\bullet} \longrightarrow R_2/RH + R_{-H} \tag{26}$$

(2) The homolytic decomposition in the absence of scavengers for the radical $^{\bullet}R$ is often followed by the reaction of the radical $^{\bullet}R$ with the transient complex with the metal–carbon bond:

$$L_{m-1}M^{n+1} - R + R^{\bullet} \xrightarrow{L} M^nL_m + R_2/(R^+ + R^-) \tag{27}$$

This reaction leads in many systems to unexpected products. The detailed mechanism of this reaction was studied only in few systems (*27,28*). Systems which follow this pathway (Eq. (9) followed by (27)), show an inverse dependence on $[M^nL_m]$ of their second order rate constant of decomposition of the transient complex with the metal–carbon bond. This is contrary to an inverse dependence on $[M^nL_m]^2$, which is observed when reaction (9) is followed by reaction (26) (radical radical reaction).

Reactions analogous to reaction (27) for methyl radicals were observed for a variety of complexes. The product of these reactions is ethane. Table IV presents a summary of their rates of reaction. As can be seen these rates are often fast, approaching the diffusion-controlled limit. The results for the homolytic decomposition of $L^2Cu^{II}–CH_2CH_2CO_2^-$ suggest that steric hindrance slows down reaction (27) considerably (*92*).

Volumes of activation for reaction (27) were measured for the (hedta)Fe^{III}–R, $^{\bullet}R=^{\bullet}CH_3$ and $CO_2^{\bullet-}$ system as –5.5 and 4.2 $cm^3\ mol^{-1}$, respectively (*46*). The positive value received for the $^{\bullet}R=CO_2^{\bullet-}$ system was contrary to the expectation that bond formation (Fe–C or C–O) in the transition state will lead to a negative $\Delta V^{\#}$. Therefore the following transition state was suggested for this system (*46*):

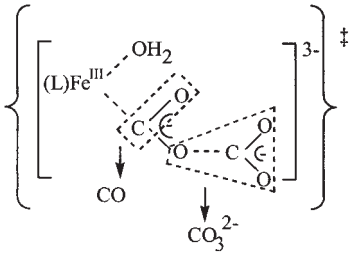

involving the formation of an Fe–O and a C–O bond and breaking of an Fe–C and C–O bond and the reduction of the central iron ion (*46*). It should be noted that the reaction products in the latter reaction are CO and CO_3^{2-}, i.e., reaction (27) yields the disproportionation products in this case.

(3) In the presence of scavengers the following general reaction takes place:

$$R^{\bullet} + S \longrightarrow \text{products} \tag{23}$$

In the presence of dioxygen, which acts as a scavenger for the radicals $^{\bullet}R$, homolytic decomposition is thus followed by (*43,72,73,84*):

$$R^{\bullet} + O_2 \longrightarrow RO_2^{\bullet} \tag{28}$$

which is usually followed by (*43,72,73,84*):

$$RO_2^{\bullet} + M^nL_m \longrightarrow L_{m-1}M^{n+1} - OOR + L \tag{29}$$

The transient complexes $L_{m-1}M^{n+1}$–OOR thus formed are an important class of intermediates by themselves (*128–131*). Moreover in several systems, which decompose via homolysis, oxygen was used as a scavenger for the methyl radical (*72,84*) and thus aided in the elucidation of the mechanism and the determination of the associated rate constants (*72,84*).

In the presence of efficient scavengers for M^nL_m and/or $^{\bullet}R$ the mechanism of decomposition of complexes with metal–carbon σ-bonds, which decompose heterolytically under routine conditions, can be shifted towards the homolytic decomposition (*49,50,124*).

Mechanistically the distinction between the homolytic and the heterolytic mechanism is based on two types of experimental data.

(1) *Kinetic Evidence*: The homolytic decomposition follows a rate law, which is second order in the L^iM^{n+1}–$CR^1R^2R^3$ intermediate and shows an inverse dependence on the $M^nL^i_m$ concentration, whereas a heterolytic decomposition mechanism obeys a first order dependence on the L^iM^{n+1}–$CR^1R^2R^3$ compound and is independent of the $M^nL^i_m$ concentration.

(2) *Product Analysis*: The products of a homolytic decomposition are expected to contain dimers of the organic radical or their disproportionation products, whereas in the heterolytic decomposition process the only expected organic products in aqueous solutions are RH (reduced organic radical) or ROH (oxidized organic radical).

C. Oxidation of $L_{m-1}M^{n+1}$–R Followed by Homolysis

Many electron acceptors are able to oxidize transient complexes with metal–carbon σ-bonds. The reaction of organochromium(III) species ($(H_2O)_5Cr$–R^{2+} and $L(H_2O)Cr$–R^{2+}, L = 1,4,8,12-tetraazacyclopentadecane) have been studied for the acceptors $Ru(bpy)_3^{3+}$, ^{2}E-$Cr(bpy)_3^{3+}$, $Ni([14]aneN_4)^{3+}$, and $IrCl_6^{2-}$ (*132,133*), and proceed according to the following general equation:

$$Cr\text{–}R^{2+} + A \longrightarrow Cr\text{–}R^{3+} + A^- \qquad (30)$$

It was reported (*134*), that dihalides $X_2^{\bullet -}$ (X = I, Br, SCN), generated by pulse radiolysis of N_2O saturated aqueous solutions of the corresponding sodium halides or sodiumthiocyanate, oxidize a variety of $L(H_2O)Cr$–R^{2+} as well, according to:

$$L(H_2O)Cr\text{–}R^{2+} + X_2^{\bullet -} \longrightarrow L(H_2O)Cr\text{–}R^{3+} + 2X^- \qquad (31)$$

The rate constants of this bimolecular reaction for a given organochromium cation change in order of the driving force, with *k*'s increasing in the series $I_2^{\bullet -} < SCN_2^{\bullet -} < Br_2^{\bullet -}$.

The rates also change in a regular way with variation of the R group on the organochromium complex. However, the fact that this change is smaller than that in a similar series of oxidations by $Ru(bpy)_3^{3+}$ and $^2E\text{-}Cr(bpy)_3^{3+}$ and that the variation in rates of the $X_2^{\bullet -}$ reagents is rather small compared to the difference in driving force (0.59 V) in this series, suggests that the rate limiting step in the $X_2^{\bullet -}$ reactions is not purely electron transfer. Thus a mechanism was suggested in which a loosely bound adduct is involved (*134*):

$$L(H_2O)Cr\text{–}R^{2+} + X_2^{\bullet -} \rightleftarrows \{X_2^{\bullet -}, L(H_2O)Cr\text{–}R^{2+}\} \quad (32)$$

$$\{X_2^{\bullet -}, L(H_2O)Cr\text{–}R^{2+}\} \longrightarrow L(H_2O)Cr\text{–}R^{3+} + 2X^- \quad (33)$$

The oxidized organochromium transient decomposes via homolysis of the chromium–carbon bond (*134*):

$$L(H_2O)Cr\text{–}R^{3+} \longrightarrow (H_2O)_2CrL^{3+} + {}^{\bullet}R \quad (34)$$

K_{34} is clearly larger for the Cr^{IV}–C complexes than for the corresponding Cr^{III}–C complexes. This observation was attributed to the high oxidation potential of the $Cr^{IV/III}$ couple. Similarly the tendency for homolysis is larger for Ni^{III}–C complexes than for the corresponding Ni^{II}–C complexes (*83*). On the other hand, Cu^{II}–C complexes are more susceptible to homolysis than the corresponding Cu^{III}–C complexes probably due the tendency of the latter to decompose via reductive heterolysis (*85,97*).

D. β-Hydride Shift Reactions

β-Hydride shift reactions were also observed, though up to now only in a few systems, e.g.,

$$L(H_2O)Co^{III}\text{–}CH(CH_3)OH^{2+} \longrightarrow L(H_2O)Co^{III}\text{–}H^{2+} + CH_3CHO \quad (70) \quad (35)$$

where L is a tetraaza-macrocyclic ligand.

A β-hydride shift involvement was also implied in the acid catalyzed decomposition of $[(H_2O)_5Cr^{III}\text{–}C(CH_3)_2OH]^{2+}$ yielding propene as a major product (*135*). It was proposed that this complex

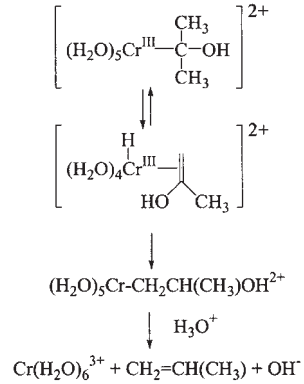

SCHEME 2.

isomerizes via a β-hydride shift step to form $[(H_2O)_5Cr^{III}–CH_2CH(CH_3)OH]^{2+}$ which decomposes via β hydroxide elimination according to Scheme 2 (*135*).

E. β-ELIMINATION REACTIONS

The β-elimination mechanism of decomposition of transient complexes of the type $L_mM^{n+1}–R$ occurs when a good leaving group, X, e.g., X = –OR, $–NR_2$, –NHC(O)R, and halides, is bound to the β-carbon:

$$L_mM^{n+1} - CR^1R^2CR^3R^4X \longrightarrow M^{n+1}L_m + R^1R^2C = CR^3R^4 + X^- \qquad (36)$$

These reactions were observed for a large variety of such complexes, see for example, X = OH (*13,50,55,57,63,70,71,77,85,88,136–138*), X = OR (*139*), $X = NR_2$ (*90,91,102,140,141*), $OP(O)(OH)_2$ (*142*), and NHC(O)R (*143*).

Decomposition reactions following the β-elimination mechanism are generally considerably faster than the decomposition reactions of the corresponding alkyl complexes. The decompositions of the $L_mM^{n+1}–CR^1R^2CR^3R^4X$ transients that follow first order rate laws, are often acid catalyzed and produce usually the corresponding alkenes, $M^{n+1}L_m$, and X^- as the final stable products. In some cases intermediates containing the alkenes bound to the metal-complex are observed (*55,71,144*). Thus the first product in all β-elimination processes seems to be a π-complex (or actually a structure between the extreme descriptions as π-complex and that as a 3-ring metallocycle)

TABLE V

SPECIFIC RATES OF β-HYDROXYL ELIMINATION FROM L_mM^{n+1}–$CR^1R^2CR^3R^4OH$ COMPLEXES

Complex	k_0 (s^{-1})	k_{H+} ($M^{-1}\,s^{-1}$)	Ref.
$[(H_2O)_5Cu^{II}–CH_2CH_2OH]^+$	3.2×10^3	3.8×10^7	(*85*)
$[(H_2O)_5Cu^{II}–CH_2CH(CH_3)OH]^+$	1.5×10^4	1.5×10^8	(*85*)
$[(H_2O)_5Cu^{II}–CH_2C(CH_3)_2OH]^+$	5.0×10^4	8.6×10^7	(*136*)
$[(H_2O)_5Cr^{III}–CH_2CH_2OH]^{2+}$	2.0	1.4×10^4	(*55*)
$[(H_2O)_5Cr^{III}–CH(CH_3)CH_2OH]^{2+}$	21	1.1×10^5	(*55*)
$[(H_2O)_5Cr^{III}–CH(CH_3)CH(CH_3)OH]^{2+}$	250	9.8×10^4	(*55*)
$[(H_2O)_5Cr^{III}–CH_2C(CH_3)_2OH]^{2+}$	100	2.7×10^6	(*13,55,144*)
$[(H_2O)_5Cr^{III}–CH_2CH_2OCH_2CH_3]^{2+}$	< 0.1	4.6×10^3	(*139*)
$[(H_2O)_5Cr^{III}–CH(OH)CH_2OH]^{2+}$	$> 5 \times 10^5$		(*13*)
$[(H_2O)_5Cr^{III}–CHOCH_2CH_2OCH_2]^{2+}$	$< 2 \times 10^{-2}$	4.8×10^{-1}	(*13*)
$(dmg\text{-}H)_2Co^{III}–CH_2CH_2OH$		0.7	(*182*)
$PPFe^{III}–CH_2CH_2OH$	80 ($10 < pH < 13$)		(*63*)
$PPFe^{III}–CH(CH_3)CH_2OH$	40 ($10 < pH < 13$)		(*63*)
$[(tspc)Co^{III}–CH_2C(CH_3)_2OH]^{4-}$	15		(*71*)
$[(tspc)Co^{III}–CH(CH_3)CH(CH_3)OH]^{4-}$	6		(*71*)
$[(tspc)Co^{III}–CH(CH_3)CH_2OH]^{4-}$	8		(*71*)
$[(tspc)Co^{III}–CH_2CH_2OH]^{4-}$	5		(*71*)

dmg-H, dimethylglyoxomato; PP, protoporphyrin; tspc, tetrasulphophthalocyanine.

between the leaving alkene and the central transition metal cation (*55,71,144*).

Comparing rates of decomposition for transient complexes containing different metal centers (Table V) it was observed that the specific rates of β-hydroxyl elimination for $Cu^{II}–CR^1R^2CR^3R^4OH$ complexes are considerably higher than those observed for $(H_2O)_5Cr^{III}R$, $(tspc)Co^{III}R$ and $PPFe^{III}R$ (*136*).

The effect of methyl substituents on the β-carbon on the rate of β-elimination is complicated, different effects are observed for the acid dependent and acid independent process and for different central cations (Table V) (*136*). Methyl substituents on the β-carbon enhance the specific rate of the acid independent path for both chromium(III) and copper(II) complexes, however no such effect was observed for the analogues (tspc)Co(III) complexes (*136*). The effect on the acid catalyzed reaction is even opposite for the chromium(III) and copper(II) complexes (*136*).

The rate constants for β-elimination processes are correlated with the C–X bond strength (*91,140*). Thus the rate determining step in these processes involves the breaking of the C–X bond. β-Elimination

reactions of NH_3 are considerably slower than those of the corresponding β-hydroxyl elimination reactions (*91,140*). The results indicate that the C–X bond strength in $[M^{n+1}–CH_2C(CH_3)_2X]^{n+}$ (X = OH, NH_3) complexes is reversed relative to the corresponding alkyls, as the metal center exerts a large inductive effect, affecting the C–X bond strength considerably (*91,140*).

Measurements of the volumes of activation of some of these reactions (141) suggest that their transitions states are of the type:

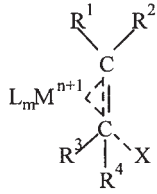

No specific pH-dependence of the volumes of activation was found in either the spontaneous or the acid catalyzed pathways, indicating that their transition states are similar (e.g., X = OH, H_2O respectively in the above scheme) and that they basically follow the same mechanism (*141*).

It is of interest to note that the transient complex

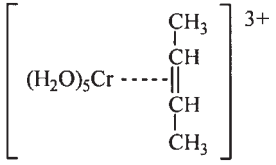

formed in the decomposition of $(H_2O)_5Cr–CH(CH_3)CH(CH_3)OH^{2+}$, decomposed to a 1:1 mixture of *cis*- and *trans*-2-butene at pH > 2, whereas at pH < 1 the thermodynamically less stable *cis*-2-butene is produced in considerable excess. This surprising result is attributed to an acid catalyzed isomerization of the $d \rightarrow \pi$ complex and a higher rate of dissociation of the *cis*-2-butene complex. This mechanism is outlined in Scheme 3.

F. β-Elimination of Carboxylates

A further mechanism of decomposition which was observed up to date only for $M^n = Cu(II)$ (*101,102*) is the β-elimination of carboxylates:

$$L_mM^{n+1}–(CR^1R^2CR^3R^4CO_2^-) \longrightarrow M^{n-1}L_m + R^1R^2C = CR^3R^4 + CO_2 \quad (37)$$

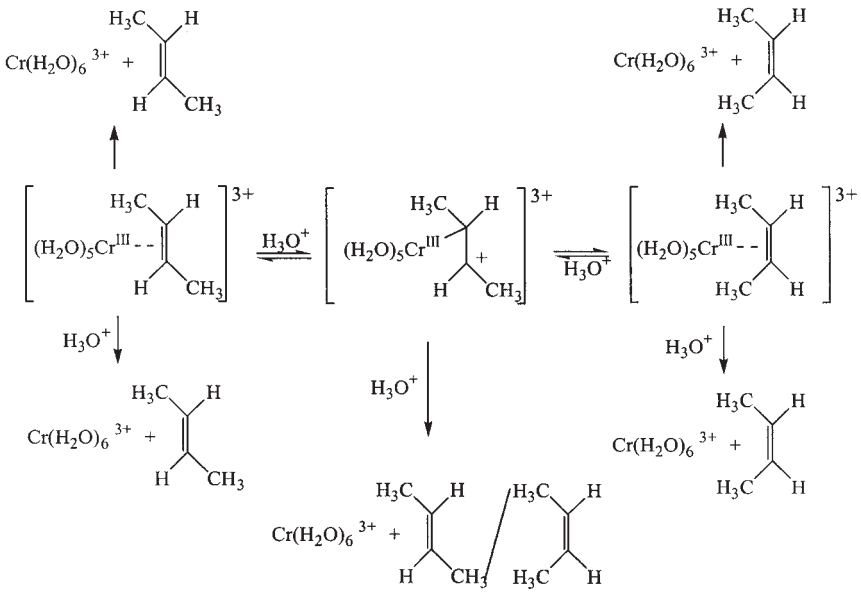

SCHEME 3.

By this reaction the reduced metal-complex, the corresponding alkene and CO_2 are formed. Thus the reaction requires that the central metal ion can be reduced.

This mechanism is of importance in radical induced amino acid damage catalyzed by copper ions. The study of the decomposition of transients with a metal–carbon σ-bond containing two potential leaving groups (both an amine and a carboxylate group) at the β position of the carbon centered radical is of special interest. It was reported that the intermediate formed with the amino acid 2-methylalanine with cupric ions decomposes via β-carboxyl elimination whereas the intermediate formed with cuprous ions decomposes via β-amine elimination (*102*).

The rate of decomposition of Cu^{III}–$CH_2C(CH_3)_2CO_2H^{2+}{}_{aq}$ is considerably slower ($k = 0.03\ s^{-1}$) than that reported for the corresponding intermediate containing instead of the carboxylate an OH group (which decomposes heterolytically analogous to reaction (18), $k = 4.5 \times 10^2\ s^{-1}$) (*97*,*101*). It was proposed, that the intermediate

$Cu^{III}–CH_2C(CH_3)_2CO_2H^{2+}_{aq}$ probably exists in aqueous solution mainly in the form

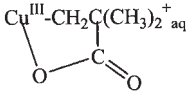

thus stabilizing this intermediate towards heterolysis.

G. CO Insertion/Methyl Migration

The insertion of ligated CO into metal–carbon σ-bonds (or rather the migration of an alkyl group to a coordinated CO) is a key step in a variety of synthetic and catalytic important processes, e.g., in hydroformylation (*145*), the Fischer-Tropsch reaction (*146*) and the synthesis of acetic acid from methanol (*147*).

$$(CO)M–R \longrightarrow M–C(R) = O \tag{38}$$

A detailed study of the CO insertion, or methyl migration, observing formation and decomposition of the transients, was performed so far only for one Cu(I) model system (*93*). It was reported that methyl radicals form transient complexes containing metal–carbon σ-bonds with carbonmonoxide ($n = 1$, 3, 4) complexes of Cu(I). These complexes decompose yielding Cu(II) and acetaldehyde as final products via an copper acetyl intermediate formed by insertion of CO/migration of CH_3 as described in Scheme 4.

The rates in the scheme are for $[CO]/[Cu^+] = 3$ and depend slightly on this ratio. However analogous studies clearly can be carried out for other systems.

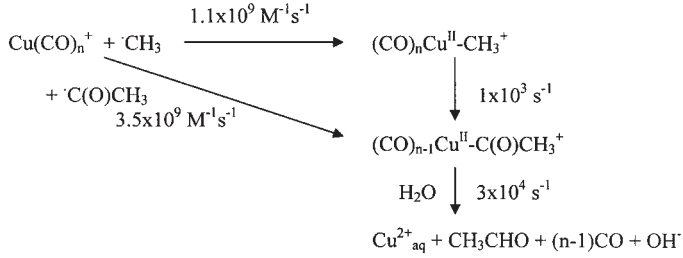

SCHEME 4.

H. Bimolecular Decomposition of the Transient Complexes

Several Cu(II) intermediates decompose via bimolecular reactions. Cu^{II}–$CH^{+}_{3\,aq}$ decomposes at pH ≥ 2.5 via

$$2Cu^{II} - CH^{+}_{3\,aq} \longrightarrow 2Cu^{+}_{aq} + C_2H_6 \qquad (39)$$

This process, which involves carbon–carbon bond formation, does not involve homolysis of the copper carbon bond followed by reactions analogous to Eqs. (26) or (27) (*86*). Whereas in highly acidic solutions (pH < 1.5) Cu^{II}–$CH^{+}_{3\,aq}$ decomposes heterolytically, via reaction (17), yielding methane as the final product, the decomposition of Cu^{II}–$CH^{+}_{3\,aq}$ at pH ≥ 2.5 obeys a second order rate law ($2k = 3.0 \times 10^8$ M^{-1} s^{-1}) (*92*), with the rate being independent of the concentrations of Cu^{2+}_{aq}, Cu^{+}_{aq}, $(CH_3)_2SO$, and CH_3CO_2Na. Ethane is the final product of this reaction (*86*). Thus Cu^{II}–$CH^{+}_{3\,aq}$ decomposes via a bimolecular or a heterolytic process depending on pH.

Decomposition reactions proceeding according to an analogous mechanism to reaction (33) have also been observed for L^2Cu^{II}–CH^{+}_3 (L^2 = 2,5,8,11-tetramethyl-2,5,8,11-tetraazadodecane; $2k = 8.6 \times 10^6$ M^{-1} s^{-1}) and for Cu^{II}–$CH_2CH_2COOH^{+}_{aq}$ (*92*). However, the corresponding L^2Cu^{II}–$CH_2CH_2COOH^{+}$ complex decomposes via homolysis in contrast to the aqua system, apparently due to steric hindrance imposed by the ligand, L^2 (*92*). Obviously the nature of R and L have a pronounced effect on the mechanism of decomposition of the intermediate complexes with metal–carbon σ-bonds. Analogous complexes to the above with R=CH_2COOH and $CH(CH_3)COOH$ decompose via heterolysis of the copper–carbon σ-bonds for both the aqua and the L^2 system forming Cu(II)L. The observation that LCu^{II}–CH_2COOH^{+} and LCu^{II}–$CH(CH_3)COOH^{+}_{aq}$ decompose heterolytically under conditions where LCu^{II}–CH^{+}_3 decompose via an alternative mechanism is not surprising as the electron withdrawing substituent bound to the α carbon, –COOH, increases the polar nature of the metal–carbon σ-bond (*92*). A homolytic process was observed for Cu^{II}–$CH_2OH^{+}_{aq}$ (*85*) and Cu^{II}–CO_{2aq} (*148*).

Reaction (39) is proposed to proceed via a transition state in which a carbon–carbon bond is formed directly while each methyl is bound to another copper (*92*):

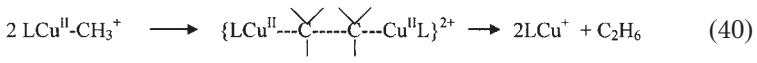

(40)

A small negative volume of activation of $-5 \pm 1\ cm^3\ mol^{-1}$ was measured for the decomposition reaction of Cu^{II}–CH^+_{3aq} supporting the suggested mechanism. Most likely the C–C bond formation process, associated with a volume collapse, is the dominant factor in determining the sign of $\Delta V^{\#}$ in this reaction. (The accompanying stretching of the Cu–C bonds will be associated with a volume increase that will partially offset this volume collapse (*108*).)

I. Methyl Transfer Reactions

In the presence of an additional metal ion or complex the R group of an intermediate containing a metal–carbon σ-bond can be transferred to it, according to:

$$L_{m-1}M^{n+1} - R + (M^nL_m)' \longrightarrow M^nL_m + (L_{m-1}M^{n+1})' - R \qquad (41)$$

where $(M^nL_m)'$ is a stronger reducing agent than M^nL_m. Reactions of this kind were observed for the reaction of several alkylcobalt(III) compounds (*50*) and of $L(H_2O)Ni^{III}$–CH^{2+}_3 (*84*) with $Cr(H_2O)^{2+}_6$.

The rate of decomposition of $L(H_2O)Ni^{III}$–CH^{2+}_3 (L = cyclam) is thus enhanced in solutions containing added $Cr(H_2O)^{2+}_6$ (*84*). The kinetics of decomposition of $L(H_2O)Ni^{III}$–CH^{2+}_3 under these conditions obey a pseudo first order rate law with the rate being proportional to $[Cr(H_2O)^{2+}_6]$ and independent of $[LNi^{2+}]$. The results thus point out, that the reaction occurring is analogous to Eq. (41) and does not proceed via an initial homolysis of the Ni–carbon bond. The specific rate of reaction found for the reaction of the Ni-complex with Cr^{II}_{aq} ($k_{41} = 1.1 \times 10^5\ M^{-1}\ s^{-1}$) (*84*) is about three orders of magnitude higher than those reported for the fastest alkyl-transfer reactions from organocobalt complexes (*50*), probably due to the higher redox potential of the Ni(III) complex (*84*).

$$M^{n-1}L + LM^{n+1}\text{–}R \longrightarrow M^nL + LM^n\text{–}R \qquad (42)$$

The reactions analogous to Eq. (42) observed for $M^n = Cu^{II}$ (*149*) and Ni^{II} (*150*) probably proceed via the same mechanism, though an outer sphere redox mechanism is a plausible alternative.

J. Rearrangement of the Carbon-Skeleton of R

In principle one can expect that the formation of transient complexes of the type L_mM^{n+1}–R might result in the rearrangement of the carbon-skeleton of R in analogy to B-12 catalyzed processes (*151*). However, only one such reaction was observed till now (*89*), probably due to the fact that very simple alkyl radicals are used in most studies. This rearrangement is discussed in Section IX.

K. $(H_2O)_5CrCHO^{2+}$ as a Hydride Transfer Reducing Agent

The formyl complex $[(H_2O)_5CrCHO]^{2+}$ is formed in aqueous solution via the reaction of aqueous Cr(II) with the dihydroxymethyl radical (*52*). The latter radical is derived from the reaction of formaldehyde (aqueous formaldehyde exists almost exclusively in the acetal form) with $^{\bullet}OH$ radicals. The initial complex formed is that of the hydrated formyl complex, which transforms rapidly to the formyl complex:

$$Cr^{2+}_{aq} + {}^{\bullet}CH(OH)_2 \longrightarrow [(H_2O)_5CrCH(OH)_2]^{2+} \longrightarrow [(H_2O)_5CrCHO]^{2+} + H_2O \quad (43)$$

Apparently the preference of the formyl ligand for the aldehyde form over the hydrated form stems mainly from the large steric requirements of the $(H_2O)_5Cr$ moiety. Surprisingly the transient formyl complex acts as a reducing agent towards the formaldehyde present in the solution, via hydride transfer to yield CO and methanol (*52*):

$$[(H_2O)_5CrCHO]^{2+} + H_2C{=}O + H_3O^+ \longrightarrow CH_3OH + CO + Cr^{III}_{aq} \quad (44)$$

VII. Alkene Complexes

Alkenes are known to form $d \rightarrow \pi$ complexes with low valent transition metal ions (or atoms), thus stabilizing their low valent complexes (*152*). Complexes of this type are key intermediates in a variety of catalytic processes, e.g., hydrogenations, polymerizations,

alkene isomerization. The kinetics of formation of these complexes were not known.

A large number of π-complexes of Cu(I) are known. Recently a detailed study of the kinetics of formation (*123*) and the stability constants of copper(I) complexes with the three acid–base forms of fumaric and maleic acid were carried out (*153*). The results demonstrate that the rate constants of the reaction

$$\begin{aligned} Cu^{I}_{aq} + HOOCCH=CHCOO^{-} \\ \longrightarrow \{Cu^{I}_{aq};\ HOOCCH=CHCOO^{-}\} \\ d \longrightarrow \pi^{*}\text{complex} \end{aligned} \tag{45}$$

approach the diffusion controlled limit. This result indicates that:

(a) The ligand exchange rate of Cu(I) complexes is very high.
(b) The formation of $d \rightarrow \pi$ bonds is extremely facile.

It was observed that the alkaline forms of the unsaturated acids form noticeably more stable complexes than the acids although deprotonation of the acids decreases the electron-attracting property of the π-ligand and thus decreases the contribution of the π-back-bonding. Clearly the negative charge on the oxygen induces an electrostatic interaction between the central metal ion and the oxygen, thus increasing the stability constants of the complexes (*153*).

Copper(I) and silver(I) complexes are exceptions of the general trend in stability constants with electron-donating or attracting substituents. Thus most known π-complexes of silver and copper are less stable than their respective ethylene complexes (*154–156*). The steric hindrance introduced by the substituents seems to have a major effect in those systems.

VIII. Complexes with Metal–Carbon σ-Bonds Formed in Redox Processes Between Transition Metal Complexes and Organic Substrates

A. Reduction of Halo–Alkanes

1. Reduction of $Cl_3CCO_2^-$ by Cu^IL Complexes

Copper(I) complexes catalyze a variety of organic reactions, which are of synthetic and industrial importance. Many of these processes

are initiated by halide abstraction from aryl or alkyl halides by the Cu(I) catalyst (*157–159*). Due to the low solubility of Cu(I) halides, and due to the disproportionation of Cu^{+}_{aq} the concentration of Cu(I) in these systems is usually very low. It was therefore of interest to check whether the addition of appropriate ligands for Cu(I), e.g., CH_3CN (*160,161*), alkenes (*162*), NH_3 (*162*), and several tri- and tetradentate ligands L with incorporated alkene groups (e.g., L^3 and L^4) (*163–165*), will accelerate these processes.

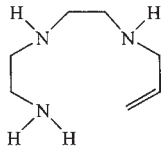

L^3

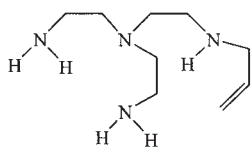

L^4

Thus a detailed study on the effect of ligands that stabilize copper(I) on the rates and mechanisms of reduction of trichloroacetic acid, $Cl_3CCO_2^-$ was carried out (*149*).

The general reaction mechanism for the reaction of Cu(I) with trichloroacetic acid in the presence of stabilizing ligands is summarized in the following equations (*149*):

$$Cu^{+}_{aq} + L \rightleftharpoons Cu^{I}L \tag{46}$$

$$Cu^{+}_{aq}/Cu^{I}L + Cl_3CCO_2^- \longrightarrow (LCu^{II}Cl)/(CuCl)^{+} + {}^{\bullet}CCl_2CO_2^- \tag{47}$$

$$Cu^{+}_{aq}/Cu^{I}L + {}^{\bullet}CCl_2CO_2^- \longrightarrow (LCu^{II}{-}CCl_2CO_2^-)/(Cu^{II}{-}CCl_2CO_2^-) \tag{48}$$

$$(LCu^{II}{-}CCl_2CO_2^-)/(Cu^{II}{-}CCl_2CO_2^-) + H_3O^{+} \longrightarrow Cu^{2+}_{aq} + HCCl_2CO_2^- + L \tag{49}$$

$$Cu^{2+}_{aq}/Cu^{II}L + {}^{\bullet}CCl_2CO_2^- \longrightarrow (LCu^{III}{-}CCl_2CO_2^-)/(Cu^{III}{-}CCl_2CO_2^-)^{+} \tag{50}$$

$$(LCu^{III}{-}CCl_2CO_2^-)/(Cu^{III}{-}CCl_2CO_2^-)^{+} + Cu^{+}_{aq}/Cu^{I}L \longrightarrow (LCu^{II}{-}CCl_2CO_2^-)/(Cu^{II}{-}CCl_2CO_2^-) + Cu^{2+}_{aq}/Cu^{II}L \tag{51}$$

(charges for CuL complexes have been omitted in this scheme, as L = neutral or –1).

The results demonstrate that the rate of the chlorine abstraction reaction (Eq. (47)), which is usually the rate determining step in this process, is affected by: (a) the redox potential of the $Cu^{II/I}L$ couple (solvents such as acetonitrile, that form complexes with Cu^{I} and anodically shift its redox potential, decrease the reactivity), (b) the hybridization on Cu^{I} in the $Cu^{I}L$ complex, (c) steric hindrance, (d) electron density on the central Cu^{I} cation, at the binding site of the chlorine atom to be abstracted (*149*). However for the complex $Cu(I)L^{4}$, which is the strongest reducing agent studied, the stability of the $L^{4}Cu^{II}–CCl_2CO_2^-$ transient is increased considerably and its decomposition becomes the rate determining step (*149*).

2. Reduction of Halo–Alkanes by $Ni^{I}L$ Complexes

Halo–alkenes are common pollutants. Therefore, there is an ongoing study on plausible approaches to the dehalogenation of halo–alkanes. One of these approaches involves their electrocatalytic reduction. $Ni^{II}L^{2+}$ (L = a tetraaza macrocyclic ligand) complexes were proposed as plausible electrocatalysts (*150*). A pulse radiolytic study on the mechanism and kinetics of the reaction:

$$Ni^{I}L^{+} + RX \longrightarrow Ni^{II}L^{2+} + {}^{\bullet}R + X^{-} \tag{52}$$

indicated that it is often followed by

$$Ni^{II}L^{2+} + {}^{\bullet}R \longrightarrow LNi^{III}–R^{2+} \tag{53}$$

$$Ni^{I}L^{+} + LNi^{III}–R^{2+} \longrightarrow LNi^{II}–R^{+} + Ni^{II}L^{2+} \tag{54}$$

$$LNi^{II}–R^{+} + H^{+} \longrightarrow Ni^{II}L^{2+} + HR \tag{55}$$

i.e., the kinetics of the latter reactions affect the nature of the final products of the dehalogenation process (*150*).

B. Decomposition of Cu(III)Peptide Complexes

Cu^{III}peptide complexes are formed via the oxidation of Cu^{II}peptide complexes by a variety of oxidizing agents, e.g., O_2 (*166*) and $RO_2^{\bullet}$ radicals (*131,143,167*). It was proposed that the decomposition of the Cu^{III}(GlyGlyHis) complex, proceeds via the mechanism outlined in Scheme 5 (*166*). The mechanism includes closure of the free

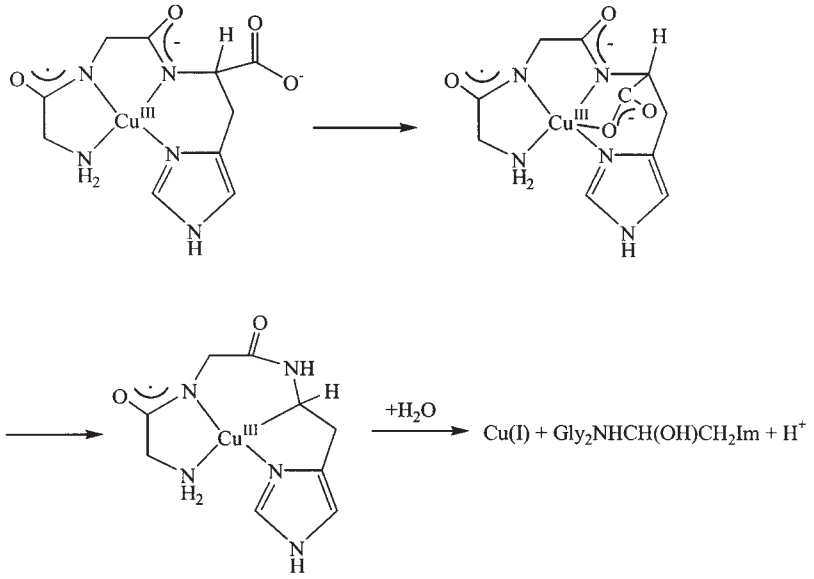

SCHEME 5.

carboxylate to form a chelate ring followed by decarboxylation, then by the formation of a Cu^{III}–carbon bond and heterolytic cleavage of the latter (*166*).

Applying pulse radiolysis to the formation of Cu^{III}(GlyGlyHis) only two consecutive reactions are observed experimentally during its decomposition. A volume of activation of $\Delta V^{\#} = +14$ cm^3 mol^{-1} was measured for the first observable step, which is in accord with the decarboxylation process being the rate determining step in this mechanism. $\Delta V^{\#} = +8$ cm^3 mol^{-1} was obtained for the second observable process in agreement with expectations for the heterolytic cleavage of the Cu^{III}–C bond, as proposed (*168*).

C. PARTICIPATION OF COMPLEXES WITH METAL–CARBON σ-BONDS IN THE REDUCTION OF ALKENES

Alkenes are known to form relatively stable $d \rightarrow \pi$ complexes with low valent transition metal ions (or atoms), thus stabilizing their low valent complexes (*152*). For example, ethylene was shown to stabilize several Ni(I) complexes (*165*).

Recently while trying to stabilize $(Ni^{I}L')^{+}$ (L′ = 1,4,8,11-tetraazacyclotetradecane) in neutral aqueous solutions it was noted that allyl

substituents on the macrocycle indeed thermodynamically stabilize $(Ni^{I}L')^{+}$ but kinetically destabilize it as the central cation reduces the allyl substituents (*169,170*). $(Ni^{I}L')^{+}$ also reduces alkenes present homogeneously in the solution, two such reactions were studied up to date (*169,171*):

(a) The reduction of ethylene yields mainly ethane with butane as a side product (traces of hexane are also obtained). The addition of ethylene accelerates the disappearance of the mono-valent nickel complex in a general acid catalyzed process. The results suggest the following mechanism:

$$\{Ni^{I}L'\}^{+} + C_2H_4 \longrightarrow \{Ni^{II}L'\}^{2+} + {}^{\bullet}C_2H_5 \longrightarrow \{L'(Ni^{III}\text{–}C_2H_5\}^{2+} \quad (56)$$

$$\{L'(Ni^{III}\text{–}C_2H_5\}^{2+} + \{Ni^{I}L'\}^{+} \longrightarrow \{L'(Ni^{II}\text{–}C_2H_5\}^{+} + \{Ni^{II}L'\}^{2+} \quad (57)$$

$$\{Ni^{I}L'\}^{+} + {}^{\bullet}C_2H_5 \longrightarrow \{L'(Ni^{II}\text{–}C_2H_5\}^{+} \quad (58)$$

$$\{L'(Ni^{II}\text{–}C_2H_5\}^{+} + H^{+} \longrightarrow \{Ni^{II}L'\}^{2+} + C_2H_6 \quad (59)$$

$$\{L'(Ni^{III}\text{–}C_2H_5\}^{2+} + {}^{\bullet}C_2H_5 \longrightarrow \{Ni^{II}L'\}^{2+} + C_4H_{10} \quad (60)$$

(b) The reduction of maleic acid proceeds via a significantly different mechanism, i.e.,

$$\{Ni^{I}L'\}^{+} + ({}^{-}O_2C)HC{=}CH(CO_2^{-}) \rightleftarrows [\{Ni^{I}L'\}^{+}; ({}^{-}O_2C)HC{=}CH(CO_2^{-})] \quad (61)$$

i.e., the formation of a $d \rightarrow \pi^*$ complex. This reaction is followed by:

$$[\{Ni^{I}L'\}^{+}; ({}^{-}O_2C)HC = CH(CO_2^{-})] \xrightarrow{H^{+}} \{Ni^{II}L'\}^{2+} + {}^{\bullet}CH(CO_2^{-})CH_2CO_2^{-} \quad (62)$$

$$\{Ni^{I}L'\}^{+} + {}^{\bullet}CH(CO_2^{-})CH_2CO_2^{+} \rightleftarrows \{L'Ni^{II}\text{–}CH(CO_2^{-})CH_2CO_2^{-}\}^{-} \quad (63)$$

$$\{L'Ni^{II}\text{–}CH(CO_2^{-})CH_2CO_2^{-}\}^{-} + {}^{\bullet}CH(CO_2^{-})CH_2CO_2^{-} \longrightarrow \{Ni^{I}L'\}^{+} + ({}^{-}CH(CO_2^{-})CH_2CO_2^{-})_2 \quad (64)$$

$$\{Ni^{II}L'\}^{2+} + {}^{\bullet}CH(CO_2^{-})CH_2CO_2^{-} \longrightarrow \{L'Ni^{III}\text{–}CH(CO_2^{-})CH_2CO_2^{-}\} \quad (65)$$

$$\{Ni^{I}L'\}^{+} + \{L'Ni^{III}\text{–}CH(CO_2^-)CH_2CO_2^-\} \longrightarrow \{L'Ni^{II}\text{–}CH(CO_2^-)CH_2CO_2^-\}^{-} + \{Ni^{II}L'\}^{2+} \quad (66)$$

The final products of this reaction were still not determined. These results thus suggest that the detailed mechanism of reduction of ethylene and maleate by $\{Ni^{I}L'\}^{+}$ yields as transients complexes with Ni–carbon bonds. The mechanism of decomposition of the latter depends on the nature of substituents on the alkyl radical.

IX. Elucidation of the Mechanisms of Catalytic Processes

Finally it should be pointed out that the pulse radiolysis technique can be applied to the elucidation of the detailed mechanisms of a variety of catalytic processes. Here two examples for this application will be presented.

a. The catalytic oxidation of cyclohexene by $S_2O_8^{2-}$ in the presence of copper ions. The oxidation of cyclohexene to cyclopentanecarbaldehyde by $S_2O_8^{2-}$ is catalyzed by copper ions (*172*). It was proposed that the mechanism of this process involves the following steps (*172*):

$$S_2O_8^{2-} \xrightarrow{\Delta} 2\,SO_4^{\cdot-} \quad (67)$$

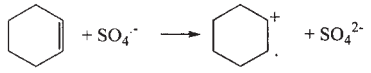

(68)

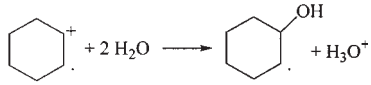

(69)

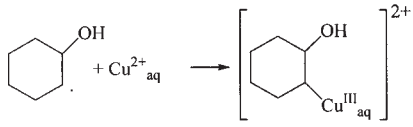

(70)

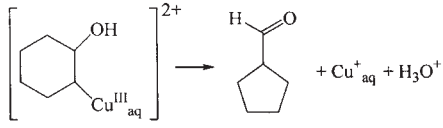

(71)

$$Cu^{+}_{aq} + S_2O_8^{2-} \longrightarrow Cu^{2+}_{aq} + SO_4^{2-} + SO_4^{\bullet -} \qquad (72)$$

As the proposed mechanism involves transients with Cu–carbon σ-bonds, via the predicted reaction of the 2-hydroxycyclohexyl radical with Cu^{2+}_{aq}, it seemed of interest to study the detailed mechanism of reaction (71). For this purpose it was decided to start with the study of reaction (70). 2-Hydroxycyclohexyl radicals are easily prepared via the reaction of •OH radicals with cyclohexene. Surprisingly it was found that its reaction with copper(II) is very slow and instead the reaction observed is that with copper(I) to yield the transient in reaction (73) (*89*). Thus even though the steady state concentration of Cu(I) in the catalytical system is rather low the 2-hydroxycyclohexyl radical will preferably react with Cu(I).

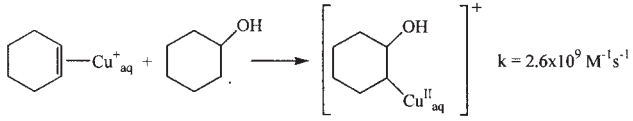

(73)

which is followed by:

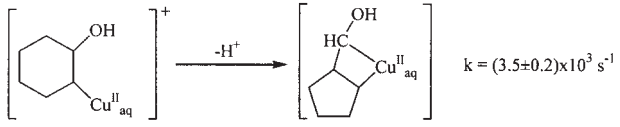

(74)

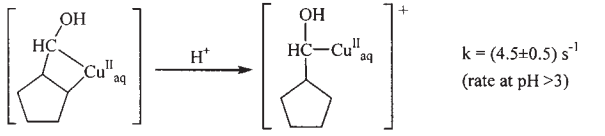

(75)

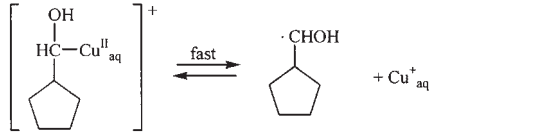

(76)

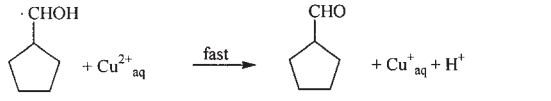

(77)

The initial transient formed, rearranges in a reaction that involves the ring contraction step in reaction (74). The lifetime of this intermediate is considerably longer than that reported for any other intermediate with a copper(II)–carbon bond in aqueous solution (*85–87,101,136*), suggesting the stabilized structure featuring the metallocycle. This intermediate decomposes via heterolysis of one of the copper(II)–carbon σ-bonds followed by homolysis of the second to form the cyclopentylmethanol radical in reactions (75) and (76), which reacts with Cu^{2+}_{aq} to form the final product cyclopentanecarbaldehyde (*89*).

Similarly the mechanism of the Cu(II) catalyzed oxidation of malic acid by $S_2O_8^{2-}$ (*173*) was reinterpreted on the basis of the properties of Cu^{II}–$CR^1R^2R^3$ and Cu^{III}–$CR^1R^2R^3$ complexes. The following catalytic Scheme 6 was proposed (*174*).

b. The "Fenton Like" reactions. The oxidation of a variety of organic substrates by a mixture of a low-valent transition metal complex and hydrogen peroxide is commonly attributed to a "Fenton-like" mechanism. This mechanism is of major importance due to its role in many catalytic oxidations (*129,175*) and its proposal as a key step in many biochemical processes (*176,177*). There is a major debate concerning the question whether free hydroxyl radicals are formed in "Fenton-like" reactions (*131*). In order to solve this question it was decided to use β-elimination processes according to Eq. (36) in the following way (*110,178,179*). Solutions containing a mixture of alcohols, e.g., $(CH_3)_2$CHOH and $(CH_3)_3$COH, in the presence of a low valent transition metal complex M^nL_m are first irradiated (source of "authentic" $^{\bullet}$OH radicals) and the relative yields of the alkenes formed in the reactions:

$$^{\bullet}OH + (CH_3)_2CHOH/(CH_3)_3COH \longrightarrow {}^{\bullet}CH_2CH(OH)CH_3/{}^{\bullet}CH_2C(CH_3)_2OH + H_2O \quad (78)$$

$$^{\bullet}CH_2CH(OH)CH_3/{}^{\bullet}CH_2C(CH_3)_2OH + M^nL_m \longrightarrow L_{m-1}M^{n+1} - CH_2CH(OH)CH_3/L_{m-1}M^{n+1} - CH_2C(CH_3)_2OH + L \quad (79)$$

$$L_mM^{n+1} - CH_2CH(OH)CH_3/L_mM^{n+1} - CH_2C(CH_3)_2OH \xrightarrow{L} M^{n+1}L_m + H_2C{=}CCH_3/H_2C{=}C(CH_3)_2 + OH^- \quad (80)$$

are measured. Then to identical solutions hydrogen-peroxide is added and the relative yields of the same alkenes are measured. If the results

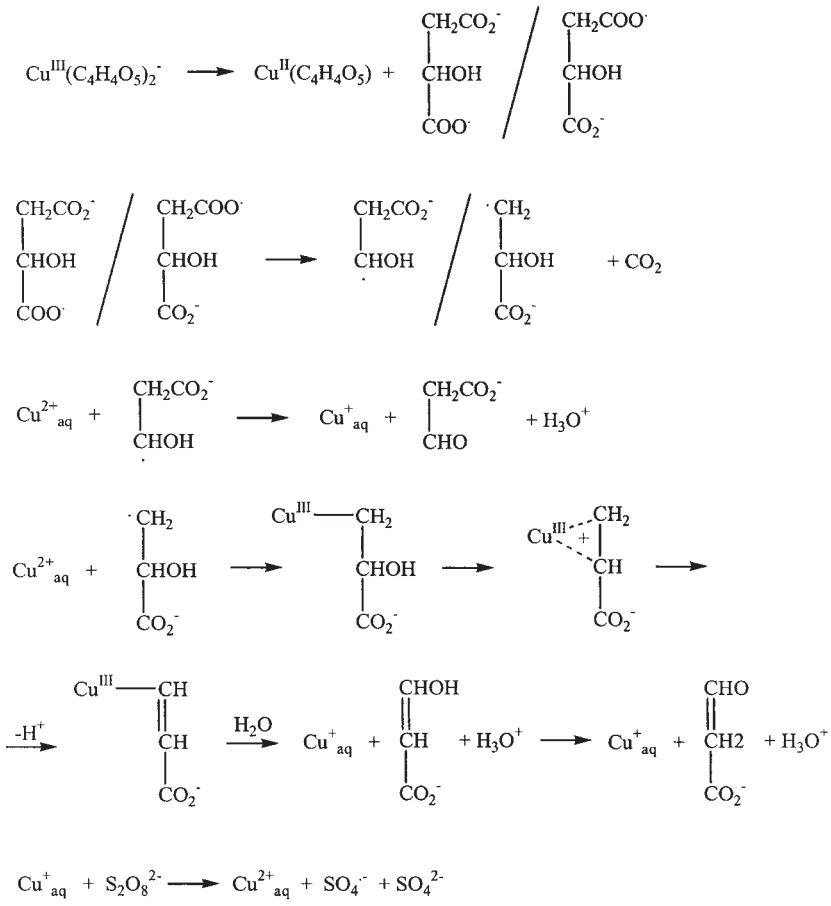

SCHEME 6.

are identical only then the hydroxyl radicals are formed in the system. The results point out that the first reaction is always the formation of a complex between the peroxide and the low valent metal complex (*180,181*):

$$M^nL_m + H_2O_2 \rightleftarrows L_{m-1}M^{n\bullet}H_2O_2 \qquad (81)$$

This reaction might be followed by one of the following reactions:

$$L_{m-1}M^{n\bullet}H_2O_2 \xrightarrow{L} M^{n+1}L_m + {}^{\bullet}OH + OH^- \qquad (82)$$

$$L_{m-1}M^{n\bullet}H_2O_2 \longrightarrow L_{m-1}M^{n+2} = O + H_2O \quad (83)$$

$$L_{m-1}M^{n\bullet}H_2O_2 \xrightarrow{RH;L} M^{n+1}L_m + {}^{\bullet}R + H_2O \quad (84)$$

The mechanism occurring depends on the nature of M^n, L, pH, and the concentration and nature of RH.

Then the reactions of the $^{\bullet}R$ radicals with the M^nL_m complexes present in solution affect the nature of the final products (*175*).

Acknowledgments

We are indebted to our co-workers whose work is cited in this manuscript. The financial help via grants from the Israel Science Foundation, The Planning and Granting Committee and the Israel Atomic Energy Committee, The German Israel Binational Science Foundation and The American Israel Binational Science Foundation, and The Alexander von Humboldt Foundation enabled these studies. Finally D.M. appreciates the continuous interest and support by Mrs. Irene Evens.

References

1. Meyerstein, D. *Acc. Chem. Res.* **1978**, *11*, 43–48.
2. Meyerstein, D. *Pure Appl. Chem.* **1989**, *61*, 885–889.
3. Tabata, Y. "*Pulse Radiolysis*"; CRC Press: Boca Raton, Florida, 1991.
4. Matheson, M. S.; Dorfman, L. "*Pulse Radiolysis*"; M.I.T. Press: Cambridge, MA, 1969.
5. Spinks, J. W. T.; Woods, R. J. "*An Introduction to Radiation Chemistry*"; 3rd edn.; John Wiley & Sons: New York, 1990.
6. Wardman, P. *J. Phys. Chem. Ref. Data* **1989**, *18*, 1637.
7. Buxton, G. V.; Greenstock, C. V.; Helman, W. P.; Ross, A. R. *J. Phys. Chem. Ref. Data* **1988**, *17*, 513.
8. Neta, P.; Huie, R. E.; Ross, A. B. *J. Phys. Chem. Ref. Data* **1988**, *17*, 1027.
9. Neta, P.; Huie, R. E.; Ross, A. B. *J. Phys. Chem. Ref. Data* **1990**, *19*, 413.
10. Neta, P.; Grodkowski, J.; Ross, A. B. *J. Phys. Chem. Ref. Data* **1996**, *25*, 709–1050.
11. Stanbury, D. M. *Adv. Inorg. Chem.* **1989**, *33*, 69.
12. Veitwitch, D.; Janata, E.; Asmus, K. D. *J. Chem. Soc., Perkin Trans.* **1980**, 146.
13. Cohen, H.; Meyerstein, D. *Inorg. Chem.* **1974**, *13*, 2434–2443.
14. Espenson, J. H.; Bakac, A.; Kim, J. H. *Inorg. Chem.* **1991**, *30*, 4830.
15. Cohen, H.; Meyerstein, D. *J. Am. Chem. Soc.* **1972**, *94*, 6944.
16. Cohen, H.; Meyerstein, D. *J. Chem. Soc., Dalton Trans.* **1977**, 2559.
17. McHatton, R. M.; Espenson, J. H. *Inorg. Chem.* **1983**, *22*, 784.
18. Grodkowski, J.; Neta, P.; Schlesener, C. J.; Kochi, J. K. *J. Phys. Chem.* **1985**, *89*, 4373.
19. Bakac, A.; Espenson, J. H.; Lovric, J.; Orhanovic, M. *Inorg. Chem.* **1987**, *26*, 4096.
20. Bakac, A.; Butkovic, V.; Espenson, J. H.; Lovric, J.; Orhanovic, M. *Inorg. Chem.* **1989**, *28*, 4323.
21. Kusaba, K.; Ogino, H.; Bakac, A.; Espenson, J. H. *Inorg. Chem.* **1988**, *28*, 970.
22. Bakac, A.; Butkovic, V.; Espenson, J. H.; Marcec, R.; Orhanovic, M. *Inorg. Chem.* **1986**, *25*, 341.

23. Steenken, S.; Neta, P. *J. Am. Chem. Soc.* **1982**, *104*, 1244.
24. Schwarz, H. A.; Dodson, W. R. *J. Phys. Chem.* **1989**, *93*, 409–414.
25. Creutz, C.; Schwarz, H. A.; Wishart, J. F.; Fujita, E.; Sutin, N. *J. Am. Chem. Soc.* **1991**, *113*, 3361–3371.
26. Kelley, D. G.; Espenson, J. H.; Bakac, A. *Inorg. Chem.* **1990**, *29*, 4996.
27. Shaham, N.; Masarwa, A.; Matana, Y.; Cohen, H.; Meyerstein, D. *Eur. J. Inorg. Chem.* **2002**, 87–92.
28. Meyerstein, D.; Schwarz, H. A. *J. Chem. Soc., Faraday Trans. I* **1988**, *84*, 2933–2949.
29. Venturi, M.; Emmi, S.; Fuochi, P. G.; Mulazzani, G. G. *J. Phys. Chem.* **1980**, *84*, 2160.
30. Cohen, H. *Ph.D. Thesis*; Ben Gurion University of the Negev: Beer Sheva, Israel, 1975.
31. Cohen, H.; Meyerstein, D. *J. Chem. Soc., Dalton Trans.* **1976**, 1976–1979.
32. Wieghardt, K.; Cohen, H.; Meyerstein, D. *Ber. Bunsen-Ges. Phys. Chem. Chem. Phys.* **1978**, *82*, 388–392.
33. Wieghardt, K.; Cohen, H.; Meyerstein, D. *Angew. Chem. Int. Ed. Engl.* **1978**, *17*, 608–609.
34. Beitz, J. V.; Miller, J. R.; Cohen, H.; Wieghardt, K.; Meyerstein, D. *Inorg. Chem.* **1980**, *19*, 966–968.
35. Cohen, H.; Nutkovich, M.; Meyerstein, D.; Wieghardt, K. *J. Chem. Soc., Dalton Trans.* **1982**, 943–950.
36. Bakac, A.; Butkovic, V.; Espenson, J. H.; Marcec, R.; Orhanovic, M. *Inorg. Chem.* **1991**, *30*, 481–483.
37. Whitburn, K. D.; Hoffman, M. Z.; Brezniak, N. V.; Simic, M. G. *Inorg. Chem.* **1986**, *25*, 3037.
38. Bakac, A.; Butkovic, V.; Espenson, J. H.; Marcec, R.; Orhanovic, M. *Inorg. Chem.* **1986**, *25*, 2562–2566.
39. Tsukahara, K.; Wilkins, R. G. *Inorg. Chem.* **1989**, *28*, 1605.
40. Simic, M. G.; Hoffman, M. Z.; Brezniak, N. V. *J. Am. Chem. Soc.* **1977**, *99*, 2166.
41. Espenson, J. H.; Bakac, A.; Kim, J. H. *Inorg. Chem.* **1991**, *30*, 4830–4833.
42. Behar, D.; Samuni, A.; Fessenden, R. W. *J. Phys. Chem.* **1973**, *77*, 2055.
43. Vaneldik, R.; Cohen, H.; Meshulam, A.; Meyerstein, D. *Inorg. Chem.* **1990**, *29*, 4156–4158.
44. Rotman, A.; Cohen, H.; Meyerstein, D. *Inorg. Chem.* **1985**, *24*, 4158–4164.
45. Vaneldik, R.; Cohen, H.; Meyerstein, D. *Inorg. Chem.* **1994**, *33*, 1566–1568.
46. Goldstein, S.; Czapski, G.; van Eldik, R.; Shaham, N.; Cohen, H.; Meyerstein, D. *Inorg. Chem.* **2001**, *40*, 4966–4970.
47. Ellis, J. D.; Green, M.; Sykes, A. G.; Buxton, G. V.; Sellers, R. M. *J. Chem. Soc., Dalton Trans.* **1973**, 1724.
48. Chen, J. T.; Espenson, J. H. *Inorg. Chem.* **1983**, *22*, 1651–1655.
49. Mulac, W. A.; Cohen, H.; Meyerstein, D. *Inorg. Chem.* **1982**, *21*, 4016–4020.
50. Espenson, J. H. ''*Advances in Inorganic and Bioinorganic Mechanisms*'', Vol. 1; Ed. Sykes, G.; Academic Press, 1982, p. 1.
51. Espenson, J. H.; Connolly, P.; Meyerstein, D.; Cohen, H. *Inorg. Chem.* **1983**, *22*, 1009–1013.
52. Cohen, H.; Meyerstein, D.; Shusterman, A. J.; Weiss, M. *J. Chem. Soc., Chem. Comm.* **1985**, 424–425.
53. Cohen, H.; Gaede, W.; Gerhard, A.; Meyerstein, D.; Vaneldik, R. *Inorg. Chem.* **1992**, *31*, 3805–3809.
54. Bakac, A.; Espenson, J. H. *Inorg. Chem.* **1989**, *28*, 3901–3904.
55. Cohen, H.; Feldman, A.; Ishshalom, R.; Meyerstein, D. *J. Am. Chem. Soc.* **1991**, *113*, 5292–5299.

56. Vaneldik, R.; Gaede, W.; Cohen, H.; Meyerstein, D. *Inorg. Chem.* **1992**, *31*, 3695–3696.
57. Espenson, J. H. *Acc. Chem. Res.* **1992**, *25*, 222–227.
58. Guldi, D. M.; Neta, P.; Hambright, P. *J. Chem. Soc., Faraday Trans. I* **1992**, *88*, 2337.
59. Cohen, H.; Meyerstein, D. *Inorg. Chem.* **1988**, *27*, 3429–3431.
60. Morehouse, K. M.; Neta, P. *J. Phys. Chem.* **1984**, *88*, 1575.
61. Guldi, D. M.; Kumar, M.; Neta, P.; Hambright, P. *J. Phys. Chem.* **1992**, *96*, 9576.
62. Sorek, Y.; Cohen, H.; Meyerstein, D. *J. Chem. Soc., Faraday Trans. I* **1985**, *81*, 233–239.
63. Sorek, Y.; Cohen, H.; Meyerstein, D. *J. Chem. Soc., Faraday Trans. I* **1986**, *82*, 3431–3438.
64. Goldstein, S.; Czapski, G.; Cohen, H.; Meyerstein, D. *J. Am. Chem. Soc.* **1988**, *110*, 3903–3907.
65. Brault, D.; Neta, P. *J. Am. Chem. Soc.* **1981**, *103*, 2705.
66. Brault, D.; Neta, P. *J. Phys. Chem.* **1982**, *86*, 3405.
67. Brault, D.; Neta, P. *J. Phys. Chem.* **1987**, *91*, 4156.
68. Cabelli, D. E.; Rush, J. D.; Thomas, M. J.; Bielski, B. H. J. *J. Phys. Chem.* **1989**, *93*, 3579.
69. Roche, T. S.; Endicott, J. F. *Inorg. Chem.* **1974**, *13*, 1575.
70. Elroi, H.; Meyerstein, D. *J. Am. Chem. Soc.* **1978**, *100*, 5540.
71. Sorek, Y.; Cohen, H.; Meyerstein, D. *J. Chem. Soc. Faraday Trans. I* **1989**, *85*, 1169–1179.
72. Sauer, A.; Cohen, H.; Meyerstein, D. *Inorg. Chem.* **1989**, *28*, 2511–2512.
73. Vaneldik, R.; Cohen, H.; Meyerstein, D. *Angew. Chem.-Int. Ed. Engl.* **1991**, *30*, 1158–1160.
74. Blackburn, R.; Kyaw, M.; Phillips, G. O.; Swallow, A. J. *J. Chem. Soc., Faraday Trans. 1* **1975**, *71*, 2277.
75. McHatton, R. C.; Espenson, J. H.; Bakac, A. *J. Am. Chem. Soc.* **1986**, *108*, 5885–5890.
76. Bakac, A.; Espenson, J. H. *Inorg. Chem.* **1989**, *28*, 4319–4322.
77. Lee, S. Y.; Espenson, J. H.; Bakac, A. *Inorg. Chem.* **1990**, *29*, 3442–3447.
78. Baral, S.; Neta, P. *J. Phys. Chem.* **1983**, *87*, 1502.
79. Kumar, M.; Natarajan, E.; Neta, P. *J. Phys. Chem.* **1994**, *98*, 8024.
80. Guldi, D. M.; Neta, P.; Hambright, P.; Rahimi, R. *Inorg. Chem.* **1992**, *31*, 4849.
81. Kelm, M.; Lilie, J.; Henglein, A.; Janata, E. *J. Phys. Chem.* **1974**, *78*, 882.
82. Ram, M. S.; Bakac, A.; Espenson, J. H. *Inorg. Chem.* **1986**, *25*, 3267–3272.
83. Kelley, D. G.; Marchaj, A.; Bakac, A.; Espenson, J. H. *J. Am. Chem. Soc.* **1991**, *113*, 7583–7587.
84. Sauer, A.; Cohen, H.; Meyerstein, D. *Inorg. Chem.* **1988**, *27*, 4578–4581.
85. Freiberg, M.; Mulac, W. A.; Schmidt, K. H.; Meyerstein, D. *J. Chem. Soc., Faraday Trans. I* **1980**, *76*, 1838–1848.
86. Cohen, H.; Meyerstein, D. *Inorg. Chem.* **1986**, *25*, 1505–1506.
87. Cohen, H.; Meyerstein, D. *Inorg. Chem.* **1987**, *26*, 2342–2344.
88. Goldstein, S.; Czapski, G.; Cohen, H.; Meyerstein, D. *Inorg. Chem.* **1988**, *27*, 4130–4135.
89. Masarwa, M.; Cohen, H.; Meyerstein, D. *Inorg. Chem.* **1991**, *30*, 1849–1854.
90. Goldstein, S.; Czapski, G.; Cohen, H.; Meyerstein, D. *Inorg. Chim. Acta* **1992**, *192*, 87–93.
91. Goldstein, S.; Czapski, G.; Cohen, H.; Meyerstein, D.; Cho, J. K.; Shaik, S. S. *Inorg. Chem.* **1992**, *31*, 798–803.
92. Navon, N.; Golub, G.; Cohen, H.; Meyerstein, D. *Organometallics* **1995**, *14*, 5670–5676.
93. Szulc, A.; Meyerstein, D.; Cohen, H. *Inorg. Chim. Acta* **1998**, *270*, 440–445.
94. Buxton, G. V.; Green, J. C. *J. Chem. Soc., Faraday Trans. I* **1977**, *74*, 697–714.
95. Freiberg, M.; Meyerstein, D. *J. Chem. Soc., Chem. Comm.* **1977**, 127–128.
96. Mulac, W. A.; Meyerstein, D. *J. Chem. Soc., Chem. Comm.* **1979**, 893–895.

97. Freiberg, M.; Meyerstein, D. *J. Chem. Soc., Faraday Trans. I* **1980**, *76*, 1825–1837.
98. Kirschenbaum, L. J.; Meyerstein, D. *Inorg. Chem.* **1980**, *19*, 1373–1379.
99. Masarwa, M.; Cohen, H.; Meyerstein, D. *Inorg. Chem.* **1986**, *25*, 4897–4900.
100. Masarwa, M.; Cohen, H.; Glaser, R.; Meyerstein, D. *Inorg. Chem.* **1990**, *29*, 5031–5035.
101. Masarwa, M.; Cohen, H.; Saar, J.; Meyerstein, D. *Israel J. Chem.* **1990**, *30*, 361–368.
102. Goldstein, S.; Czapski, G.; Cohen, H.; Meyerstein, D. *Inorg. Chem.* **1992**, *31*, 2439–2444.
103. Abe, Y.; Ogino, H. *Bull. Chem. Soc. Jpn.* **1989**, *62*, 56.
104. Sauer, A.; Cohen, H.; Meyerstein, D. *Inorg. Chim. Acta* **1989**, *155*, 101–104.
105. Gaede, W.; VanEldik, R.; Cohen, H.; Meyerstein, D. *Inorg. Chem.* **1993**, *32*, 1997–2000.
106. Bakac, A.; Espenson, J. H. *J. Am. Chem. Soc.* **1986**, *108*, 713–719.
107. Cohen, H.; Meyerstein, D. *Inorg. Chem.* **1984**, *23*, 84–87.
108. Shaham, N.; Cohen, H.; van Eldik, R.; Meyerstein, D. *J. Chem. Soc., Dalton Trans.* **2000**, 3356–3359.
109. Van Eldik, R.; Meyerstein, D. *Acc. Chem. Res.* **2000**, *33*, 207–214.
110. Masarwa, M.; Cohen, H.; Meyerstein, D.; Hickman, D. L.; Bakac, A.; Espenson, J. H. *J. Am. Chem. Soc.* **1988**, *110*, 4293–4297.
111. Ogino, H.; Shimura, M.; Tanaka, N. *J. Chem. Soc., Chem. Commun.* **1983**, 1063.
112. Ferraudi, G. *Inorg. Chem.* **1978**, *17*, 2506–2508.
113. Mansano-Weiss, C.; Epstein, D. M.; Cohen, H.; Masarwa, A.; Meyerstein, D. *Inorg. Chim. Acta* **2002**, *339*, 283–291.
114. Scaiano, J. C.; Leigh, W. J.; Ferraudi, G. *Can. J. Chem.* **1984**, *62*, 2355.
115. Pryor, W. A. *ACS Symposium Series* **1985**, *277*, 77.
116. Goldstein, S.; Czapski, G. *Free Rad. Biol. Med.* **1986**, *2*, 3.
117. Mayouf, A.; Lemmetyinen, H.; Sychttchikowa, I.; Koskikallio, J. *Int. J. Chem. Kin.* **1992**, *24*, 579.
118. Halpern, J. *Pure Appl. Chem.* **1979**, *51*, 2171.
119. Halpern, J. *Pure Appl. Chem.* **1983**, *55*, 1059.
120. Finke, R. G.; Schiraldi, D. A.; Mayer, B. *Coord. Chem. Rev.* **1984**, *54*, 1.
121. Woska, D. C.; Wayland, B. B. *Inorg. Chim. Acta* **1998**, *270*, 197.
122. Schofield, M. H.; Halpern, J. *Inorg. Chim. Acta* **2003**, *345*, 353–358.
123. Meyerstein, D. *Inorg. Chem.* **1975**, *14*, 1716–1717.
124. Kirker, G. W.; Bakac, A.; Espenson, J. H. *J. Am. Chem. Soc.* **1982**, *104*, 1249–1255.
125. Espenson, J. H. *Progress in Inorganic Chemistry* **1983**, *30*, 189–212.
126. Cohen, H.; Meyerstein, D. Unpublished results.
127. Sisley, M. J.; Rindermann, W.; van Eldik, R.; Swaddle, T. W. *J. Am. Chem. Soc.* **1984**, *106*, 7432.
128. ''*Catalytic Oxidations with Hydrogen Peroxide as Oxidant*''; Ed. Strukul, G.; Kluwer Academic Publishers: Netherlands, 1992.
129. Sheldon, R. A.; Kochi, J. K. ''*Metal Catalyzed Oxidations of Organic Compounds*''; Academic Press: New York, 1981.
130. Sawyer, D. T. ''*Oxygen Chemistry*''; Oxford University Press: New York, 1991.
131. Meyerstein, D. *''Metal Ions in Biological Systems*'', Vol. 36; 1999, pp. 41–77.
132. Steffan, C. R.; Espenson, J. H.; Bakac, A. *Inorg. Chem.* **1991**, *30*, 1134–1137.
133. Katsuyama, T.; Bakac, A.; Espenson, J. H. *Inorg. Chem.* **1989**, *28*, 339–341.
134. Shi, S.; Espenson, J. H.; Meyerstein, D.; Meisel, D. *Inorg. Chem.* **1991**, *30*, 4468–4470.
135. Shaham, N.; Cohen, H.; Meyerstein, D. *J. Chem. Soc., Dalton Trans.* **1999**, 3805–3808.
136. Cohen, H.; Meyerstein, D. *J. Chem. Soc., Faraday Trans. I* **1988**, *84*, 4157–4160.
137. Mulac, W. A.; Meyerstein, D. *J. Am. Chem. Soc.* **1982**, *104*, 4124–4128.

138. Sorek, Y.; Cohen, H.; Mulac, W. A.; Schmidt, K. H.; Meyerstein, D. *Inorg. Chem.* **1983**, *22*, 3040–3046.
139. Cohen, H.; Meyerstein, D. *Angew. Chem.-Int. Edit. Engl.* **1985**, *24*, 779–781.
140. Goldstein, S.; Czapski, G.; Cohen, H.; Meyerstein, D.; Shaik, S. *J. Chem. Soc., Faraday Trans.* **1993**, *89*, 4045–4051.
141. Cohen, H.; Vaneldik, R.; Gaede, W.; Gerhard, A.; Goldstein, S.; Czapski, G.; Meyerstein, D. *Inorg. Chim. Acta* **1994**, *227*, 57–61.
142. Goldstein, S.; Czapski, G.; Cohen, H.; Meyerstein, D. *Free Radic. Biol. Med.* **1990**, *9*, 371–379.
143. Goldstein, S.; Czapski, G.; Cohen, H.; Meyerstein, D. *Free Radic. Biol. Med.* **1994**, *17*, 11–18.
144. Cohen, H.; Meyerstein, D.; Shusterman, A. J.; Weiss, M. *J. Am. Chem. Soc.* **1984**, *106*, 1876–1877.
145. Masters, C. ''*Homogeneous Transition Metal Catalysis*''; Chapman Hall: London, 1981.
146. Anderson, R. B. ''*The Fischer Tropsch Synthesis*''; Academic Press: London, 1984.
147. Dekleva, T. W.; Forester, D. *Adv. Catal.* **1986**, *34*, 81.
148. Das, S.; Johnson, J. R. *J. Chem. Soc., Faraday Trans. 1* **1980**, *74*, 1779.
149. Navon, N.; Burg, A.; Cohen, H.; vanEldik, R.; Meyerstein, D. *Eur. J. Inorg. Chem.* **2002**, 423–429.
150. Shandalov, E.; Zilbermann, I.; Maimon, E.; Nahmani, Y.; Cohen, H.; Adar, E.; Meyerstein, D. Submitted for publication.
151. Marzilli, L. G. ''*Bioinorganic Catalysis*''; Marcel Dekker: New York, 1993.
152. Cotton, F. A.; Wilkenson, G. ''*Advanced Inorganic Chemistry*'', 6th edn.; Interscience Publishers: New York, 1999, p. 680.
153. Navon, N.; Masarwa, A.; Cohen, H.; Meyerstein, D. *Inorg. Chim. Acta* **1997**, *261*, 29–35.
154. Buxton, G. V.; Green, J. C.; Sellers, R. M. *J. Chem. Soc., Dalton Trans.* **1976**, 2160.
155. Pruchnik, F. P. ''*Organometallic Chemistry of the Transition Elements*''; Plenum: New York, 1990.
156. Salomon, R. G.; Kochi, J. K. *J. Am. Chem. Soc.* **1973**, *95*, 1889.
157. Kochi, J. K. ''*Organometallic Mechanisms and Catalysts*''; Academic Press: New York, 1978.
158. Brandsma, L.; Vasilevsky, S. F.; Verkruijsse, H. D. ''*Application of Transition Metal Catalysis in Organic Synthesis*''; Springer: Berlin, 1998.
159. Cornils, B.; Herrmann, W. A. ''*Applied Homogeneous Catalysis with Organometallic Compounds*''; VCH: Weinheim, 1996.
160. Zuberbuehler, A. D. *Helv. Chim. Acta* **1970**, *53*, 278.
161. Guenter, A.; Zuberbuehler, A. D. *Chimia* **1970**, *24*, 340–342.
162. Cotton, F. A.; Wilkenson, G. ''*Advanced Inorganic Chemistry*''; 5th edn.; Interscience Publishers: New York, 1988.
163. Navon, N.; Cohen, H.; Meyerstein, D. *Inorg. Chem.* **1997**, *36*, 3781–3783.
164. Navon, N.; Golub, G.; Cohen, H.; Paoletti, P.; Valtancoli, B.; Bencini, A.; Meyerstein, D. *Inorg. Chem.* **1999**, *38*, 3484–3488.
165. Navon, N.; Cohen, H.; Paoletti, P.; Valtancoli, B.; Bencini, A.; Meyerstein, D. *Ind. Eng. Chem. Res.* **2000**, *39*, 3536–3540.
166. Margerum, D. W.; Scheper, W. M.; McDonald, M. R.; Fredericks, F. C.; Wang, L.; Lee, H. D. ''*Bioinorganic Chemistry of Copper*''; Chapman & Hall: New York, 1993.
167. Goldstein, S.; Czapski, G.; Meyerstein, D. *J. Am. Chem. Soc.* **1990**, *112*, 6489–6492.

168. Goldstein, S.; Czapski, G.; Cohen, H.; Meyerstein, D.; Vaneldik, R. *Inorg. Chem.* **1994**, *33*, 3255–3260.
169. Zilbermann, I.; Raznoshik, H.; Masarwa, A.; Maimon, E.; Cohen, H.; Meyerstein, D. Unpublished results.
170. Raznoshik, H.; Zilbermann, I.; Maimon, E.; Cohen, H.; Meyerstein, D. *ICCC34*: Edinburgh, Scotland, 2000.
171. Raznoshik, H.; Maimon, E.; Zilbermann, I.; Cohen, H.; Meyerstein, D. *26th International Symposium on Macrocyclic Chemistry*: Fukuoka, Japan, 2001.
172. Arroldi, C.; Citero, A.; Minski, F. *J. Chem. Soc., Perkin Trans.* **1983**, *2*, 531.
173. Agarwal, S. C.; Chandra, G.; Jha, S. K. *J. Inorg. Nucl. Chem.* **1979**, *41*, 889.
174. Meyerstein, D. *J. Inorg. Nucl. Chem.* **1981**, *43*, 401–402.
175. Walling, C. *Acc. Chem. Res.* **1975**, *8*, 125–131.
176. Halliwell, B.; Gutteridge, J. M. C. "*Free Radicals in Biology and Medicine*"; Claredon Press: Oxford, 1985.
177. Rice-Evans, C. "*Free Radicals, Cell Damage and Disease*"; Richelieu Press: London, 1986.
178. Luzzatto, E.; Cohen, H.; Stockheim, C.; Wieghardt, K.; Meyerstein, D. *Free Radic. Res.* **1995**, *23*, 453–463.
179. Bamnolker, H.; Cohen, H.; Meyerstein, D. *Free Radic. Res. Commun.* **1991**, *15*, 231–241.
180. Goldstein, S.; Meyerstein, D. *Acc. Chem. Res.* **1999**, *32*, 547–550.
181. Goldstein, S.; Meyerstein, D.; Czapski, G. *Free Radic. Biol. Med.* **1993**, *15*, 435–445.
182. Espenson, J. H.; Wang, D. M. *Inorg. Chem.* **1979**, *18*, 2853–2859.

This Page Intentionally Left Blank

TRANSITION METAL COMPLEXES WITH BIS(HYDRAZONE) LIGANDS OF 2,6-DIACETYLPYRIDINE. HEPTA-COORDINATION OF 3d METALS

IVANA IVANOVIĆ-BURMAZOVIĆ[a] and KATARINA ANDJELKOVIĆ

Faculty of Chemistry, University of Belgrade, P.O. Box 158, 11000 Belgrade, Serbia and Montenegro
[a]Present address: Institute for Inorganic Chemistry, University of Erlangen-Nürnberg, 51058 Erlangen, Germany

I. Introduction
II. Aspects Studied
  A. Cobalt (II) Complexes
  B. Copper(II) Complexes
  C. Nickel(II) Complexes
  D. Iron (III) Complexes
  E. Manganese(II) and Zinc(II) Complexes
  F. Mo(V), La(III), and U(VI) Complexes
III. Concluding Discussion
  References

I. Introduction

Among hepta-coordinated complexes, structures with pentagonal–bipyramidal (PBP) geometry are found most frequently. Synthesis and X-ray structural analyses of a number of PBP complexes were performed by Nelson (*1*), Palenik (*2*), and Pelizzi (*3*), among other authors. However, systematic studies on the possibility of PBP geometry formation around different 3d metals are rather scarce in the literature. The ligands possessing only five donor atoms in a rigid position stabilized by resonance or within a macrocyclic system, force the metals independent of their d^n configuration to form the PBP geometry. On the other hand, synthesis of both ligands containing a higher number of potential donor atoms and non-planar ligands of an increased conformational flexibility, provides a possibility to examine to which extent the PBP geometry of the coordination sphere of 3d metals is favored by

ADVANCES IN INORGANIC CHEMISTRY
VOLUME 55 ISSN 0898-8838 DOI 10.1016/S0898-8838(03)55006-1

© 2004 Elsevier Inc.
All rights reserved.

ligand rigidity and/or by electron configuration of the central metal ion. However, this is far from exhausting all relevant questions. For example, the ability of ligand deprotonation of the most frequently employed 2,6-diacetylpyridine hydrazones, enables to follow a possible change in PBP geometry of the coordination sphere of 3d metals provoked by an increased negative charge on the ligand. The influence of this geometry, unusual for 3d metals, on physical and chemical characteristics of the produced compounds has not been studied in sufficient detail. In addition, the effect of the degree of deprotonation of coordinated polydentate ligands on the ligand field strength and spin state of 3d metal ions, and thus on the stability of the PBP geometry, has not been examined. Theoretical studies (*2*) on electronic and structural characteristics of 3d metal PBP complexes, employing $[Fe(DAPSC)(H_2O)_2]^{2+}$ (where DAPSC represents 2,6-diacetylpyridine-bis(semicarbazone)) as a model compound, showed that just the spin state of the central metal ion has a crucial influence on the bond lengths, angles and geometry within the frame of the PBP coordination sphere of this type of complexes. However, variation of factors that would lead to changes in the spin state of the metal ion and the detection of changes in the geometry of the 3d metal coordination environment, have not been elaborated either theoretically or experimentally. As a result of our interest in both the coordination chemistry of 2,6-diacetylpyridine hydrazones and 3d metal hepta-coordinate complexes, several of our earlier studies (*4–13*) have been performed with the aim to solve some of the above-mentioned problems.

II. Aspects Studied

The products of the condensation reactions of 2,6-diacetylpyridine (dap) with hydrazides of different acids were found to be the most suitable for the PBP complex-formation because they are the most frequently coordinated as planar pentadentates forming four five-membered chelate rings (Tables I and II show 2,6-diacetylpyridine and related pyridine derivatives mainly used in the synthesis of 3d metal hepta-coordinate complexes). However, they also have the ability to appear as ligands of variable dentacity and a great flexibility in producing different conformations during their coordination to metals. This enables the formation of stereochemically different complexes and opens a new field of research. Not only are PBP structures included in the present report, also how multidentate coordination through different donor atoms affects the formation of different geometries

TABLE I

COMPLEXES OF 3d METALS WITH COORDINATION NUMBER SEVEN AND MACROCYCLIC 2,6-DIACETYLPYRIDINE AND SOME RELATED PYRIDINE LIGAND SYSTEMS

Ligand structure	Designation and number of the ligand	Complexes		References
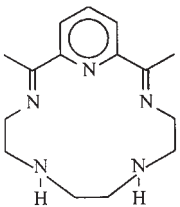	B	$[FeBX_2]ClO_4$		(*14,15*)
			X = Cl^-, Br^-, I^-;	
	I	$[FeBCl_2]BF_4$		(*14,15*)
		$[FeB(NCS)_2]Y$		(*14,15,16*[a]*,17*[a])
			Y = ClO_4^-, NCS^-;	
		$[FeB(H_2O)_2]Cl(ClO_4)$		(*18,19*[a])
		$[FeBX_2] \cdot 2H_2O$		(*18*)
			X = Br^-, I^-;	
		$[B(NCS)Fe–O–Fe(NCS)B](ClO_4)_2$		(*14,15*)
		$[B(H_2O)Fe–O–Fe(H_2O)B]$		(*16*[a])
		$[MB(NCS)_2]$		(*18,20*[a]*,21,22*)
			M = Fe(II), Zn(II), Mn(II);	
		$[MnBX_2]$		(*22*)
			X = Cl^-, BPh_4^-;	
		$[MnBX(ClO_4)]$		(*22*)
			X = Cl^-, NCS^-;	
		$[MnB(H_2O)_2]Cl_2 \cdot 4H_2O$		(*22*)
		$[MnB(H_2O)_2][BPh_4]_2$		(*22*)
		$[MnB(Cl)(H_2O)][ClO_4] \cdot H_2O$		(*22*)
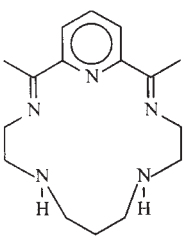	C	$[FeCX_2]Y$		(*17*)
			X = Cl^-, Br^-, NCS^-, N_3^-;	
	II		Y = ClO_4^-, PF_6^-, BPh_4^-, $FeCl_4^-$, $FeBr_4^-$;	
		$[FeC(NCS)_2]ClO_4$		(*17*[a])

(*Continued*)

TABLE I
CONTINUED

Ligand structure	Designation and number of the ligand	Complexes		References
		$[FeCBr_2] \cdot 2H_2O$		(*18*)
		$[FeCI_2] \cdot 3H_2O$		(*18*)
		$[FeC(NCS)_2]$		(*18,20*[a])
		$[MnCX_2]$	$X = Cl^-$, NCS^-;	(*22*)
		$[MnC(NCS)(ClO_4)]$		(*22*)
		$[MnC(Cl)(H_2O)]Cl \cdot H_2O$		(*22*)
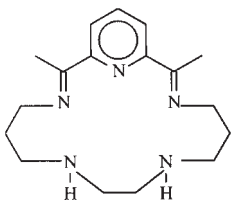	L^3 **III**	$[MnL^3(NCS)_2]$		(*22*[a])
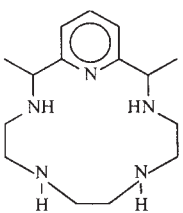	pyane **IV**	$[Fe(pyane)X_2]PF_6$	$X = Cl^-$, Br^-, NO_3^-, NCS^-, N_3^-, $C_2O_4^{2-}$;	(*23*)
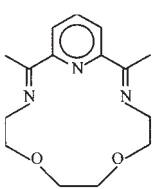	L^4 **V**	$[ML^4(NCS)_2]$	$M = Mn(II)$, $Fe(II)$, $Zn(II)$;	(*24*[a])
		$[FeL^4Cl_2][FeCl_4]$		(*24*)
		$[FeL^4X_2](ClO_4)$	$X = Cl^-$, NCS^-;	(*24*)
		$[FeL^4(CN)_2]H_2O$		(*25*)

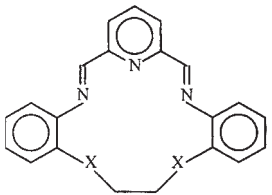	L X = NH, S, O; **VI**	$[MLY_2]$	M = Mn(II), Zn(II); $Y = ClO_4^-$, NO_3^-;	(*26*[a])
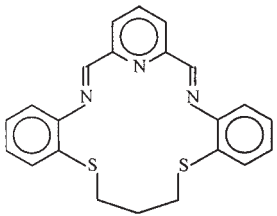	L′ **VII**	$[ZnL'(H_2O)_2](ClO_4)_2 \cdot CH_3CN$		(*27*[a])
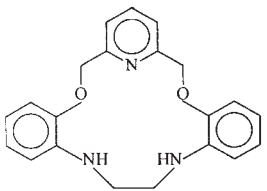	L **VIII**	$[Zn(L)(H_2O)(NO_3)]NO_3$		(*28*[a])
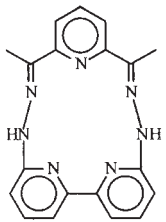	L **IX**	$[ZnL(H_2O)_2](NO_3)_2$		(*29*[a])

(*Continued*)

TABLE I
CONTINUED

Ligand structure	Designation and number of the ligand	Complexes		References
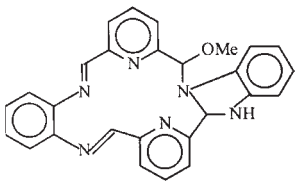	L^2	$[ML^2(H_2O)(MeOH)](ClO_4)_2$	M = Mn(II), Fe(II), Co(II);	(*30*[a])
	X	$[ML^2(NCS)_2]$	M = Mn(II), Fe(II), Co(II);	(*30*)
		$[ZnL^2(H_2O)](ClO_4)_2$		(*30*)
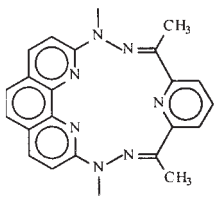	L^1 R = H **XI**	$[CoL^1(H_2O)_2](BF_4)_2$		(*31*[a])
		$[ML^2(H_2O)_2](BF_4)_2$		(*32*[a],*33*,*34*[a],*35*[a])
	L^2 R = CH_3 **XII**	$[CoL^2(CH_3OH)_2](BF_4)_2$	M = Fe(II), Ni(II), Co(II);	(*36*[a])
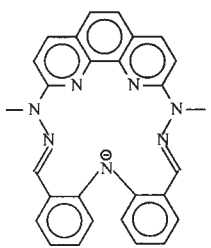	L^3 **XIII**	$[CoL^3(py)_2](BPh_4)$		(*37*[a])

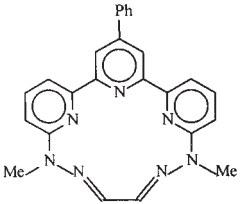	L **XIV**	$[NiLX_2](BF_4)_2$	X = CH_3CN, C_2H_5OH;	(*38*[a])
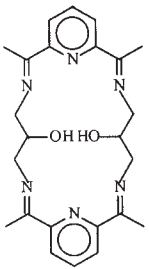	H_2L **XV**	$[Mn_4(HL)L(NCS)_4]NCS$		(*39*[a])
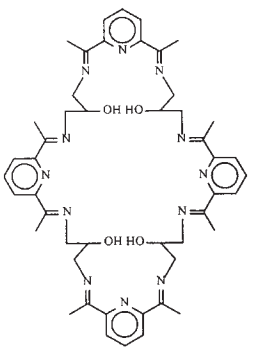	H_4L' **XVI**	$[Mn_4L'(ClO_4)_4] \cdot 4H_2O$		(*39*[a])

[a]X-ray crystal structure analysis done.

TABLE II

COMPLEXES OF 3d METALS WITH CO-ORDINATION NUMBER SEVEN AND ACYCLIC 2,6-DIACETYLPYRIDINE AND SOME RELATED PYRIDINE LIGAND SYSTEMS

Ligand structure	Designation and number of the ligand	Complexes		References
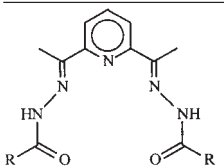 R = –CH_3 R = –NH_2	H_2dapac **XVII**	$[M(H_2dapac)(H_2O)_2](NO_3)_2 \cdot H_2O$	M = Mn(II), Ni(II), Cu(II);	(*40*[a])
	H_2dapsc **XVIII**	$[Cr(H_2dapsc)(H_2O)_2](NO_3)_2(OH)(H_2O)$		(*41*[a])
		$[Cr(Hdapsc)(H_2O)_2](NO_3)_2(H_2O)$		(*42*[a])
		$[M(H_2dapsc)(H_2O)Cl]Cl \cdot 2H_2O$	M = Mn(II),Fe(II),Co(II),Zn(II);	(*43*[a],*44*[a])
		$[Fe(H_2dapsc)Cl_2]Cl \cdot 2H_2O$		(*41*[a])
		$[M(H_2dapsc)(H_2O)_2](NO_3)_2 \cdot H_2O$	M = Ni(II), Cu(II);	(*45*[a])
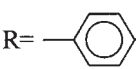	H_2dapb **XIX**	$[Mn(H_2dapb)(H_2O)(Cl)]Cl$		(*46*[a])
		$[Fe(H_2dapb)Cl_2]$		(*47*)
		$[Co(H_2dapb)(H_2O)(NO_3)](NO_3)_2$		(*48*[a])
		$[Ni(H_2dapb)(H_2O)_2](NO_3)_2$		(*48*[a])
		$Zn(H_2dapb)Cl_2 \cdot 3H_2O$		(*46*)
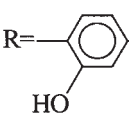	H_2daps	$[Fe(H_2daps)Cl_2] \cdot H_2O \cdot 0.5C_6H_5Me$		(*49*[a])
		$[Ni(H_2daps)(H_2O)_2](NO_3)_2 \cdot 1.5H_2O$		(*50*[a])
		$[Co(H_2daps)(H_2O)_2](NO_3)_2 \cdot H_2O$		(*51*[a])
		$[M(H_2daps)Cl_2]_2 \cdot 4H_2O$	M = Co(II), Ni(II), Zn(II);	(*52*)
		$[Fe_2(daps)Cl_2(C_2H_5OH)_2]$		(*53*[a])

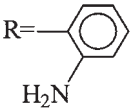	H_2dapab **XXI**	$[Mn(H_2dapab)(Cl)(CH_3OH)]Cl \cdot H_2O$		(*54*[a])
		$[Ni(H_2dapab)Cl_2] \cdot H_2O$		(*54*)
		$[M(H_2dapab)Cl_2] \cdot 4H_2O$	M = Co(II), Zn(II);	(*54*)
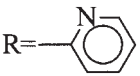	H_2dappc **XII**	$[Mn(H_2dappc)(Cl)(H_2O)]Cl4 \cdot H_2O$		(*55*[a])
		$[Mn(dappc)(H_2O)_2]$		(*56*[a])
		$[Co(H_2dappc)(H_2O)_2]Cl_2 \cdot 3H_2O$		(*56,57*[a])
		$Ni(H_2dappc)Cl_2 \cdot 5H_2O$		(*56*)
		$Zn(H_2dappc)Cl_2 \cdot 6H_2O$		(*56*)
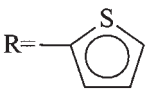	H_2dapt **XXIII**	$M(H_2dapt)Cl_2 \cdot 4H_2O$	M = Co(II), Ni(II), Zn(II);	(*58*)
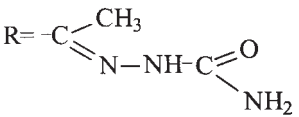	H_4L **XXIV**	$Co(H_4L)(H_2O)_2(NO_3)_2 \cdot 2H_2O$		(*59*[a])
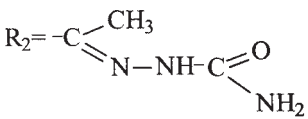	H_3L' **XXV**	$Zn(H_3L')(H_2O)_2(ClO_4)_2$		(*59*[a])
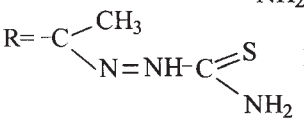	H_2dapipt **XXVI**	$Zn(H_2dapipt)(H_2O)_2(ClO_4)_2$		(*60*[a])
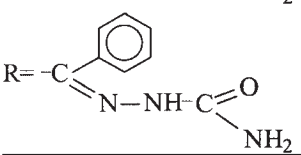	H_4dapis **XXVII**	$Co(H_4dapis)(H_2O)_2Cl_2 \cdot 9/2H_2O$		(*61*[a])

(*Continued*)

TABLE II
CONTINUED

Ligand structure	Designation and number of the ligand	Complexes		References
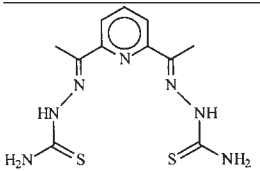	H_2daptsc **XXVIII**	$Fe(H_2daptsc)(NCS)_2$		(*62*[a])
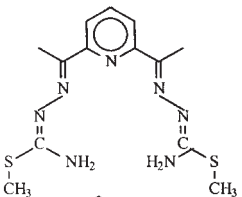	H_2L **XXIX**	$Mn(H_2L)(NCS)(CH_3OH)(NCS)$		(*63*)
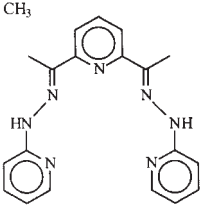	H_2dapp **XXX**	$M(H_2dapp)(H_2O)_2Cl_2$	M = Co(II), Zn(II);	(*64*[a],*65*[a]) (*1*[a])
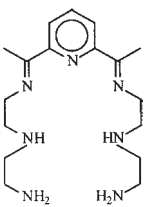	L **XXXI**	$[ML]X_2$	M = Cu(II), Mn(II), Fe(II), Co(II), Ni(II), Zn(II); X = ClO_4^-, BPh_4^-;	(*1*[a])

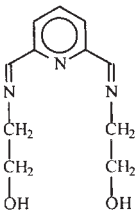	L^1 **XXXII**	$[MnL^1Cl_2] \cdot H_2O$	(*66*)
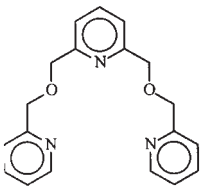	L^1 **XXXIII**	$[CoL^1(H_2O)_2]Cl_2$	(*67*[a])
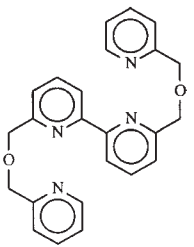	L^2 **XXXIV**	$[CoL^2(H_2O)]Cl_2$	(*67*[a])
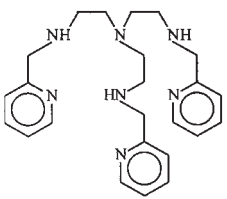	TPAA **XXXV**	$[MnTPAA](PF_6)_2$[b] $[FeTPAA](ClO_4)_2$	(*68*[a]) (*69*[a])

(*Continued*)

TABLE II
CONTINUED

Ligand structure	Designation and number of the ligand	Complexes	References
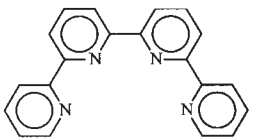	L **XXXVI**	$[\{FeL(ClO_4)\}_2O]$	(*70*[a])
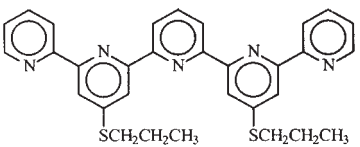	L **XXXVII**	$[CoLCl_2]$	(*71*[a])
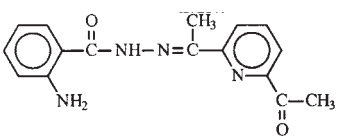	HL **XXXVIII**	$[Mn(HL)(H_2O)_2(Cl)]Cl \cdot H_2O$	(*3*[a])

[a]X-ray crystal structure analysis done.
[b]CTP (capped trigonal prism) complexes; all the others are the PBP (pentagonal–bipyramidal) complexes.

around various metal ions, is considered. Bis(hydrazine) ligands of dap can be coordinated as neutral, single, or double deprotonated polydentates depending on the central metal ion, thus allowing studies on the influence of the degree of ligand deprotonation on the coordination number, geometry, magnetic properties, and UV/VIS spectra of the synthesized complexes.

With the aim to systematically examine the above-mentioned problems in the present report, the polydentate H_2dapsox ligand (H_2dapsox = 2′,2‴-(2,6-pyridindiyldiethylidene)dioxamohydrazide) (*4*) is considered in more details. At first sight, this ligand did not point to an increased flexibility in coordination as compared to H_2dapa, H_2daps, H_2dappc, and H_2dapt (Table II). However, with eleven potential donor atoms and the possibility to exist in neutral, mono-, and di-anionic form (*6*), H_2dapsox is an extremely suitable ligand to resolve the outlined problems.

Its coordination with Co(II), Cu(II), Ni(II), Fe(III), Mn(II), and Zn(II) ion in differently charged forms, served to investigate the effect of the degree of deprotonation on the electronic configuration of different metals, and the influence of the electronic configuration on both the geometry and physicochemical characteristics of the resulting complexes. In addition, the influence of the synthetic approach (template or direct method) on the structure and stability of the resulting compounds will be treated. Studies were also extended to include Mo(V), La(III), and U(VI) complexes of this ligand.

A. Cobalt (II) Complexes

The synthesis of Co(II) complexes containing the H_2dapsox ligand was studied first, since most of the structurally characterized hepta-coordinate species of 3d metals represent Co(II) complexes. Forty Co(II) complexes with coordination number seven have been synthesized so far and 32 of them were characterized by X-ray structural analysis. Most of these structures contain planar pentadentates: eight were prepared with acyclic (*43,44,48,51,57,59,61,64,65,67*) and five with macrocyclic (*30,31,35–37*) pentadentates. As far as non-planar ligands are concerned, one structure with acyclic (*71*) and seven structures with cyclic pentadentates (*72–75*), one with cyclic tetradentate (*76*), three structures with acyclic (*67,77*) and one with cyclic hexadentate [*72*], and one each with acyclic (*78*) and cyclic (*79*) heptadentate. It is interesting to emphasize that Co(II) can form hepta-coordinate PBP complexes not only with polydentates, but also by a combination of mono and bidentate nitrate groups (*80*), by a combination of bidentately

coordinated nitrate ions with monodentates (*81,82*) or tridentates (*83*), and with bidentately bound nitrite ions and monodentates (*84*).

All Co(II) complexes with planar pentadentate ligands are characterized by the formation of four five-membered chelate rings in the equatorial plane, while water molecules usually occupy apical positions. Although side chains of some acyclic pentadentates (**XXII**, **XXIII**, **XXIV**, **XXVII**)[1] could also form six-membered rings, such complexes have not been synthesized so far. The macrocyclic pentadentate **XIII**, represents the only example of six-membered ring-formation around Co(II) in the plane with five-membered rings since its rigidity makes other coordination modes impossible. On the other hand, in the case of tripodal heptadentate ligands (such as $(pyo)_3tren$) (*78*), Co(II) complexes with coordination number 7 are formed only when there is the possibility for the formation of six-membered chelate rings in addition to five-membered ones formed by coordination through the tertiary amine and three imine nitrogen atoms. When the tripodal heptadentate ligands force the formation of five-membered chelate rings (*78*), only trigonal antiprismatic Co(II) complexes with coordination number 6 were formed.

Coordination of the neutral form of the pentadentate ligand represents another characteristic of the Co(II) complexes. The complex with the monoanionic ligand **XIII** presents the only exception. Coordination of anions with Co(II) in hepta-coordinate structures was observed with the non-planar hexadentate EDTA ligand (*85*), tridentate purpurate ion (*83*), nitrite (*84*), and nitrate ions (*80–82*). On the other hand, if $(sal)_3tren$ (*78*) (from the class of tripodal heptadentates) coordinates as trianion, disregarding its ability to form six-membered rings (as $(pyo)_3tren$) suitable for hepta-coordination, the resulting Co(II) complex is six-coordinate. This illustrates how negative charge on the heptadentate ligand destabilizes a monocapped trigonal antiprismatic Co(II) structure (*78*). What would happen to the PBP structure in the case of an increased negative charge on the pentadentate ligand still remains to be an open question. In order to answer this question, the complexes $[Co(H_2dapsox)(H_2O)(MeOH)](ClO_4)_2$ (**1**),[2] $[Co(Hdapsox)(H_2O)_2]ClO_4$ (**2**), and $[Co(dapsox)(H_2O)_2] \cdot 6H_2O$ (**3**) were synthesized.

For the synthesis of the Co(II) complex with $H_2dapsox$, direct and template methods were employed, which afforded an identical product **1**

[1]Roman numerals are related to the ligands listed in Tables I and II.

[2]Arabic numerals are related to the complexes synthesized in our work, which is presented with Schemes.

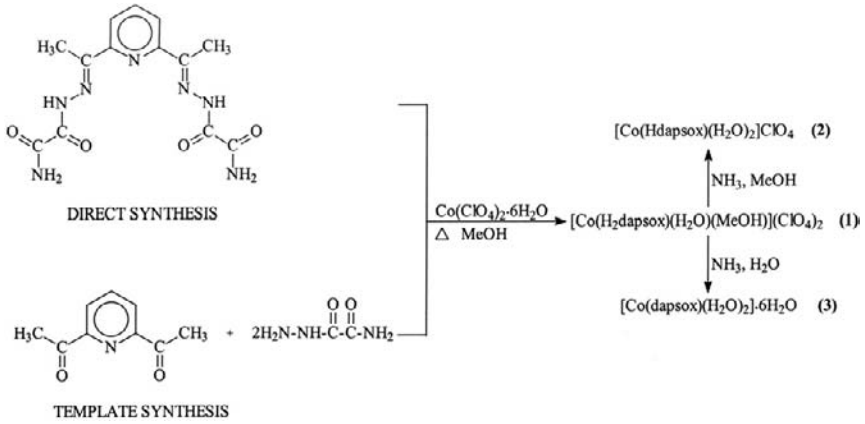

SCHEME 1.

(Scheme 1). In addition to the determination of molar conductivity, magnetic moment, and IR spectra, the complex was characterized by X-ray structural analysis (*4*). This indicates that the cationic complex with neutral H_2dapsox is symmetrically coordinated as a pentadentate ligand. Co(II) occurs in a PBP environment with water and methanol molecules in apical positions (Fig. 1). Although the side chains are symmetrically coordinated, Co–O(eq) bond lengths differ significantly.

Complexes **2** and **3** with the monoanionic and dianionic pentadentate ligand, respectively, were isolated (Scheme 1). IR, Λ_M, and μ_{eff} data suggested an identical coordination mode for the single and double deprotonated ligand, as well as an identical geometry of the produced complexes. This was also confirmed by X-ray analysis of **3** (*5*). Co(II) occurs in the PBP environment with water molecules in the apical positions (Fig. 2). In relation to the structure with the neutral ligand, the Co–O(eq) bonds are almost of the same length, and the structure is characterized by a higher symmetry, lower rigidity, and more pronounced planarity in the equatorial plane (*5*).

As far as electron absorption spectra of the Co(II) PBP complex are concerned, they have still been insufficiently explained (*1,56,67,86*). Gerloch *et al.* (*86*) discussed the spectra of the $[Co(H_2dapsc)(Cl)(H_2O)]^+$ and $[Co(H_2dapsc)(H_2O)_2]^{2+}$ cations in some detail and the bands at 632, 562, 549(sh), and 507(sh) nm of the former, and those at 628, 540, and 526(sh) nm of the latter complex, were ascribed to transitions between components of the ^{4}P term. These authors found that all spin-allowed d–d transitions occur at energies below 500 nm,

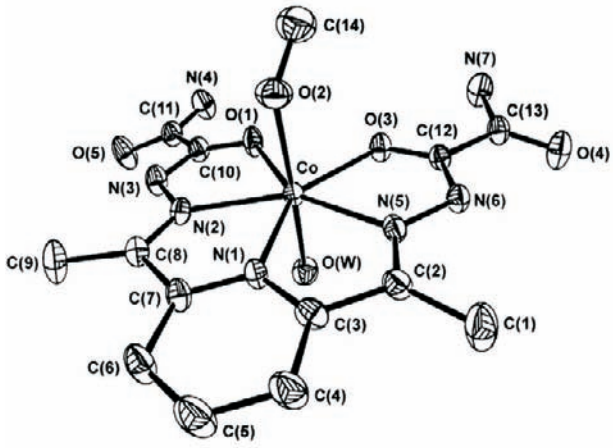

FIG. 1. The structure of complex cation $[Co(H_2dapsox)(H_2O)(MeOH)]^{2+}$ (*4*).

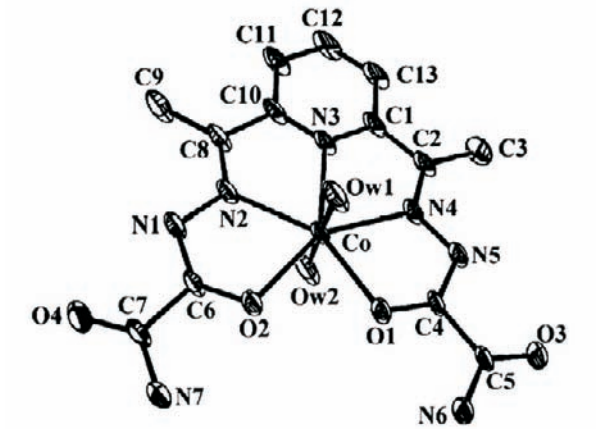

FIG. 2. The structure of $[Co(dapsox)(H_2O)_2$ (*5*).

although this region is overlapped by intense "charge-transfer" and intra-ligand transitions. In the studies reported later, systems producing intensive bands at wavelengths below 500 nm were used, and in the spectra of the complexes only a single d–d transition could be seen (at 549 nm (*56*), i.e., 534 nm (*67*), i.e., 653 nm (*1*)). In contrast to these complexes, the spectrum of H_2dapsox shows two bands at 277 and

TABLE III

POSITION OF THE BANDS (λ, nm) IN ABSORPTION SPECTRA OF H_2dapsox AND Co(II) COMPLEXES (IN MeOH, AT 293 K)

Compound	d*xz*(d*yz*) → d*xy*	d*xz*(d*yz*) → dx^2–y^2	d*z*(d*yz*) → dz^2	Intraligand transitions
H_2dapsox	–	–	–	315 277
[Co(H_2dapsox)(H_2O)(MeOH)](ClO_4)	637	552	443	317 280
[Co(Hdapsox)(H_2O)$_2$]ClO_4	615	531	442	326 287
[Co(dapsox)(H_2O)$_2$]	570	490	440	340 296

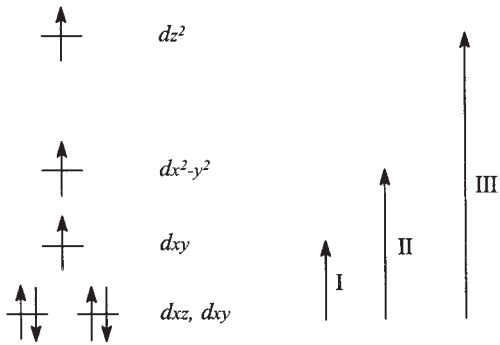

SCHEME 2.

315 nm (Table III), thus in the region above 350 nm the possibility for the overlap of d–d bands with intra-ligand transitions is eliminated. Furthermore, since Co(II) complexes with three different forms of pentadentate ligands were synthesized for the first time in earlier studies (*4,5*), it was possible to improve the understanding of the properties of the bands in the electronic spectra. From Table III and Scheme 2 it can be seen that: (a) there are d–d bands of PBP Co(II) complexes in the region below 500 nm and (b) the degree of ligand deprotonation has almost no influence on the d*xz*(*yz*) → dz^2 transition, while affecting the other two bands. This is in accordance with the fact that deprotonation of H_2dapsox primarily results in an increase in energy of the dx^2–y^2 and *dxy* orbitals. The increase in the ligand field strength is more pronounced during the transition from the single to the double deprotonated form, than during transition of the neutral to the mono-anionic form of the ligand. Also, the shift in the intra-ligand transition bands toward the visible region was

observed as a result of an increased degree of delocalization as a result of deprotonation.[3]

In spite of the presence of two vicinal C = O groups in both side chains and the application of both synthetic methods, Co^{2+} forms a complex with four five-membered chelate rings, which was also the case with previously synthesized complexes (*60,72,74*). This is the consequence of the higher stability of the five-membered ring compared to the six-membered chelate ring. Besides, total planarity of 13 atoms surrounding the equatorial pentagon also plays a certain role (*2*). Considerations of structural models revealed that the formation of six-membered rings is quite possible, but they would significantly deviate from planarity with a boat conformation. Co^{2+} forms a stable PBP structure with the symmetrical dianionic, as well as asymmetrical mono-anionic forms of the polydentate ligand. Furthermore, although deprotonation-related strengthening of the ligand field was found to be present (Table III), it does not change the high-spin Co(II) configuration into the low-spin one. The stability of the PBP geometry around the Co^{2+} ion, which is a consequence of symmetrical distribution of electrons in dz^2, dx^2–y^2, and dxy orbitals, and symmetrical electron distribution in dxz and dz orbitals (Scheme 2), makes the energy required for conversion from the high-spin to the low-spin configuration very high.

B. Copper(II) Complexes

In the available literature, only a few hepta-coordinate PBP structures of Cu(II) complexes have been described so far and $[Cu(H_2dapsc)(H_2O)_2](NO_3)_2 \cdot H_2O$ (*45*) was the first. It has a rigid unflexible ligand **XVIII** with pentadentate properties and this is also the case with the $[Cu(H_2dapac)(H_2O)_2](NO_3)_2 \cdot H_2O$ complex (*40*) **XVII**. The third complex $[Cu(H_2L)](ClO_4)_2$ (*1*) was produced with a significantly more flexible heptadentate ligand **XXXI**, obtained by condensation of dap and two moles of diethylene triamine. However, it was impossible to obtain a system with a non-planar heptadentate ligand that forms the PBP geometry around the Cu(II) ion, either through direct or template synthesis, and the only way was via transmetallation starting with the alkaline–earth complex. One of

[3]Detailed analyses of UV/VIS spectra of these complexes are hindered by the fact that their stability in solution is significantly lower, because the solution becomes relatively quickly turbid and precipitation of the free ligand occurs.

the seven Cu–N bonds is significantly longer (2.565(24) Å) and this is the bond with the imine nitrogen in the equatorial plane. All three complexes contain the coordinated polydentate chelate in the neutral form.

In the case of other derivatives of dap and acylhydrazones (Table II), it was impossible to isolate Cu(II) complexes with a neutral form of these ligands. Syntheses with Cu(II) chloride or nitrate did not afford defined products and only those with Cu(II) acetate produced stoichiometrically defined substances. The complexes produced have a PBP structure and contain a doubly-deprotonated polydentate ligand. Their more precise characterization has not been performed so far and only on the basis of IR spectra of [Cu(dapb)] (*46*), [Cu(daps)] (*52*), and [Cu(dapab)] (*54*), a dimeric or polymeric structure was suggested, whereas there are no data available on the coordination number. $[Cu_2(dappc)(H_2O)_3]_2[Cu_2(dappc)(H_2O)_2(ClO_4)]_2(ClO_4)_6 \cdot 2H_2O$ (*87*), $[Cu_2(dappc)Cl_2]_2 \cdot 2H_2O$ (*88*), $[Cu_2(dapip')Br]_2 \cdot 2H_2O$ (*87*), and $[Cu(dapt)]_2$ (*89*) are the only structurally defined compounds with doubly-deprotonated 2,6-diacetylpyridine-bis(acylhydrazone). Both cations of the first complex consist of tetrameric Cu(II) units, where deformed octahedral geometry occurs around two Cu(II) ions and square–pyramidal geometry around the other two Cu(II) ions. In the case of $[Cu_2(dappc)Cl_2]_2 \cdot 2H_2O$ and $[Cu_2(dapip')Br]_2 \cdot 2H_2O$, which also have tetrameric structure, there is a square–pyramidal geometry around each Cu(II) ion. $[Cu_2(dapip')Br]_2 \cdot 2H_2O$ represents the first example of a structure with mixed bis(acylhydrazone) of 2,6-diacetylpyridine. One chain is the same as in ligand **XXII** and the other like that in 2,6-diacetylpyridine-bis[2-(2′-pyridinecarbonylhydrazono)phenylacetohydrazone] (H_2dapip) (*87*). The last example of a Cu(II) complex with the dianion of 2,6-diacetylpyridine-bis(acylhydrazone), is the dimeric $[Cu(dapt)]_2$ structure with deformed octahedral environment around both Cu(II) ions (*89*).

The data presented above demonstrate that ligands of the acylhydrazone 2,6-diacetylpyridine class coordinate with Cu(II) in neutral form as pentadentates and in the doubly-deprotonated form as octadentates forming dimeric or tetrameric structures. On the other hand, $[Cu(dapsox)H_2O]H_2O$ (**4**) (*6*) obtained throughout the studies, is a monomeric complex with square–pyramidal geometry with the doubly-deprotonated ligand coordinated as a tetradentate. Singly-deprotonated forms of bis(acylhydrazones) have not been considered in the available literature so far, and this prompted the synthesis and structural characterization of the first complex of this group, viz. $[Cu(Hdapsox)H_2O]ClO_4$ (**5**) (*7*).

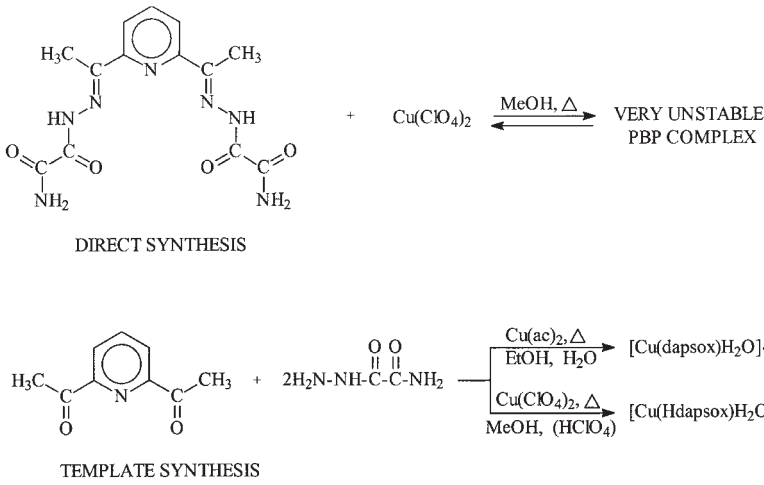

SCHEME 3.

These two types of complexes with the singly- and doubly-deprotonated H_2dapsox ligand were obtained by template synthesis (Scheme 3) throughout our studies. It was impossible to produce the complex with the neutral ligand because even perchloric acid could not protonate the coordinated anion. Direct synthesis afforded an unstable product and the starting ligand precipitated during cooling of the reaction mixture.

In addition to IR and electron spectroscopy, structure analyses of both complexes (*6,7*) showed that the mono- and di-anionic forms of the H_2dapsox ligand coordinate with Cu(II) in an identical way as tetradentates. In spite of the ligand symmetry, it is asymmetrically coordinated *via* the pyridine nitrogen, deprotonated hydrazide nitrogen, and terminal carbonyl groups, while the other chain can include only imino nitrogen in the coordination mode because of the formation of the central six-membered ring. The square–pyramidal structure of both complexes is supplemented by water molecules. The structure with the doubly deprotonated ligand is unique because similar ligand systems with so many potential donor atoms always form polynuclear structures during coordination to Cu(II) (*87,88*), whereas this structure is monomeric. Besides the structure of the Cr(III) complex (*42*) with ligand **XX** of the same class, complex **5** represents the only structure with monodeprotonated bis(acylhydrazone) of

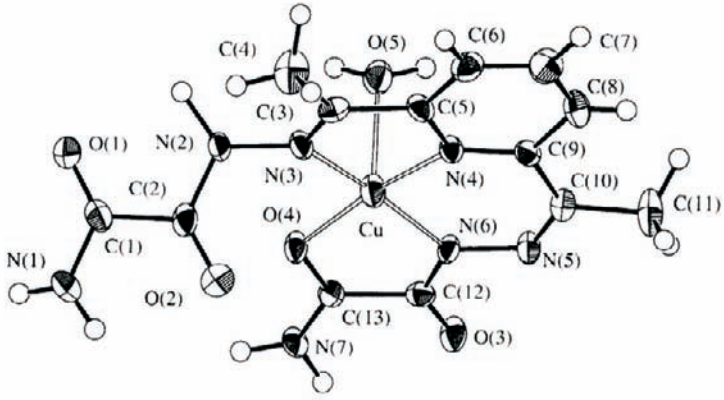

FIG. 3. The structure of complex cation $[Cu(Hdapsox)(H_2O)]^+$ (*7*).

2,6-diacetylpyridine (Fig. 3).[4] Steric strain within both structures is mainly localized on the bite angles of the five-membered rings. Comparison of structures **4** and **5** revealed no crucial differences with respect to bond length between the Cu(II) ion and the donor atoms. Somewhat more pronounced differences have been observed in intraligand bonds of the pendant arm, which is deprotonated in structure **4** and neutral in structure **5**. The neutral pendant arm in **5** has a more pronounced hydrazide form (*7*), while negatively charged pendant arm in complex **4** occurs mostly in the α-oxyazine form (*6*).

Electron absorption spectra of the complexes **4** and **5** (*10*) showed that double deprotonation of the ligand leads to a significant shift of the $B_1 \rightarrow A_1$ and $B_1 \rightarrow E$ bands toward higher energies demonstrating a significant strengthening of the ligand field in the *xy* plane. However, strengthening of the ligand field cannot result in a change in the electronic configuration of the Cu(II) ion, because it is a d^9 system, and thus, there is no change in geometry provoked by an increase in negative charge on the polydentate ligand.

[4]The above-mentioned Cr(III) complex was first defined as $[Cr(H_2dapsc)(H_2O)]^{3+}$ [41], and during structural analyses performed later[42] it was established that it in fact represents the $[Cr(Hdapsc)(H_2O)_2]^{2+}$ cation, confirming the coordination of the mono-anionic form of the pentadentate ligand.

C. Nickel(II) Complexes

In the available literature, only six PBP structures of Ni(II) have been reported so far (*34,38,40,45,48,50*) and four of them include acyclic pentadentates (**XVII–XX**). These pentadentates are equatorially coordinated in their neutral form with weak conformational flexibility. Apical positions are always occupied by water molecules, while nitrate anions always represent counter ions in the structure. The change of any of the mentioned structural elements (polydentate, axial ligands, or counter ion) affords complexes of which the structure has not been determined (*52,54,56,58*). These are complexes with the same type of ligands **XX–XXIII**, containing Cl^- ions and water molecules, but it is still unknown which of these two monodentate ligands occupies the apical positions. It is questioned whether both monodentates actually occur in the coordination sphere, and because of that it is impossible to discuss the geometry of these complexes in more detail.

The remaining two complexes of known X-ray structure (*34,38*) represent complexes with the macrocyclic ligands **XII** and **XIV**, characterized by an even lower conformational flexibility. All above-mentioned complexes were formed solely with rigid planar pentadentates. The reason is a rather high instability of PBP complexes of Ni(II), where the Ni–O(hydrazide) bonds are longer than in analogous complexes of other metals with bis(acylhydrazones) of 2,6-diacetylpyridine. In addition to this bond elongation, a pronounced asymmetry in the two Ni–O bonds was observed (*48*). A strong tendency of the d^8 system toward a geometry in which the metal–ligand bonds are orthogonally positioned to one another (octahedral, square–pyramidal, and square–planar) was observed in attempts to synthesize Ni(II) complexes with different macrocyclic ligands (*90–92*), and is also apparent from a comparison of the crystal field stabilization energies of different stereochemical configurations of the d^8 system (*91*) (Table IV). Because of that, it is possible to realize the PBP environment of the Ni(II) ion only by employing very rigid ligand systems. In attempts to produce such a geometry, the macrocyclic pentadentate ligands **I**, **II**, **III**, and **V** were used, but even then the obtained complexes had octahedral structures (*90*). Addition of a solvent molecule (ROH) to the azomethine C=N bond occurred, thus producing a more flexible macrocyclic compound which could adapt the octahedral geometry (*90*). Geometrical constraints within such a structure led to the opening of the macrocycle and a hydrolytic process, which resulted in a higher stability of the octahedral complex (*90*).

TABLE IV

COMPARISON OF CRYSTAL FIELD STABILIZATION ENERGIES (IN Dq) IN D_{5h}, O_h, AND C_{4v}, ENVIRONMENTS OF Fe(III), Mn(II), Fe(II), Co(II), Ni(II), Cu(II), AND Zn(II) IONS WITH HIGH SPIN CONFIGURATIONS (*93*)

	Ion	D_{5h}	O_h	C_{4v}
d^5	Fe(III)	0	0	0
d^5	Mn(II)	0	0	0
d^6	Fe(II)	5.28	4	4.57
d^7	Co(II)	10.56	8	9.14
d^8	Ni(II)	7.74	12	10
d^9	Cu(II)	4.93	6	9
d^{10}	Zn(II)	0	0	0

Furthermore, isomerization of the heptadentate **XXXI**, coordinated to Ni(II) via transmetallation (*91*), occurs again aimed at its adaptation to a octahedral coordination sphere around ions with d^8 configuration. In the case of the more flexible pentadentate ligands, **XXXII** and its analogue with three methylene groups (L_2) (*92*), formation of monomeric (with **XXXII**) and dimeric (with L_2), but also of polymeric (with L_2) Ni(II) complexes with an octahedral environment around the metal is possible (*94*).

The complex with ligand **XXIV**, which has 15 potential donor atoms, represents the only example of a Ni(II) structure with the deprotonated ligand from the class of bis(acylhydrazones) of 2,6-diacetylpyridine. A large number of donor atoms enables the formation of the tetrameric structure (*59*) and enables the formation of different coordination geometries around Ni(II). However, the coordination sphere around all four Ni(II) ions in this tetrameric structure is again octahedral.

In order to examine the effect of varying the charge on the pentadentate ligand on both the structure and characteristics of the produced Ni(II) complexes, the complexes $[Ni(Hdapsox)(MeOH)_2]ClO_4$ (**6**) (*7*), [Ni(dapsox)] (**7**) (*11*), and $[Ni(H_2dapoamh)_2](ClO_4)_2$ (**8**) (*11*) were synthesized, representing complexes with mono-anionic, di-anionic, and neutral forms of potential pentadentate ligands, respectively (Scheme 4).

Similar to the Cu(II) complex, direct synthesis afforded an unstable Ni(II) complex and precipitation of the starting ligand occurred. Template synthesis, even with $HClO_4$ produced the complex with the monoanionic $Hdapsox^-$ ligand (complex **6**), and heating in alkaline

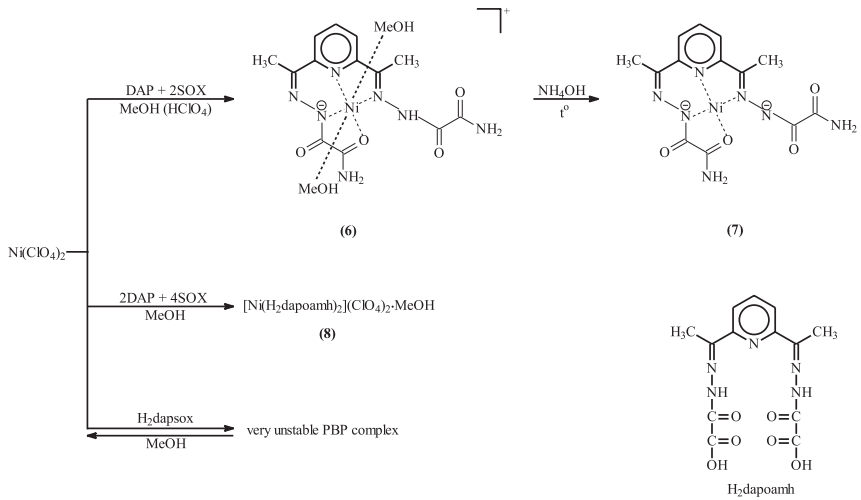

SCHEME 4.

medium led to the precipitation of a sparingly soluble complex with a doubly deprotonated ligand (complex **7**). IR spectra and thermal analysis (*94*) confirm that the same mode of coordination for both deprotonated forms of the H_2dapsox ligand in Ni(II) complexes occurred as that observed in the case of Cu(II) complexes, i.e., the ligand was asymmetrically tetradentately coordinated (Scheme 4). Such coordination in the presence of two MeOH molecules and magnetic moment of 2.1 BM pointed to a deformed octahedral geometry for the monodeprotonated complex. The electronic absorption spectrum of complex **6** corresponds to that of the tetragonally elongated octahedral complex of the Ni(II) ion (*95,96*).

The complex with the di-anionic ligand has diamagnetic properties, which together with the absence of solvent molecules and anions in the structure points to its square–planar geometry. Strengthening of the ligand field, caused by ligand deprotonation, in case of Ni(II) led to electron pairing and also resulted in a change in geometry from octahedral to square–planar.

A change in the stoichiometric ratio of $Ni(ClO_4)_2$, dap and sox from 1:1:2 to 1:2:4 enabled coordination of neutral bis(acylhydrazone), but during the synthesis hydrolysis of the amide groups and coordination of two molecules of the newly formed condensation product H_2dapoamh (H_2dapoamh = dioxo-2,6-pyridinediylbis(ethylidyne-1-hydra-zinyl-2-ylidene) diacetic acid) took place (Scheme 4). X-ray structure analysis of complex **8** (Fig. 4) shows that two H_2dapoamh are tridentately coordinated

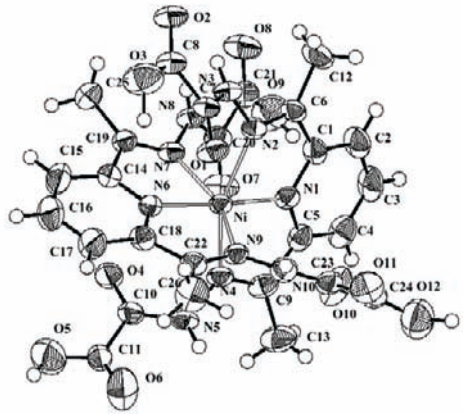

FIG. 4. The structure of complex cation $[Ni(H_2dapoamh)_2]^{2+}$ (*11*).

to Ni(II), which is unusual taking into account the significantly higher number of potential donor atoms. This is the only example of tridentate coordination of ligands from the class of bis(acylhydrazones) of dap and also serves to form the octahedral geometry favored by the Ni(II) ion. It is interesting that the hydrazide oxygen atoms O1, O4, O7, and O10 form long-range Ni $\cdots$ O intramolecular contacts (*11*), producing a deformed tetrahedral secondary coordination sphere around the primary octahedral coordination sphere. Thus H_2dapoamh realizes pseudo-pentadentate coordination since pentadentate binding represents the most suitable binding mode for ligands of this class.

D. IRON (III) COMPLEXES

Although in the case of ions with spheric symmetrical electron distribution, stable PBP complexes are expected (*23,45*), only a few Fe(III) complexes of this geometry have been synthesized and characterized so far. There are twelve Fe(III) complexes of coordination number seven characterized by X-ray analysis (*97*). $[Fe(EDTA)(H_2O)]^-$ represents the first among such complexes and the first PBP complex of 3d metals in general (*97*). Later on, four analogous complexes (*97,98*) with a rather deformed PBP structure have been synthesized. A regular pentagonal–bipyramidal structure was found in $[Fe(B)X_2]Y$, $[Fe(C)X_2]Y$ (Table I), and $[Fe(L)Cl_2](PF_6)$ (*99*) with pentadentate N5 macrocyclic systems. Among Fe(III) complexes of this geometry with bis(acylhydrazones) of dap, only $[Fe(H_2dapsc)Cl_2]Cl \cdot 2H_2O$ (*41*), $[Fe(H_2daps)Cl_2]Cl$ (*49*), and

$[Fe_2(daps)Cl_2(EtOH)_2]$ (*53*) have been structurally characterized (Table II). The first two represent monomeric complexes with neutral pentadentate ligands, whereas the third is a binuclear complex with tetra-deprotonated $daps^{4-}$ as a heptadentate ligand and two non-equivalent Fe(III) ions, one in a PBP and the other one in an octahedral environment (*53*).

The remaining two hepta-coordinate structures of Fe(III) are μ-oxo dimers. The first of them $[(H_2O)BFe–O–FeB(H_2O)](ClO_4)_4$ includes a macrocyclic ligand (Table I), and the other one $[Fe_2O(NO_3)_4(bpy)_2]$ (bpy = 2,2′-bipyridine), bidentate ligands (*100,101*). The PBP geometry of the μ-oxo-diiron(III) complexes is unusual since these complexes have square–pyramidal or octahedral structures with the exception of the above-mentioned two complexes.

Only three PBP complexes of Fe(III) with acyclic ligands from the class of bis(acylhydrazone) of dap have been structurally characterized at present (*41,49,53*) and this prompted studies in that direction. Both direct and template synthesis afforded the complex $[Fe(Hdapsox)Cl_2] \cdot 1/2H_2O$ (**9**) with a monoanionic H_2dapsox ligand (*7*). Protonation of the coordinated ligand was unsuccessful even upon addition of HCl to the reaction mixture (Scheme 5). In spite of asymmetrical mono-deprotonation, the ligand was symmetrically pentadentately

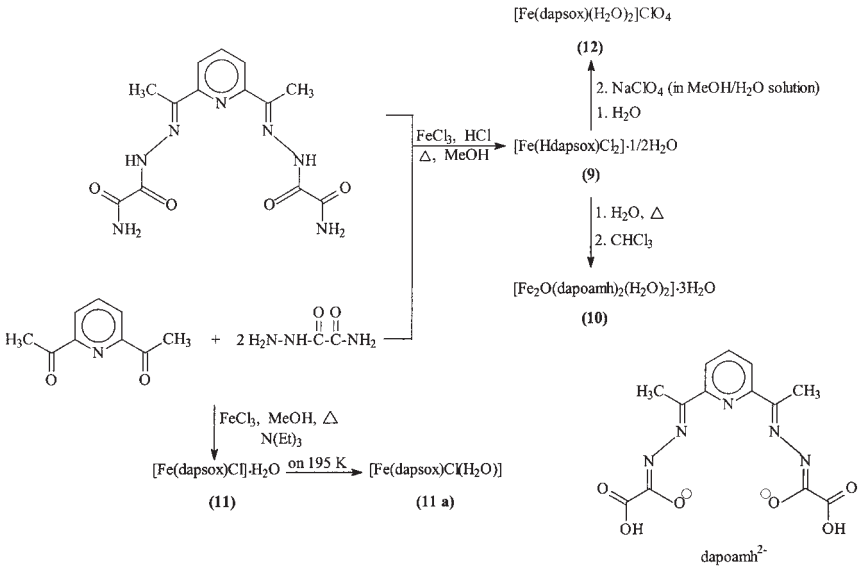

SCHEME 5.

coordinated, as in the case of the Co(II) complex **2** (Scheme 6). Such a coordination mode with two Cl^- ions forms the PBP environment of high-spin Fe(III). Thermal analysis (*94*) revealed an interesting three-step decomposition of the pentadentate ligand, i.e., the decomposition processes of the neutral and deprotonated chain were clearly distinguishable during thermal decomposition.

Synthesis of the Fe(III) complex with the doubly deprotonated polydentate ligand was performed employing three approaches and as a result three different products **10**, **11**, and **12** were obtained (Scheme 5). The first product was formed by hydrolysis of **9** and it represents the first PBP μ-oxo dimer of Fe(III) with an acyclic ligand in the coordination sphere (*10*). At the same time it is the first diamagnetic complex of Fe(III) that has ever been synthesized. Structural analysis (Fig. 5) confirmed double deprotonation and hydrolysis of the starting H_2dapsox ligand, as well as symmetrical penta-coordination of the newly formed dapoamh^{2-} (Scheme 5). The simultaneous presence of a protonated carboxyl and deprotonated hydrazide NH group in the structure is rather interesting. A coplanarity of four five-membered chelate rings, as a consequence of conjugation over the entire pentadentate ligand (*10,97*), is even more pronounced than in the case of the Co(II) complex **3** with dianionic H_2dapsox. Pentagons around two Fe(III) ions are rotating around the Fe–O–Fe bond under an angle of 140°. This structure is also interesting because the Fe(III) ions have low-spin configurations different from the high-spin configuration of complex **9**, which was used in the synthesis as the starting material. It was impossible to compare structural parameters because this was the first low-spin PBP complex of Fe(III). However, M–L bonds were found to be longer than expected in the case of the low-spin Fe(III) complex (*10*).

Template synthesis (Scheme 5) in the presence of triethylamine as a proton acceptor afforded another Fe(III) complex with a dianion in

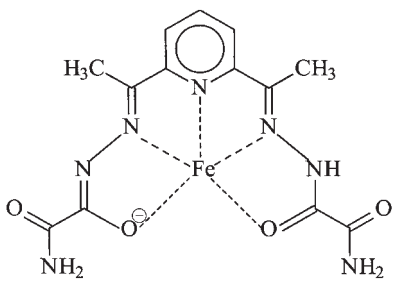

SCHEME 6.

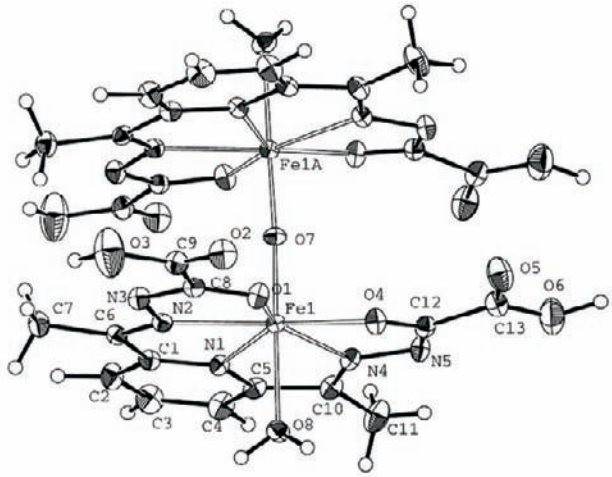

FIG. 5. The structure of $[Fe(dapoamh)(H_2O)]_2O$ (*10*).

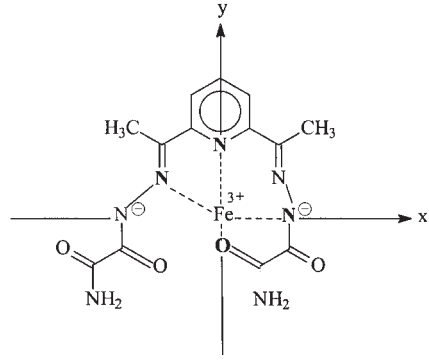

SCHEME 7.

the coordination sphere **11** (*10*). This complex has a square–pyramidal geometry with an asymmetric tetradentately coordinated dianion as in the case of Cu(II) and Ni(II) ions (Scheme 7) and chloride ion in the apical position. The mechanism of the two-step thermal decomposition of the tetradentate chelate was found to be identical to that described for Cu(II) and Ni(II) complexes (*94*). EPR spectra and magnetic moment measurements at different temperatures (*10*), undoubtedly pointed to the rare $S = 3/2$ spin-state of the square–pyramidal complex **11** at room temperature, which with a decrease in temperature transforms to an

octahedral low-spin ($S=1/2$) Fe(III) complex with unpaired electrons in the d*xy* orbital. This temperature dependent conversion from a square–pyramidal to an octahedral structure results from the coordination of water molecules present in the crystal lattice (*10*). The low-spin conformation ($S=1/2$) of Fe(III) in the dimer **10**, as well as in **11**, is a consequence of a strong ligand field of the doubly deprotonated pentadentate in the *xy* plane, but also the consequence of participation of the apical water molecules in strong hydrogen bonding, having an effect similar to that observed when hydroxyl groups are apically coordinated, which significantly strengthens the ligand field along the *z* axis. The interaction of the two low-spin Fe(III) ions in the dimer causes diamagnetism, demonstrating that the unpaired electron also occupies the d*xy* orbital. Recording UV/VIS spectra of aqueous solutions of **9** at different temperatures, established the reaction pathway for the hydrolytic processes affording the dinuclear μ-oxo complex **10** as final product (*10*). Equilibrium hydrolytic processes in aqueous solution lead to the formation of the doubly deprotonated monomeric PBP complexes [Fe(dapsox)Cl(H_2O)]* [5] and [Fe(dapoamh)Cl(H_2O)] as intermediates.

Since these intermediates were characterized (*10*) as monomeric PBP complexes of Fe(III) with a dianionic acyclic pentadentate ligand, it was the intention to isolate and structurally characterize some of them, since no examples of such structures have been reported in the literature. With this aim, the [Fe(dapsox)(H_2O)$_2$]ClO_4 complex **12** was synthesized, which is analogous to the intermediate [Fe(dapsox)Cl(H_2O)]*. The results of an X-ray structural analysis (Fig. 6) confirmed the PBP structure of the complex and double deprotonation of the ligand. This structure is the first example of a monomeric structure of Fe(III) with an anionic pentadentate ligand and confirms previously suggested hydrolytic processes (*10*) which led to the production of complex **10**.

In these studies a monomeric high-spin PBP complex of Fe(III) **9** with the monoanionic form of the pentadentate ligand was produced. Further deprotonation of the ligand afforded the diamagnetic μ-oxo dimer **10** with low-spin Fe(III) ions. In spite of the change in electronic configuration of the Fe(III) ions provoked by an increase in the strength of the ligand field of the doubly deprotonated polydentate ligand, complex **10** preserved the PBP geometry of the starting complex **9**. On the

[5] An asterisk was introduced to distinguish this complex from the octahedral complex produced by treating [Fe(dapsox)Cl] · H_2O (**11**) at low temperatures.

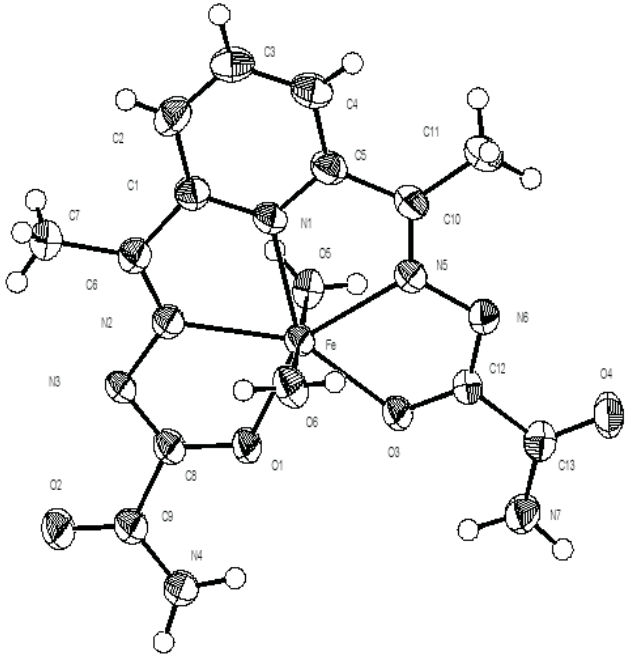

FIG. 6. The structure of complex cation $[Fe(dapsox)(H_2O)_2]^+$ (*12*).

other hand, template synthesis afforded the square–pyramidal complex **11**, also with the dianionic form of H_2dapsox, which represents a complex of intermediate spin state because of its lower coordination number 5. Conversion of this complex to the octahedral one at lower temperatures produced low-spin $[Fe(dapsox)Cl(H_2O)]$. These examples clearly demonstrate the effects of different synthetic methods, as well as charge on the polydentate ligand, on the electronic configuration of the central metal ion and on the geometry and magnetic characteristics of the produced complexes.

E. MANGANESE(II) AND ZINC(II) COMPLEXES

Following Co(II) complexes, the most frequently found hepta-coordinate structures among 3d metals are those of Mn(II) complexes. Based on literature data, 21 X-ray analyses of Mn(II) complexes with coordination number seven have been reported so far. They include

complexes with hepta-, hexa-, penta-, tetra-, and tridentate ligands. Two structures obtained with tripodal heptadentates **XXXV** (Table II) and $(pyo)_3$tren (*78*) are known at present. Also, three complexes with hexadentate ligands of the EDTA type have been obtained so far (*77,85,102*). Only one structure with the tetradentate **XXXVIII** ligand and one with the tridentate purpurate ion (*103*) was described, while most of the hepta-coordinate Mn(II) complexes include planar pentadentate ligands. Four complexes involve macrocyclic ligands (*22,24,26,104*), and eight complexes acyclic bis(imine) derivatives of dap (**XVII**, **XVIII**, **XXI**, **XXII**, **XXIX**, **XXXI**). Only in one of these structures, bis(acylhydrazone) of 2,6-diacetylpyridine is coordinated in the dianionic form (*56*). The last two complexes have an interesting tetrameric structure with the macrocyclic ligands **XV** and **XVI**, the former possessing eight potential donor atoms and the latter sixteen, all of them being included in the formation of the PBP geometry around four Mn(II) ions.

In contrast to the variety within the structures of Mn(II) hepta-coordinate species, out of ten known PBP structures of Zn(II), eight include planar pentadentates (derivatives of dap), four macrocylic (**VI**, **VII**, **VIII,** and **IX**) and four acyclic systems (**XVIII**, **XXV**, **XXVI**, and **XXX**). In the remaining two complexes, the PBP geometry around the Zn(II) ion was formed by a combination of a tridentate ligand and bidentate NO_3^- ions (*83*), i.e., by a combination of a monodentate ligand and again the bidentate nitrate ions (*81*). However, these structures might be better described as pseudo-PBP, taking into consideration that they contain one much longer Zn–O(nitrato) bond compared to the others, i.e., one NO_3^- ion has rather monodentate than bidentate character.

Mn(II) and Zn(II) complexes synthesized (*13*) with the H_2dapsox ligand (Scheme 8) have PBP geometry. They were characterized by elemental analysis, determination of molar conductivity, magnetic moment (in the case of Mn(II)), IR, UV/VIS (in the case of Mn(II)), and NMR (in the case of Zn(II)) spectra, as well as by thermal analysis (*13,94*). The results confirmed pentadentate coordination of the neutral H_2dapsox ligand form, similar to the Co(II) complex **1**. Comparison of IR spectra and results of detailed thermal analysis (*13,94*) revealed the similarity in the stability of the Mn(II) and Co(II) complex **1**, while NMR spectra (^{1}H and ^{13}C) and thermal analysis of the Zn(II) complex (*13,94*), pointed to a significantly lower stability of the complex. Among all complexes with the H_2dapsox ligand and its deprotonated forms, only the zinc complex was found to be very unstable (*13,94*). During thermal decomposition of the PBP Zn(II) complex, an intermediate

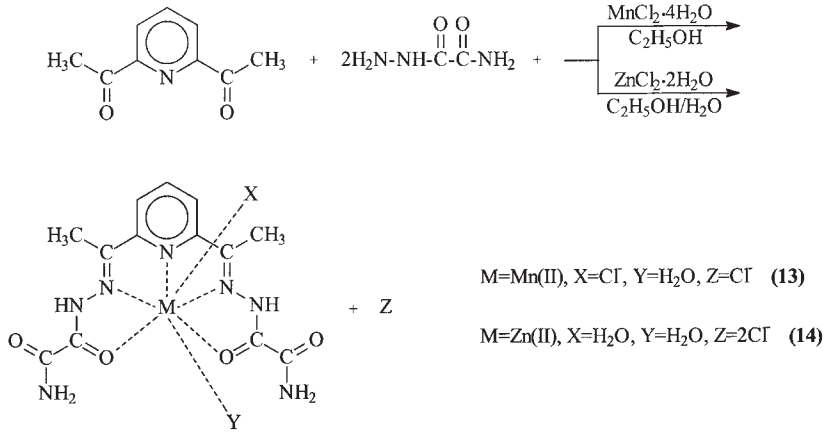

SCHEME 8.

complex of helicoidal structure with coordination number five was isolated. Dissolution in absolute ethanol and mild heating led to decomposition of this complex and precipitation of H_2dapsox, demonstrating that the helicoidal structure has lower stability in solution than in the solid state, and also a lower stability than the corresponding PBP structure. This explains the fact that starting with a mixture of dap and sox in absolute methanol in the presence of anhydrous $ZnCl_2$, H_2dapsox was produced, while if the reaction proceeded in a water–alcohol solution in the presence of hydrated $ZnCl_2$, the PBP complex was obtained. In the former case, Zn served only as a catalyst for the condensation reaction in which the helicoidal penta-coordinate Zn(II) complex only represents an intermediate state. In the latter case, the presence of water enabled the formation of a more stable PBP complex, due to a high tendency of Zn(II) to coordinate water molecules, resulting in the shortest metal–water bonds among PBP complexes of 3d metals (*43,52*).

F. Mo(V), La(III), AND U(VI) COMPLEXES

In order to investigate the coordination possibilities of bis(acylhydrazones) of dap, complexes of the larger metal ions and H_2dapsox were synthesized: $[Mo_2O_2(H_2dapsox)_2]Cl_6 \cdot 4H_2O$ **15** (*9*), $[La(H_2dapsox)(NO_3)_x](NO_3)_{3-x}$ **16** (*9*), and $[UO_2(dapsox)]$ **17** (*8*). These complexes were characterized by IR, EPR (in the case of complex **15**), ^{1}H and ^{13}C NMR

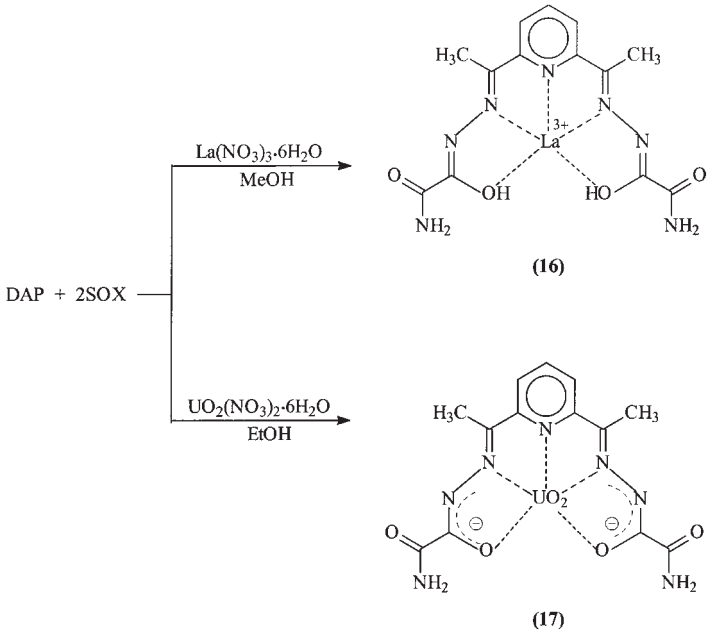

SCHEME 9.

spectra (in the case of complex **17**), electron absorption spectra and thermal analysis.

The lanthanum complex (Scheme 9) has the coordination number nine with two NO_3^- ions bidentately bound in the solid state, while in solution only one nitrate group is coordinated. H_2dapsox is symmetrically pentadentately coordinated in the α-oxyazine form (Scheme 9).

The complex of the uranyl ion (Scheme 9) is characterized by a PBP geometry with oxo oxygen atoms in the *trans* positions and also symmetrically coordinated bis(acylhydrazone). However, during the synthesis, spontaneous double deprotonation of the ligand (without addition of a proton acceptor) and its coordination in the dianionic form (Scheme 9) took place. In the case of the other central metal ions (Co(II), Cu(II), Ni(II), and Fe(III)), no spontaneous double deprotonation of the coordinated ligand either in the solid state or in solution was observed (*4–7*), and in the case of a complex with the MoO^{3+} cation (Scheme 10), deprotonation occurred only in aqueous solution. Thermal analysis showed that among all complexes with the H_2dapsox ligand and its mono- and di-anionic forms (*8,94*), only the complex with the

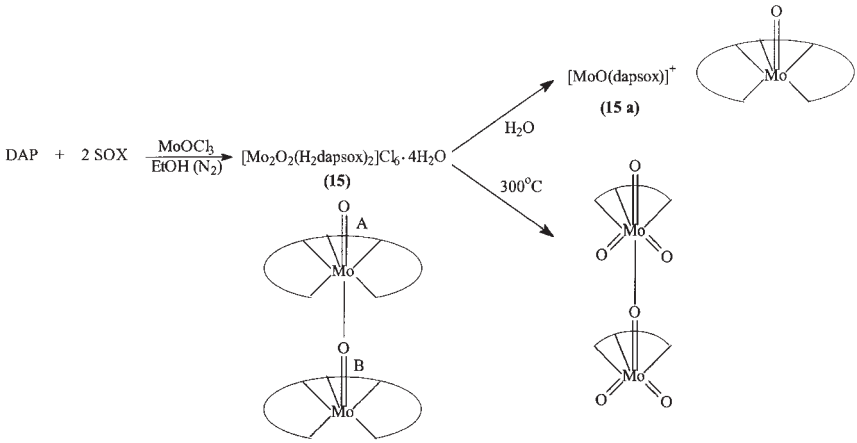

SCHEME 10.

uranyl ion was the most stable. The strong bonds between the donor atoms and the central metal ion, together with more pronounced shifts of the peaks in the ^{13}C spectrum resulting from coordination of the UO_2^{2+} cation by H_2dapsox (*8*), demonstrate a significant effect of the UO_2^{2+} group on the coordinated ligand system, and this is the reason for spontaneous double deprotonation.

The $[Mo_2O_2(H_2dapsox)_2]Cl_6 \cdot 4H_2O$ complex appeared to be a rather interesting one. Molybdenum chemistry is dominated by dimeric species with single or double bridged oxygen atoms. In the structures with a single bridged oxygen atom, Mo–O terminal bonds are *cis* or *trans* orientated; normal orientation has not been described so far and the linear one was found only in the tetraphenylporphyrin (TPP) dimer (*105–107*). Because of *cis* or *trans* configuration of the above bonds, Mo(V) dimers have diamagnetic properties. The linear complex with TPP represents the only paramagnetic molybdenum dimer (*105*). Complex **15**, represents the second example of a paramagnetic dimolybdenum(V) compound. A dimeric structure (Scheme 10) with the symmetric pentadentately coordinated neutral H_2dapsox ligand was established by IR and thermal analysis. These data also pointed to delocalization in the plane of the pentadentate ligand, as well as to the coordination of an α-oxyazine form (*9*). This structure is unique, because one terminal oxygen atom plays at the same time the role of the bridging oxygen atom, and this is the first example of a dimer with a Mo_2O_2 fragment. PBP geometry occurs around one Mo, with PP

(pentagonal–pyramidal) geometry around the other one (Scheme 10). Thermal decomposition of the complex at about 300 °C affords an intermediate Mo(VI) dimer, which belongs to the rare trioxo complexes (*108–110*). Thermal stability points to the stability of the dimeric structure in the solid state, since no sign of either polymerization or cleavage of the Mo–O bond was observed. However, the dimeric structure breaks in solution and pentadentate deprotonation occurs, thus producing the monomeric pentagonal–pyramidal complex with the dianionic H_2dapsox ligand (*9*).

The magnetic characteristics of both the dimeric and monomeric complexes are rather interesting. Taking into account the linear structure of the dimer, paramagnetism was expected because the d*xy* orbital with the unpaired electron has no possibility to overlap with the pπ orbitals of the bridging oxygen and there is no formation of a three-center π bond through Mo–O–Mo atoms, which would lead to diamagnetism. Although only the dimer **15** and the dimer with a TPP structure were found to be paramagnetic, they differed significantly. Since our dimer is penta-coordinate in the *xy* plane, the d*xy* orbital with the unpaired electron is not non-bonding, but together with the $dx^2–y^2$ orbital takes part in bond formation with the pentadentate ligand. In the TPP dimer, the unpaired electron is strictly localized in the anti-bonding d*xy* orbital and as a consequence, there is no magnetic coupling between the two Mo centres and μ_{eff} is 1.7 BM, whereas in our case it is 0.95 BM, which points to a significant interaction of the unpaired electrons. Similar interaction has been previously established in the Fe(III) dimer, but it was more intense and led to diamagnetism. A higher degree of electron delocalization in the *xy* plane due to the presence of the deprotonated pentadentate ligand, assists a stronger interaction between the two Fe(III) ions in the dimer **10** (*10,97*).

The EPR spectrum of **15** in aqueous solution (*9*) confirmed the monomeric structure. It also confirmed deprotonation and a high degree of delocalization in the *xy* plane, as seen from an extremely high $g_{\|}$ value and large g-anisotropy. According to the degree of g-anisotropy, Mo enzymes and monomeric complexes were classified into two groups (*111*), the first including octahedral and the second one square–pyramidal complexes. However, our complex does not belong to either of these two groups, as judged from the EPR parameters. Since this complex represents one of the pentagonal–pyramidal Mo(V) complexes that have not been described in the literature, it remains to be examined whether the other complexes of this geometry would reveal similar EPR characteristics.

III. Concluding Discussion

A schematic presentation of the complex structures synthesized is presented in Scheme 11. The stability of complexes with PBP geometry of ions with spherically symmetrical electron distribution has been observed earlier (*23,45*), as in the case of high-spin Fe(III) **9** and

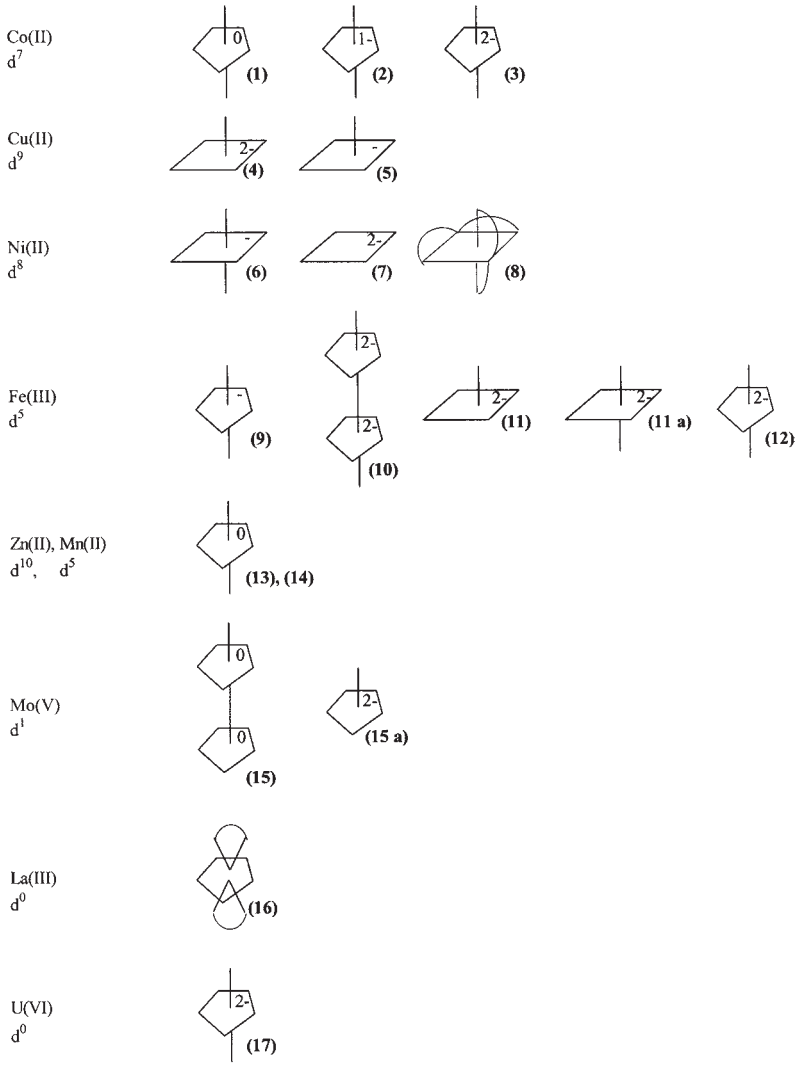

SCHEME 11.

Mn(II) **13** complexes described in the present report. No matter whether the template or direct synthetic method was employed, these Fe(III) and Mn(II) complexes preserved their PBP geometry. However, Ni(II) and Cu(II) complexes of this geometry are rare and unstable, and it was impossible to synthesize them by template synthesis, but only by applying the direct synthetic or transmetallation method (*45,48,112*). Syntheses of pentadentate planar macrocyclic ligands with Ni(II) or Cu(II) ions as templates were unsuccessful (*90*), because they require formation of a PBP geometry around the template ions, and this geometry is not supported by such ions. So, direct synthesis performed with the already formed H_2dapsox ligand, which favors the PBP geometry, afforded in the case of Ni(II) and Cu(II) ion very unstable, rapidly decomposing PBP complexes. Since the application of template synthesis results in the formation of the octahedral Ni(II) **6** and square–pyramidal Cu(II) complexes **4** and **5**, coordination during template synthesis is primarily dictated by the d^n configuration of the metal ion, whereas during direct synthesis it is dictated by the conformational flexibility of a ligand.

However, very stable Co(II) complexes with a PBP geometry were obtained and their formation was independent on both reaction pathway and charge on the pentadentate ligand, although the d orbitals of Co(II) ion are not evenly filled with electrons. Orbitals of the donor atoms in the PBP geometry are directed toward dxy, dx^2–y^2, and dz^2 orbitals of the central metal ion (Scheme 12), causing a splitting of the d orbitals into three groups: e''_1[(xz), (yz)], e'_2[(x^2–y^2), (xy)], and a'_1(z^2). Because of the pentadentate character with the N_3O_2 set of donors in the xy plane, the actual symmetry is lower than D_{5h}, which mostly affects the e'_2 state, splitting it further (Scheme 2). In any case, symmetrical distribution of electrons within the dxy, dx^2–y^2, and dz^2 orbitals, pointing directly at the donor atoms in the PBP geometry, is of key importance for the stability of PBP complexes, whereas completely symmetrical occupation of d orbitals with electrons is not indispensable. So, d^5, d^6, and d^7 high-spin configurations are stable in the PBP environment (Fe(III), Mn(II), Fe(II), and Co(II)), because of symmetrical distribution of electron density in the above mentioned dxy, dx^2–y^2, and dz^2 orbitals. For that reason, in addition to high-spin d^5 configuration, high-spin d^7 configuration is also stable in the PBP environment. Asymmetrical monodeprotonation of the pentadentate (e.g., in the Co(II) complex **2** and Fe(III) complex **9**), as well as double deprotonation (in the case of the Co(II) complex **3** and Mn(II) complexes with **XXII** and purpurate (*103*), respectively) which provokes a significant increase in ligand field strength (as reported in our previous studies (*10,11*),

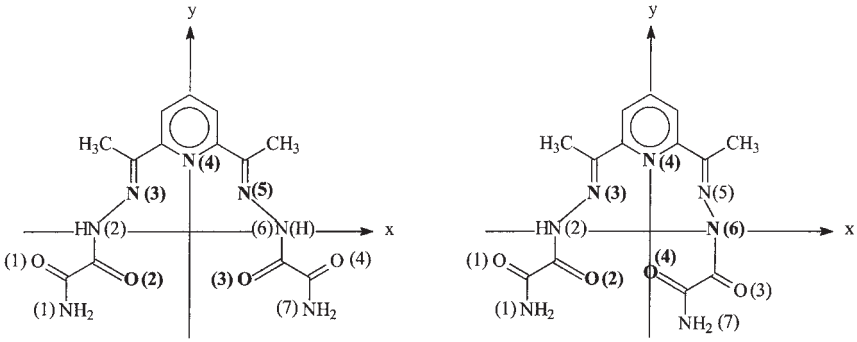

SCHEME 12.

does not lead to electron pairing in these electron configurations. This means that 3d ions with d^0, d^1, d^2, d^{10} and high-spin d^6 configuration, are also able to form PBP structures, as confirmed by the synthesis of PBP complexes with Cr(VI) (*113*), Ti(III) (*114*), V(III) (*115*), Cr(IV) (*116,117*), Fe(II) (*19,20,32,43,44,49,62,69,70*), and Zn(II) (Section II.E). There are, although, certain differences in the stability of these complexes provoked by some additional influences such as ionic radius, charge of the metal atom and crystal field stabilization energy (Table IV). Based on the value of the ionic radius and because of the spherically symmetric high-spin d^5 electron configuration, Mn(II) PBP complexes could be the most stable among 3d metals. However, this is not quite true, since it is different from Co(II) and Fe(II), there is no crystal field stabilization in Mn(II). In Cr(IV), V(III), and Ti(III) crystal field stabilization occurs, but their ionic radii are smaller than those of either Mn(II), Fe(II), and Co(II), and this, together with their high positive charge, makes their PBP complexes less stable. Because of that, these structures are very rare (*114–117*). Zn(II) with spherically symmetrical distribution of electron density and an ionic radius close to that of Co(II) (smaller than the radius of Mn(II) and Fe(II)), has no crystal field stabilization energy. Complete filling of the dz^2, $dx^2–y^2$, and dxy orbitals with electrons leads to significant repulsive interactions with donor atomic orbitals, which all together influence a rather high instability of the PBP Zn(II) complex, as confirmed by earlier studies (*13,94*). Zn(II) only forms these complexes with rigid planar neutral pentadentates, and increasing negative polydentate charge results in a decrease in the coordination number from seven to six (*58,64,65*) or even to five (*118*). Similarly, in the case of Fe(III), even a smaller ionic radius (*93*), a higher charge on the metal ion and the absence of crystal

field stabilization energy, result in a decreased stability of its PBP structures. Although Fe(III) ion forms a PBP complex with the mono-anion $Hdapsox^-$, template synthesis with the polydentate di-anion afforded a square–pyramidal complex with three unpaired electrons, which points to a lower tendency of Fe(III) to form the PBP geometry as compared to Mn(II), Co(II), and Fe(II).

Only the three ions Mn(II), Co(II), and Fe(II), produce the most stable PBP complexes. However, Co(II) has the highest crystal field stabilization energy (Table IV) and, in spite of its smaller ionic radius, this contributes greatly to the stability of these structures (Mn(II) has no crystal field stabilization energy and in the case of Fe(II) this energy is lower than in Co(II)). In case of the Fe(II) ion, asymmetrical occupation of orbitals within the $e_1''(dxz, dyz)$ level leads to a decreased stability of its PBP environment. For that reason, seven out of nine known PBP structures were formed with planar pentadentates and only one with a tetradentate and one with a heptadentate geometry (Tables I and II). When the axial monodentate ligand in the PBP Fe(II) complex, with the pentadentate **V**, is replaced by the strong-field CN^- ligand, the PBP geometry of the complex transforms into the octahedral one (*25*). Based on the above presented considerations, PBP complexes of Co(II) and Mn(II) seem to be the most stable among 3d metals, followed by Fe(II) complexes and then by the complexes of other ions with symmetrical distribution of electrons in the dz^2, $dx^2–y^2$, and dxy orbitals. The highest number of 3d PBP structures of just Co(II) and Mn(II) has been synthesized. However, they include not only complexes with rigid pentadentates but also with hepta-, hexa-, tetra-, tri-, and bidentates.

Asymmetrical electron distribution in dz^2, $dx^2–y^2$, and dxy orbitals, as in d^3, d^8, d^9, and low-spin d^5 and d^6 configurations, destabilizes the PBP geometry. Although, if the ligand itself favors this geometry, then its distortion and tendency for asymmetrical binding takes place (*45,119*), which, if the ligand allows it, results in a change in geometry. In the Ni(II) and Cu(II) complexes **6** and **5**, not only asymmetrical coordination, but also asymmetrical single deprotonation of the ligand occurred. In the case of the $[Cr(Hdapsc)(H_2O)_2](NO_3)_2$ complex (*42*) with d^3 configuration of the metal ion, the ligand only allows asymmetrical monodeprotonation. Reduction of the PBP Cr(IV) complex results in the transition of a d^2 to d^3 configuration, which leads to the formation of octahedral complexes (*117*). Similarly, the transition of the high-spin Fe(II) configuration (in complexes with ligand **V**) into the low-spin configuration results in the conversion from the PBP to the octahedral geometry (*25*). However, in the case of complexes **10** and

12 with low-spin Fe(III), in spite of asymmetrical d-electrons distribution, the PBP environment was preserved. The reason for this phenomenon could be explained in terms of the stability of bonds established in the starting complex **9** (Schemes 5 and 6) which cannot be easily broken, while complete delocalization of electrons along the entire dianionic pentadentate ligand in these complexes expresses an additional stabilizing effect. The so-called "ring current" factor is well known and here π orbitals of four, or even better, of five equatorial donor atoms form a stabilizing π-bonding orbital, the so-called ring π orbital (*115*).

In d^8 configuration (Scheme 12), entrance of electrons into the d*xy* orbital weakens the bonds of the Ni(II) ion with N3 and N5, as well as with O2 and O3 atoms, whereas because of lower electron density in the $dx^2–y^2$ orbital, the Ni–N2 and Ni–N6 bonds, which are directly pointed to the $dx^2–y^2$ orbital, strengthen (Scheme 12). This leads to coordination of one of these two nitrogen atoms. Coordination through the hydrazine NH group results in its deprotonation (as in $[Cu_2(dappc)(H_2O)_3]_2[Cu_2(dappc)(H_2O)_2(ClO_4)]_2(ClO_4)_6 \cdot 2H_2O$ (*87*), $[Cu_2(dappc)Cl_2]_2 \cdot 2H_2O$ (*88*), $[Cu_2(dapip')Br]_2 \cdot 2H_2O$ (*87*), and the Ni(II) tetramer with ligand **XXIV** (*59*)), whereas the reverse does not have to hold good. More precisely, deprotonation of the hydrazine NH group does not require its coordination (examples are: Cr(III) (*42*), dimeric Zn(II) (*58,65*), dimeric Cu(II) (*89*), and Fe(III) complex **9** described in this report). Coordination of hydrazine nitrogen also favors coordination of the primary C=O group (O4) of the same chain (Scheme 12), since in this way a more stable five-membered ring is formed. Steric reasons are responsible for the fact that the second chain can include only imino nitrogen N3 in coordination. These are the reasons for single deprotonation and asymmetrical coordination of $Hdapsox^-$ in the octahedral Ni(II) complex **6** (Schemes 4 and 12). For the same reasons, in the case of Cu(II) ion, coordination of the N3, N6, and O4 atoms and deprotonation of the N6 atom take place (Scheme 12) (As Cu(II) is a d^9 system, the additional electron occupies the dz^2 instead of the $dx^2–y^2$ orbital, resulting in the square–pyramidal geometry).

In the Fe(III) complex **9**, monodeprotonation is not provoked by a tendency for an asymmetric structure, but by a high positive charge on the metal ion. Since Cr(III) and high-spin Fe(III) ions have almost the same ionic radii (*93*) and the same +3 charge, a similar influence on the acidity of coordinated acylhydrazone, i.e., on its single deprotonation (*42*), is to be expected. Although coordination to Fe(III) ion is not realized via the hydrazide nitrogen (Scheme 6), coordination of the hydrazide C=O oxygen was sufficient for a pronounced increase in

the acidity of its NH group. This was confirmed by the structure of the dinuclear Fe(III) complex **10** (*10*), where two carboxyl groups of dapoamh^{2-} are protonated, whereas the hydrazide nitrogen atoms are deprotonated (Scheme 5). Coordination of the hydrazide C=O group makes its NH group more acidic than the carboxyl group, whereas coordination through nitrogen itself leads to a more drastic increase in acidity, so that protonation is impossible to occur even at pH = 0.

Based on electron absorption spectra and magnetic properties of the complexes described in the present report, conclusions related to the effect of the degree of ligand deprotonation on the ligand field strength can be drawn. Doubly deprotonated dapsox^{2-} (similar to its derivative dapoamh^{2-}) represents a ligand of a much stronger field as compared to its monoanionic form Hdapsox^{-}. Absorption spectra of Cu(II) complexes **4** and **5** strongly support such a conclusion (*10*). Furthermore, deprotonation of the octahedral paramagnetic Ni(II) complex **6** resulted in precipitation of the diamagnetic square–planar complex **7** with doubly deprotonated dapsox^{2-} (Scheme 4).

A comparison of the magnetic moments and electronic spectra of the synthesized high-spin Co(II) complexes (**1**, **2**, and **3**), revealed certain, although not drastic differences in the shift of bands toward higher energies (Table III). A more pronounced shift of bands was observed during the transition of monoanionic to dianionic forms of the ligand than in the case of the transition from neutral to the singly-deprotonated ligand. However, since Co(II) has a pronounced tendency to form the PBP geometry, ligand deprotonation does not result in electron pairing because that would change the symmetrical electron occupancy of the dz^2, dx^2–y^2, and dxy orbitals, which is necessary for the stability of the PBP geometry. Consequently, all three Co(II) complexes (**1**, **2**, and **3**) have PBP structures. Both the Cu(II) complexes (**4** and **5**) have a square–pyramidal geometry, because in the d^9 configuration, strengthening of the ligand field cannot lead to a change in electron configuration. On the other hand, strengthening of the ligand field leads to electron pairing in Fe(III) and Ni(II) complexes, and affects the geometry of their coordination sphere. Thus, the octahedral Ni(II) complex **6** becomes square–planar on double deprotonation. The Fe(III) complex **9** with the monoanionic form of the Hdapsox^{-} ligand, represents a PBP complex with $S = 5/2$, whereas complex **11** with the dianionic dapsox^{2-} ligand has a square–pyramidal geometry with $S = 3/2$, and at lower temperatures it transforms into a deformed octahedral complex with $S = 1/2$. However, the diamagnetic dimer of low-spin Fe(III) **10**, preserves the PBP geometry, because the

energy necessary for breaking the bonds of the Fe(III) ion with the donor atoms (already established in the starting high-spin complex) is probably higher than the energy difference between such a PBP structure of low-spin Fe(III) and the more favorable octahedral structure. However, asymmetric electron distribution in the dxy, dx^2–y^2, and dz^2 orbitals, as in the case of the low-spin Fe(III) ion, does not contribute to the stability of the PBP geometry and this is the reason for the longer Fe–N and Fe–O bonds in complex **10** than expected in the case of a low-spin Fe(III) structure.

Finally, the diamagnetic character of the dinuclear Fe(III) complex **10** and the magnetic moment of the paramagnetic Mo(V) dimer **15**, show that the degree of deprotonation of the polydentate ligand affects not only the magnetic properties and spectral parameters of the central metal ion, but also the character of the bond between the metal ion and donor atoms. High degree of delocalization of the dapsox^{2-} ligand and its derivative dapoamh^{2-} (which is connected with the earlier mentioned effect of stabilizing the ring π-bonding of the ligand orbitals), increases the covalent character of the metal–ligand bonds within the xy plane (*9,97*). In the dimers **10** and **15**, the unpaired dxy electrons of the metal ions are included in this delocalization, which plays a key role in strengthening the magnetic interaction between the metal ions in the dimeric systems (*9,10*). This fact has not been reported in the available literature until now.

Acknowledgments

This work was supported by the Ministry for Science and Technology of Serbia through Project no. 1713.

References

1. Drew, M. G. B.; Nelson, J.; Nelson, S. M. *J. Chem. Soc., Dalton Trans.* **1981**, 1685.
2. Sommerer, S. O.; Baker, J. D.; Zerner, M. C.; Palenik, G. J. *Inorg. Chem.* **1992**, *31*, 563.
3. Pelizzi, C.; Pelizzi, G.; Tarasconi, P. *J. Chem. Soc., Dalton Trans.* **1985**, 215.
4. Andjelković, K.; Ivanović, I.; Prelesnik, B. V.; Leovac, V. M.; Poleti, D. *Polyhedron* **1996**, *15*, 4361.
5. Ivanović, I.; Andjelković, K.; Beljanski, V.; Prelesnik, B.; Leovac, V. M.; Momirovic, M. *J. Coord.Chem.* **1997**, *42*, 335.
6. Andjelković, K.; Ivanović, I.; Niketić, S. R.; Prelesnik, B.; Leovac, V. M. *Polyhedron* **1997**, *16*, 4221.
7. Ivanović-Burmazović, I.; Bacchi, A.; Pelizzi, G.; Leovac, V. M.; Andjelković, K. *Polyhedron* **1998**, *18*, 119.
8. Ivanović-Burmazović, I.; Šumar, M.; Brčeski, I.; Hodžić, I.; Andjelković, K. *Mat. Sci. Forum* **2000**, *352*, 277.

9. Andjelković, K.; Ivanović-Burmazović, I.; Gruden, M.; Niketić, S. R. *J. Coord. Chem.* **2001**, *53*, 289.
10. Bacchi, A.; Ivanović-Burmazović, I.; Pelizzi, G.; Andjelković, K. *Inorg. Chim. Acta* **2001**, *313*, 109.
11. Pelizzi, G.; Bacchi, A.; Ivanović-Burmazović, I.; Gruden, M.; Andjelković, K. *Inorg. Chem. Comm.* **2001**, *4*, 311.
12. Andjelković, K.; Bacchi, A.; Pelizzi, G.; Jeremić, D.; Ivanović-Burmazović, I. *J. Coord. Chem.* **2002**, *55*, 1385.
13. Šumar, M.; Ivanović-Burmazović, I.; Hodzić, I.; Andjelković, K. *Synth. React. Inorg. Met.-org. Chem.* **2002**, *32*, 721.
14. Nelson, S.M.; Bryan, P.; Busch, D.H. *J. Chem. Soc., Chem. Commun.* **1966**, 641.
15. Nelson, S. M.; Busch, D. H. *Inorg. Chem.* **1969**, *8*, 1859.
16. Fleischer, E.; Hawkinson, S. *J. Am. Chem. Soc.* **1967**, *89*, 720.
17. Drew, M.G.B.; Othman, A.H.; McIlroy, P.D.A.; Nelson, S.M. *J. Chem. Soc., Dalton Trans.* **1975**, 2507.
18. Drew, M.G.B.; Grimshaw, J.; McIlroy, P.D.A.; Nelson, S.M. *J. Chem. Soc., Dalton Trans.* **1976**, 1388.
19. Drew, M. G. B.; Othman, A. H.; McIlroy, P. D. A.; Nelson, S. M. *Acta Cryst.* **1976**, *B32*, 1029.
20. Drew, M. G. B.; Othman, A. H.; Nelson, S. M. *J. Chem. Soc., Dalton Trans.* **1976**, 1394.
21. Drew, M. G. B.; Nelson, S. M. *Acta Cryst.,* **1975**, *A31*, S140.
22. Drew, M. G. B.; Othman, A. H.; McFall, S. G.; McIlroy, P. D. A.; Nelson, S. M. *J. Chem. Soc., Dalton Trans.* **1977**, 438.
23. Rakowski, M. C.; Rycheck, M.; Busch, D. H. *Inorg. Chem.* **1975**, *14*, 1194.
24. Drew, M. G. B.; Othman, A. H.; McFall, S. G.; McIlroy, P. D. A.; Nelson, S. M. *J. Chem. Soc., Dalton Trans.* **1977**, 1173.
25. Nelson, S. M.; McIlroy, P. D. A.; Stevenson, C. S.; Konig, E.; Ritter, G.; Waigel, J. *J. Chem. Soc., Dalton Trans.* **1986**, 991.
26. Alcock, N. W.; Liles, D. C.; McPartlin, M.; Tasker, P. A. *J. Chem. Soc., Chem. Commun.* **1974**, 727.
27. Liles, D. C.; McPartlin, M.; Tasker, P. A. *J. Chem. Soc., Dalton Trans.* **1987**, 1631.
28. Adam, K. R.; Donnelly, S.; Leong, A. J.; Lindoy, L. F.; McCool, B. J.; Bashall, A.; Dent, M. R.; Murphy, B. P.; McPartlin, M. *J. Chem. Soc., Dalton Trans.* **1990**, 1635.
29. Haque, Z. P.; Liles, D. C.; McPartlin, M.; Tasker, P. A. *Inorg. Chim. Acta Lett.* **1977**, *23*, L21.
30. Nelson, S. M.; Esho, F. S.; Drew, M. G. B.; Bird, P. *J. Chem. Soc., Chem. Commun.* **1979**, 1035.
31. Ansell, C. W. G.; Lewis, J.; Raithby, P. R.; Ramsden, J. N. *J. Chem. Soc., Dalton Trans.* **1982**, 2127.
32. Bishop, M. M.; Lewis, J.; O'Donoghue, T. D.; Raithby, P. R.; Ramsden, J. N. *J. Chem. Soc., Chem. Commun.* **1978**, 828.
33. Bishop, M. M.; Lewis, J.; O'Donoghue, T. D.; Raithby, P. R.; Ramsden, J. N. *J. Chem. Soc., Dalton Trans.* **1980**, 1390.
34. Ansell, C. W. G.; Lewis, J.; Raithby, P. R.; Ramsden, J. N.; Schroder, M. *J. Chem. Soc., Chem. Commun.* **1982**, 546.
35. Hanton, L. R.; Raithby, P. R. *Acta Cryst.* **1980**, *B36*, 1489.
36. Ansell, C. W. G.; Lewis, J.; Liptrot, M. C.; Raithby, P. R.; Schroder, M. *J. Chem. Soc., Dalton Trans.* **1982**, 1593.
37. Ansell, C. W. G.; Lewis, J.; Raithby, P. R. *J. Chem. Soc., Dalton Trans.* **1982**, 2557.

38. Constable, E. C.; Lewis, J.; Liptrot, M. C.; Raithby, P. R.; Schroder, M. *Polyhedron* **1983**, *4*, 301.
39. Brooker, S.; McKee, V.; Shepard, W. B.; Pannell, L. K. *J. Chem. Soc., Dalton Trans.* **1987**, 2555.
40. Ianelli, S.; Pelizzi, C.; Pelizzi, G.; Tarasconi, P. *J. Chem. Crystall.* **1996**, *26*, 195.
41. Palenik, G. J.; Wester, D. W.; Rychlewska, U.; Palenik, R. C. *Inorg. Chem.* **1976**, *15*, 1814.
42. Bino, A.; Frim, R.; van Genderen, M. *Inorg. Chim. Acta* **1987**, *127*, 95.
43. Palenik, G. J.; Wester, D. *Inorg. Chem.* **1978**, *17*, 864.
44. Wester, D.; Palenik, G. J. *J. Am. Chem. Soc.* **1973**, *95*, 6505.
45. Wester, D.; Palenik, G. J. *J. Am. Chem. Soc.* **1974**, *96*, 7565.
46. Lorenzini, C.; Pelizzi, C.; Pelizzi, G.; Predieri, G. *J. Chem. Soc., Dalton Trans.* **1983**, 721.
47. Al-Shihri, A. S. M.; Dilworth, J. R.; Howe, S. D.; Silver, J.; Thompson, R. M. *Polyhedron* **1993**, *12*, 2297.
48. Giordano, T. J.; Palenik, G. J.; Palenik, R. C.; Sullivan, D. A. *Inorg. Chem.* **1979**, *18*, 2445.
49. Bonardi, A.; Carini, C.; Merlo, C.; Pelizzi, C.; Pelizzi, G.; Tarasconi, P.; Vitali, F. *J. Chem. Soc., Dalton Trans.* **1990**, 2771.
50. Pelizzi, C.; Pelizzi, G.; Porretta, S.; Vitali, F. *Acta Cryst.* **1986**, *C42*, 1131.
51. Gaines, S. W.; Palenik, G. J.; Palenik, R. C. *Cryst. Struct. Comm.* **1981**, *10*, 673.
52. Pelizzi, C.; Pelizzi, G.; Vitali, F. *J. Chem. Soc., Dalton Trans.* **1987**, 177.
53. Bonardi, A.; Merlo, C.; Pelizzi, C.; Pelizzi, G.; Tarasconi, P.; Cavatorta, F. *J. Chem. Soc., Dalton Trans.* **1991**, 1063.
54. Pelizzi, C.; Pelizzi, G.; Predieri, G.; Vitali, F. *J. Chem. Soc., Dalton Trans.* **1985**, 2387.
55. Nardelli, M.; Pelizzi, C.; Pelizzi, G. *Transition Met. Chem.* **1977**, *2*, 35.
56. Pelizzi, C.; Pelizzi, G.; Predieri, G.; Resola, S. *J. Chem. Soc., Dalton Trans.* **1982**, 1349.
57. Pelizzi, C.; Pelizzi, G.; Vitali, F. *Transition Met. Chem.* **1986**, *11*, 401.
58. Lorenzini, C.; Pelizzi, C.; Pelizzi, G.; Predieri, G. *J. Chem. Soc., Dalton Trans.* **1983**, 2155.
59. Ianelli, S.; Minardi, G.; Pelizzi, C.; Pelizzi, G.; Reverberi, L.; Solinas, C.; Tarasconi, P. *J. Chem. Soc., Dalton Trans.* **1991**, 2113.
60. Rodriguez-Arguelles, M. C.; Ferrari, M. B.; Fava, G. G.; Pelizzi, C.; Tarasconi, P.; Albertini, R.; Dall'Aglio, P. P.; Lunghi, P.; Pinelli, S. *J. Inorg. Biochem.* **1995**, *58*, 157.
61. Belletti, D.; Carcelli, M.; Pelizzi, C.; Pelizzi, G. *J. Crystall. Spectr. Research* **1992**, *22*, 185.
62. Dessy, G.; Fares, V. *Cryst. Struct. Comm.* **1981**, *10*, 1025.
63. Leovac, V. M.; Ivegeš, E. Z.; Češljević, V. I.; Divjaković, V.; Klement, U. *J. Serb. Chem. Soc.* **1997**, *62*, 837.
64. Wester, D.; Palenik, G.J. *J. Chem. Soc., Chem. Commun.* **1975**, 74.
65. Wester, D.; Palenik, G. J. *Inorg. Chem.* **1976**, *15*, 755.
66. Brooker, S.; McKee, V. *J. Chem. Soc., Dalton Trans.* **1990**, 2397.
67. Newkome, G. R.; Gupta, V. K.; Fronczek, F. R.; Pappalardo, S. *Inorg. Chem.* **1984**, *23*, 2400.
68. Deroche, A.; Morgenstern-Bardarau, I.; Cesario, M.; Guilhem, J.; Keita, B.; Nadjo, L.; Honee-Levin, C. *J. Am. Chem. Soc.* **1996**, *118*, 4567.
69. Morgenstern-Bardarau, I.; Lambert, F.; Renault, J. P.; Cesario, M.; Marechal, J. D.; Maseras, F. *Inorg. Chim. Acta* **2000**, *297*, 338.
70. Che, C.M.; Chan, C.W.; Yang, S.M.; Guo, C.X.; Lee, C.Y.; Peng, S.M. *J. Chem. Soc., Dalton Trans.* **1995**, 2961.

71. Gheysen, K. A.; Potts, K. T.; Hurrell, H. C.; Abruna, H. D. *Inorg. Chem.* **1990**, *29*, 1589.
72. Strel'tsova, N. R.; Ivakina, L. V.; Storozhenko, P. A.; Bel'skii, V. K.; Bulychev, B. K.; Gorbunov, A. I. *Zhurnal Obshchei Himii* **1989**, *59*, 40.
73. Kireeva, O. K.; Bulychev, B. M.; Streltsova, N. R.; Belsky, V. K.; Dunin, A. G. *Polyhedron* **1992**, *11*, 1801.
74. Massa, W.; Frust, T.; Dehnicke, K. *Z. Naturfosch.* **1990**, *456*, 563.
75. Streltsova, N. R.; Belsky, V. K.; Bulychev, B. M.; Kireeva, O. K. *Inorg. Chim. Acta* **1991**, *189*, 111.
76. Holt, E. M.; Alcock, N. W.; Hendrixson, R. R.; Malpass, G. D. Jr.; Ghirardelli, R. G.; Palmer, R. A. *Acta Cryst.* **1981**, *B37*, 1080.
77. Nakasuka, N.; Azuma, S.; Katayama, C.; Honda, M.; Tanaka, J.; Tanaka, M. *Acta. Cryst.* **1985**, *C41*, 1176.
78. Gou, S.; You, X.; Yu, K.; Lu, J. *Inorg. Chem.* **1993**, *32*, 1883.
79. Mathieu, F.; Weiss, R. *Chem. J. Soc., Chem. Commun.* **1973**, 816.
80. Morozov, I. V.; Kemnitz, E.; Troyanov, S. I. *Z. Anorg. Allg. Chem.* **1999**, *625*, 1664.
81. Cameron, A.F.; Taylor, D.W.; Nuttall, R.H. *J. Chem. Soc., Dalton Trans.* **1972**, 1603.
82. Albright, J. O.; Clardy, J. C.; Verkade, J. G. *Inorg. Chem.* **1977**, *16*, 1575.
83. White, A.H.; Willis, A.C. *J. Chem. Soc., Dalton Trans.* **1977**, 1377.
84. Goodgame, D. M. L .; Hitchman, M. A.; Marsham, D. F.; Souter, C. E. *J. Chem. Soc., A* **1969**, 2464.
85. Nesterova, Y. A. M.; Porai-Koshits, M. A. *Koord. Khim.* **1982**, *8*, 994.
86. Gerloch, M.; Morgenstern-Bardarau, I.; Audiere, J. P. *Inorg. Chem.* **1979**, *18*, 3220.
87. Bonardi, A.; Ianelli, S.; Pelizzi, C.; Pelizzi, G.; Solinas, C. *Inorg. Chim. Acta* **1991**, *187*, 167.
88. Mangia, A.; Pelizzi, C.; Pelizzi, G. *Acta Cryst.* **1974**, *B30*, 2146.
89. Carcelli, M.; Mazza, P.; Pelizzi, C.; Pelizzi, G.; Zani, F. *J. Inorg. Biochem.* **1995**, *57*, 43.
90. Cairus, C.; McFall, S.G.; Nelson, S.M.; Drew, M.G.B. *J. Chem. Soc., Dalton Trans.* **1979**, 446.
91. Drew, M.G.B.; Nelson, J.; Nelson, S.M. *J. Chem. Soc., Dalton Trans.* **1981**, 1691.
92. Brooker, S.; McKee, V. *J. Chem. Soc., Dalton Trans.* **1990**, 3183.
93. Basolo, F.; Pearson, R. G. "*Mechanisms of Inorganic Reactions*"; Wiley: New York, 1968.
94. Andjelković, K.; Šumar, M.; Ivanović-Burmazović, I. *J. Therm. Anal.* **2001**, *66*, 759.
95. Lever, A. B. P.; London, G.; McCarthy, P. J. *Can. J. Chem.* **1977**, *55*, 3172.
96. Ivanović-Burmazović, I. Ph.D. dissertation, University of Belgrade, 1999.
97. Ivanović-Burmazović, I.; Hamza, M. S. A.; van Eldik, R. *Inorg. Chem.* **2002**, *41,* 5150 and references therein.
98. Sanchiz, J.; Domingues, S.; Maderos, A.; Brito, F.; Arrieta, J. M. *Inorg. Chem.* **1997**, *36*, 4108.
99. Zhang, D.; Busch, D. H.; Lennon, P. L.; Weiss, R. H.; Neumann, W. L.; Riley, D. P. *Inorg. Chem.* **1998**, *37*, 956.
100. Taft, K. L.; Masschelein, A.; Liu, S.; Lippard, S. J. *Inorg. Chim. Acta* **1992**, *198–200*, 627.
101. Matsushima, H.; Iwasawa, K; Ide, K.; Reza, Md. Y.; Koikawa, M.; Tokii, T. *Inorg. Chim. Acta* **1998**, *274*, 224.
102. Inoue, M. B.; Navarro, R. E.; Inoue, M.; Fernando, Q. *Inorg. Chem.* **1995**, *34*, 6074.
103. Favas, M.C.; Kepert, D.L.; White, A. H.; Willis, A.C. *J. Chem. Soc., Dalton Trans.* **1977**, 1350.

104. Riley, D. P.; Henke, S. L.; Lennon, P. J.; Weiss, R. H.; Neumann, W. L.; Rivers, W. J.; Aston, K. W. Jr.; Sample, K. R.; Rahman, H.; Ling, C. S.; Shiel, J. J.; Busch, D. H.; Szulbinski, W. *Inorg. Chem.* **1996**, *35*, 5213.
105. Johnson, J. F.; Scheidt, W. R. *J. Am. Chem. Soc.* **1977**, *99*, 294.
106. Johnson, J. F.; Scheidt, W. R. *Inorg. Chem.* **1978**, *17*, 1280.
107. Cheng, B.; Scheidt, W. R. *Acta Crist.* **1996**, *C52*, 832.
108. Roy, P. S.; Wieghardt, K. *Inorg. Chem.* **1987**, *26*, 1885.
109. Cotton, F. A.; Elder, R. C. *Inorg. Chem.* **1964**, *3*, 397.
110. Park, J. J.; Glick, M. D.; Hoard, J. L. *J. Am. Chem. Soc.* **1968**, *91*, 301.
111. Kikuchi, T.; Sugiura, Y.; Tanaka, H. *Inorg. Chim. Acta* **1982**, *66*, L5.
112. Drew, M. G. B.; Nelson, J.; Nelson, S. M. *J. Chem. Soc., Dalton Trans.* **1981**, 1691.
113. Stomberg, R.; Ainalem, B. *Acta. Chem. Scand.* **1968**, *22*, 1439.
114. Drew, M. G. B.; Fowles, G. W. A.; Lewis, D. F. *J. Chem. Soc., Chem. Comm.* **1969**, 876.
115. Levenson, R. A.; Towns, R. L. R. *Inorg. Chem.* **1974**, *13*, 105.
116. Stomberg, R. *Nature* **1964**, *201*, 486.
117. Hourse, D. A.; Hughes, R. G.; Garner, C. S. *Inorg. Chem.* **1967**, *6*, 1077.
118. Goedken, V. L.; Christoph, G. G. *Inorg. Chem.* **1973**, *12*, 2316.
119. Gerloch, M.; Morgenstern-Bardarau, I. *Inorg. Chem.* **1979**, *18*, 3225.

POTENTIAL APPLICATIONS FOR THE USE OF LANTHANIDE COMPLEXES AS LUMINESCENT BIOLABELS

GRAHAM R. MOTSON[a], JEAN S. FLEMING[b,*] and SALLY BROOKER[a,*]

[a]Department of Chemistry, University of Otago, PO Box 56, Dunedin, New Zealand
[b]Department of Anatomy and Structural Biology, Otago School of Medical Sciences, PO Box 913, Dunedin, New Zealand

I. Scope
II. Introduction
III. Properties of Lanthanide(III) Ions
  A. Photophysical Properties
  B. Coordination Chemistry
IV. Ligand Systems Explored
  A. Acyclic Systems
  B. Cyclic Systems
  C. Summary
V. Biochemical Applications
  A. Protein Detection
  B. Nucleic Acid Detection
  C. Suitable Linker Groups
VI. Concluding Remarks
VII. Glossary
References

I. Scope

Whilst there have been a number of excellent reviews on the design, synthesis, structural determination, and photophysics of luminescent lanthanide complexes (*1–6*), detailed information for coordination chemists on how these compounds may be used as analytes in the biochemical and biological sciences has been somewhat less readily

*Corresponding authors

ADVANCES IN INORGANIC CHEMISTRY
VOLUME 55 ISSN 0898-8838 DOI 10.1016/S0898-8838(03)55007-3

© 2004 Elsevier Inc.
All rights reserved.

accessible (*4–8*). The aim of this review is to provide an overview of the "complete story", from ligand design and synthesis through photophysical characterization to how such complexes could ultimately be used in a variety of analytical techniques.

II. Introduction

Lanthanide coordination chemistry has seen a considerable increase in interest in recent years due to potential applications in a variety of fields, including catalysis (*9*), biochemical analysis (*3–8,10–14*), and non-invasive diagnostics (*8,15,16*).

Of particular interest to this review is the use of luminescent lanthanide (especially europium and terbium) materials as non-radioactive markers (*3,5,8,10–12,16*). In addition to the safety advantages over radioactive labels, lanthanide complexes remain luminescent as long as the complex remains intact, allowing repeated detection of analytes over a much longer time period than radioactive labels.

Europium and terbium complexes have inevitably received the most attention, due to their visible emission and millisecond domain lifetimes. The long lifetimes mean that time resolved (TR) methods can be employed: background fluorescence from the surrounding medium is allowed to dissipate before measurement of the lanthanide phosphorescence. The last 10 years have seen an upsurge in studies of the near-infra-red (NIR) luminescence from complexes of neodymium and ytterbium (*6,17*). Whilst their lifetimes are much shorter than those of europium and terbium (of the order of microseconds), their emission is in the NIR region of the spectrum, and consequently the metal excited states can be populated by ligands that absorb at much lower energies than conventional lanthanide antennae. This may allow in vivo use, due to the relative transparency of tissue at these wavelengths, although detection of their emission generally requires more expensive equipment.

The addition of an appropriate receptor group to the lanthanide complex would enable its use as a probe for various chemical and biochemical species by allowing selective linking of the lanthanide complex to biomolecules such as DNA, RNA, and proteins, including antibodies. This is discussed further in Section V.

Lanthanide complexes may also be employed as contrast agents in Magnetic Resonance Imaging (MRI), a non-invasive diagnostic tool

(*16,18*). This is based on spatial nuclear magnetic resonance of water protons within the body. For a contrast agent to be effective, direct coordination of water molecules to the lanthanide is necessary to impart efficient relaxation of the water protons. Therefore, whilst this has been covered comprehensively in a number of recent reviews (*19*), it is important to realize that since a molecule that is ineffective as a luminescent material may have uses in MRI, the two themes of research often run in parallel.

III. Properties of Lanthanide(III) Ions

A. Photophysical Properties

There are a number of discussions of the photophysical properties of the lanthanide elements and previous reviews of this area have covered this subject (*3,5*). The features essential to the subject of this review are given below.

Many of the trivalent lanthanide ions exhibit long-lived excited states. These excited states cannot be populated directly, since the lanthanide(III) ions themselves have very low absorption coefficients, due to the fact that the f–f transitions are formally forbidden by the LaPorte rule. In addition, a number of transitions are also forbidden by the spin crossover rule. Typically, these extinction coefficients are of the order of 1 M^{-1} cm^{-1} (*20*).

The f electrons are well shielded from ligand field effects by the outer s and p electrons, and are therefore virtually unaffected by coordination environment. This gives rise to line-like spectra, which are characteristic of the individual elements. Some of these transitions are given in Table I and some of the pertinent energy levels shown schematically in Fig. 1.

The low absorption cross-sections of the trivalent ions means that an indirect method of populating the metal excited states is required to generate a significant emission. Such a mechanism is the Antenna Effect.

1. The Antenna Effect

The mechanism for sensitized luminescence using the antenna effect is shown schematically in Fig. 2.

Absorption by the chromophore ligand is commonly (*6*) followed by inter-system crossing (ISC) to the triplet state of the ligand. This state can decay either by emission (ligand phosphorescence) or by

TABLE I

SELECTED LANTHANIDE EMISSION INFORMATION (*20,199*)

Lanthanide (III)	Emissive (initial) state configuration	Final state configuration	Transition wavelength/nm
Nd	$^4F_{3/2}$	$^4I_{9/2}$	880
		$^4I_{11/2}$	1060
		$^4I_{13/2}$	1370
		$^4I_{15/2}$	1900
Eu	$^5D_0$	$^7F_0$	580
		$^7F_1$	595
		$^7F_2$	615
		$^7F_3$	645
		$^7F_4$	690
		$^7F_5$	750
		$^7F_6$	825
Tb	$^5D_4$	$^7F_6$	450
		$^7F_5$	550
		$^7F_4$	590
		$^7F_3$	620
		$^7F_2$	650
Yb	$^2F_{5/2}$	$^2F_{7/2}$	980

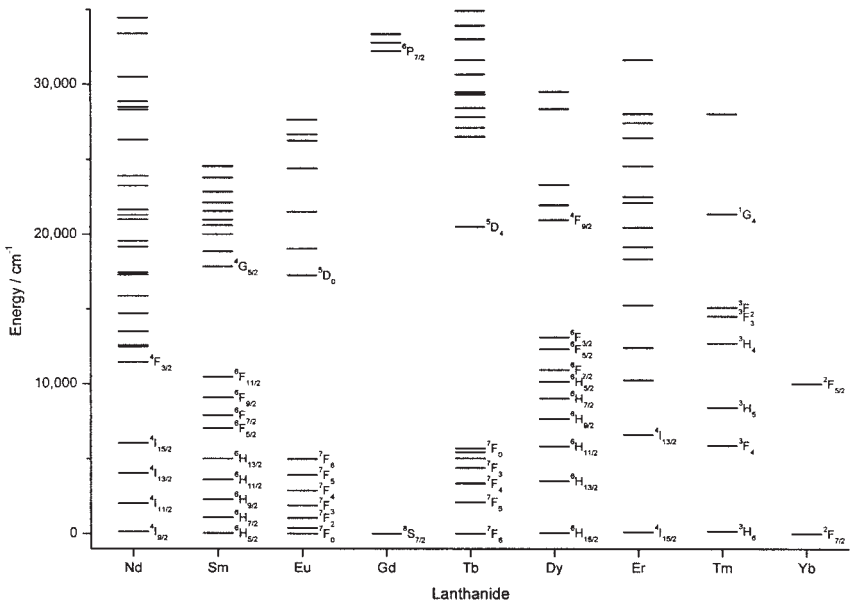

FIG. 1. Energy levels of selected lanthanide(III) ions (*199*).

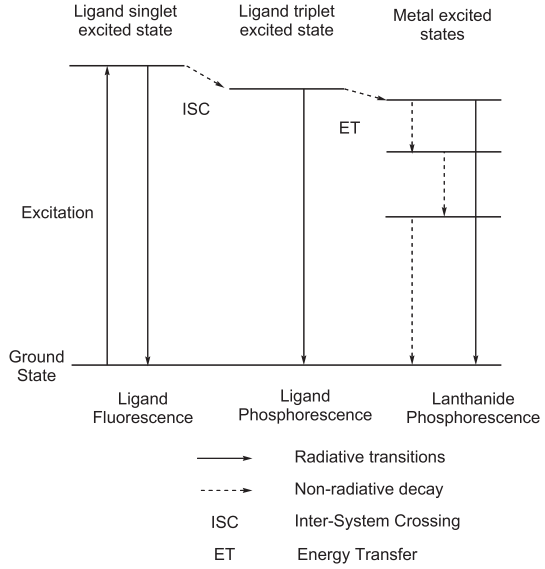

FIG. 2. Antenna mechanism for sensitized lanthanide phosphorescence.

non-radiative energy transfer (ET) to the excited state of the metal center. The metal excited state can then decay either by radiative (lanthanide phosphorescence) or non-radiative mechanisms.

To work efficiently (thereby producing large quantum yields), the relative energies of these various states are of great importance, and particularly the energy difference between the ligand triplet state and the metal excited state. Obviously, the ligand triplet state must be higher in energy; however, it is also important that there is a significant difference in energy, to prevent back transfer from the metal excited state to the ligand triplet state. Investigations into the dependence of the ligand triplet energy suggest a minimum gap of 1850 cm^{-1} for terbium complexes (*21*).

Among the non-radiative decay mechanisms is coupling to vibrational overtones of O–H, N–H, and C–H bonds. This is a particularly effective route if O–H containing solvent molecules are coordinated directly to the metal center. As such, this effect can impart information on solution-state structures of complexes. This is discussed further in Section III.A.2.

2. Determination of Coordinated Solvent Molecules

The quenching of the metal excited state by coupling to the O–H vibrational overtones has already been mentioned. Horrocks and Sudnick (*22*) showed that this effect (shown in Fig. 3) can be utilized in the elucidation of the structure of the complex in solution.

The vibronic decay pathway to the O–D oscillator is much less efficient. Thus, by comparison of the luminescence lifetimes in H_2O and D_2O an approximation for the number of coordinated solvent water molecules, q, in aqueous solution can be calculated by Eq. (1).

$$q = A_{\mathrm{Ln}}\left(\frac{1}{\tau_{\mathrm{H_2O}}} - \frac{1}{\tau_{\mathrm{D_2O}}}\right) \tag{1}$$

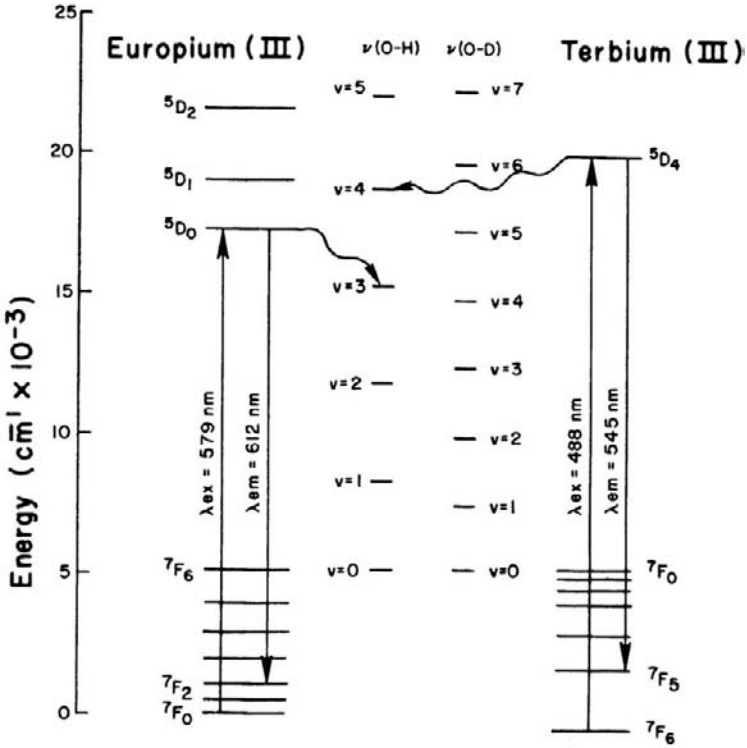

FIG. 3. Deactivation of europium and terbium excited states by energy transfer to O–H and O–D oscillator overtone vibrations. Reprinted with permission from *Acc. Chem. Res.* **1981**, *14*, 384–392. Copyright 1981 American Chemical Society.

A_{Ln} is a constant for the specific lanthanide, and takes the values of 1.05 and 4.2 for Eu^{3+} and Tb^{3+}, respectively. By assuming that the one O–H group in methanol has half the deactivating effect as the two in water (*23*), Eq. (1) can also hold true in methanol, using values of A_{Ln} of 2.1 and 8.4 for europium and terbium, respectively (*6*).

These q values are given an estimated uncertainty of ± 0.5. This can be improved by the use of the modified Horrocks equation determined by Parker and co-workers (*24*), which takes into account closely diffusing second sphere solvent molecules and proximate N–H bonds in the ligand; see Eqs. (2) and (3).

$$q_{Eu} = 1.2\left[\left(\frac{1}{\tau_{H_2O}} - \frac{1}{\tau_{D_2O}}\right) - (0.25 + 0.075x)\right] \tag{2}$$

where x is the number of oxygen bound amide N–H groups.

$$q_{Tb} = 5\left[\left(\frac{1}{\tau_{H_2O}} - \frac{1}{\tau_{D_2O}}\right) - 0.06\right] \tag{3}$$

Again, solvation numbers in methanol can be calculated by altering the constants to account for halving the number of O–H oscillators per solvent molecule, giving Eqs. (4) and (5):

$$q_{Eu} = 2.4\left[\left(\frac{1}{\tau_{H_2O}} - \frac{1}{\tau_{D_2O}}\right) - (0.125 + 0.0375x)\right] \tag{4}$$

$$q_{Tb} = 5\left[\left(\frac{1}{\tau_{H_2O}} - \frac{1}{\tau_{D_2O}}\right) - 0.03\right] \tag{5}$$

These corrections, whilst applicable to a variety of systems, were determined for use with cyclen derivatives. A more wide ranging correction for q values of europium complexes has been postulated by Supkowski and Horrocks (*25*), using data for 25 complexes taken from the literature. Their new equation is:

$$q_{Eu} = 1.11\left[\frac{1}{\tau_{H_2O}} - \frac{1}{\tau_{D_2O}} - 0.31 + 0.45n_{OH} + 0.99n_{NH} + 0.075n_{O=CNH}\right] \tag{6}$$

where n_{OH} is the number of alcoholic O–H oscillators in the first coordination sphere, n_{NH} is the number of amine N–H oscillators

in the first coordination sphere, and $n_{O=CNH}$ is the number of amide N–H oscillators in which the amide carboxylic oxygen is in the first coordination sphere.

Whilst such an approach can also be adopted with reasonable success for ytterbium, the effect of C–H oscillators becomes too significant for neodymium and erbium.

3. Quantum Yield

An important measure of the luminescence is the quantum yield. In effect, this is the probability that a photon will be emitted by the lanthanide given that one photon has been absorbed by the antenna ligand. Since measurement of absolute quantum yields is particularly difficult, the overall quantum yield (Φ) is normally measured with reference to certain standards (*26*); these are routinely $[Ru(bpy)_3]^{2+}$ in water or SulfoRhodamine 101 in methanol for Eu^{3+}, and quinoline sulfate in 0.1 M HCl or fluorescein in 1 N NaOH for Tb^{3+} (*27,28*). A method has been developed that measures energy transfer from the lanthanide complex to an acceptor of known quantum yield (*28*).

The highest quantum yields are obtained by exciting the lowest singlet state of the ligand, since more energy is lost during the transfer to the metal through more numerous non-radiative deactivation processes if a ligand state with higher energy is excited (*29*).

Since the antenna mechanism is an indirect route, there are probabilities associated with each of the processes, i.e.,

$$\Phi_{overall} = \varphi_{ISC} \cdot \varphi_{ET} \cdot \varphi_{Ln} \tag{7}$$

where φ_{ISC}, φ_{ET}, and φ_{Ln} are the quantum yields of the inter-system crossing, energy transfer, and lanthanide emission processes, respectively (*30*). In many cases, the efficiency of the sensitizing ligand gives values of φ_{ISC} and φ_{ET} near to unity.

Due to the competing non-radiative decay routes for the lanthanide excited state, there is an intrinsic limit to the overall quantum yield in luminescent lanthanide complexes. It has been estimated that these values are 0.50 and 0.75 for europium and terbium, respectively (*27*). Although quantum yields exceeding these have been reported (*31,32*), care should be taken in analyzing quantum yield results in the literature, as these are often given for the energy transfer process alone, and not the overall quantum yield, and in other cases it is unclear as to which process(es) the quoted quantum yield refers to.

B. Coordination Chemistry

As hard metal centers, lanthanide(III) ions have a general preference for hard donor atoms (*33,34*). Much of their early coordination chemistry involved anionic oxygen donors and it is well established that carboxylates and β-diketonates are very good at coordinating lanthanide ions.

Because the 4f orbitals are deeply buried, they play little part in metal-ligand bonding, which is predominantly ionic in character. Subsequently, coordination numbers and geometries are mostly controlled by spatial requirements of ligands. Coordination numbers of 8 or 9 are most common, but have been reported up to 12 (*34,35*).

IV. Ligand Systems Explored

As has already been discussed, there are three key requirements of ligands for use in the sensitized luminescence of lanthanides: (i) strong absorption in an accessible part of the spectrum; (ii) efficient transfer of energy to the metal excited state; and (iii) good encapsulation of the metal to prevent deactivation of the excited state by coordinated or closely diffusing solvent molecules. In addition, to be an effective biochemical marker it should be easily functionalized with an appropriate receptor group or linker (so that it can ultimately be attached to the target biomolecule). The complex should be highly stable (*5*) under physiological conditions (aqueous solution, neutral pH); obviously, it should be highly soluble in water.

Various approaches have been taken to the synthesis of effective luminescent materials, using a variety of large encapsulating antenna-containing ligands, including podands, calixarenes, macrocycles, and macrobicycles (cryptands). These have been divided into acyclic (sub-section A) and cyclic (sub-section B). Representative ligands and complexes will be presented and discussed.

A. Acyclic Systems

1. Podands

Various podand-type ligands have been developed with carbon, nitrogen, and boron bridgehead atoms. The selection of ligands discussed in this section is shown in Scheme 1.

A number of ligands containing benzimidazole chromophores have been developed, and coordinated with lanthanide(III) ions. Reaction

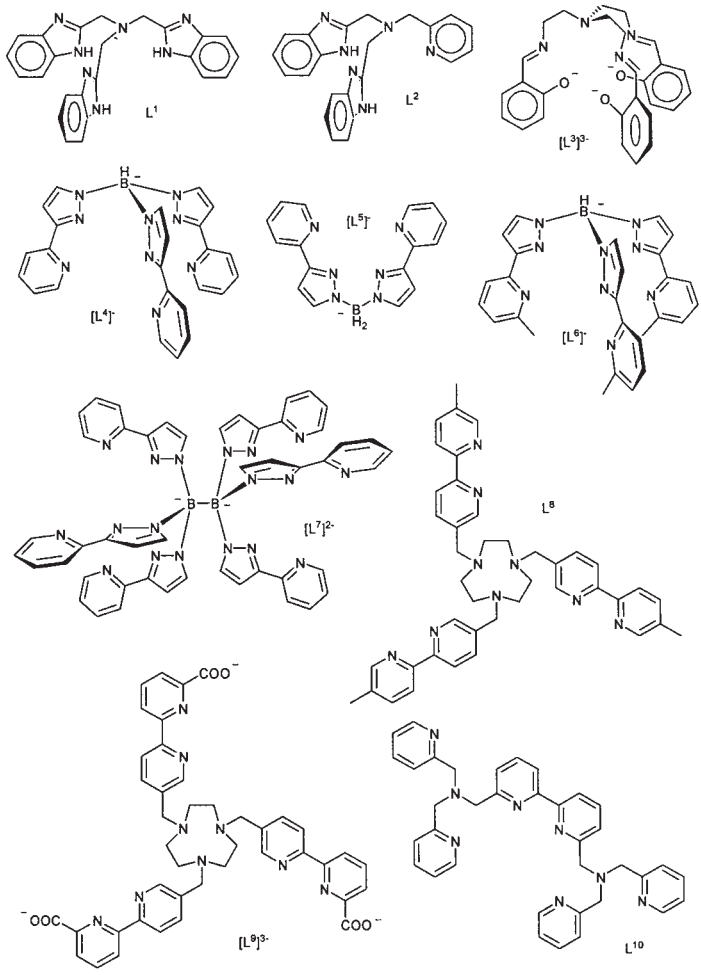

SCHEME 1. Selected podand ligands.

of ligand L^1 with the appropriate lanthanide(III) nitrate in methanol results in 10-coordinate complexes of the type $[Ln(L^1)(NO_3)_3]$ (*36*); the samarium, europium, terbium, and dysprosium complexes have been shown to exhibit sensitized luminescence.

The unsymmetrical derivative, L^2, in which one benzimidazole group is replaced by a 2-pyridyl moiety, and its complexes with europium and terbium have been further studied for their photophysical properties (*37*). The coordinated nitrate anions in the $[Ln(L^2)(NO_3)_3]$

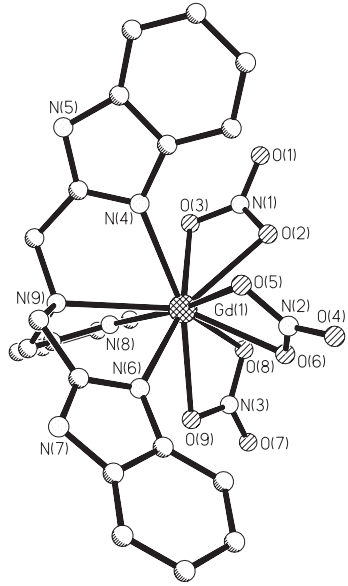

FIG. 4. Molecular structure of $[Gd(L^2)(NO_3)_3]$. This figure was generated from data obtained from the Cambridge Crystallographic Data Centre as published originally in Ref. (*37*).

complexes (see Fig. 4) dissociate in coordinating solvents such as methanol, leading to coordination of approximately three solvent molecules, significantly diminishing the luminescent lifetimes ($\tau_{Eu} = 0.36$ ms, $\Phi_{Eu} = 0.031$; $\tau_{Tb} = 0.95$ ms, $\Phi_{Tb} = 0.38$). The quantum yields (measured in acetonitrile solution) of the $[Ln(L^2)Cl_3(H_2O)]$ complexes are much lower, an effect of the coordinated water molecule ($\tau_{Eu} = 0.31$ ms, $\Phi_{Eu} = 0.001$; $\tau_{Tb} = 0.80$ ms, $\Phi_{Tb} = 0.18$).

Related complexes where two ligands encapsulate the lanthanide center have been reported (*38,39*). Coordination of a second antenna ligand may increase the luminescence by excluding deactivating solvent molecules; to date, however, photophysical studies for these complexes have not been published. A recent paper details ternary complexes with an additional chromophore, antipyrene (antipy) (*40*). The complexes $[Eu(L^2)(antipy)_3]^{3+}$ and $[Tb(L^2)(antipy)_3]^{3+}$ both exclude coordinating solvent molecules and provide an additional excitation route, leading to high quantum yields ($\Phi_{Eu} = 0.097$, $\Phi_{Tb} = 0.420$) and millisecond lifetimes.

A number of other acyclic ligand systems have been developed that use tris(aminoethyl)amine (tren) as a central unit (for macrobicycles

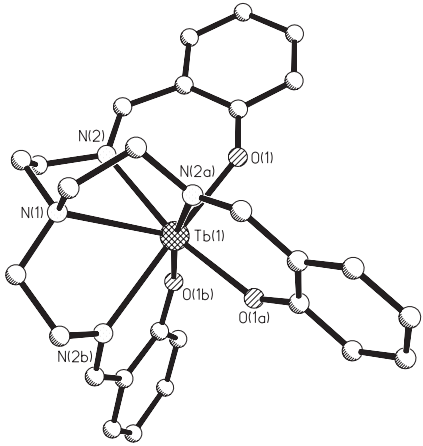

FIG. 5. Molecular structure of [Tb(L^3)]. This figure was generated from data obtained from the Cambridge Crystallographic Data Centre as published originally in Ref. (*41*).

based on tren see Section IV.B.4). Condensation reactions with *ortho*-formylphenols can give potentially heptadentate podand ligands with a variety of chromophoric groups. The unusually 7-coordinate [Ln(L^3)] complexes (see Fig. 5) can be synthesized via template reactions under various conditions (*41,42*). A number of derivative ligands have also been complexed with lanthanide(III) ions (*43–45*). Of these, the structurally characterized complexes also feature 7-coordinate lanthanide ions (*45*).

A variety of tris(pyrazolyl)borate ligands have been developed. Whilst this class of complexes has been thoroughly examined in a recent review (*46*), significant results with regard to the luminescence of these species are discussed here. McCleverty, Ward and co-workers have produced a range of "second generation" tris(pyrazolyl)-borates, substituting the pyrazolyl ring in the 3-position with a coordinating 2-pyridyl group. This ligand and derivatives thereof, have yielded a number of different complexes, with varying photophysical properties.

The parent ligand tris(pyrazolyl)borate, $[L^4]^-$, forms 1:1 and 1:2 metal:ligand complexes [Ln(L^4)(NO_3)$_2$] and $[Ln(L^4)_2]^+$; the molecular structure of the latter is shown in Fig. 6. In solution, dissociation of the nitrate anions in the former complex leave the lanthanide ion open to coordination by solvent molecules (*47*). Photophysical studies in water and methanol (*48*) confirm this; use of the Horrocks equation

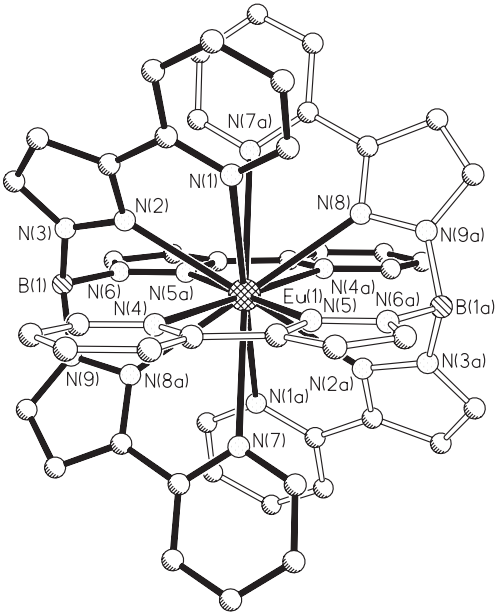

FIG. 6. Molecular structure of $[Eu(L^4)_2]^+$. This figure was generated from data obtained from the Cambridge Crystallographic Data Centre as published originally in Ref. (*47*).

suggests the coordination of 2–3 solvent molecules. Luminescence lifetimes and quantum yields for $[Ln(L^4)(NO_3)_2]$ (in aqueous solution, $\tau_{Eu} = 0.4$ ms, $\Phi_{Eu} = 0.001$; $\tau_{Tb} = 0.9$ ms, $\Phi_{Tb} = 0.13$) are greatly enhanced by use of deuterated solvents (e.g., D_2O: $\tau_{Eu} = 2.1$ ms, $\Phi_{Eu} = 0.013$; $\tau_{Tb} = 2.4$ ms, $\Phi_{Tb} = 0.46$) or dichloromethane ($\tau_{Eu} = 1.7$ ms, $\Phi_{Eu} = 0.050$; $\tau_{Tb} = 2.0$ ms, $\Phi_{Tb} = 0.41$).

The $[Ln(L^4)_2]^+$ complexes offer greater protection to the metal center, being encapsulated by both ligands in a 12-coordinate manner. Unfortunately, solubility has prevented the photophysical study of these complexes in solvents other than dichloromethane, in which high quantum yields ($\Phi_{Tb} = 0.42$ for $[Tb(L^4)_2][BPh_4]$, and $\tau_{Tb} = 1.7$ ms) and remarkably long lifetimes ($\tau_{Eu} = 3.5$ ms for $[Eu(L^4)_2][BPh_4]$, and $\Phi_{Eu} = 0.074$) are observed (*48*).

The related bis(pyrazolyl)borate ligand $[L^5]^-$ forms 10-coordinate complexes of the type $[Ln(L^5)_2(NO_3)]$. The terbium complex in particular has promising luminescence characteristics, with a lifetime of 2.6 ms and quantum yield of 0.36 in methanol (*49*). However, the complexes are not stable in water.

Methyl groups in the C^6 positions of the pyridyl rings provide a degree of steric hindrance at the metal center in the derivative tris(pyrazolyl)borate ligand $[L^6]^-$ (*50*). This prevents the ligand acting in a fully hexadentate manner, and results in coordination of a water molecule in the solid state structure of the $[Ln(L^6)(NO_3)_2(H_2O)]$ complexes. Solubility problems meant that luminescence data were collected for dichloromethane solutions only. The metal-centered emission is markedly less intense than in the parent $[L^4]^-$ complexes; this is ascribed to a combination of the quenching effect of the coordinated water molecule and poorer energy transfer due to partial coordination of the ligand.

An attempt to synthesize binuclear complexes led to the development of the "back-to-back" ligand $[L^7]^{2-}$. The lanthanide coordination environment of the resultant $[\{Ln(NO_3)_2\}_2(L^7)]$ complexes is the same as that in the parent mononuclear $[L^4]^-$ complexes, as shown in Fig. 7. Despite the possibility of displacement of the nitrate anions by solvent molecules, a reasonable lifetime (0.9 ms) and quantum yield (0.13) is recorded for aqueous solutions of the terbium complex (*49*).

The ligand L^8 is described by the authors as a podand, although the apical group is a polyazamacrocycle (*51*). The photophysical

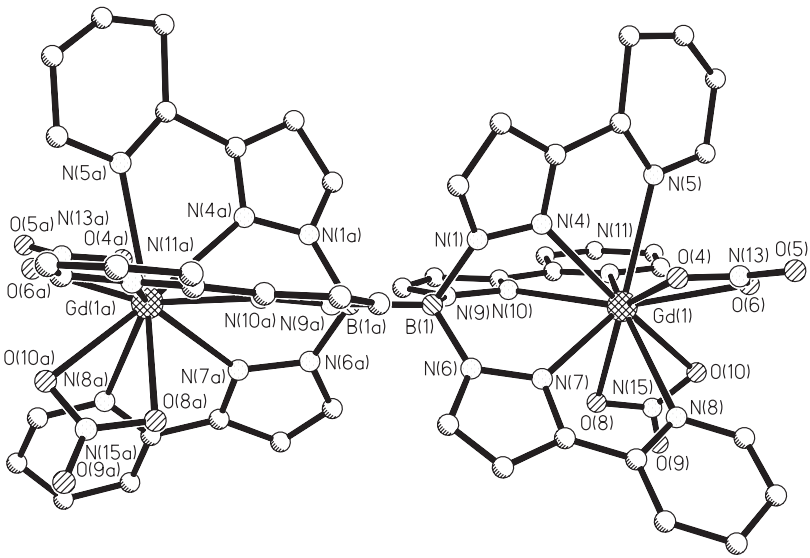

FIG. 7. Molecular structure of $[\{Gd(NO_3)_2\}_2(L^7)]$. This figure was generated from data obtained from the Cambridge Crystallographic Data Centre as published originally in Ref. (*49*).

properties of the europium complex $[Eu(L^8)]^{3+}$ are better than the terbium analogue of related ligands with a tetraazamacrocyclic apical group, with a lifetime of 1.71 ms and quantum yield of 0.35. However, it is not clear whether these measurements were taken in aqueous or acetonitrile solution.

A derivative ligand, $[L^9]^{3-}$, has been developed with carboxylate groups in the 6′-position of the bipyridyl chromophores (*52*). These coordinate to lanthanide(III) ions through the N,N,COO^- units, leaving the triazamacrocycle uncoordinated, to give 9-coordinate complexes (see Fig. 8). These successfully exclude water molecules in aqueous solution, giving luminescence which is strong and long-lived in the case of europium ($\tau_{Eu} = 1.85$ ms, $\Phi_{Eu} = 0.12$; $\tau_{Tb} = 0.50$ ms, $\Phi_{Tb} = 0.10$). The combination of photophysical properties, stability, and solubility of these complexes suggest that they may be suitable for use in biochemical assays. As further evidence of this, luminescence microscopy of acrylic beads containing either the europium complex or fluorescein show a 1000-fold increase in the Eu^{3+}:fluorescein intensity ratio under time-resolved conditions compared to steady-state conditions, as shown in Fig. 9.

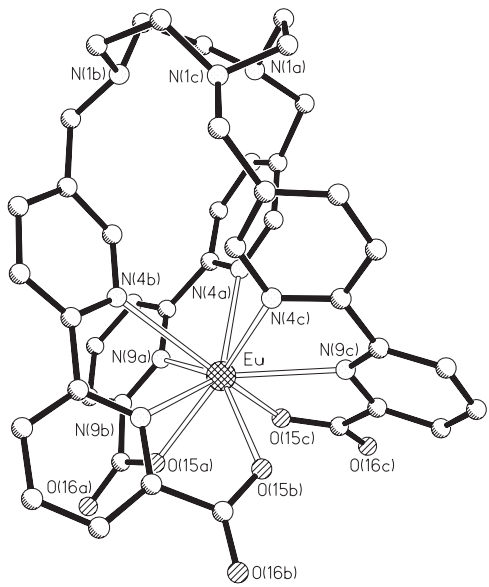

FIG. 8. Molecular structure of $[Ln(HL^9)]^+$. This figure was generated from data obtained from the authors of Ref. (*52*).

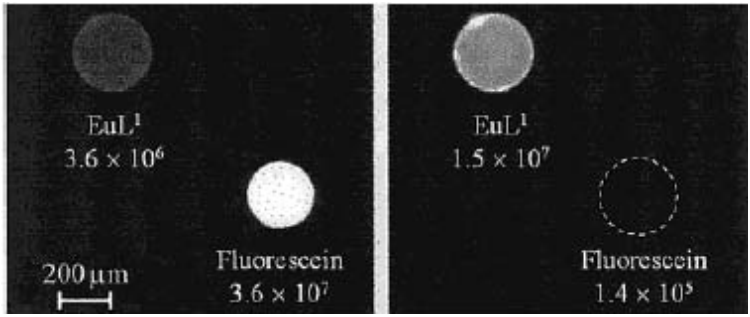

FIG. 9. Microscope luminescence imaging of a model system consisting of oxirane acrylic beads (diameter < 250 μm) containing $[Eu(HL)]^+$ or fluorescein. The left panel shows the prompt fluorescence image and the right panel the TR luminescence image. The figures represent the average luminescence intensities measured for each bead. Reprinted with permission from *J. Am. Chem. Soc.* **2001**, *123*, 2436–2437. Copyright 2001 American Chemical Society.

L^{10} uses the bipyridyl chromophore as the apical group of the podand, appending a dipyridylamine group to each side of the central bipyridyl (*53*). The ligand forms 1:1 complexes with lanthanide(III) ions, shown by X-ray crystallography of the gadolinium complex to be of the form $[Ln(L^{10})Cl_2]Cl$, with one of the pendant pyridyl groups remaining uncoordinated. From photophysical studies of the europium complex in water and methanol (and in the deuterated forms of these), it appears that this pyridyl group coordinates in solution, replacing one of the chloride ions; Horrocks analysis suggests a solvation number of 0.5. The aqueous lifetime and quantum yield (0.78 ms and 0.046, respectively) are somewhat better than the tris(bipyridyl) cryptand (see Section IV.B.4). The small quantum yield is ascribed to an inefficient transfer of energy from the pyridine groups to the metal. Instability to dissociation in water is also reported.

2. Non-podand Ligands

A number of non-podand (i.e., those without an apical atom or group) acyclic ligand systems have been developed for lanthanide luminescence applications. Many of these are designed as helicating ligands such that the lanthanide ion is well encapsulated despite the linearity of the ligand.

This approach is demonstrated by the ligands L^{11}–L^{15}, developed by Bünzli, Piguet and co-workers, shown in Scheme 2. These are

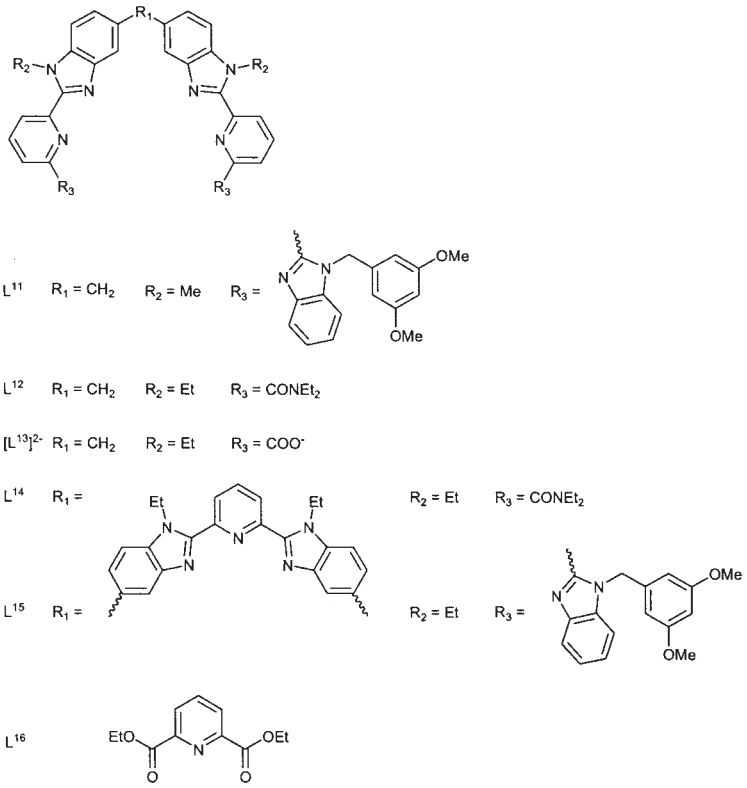

SCHEME 2. Selected Bünzli/Piguet ligands.

designed to give dimetallic (L^{11}–L^{13}) and trimetallic (L^{13}–L^{14}) triple helicate complexes; a number of such complexes have been synthesized and structurally characterized (*54–58*).

Photophysical studies of $[Eu_2(L^{12})_2]^{6+}$ in acetonitrile/water mixtures suggest that this complex is not stable in water. Addition of up to 2.5 M water to a 10^{-3} M acetonitrile solution of the complex gave no significant changes to the quantum yield; further addition of water induced a drastic decrease in the quantum yield. Similar results are observed for complexes of L^{16} (*59*).

A greater stability is observed for $[Ln_2(L^{13})_3]$ (see Fig. 10) (*56*); these complexes are stable in water in the pH range 4–13, with a stability similar to $[Ln(DOTA)]^-$ (DOTA = 1,4,7,10-tetraazacyclododecane-1,4,7,10-tetraacetic acid). The europium complex exhibits a quantum yield of only 0.0137, but has an extremely long lifetime (2.53 ms) in

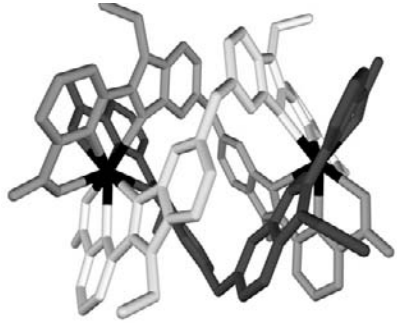

FIG. 10. Molecular structure of $[Tb_2(L^{13})_3]$, with each ligand shaded differently. This figure was generated from data obtained from the Cambridge Crystallographic Data Centre as published originally in Ref. (*56*).

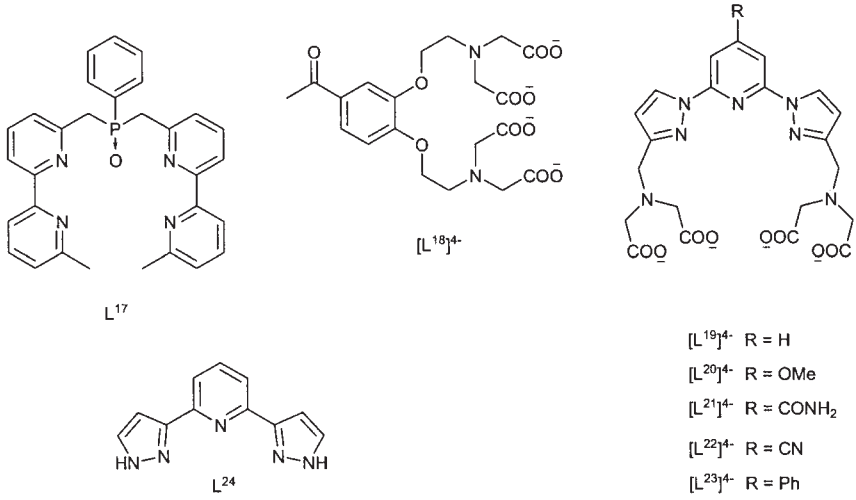

SCHEME 3. Selected acyclic ligands.

aqueous solution. This is a result of the exclusion of water from the primary coordination sphere.

The bipyridyl chromophore has been extensively used in lanthanide coordination chemistry. In addition to those based on the Lehn cryptand (see Section IV.B.4), a number of acyclic ligands have also employed this group. One such ligand is L^{17}, which binds to lanthanide ions such that one face of the ligand is left open (Scheme 3) (*60*). As expected, luminescence is extremely weak in water and methanol, but stronger in acetonitrile ($\Phi = 0.30$, 0.14 for europium and terbium, respectively). In addition, the nature of the counter ion can

have a dramatic effect on the emission intensity. Such a result may enable complexes of this type to be used for the sensing of anions.

Due to the presence of hard anionic oxygen atoms, phenolate and carboxylate groups are often employed as donors in lanthanide coordination chemistry. Ligand $[L^{18}]^{4-}$ is reported as "an excellent triplet sensitizer for lanthanide luminescence" (*61*). Indeed aqueous lifetimes of 0.57 and 1.61 ms are reported for europium and terbium, respectively; quantum yields of 0.20 and 0.95 respectively refer to the efficiency of the energy transfer process alone.

Recently, a series of derivative ligands, $[L^{19}]^{4-}$–$[L^{23}]^{4-}$, has been reported (*32,62*), where the acetophenone chromophore in $[L^{18}]^{4-}$ is replaced by a dipyrazolylpyridine chromophore. These form lanthanide complexes that are stable in aqueous solution, and which possess very promising photophysical attributes. The europium and terbium complexes of all these ligands have long lifetimes (1.3–1.4 ms for europium and 2.3–2.8 ms for terbium) in water that are largely unchanged by solvent deuteration, indicating the effective exclusion of solvent from the primary coordination sphere.

The potential of this class of ligand is illustrated by the use of H_4L^{23} in the time resolved fluoroimmunoassay of two serum proteins, α-fetoprotein (AFP) and carcinoembryonic antigen (CEA) (*62*). The succinimidyl monoester of H_4L^{23} (prepared by treating H_4L^{23} with 1,3-dicyclohexylcarbodiimide and N-hydroxysuccinimide) was used to label ca. 26 amine moieties in streptavidin (the same bond formation reaction, albeit between very different compounds, is shown in Fig. 31) and Tb^{3+} inserted. The resulting terbium-labeled streptavidin, which binds strongly and specifically to biotin (a useful fact that is often exploited in this way), was strongly luminescent and stable in buffers from pH 6.0 to 8.5. The detection limits of the resulting sandwich-type time resolved fluoroimmunoassays were low enough to measure the AFP and CEA proteins sensitively and accurately in human sera. The binding reaction was similar to that shown in Fig. 21C, except that the streptavidin terbium complex replaced the tertiary antibody, the secondary antibody (to AFP or CEA) was biotinylated and the antigen was AFP or CEA. Sequential, but simultaneous measurement of these two serum proteins was also possible by employing a europium-labeled anti-AFP secondary antibody (see Fig. 21B) in combination with a biotinylated anti-CEA secondary antibody (the biotin moiety again being used to bind the streptavidin moiety) and the terbium-labeled streptavidin (see Fig. 21C). To provide a clear distinction, the Eu^{3+} complex phosphorescence was measured at 615 nm before the addition of the Tb^{3+} complex and its phosphorescence measurement at 545 nm.

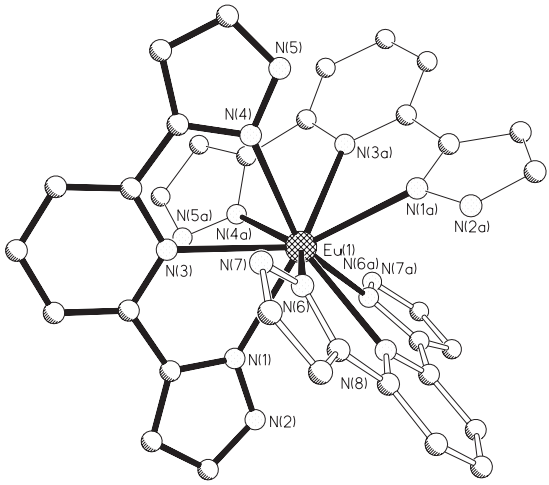

FIG. 11. Molecular structure of $[Eu(L^{23})_3]^{3+}$, clearly showing the three ligands. This figure was generated from data obtained from the Cambridge Crystallographic Data Centre as published originally in Ref. (*63*).

The importance of the carboxylate donors is underlined by a study of the lanthanide coordination chemistry of the similar terdentate ligand 2,6-bis(1*H*-pyrazol-3-yl)pyridine, L^{24} (*63*). The complex structure of $[Tb(L^{24})_3][PF_6]_3$, shown in Fig. 11, appears to be fairly robust in methanolic solution, with Horrocks analysis ($q = 0.6$) suggesting the 9-coordinate structure is retained; the small quenching effect of outer sphere coordination explains the q-value. However, in aqueous solution, the lability of the ligands dramatically changes the luminescence. Whilst the emission decays are not exactly single exponential, approximate lifetimes in H_2O and D_2O suggest a solvation value of 4–5.

B. CYCLIC SYSTEMS

1. Cyclen-derivative Macrocycles

The tetraazamacrocycle DOTA (1,4,7,10-tetraazacyclododecane-1,4,7,10-tetraacetic acid) forms stable complexes with the trivalent lanthanides, and consequently has been used in MRI as its gadolinium complex under the trade name DOTAREM. A vast number of ligands have been developed that use the tetraazacyclododecane (cyclen) ring with a variety of pendant groups; many of these have

been the work of Parker, Beeby and co-workers. In addition to the systems described below (shown in Scheme 4), developments have included the study of systems for sensing of pH, dissolved oxygen and the presence of anions such as bicarbonate or carboxylates in solution by quenching or enhancement of europium and terbium luminescence (*64*). Complexes suitable for use as "molecular logic gates" have also been reported (*65*).

Much work has been done to establish the factors that are important in creating complexes with highly efficient, long-lived luminescence. As with all ligand systems, this includes the efficiency of population of the ligand triplet state and energy transfer to the lanthanide center, i.e., an appropriate choice of chromophore. Ligand $[L^{25}]^{3-}$, mono-substituted with a benzophenone moiety, shows a ligand triplet yield of unity and efficient sensitization of europium and terbium as a result (*66*). Although deuteration studies show a q value of 1.25, the metal-centered luminescence is still reasonably long-lived (0.61 and 1.14 ms in water for europium and terbium, respectively) and strong ($\Phi_{Eu} = 0.095$, $\Phi_{Tb} = 0.27$).

Chromophores where the singlet–triplet energy gap in the ligand is small can allow the use of longer wavelengths to excite the lanthanide complex; this may help to eliminate background autofluorescence, as well as avoiding the need for expensive quartz optics. The absorption band of the benzophenone ligand $[L^{25}]^{3-}$ extends to 370 nm. Acridone (see $[L^{26}]^{3-}$–$[L^{28}]^{3-}$) has also been shown to be an appropriate chromophore (*67,68*), allowing moderate emission by excitation between 395 and 430 nm. The lower quantum yields and shorter lifetimes reflect the presence of two water molecules in the primary coordination sphere.

For those complexes where the chromophore is not coordinated to the metal center directly, the orientation of the chromophore is important to ensure efficient energy transfer. The series of ligands L^{29}–L^{32} were investigated for correlations between structural parameters found in the solid state (see, for example, Fig. 12) and solution (by NMR spectroscopy) and photophysical properties (*69,70*). It was found that both chromophore-metal separation and the angle of orientation have a direct influence on the quantum yield of the europium complexes. For example, the difference in quantum yield between $[Eu(L^{29})]^{3+}$ and $[Eu(L^{30})]^{3+}$ (0.06 and 0.02, respectively) cannot be attributed solely to the chromophore-metal separation, so may also depend on the better orientation of the chromophore in the L^{29} system as measured by the angle α between the metal center, the amide nitrogen atom, and the center of the phenyl ring.

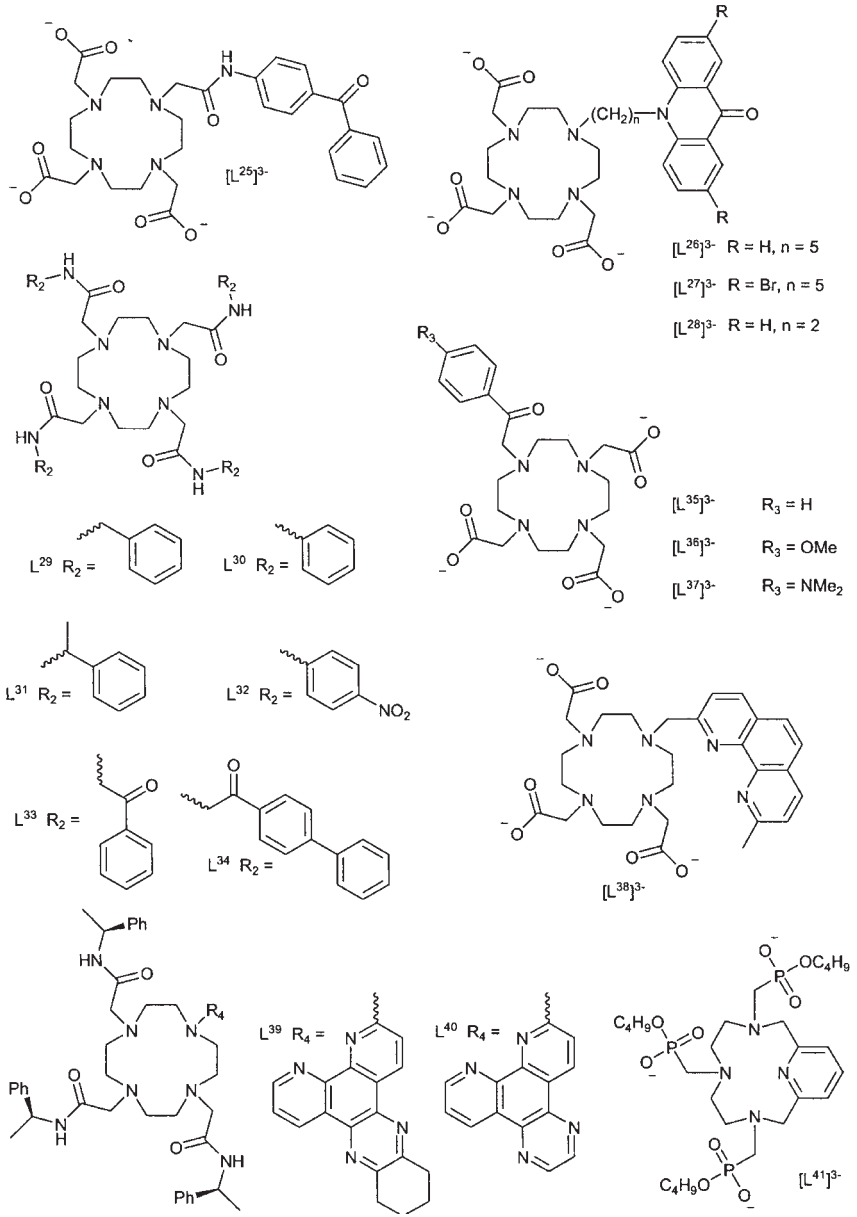

SCHEME 4. Selected DOTA-derived ligands.

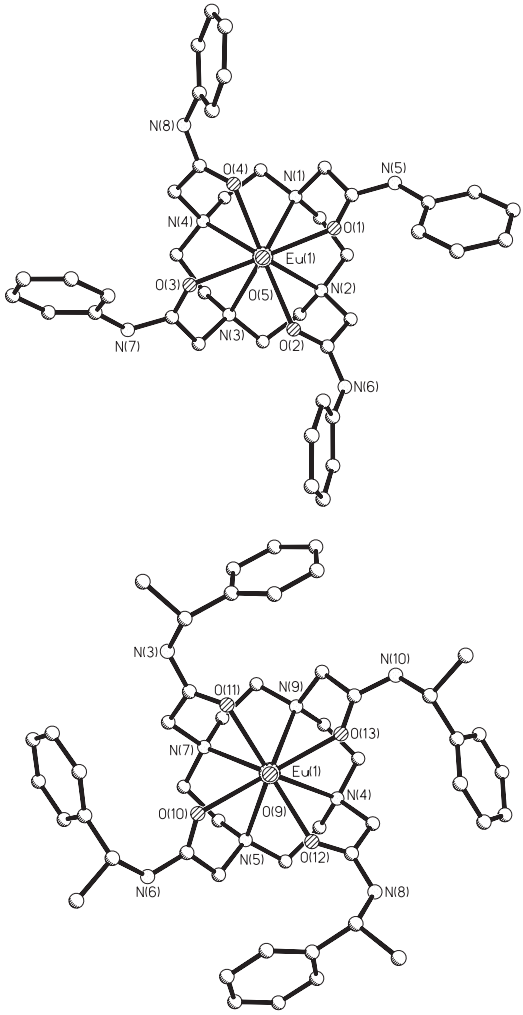

FIG. 12. Molecular structures of $[Eu(L^{30})(H_2O)]^{3+}$ (top) and $[Eu(L^{31})(H_2O)]^{3+}$ (bottom; used as a model for $[Eu(L^{29})(H_2O)]^{3+}$). These figures were generated from data obtained from the Cambridge Crystallographic Data Centre as published originally in Refs. (*69,70*).

Ligands L^{33} and L^{34} are both good sensitizers of europium, whilst the former also efficiently sensitizes terbium emission (*29*). The quantum yield of $[EuL^{34}]^{3+}$ in aqueous solution, 0.247, is among the highest reported for any europium complex. The lower triplet energy of L^{34} results in back transfer of energy from the terbium excited state to

the ligand. Derivative ligands that allow for coupling to biological molecules are currently under development.

Fine-tuning of the electronic properties of the chromophore is essential, as shown by the series of ligands $[L^{35}]^{3-}$–$[L^{37}]^{3-}$. Both EuL^{35} and EuL^{36} are emissive, with aqueous luminescence lifetimes of approximately 0.6 ms. The presence of a *para*-NMe_2 group results in loss of luminescence due to the lowering of the triplet energy of the ligand to 21,000 cm^{-1}, making it too low in energy to efficiently populate the europium and terbium excited states.

Phenanthroline has also been shown to be an excellent chromophore (*27*). Although there is evidence to suggest that the two phenanthroline N atoms in ligand $[L^{38}]^{3-}$ are not equally involved in coordination to the metal center, the presence of the coordinating chromophore helps to exclude water from the primary coordination sphere, as shown by both photophysical studies of the europium and terbium complexes, and relaxivity of the gadolinium complex. Whilst the europium complex exhibits excellent luminescence ($\tau = 1.24$ ms, $\Phi = 0.21$), the terbium emission is significantly quenched by the presence of oxygen: the lifetime and quantum yield are 0.31 and 0.11 ms respectively, compared with 1.51 and 0.51 ms in degassed aqueous solution. This is a result of diffusional quenching of the phenanthroline triplet state by dissolved oxygen.

The creation of luminescent complexes where the tetraazatriphenylene chromophores can also intercalate DNA allows them to be used as DNA probes (*71*). In aqueous solution the europium and terbium complexes of L^{39} and L^{40} have long-lived (1.05–1.85 ms) and highly emissive ($\Phi_{Eu} = 0.16$–0.21, $\Phi_{Tb} = 0.36$–0.40) excited states. The emission intensity is reduced on addition of poly(dAdT), poly(dGdC) and calf thymus DNA; this quenching is accompanied by a decrease in luminescence lifetime. This is shown to be consistent with an intercalative binding to the DNA or polynucleotides, the luminescence quenching occurring by a charge-transfer mechanism.

A closely related ligand is $[L^{41}]^{3-}$ where one side of the cyclen ring is replaced by a pyridyl group (*72*). In addition to the high quantum yield of the terbium complex ($\Phi = 0.51$), the complex exhibits in vivo and in vitro tissue selectivity, allowing it to be used for imaging of adenocarcinoma cells.

2. Other Macrocycles

Schiff base approaches have been used to synthesize mono-, di-, and trinuclear lanthanide complexes (*73*–*78*). Complexes of the macrobicyclic

(cryptand) Schiff bases are discussed later (see Section IV.B.4). To the best of our knowledge, most of the "single ring" Schiff base macrocyclic lanthanide complexes have not been studied for their photophysics, and those that have relate mainly to energy transfer between lanthanide centers (*75*).

3. Calixarenes

Photophysical studies have been conducted on a number of lanthanide complexes of calix[n]arenes, and a significant number of these are discussed in a recent review (*79*). The first europium and terbium calixarene complexes showed promising photophysical properties, with terbium luminescence lifetime of 1.5 ms and quantum yield of 0.20 in aqueous solution (*80*).

Replacement of the calixarene ring CH_2 groups with S or SO_2 and substitution of the *tert*-butyl group with sulfonate led to both greater water solubility and better complexation ability (e.g., $[L^{42}]^{4-}$ to L^{47}, Scheme 5) (*81*). Because of the high degree of solvent coordination ($q > 3$ in all cases) luminescence lifetimes of the terbium complexes were all below 1 ms; however, quantum yields were still reasonable [$\Phi = 0.12$–0.15] for ligands $[L^{42}]^{4-}$ to $[L^{44}]^{4-}$ (Scheme 5). Modification of these ligand systems is underway to try to exclude the presence of solvent molecules.

High quantum yields and long lifetimes have been reported for a series of calixcrowns with appended bipyridyl chromophores, such as L^{48} (*82*). Photophysical studies in acetonitrile gave lifetimes of 0.95–1.38 and 1.83–1.93 ms, and quantum yields of 0.18–0.32 and 0.32–0.39 for europium and terbium complexes, respectively.

The ether-amide functionalized calix[4]arene L^{49} has been complexed with various lanthanide ions, and the lutetium(III) complex has been structurally characterized (Fig. 13) (*83*). The large distance between the chromophore and the lanthanide, and the large energy difference between the ligand singlet and triplet states, suggests that metal-centered luminescence will be inefficient. Indeed, the emission spectra for both the europium(III) and terbium(III) complexes show residual emission from the ligand triplet state, indicating incomplete energy transfer. However, reasonable emission lifetimes (0.73 and 1.45 ms for europium and terbium complexes, respectively) and quantum yields (0.02 and 0.058, respectively) are recorded in acetonitrile solution.

The bipyridyl-*N*,*N*′-dioxide chromophore has been appended to a calix[4]arene to give L^{50}, and complexed with europium and terbium

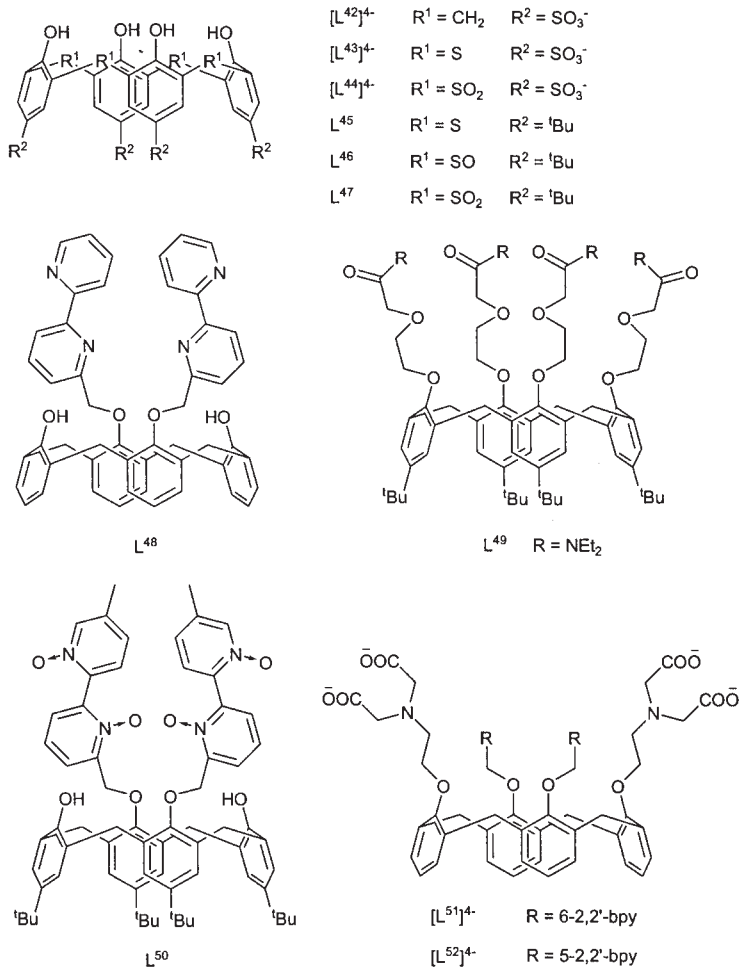

SCHEME 5. Selected calixarene-derived ligands.

(*84*). The europium complexes are highly luminescent, with quantum yields of up to 0.19 in methanol. The ligand triplet state is too low in energy to efficiently populate the terbium excited state, and no metal-centered emission is observed.

Complexes of calixarenes with bipyridyl chromophores can be stabilized by the addition of anionic side arms, such as iminodiacetate units (*85*). Whilst the lanthanide complexes of ligands $[L^{51}]^{4-}$ and $[L^{52}]^{4-}$ are not soluble in water, their photophysical properties in

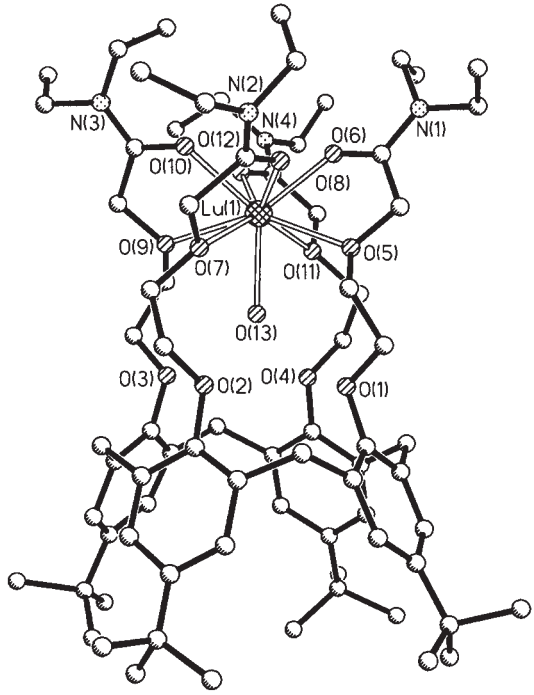

FIG. 13. Molecular structure of $[Lu(L^{49})(H_2O)]^{3+}$. This figure was generated from data obtained from the Cambridge Crystallographic Data Centre as published originally in Ref. (*83*).

methanol are reasonable, with lifetimes of 0.31–1.14 ms and quantum yields of up to 0.05 (europium) and 0.13 (terbium). It was shown that the substitution pattern of the bipyridyl chromophore had a larger bearing on complex stability than photophysics.

Calixarenes are a promising class of ligand with regard to the development of luminescent lanthanide biolabels with the necessary stability, luminescence and, ultimately, solubility properties.

4. Macrobicycles

The first cage lanthanide complexes studied for their photophysics were the simple 2.2.1 cryptands. The lack of a strongly absorbing chromophore, and easy approach of solvent molecules meant that their luminescence properties were disappointing in comparison to many recently studied complexes. The Lehn cryptand (L^{53}) (Scheme 6

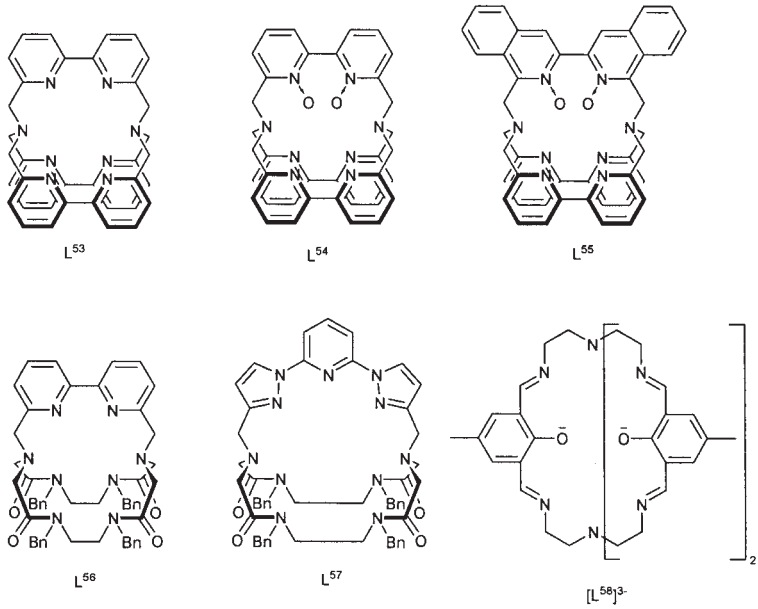

SCHEME 6. Selected macrobicyclic ligands.

and Fig. 14) and its derivatives aim to combat these problems by incorporating strongly absorbing chromophores such as 2,2′-bipyridine (bpy) groups (*86,87*). The photophysics of the europium and terbium complexes of L^{53} suggested the promise of these types of ligands, with aqueous lifetimes for both complexes of approximately 0.35 ms and quantum yields of 0.03; these were limited by the coordination of 2–3 water molecules (*87*).

Alteration of the chromophore by conversion of some of the bipyridyl groups to their N-oxide derivative leads to a significant improvement in the luminescence performance (*88*). Although the lifetimes of the europium complexes of ligands L^{54} and L^{55} were still less than a millisecond, the quantum yields of 0.15 and 0.20 respectively are significantly better.

Recently, two cryptands and their lanthanide complexes have been synthesized which include either a bipyridyl (L^{56}) or pyridyl (L^{57}) chromophore (*89*). These have proved effective at populating the lanthanide excited states. Aqueous luminescence lifetimes of up to 1.12 ms and quantum yields of up to 0.02 (europium) and 0.25 (terbium) are reported. The better luminescence from complexes of ligand L^{57} is due to the better exclusion of water from the lanthanide center.

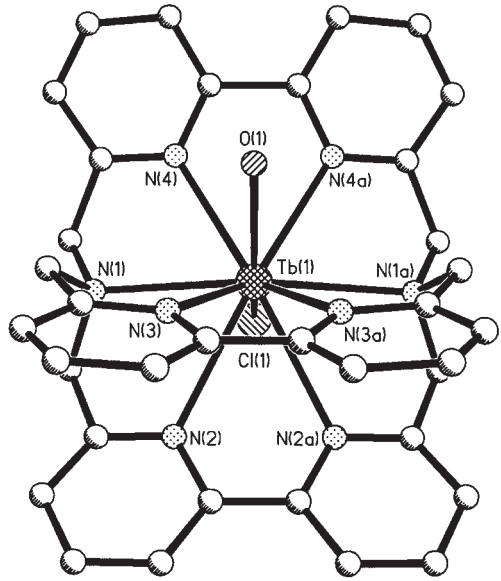

FIG. 14. Molecular structure of $[Tb(L^{53})(H_2O)Cl]^{2+}$. This figure was generated from data obtained from the Cambridge Crystallographic Data Centre as published originally in Ref. (*86*).

Mono- and bimetallic lanthanide complexes of the tren-based macrobicyclic Schiff base ligand $[L^{58}]^{3-}$ have been synthesized and structurally characterized (Fig. 15), and their photophysical properties studied (*90,91*). The bimetallic cryptates only form with the lanthanides from gadolinium to lutetium due to the lanthanide contraction. The triplet energy of the ligand (ca. 16,500 cm^{-1}) is too low to populate the terbium excited state. The aqueous lifetime of the emission from the europium complex is less than 0.5 ms, due in part to the coordination of a solvent molecule in solution. A recent development is the study of d–f heterobimetallic complexes of this ligand (*92*); the Zn–Ln complexes show improved photophysical properties over the homobinuclear and mononuclear complexes, although only data in acetonitrile have been reported to date.

C. SUMMARY

Currently the best lanthanide complexes have millisecond excited state lifetimes in aqueous solution (*52,56,93*) and quantum yields of approximately 0.3 (Eu^{3+}) and 0.6 (Tb^{3+}) (*27*). While almost all of the

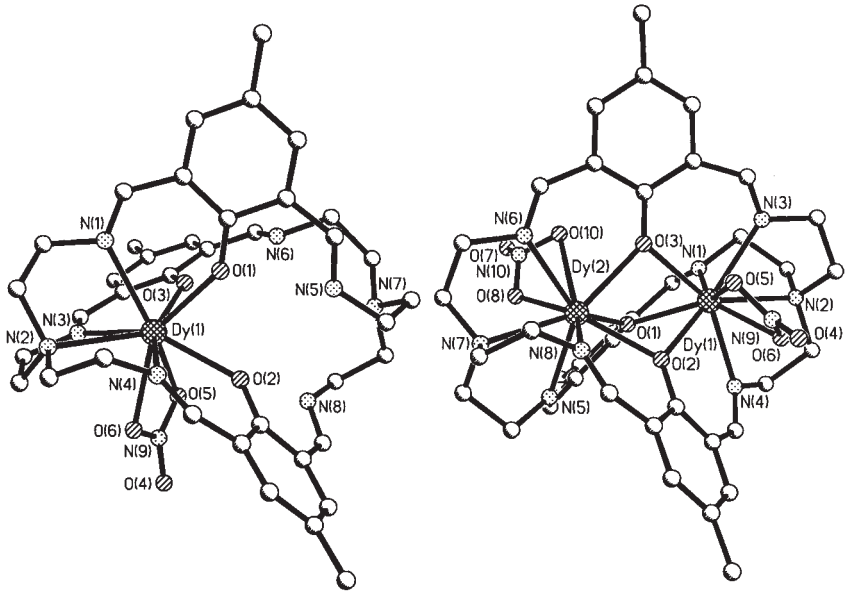

FIG. 15. Molecular structures of $[Dy(L^{55})(NO_3)]^-$ (left) and $[\{Dy(NO_3)_2\}_2(L^{55})]^+$ (right). These figures were generated from data obtained from the Cambridge Crystallographic Data Centre as published originally in Ref. (*90*).

studies to date have focused on mono-metallic lanthanide complexes, there have been a few isolated exceptions (*56,57,77,78,90,91,94,95*). It remains to be seen what advantages may accrue from systems employing more than one lanthanide ion.

V. Biochemical Applications

The past 50 years have seen the arrival of an increasing number of new methodologies for the analysis of biological molecules, including nucleic acids, proteins, carbohydrates, and lipids. Modern quantitation assays require sensitivity, but are usually automated and with high throughput, often requiring multiplex labeling (more than one label of different colors or characteristics), for applications such as diagnostics or drug screening (*96*). It should also be noted that labeling of biological molecules needs to be completed in buffered aqueous solutions and at approximately neutral pH, so as not to denature the molecules and change their structure and biological

function. The label can be used to tag all molecules in a mixture, before separation of tagged molecules by size or chemistry and subsequent identification, or certain molecules can be identified in a mixture, by the specific binding of a label. In both cases, the label must contain a visualization component, for example a radioactive or luminescent moiety, as well as a suitable binding group (receptor) for hybridization or conjugation to the biomolecule. When specific, not total, tagging is required, the binding group may be a specific recognition molecule: a known gene sequence (nucleic acid probe) for nucleic acid recognition, or an antibody for the recognition of specific proteins or haptens.

The original protocols utilized the sensitivity of radioactive labels in the detection and analysis of proteins by radioimmunoassay and in the sequencing of DNA, for example. However, the radioactive isotopes used (mainly ^{125}I and ^{32}P) often have significant health risks associated with their use and their relatively short half lives (weeks to months) mean that experiments must be performed directly after labeling and frequent labeling experiments are required (*97*). Despite the development of a variety of non-radioactive labeling methods, involving enzyme-linked color reactions and fluorescent dyes, these methods often use several antibodies for detection, making them expensive. They can also be less sensitive than radio-labeling and non-specific color reactions or the epifluorescence of the sample can make non-radioactive labels less specific. An easy to use, safe, stable, inexpensive, and sensitive label is still being sought for the detection and assay of biological molecules.

A. Protein Detection

1. Protein Staining and Assay

A variety of methods are available to detect proteins separated by electrophoresis or to measure the concentration of total protein in a solution. These methods are normally based on the binding of a dye to one of the amino acids in protein, or a color reaction with an amino acid side chain. The most commonly used stains for protein detection on gels are Coomassie Brilliant Blue (*98*) and silver stain (*99,100*). These methods detect any protein residues, either in solution or on an electrophoresis gel. Their main requirement is sensitivity, not specificity. New, more sensitive dyes are being developed for the proteomic analysis of protein structure and sequence, for example Ruby Red (*101*).

2. Immunoassay

The detection of a specific protein in a mixture of biomolecules commonly utilizes the specific reaction between an antibody and its antigen. The mammalian immune system can recognize proteins and other molecules that are foreign to that animal and responds with the production of a population of antibodies. These antibodies specifically recognize only the foreign molecule (antigen) and bind to it tightly, this being the first stage of removal by the immune system (*102*). This biological reaction has been used for the assay of proteins, peptides, and other molecules for the past 40 years. Small molecules such as steroid hormones, neurotransmitters and other organic chemicals, usually do not elicit an effective immune response on their own. These non-immunogenic molecules (haptens) can be covalently coupled (conjugated) to a carrier protein in order to induce an immune response specific to the carrier protein antigen complex and hence, in effect, to the hapten (*103*). A mixture of immunoglobulins (polyclonal antibodies) is produced by injection of a single foreign antigen into a living animal. Each different antibody in the mixture binds to a subtly different site (epitope) on the antigen by multiple, non-covalent interactions and is produced by a different clone (family) of activated B-lymphocytes in the thymus gland (*103*). Antibodies derived from single antibody-producing B-cells that are immortalized in the laboratory by fusion to a B-lymphocyte tumor cell line to form hybridoma clones, are called monoclonal antibodies. A monoclonal antibody consists of a single immunoglobulin type with only one type of binding site for the antigen (*103*).

Proteins, peptides, and haptens can be sensitively and specifically detected in solution and on solid supports, using the specific antigen–antibody binding reaction. Either the antigen or the antibody can be labeled, and a variety of radioactive or non-radioactive systems have been employed. An immunoassay is a competitive binding assay for molecules in solution, which utilizes a low concentration of labeled pure antigen that competes for antibody binding sites with unlabeled standard or unknown unlabeled antigen. If no unlabeled antigen is present, binding of the "tracer" labeled antigen will be maximal. Binding will decrease as the concentration of unlabeled antigen increases and competes for the antibody binding site (Fig. 16). Immunoassays are available for a huge variety of molecules now, ranging from small metabolites such as cyclic AMP, to steroid hormones, neurotransmitters, carbohydrates, peptides, and proteins (*103*).

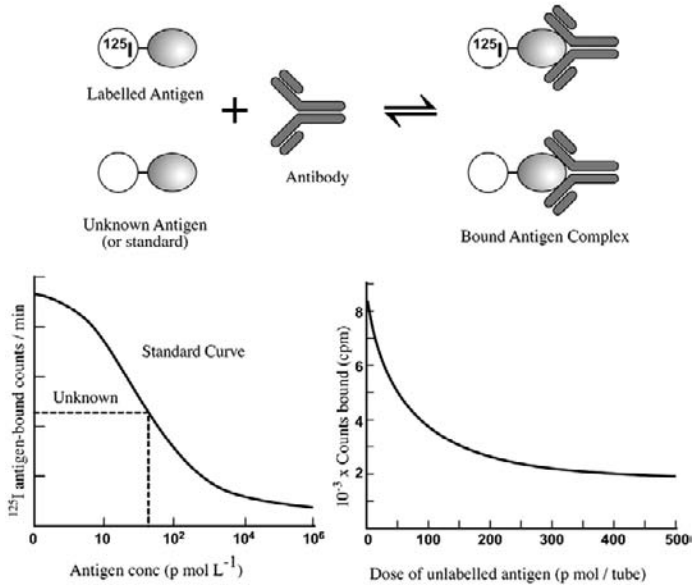

FIG. 16. The principal of the immunoassay. Labeled antigen (in this case ^{125}I-labeled antigen) competes with unlabeled antigen for binding sites on a set concentration of antibody. Adapted from Ref. (*200*).

a. Radioimmunoassay The competitive binding equilibrium that is the basis of immunoassays has been adapted into a variety of protocols. In a radioimmunoassay, a pure sample of the substance to be measured is labeled with a radioactive molecule. For peptides and proteins the radioactive iodinating agent is normally $^{125}I_2$ (although ^{125}ICl is a more effective agent, the molecule is not available at sufficiently high specific activity for the preparation of labeled proteins). Molecular iodine iodinates by an addition reaction at a double bond on a group, such as the side chain on the amino acids tyrosine or histidine (*104*).

The most common method of radiolabeling employs Chloramine-T, the sodium salt of the N-monochloro derivative of *p*-toluenesulfonamide (Fig. 17). It breaks down slowly in aqueous solution to hypochlorous acid and is used as a mild oxidizing agent in radioiodination reactions. Other oxidation reagents used in radioiodination include 1,3,4,6-tetrachloro-3*a*,6*a*-diphenylglycoluril (known commercially as Iodo-gen, Fig. 17) or Bolton and Hunter reagent (*104*).

In the presence of chloramine-T under mildly alkaline conditions (pH 7.5), NaI is oxidized to form cationic iodine I^+. At this pH the tyrosine will be only slightly anionic as the pK_a of the phenolic side

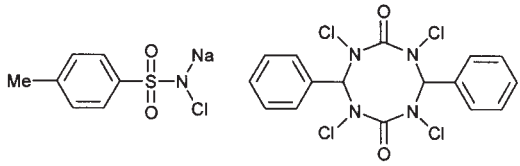

FIG. 17. Chloramine-T (left) and Iodo-gen (right) reagents, used in radio-iodination reactions.

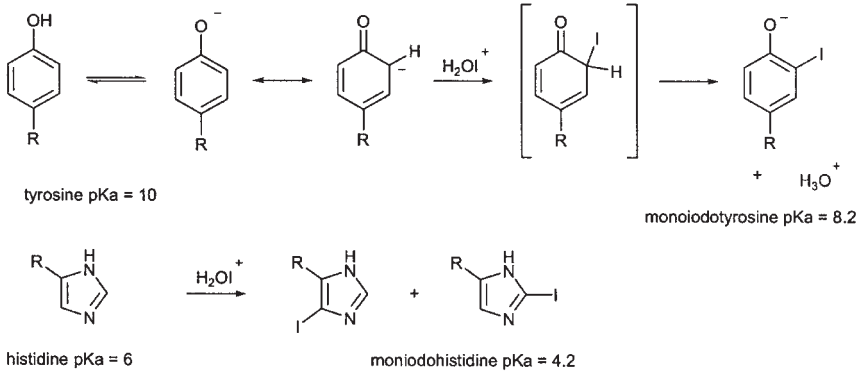

FIG. 18. Iodination of tyrosine (top) and histidine (bottom) amino acid residues in proteins by electrophilic substitution.

chain is over 10, but the iodination reaction, forming monoiodotyrosine (Fig. 18), will proceed through this small proportion of ionized groups. This also minimizes secondary reactions, including the oxidation of methionines in the labeled protein, which may interfere with the specific binding reaction between the labeled protein and the antibody in the radioimmunoassay and allows the optimal incorporation of one iodine atom per protein molecule (*105*).

Once radio-iodinated, the labeled protein or peptide is then purified from the remaining unbound radioactive iodide by gel filtration (*106*). Use of radioactive iodine poses a significant health threat, because of its ability to accumulate in the thyroid gland, the source of iodinated thyroid hormones. Iodination reactions need to be carried out in filtered fume hoods, behind lead shielding, and the operator requires regular monitoring of the thyroid for accumulation of radioactivity. The ^{125}I isotope has a relatively short half life of 59.6 days (*107*) and the labeled proteins can be unstable, necessitating regular radio-iodination reactions.

Small organic molecules can be labeled with ^{14}C-carbon by chemical or enzymatic incorporation of ^{14}C into the molecular structure. These molecules are commercially available for use in radioimmunoassay (*108*). Steroid molecules are more commonly labeled with ^{3}H during chemical synthesis. These radioisotopes have much longer half lives (5730 and 12.4 years, respectively) and several atoms of the radioisotope can often be incorporated per labeled molecule (*107*). The emitted beta radiation is not as powerful as the gamma radiation emitted from the ^{125}I isotope, requiring longer counting times and making the assays less sensitive (*109*).

b. Enzyme-linked Immunosorbent Assay (ELISA) An ELISA is an immunoassay in a multi-well plate format, which utilizes a color reaction catalyzed by an enzyme for detection of the antigen. Proteins, whether antibody or antigen, may be passively adsorbed to a solid plastic surface such as the wells of a 96 well microtitre plate. The standard procedure uses sodium carbonate buffer at pH 9.2 and incubation for 12–20 h (*110*). Immobilization of one component allows the use of small volumes and multiple-well pipetting, and the simultaneous assay of multiple samples.

The enzymes commonly used as labels in ELISA and other immunochemical reactions include horse radish peroxidase (HRP) and alkaline phosphatase (AP). The enzyme can be covalently coupled to the antibody using glutaraldehyde conjugation to reactive amino groups on the enzyme (lysines) in a phosphate buffered aqueous solution at neutral pH, as shown in Fig. 19 (*103*). Alternatively, carbohydrates present in the immunoglobulin structure can be cleaved by periodate treatment (see Fig. 20) and bound to free amino groups on the enzyme through a Schiff base reaction (*103*).

As shown in Fig. 21, in a direct ELISA the unlabeled antigen (a range of standard antigen concentrations or unknown samples) is attached to the solid phase. Enzyme-conjugated (labeled) primary antibody is then added. After incubation and washing of the plate

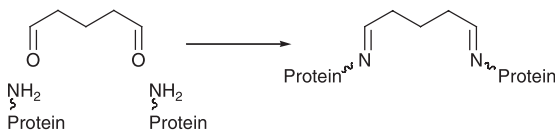

FIG. 19. Schiff base condensation of glutaraldehyde with enzyme amino groups.

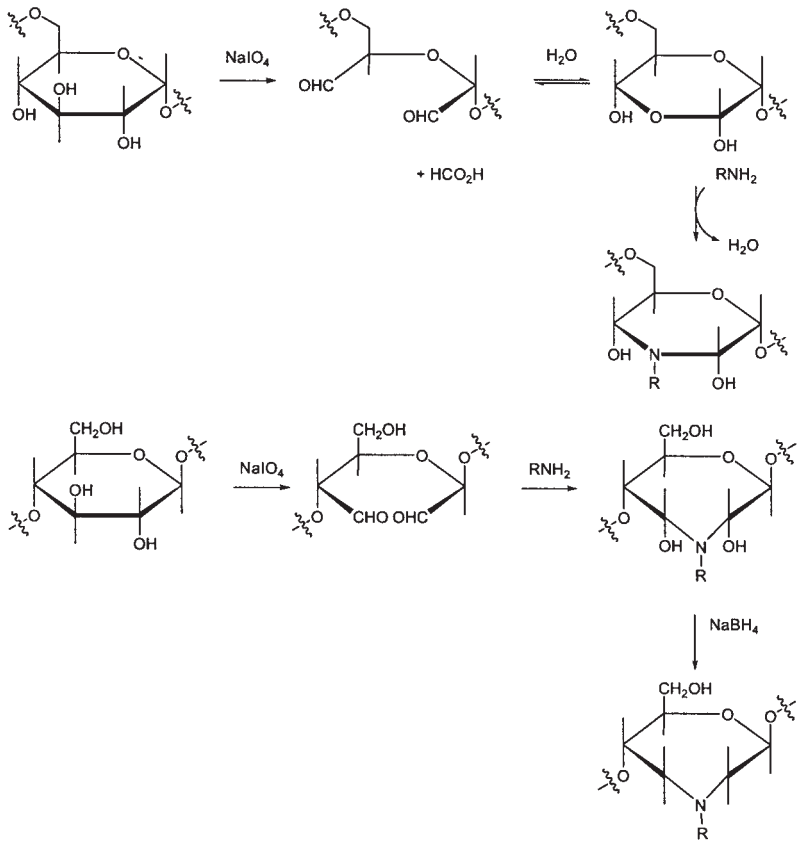

FIG. 20. Periodate treatment of glycoprotein or carbohydrates (top is a 1,6-linked polymer of glucose; bottom is a 1,4-linked polymer of glucose i.e., cellulose) creates aldehydes, which can then be conjugated to dye-amine derivatives (*116,201*).

the enzyme substrate solution is added to each well and color allowed to develop. The intensity of the color in the multi-well plates is then measured in a multi-channel spectrophotometer. Alternatively, an unlabeled primary antibody can be attached to the base of the wells and antigen added. Dilutions of standard antigen or test samples of unlabeled antigen are added to different wells. Antigen is then detected by addition of an enzyme-conjugated secondary antibody or by sandwiching the antigen between an immobilized, species-specific primary antibody and an enzyme-labeled antigen-directed secondary antibody (Fig. 21C) (*111*). In all cases, after the enzyme substrate is

added, the amount of color produced is proportional to the amount of antigen present. More complicated ELISA assays use an enzyme-labeled secondary antibody directed against the primary antibody (indirect ELISA).

c. Fluorescence Immunoassays Fluorescence immunoassays have been widely used over the past 20 years, in parallel to the development of instrumentation for automation. Most fluorescence homogeneous immunoassays allow rapid and direct measurement of a specific antigen (which might be a hapten, carbohydrate, nucleic acid, peptide, or protein) in a mixture without purification or separation steps. The simplest form of fluorescence immunoassay utilizes an enzyme substrate that yields a fluorescent product on cleavage by a specific enzyme, such as the CSPD®, and CDP-*Star*® substrates for AP (Fig. 22), available from Applied Biosystems Ltd (*112*).

The fluorescence polarization immunoassay is used for routine, automated immunoassay of small molecules, such as drugs. It depends on the principle that a fluorophore attached to a macromolecule such as an antibody is not free to rotate in solution. If polarized light is used to stimulate the fluorophore to fluoresce, emission from the bound fluorophore (attached to the antibody, which is bound to a surface) will continue to be polarized, but polarization will be lost from free fluorophore (*111*).

Reagents for the conjugation (covalent bonding) of fluorescent dyes to proteins are readily available commercially (*113,114*). Fluorescent probes can be used to tag not only proteins, but also nucleotides, lipids, oligosaccharides, or other biological molecules. Free amino groups of the protein to be labeled react with a N-hydroxysuccinimide ester-derivative of the fluorescent dye (Fig. 23), forming a stable amide bond. The water-soluble cyanine dyes, Cy3, Cy5 and Cy7, are often used for this purpose. Alternatively dye maleimides or methanethiosulfonate (MTS) (*115*) reagents can be reacted with free sulfhydryl groups, such as the cysteine amino acids in proteins or peptides, forming disulfide bonds (Fig. 24) (*116,117*).

In the past, the sensitivity of the fluorescence immunoassay has been limited by background fluorescence, often from proteins, plastics or detergents. As described above in Section III.A.1, lanthanides give intense phosphorescence when coupled to, and shielded by, appropriate organic ligands. Time resolved luminescence immunoassay takes advantage of the long decay time (10^{-5} to 10^{-3} s) of the phosphorescence of lanthanide complexes, to remove background, significantly improving the sensitivity of the immunoassay. Initial difficulties

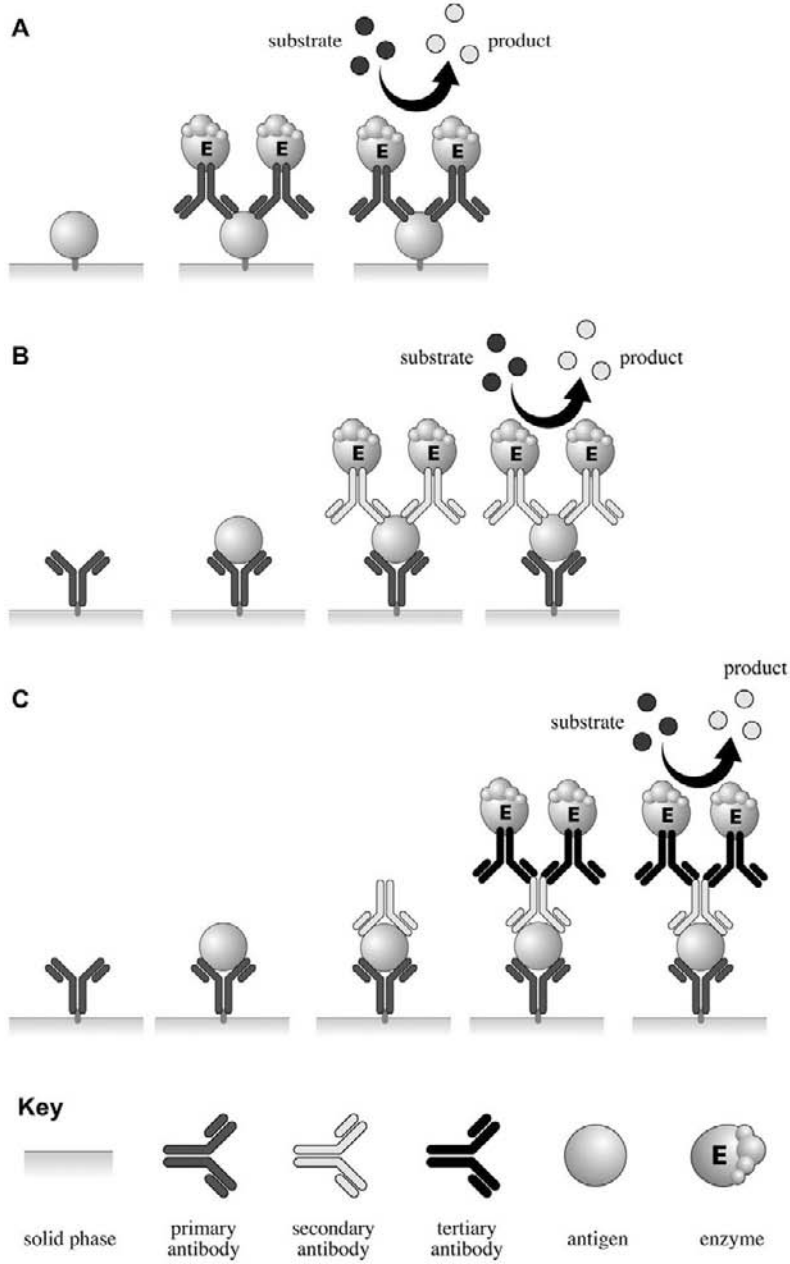
A
substrate
product
E
E
E
E
B
substrate
product
E
E
E
E
C
product
substrate
E
E
E
E
Key
solid phase
primary antibody
secondary antibody
tertiary antibody
antigen
E
enzyme

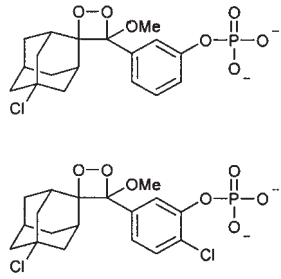

FIG. 22. CSPD® Substrate (top) and CDP-*Star*® Substrate (bottom), enzyme substrates which alkaline phosphatase (AP) cleaves to form fluorescent products.

coupling the first-generation lanthanide complexes to proteins were rapidly overcome. The early dissociation-enhanced lanthanide fluoroimmunoassay (DELFIA) system, using a non-fluorescent chelate label, linked to the second antibody by conjugation through free amino groups on lysine amino acids in the immunoglobulin, is shown in Fig. 25A. Once the immune reaction is complete, the lanthanide ion is dissociated from the chelate at low pH and an enhancement solution added to elicit luminescence from the free lanthanide (*5,110,118*). More complex time resolved fluorescence immunoassays use a sandwich format, with two monoclonal antibodies reacting with different parts of the antigen. One antibody is immobilized onto the microtitre plate well and the second is labeled with the lanthanide complex (Fig. 25B) (*62,110,118,119*). Time-resolved fluorometry with lanthanide chelate labels is now used extensively in diagnostics, as well as in a range of assay formats for drug screening. A comprehensive description of the applications of the DELFIA system can be found in the review by Sammes and Yahioglu (*5*). Although the small size of the molecules to be labeled has ensured the continued use of internal radiolabels, rather than a larger, external label, such as a lanthanide chelate,

---

FIG. 21. Principles of ELISA. A: In a direct ELISA the unlabeled antigen is attached to the solid phase. Enzyme-conjugated antibody is then added, followed by the enzyme substrate solution and color is allowed to develop. B: ELISA with unlabeled antibody attached to the solid support. A variable amount of antigen is then added. A secondary antibody labeled with enzyme, followed by substrate solution, is added to all wells. The amount of color produced is proportional to the amount of antigen present. C: Sandwich ELISA assay with the antigen sandwiched between an immobilized, antigen-specific primary antibody and an antigen- or species-specific secondary antibody. An enzyme-labeled tertiary antibody increases the assay specificity and sensitivity.

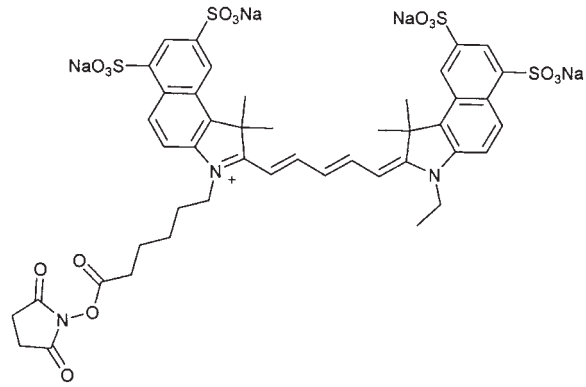

FIG. 23. N-hydroxysuccinimide Cy5, an example of an activated water-soluble cyanine dye for the labeling of free amino groups.

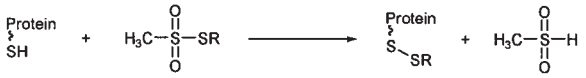

FIG. 24. Methanethiosulfonate (MTS) reagent reacting with a thiol (sulfhydryl), typically of a cysteine residue in a protein, forming a disulfide bond and thus introducing the dye moiety (label)—SR.

the continuing problem of radio-isotope safety and disposal, as well as the drive to automation and assay miniaturization, has meant that methods using these non-radioactive labels are now being developed (*96*).

3. Western Blotting

The binding of an antibody to its antigen has also been utilized in the detection of specific proteins on a solid support, such as a western blot, where size-separated proteins are immobilized on a nitrocellulose or nylon membrane (see Section V.B). In this case, the primary

---

FIG. 25. (A) DELFIA (Dissociation Enhanced Lanthanide Fluoro-ImmunoAssay) system. This heterogeneous immunoassay system uses a primary antibody bound to a solid support, to which a variable amount of unlabeled antigen is bound. The secondary antibody is labeled with a non-phosphorescent lanthanide chelate, which becomes phosphorescent after dissociation from the antibody, due to the addition of an enhancement solution [which typically contains a mixture of sensitizer (typically a β-diketonate) and micelle inducing surfactant (*5*). (B) Heterogeneous fluoroimmunoassay using a secondary antibody directly labeled with a phosphorescent lanthanide chelate.

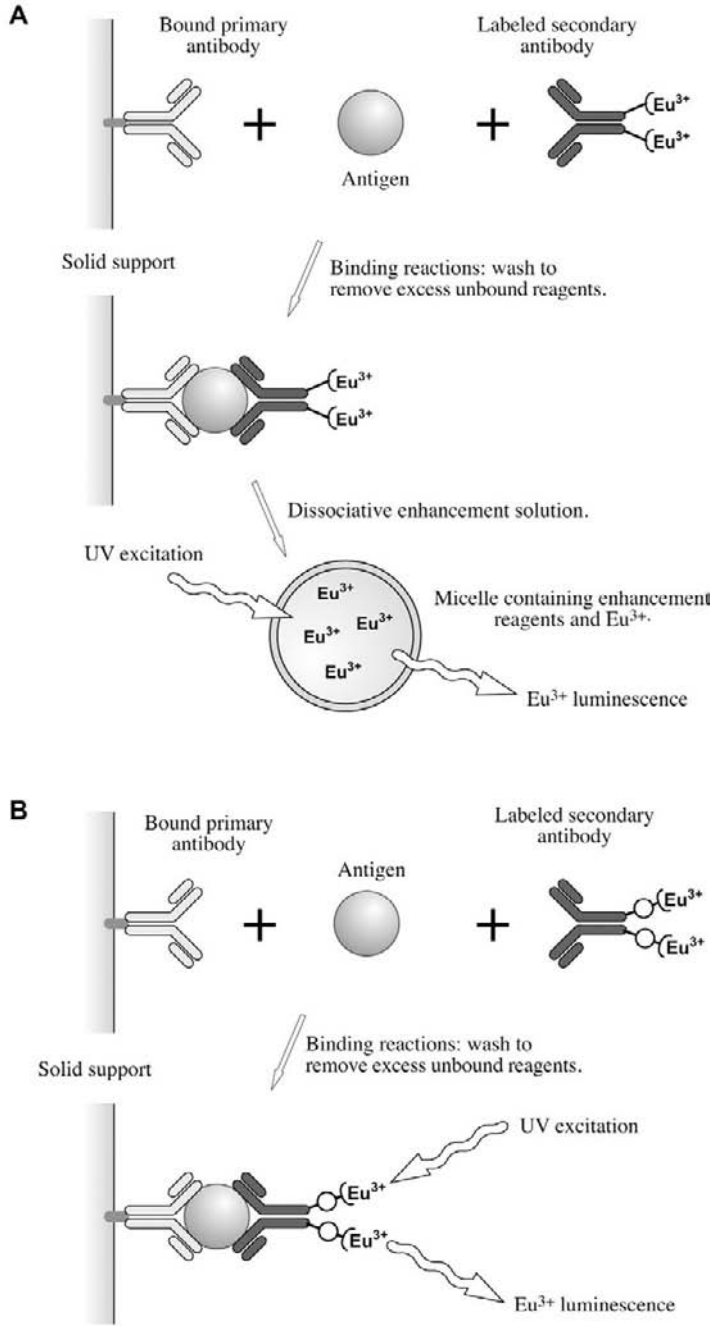
A
Bound primary antibody
Labeled secondary antibody
Antigen
Solid support
Binding reactions: wash to remove excess unbound reagents.
Dissociative enhancement solution.
UV excitation
Micelle containing enhancement reagents and Eu3+.
Eu3+ luminescence
B
Bound primary antibody
Antigen
Labeled secondary antibody
Solid support
Binding reactions: wash to remove excess unbound reagents.
UV excitation
Eu3+ luminescence

antibody (which binds to the protein on the membrane or support) or a secondary antibody (which specifically detects the primary antibody) is labeled with either a radioactive label, or by conjugation of the antibody to an enzyme (such as AP or HRP) that can catalyze a color reaction, or by conjugation to an enzyme which can catalyze the degradation of a substrate to produce a fluorescent or chemiluminescent signal (*120–130*). The blot, containing the immobilized, separated protein mixture, is incubated with the primary antibody in an aqueous solution at neutral pH and at approximately 4 °C. After washing to remove non-specifically bound antibody, the protein of interest is visualized by the binding of a secondary antibody. After the addition of substrate, antigen bands can be visualized by exposure of the blot to fluorescence scanning equipment or an X-ray film (*113,131*).

4. Receptor-ligand Binding Reactions

Hormones and other signaling molecules, such as growth factors, must bind to a specific protein receptor to transmit their message to the target cell. Protein and peptide hormones have membrane receptors, whereas lipid-soluble steroid hormones have intracellular receptor proteins. The kinetics of the binding reaction of a receptor protein with its ligand can yield much information on the affinity of the receptor for different ligands and on the number of receptors synthesized by a particular cell population. Furthermore, a competitive receptor–ligand binding assay can be used to assess the amount of ligand present in a complex mixture, in a similar way to immunoassay (*132*). In vitro receptor–ligand binding characteristics can be assessed using a labeled ligand, in a parallel manner to the antibody–antigen reactions described above.

5. Immunohistochemistry and Receptor Autoradiography

Proteins can be detected in tissue sections or cell cultures using similar immune detection systems. Use of an antibody to detect specific proteins in tissues is called immunohistochemistry, whereas detection of proteins in cell suspensions is called immunocytochemistry. Tissues can be prepared by fixation and embedding in paraffin wax, or by rapid freezing in a compound that inhibits ice formation in the tissue, so as to preserve cell morphology. Some antibodies do not work well with paraffin-embedded tissues, probably because the antibody cannot access the antigen properly (*133*). The most common labeling system used for detection of the bound antibody is an enzyme-coupled secondary antibody that produces a color reaction

in the cells containing the protein of interest. The use of a secondary antibody system allows amplification of a weak signal and increases the specificity of detection (*134*). The antibodies used for detection are conjugated either with enzymes such as AP or HRP, or to fluorophores (as described in Section V.A.2). Antibodies conjugated with enzymes can be detected with chromogenic or fluorescent substrates (*135*). Radiolabeled-ligands are commonly used to detect binding sites (i.e., receptors) in whole animals or cells in vivo, or on tissue sections in vitro (*136–142*). Small latex beads carrying fluorescent lanthanides are available now for time-resolved imaging of specific proteins or ligands in tissues, using these methods (*143*).

6. Future Applications

Safe and sensitive labels will be required in the future for in vivo protein detection, for example to monitor the delivery of peptide or protein drugs or vaccines in patients. Some pre-clinical models are available for this purpose, but these normally involve the use of transgenic animals or cells, with reporter genes such as jellyfish green fluorescent protein, to follow the expression of a particular protein in the living cell (*144–146*). Development of fluorescent labels that could be used to monitor protein synthesis, secretion, binding, distribution or degradation in vivo, with no additional harm to the patient, would be of great use in the development of new drug systems.

B. Nucleic Acid Detection

The sequencing of the human genome (*147–149*) heralds an era when diagnosis of genetic traits and detection of gene expression will become routine. The detection of nucleic acids (deoxyribonucleic acid or DNA and ribonucleic acid or RNA) utilizes a nucleic acid probe, which is a relatively short strand of DNA or RNA that locates and binds to (hybridizes with) its complementary sequence in samples containing mixtures of single stranded DNA or RNA. The visualization is achieved by, for example, incorporating radioactive atoms into the nucleic acid probe when it is synthesized (see Section V.B.3.a). Our ability to synthesize gene probes and to amplify the target sequence using the polymerase chain reaction (PCR, see Section V.B.2), has made nucleic acid identification for diagnostic or research purposes relatively straightforward. The PCR is capable of amplifying a DNA sequence over a million times, so that the piece of DNA can be stained and seen on an electrophoresis gel.

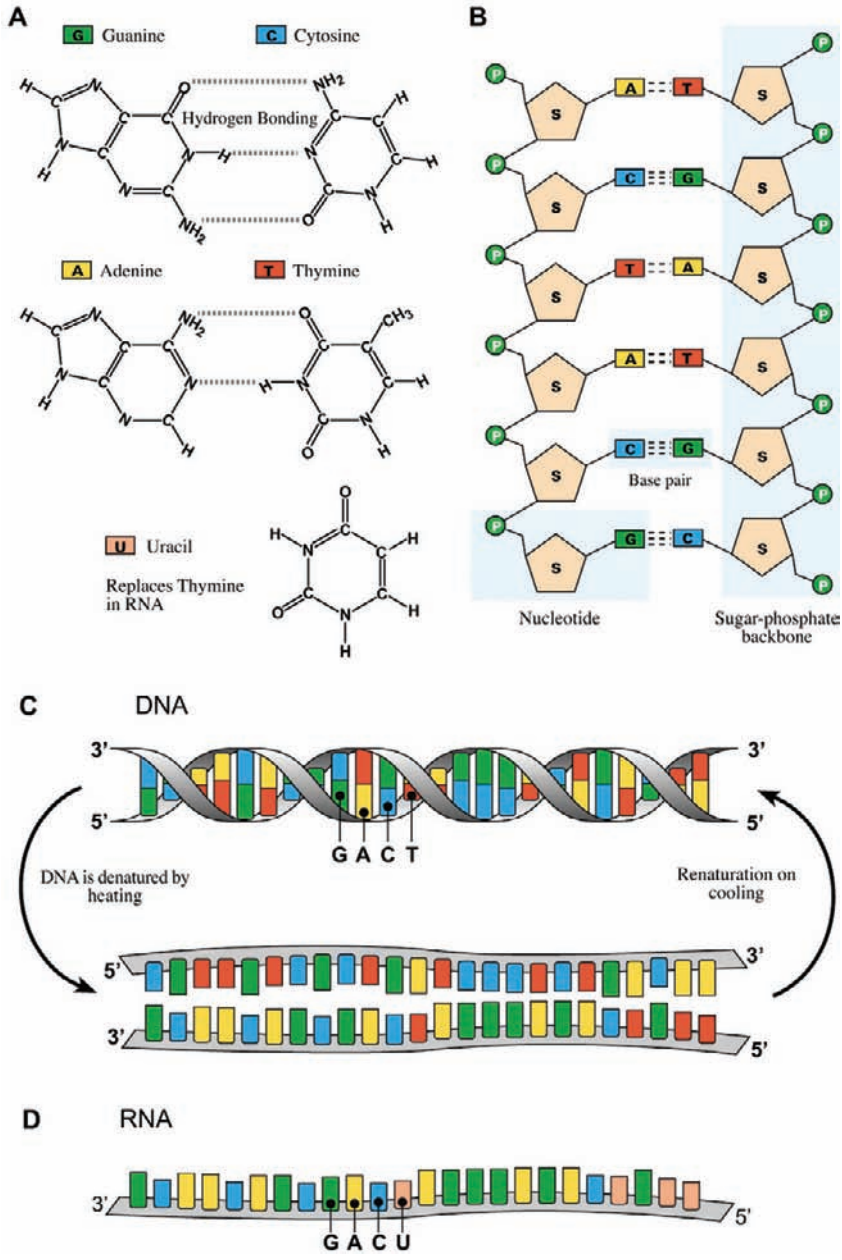
A
G Guanine
C Cytosine
Hydrogen Bonding
A Adenine
T Thymine
U Uracil
Replaces Thymine in RNA
B
Base pair
Nucleotide
Sugar-phosphate backbone
C DNA
3'
5'
G A C T
DNA is denatured by heating
Renaturation on cooling
D RNA
G A C U

DNA is double stranded, with the two complementary deoxyribose nucleotide chains running in opposite directions, held together in the classic double helix by hydrogen bonds between nucleotide bases (Fig. 26A–B). Adenine (A) always hydrogen bonds to thymine (T), whereas cytosine (C) bonds to guanine (G). The spontaneous attraction of A for T (two hydrogen bonds) and C for G (three hydrogen bonds) allows the recognition of homologous sequences of single stranded DNA in aqueous solutions and the strong and specific hybridization of one sequence with its homologous sequence to reform the double helix (Fig. 26C) (*150*).

RNA, on the other hand, is normally single stranded in vivo (Fig. 26D) and is therefore less stable and more prone to enzymatic degradation than DNA. The process by which the information in the DNA (genes) is transcribed into a messenger, mRNA, and translated into a protein, is known as gene expression. Analysis of gene expression requires the detection of the labile mRNA species. Modern methods of RNA analysis often involve the copying of the single stranded mRNA species to a more stable, double-stranded (complementary) cDNA, using an enzyme called reverse transcriptase (originally found in retroviruses), before detection.

Nucleic acids can be transferred from electrophoresis gels, or colonies of bacteria growing on agar media, to more solid supports such as nylon or nitrocellulose membranes, by simple capillary transfer or blotting. The transfer of DNA in this way was developed first by a scientist named Southern and is referred to as Southern blotting (*151*). When it was shown that both RNA and proteins could be similarly transferred to membranes, the methods were given the names northern blotting and western blotting, respectively. The membrane (or blot) can then be hybridized with a suitable labeled gene probe and specific nucleic acids identified (*152*).

1. Non-specific Nucleic Acid Staining

Analysis of DNA or RNA frequently starts with the size separation of extracted nucleic acids by electrophoresis on agarose or

FIG. 26. Nucleic acid structures. A: The structure of the four bases in DNA, guanine (G), cytosine (C) adenine (A) and thymine (T). Uracil (U) replaces thymine (T) in RNA. B: The spontaneous attraction of A for T and C for G allows the recognition of homologous sequences in aqueous solutions and the strong and specific hybridization of one sequence with its homologous sequence. C: DNA forms a double helix at body temperature, which can be denatured to separate the strands by heating. D: single stranded mRNA structure.

polyacrylamide gels. Detection of nucleic acids on gels or solid supports is readily accomplished using dyes that fluoresce under UV illumination on intercalation with the DNA or RNA. The most commonly used reagent for this purpose is ethidium bromide, but more modern reagents include SYBR® Green, methylene blue or acridine orange. These reagents are not selective and allow visualization of all nucleic acids on the gel. As all dyes that bind DNA are potentially mutagenic, the more recent reagents are designed to have increased sensitivity as well as decreased mutagenicity (*153*).

2. Polymerase Chain Reaction: DNA Amplification with a Thermostable Enzyme

The PCR is a three-step cyclic process that repeatedly duplicates a specific DNA sequence, contained between two oligonucleotide sequences called primers (*154,155*). The two primers form the ends of the sequence of DNA to be amplified and are normally referred to as the "forward" and "reverse" primers. The forward primer is complementary to the sense strand of the DNA template and is extended 5′ to 3′ along the DNA by DNA polymerase enzyme (Fig. 27). The reverse primer is complementary to the antisense strand of the DNA template and is normally situated 200–500 base pairs downstream from the forward primer, although much longer sequences (up to 50 kbase) can now be amplified by PCR. The process employs a thermostable DNA polymerase enzyme (such as the Taq polymerase from *Thermus aquaticus* BM) extracted from bacteria found in hot water sources, such as thermal pools or deep-water vents. These enzymes are not destroyed by repeated incubation at 94 °C, the temperature at which all double stranded DNA denatures or melts to its two separate strands (*155*).

The first step of a PCR involves DNA denaturation at 90–95 °C, in a buffered, neutral, aqueous solution containing DNA polymerase, the four deoxynucleotide triphosphates and Mg^{++}, in the presence of a large excess of the two primers (Fig. 27). In the second step, the temperature of the reaction is lowered to about 10 °C below the melting temperature of the primers and the primers (which are considerably smaller than the DNA) are allowed to hybridize to their complementary sequence on the DNA template molecule. This temperature is still too high for the DNA to fully renature. The temperature is then raised to 72 °C, the optimal temperature for extension of the primers by the DNA polymerase, which catalyses the addition of nucleotide triphosphates to extend the sequence in each direction from the

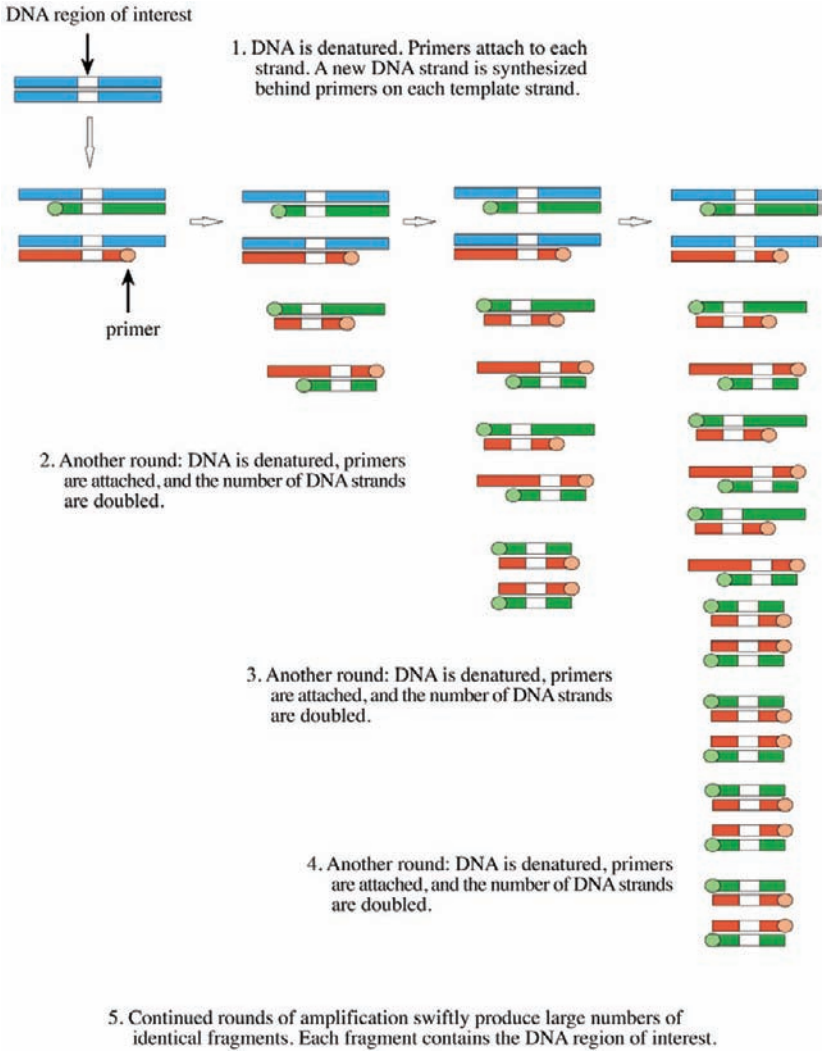

FIG. 27. The polymerase chain reaction. DNA amplification with a thermostable DNA polymerase enzyme.

forward and reverse primers, making complementary strands towards the other primer (Fig. 27). After one cycle of denaturation, annealing and primer extension, the sequence between the two primers has been doubled. The first cycle yields new DNA that extends beyond the position of the second primer in both directions, but in the second

and subsequent cycles the concentration of DNA bounded at both ends by the two primer sequences becomes much greater than that of DNA bounded only at one end, so effectively the concentration of these molecules become insignificant in the final PCR product. Repeat cycling of the reaction 30–35 times in a thermocycler results in the amplification of the desired sequence as much as a million times. The DNA can then be visualized on an agarose gel with ethidium bromide, and used for further manipulations (*155*). The PCR can also be used to analyze amounts of specific mRNA species, but the mRNA is first converted to cDNA with reverse transcriptase, as the DNA polymerase only recognizes deoxyribonucleotides and cannot extend a hybridized primer on mRNA (*154*).

3. Detection of Specific Sequences by Gene Probe Hybridization

A labeled gene probe (nucleic acid probe) is required to detect a specific gene sequence or mRNA species. Hybridization (binding) of the labeled gene probe to the target on solid supports or within tissue, allows visualization of the specific gene or mRNA species. The specific recognition component in a labeled gene probe may be single- or double-stranded DNA, single-stranded RNA, or an oligonucleotide sequence of the gene to be visualized. The visualization component is an integral part of this recognition component as it is synthesized from labeled nucleotides (see Section V.B.3.a), typically in one of two ways: by enzymatic synthesis in a neutral, buffered, aqueous solution, of copies of the gene probe sequence with labeled nucleotides, or by enzymatic incorporation of labeled nucleotides at the ends of the gene probe sequence (Fig. 28).

a. Labeling and detection of gene probes Modern DNA labeling techniques must be safe, fast, specific, and sensitive. Various methods have been devised as alternatives to radioisotope labels, but no single label has yet emerged as an ideal replacement (*5*). The radioisotopes still commonly used to label nucleic acid probes are ^{32}P, ^{33}P, ^{14}C, and ^{35}S, incorporated into a nucleotide triphosphate (NTP), such as ATP or CTP (Fig. 29). For the production of radio-labeled RNA probes ("riboprobes"), the RNA-specific NTP, UTP, is used. Radioactive nucleotides such as ^{32}P-deoxy-ATP or ^{33}P-UTP are available commercially (*108*). These radiolabels have great sensitivity, but are difficult to work with, because of their short half life and safety risks. Methods of non-radioactive labeling have now been developed and biotin,

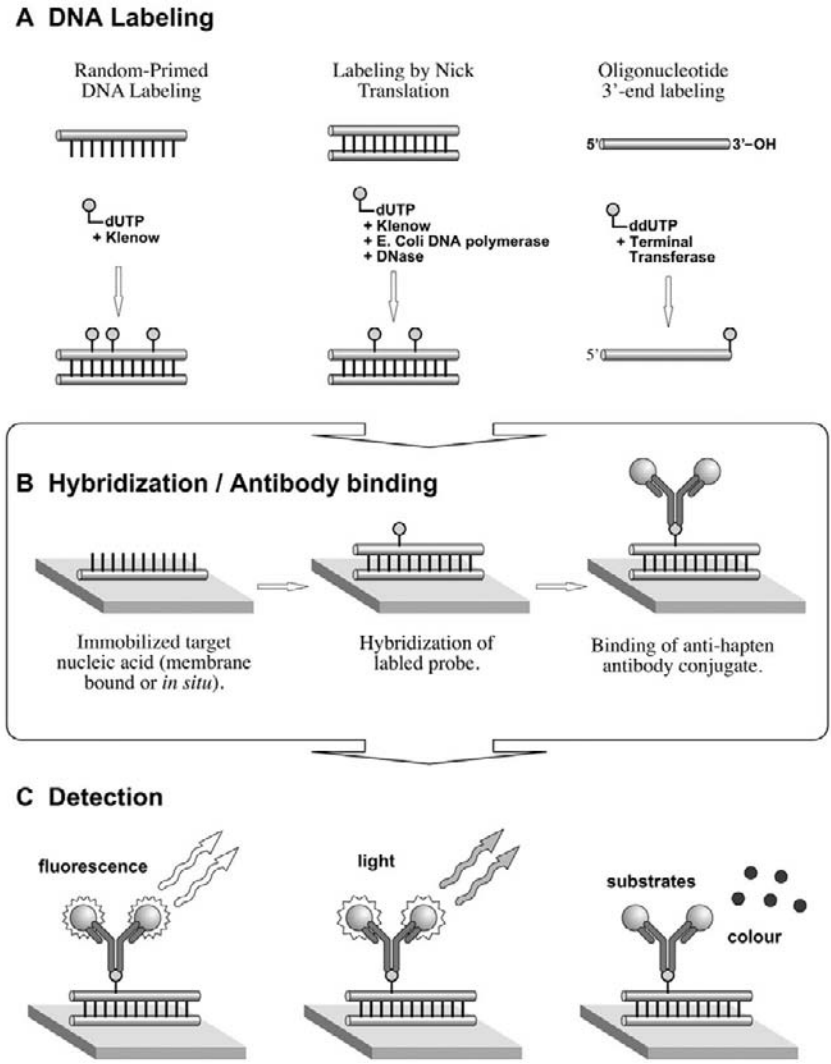

FIG. 28. Synthesis of labeled DNA probes. A: Labeled DNA can be generated using different enzymes (Klenow fragment of DNA polymerase or a terminal transferase) to incorporate labeled nucleotides into specific DNA sequences. Probes can be labeled using radioactive nucleotides or nucleotides labeled with an immunogenic molecule such as biotin. B: The labeled probe is then hybridized to the target nucleic acid, which is either bound to a membrane or in a tissue section or cell. An antibody is then used to detect the non-radioactively-labeled probe. C: The antibody may be conjugated to a fluorescent or chemiluminescent dye, or an enzyme that produces a color reaction. The target nucleic acid is thus visualized.

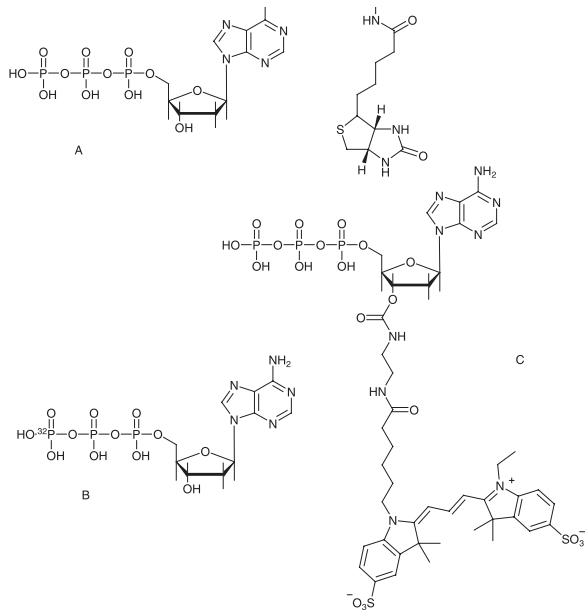

FIG. 29. Structure of a variety of labeled nucleotides. A: biotin-labeled UTP; B: Gamma labeled ^{32}P-ATP; C: The ribose-modified fluorescent ATP analogue, Cy3-EDA-ATP, which was synthesized by conjugating Cy3 reactive dye with 2′(3′)-*O*-[*N*-(2-aminoethyl)carbamoyl] ATP (EDA-ATP).

fluorescein and digoxigenin are now used regularly in antibody-based replacements for radio-labeled probes (*156–158*). Figure 29 illustrates the structures of three commonly labeled NTPs (gene probes typically consist of 50–60% G and C).

Whereas radio-labeled probes are detected by autoradiography or imaging with instruments capable of detecting the particles emitted by radioactive decay, non-radioactive labels can be detected either directly or indirectly. Fluorochromes, such as fluorescein, may be detected directly using imaging systems capable of detecting fluorescence. Alternatively, specific antibodies can be used to detect both fluorescent species and non-radioactive labels such as digoxigenin (Fig. 30). The antibody recognizes the label incorporated into the nucleic acid probe (*159*). Antibody systems involving more than one antibody, can also be used to amplify the signal from the probe. Normally the secondary antibody is directly coupled to an enzyme, so that addition of the enzyme substrate leads to the production of a colored product (Fig. 28).

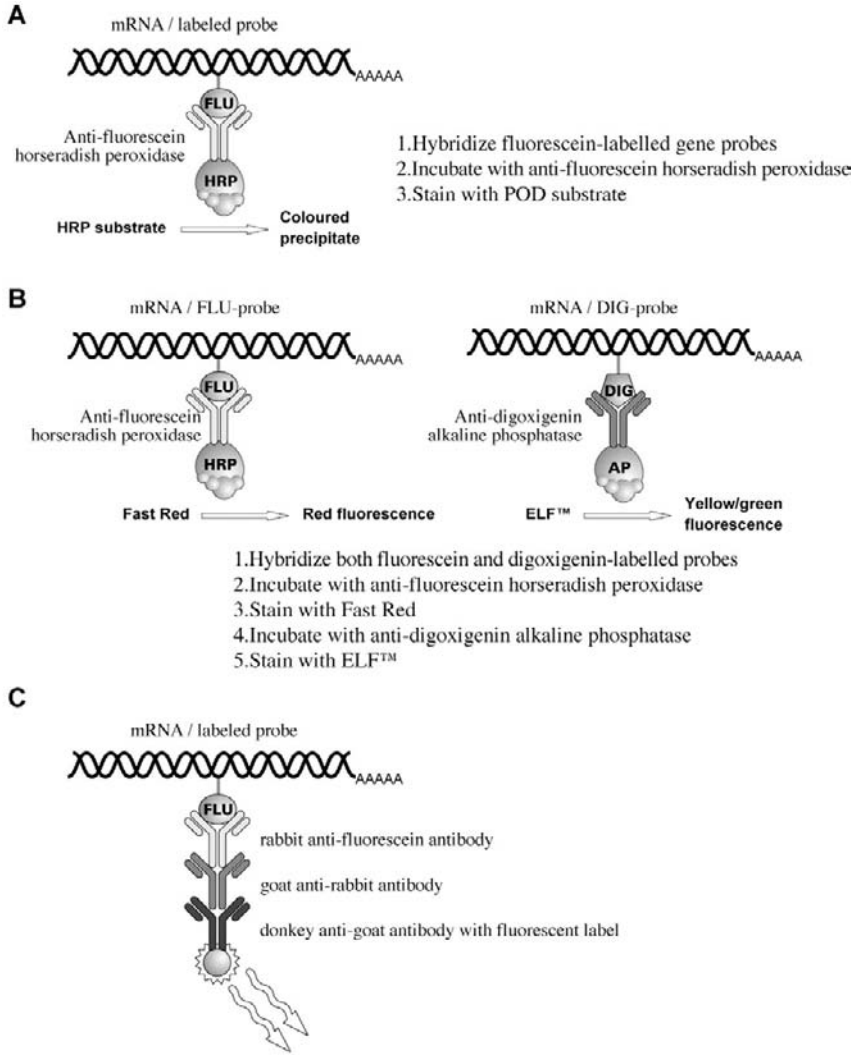

FIG. 30. Detection of mRNA on a membrane or in situ with labeled gene probes. A: Detection of mRNA with a fluorescein-labeled single stranded nucleic acid probe, using POD-conjugated anti-fluorescein antibody. B: Use of two gene probes labeled with different molecules (fluorescein and digoxigenin) and detected with specific antibodies, both coupled to AP and using two substrates, leading to differently colored products. This in situ hybridization scheme allows the simultaneous detection of two mRNA species in a tissue or cell preparation. C: Amplification systems involving more than one antibody can be used to increase specificity and signal intensity.

Chemiluminescent labeling systems have been developed, based on the incorporation of fluorescein-11-dUTP into a DNA probe. An anti-fluorescein antibody covalently bound to the enzyme HRP is then bound to the incorporated fluorescein label. HRP catalyses the breakdown of luminol and the chemiluminescent signal is detected by autoradiography with X-ray film or by fluorescence scanning instrumentation. Chemiluminescence is more sensitive than enzyme-based color detection systems. Furthermore the labeled gene probes are stable and give results quickly (*160*).

Similar systems have been developed using fluorescent cyanine dyes conjugated to nucleotide triphosphate structures (Fig. 29C). Commercially available systems enable the generation of high-quality fluorescent probes for micro-array hybridizations of thousands of gene sequences. By incorporating different colored dyes into the cDNA probes derived from two different populations (for example, control cells and treated cells) and simultaneously hybridizing both probes to a micro-array of all the genes in the human genome, a picture can be derived of the differences in gene expression in the two cell populations (*123*).

Lanthanide-labeled oligonucleotide probes are now available commercially (*161*). Oligonucleotides are synthesized containing free amino groups, which are then labeled with a lanthanide chelate via a Schiff base conjugation [similar to the reaction shown in Fig. 19 but with a monoaldehyde functional group (linker) of a lanthanide complex in place of glutaraldehyde].

b. Time-resolved fluorometry PCR assays PCR has been used extensively to increase our ability to detect small amounts of a specific gene sequence, whether for mutation screening of neonatal blood samples or for the detection of viral infection. A number of researchers (*162–164*) have combined time-resolved fluorometry using lanthanide chelates as luminescent labels, with gene amplification by PCR, to detect specific sequences with accuracy and sensitivity. The methods employed often use biotinylated PCR primers so that the resulting amplified DNA sequence can be captured on streptavidin-coated microtitre wells. The immobilized PCR product is then hybridized to lanthanide-labeled oligonucleotide probes. Measurement of luminescence after a time delay highly increases the sensitivity of the assays, improves the interpretation of borderline PCR results and allows automation of the assay. Time-resolved fluorometry is now being used increasingly for real-time, quantitative PCR (*165,166*).

4. Real-time Gene Expression Analysis

The PCR described above has now been automated to allow accurate quantitation of the amplification of a specific DNA sequence. In the simplest form of "real-time" PCR, fluorescent dyes such as SYBR Green are added to the PCR, which fluoresce when intercalated in the DNA structure. As the amount of DNA increases, the amount of fluorescence increases in parallel. The LightCycler system available from Roche Applied Science (*167–173*) uses glass capillaries to hold the amplification reaction, allowing rapid transition between temperatures, as well as the concentration and collection of light signals from the top of the capillary. During thermal cycling, reactions are monitored continuously on-line and the kinetics of the reaction, including the melting temperature of the resultant amplicon (a characteristic of its specific sequence) and the amount of amplicon at any time are automatically calculated. The Applied Biosystems Taqman system uses a specific, dual-labeled probe sequence that hybridizes to the target sequence between the two primers. Energy transfer between the two fluorescent dyes on the probe – a reporter dye and a quencher dye – prevents fluorescent emission. As the DNA polymerase extends the sequence from the primer during the PCR, it displaces and degrades the central probe, thus separating the quencher dye from the reporter and allowing emission. Each time a new copy of the cDNA is produced the amount of fluorescence increases (*174–183*). A variation on this idea involves the use of two internal probes, one labeled at one end with one fluorophore and the other labeled at the opposite end with a second fluorophore, such that the two probes lie next to each other when hybridized to the target sequence. When juxtaposed, fluorescence resonance energy transfer occurs between the two fluorophores and light is emitted. The emitted fluorescence is proportional to the amount of target sequence in the mix.

Real-time RNA analysis is also possible by these methods, once the RNA species have been converted to cDNA using reverse transcription. Thermostable reverse transcriptase enzymes are now available commercially, allowing one-step reverse transcription and DNA amplification (*184–187*).

5. In situ Hybridization

Labeled gene probes can also be used to detect specific genes or mRNA in tissue sections or in chromosome spreads. This technique is known as in situ hybridization. The detection of specific genes or gene

clusters on chromosomes, with a range of large gene probes labeled with different fluorescent dyes (Fluorescence In Situ Hybridization or FISH) has been termed "chromosome painting". Radio-labeled gene probes are not used for gene detection on chromosomes, because of the scatter of the radioactive particles under the microscopic magnification required for detection.

In situ hybridization in tissue sections allows the visualization of the production of a known mRNA by specific cells. This method has become a key technique in gene expression analysis, as it allows the investigator to identify the cells (often in a complex tissue structure) that contain a specific mRNA. Radio-labeled probes have the sensitivity required for detection of rare mRNA species (*135*), but non-radioactive labels are being used increasingly. The use of an antibody system to detect a molecule (antigen) incorporated into the gene probe allows amplification of a weak signal and increases the specificity of detection (Fig. 30). The antibodies used for detection are conjugated either to enzymes such as AP or HRP, or to fluorophores. Antibodies conjugated to enzymes, which are bound to nucleic acids, can be visualized with chromogenic or fluorescent substrates. The use of different antigen molecules and detection systems allows the simultaneous detection of more than one mRNA species (*159*).

6. Requirements for any New Generation of Labels

Any new labeling system for nucleic acid characterization will require the following properties. Primarily the label will need to give a strong enough signal for the specific detection of a nucleic acid at a very low concentration in a complex mixture of others, with a decreased likelihood of non-specific labeling. The label would have to be competitive, price-wise, with the radioactive and other non-radioactive labels available currently. It would need to be safe to handle and non-toxic to cells – both those of the user and those under investigation. The label would need to be stable, with the ability for labeled molecules to be stored without degradation for years, rather than weeks. The possibility of a variety of different labels (i.e., different colors) would be an advantage in automated multiplex applications with multiple labels. Finally, any new labeling system would need to be compatible with other labeling systems and with the methods of analysis used in current and future molecular biology.

An ability to be taken up into living cells and activated by some external signal, to study DNA replication in vivo for example, would confer a considerable advantage over other labels (*188–190*).

New methods for in vivo measurement of gene expression are appearing regularly. Imaging of endogenous gene expression in living cells or the whole animal requires special marker genes that encode either cell surface receptors or intracellular enzymes. These gene products can be targeted by high affinity imaging labels that bind to the receptor or enzyme, evoking a reaction that can be detected by magnetic resonance or bioluminescent imaging (*191–193*). Intracellular monitoring requires both the expression of the marker gene only in the cells of interest, and the ability of the label to penetrate the cells. Use of a cell surface receptor removes the need for the label to cross the membrane. These new methods are being used to follow the interactions of proteins within cells in real time and also for the monitoring of gene delivery in the development of gene therapies (*191,193*).

C. Suitable Linker Groups

For the two types of biological target molecules, different classes of receptor groups are required. For applications involving the labeling of DNA, functional groups that can either intercalate the DNA strands through π-stacking interactions, or can be covalently bonded to the DNA (either through the phosphate sugar backbone or directly to the bases themselves) are required. Protein recognition requires covalent bonds (referred to in biochemistry as conjugation) to be made to a chemically accessible part of the protein. Many of the linker groups employed in attaching labels by covalent bond formation have been presented in the previous sections, V.A. and V.B. Here some additional examples of labeling methods for DNA are presented and the labeling of proteins is summarized.

1. Detection of DNA

A number of aromatic groups are known to intercalate DNA. Among these are tetraazatriphenylenes, which have been shown to bind to the minor groove of DNA. These functional groups have been incorporated into a luminescent lanthanide complex (*71*), where it serves not only to bind to DNA, but also acts as the antenna ligand. As a consequence of this, intercalation prevents luminescence by quenching the ligand excited state (*194*).

If designed the other way around systems which involve quenching can be very useful. Incorporating a quenching unit into the label that

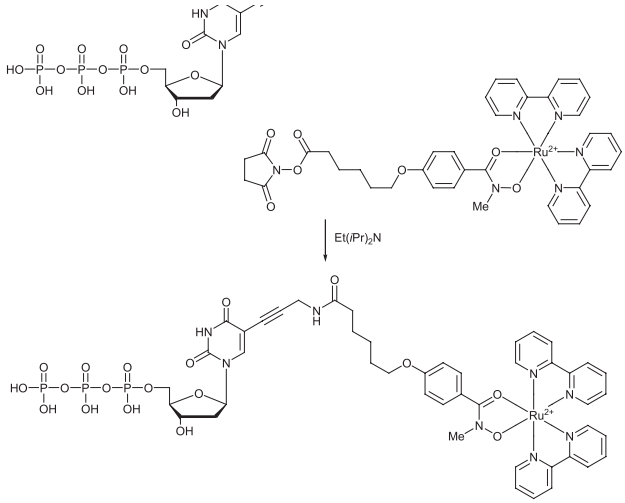

FIG. 31. Connection of 5-(3″-aminopropynyl)-2′-deoxyuridine-5′-triphosphate to the succinimide active ester arm of a ruthenium polypyridyl complex.

is turned off (i.e., no longer quenches the luminescent part of the label) on conjugation, intercalation or combination of DNA strands, a more positive result can be obtained (*195*). The same effect is achieved by elimination of the quenching unit (*196*).

Tor and co-workers have developed a strategy for appending ruthenium(II) and osmium(II) polypyridyl complexes to nucleotides, by using succinimide esters as shown in Fig. 31 (*197*). These have been shown to incorporate into DNA without altering the global conformation, and still exhibit metal-centered luminescence (*198*).

2. Protein Conjugation

In conjugating (covalently bonding) a luminescent label to a protein [including, in many cases avidin or streptavidin for subsequent conjugation to biotinylated biomolecules (*5,62*)], chemically accessible groups in the protein are targeted. The most common among these is an amine group in a lysine residue, although the thiol groups in cysteine can also be targeted. Both of these can be achieved with, for example, the use of activated ester groups such N-succinimide esters, iodide or isothiocyanates (*7,11,62*).

VI. Concluding Remarks

The key advantage that lanthanide labels have over other types of fluorescent labels is that time resolved techniques can be employed, allowing fluorescence from the surrounding biological medium to dissipate before detection of the long lived lanthanide phosphorescence. The safety advantages they have over radioactive labels are clear.

Lanthanide label kits are commercially available and will become more and more widely used as the nature of the visibly luminescent europium (red) and terbium (green) complexes utilized is optimized. Significant growth can also be expected in the development of lanthanide labels based on neodymium and ytterbium as their luminescence in the NIR, whilst of shorter lifetimes and requiring specialist detection equipment, is at a wavelength where tissue is optimally transparent, making in vivo uses a distinct possibility.

VII. Glossary

antibody	generated by the immune system in response to the presence of an antigen, a glycoprotein which can be used for the recognition of a specific protein (antigen) or hapten
antigen	foreign molecule recognized by immune system as non-self
AP	alkaline phosphatase (an enzyme)
ATP	adenosine triphosphate
blot	separated protein, DNA, or RNA immobilized by covalent binding to a nitrocellulose or nylon membrane
cDNA	complementary DNA
clones	families of cells with identical DNA
conjugate	link by covalent bond
DELFIA	dissociation-enhanced lanthanide fluoroimmunoassay
DNA	deoxyribonucleic acid
ELISA	enzyme-linked immunosorbent assay, an immunoassay in a multiwell plate formation
epitope	binding site on an antigen
FISH	fluorescent in situ hybridization, to identify specific genes on chromosomes or mRNA species in cells or tissues

fluorescence	emission resulting from relaxation to the ground state from an excited state of the same multiplicity (e.g., S_1 to S_0), that ceases almost immediately (cf. phosphorescence) after removal of the excitation source
gene probe	nucleic acid probe, a known gene sequence, used for recognition of a specific gene or mRNA
GTP	guanosine triphosphate one of the four nucleotide bases that make up DNA
hapten	small, non-immunogenic molecule e.g., steroid hormones, neurotransmitters, other organic molecules
HRP	horse radish peroxidase (an enzyme)
hybridization	binding of single strand of DNA, or RNA, to its complementary sequence
immunoassay	competitive binding assay for molecules (antigens) in solution
immunocytochemistry	protein detection in cell cultures or suspensions, using an antibody
immunohistochemistry	protein detection in tissue sections, using an antibody
linker	functional group within the label which is used to covalently attach the label to target biomolecule
luminescence	general term for emission resulting from relaxation from an excited state (see also fluorescence and phosphorescence)
mRNA	messenger RNA, single stranded nucleic acid transcribed from the DNA
monoclonal antibody	single immunoglobulin (antibody) produced by a clone of immortalized B-lymphocytes
multiwell plate	plastic dish containing a variable number of indentations or wells, used in multi-sample assays
northern blot	size-separated RNA, immobilized on a nitrocellulose or nylon membrane
NTP	nucleotide triphosphate
nucleic acid probe	see gene probe
PCR	polymerase chain reaction; method which generates many copies of a specific DNA sequence
phosphorescence	emission resulting from relaxation to the ground state from an excited state of different

	multiplicity (e.g., T_1 to S_0), that may persist for relatively long periods (cf. fluorescence) after removal of the excitation source
polyclonal antibodies	mixture of immunoglobulins
receptor	binding group or site (a) links label to biomolecule (*Chem*) or (b) hormone, neurotransmitter or growth factor binding protein (*Biochem*)
riboprobe	labeled RNA probe
RNA	ribonucleic acid; normally single stranded
Southern blot	size-separated DNA, immobilized on a nitrocellulose or nylon membrane
UTP	uridine triphosphate
western blot	size-separated proteins, immobilized on a nitrocellulose or nylon membrane

Acknowledgments

We thank the Royal Society (UK) for a postdoctoral fellowship (GRM) and the University of Otago for a research grant. We are grateful to Michael Crawford for production of biological artwork, Jesse Gale for technical advice on radio-iodination of proteins, Drs Sarah L. Heath and David S. Larsen for helpful discussions, Drs Sally P.A. McCormick, Stephen Faulkner, and Wolfgang Mohr for critically reading this manuscript, Tanya K. Ronson for her help with the references and Dr Katie Heslop for additional help with manuscript production.

References

1. Parker, D.; Dickins, R. S.; Puschmann, H.; Crossland, C.; Howard, J. A. K. Being excited by lanthanide coordination complexes: aqua species, chirality, excited-state chemistry, and exchange dynamics. *Chem. Rev.* **2002**, *102*, 1977–2010.
2. Bünzli, J.-C. G.; Piguet, C. Lanthanide-containing molecular and supramolecular polymetallic functional assemblies. *Chem. Rev.* **2002**, *102*, 1897–1928.
3. Sabbatini, N.; Guardigli, M.; Lehn, J.-M. Luminescent lanthanide complexes as photochemical supramolecular devices. *Coord. Chem. Rev.* **1993**, *123*, 201–228.
4. Sabbatini, N.; Guardigli, M.; Manet, I. Lanthanide complexes of encapsulating ligands as luminescent devices. *Adv. Photochem.* **1997**, *23*, 213–278.
5. Sammes, P. G.; Yahioglu, G. Modern bioassays using metal chelates as luminescent probes. *Nat. Prod. Rep.* **1996**, 1–28.
6. Faulkner, S.; Matthews, J. L. Fluorescent and Luminescent Complexes for Biomedical Applications, "*Comprehensive Coordination Chemistry II*", Vol. 9; Eds. McCleverty, J.; Meyer, T. J.; Pergamon, 2003, p. in press, in press.
7. Yam, V. W.-W.; Lo, K. K.-W. Recent advances in utilization of transition metal complexes and lanthanides as diagnostic tools. *Coordi. Chem. Rev.* **1998**, *184*, 157–240.

8. Selvin, P. R. Principles and biophysical applications of lanthanide-based probes. *Annu. Rev. Biophys. Biomol. Struct.* **2002**, *31*, 275–302.

9. Inanaga, J.; Furuno, H.; Hayano, T. Asymmetric catalysis and amplification with chiral lanthanide complexes. *Chem. Rev.* **2002**, *102*, 2211–2225.

10. Bünzli, J.-C. G.; Choppin, G. R. Lanthanide probes in life, chemical, and earth sciences: theory and practice. Elsevier: New York; ISBN: 0-444-88199-9.

11. Lamture, J. B.; Wensel, T. G. A novel reagent for labeling macromolecules with intensely luminescent lanthanide complexes. *Tetrahedron Lett.* **1993**, *34*, 4141–4144.

12. Price, C. P.; Newman, D. J. *"Principles and Applications of Immunoassay"*, 2nd edn.; Macmillan Reference. ISBN: 0-333-62504-8.

13. Schepartz, A.; Kim, P. S. Interaction, assembly and processing at the chemistry–biology interface. *Curr. Opin. Chem. Biol.* **1998**, *2*(1), 9–10.

14. Benkovic, S. J.; Walsh, C. T. Mechanisms research highlights at the chemistry–biology interface. *Curr. Opin. Chem. Biol.* **1999**, *3*(5), 571–572.

15. Parker, D. Targeting metal complexes. *Chem. Britain* **1994**, 818–822.

16. Parker, D.; Williams, J. A. G. Getting excited about lanthanide complexation chemistry. *J. Chem. Soc., Dalton Trans.* **1996**, 3613–3628.

17. Klink, S. I.; Hebbik, G. A.; Grave, L.; Peters, F. G. A.; Van Veggel, F. C. J. M.; Reinhoudt, D. N.; Hofstraat, J. W. Near-infrared and visible luminescence from terphenyl-based lanthanide(III) complexes bearing amido and sulfonamido pendant arms. *Eur. J. Org. Chem.* **2000**, 1923–1931.

18. Caravan, P.; Ellison, J. J.; McMurry, T. J.; Lauffer, R. B. Gadolinium(III) chelates as MRI contrast agents: structure, dynamics, and applications. *Chem. Rev.* **1999**, *99*(9), 2293–2352.

19. See for example *Topics in Current Chemistry*, Volume 221 – Contrast Agents I.

20. Carnall, W. T. The absorption and fluorescence spectra of rare earth ions in solution, "*Handbook on the Physics and Chemistry of the Rare Earths*", Vol. 4; Eds. Gschneider K. A., Jr.; Eyring, L.; North-Holland Publishing Company: Amsterdam, 1979, pp. 171–208.

21. Latva, M.; Takalo, H.; Mukkala, V.-M.; Matachescu, C.; Rodríguez-Ubis, J.-C.; Kankare, J. Correlation between the lowest triplet state energy level of the ligand and lanthanide(III) luminescence quantum yield. *J. Luminesc.* **1997**, *75*, 149–169.

22. Horrocks, W. de W. Jr.; Sudnick, D. R. Lanthanide ion probes of structure in biology. Laser-induced luminescence decay constants provide a direct measure of the number of metal-coordinated water molecules. *J. Am. Chem. Soc.* **1979**, *101*(2), 334–340.

23. Holz, R. C.; Allen Chang, C.; Horrocks, W. De W. Jr. Spectroscopic characterization of the europium(III) complexes of a series of N,N′-bis(carboxymethyl macrocyclic ether bis(lactones). *Inorg. Chem.* **1991**, *30*, 3270–3275.

24. Beeby, A.; Clarkson, I. M.; Dickins, R. S.; Faulkner, S.; Parker, D.; Royle, L.; de Sousa, A. S.; Williams, J. A. G.; Woods, M. Non-radiative deactivation of the excited states of europium, terbium and ytterbium complexes by proximate energy-matched OH, NH and CH oscillators: an improved luminescence method for establishing solution hydration states. *J. Chem. Soc., Perkin Trans. 2* **1999**, (3), 493–503.

25. Supkowsky, R. M.; Horrocks, de W. On the determination of the number of water molecules, q, coordinated to europium(III) ions in solution from luminescence decay lifetimes. *Inorg. Chim. Acta* **2002**, *340*, 44–48.

26. Haas, Y.; Stein, G. Pathways of radiative and radiationless transitions in europium(III) solutions: role of solvents and anions. *J. Phys. Chem.* **1971**, *75*(24), 3668–3677.

27. Quici, S.; Marzanni, G.; Cavazzini, M.; Anelli, P. L.; Botta, M.; Gianolio, E.; Accorsi, G.; Armaroli, N.; Barigelletti, F. Highly luminescent Eu^{3+} and Tb^{3+} macrocyclic complexes bearing an appended phenanthroline chromophore. *Inorg. Chem.* **2002**, *41*, 2777–2784.

28. Xiao, M.; Selvin, P. R. Quantum yields of luminescent lanthanide chelates and far-red dyes measured by resonance energy transfer. *J. Am. Chem. Soc.* **2001**, *123*, 7067–7073.

29. Zucchi, G.; Ferrand, A.-C.; Scopelliti, R.; Bünzli, J.-C. G. Highly luminescent, visible-emitting lanthanide macrocyclic chelates stable in water and derived from the cyclen framework. *Inorg. Chem.* **2002**, *41*, 2459–2465.

30. Beeby, A.; Bushby, L. M.; Maffeo, D.; Williams, J. A. G. Intramolecular sensitisation of lanthanide(III) luminescence by acetophenone-containing ligands: the critical effect of para-substituents and solvent. *J. Chem. Soc., Dalton Trans.* **2002**, 48–54.

31. Sato, S.; Wada, M. Relations between intramolecular energy transfer efficiences and triplet energies in rare earth beta-diketone chelates. *Bull. Chem. Soc. Japan* **1970**, *43*, 1955.

32. Brunet, E.; Juanes, O.; Sedano, R.; Rodríguez-Ubis, J.-C. Lanthanide complexes of polycarboxylate-bearing dipyrazolylpyridine ligands with near-unity luminescence quantum yields: the effect of pyridine substitution. *Photochem. Photobiol. Sci.* **2002**, *1*, 613–618.

33. Jørgensen, C. K.; Reisfeld, R. Chemistry and spectroscopy of rare earths. *Top. Curr. Chem.* **1982**, *100*, 127–167.

34. Richardson, F. S. Terbium(III) and europium(III) ions as luminescent probes and stains for biomolecular systems. *Chem. Rev.* **1982**, *82*, 541–552.

35. Housecroft, C. E.; Sharpe, A. G. "*Inorganic Chemistry*", 1st edn.; Pearson Education: Harlow, Essex, UK, 2001. ISBN: 0-582-31080-6.

36. Su, C.-Y.; Kang, B.-S.; Mu, X.-Q.; Sun, J.; Tong, Y.-X.; Chen, Z.-N. Studies on lanthanide complexes of the tripodal ligand tris(benzimidazol-2-ylmethyl)amine (ntb). Crystal structures of $[Ln(ntb)(NO_3)_3]\cdot H_2O$ (Ln = Ce, Er). *Aust. J. Chem.* **1998**, *51*(7), 565–571.

37. Yang, X.-P.; Su, C.-Y.; Kang, B.-S.; Feng, X.-L.; Xiao, W.-L.; Liu, H.-Q. Studies on lanthanide complexes of the tripodal ligand bis(2-benzimidazolylmethyl)(2-pyridylmethyl)amine. Crystal structures and luminescence properties. *J. Chem. Soc., Dalton Trans.* **2000**, (19), 3253–3260.

38. Su, C.-Y.; Kang, B.-S.; Liu, H.-Q.; Wang, Q.-G.; Mak, T. C. W. Construction of two- and three-dimensional supramolecular networks with an encapsulated lanthanide(III) complex as building block and hydrogen-bonded 4,4′-bipyridyl as spacer. *Chem. Commun.* **1998**, (15), 1551–1552.

39. Su, C.-Y.; Kang, B.-S.; Liu, H.-Q.; Wang, Q.-G.; Chen, Z.-N.; Lu, Z.-L.; Tong, Y.-X.; Mak, T. C. W. Luminescent lanthanide complexes with encapsulating polybenzimidazole tripodal ligands. *Inorg. Chem.* **1999**, *38*(7), 1374–1375.

40. Yang, X.-P.; Kang, B.-S.; Wong, W.-K.; Su, C.-Y.; Liu, H.-Q. Synthesis, crystal structures, and luminescent properties of lanthanide complexes with tripodal ligands bearing benzimidazole and pyridine groups. *Inorg. Chem.* **2003**, *42*, 169–179.

41. Kanesato, M.; Yokoyama, T. Synthesis and structural characterisation of Ln(III) complexes (Ln = Eu, Gd, Er, Tm, Lu) of tripodal tris[2-(salicylideneamino)ethyl] amine. *Chem. Lett.* **1999**, 137–138.

42. Bernhardt, P. V.; Flanagan, B. M.; Riley, M. J. Isomorphous lanthanide complexes of a tripodal N_4O_3 ligand. *Aust. J. Chem*. **2000**, *53*, 229–231.
43. Casellato, U.; Tamburini, S.; Tomasin, P.; Vigato, P. A.; Botta, M. Lanthanide(III) complexes with a podand Schiff base containing an N_4O_3 coordination site. *Inorg. Chim. Acta* **1996**, *247*, 143–145.
44. Costes, J.-P.; Dupuis, A.; Commenges, C.; Lagrave, S; Laurent, J.-P. Mononuclear lanthanide complexes of tripodal ligands: synthesis and spectroscopic studies. *Inorg. Chim. Acta* **1999**, *285*, 49–54.
45. Mizukami, S.; Houjou, H.; Kanesato, M.; Hiratani, K. Adjustment of twist angles in pseudo-helical lanthanide complexes by the size of metal ions. *Chem. Eur. J.* **2003**, *9*, 1521–1528.
46. Marques, N.; Sella, A.; Takats, J. Chemistry of the lanthanides using pyrazolylborate ligands. *Chem. Rev*. **2002**, *102*(6), 2137–2159.
47. Jones, P. L.; Amoroso, A. J.; Jeffery, J. C.; McCleverty, J. A.; Psillakis, E.; Rees, L. H.; Ward, M. D. Lanthanide complexes of the hexadentate N-donor podand tris[3-(2-pyridyl)pyrazolyl]hydroborate: solid-state and solution properties. *Inorg. Chem*. **1997**, *36*(1), 10–18.
48. Armaroli, N.; Balzani, V.; Barigelletti, F.; Ward, M. D.; McCleverty, J. A. Luminescence properties of Eu^{3+}, Tb^{3+} and Gd^{3+} complexes of the hexadentate N-podand tris-[3-(2-pyridyl)pyrazol-1yl]hydroborate. *Chem. Phys. Lett*. **1997**, *276*, 435–440.
49. Armaroli, N.; Accorsi, G.; Barigelletti, F.; Couchman, S. M.; Fleming, J. S.; Harden, N. C.; Jeffery, J. C.; Mann, K. L. V.; McCleverty, J. A.; Rees, L. H.; Starling, S. R.; Ward, M. D. Structural and photophysical properties of mononuclear and dinuclear lanthanide(III) complexes of multidentate podand ligands based on poly(pyrazollyl)borates. *Inorg. Chem*. **1999**, *38*, 5769–5776.
50. Reeves, Z. R.; Mann, K. L. V.; Jeffery, J. C.; McCleverty, J. A.; Ward, M. D.; Barigelletti, F.; Armaroli, N. Lanthanide complexes of a new sterically hindered potentially hexadentate podand ligand based on a tris(pyrazolyl)borate core; crystal structures, solution structures and luminescence properties. *J. Chem. Soc., Dalton Trans*. **1999**, 349–355.
51. Ulrich, G.; Hissler, M.; Ziessel, R.; Manet, I.; Sarti, G.; Sabbatini, N. Synthesis of novel podands bearing bipyridine or bipyridine-*N*,*N*′-dioxide chromophores and luminescence of their Eu^{3+} and Tb^{3+} complexes. *New J. Chem*. **1997**, *21*(2), 147–150.
52. Charbonnière, L.; Ziessel, R.; Guardigli, M.; Roda, A.; Sabbatini, N.; Cesario, M. Lanthanide tags for time-resolved luminescence microscopy displaying improved stability and optical properties. *J. Am. Chem. Soc*. **2001**, *123*, 2436–2437.
53. Døssing, A.; Toftlund, H.; Hazell, A.; Bourassa, J.; Ford, P. C. Crystal structure, luminescence and other properties of some lanthanide complexes of the polypyridine ligand 6,6′-bis[bis(2-pyridylmethyl)aminomethyl]-2,2′-bipyridine. *J. Chem. Soc., Dalton Trans*. **1997**, (3), 335–339.
54. Piguet, C.; Bünzli, J.-C. G.; Bernardinelli, G.; Hopfgartner, G.; Williams, A. F. Self-assembly and photophysical properties of lanthanide dinuclear triple-helical complexes. *J. Am. Chem. Soc*. **1993**, *115*, 8197–8206.
55. Martin, N.; Bünzli, J.-C. G.; McKee, V.; Piguet, C.; Hopfgartner, G. Self-assembled dinuclear lanthanide helicates: substantial luminescence enhancement upon replacing terminal benzimidazole groups by carboxamide binding units. *Inorg. Chem*. **1998**, *37*, 577–589.

56. Elhabiri, M.; Scopelliti, R.; Bünzli, J.-C. G.; Piguet, C. Lanthanide helicates self-assembled in water: a new class of highly stable and luminescent dimetallic carboxylates. *J. Am. Chem. Soc.* **1999**, *121*, 10747–10762.

57. Andre, N.; Scopelliti, R.; Hopfgarter, G.; Piguet, C.; Bünzli, J.-C. G. Discriminating between lanthanide ions: self-assembly of heterodimetallic triple-stranded helicates. *Chem. Commun.* **2002**, 214–215.

58. Bocquet, B.; Bernardinelli, G.; Ouali, N.; Floquet, S.; Renaud, F.; Hopfgartner, G.; Piguet, C. The first self-assembled trimetallic lanthanide helicate: different coordination sites in symmetrical molecular architectures. *Chem. Commun.* **2002**, 930–931.

59. Renaud, F.; Piguet, C.; Bernardinelli, G.; Bünzli, J.-C. G.; Hopfgartner, G. In search for mononuclear helical lanthanide building blocks with predetermined properties: lanthanide complexes with diethyl pyridine-2,6-dicarboxylate. *Chem. Eur. J.* **1997**, *3*(10), 1660–1667.

60. Charbonnière, L. J.; Ziessel, R.; Montalti, M.; Prodi, L.; Zaccheroni, N.; Boehme, C.; Wipff, G. Luminescent lanthanide complexes of a bis-bipyridine-phosphine-oxide ligand as tools for anion detection. *J. Am. Chem. Soc.* **2002**, *124*(26), 7779–7788.

61. Rodríguez-Ubis, J.-C.; Alonso, M. T.; Juanes, O.; Sedano, R.; Brunet, E. The discovery of a simple ligand based on acetophenone bearing excellent quantum yields for the excitation of Eu^{3+} and Tb^{3+}. *J. Lumin.* **1998**, *79*, 121–125.

62. Yuan, J.; Wang, G.; Majima, K.; Matsumoto, K. Synthesis of a terbium fluorescent chelate and its application to time-resolved fluoroimmunoassay. *Anal. Chem.* **2001**, *73*(8), 1869–1876.

63. Bardwell, D. A.; Jeffery, J. C.; Jones, P. L.; McCleverty, J. A.; Psillakis, E.; Reeves, Z. R.; Ward, M. D. Lanthanide complexes of the tetradentate N-donor ligand dihydrobis[3-(2-pyridyl)pyrazolyl]borate and the terdentate N-donor ligand 2,6-bis(1H-pyrazol-3-yl)pyridine: syntheses, crystal structures and solution structures based on luminescence lifetime studies. *J. Chem. Soc., Dalton Trans.* **1997**, 2079–2086.

64. Parker, D. Luminescent lanthanide sensors for pH, pO_2 and selected anions. *Coord. Chem. Rev.* **2000**, *205*, 109–130.

65. Gunnlaugsson, T.; Donall, A. M. D.; Parker, D. Luminescent molecular logic gates: the two-input inhibit (INH) function. *Chem. Commun.* **2000**, 93–94.

66. Beeby, A.; Bushby, L. M.; Maffeo, D.; Williams, J. A. G. The efficient intramolecular sensitisation of terbium(III) and europium(III) by benzophenone-containing ligands. *J. Chem. Soc., Perkin Trans. 2* **2000**, 1281–1283.

67. Dadabhoy, A.; Faulkner, S.; Sammes, P. G. Long wavelength sensitizers for europium(III) luminescence based on acridone derivatives. *J. Chem. Soc., Perkin Trans. 2* **2002**, (2), 348–357.

68. Dadabhoy, A.; Faulkner, S.; Sammes, P. G. Small singlet-triplet energy gap of acridone enables longer wavelength sensitization of europium(III) luminescence. *J. Chem. Soc., Perkin Trans. 2* **2000**, (12), 2359–2360.

69. Dickins, R. S.; Howard, J. A. K.; Lehmann, C. W.; Moloney, J.; Parker, D.; Peacock, R. D. Structural rigidity and luminescence of chiral lanthanide tetraamide complexes based on 1,4,7,10-tetraazacyclododecane. *Angew. Chem. Int. Ed.* **1997**, *38*, 521–523.

70. Zucchi, G.; Scopelliti, R.; Bünzli, J.-C. G. Importance of the chromophore orientation to the ligand-to-metal energy transfer in lanthanide complexes with pendant-arm fitted cyclen derivatives. *J. Chem. Soc., Dalton Trans.* **2001**, (13), 1975–1985.

71. Bobba, G.; Frias, J. C.; Parker, D. Highly emissive, nine-coordinate enantiopure lanthanide complexes incorporating tetraazatriphenylenes as probes for DNA. *Chem. Commun.* **2002**, 890.

72. Bornhop, D. J.; Hubbard, D. S.; Houlne, M. P.; Adair, C.; Kiefer, G. E.; Pence, B. C.; Morgan, D. L. Fluorescent tissue site-selective lanthanide chelate, Tb-PCTMB for enhanced imaging of cancer. *Anal. Chem.* **1999**, *71*(14), 2607–2616.

73. Fenton, D. E.; Vigato, P. A. Macrocyclic Schiff base complexes of lanthanides and actinides. *Chem. Soc. Rev.* **1988**, *17*, 69–90.

74. Fenton, D. E.; Kitchen, S. J.; Spencer, C. M.; Tamburini, S.; Vigato, P. A. Complexes of ligands providing endogenous bridges. Part 5. Solution studies on a novel '3 + 3' hexamine Schiff-base macrocyclic complex of lanthanum. *J. Chem. Soc., Dalton Trans.* **1988**, 685–690.

75. Howell, R. C.; Spence, K. V. N.; Kahwa, I. A.; White, A. J. P.; Williams, D. J. The preparation and crystal and molecular structures of new luminescent Schiff-base complexes featuring coupled lanthanide(III) cations. *J. Chem. Soc., Dalton Trans.* **1996**, 961–968.

76. Bastida, R.; de Blas, A.; Castro, P.; Fenton, D. E.; Macias, A.; Rial, R.; Rodríguez, A.; Rodríguez-Blas, T. Complexes of lanthanide(III) ions with macrocyclic ligands containing pyridine head units. *J. Chem. Soc., Dalton Trans.* **1996**, 1493–1497.

77. Wang, Z.; Reibenspies, J.; Martell, A. E. Design, synthesis and X-ray structural characterization of new dinucleating macrocyclic ligands and a novel phenolate-bridged dilanthanum(III) complex. *Inorg. Chem.* **1997**, *36*, 629–636.

78. Aspinall, H. C.; Black, J.; Dodd, I.; Harding, M. M.; Winkley, S. J. A lanthanide-templated Schiff-base condensation reaction to give a trinuclear macrocyclic complex. *J. Chem. Soc., Dalton Trans.* **1993**, 709–714.

79. Sabbatini, N.; Guardigli, M.; Manet, I.; Ziessel, R. Luminescent probes [involving calixarenes], "*Calixarenes 2001*"; Ed. Asfari, Z.; Kluwer Academic Publishers, 2001.

80. Sabbatini, N.; Guardigli, M.; Mecati, A.; Balzani, V.; Ungaro, R.; Ghidini, E.; Casnati, A.; Pochini, A. Encapsulation of lanthanide ions in calixarene receptors. A strongly luminescent terbium(3 +) complex. *J. Chem. Soc., Chem. Commun.* **1990**, (12), 878–879.

81. Iki, N.; Horiuchi, T.; Oka, H.; Koyama, K.; Morohashi, N.; Kabuto, C.; Miyano, S. Energy transfer luminescence of Tb^{3+} ion complexed with calix[4]arenetetrasulfonate and the thio and sulfonyl analogue. The effect of bridging groups. *J. Chem. Soc., Perkin Trans. 2* **2001**, 2219–2225.

82. Fischer, C.; Sarti, G.; Casnati, A.; Carrettoni, B.; Manet, I.; Schuurman, R.; Guardigli, M.; Sabbatini, N.; Ungaro, R. 2,2′-Bipyridine lariat calixcrowns: a new class of encapsulating ligands forming highly luminescent Eu^{3+} and Tb^{3+} complexes. *Chem. Eur. J.* **2000**, *6*(6), 1026–1034.

83. de Maria Ramírez, F.; Charbonnière, L.; Muller, G.; Scopelliti, R.; Bünzli, J.-C. G. A p-tert-butylcalix[4]arene functionalised at its lower rim with ether-amide pendant arms acts as an inorganic-organic receptor: structural and photophysical properties of its lanthanide complexes. *J. Chem. Soc., Dalton Trans.* **2001**, (21), 3205–3213.

84. Prodi, L.; Pivari, S.; Bolletta, F.; Hissler, M.; Ziessel, R. Synthesis of functionalized calix[4]arene ligands incorporating bipyridine N,N′-dioxide chromophores and luminescence of their lanthanide complexes. *Eur. J. Inorg. Chem.* **1998**, 1959–1965.

85. Casnati, A.; Baldini, L.; Sansone, F.; Ungaro, R.; Armaroli, N.; Pompei, D.; Barigelletti, F. Synthesis, complexation and photophysics in protic solvents of lanthanide complexes of novel calix[4]arene polycarboxylic-2,2′-bipyridine mixed ligands. *Supramol. Chem.* **2002**, *14*(2–3), 281–289.

86. Bkouche-Waksman, I.; Guilhem, J.; Pascard, C.; Alpha, B.; Deschenaux, R.; Lehn, J.-M. 110. Crystal structures of the lanthanum(III), europium(III), and terbium(III) cryptates of tris(bipyridine) macrobicyclic ligands. *Helv. Chim. Acta* **1991**, *74*, 1163–1170.

87. Alpha, B.; Ballardini, R.; Balzani, V.; Lehn, J.-M.; Perathoner, S.; Sabbatini, N. Antenna effect in luminescent lanthanide cryptates: a photophysical study. *Photochem. Photobiol*. **1990**, *52*(2), 299–306.

88. Prodi, L.; Maestri, M.; Balzani, V.; Lehn, J.-M.; Roth, C. Luminescence properties of cryptate europium(III) complexes incorporating heterocyclic N-oxide groups. *Chem. Phys. Lett*. **1991**, *180*, 45–50.

89. Galaup, C.; Azéma, J.; Tisnès, P.; Picard, C.; Ramos, P.; Juanes, O.; Brunet, E.; Rodríguez-Ubis, J.-C. Luminescence of Eu^{3+} and Tb^{3+} complexes of two macrobicyclic ligands derived from a tetralactam ring and a chromophoric antenna. *Helv. Chim. Acta* **2002**, *85*(6), 1613–1625.

90. Platas, C.; Avecilla, F.; de Blas, A.; Rodríguez-Blas, T.; Geraldes, C. F. G. C.; Toth, E.; Merbach, A. E.; Bünzli, J.-C. G. Mono and bimetallic lanthanide(III) phenolic cryptates obtained by template reaction: solid state structure, photophysical properties and relaxivity. *J. Chem. Soc., Dalton Trans*. **2000**, 611–618.

91. Avecilla, F.; de Blas, A.; Bastida, R.; Fenton, D. E.; Mahia, J.; Macías, A.; Platas, C.; Rodríguez, A.; Rodríguez-Blas, T. The template synthesis and X-ray structure of the first dinuclear lanthanide(III) iminophenolate cryptate. *Chem. Commun*. **1999**, 125–126.

92. Rodríguez-Cortiñas, R.; Avecilla, F.; Platas-Iglesias, C.; Imbert, D.; Bünzli, J.-C. G.; de Blas, A.; Rodríguez-Blas, T. Structural and photophysical properties of heterobimetallic 4f-Zn iminophenolate cryptates. *Inorg. Chem*. **2002**, *41*(21), 5336–5349.

93. Dickins, R. S.; Gunnlaugsson, T.; Parker, D.; Peacock, R. D. Reversible anion binding in aqueous solution at a cationic heptacoordinate lanthanide centre: selective bicarbonate sensing by time-delayed luminescence. *Chem. Commun*. **1998**, *16*, 1643–1644.

94. Matthews, K. D.; Kahwa, I. A.; Williams, D. J. Preparation, structure, and luminescence of dinuclear lanthanide complexes of a novel imine-amine phenolate macrocycle. *Inorg. Chem*. **1994**, *33*, 1382–1387.

95. Costes, J.-P.; Dahan, F.; Dupuis, A.; Lagrave, S.; Laurent, J.-P. Homo- (4f, 4f) and Heterodimetallic (4f, 4f') Complexes. The first structurally characterized example of a heterodimetallic (Yb, La) complex (1'). Magnetic properties of 1' and of a homodinuclear (Gd, Gd) analogue. *Inorg. Chem*. **1998**, *37*, 153–155.

96. Hemmila, I.; Webb, S. Time-resolved fluorometry: an overview of the labels and core technologies for drug screening applications. *DDT* **1997**, *2*(9), 373–381.

97. Sharma, B. P.; Singh, P.; Sharma, R. S.; Tyle, P. Diagnostics – Where we were, where we are, and where we are going: an introduction, "*Diagnostics in the year 2000. Antibody, Biosensor and Nucleic Acid Technologies*"; Eds. Singh, P.; Sharma, B. P.; Tyle, P.; Van Nostrand Reinhold: New York, 1993, pp. 1–7.

98. Diezel, W.; Kopperschlager, G.; Hofmann, E. An improved procedure for protein staining in polyacrylamide gels with a new type of Coomassie Brilliant Blue. *Anal. Biochem*. **1972**, *48*(2), 617–620.

99. Sinha, P.; Poland, J.; Schnolzer, M.; Rabilloud, T. A new silver staining apparatus and procedure for matrix-assisted laser desorption/ionization-time of flight analysis of proteins after two-dimensional electrophoresis. *Proteomics* (Germany) **2001**, *1*(7), 835–840.

100. Yan, J. X.; Wait, R.; Berkelman, T.; Harry, R. A.; Westbrook, J. A.; Wheeler, C. H.; Dunn, M. J. A modified silver staining protocol for visualization of proteins compatible with matrix-assisted laser desorption/ionization and electrospray ionization-mass spectrometry. *Electrophoresis* **2000**, *21*(17), 3666–3672.

101. Yan, J. X.; Harry, R. A.; Spibey, C.; Dunn, M. J. Postelectrophoretic staining of proteins separated by two-dimensional gel electrophoresis using SYPRO dyes. *Electrophoresis* **2000**, *21*(17), 3657–3665.

102. Roitt, I. M.; Brostoff, J.; Male, D. K. ''*Immunology*''; 3rd edn. Mosby: St. Louis, MO, 1993.

103. Crowther, J. R. ELISA. Theory and practice, ''*Methods in Molecular Biology*'', Vol. 42; Ed. Walker, J. M.; Humana Press: Totowa, New Jersey, 1995, p. 223.

104. Grassi, J.; MacLouf, J.; Pradelles, P. Radioiodination and other labelling techniques, ''*Radioimmunoassay in Basic and Clinical Pharmacology*''; Eds. Patrono, C.; Peskov, B. A.; Springer-Verlag: Berlin, Germany, 1987, pp. 103–107.

105. Glanzer, K.; Appenheimer, M.; Kruck, F.; Vetter, W.; Vetter, H. Measurement of 8-arginine-vasopressin by radioimmunoassay. Development and application to urine and plasma samples using one extraction method. *Acta Endocrinol.* (Denmark) **1984**, *106*(3), 317–329.

106. Andrews, P. Estimation of molecular size and molecular weights of biological compounds by gel filtration. *Methods Biochem. Anal.* **1970**, *18*, 1–53.

107. Amersham-Biosciences. Radiochemicals and Radiation Safety. *Biodirectory 2002* **2002**, 149.

108. Amersham-Biosciences. Radiochemicals. *Biodirectory 2002* **2002**, 110–148.

109. Amersham-Biosciences. Technical information – Radiochemicals. *Biodirectory 2002* **2002**, 177–181.

110. Stenman, U.-H.; Alfthan, H. Time-resolved fluoroimmunoassays, ''*Diagnostics in the year 2000. Antibody, Biosensor, and Nucleic Acid Technologies*''; Eds. Singh, P.; Sharma, B. P. ; Tyle, P.; Van Norstrand Reinhold: New York, 1993, pp. 53–64.

111. Wang, P. P.; Boeckx, R. L. Fluorescence polarization immunoassay and therapeutic drug monitoring and toxicology, ''*Diagnostics in the year 2000. Antibody, Biosensor, and Nucleic Acid Technologies*''; Eds. Singh, P.; Sharma, B. P.; Tyle, P.; Van Norstrand Reinhold: New York, 1993, pp. 39–52.

112. Applied Biosystems Ltd. ''*CDP-Star® & CSPD® Chemiluminescent Substrates for Alkaline Phosphatase*'', 2003. www.appliedbiosystems.com/products/productdetail.cfm?prodid = 114.

113. Amersham-Biosciences. Protein labelling and detection. *Biodirectory 2002* **2002**, 410–417.

114. Roche-Applied-Science. Protein labelling kits. *2002 Biochem. Catalog* **2002**, 322–323.

115. Javitch, J. A.; Li, X.; Kaback, J.; Karlin, A. A cysteine residue in the third membrane-spanning segment of the human D2 dopamine receptor is exposed in the binding-site crevice. *Proc. Natl. Acad. Sci. U S A* **1994**, *91*, 10355–10359.

116. Phillips, T. M.; Dickens, B. F. Affinity and immunoaffinity purification techniques, ''*The Biotechniques Series on Molecular Laboratory Methods*''; Eaton: Natick, MA, 2000.

117. Gruber, H. J.; Kada, G.; Pragl, B.; Riener, C.; Hahn, C. D.; Harms, G. S.; Ahrer, W.; Dax, T. G.; Hohenthanner, K.; Knaus, H. G. Preparation of thiol-reactive Cy5 derivatives from commercial Cy5 succinimidyl ester. *Bioconjug. Chem. 11*(2), 161–166.

118. Gudgin Dickinson, E. F.; Pollak, A.; Diamandis, E. P. Time-resolved detection of lanthanide luminescence for ultrasensitive bioanalytical assays. *J. Photochem. Photobiol. B: Biol.* **1995**, *27*, 3–19.

119. Deshpande, S. S.; Sharma, B. P. Diagnostics. Immunoassays, nucleic acid probes, and biosensors – two decades of development, current status, and future projections in clinical, environmental, and agricultural applications, ''*Diagnostics in the year 2000. Antibody, Biosensor, and Nucleic Acid Technologies*'', Eds. Singh, P.; Sharma, B. P.; Tyle, P.; Van Nostrand Reinhold: New York, 1993, pp. 459–525.

120. Hartig, W.; Kirazov, L.; Bruckner, G.; Holzer, M.; Gartner, U.; Bigl, V. Blot analyses and immunocytochemistry of neural antigens with digoxigenylated primary and secondary antibodies. *Brain Res. Protoc.* **1997**, *2*(1), 35–43.

121. Constantine, N. T.; Bansal, J.; Zhang, X.; Hyams, K. C.; Hayes, C. Enhanced chemiluminescence as a means of increasing the sensitivity of western blot assays for HIV antibody. *J. Virol. Methods* **1994**, *47*(1–2), 153–164.

122. Kain, S. R.; Mai, K.; Sinai, P. Human multiple tissue western blots: a new immunological tool for the analysis of tissue-specific protein expression. *Biotechniques* **1994**, *17*(5), 982–987.

123. Roda, A.; Pasini, P.; Guardigli, M.; Baraldini, M.; Musiani, M.; Mirasoli, M. Bio- and chemiluminescence in bioanalysis. *Fresenius' J. Anal. Chem.* **2000**, *366*(6–7), 752–759.

124. Krajewski, S.; Zapata, J. M.; Reed, J. C. Detection of multiple antigens on western blots. *Anal. Biochem.* **1996**, *236*(2), 221–228.

125. Conrad, C. C.; Malakowsky, C. A.; Talent, J.; Rong, D.; Lakdawala, S.; Gracy, R. W. Chemiluminescent standards for quantitative comparison of two-dimensional electrophoresis western blots. *Proteomics* (Germany) **2001**, *1*(3), 365–369.

126. Cosma, A. Affinity biotinylation: nonradioactive method for specific selection and labeling of cellular proteins. *Anal. Biochem.* **1997**, *252*(1), 10–14.

127. Heinicke, E.; Kumar, U.; Munoz, D. G. Quantitative dot-blot assay for proteins using enhanced chemiluminescence. *J. Immunol. Methods* **1992**, *152*(2), 227–236.

128. Kemper, C.; Berggren, K.; Diwu, Z.; Patton, W. F. An improved, luminescent europium-based stain for detection of electroblotted proteins on nitrocellulose or polyvinylidene difluoride membranes. *Electrophoresis* **2001**, *22*(5), 881–889.

129. Liu, R. H.; Jacob, J.; Tennant, B. Chemiluminescent detection of protein molecular weight markers in western blot techniques. *Biotechniques* **1997**, *22*(4), 594–595.

130. Huang, D.; Amero, S. A. Measurement of antigen by enhanced chemiluminescent western blot. *Biotechniques* **1997**, *22*(3), 454–456, 458.

131. Roche Applied Science. Protein and antibody labelling and detection. *2002 Biochemicals Catalog* **2002**, 330–333.

132. Fleming, J. S.; Lun, S.; Smith, P.; McNatty, K. P. Pituitary binding sites for gonadotrophin releasing hormone in Booroola Merino ewes which were non-carriers or homozygotes of the fecundity gene F. *J. Neuroendocrinol.* **1990**, *2*, 601–604.

133. Brown, C. Antigen retrieval methods for immunohistochemistry. *Toxicol. Pathol.* **1998**, *26*(6), 830–831.

134. Franco, D.; de Boer, P. A.; de Gier de Vries, C.; Lamers, W. H.; Moorman, A. F. Methods of in situ hybridization, immunohistochemistry and beta-galactosidase reporter gene detection. *Eur. J. Morphol.* **2001**, *39*(1), 3–25.

135. Fleming, J. S.; Hope, N. M.; Bolter, C. J. Clusterin is expressed in the anterior and intermediate lobes, but not in the posterior pituitary of sheep. *J. Mol. Endocrinol.* **1999**, *23*(2), 199–208.

136. Sovago, J.; Dupuis, D. S.; Gulyas, B.; Hall, H. An overview on functional receptor autoradiography using [35S]GTP-gamma S. *Brain Res. Rev.* **2001**, *38*(1–2), 149–164.

137. Cyr, M.; Ghribi, O.; Thibault, C.; Morissette, M.; Landry, M.; di Paolo, T. Ovarian steroids and selective estrogen receptor modulators activity on rat brain NMDA and AMPA receptors. *Brain Res. Rev.* **2001**, *37*(1–3), 153–161.

138. Blasberg, R. G. Receptor binding radiotracers: personal history of the past 20 years. *Nucl. Med. Biol.* **2001**, *28*(5), 573–583.

139. Yamashita, S. Histochemistry and cytochemistry of nuclear receptors. *Prog Histochem. Cytochem.* **2001**, *36*(2), 91–176.

140. Qume, M. Overview of ligand-receptor binding techniques. *Methods Mol. Biol.* **1999**, *106*, 3–23.

141. Beaudet, A.; Dournaud, P.; Boudin, H. Complementarity of radioautographic and immunohistochemical techniques for localizing neuroreceptors at the light and electron microscopy level. *Braz. J. Med. Biol. Res.* **1998**, *31*(2), 215–223.

142. Stumpf, W. E. Receptor localization of steroid hormones and drugs: discoveries through the use of thaw-mount and dry-mount autoradiography. *Braz. J. Med. Biol. Res.* **1998**, *31*(2), 197–206.

143. Hemmilá, I.; Mukkala, V.-M. Time-resolution in fluorometry technologies, labels, and applications in bioanalytical assays. *Crit. Rev. Clin. Lab. Sci.* **2001**, *38*(6), 441–519.

144. Del Rio, M.; Larcher, F.; Serrano, F.; Meana, A.; Munoz, M.; Garcia, M.; Munoz, E.; Martin, C.; Bernad, A.; Jorcano, J. L. A preclinical model for the analysis of genetically modified human skin in vivo. *Hum. Gene. Ther.* **2002**, *13*(8), 959–968.

145. Yang, X.; Atalar, E.; Li, D.; Serfaty, J. M.; Wang, D.; Kumar, A.; Cheng, L. Magnetic resonance imaging permits in vivo monitoring of catheter-based vascular gene delivery. *Circulation* **2001**, *104*(14), 1588–1590.

146. Kishimoto, J.; Ehama, R.; Ge, Y.; Kobayashi, T.; Nishiyama, T.; Detmar, M.; Burgeson, R. E. In vivo detection of human vascular endothelial growth factor promoter activity in transgenic mouse skin. *Am. J. Pathol.* **2000**, *157*(1), 103–110.

147. Venter, J. C.; Adams, M. D.; Myers, E. W.; Li, P. W.; Mural, R. J.; Sutton, G. G.; Smith, H. O.; Yandell, M.; Evans, C. A.; Holt, R. A.; Gocayne, J. D.; Amanatides, P.; Ballew, R. M.; Huson, D. H.; Wortman, J. R.; Zhang, Q.; Kodira, C. D.; Zheng, X. H.; Chen, L.; Skupski, M.; Subramanian, G.; Thomas, P. D.; Zhang, J.; Gabor Miklos, G. L.; Nelson, C.; Broder, S.; Clark, A. G.; Nadeau, J.; McKusick, V. A.; Zinder, N.; Levine, A. J.; Roberts, R. J.; Simon, M.; Slayman, C.; Hunkapiller, M.; Bolanos, R.; Delcher, A.; Dew, I.; Fasulo, D.; Flanigan, M.; Florea, L.; Halpern, A.; Hannenhalli, S.; Kravitz, S.; Levy, S.; Mobarry, C.; Reinert, K.; Remington, K.; Abu Threideh, J.; Beasley, E.; Biddick, K.; Bonazzi, V.; Brandon, R.; Cargill, M.; Chandramouliswaran, I.; Charlab, R.; Chaturvedi, K.; Deng, Z.; di Francesco, V.; Dunn, P.; Eilbeck, K.; Evangelista, C.; Gabrielian, A. E.; Gan, W.; Ge, W.; Gong, F.; Gu, Z.; Guan, P.; Heiman, T. J.; Higgins, M. E.; Ji, R. R.; Ke, Z.; Ketchum, K. A.; Lai, Z.; Lei, Y.; Li, Z.; Li, J.; Liang, Y.; Lin, X.; Lu, F.; Merkulov, G. V.; Milshina, N.; Moore, H. M.; Naik, A. K.; Narayan, V. A.; Neelam, B.; Nusskern, D.; Rusch, D. B.; Salzberg, S.; Shao, W.; Shue, B.; Sun, J.; Wang, Z.; Wang, A.; Wang, X.; Wang, J.; Wei, M.; Wides, R.; Xiao, C.; Yan, C.; Yao, A.; Ye, J.; Zhan, M.; Zhang, W.; Zhang, H.; Zhao, Q.; Zheng, L.; Zhong, F.; Zhong, W.; Zhu, S.; Zhao, S.; Gilbert, D.; Baumhueter, S.; Spier, G.; Carter, C.; Cravchik, A.; Woodage, T.; Ali, F.; An, H.; Awe, A.; Baldwin, D.; Baden, H.; Barnstead, M.; Barrow, I.; Beeson, K.; Busam, D.; Carver, A.; Center, A.; Cheng, M. L.; Curry, L.; Danaher, S.; Davenport, L.; Desilets, R.; Dietz, S.; Dodson, K.; Doup, L.; Ferriera, S.; Garg, N.; Gluecksmann, A.; Hart, B.; Haynes, J.; Haynes, C.; Heiner, C.; Hladun, S.; Hostin, D.; Houck, J.; Howland, T.; Ibegwam, C.; Johnson, J.; Kalush, F.; Kline, L.;

Koduru, S.; Love, A.; Mann, F.; May, D.; McCawley, S.; McIntosh, T.; McMullen, I.; Moy, M.; Moy, L.; Murphy, B.; Nelson, K.; Pfannkoch, C.; Pratts, E.; Puri, V.; Qureshi, H.; Reardon, M.; Rodriguez, R.; Rogers, Y. H.; Romblad, D.; Ruhfel, B.; Scott, R.; Sitter, C.; Smallwood, M.; Stewart, E.; Strong, R.; Suh, E.; Thomas, R.; Tint, N. N.; Tse, S.; Vech, C.; Wang, G.; Wetter, J.; Williams, S.; Williams, M.; Windsor, S.; Winn Deen, E.; Wolfe, K.; Zaveri, J.; Zaveri, K.; Abril, J. F.; Guigo, R.; Campbell, M. J.; Sjolander, K. V.; Karlak, B.; Kejariwal, A.; Mi, H.; Lazareva, B.; Hatton, T. The sequence of the human genome. *Science* **2001**, *291*(5507), 1304–1351.

148. Waterston, R. H.; Lander, E. S.; Sulston, J. E. On the sequencing of the human genome. *Proc. Natl. Acad. Sci. U.S.A.* **2002**, *99*(6), 3712–3716.

149. Olivier, M.; Aggarwal, A.; Allen, J.; Almendras, A. A.; Bajorek, E. S.; Beasley, E. M.; Brady, S. D.; Bushard, J. M.; Bustos, V. I.; Chu, A.; Chung, T. R.; de Witte, A.; Denys, M. E.; Dominguez, R.; Fang, N. Y.; Foster, B. D.; Freudenberg, R. W.; Hadley, D.; Hamilton, L. R.; Jeffrey, T. J.; Kelly, L.; Lazzeroni, L.; Levy, M. R.; Lewis, S. C.; Liu, X.; Lopez, F. J.; Louie, B.; Marquis, J. P.; Martinez, R. A.; Matsuura, M. K.; Misherghi, N. S.; Norton, J. A.; Olshen, A.; Perkins, S. M.; Perou, A. J.; Piercy, C.; Piercy, M.; Qin, F.; Reif, T.; Sheppard, K.; Shokoohi, V.; Smick, G. A.; Sun, W. L.; Stewart, E. A.; Fernando, J.; Tejeda, J. F.; Tran, N. M.; Trejo, T.; Vo, N. T.; Yan, S. C.; Zierten, D. L.; Zhao, S.; Sachidanandam, R.; Trask, B. J.; Myers, R. M.; Cox, D. R. A high-resolution radiation hybrid map of the human genome draft sequence. *Science* **2001**, *291*(5507), 1298–1302.

150. Lewin, B. ''*Genes VII*''; 7th edn.; Oxford University Press: Oxford, 1999, p. 990.

151. Southern, E. M. Detection of specific sequences among DNA fragments separated by gel electrophoresis. *J. Mol. Biol.* **1975**, *98*(3), 503–517.

152. Fleming, J. S.; Tisdall, D. J.; Greenwood, P. J.; Hudson, N. L.; Heath, D. A.; McNatty, K. P. Expression of the genes for alpha inhibin, beta A inhibin and follistatin in the ovaries of Booroola ewes which were homozygotes or non-carriers of the fecundity gene FecB. *J. Mol. Endocrinol.* **1992**, *8*(3), 265–273.

153. Sigma-Aldrich. Electrophoresis – Gel stains, ''*Products for Life Science Research*'', 2000, pp. 825–829. www.sigma-aldrich.com.

154. Saiki, R. K.; Scharf, S.; Faloona, F.; Mullis, K. B.; Horn, G. T.; Erlich, H. A.; Arnheim, N. Enzymatic amplification of beta-globin genomic sequences and restriction site analysis for diagnosis of sickle cell anemia. *Science* **1985**, *230*(4732), 1350–1354.

155. Mullis, K. B. The polymerase chain reaction (Nobel Lecture). *Angew. Chem. Int. Ed. Engl.* **1994**, *33*, 1209–1213.

156. Cimino, G. D.; Gamper, H. B.; Isaacs, S. T.; Hearst, J. E. Psoralens as photoactive probes of nucleic acid structure and function: organic chemistry, photochemistry, and biochemistry. *Annu. Rev. Biochem.* **1985**, *54*, 1151–1193.

157. Mansfield, E. S.; Worley, J. M.; McKenzie, S. E.; Surrey, S.; Rappaport, E.; Fortina, P. Nucleic acid detection using non-radioactive labelling methods. *Mol. Cell. Probes* **1995**, *9*(3), 145–156.

158. Schmitz, G. G.; Walter, T.; Seibl, R.; Kessler, C. Nonradioactive labeling of oligonucleotides in vitro with the hapten digoxigenin by tailing with terminal transferase. *Anal. Biochem.* **1991**, *192*(1), 222–231.

159. Jowett, T. ''*Tissue In situ Hybridization: Methods in Animal Development*''; John Wiley & Sons, Inc.: New York, 1997, p. 121.

160. Osborn, J. A review of radioactive and non-radioactive-based techniques used in life science applications. Part I: Blotting techniques. *Life Science News, Amersham Pharmacia Biotech* **2000**, *6*, 1–6.

161. Perkin Elmer Life Sciences "*Applications of Time-resolved Fluorometry with the DELFIA® Method*", 2003. http://lifesciences.perkinelmer.com.

162. Hukkanen, V.; Rehn, T.; Kajander, R.; Sjoroos, M.; Waris, M. Time-resolved fluorometry PCR assay for rapid detection of herpes simplex virus in cerebrospinal fluid. *J. Clin. Microbiol.* **2000**, *38*(9), 3214–3218.

163. Seddon, H. R.; Gray, G.; Pollitt, R. J.; Iitia, A.; Green, A. Population screening for the common G985 mutation causing medium-chain acyl-CoA dehydrogenase deficiency with Eu-labeled oligonucleotides and the DELFIA system. *Clin. Chem.* **1997**, *43*(3), 436–442.

164. Nurmi, J.; Kiviniemi, M.; Kujanpaa, M.; Sjoroos, M.; Ilonen, J.; Lovgren, T. High-throughput genetic analysis using time-resolved fluorometry and closed-tube detection. *Anal. Biochem.* **2001**, *299*(2), 211–217.

165. Bortolin, S.; Christopoulos, T. K.; Verhaegen, M. Quantitative polymerase chain reaction using a recombinant DNA internal standard and time-resolved fluorometry. *Anal. Chem.* **1996**, *68*(5), 834–840.

166. Galvan, B.; Christopoulos, T. K. Quantitative reverse transcriptase-polymerase chain reaction for prostate-specific antigen mRNA. *Clin. Biochem.* **1997**, *30*(5), 391–397.

167. Gutzmer, R.; Mommert, S.; Kiehl, P.; Wittmann, M.; Kapp, A.; Werfel, T. Detection of clonal T cell receptor gamma gene rearrangements in cutaneous T cell lymphoma by LightCycler-polymerase chain reaction. *J. Invest. Dermatol.* **2001**, *116*(6), 926–932.

168. Espy, M. J.; Teo, R.; Ross, T. K.; Svien, K. A.; Wold, A. D.; Uhl, J. R.; Smith, T. F. Diagnosis of varicella-zoster virus infections in the clinical laboratory by LightCycler PCR. *J. Clin. Microbiol.* **2000**, *38*(9), 3187–3189.

169. Nakao, M.; Janssen, J. W.; Flohr, T.; Bartram, C. R. Rapid and reliable quantification of minimal residual disease in acute lymphoblastic leukemia using rearranged immunoglobulin and T-cell receptor loci by LightCycler technology. *Cancer Res.* **2000**, *60*(12), 3281–3289.

170. Espy, M. J.; Uhl, J. R.; Mitchell, P. S.; Thorvilson, J. N.; Svien, K. A.; Wold, A. D.; Smith, T. F. Diagnosis of herpes simplex virus infections in the clinical laboratory by LightCycler PCR. *J. Clin. Microbiol.* **2000**, *38*(2), 795–799.

171. Kreuzer, K. A.; Lass, U.; Bohn, A.; Landt, O.; Schmidt, C. A. LightCycler technology for the quantitation of bcr/abl fusion transcripts. *Cancer Res.* **1999**, *59*(13), 3171–3174.

172. Nozaki, A.; Kato, N. Quantitative method of intracellular hepatitis C virus RNA using LightCycler PCR. *Acta Med. Okayama* **2002**, *56*(2), 107–110.

173. Schnerr, H.; Niessen, L.; Vogel, R. F. Real time detection of the tri5 gene in Fusarium species by lightcycler-PCR using SYBR Green I for continuous fluorescence monitoring. *Int. J. Food Microbiol.* **2001**, *71*(1), 53–61.

174. Hackett, S. J.; Carrol, E. D.; Guiver, M.; Marsh, J.; Sills, J. A.; Thomson, A. P.; Kaczmarski, E. B.; Hart, C. A. Improved case confirmation in meningococcal disease with whole blood Taqman PCR. *Arch. Dis. Child.* **2002**, *86*(6), 449–452.

175. Bhudevi, B.; Weinstock, D. Fluorogenic RT-PCR assay (TaqMan) for detection and classification of bovine viral diarrhea virus. *Vet. Microbiol.* **2001**, *83*(1), 1–10.

176. Loeb, K. R.; Jerome, K. R.; Goddard, J.; Huang, M.; Cent, A.; Corey, L. High-throughput quantitative analysis of hepatitis B virus DNA in serum using the TaqMan fluorogenic detection system. *Hepatology* **2000**, *32*(3), 626–629.

177. Guiver, M.; Borrow, R.; Marsh, J.; Gray, S. J.; Kaczmarski, E. B.; Howells, D.; Boseley, P.; Fox, A. J. Evaluation of the Applied Biosystems automated Taqman polymerase chain reaction system for the detection of meningococcal DNA. *FEMS Immunol. Med. Microbiol.* **2000**, *28*(2), 173–179.

178. Pusterla, N.; Huder, J. B.; Leutenegger, C. M.; Braun, U.; Madigan, J. E.; Lutz, H. Quantitative real-time PCR for detection of members of the Ehrlichia phagocytophila genogroup in host animals and Ixodes ricinus ticks. *J. Clin. Microbiol.* **1999**, *37*(5), 1329–1331.

179. Drosten, C.; Weber, M.; Seifried, E.; Roth, W. K. Evaluation of a new PCR assay with competitive internal control sequence for blood donor screening. *Transfusion* **2000**, *40*(6), 718–724.

180. Weinberger, K. M.; Wiedenmann, E.; Bohm, S.; Jilg, W. Sensitive and accurate quantitation of hepatitis B virus DNA using a kinetic fluorescence detection system (TaqMan PCR). *J Virol Methods* **2000**, *85*(1–2), 75–82.

181. Yajima, T.; Yagihashi, A.; Kameshima, H.; Furuya, D.; Kobayashi, D.; Hirata, K.; Watanabe, N. Establishment of quantitative reverse transcription–polymerase chain reaction assays for human telomerase-associated genes. *Clin. Chim. Acta* **2000**, *290*(2), 117–127.

182. Becker, K.; Pan, D.; Whitley, C. B. Real-time quantitative polymerase chain reaction to assess gene transfer. *Hum. Gene. Ther.* **1999**, *10*(15), 2559–2566.

183. Holloway, J. W.; Beghe, B.; Turner, S.; Hinks, L. J.; Day, I. N.; Howell, W. M. Comparison of three methods for single nucleotide polymorphism typing for DNA bank studies: sequence-specific oligonucleotide probe hybridisation, TaqMan liquid phase hybridisation, and microplate array diagonal gel electrophoresis (MADGE). *Hum. Mutat.* **1999**, *14*(4), 340–347.

184. Sellner, L. N.; Turbett, G. R. Comparison of three RT-PCR methods. *Biotechniques* **1998**, *25*(2), 230–234.

185. Carninci, P.; Nishiyama, Y.; Westover, A.; Itoh, M.; Nagaoka, S.; Sasaki, N.; Okazaki, Y.; Muramatsu, M.; Hayashizaki, Y. Thermostabilization and thermoactivation of thermolabile enzymes by trehalose and its application for the synthesis of full length cDNA. *Proc. Natl. Acad. Sci. U.S.A.* **1998**, *95*(2), 520–524.

186. Stone, B. B.; Nietupski, R. M.; Breton, G. L.; Weisburg, W. G. Comparison of Mycobacterium 23S rRNA sequences by high-temperature reverse transcription and PCR. *Int. J. Syst. Bacteriol.* **1995**, *45*(4), 811–819.

187. Myers, T. W.; Gelfand, D. H. Reverse transcription and DNA amplification by a Thermus thermophilus DNA polymerase. *Biochemistry* **1991**, *30*(31), 7661–7666.

188. Dabiri, G. A.; Turnacioglu, K. K.; Sanger, J. M.; Sanger, J. W. Myofibrillogenesis visualized in living embryonic cardiomyocytes. *Proc. Natl. Acad. Sci. U S A* **1997**, *94*(17), 9493–9498.

189. Scheffel, U.; Dannals, R. F.; Cline, E. J.; Ricaurte, G. A.; Carroll, F. I.; Abraham, P.; Lewin, A. H.; Kuhar, M. J. [$^{123/125}$I]RTI-55, an in vivo label for the serotonin transporter. *Synapse* **1992**, *11*(2), 134–139.

190. Herring, M. B.; Gunther, G. R.; Etchberger, K. J. ^{111}Indium is an unreliable in vivo label for vascular endothelial cells. *Ann. Vasc. Surg.* **1991**, *5*(5), 424–428.

191. Bogdanov, A. Jr.; Weissleder, R. In vivo imaging of gene delivery and expression. *Trends Biotechnol.* **2002**, *20*(8 (Suppl)), S11–S18.

192. Fenster, A. A TRENDS guide to imaging technologies. *Trends Biotechnol.* **2002**, *20*(8 (Suppl)), S1–S2.

193. O'Connell-Rodwell, C. E.; Burns, S. M.; Bachmann, M. H.; Contag, C. H. Bioluminescent indicators for in vivo measurements of gene expression. *Trends Biotechnol.* **2002**, *20*(8 (Suppl)), S19–S23.

194. Bobba, G.; Dickins, R. S.; Kean, S. D.; Mathieu, C. E.; Parker, D.; Peacock, R. D.; Siligardi, G.; Smith, M. J.; Williams, J. A. G.; Geraldes, C. F. G. C. Chiroptical, ESMS and NMR spectroscopic study of the interaction of enantiopure lanthanide

complexes with selected self-complementary dodecamer oligonucleotides. *J. Chem. Soc., Perkin Trans. 2* **2001**, (9), 1729–1737.

195. Maxwell, D. J.; Taylor, J. R.; Nie, S. Self-assembled nanoparticle probes for recognition and detection of biomolecules. *J. Am. Chem. Soc.* **2002**, *124*, 9606–9612.

196. Sando, S.; Kool, E. T. Quencher as leaving group: efficient detection of DNA-joining reactions. *J. Am. Chem. Soc.* **2002**, *124*(10), 2096–2097.

197. Weizman, H.; Tor, Y. Redox-active metal-containing nucleotides: synthesis, tunability, and enzymatic incorporation into DNA. *J. Am. Chem. Soc.* **2002**, *124*, 1568–1569.

198. Hurley, D. J.; Tor, Y. Ru(II) and Os(II) nucleosides and oligonucleotides: synthesis and properties. *J. Am. Chem. Soc.* **2002**, *124*(14), 3749–3762.

199. Carnall, W. T.; Fields, P. R.; Rajnak, K. Electronic energy levels of the trivalent lanthanide aquo ions. I–IV. *J. Chem. Phys.* **1968**, *49*(10), 4424–4455.

200. Fleming, J. S.; Allison, J. V.; Bray, J. J. Endocrine system, ''*Lecture Notes on Human Physiology*'', 4th edn.; Eds. Bray, J. J.; Cragg, P. A.; Macknight, A. D. C.; Mills, R. G.; Blackwell Science: London, 1999, pp. 234–263.

201. Stick, R. V. ''*Carbohydrates: The Sweet Molecules of Life*''; Academic Press: Bodmin (UK), 2001. ISBN: 0-12-670960-2.

INDEX

ABTS, 233–234
Acetonitrile, carboxylic group activation, 221
Acid catalyzed decarboxylation/aquation, 157
Acid dissociation constants, 158
  for α-hydroxyalkyl complexes, 279–280
Acyclic ligands, 378
Acyclic systems, 369
Acylperoxyl radicals, cross-coupling with, 51
Alcohol dehydrogenase (ADH) quinohemoprotein, 207
Alcohols
  catalytic oxidation by O_2, 46–50
  oxidation, 106–108
Aliphatic carbon-centered radicals, reaction with transition metal complexes in aqueous solutions, 274–275
Alkaline phosphatase (AP), 395
Alkene complexes, 298–299
Alkenes, reduction of, 302–304
n-Alkylferricenium cations, 219
n-Alkylferricenium ions, 219
Alkylferrocenes, 218, 238
Alkylperoxyl radicals, 29
Amines, oxidation, 106–108
Aminomethylferrocene, hemin modification by, 233
5-(3″-Aminopropynyl)-2′-deoxyuridine-5′-triphosphate, 416
Anionic inhibitors, recognition of, 187–188
Antenna Effect, 363–365
Antenna mechanism, 368
  for lanthanide phosphorescence, 365
Aqueous media, atom transfer and free radical chemistry in, 1–59
Aqueous solutions, radiolysis of, 272–274
$ArOH^+$, structure, 19
Aspergillus niger, 203, 210, 244–245
  glucose oxidase from, 203–205, 210–224, 262
Atom transfer in aqueous media, 1–59
Autooxidation of hydrazine, 104–106

Bacillus subtilis, 181
Benzaldehyde formation in $Cr_{aq}OO^{2+}$-catalyzed reaction, 48
β-elimination of carboxylates, 293–295
β-elimination reactions, 291–293
Bienzyme biosensor incorporating HRP, 225
Bimolecular decomposition of transient complexes, 296–297
Bimolecular redox reactions, intramolecular redox assistance of, 117–120
Binuclear carbonato bridged complexes, 144
Bipyridyl chromophore, 378
Bipyridyl-*N,N′*-dioxide chromophore, 385
Bis(hydrazone) ligands of 2,6-diacetylpyridine, 315–360
Bünzli/Piguet ligands, 377
n-Butyldiazoate, 103

^{13}C NMR spectroscopy, 166
^{113}Cd NMR studies, 166
Caldariomyces fumago, 255
Calixarene complexes, 386–387
Calixarene-derived ligands, 386
Calixarenes, 385–387
Carbodiimide modification of GO, 220
Carbon dioxide *see* CO_2
Carbon monoxide *see* CO
Carbon-skeleton, rearrangement of, 298
Carbonate/bicarbonate
  bonding modes, 139
  metal–oxygen bond lengths, 139
Carbonato complexes, 127–199
  aquation/decarboxylation, 153–159, 186–188
  chelated, 156–159
  coordination modes, 145
  formation of, 146–153
  general chemistry, 128
  μ_3-bridged, 141–145
  stability constants, 133

Carbonic acid dehydration, 131–133
Carbonic anhydrase isoenzymes, 160
Carbonic anhydrase models, 127–199
Carbonic anhydrase-related proteins (CA-RP), 160
Carbonic anhydrases (CAs)
  activators, 179–180
  binding sites, 162
  catalytic mechanism, 167–169
  classification, 159–161
  CO_2 catalyzed, 168
  Co-substituted, 164–165
  coordination pattern of different inhibitors with Zn–CA (wild type) and Co–CA II and their association constants, 178
  δ-class, 185–190
  discovery, 159–161
  γ-class, *Methanosarcina thermophila*, 183–185
  mechanism of inhibition, 176–179
  mechanistic insight for catalyzed reaction, 174–176
  transfer of H^+ between active site and reaction medium, 167–169
α-Carbonic anhydrases (CAs), 161
  structure of, 161–180
β-Carbonic anhydrases (CAs)
  CO_2 hydration mechanism for, 183
  from Red Alga, 180–183
  hydrogen bonding at active site, 182
Carboxylates, β-elimination of, 293–295
Carboxylic acid, cyclic voltammogram, 211
Carboxylic oxygen, 368
Carcinoembryonic antigen (CEA), 379
Catalytic oxidation
  of alcohols by O_2, 46–50
  of cyclohexene, 304–306
Catalytic processes, mechanisms of, 304–308
CdBCA II, 166
CdHCA I, 166
CDP-*star* substrate, 399
Cetyltrimethylammonium bromide (CTAB), 217–218
CH_2O yields in $Cr_{aq}OO^{2+}$-catalyzed oxidation of HNO_2/CH_3OH, 47
Chemical Kinetics Simulator, 49
Chemiluminescent labeling, 412
Chiral complexes, 253–256
  examples, 254
Chlamydomonas reinhardtii, 160
Chloramine-T, 393–394
Chromium complexes, 4–7, 10–13
Chromium compounds, spectra, 278
CMe_3CHO reaction with, $\{Cr_{aq}O^{2+} + Cr_{aq}OO^{2+}\}$, 27–29
$CMe_3OO^{\bullet}/CMe_3C(O)OO^{\bullet}$ cross reaction, 26–27
CO insertion/methyl migration, 295
CO_2
  base hydrolysis, 132
  equilibrium constant, 130
  hydration mechanism, 182–183
    for β-CA, 183
    for γ-class CA, 185
  interconversion with HCO_3^-, 169
  kinetics of hydration, 131–133
  solubility and equilibria in solution, 129–131
  solubility equilibrium, 129
  uncatalyzed hydration/dehydration mechanism, 132
  uptake and dehydration reaction, 176
  uptake reaction, 147–149
Cobalt complexes, 3–7, 158
CoBCA II, 165
CoBCA III, 165
$[Co(dapsox)(H_2O)]_2$, 330
$[Co(H_2dapsox)(H_2O)(MeOH)]^{2+}$, 330
CoHCA I, 165
Co(II) complexes, 327–332, 337, 351–353, 355
Co(III) coordinated imidazole, 149
Comamonas testosteron, 207
Contrast agents, 362
Coomassie Brilliant Blue, 391
Coordinated solvent molecules, 366–368
Copper–carbonic anhydrase (CuCA) complexes, ^1H NMR data of, 141–142, 165
Copper complexes, 141–142
Copper–quinoproteins, 207
Copper(II), pH dependent complexation of, 136
Copper(II) complexes, 332–335
$Cr_{aq}O^{2+}$, thermodynamic data, 30

$Cr_{aq}OO^{2+}$
  as catalyst for oxidations with O_2 in presence of HNO_2, 51
  radical reactivity, 50
  reactions with N- and O-centered radicals, 43
  thermodynamic data, 30
$Cr_{aq}OO^{2+}/CMe_3C(O)OO^{\bullet}$ cross reaction, 24–26
Creutz-Taube analogs, 63
Cr(III), 354
Cr(IV) complexes, 352–353
  rate constants for reactions with rhodium hydrides, 13
Cr(V) complexes, rate constants for reactions with rhodium hydrides, 13
Cr(VI) complexes, 352
Crystal field stabilization energies, 337
CSPD substrate, 399
$[Cu(Hdapsox)(H_2O)]^{+}$, 335
Cu(I) complexes, reduction by $Cl_3CCO_2^-$, 299–301
Cu(II) complexes, 327, 337–338, 351, 353–355
Cu(II)–carbonato complexes, proposed structures, 137
Cu(III) peptide complexes, decomposition of, 301–302
Cyano-bridge formation and electron transfer reactivity, 115–117
Cyano-protonated complexes, 77
Cyclen-derivative macrocycles, 380–384
Cyclen derivatives, 367
Cyclic systems, 380–390
Cyclohexene, catalytic oxidation of, 304–306

Decarboxylation of $[(NH_3)_5CoOCO_2H]^{2+}$, 155
Decarboxylation rate constant, 158–159
Dehydrogenases, pyrroloquinoline quinone (PQQ), 207–208
DELFIA system, 399–400
Density functional theoretical (DFT) calculations, 64, 75, 85, 90, 94, 97–98, 121, 140
2,6-Diacetylpyridine, transition metal complexes with bis(hydrazone) ligands of, 315–360
(*S*)-*N*,*N*-dimethyl-1-ferrocenylethylamine, 253–254
1,2-Dimethylhydrazine, 79
Dioxygen activation by transition metal complexes, 1–59
Disproportionation of hydroxylamine, 108–109
Dissociation rate constants of NP complexes, 68
Dissociation-enhanced lanthanide fluoroimmunoassay (DELFIA) system, 399–400
DNA, 403–415
  amplification, 413
    with thermostable enzyme, 406–408
  denaturation, 406
  detection of, 415–416
  labeling techniques, 408–412
  polymerase enzyme, 406
  replication, 414
DOTA, 380
DOTA-derived ligands, 382
DOTAREM, 380
$[\{Dy(NO_3)_2\}_2(L^{55})]^{+}$, 390
$[Dy(L^{55})(NO_3)]^{-}$, 390

Electron absorption spectra, 335
Electron shuttle, 225
Electron transfer
  mediated, 203
  non-mediated, 203
  reactivity and cyano-bridge formation, 115–117
Electrophilic reactions of bound NO, 79–104
Enantioselective electron transfer, 255
Enantioselectivity factors, 255–256
Enemark–Feltham notation (E–F), 65
Enzyme-activator complexes, 180
Enzyme-linked immunosorbent assay (ELISA), 395–397
Enzymes, 203–208
EPR spectra, 67, 166, 349
EPR spectroscopy, 72
ESR spectra, 5–6, 11
$[Eu(HL)]^{+}$, 376
$[Eu(L^4)_2]^{+}$, 373
$[Eu(L^{23})_3]^{3+}$, 380
$[Eu(L^{30})(H_2O)]^{3+}$, 383
Europium complexes, 362, 367, 388

FAD, 223
$FADH_2$, 222

$FADH_2$/FAD couples, 212
Faraday constant, 222
Fc–FAD, 224
Fc–Hemin, 233
Fc–HRP, 233
  kinetic characteristics, 234
  model, 236
  steady-state rate, 235
Fc_{14}–GO cyclic voltammogram, 220
$[Fe(CN)_5H_2O]^{3-}$, reaction with O_2 and H_2O_2, 110
$[Fe(dapoamh)(H_2O)]_2O$, 342
$[Fe(dapsox)(H_2O)_2]^+$, 344
Fe(II) complexes, 337, 351–353
Fe(II)–Fe(III) redox couples, redox potentials, 116
Fe(III) complexes, 327, 337, 339–344, 351–356
  of protoporphyrin IX, 206
Fe(III)–porphyrins, 71–72
Fenton-like reactions, 306–308
Fenton-type chemistry, 9, 14
Ferricenium cations, 212
  ferrocenes oxidation by hydrogen peroxide, 224–225
Ferricenium half-reactions, 214–215
Ferricenium ions, 214, 216
  rate constant for oxidation of reduced GO by, 218
Ferricenium salts, 213
Ferrocene carboxylic acid, 220
Ferrocene-containing reactive mediators, 236–239
Ferrocene–GO–glucose system, 212
Ferrocene units, attaching to GO, 220
Ferrocenes, 210–239
  as substrates of HRP, 226
  Groups I and II, 227–229
  half-reaction, pH-dependence of, 215
  modification by GO, 221
  oxidation into ferricenium cations by hydrogen peroxide, 224–225
  rate constants for oxidation of, 231
  redox potentials of, 217
  substituents, 217
p-Ferrocenylaniline, 238
Ferrocyanide, rate constants for oxidation of, 231
α-Fetoprotein (AFP), 379
Flash-photolysis, 75
Flavin adenine dinucleotide, oxidized and reduced forms of, 204
Fluorescence immunoassays, 397–400
Fluorescence In Situ Hybridization (FISH), 414
Fluorochromes, 410
Fluroescein, 410
Free radical chemistry in aqueous media, 1–59
FTIR spectroscopy, 73

$[\{Gd(NO_3)_2\}_2(L^7)]$, 374
$[Gd(L^2)(NO_3)_3]$, 371
Gene expression, new methods for in vivo measurement, 415
Gene probes
  hybridization, 408–412
  labeling and detection, 408–412
Gluconobacter sp. 33, 207
δ-D-Gluconolactone, 203
β-D-Glucopyranose, 202–203
D-Glucose, fading of Fc^+PF_6 in the presence of, 214
L-Glucose, 202
Glucose dehydrogenase (GDH), 207
Glucose/gluconolactone couples, 212
Glucose half-reaction, kinetic parameters, 215
Glucose oxidase (GO)
  and PQQ-dependent oxidoreductases, 240–249
  attaching ferrocene units to, 220
  carbodiimide modification of, 220
  fading of Fc^+PF_6 in the presence of, 214
  ferrocenes modification by, 221
  from *A. niger*, 203–205, 210–224, 262
  Group II electron acceptors of, 215–216
  mass balance equation, 215
  oxidized, 214
  reduced, 213–214, 219
  transition-metal chemistry, 201–269
Glucose oxidase (GO)-catalyzed oxidation, pH-dependence of, 242
Glucose oxidase (GO)-catalyzed reduction, pH profile for steady-state rate of, 216
Glucose oxidase (GO)–$CH_2NH(CH_2)_nNHCH_2$–Fc, 221
Glucose oxidase (GO)–ferricenium intermediates, 215

Glutaraldehyde, Schiff base condensation of, 395
GO–ferricenium complex, 216

^{1}H NMR data of copper–carbonic anhydrase (CuCA) complexes, 165
H_2dapsox, 331
H_2O splitting step, 169–171
Halo-alkanes, reduction of, 299–301
HCA I, 165, 167–170
HCA II, 161, 167–170, 187
  catalytic activity, 164
  CO_2 catalyzed hydration and dehydration reaction, 175
  CO_2 hydration mechanism, 171
  Co^{II}–HCO_3^- adduct of Co^{II}-substituted, 172
  direct and indirect metal ligands, 162
  electronic mechanism for catalysis, 171–174
  high activity form, 161–180
  rearrangement of bicarbonate during CO_2 hydration, 173
  thiocyanate adduct, 163
  wild-type structure, 164–165
  X-ray crystal structure data, 161
  X-ray structure data, 163
HCA II–cyanamide complex, 160
HCA II–cyanamide–water ternary complex, 160
HCA III, 167–169, 171
Hemin, 206
Hemin modification by aminomethylferrocene, 233
Hepta-coordinated complexes, 315–360
High-valent oxo intermediates, 9–12
HNO_2
  as source of NO and NO_2, 39–42
  reactions of, 31–46
Horseradish peroxidase *see* HRP
HRP, 203, 205–207, 224–239, 249–253, 395
  bienzyme biosensor incorporating, 225
  Compound I, 205–207, 230–231, 239
  Compound II, 205–207, 227, 230–231, 239
  cyclic voltammograms, 234
  ferrocenes as substrates of, 226
  inactivation, 249
  kinetic characteristics, 234
  mechanism of catalysis by, 205
  oxidative mediators in catalysis by, 261
  recognition of planar chirality by, 255
  steady-state rate, 235
HRP-catalyzed oxidation
  of FA and FP by hydrogen peroxide, 237–238
  of phenols, 229–230
  of Ru^{II} into Ru^{III} by H_2O_2, 257
  of ruthenium complexes, 250–253, 259
Human carbonic anhydrase *see* HCA
Human erythrocytes, 161–180
Hydrazine, 88–96
  autooxidation of, 104–106
Hydride abstraction by LMO complexes, 12–16
β-Hydride shift reactions, 290–291
Hydride transfer reducing agent, 298
Hydrogen abstraction
  by $Cr_{aq}OO^{2+}$ from C–H, O–H, and Rh–H bonds, 50
  from Rh–H, O–H, and C–H bonds by chromyl ions and $Cr_{aq}OO^{2+}$, 29
Hydrogen atom abstraction
  by LMO complexes, 12–16
  summary of kinetic data, 29
Hydrogen atom transfer from rhodium hydrides to superoxometal complexes, 17–18
Hydrogen peroxide
  ferrocenes oxidation into ferricenium cations by, 224–225
  HRP-catalyzed oxidation of FA and FP by, 237–238
Hydroperoxides, 9
Hydroperoxo complexes, 7–9
  UV data, 7
α-Hydroxyalkyl complexes, acid dissociation constants for, 279–280
2-Hydroxycyclohexyl radicals, 305
Hydroxylamine, disproportionation of, 108–109
N-Hydroxysuccinimide Cy5, 400

Immunoassay, 392–400
Immunohistochemistry, 402–403
In situ hybridization, 413–414
Inter-system crossing (ISC), 363
Intramolecular electron-transfer, 120
  in ion pairs, 120

Intramolecular redox assistance of bimolecular redox reactions, 117–120
Iodination reaction, 394
Ion pairs, intramolecular electron-transfer in, 120
Isotopic exchange equilibria, 130

La(III) complexes, 327, 346–349
Lanthanide antennae, 362
Lanthanide complexes
  biochemical applications, 390–416
  luminescent, 361
  luminescent biolabels, 361–432
  macrobicycles, 387–389
Lanthanide coordination chemistry, potential applications, 362
Lanthanide emission information, 364
Lanthanide-labeled oligonucleotide probes, 412
Lanthanide phosphorescence, antenna mechanism for, 365
Lanthanide(III) ions
  coordination chemistry, 369
  energy levels, 364
  photophysical properties, 363
  properties of, 363–369
LaPorte rule, 363
Lehn cryptand, 387
Ligand phosphorescence, 363
Ligand systems, exploration, 369–390
Ligand-to-metal charge-transfer (LMCT), 63, 278–279
LightCycler system, 413
Lindskog like pathway, 173
Lindskog structure, 138–139
Linear-free-energy-relationship (LFER), 82, 84, 228
Linker groups, 415–416
Lipscomb pathway, 173
Lipscomb structure, 138–139, 155
Lithium *n*-butylamide and *n*-butylamine reactions, 102–103
$L_{m-1}M^{n+1}$–R oxidation, followed by homolysis, 289–290
LMO complexes, hydrogen atom and hydride abstractions by, 12
LMOO complexes, reactions with nitrogen oxides and HNO_2, 31–46
$[Ln(HL^9)]^+$, 375
Low active isoenzyme, 167
$[Lu(L^{49})(H_2O)]^{3+}$, 387
Luminescent biolabels, lanthanide complexes as, 361–432

Macrobicyclic ligands, 388
Magnetic Resonance Imaging (MRI), 362–363, 380
Marcus formalism, 229
Mass spectrometry, 88
Mediated electron transfer (MET), 202, 262
Mediators
  bioorganometallic concept of design, 237
  cyclometalated Os^{II}, 257–261
  cyclometalated Ru^{II}, 257–261
  inorganic and organometallic complexes frequently used as, 209
  properties of, 208–210
  rate constants for oxidation of GO(red) by electrochemically generated oxidized form of, 211
  reactivity, 243
  redox potentials of, 211
MET, 207, 261
Metal-activated oxygen, 1
Metal bicarbonate complexes, rearrangement of, 148
Metal–carbon σ-bond
  heterolysis of, 280–283
  homolysis of, 283–289
Metal carbonates
  chemistry of, 133–145
  coordination modes of carbonate in, 134
  solid state studies, 133–145
  solution equilibria, 133–145
Metal-oxo species, relative reactivities toward substrates X in aqueous solution, 15
Metal-to-ligand charge-transfer (MLCT), 62–63
Metal-to-particle charge-transfer (MPCT), 116–117
Methanethiosulfonate (MTS) reagent, 400
Methanol, solvation numbers in, 367
Methanosarcina thermoautotrophicum, 181
Methanosarcina thermophila, 160
  γ-class carbonic anhydrase, 183–185
Methyl groups, 374
Methyl radicals, rate constants for, 287

Methyl transfer reactions, 297
2-Methylferrocene carboxylic acid, 255
Michaelis–Menten behavior, 154
Michaelis–Menten kinetics, 214–215
MnCA, 166
Mn(II) complexes, 327, 337, 344–346, 351–353
Monodentate bicarbonato complexes, 158
Mo(V) complexes, 327, 346–349, 356
mRNA, 411, 414
Mycobacterium tuberculosis, 181

Near-infra-red (NIR) luminescence, 362
Neodymium complexes, 362
NH_3 formation, 92
Nickel complexes, 145
$[Ni(H_2dapoamh)_2]^{2+}$, 339
Ni(I) complexes, reduction of halo-alkanes, 301
Ni(II) complexes, 327, 336–339, 351, 353–355
Nitric oxide *see* NO
Nitrite reduction, 73
Nitrogen oxides, reactions of, 31–46
Nitroprusside ion *see* NP
Nitrosyl complexes, 64–66
  with OH^-, reactivity of, 80–88
Nitrosyl–iron complexes, 64–65
NO, 63
  bound
    electrophilic reactions, 79–104
    redox reactivity, 75–79
  coordination chemistry, 66–75
  formation and dissociation reactions, 66–75
  release from NP, 64
N_2O formation, 90, 94
$NO/Cr_{aq}OO^{2+}$ reaction, 36–39
$NO_2/CrOO^{2+}$ reaction, 42–46
$NO/L^2(H_2O)RhOO^{2+}$ reaction, 33–36
Non-podand ligands, 376–380
Non-radiative decay mechanisms, 365
Non-radiative energy transfer (ET), 365
Non-radioactive markers, 362
NP, 62
  addition reactions of bases to, 64
  addition reactions of thiolates to, 112
  and ferri-hemes, 74
  DFT computed LUMO, 76
  dissociation rate constants, 68
  electrophilic reaction
    with SH^- and SR^-, 111–115
    with sulfite, 110
  general properties, 64–66
  irreversible electroreduction, 79
  mechanistic scheme for reaction with NO, 71
  NO release from, 64
  one-electron electrochemical reduction, 75
  photochemical process, 74
  proposed mechamism involving initial reduction, 70
  rate law, 80
  reactivity
    with aliphatic amines in organic solvents, 100–103
    with hydrazine (Hz), MeHz, and 1,1-Me_2Hz, 88–96
    with NH_2OH, NH_3, and N_3, 98–100
    with OH^-, 81
    with thiolates, 114
    with trioxodinitrate, 103–104
Nucleic acids
  detection, 403–415
  non-specific staining, 405–406
Nucleid acids, requirements for new generation of labels, 414–415
Nucleophile B, 92
Nucleotides, labeled, 410

O_2, catalytic oxidation of alcohols by, 46–50
n-Octylferrocene, 217
One-step reverse transcription, 413
O–O bond length, 3, 9
O–O stretch, 3, 9
Os(II) complexes, 241
  cyclometalated, 258
Os(II) polypyridyl complexes, 416
Osmium complexes, 79, 239–253
  crystal structures, 256
  rate constants for oxidation of, 249
Oxidative dehydrogenation reactions of alcohols and amines, 106
Oxidative mediators, 261
Oxidoreductases, 201–202, 207

PBP complexes, 315–316, 329, 336, 339–341, 343, 351–353, 355
PBP environment, 329, 354

PBP geometry, 315–316, 348, 350–351, 353, 355–356
PBP structures, 316, 352–353, 355
Pentacyano(L)ferrate complexes, redox reactivity of coordinated ligands in, 61–126
Pentagonal–bipyramidal *see* PBP
Pentamethylferrocene, 228
Periodate treatment, 396
pH conditions, 89–90
pH-dependence of ferrocene half-reaction, 215
pH-dependence of GO-catalyzed oxidation, 242
pH-dependent complexation of copper(II), 136
pH profile for steady-state rate of GO-catalyzed reduction, 216
Phenol, 19
Phenols, HRP-catalyzed oxidation of, 229–230
2-Phenylimidazole, 258
2-Phenylpyridine, 258
Pivaldehyde, 20–27
Pivaloyl radicals, decarbonylation, 23
Planar chirality, 254–255
Podands, 369–376
Polymerase chain reaction (PCR), 403, 406–408
  real-time, 413
  time-resolved fluorometry assays, 412
Porphyridium purpureum, 180–183
Protein conjugation, 416
Protein detection, 391–403
  future applications, 403
Protein staining and assay, 391
Protonation constant, 157
Protoporphyrin IX, iron(III) complex of, 206
Pseudo-mediatorless electron transfer, 220
Pseudomonas extorquens, 210
Psuedomonas putida, 232
Pulse radiolysis, 271–313
Pyrroloquinoline quinone (PQQ) dehydrogenases, 207–208
Pyrroloquinoline quinone (PQQ)-dependent alcohol dehydrogenase, 210
Pyrroloquinoline quinone (PQQ)-dependent enzymes, 203
Pyrroloquinoline quinone (PQQ)-dependent oxidoreductases and glucose oxidase, 240–249

Quantum yield, 368
Quinohemoproteins, 207
Quinoproteins, 207

Radioimmunoassay, 393–395
Radio-iodination reactions, 394
Radio-labeled probes, 410
Radiolysis of aqueous solutions, 272–274
Rapid scan spectrophotometry, 154
Rate constants
  for methyl radicals, 287
  for oxidation of ferrocenes and ferrocyanide, 231
  for oxidation of Os complexes, 249
  for oxidation of reduced GO, 244–245
    by electrochemically generated oxidized form of mediator, 211
    by ferricenium ions, 218
  for oxidation of Ru complexes, 249
Real-time gene expression analysis, 413
Receptor autoradiography, 402–403
Receptor groups, 415
Receptor–ligand binding reactions, 402
Recombinant HRP isoenzyme *C*, 206
Redox potentials, 209
  cyclometalated Ru^{II} and Os^{II} complexes, 258
  Fe(II)–Fe(III) redox couples, 116
  ferrocenes, 217
  mediators, 211
  oxidation of reduced GO, 244–245
Redox reactivity
  bound NO, 75–79
  coordinated ligands in pentacyano(L)ferrate complexes, 61–126
Resonance Raman spectrum, 4
Rhodium complexes, 3–9
Rhodium hydrides, 16–18
  Cr(IV) and Cr(V) complexes rate constants for reactions with, 13
Ring-closure rate constant, 152
Ring-opening rate constant, 158
RNA, 403–415
  real-time analysis, 413
Ruby Red, 391

Ru(II) complexes, 240–241
  cyclometalated, 258
Ru(II) polypyridyl complexes, 416
Ruthenium complexes, 7–8, 239–253
  addition rate constants, activation parameters and corresponding ν_{NO}, $E_{NO^+/NO}$, and K_{eq} values, 83
  crystal structures, 256
  HRP-catalyzed oxidation of, 250–253, 259
  rate constants for oxidation of, 249
  structural and electronic parameters derived from calculations using pseudopotentials for metal centers, 86

Schiff base approaches, 384–385
Schiff base condensation of glutaraldehyde, 395
Self-exchange rate constants, 209
Sodium dodecylsulfate (SDS), 217–218
Solvation numbers in methanol, 367
Spectral transformations, 17
Stopped-flow technique, 111, 151
Sulfite coordination chemistry, 110–111
Superoxide-to-metal charge transfer, 7
Superoxo complexes
  preparation and characterization, 3–7
  rate constants for formation and homolysis, 3
  reactions with Rh–H, O–H, and C–H bonds, 16–31
  UV data, 7
Superoxometal-catalyzed co-oxidation of alcohols and nitrous acid with molecular oxygen, 49

$[Tb_2(L^{13})_3]$, 378
$[Tb(L^3)]$, 372
$[Tb(L^{53})(H_2O)Cl]^{2+}$, 389
Terbium complexes, 362, 388
Thalassiosira weissflogii, 185
Thermal intramolecular redox reaction, 75
Thermus aquaticus BM, 406
Ti(III), 352
Time resolved (TR) methods, 362
T-jump technique, 111, 151

Transient complexes
  bimolecular decomposition of, 296–297
  L_mM^{n+1}–R, mechanisms of decomposition, 280–298
  with metal–carbon σ-bonds, volumes of activation and reaction for formation and homolysis of, 286
Transition-metal complexes
  chemical structures, 2
  dioxygen activation by, 1–59
  examples, 2
  reactivity of, 12–50
  with bis(hydrazone) ligands of 2,6-diacetylpyridine, 315–360
  with metal–carbon bonds in aqueous solutions, 271–313
  with metal–carbon σ-bonds
    formation of, 275–278
    formed in redox processes with organic substrates, 299–304
    in reduction of alkenes, 302–304
    properties of, 278–280
    spectra, 278–279
Transition-metal cyanometallates, 61
Transition-metal model complexes, 186–188
Trioxodinitrate, 103–104
Tris(pyrazolyl)borate ligands, 372

UV spectral data, 9
UV–VIS absorption, 88
UV–VIS spectra, 11, 343
U(VI) complexes, 327, 346–349

V(III) complexes, 352
Volume profile analysis, 175

Western blotting, 400–402

X-ray crystallography, 1

Ytterbium complexes, 362

Zinc-bound H_2O, pK_a, 167
Zinc complexes, 142–145, 150
Zn(II) complexes, 327, 337, 344–346, 352, 354
Zn–phenol–pendant, crystallographic data, 188
Zwitterionic form, 155

This Page Intentionally Left Blank

CONTENTS OF PREVIOUS VOLUMES

VOLUME 41

The Coordination Chemistry of Technetium
John Baldas

Chemistry of Pentafluorosulfanyl Compounds
R. D. Verma, Robert L. Kirchmeier, and Jean'ne M. Shreeve

The Hunting of the Gallium Hydrides
Anthony J. Downs and Colin R. Pulham

The Structures of the Group 15 Element(III) Halides and Halogenoanions
George A. Fisher and Nicholas C. Norman

Intervalence Charge Transfer and Electron Exchange Studies of Dinuclear Ruthenium Complexes
Robert J. Crutchley

Recent Synthetic, Structural, Spectroscopic, and Theoretical Studies on Molecular Phosphorus Oxides and Oxide Sulfides
J. Clade, F. Frick, and M. Jansen

Stucture and Reactivity of Transferrins
E. N. Baker

INDEX

VOLUME 42

Substitution Reactions of Solvated Metal Ions
Stephens F. Lincoln and André E. Merbach

Lewis Acid–Base Behavior in Aqueous Solution: Some Implications for Metal Ions in Biology
Robert D. Hancock and Arthur E. Martell

The Synthesis and Structure of Organosilanols
Paul D. Lickiss

Studies of the Soluble Methane Monooxygenase Protein System: Structure, Component Interactions, and Hydroxylation Mechanism
Katherine E. Liu and Stephen J. Lippard

Alkyl, Hydride, and Hydroxide Derivatives in the *s*- and *p*-Block Elements Supported by Poly(pyrazolyl)borato Ligation: Models for Carbonic Anhydrase, Receptors for Anions, and the Study of Controlled Crystallographic Disorder
Gerard Parkin

INDEX

VOLUME 43

Advances in Thallium Aqueous Solution Chemistry
Julius Glaser

Catalytic Structure–Function: Relationships in Heme Peroxidases
Ann M. English and George Tsaprailis

Electron-, Energy-, and Atom-Transfer Reactions between Metal Complexes and DNA
H. Holden Thorp

Magnetism of Heterobimetallics: Toward Molecular-Based Magnets
Olivier Kahn

The Magnetochemistry of Homo- and Hetero-Tetranuclear First-Row *d*-Block Complexes
Keith S. Murray

Diiron–Oxygen Proteins
K. Kristoffer Andersson and Astrid Gräslund

Carbon Dioxide Fixation Catalyzed by Metals Complexes
Koji Tanaka

INDEX

VOLUME 44

Organometallic Complexes of Fullerenes
Adam H. H. Stephens and Malcolm L. H. Green

Group 6 Metal Chalcogenide Cluster Complexes and Their Relationships to Solid-State Cluster Compounds
Taro Saito

Macrocyclic Chemistry of Nickel
Myunghyun Paik Suh

Arsenic and Marine Organisms
Kevin A. Francesconi and John S. Edmonds

The Biochemical Action of Arsonic Acids Especially as Phosphate Analogues
Henry B. F. Dixon

Intrinsic Properties of Zinc(II) Ion Pertinent of Zinc Enzymes
Eiichi Kimura and Tohru Koike

Activation of Dioxygen by Cobalt Group Metal Complexes
Claudio Bianchini and Robert W. Zoellner

Recent Developments in Chromium Chemistry
Donald A. House

INDEX

VOLUME 45

Syntheses, Structures, and Reactions of Binary and Tertiary Thiomolybdate Complexes Containing the (O)Mo(S_x) and (S)Mo(S_x) Functional Groups ($x = 1, 2, 4$)
Dimitri Coucouvanis

The Transition Metal Ion Chemistry of Linked Macrocyclic Ligands
Leonard F. Lindoy

Structure and Properties of Copper–Zinc Superoxide Dismutases
Ivano Bertini, Stefano Mangani, and Maria Silvia Viezzoli

DNA and RNA Cleavage by Metal Complexes
Genevieve Pratviel, Jean Bernadou, and Bernard Meunier

Structure–Function Correlations in High Potential Iron Problems
J. A. Cowan and Siu Man Lui

The Methylamine Dehydrogenase Electron Transfer Chain
C. Dennison, G. W. Canters, S. de Vries, E. Vijgenboom, and R. J. van Spanning

INDEX

VOLUME 46

The Octahedral M_6Y_6 and M_6Y_{12} Clusters of Group 4 and 5 Transition Metals
Nicholas Prokopuk and D. F. Shriver

Recent Advances in Noble–Gas Chemistry
John H. Holloway and Eric G. Hope

Coming to Grips with Reactive Intermediates
Anthony J. Downs and Timothy M. Greene

Toward the Construction of Functional Solid-State Supramolecular Metal Complexes Containing Copper(I) and Silver(I)
Megumu Munakata, Liang Ping Wu, and Takayoshi Kuroda-Sowa

Manganese Redox Enzymes and Model Systems: Properties, Structures, and Reactivity
Neil A. Law, M. Tyler Caudle, and Vincent L. Pecoraro

Calcium-Binding Proteins
Bryan E. Finn and Torbjörn Drakenberg

Leghemoglobin: Properties and Reactions
Michael J. Davies, Christel Mathieu, and Alain Puppo

INDEX

VOLUME 47

Biological and Synthetic [Fe_3S_4] Clusters
Michael K. Johnson, Randall E. Duderstadt, and Evert C. Duin

The Structures of Rieske and Rieske-Type Proteins
Thomas A. Link

Structure, Function, and Biosynthesis of the Metallosulfur Clusters in Nitrogenases
Barry E. Smith

The Search for a "Prismane" Fe–S Protein
Alexander F. Arendsen and Peter F. Lindley

NMR Spectra of Iron–Sulfur Proteins
Ivano Bertini, Claudio Luchinat, and Antonio Rosato

Nickel–Iron–Sulfur Active Sites: Hydrogenase and CO Dehydrogenase
Juan C. Fontecilla-Camps and Stephen W. Ragsdale

FeS Centers Involved in Photosynthetic Light Reactions
Barbara Schoepp, Myriam Brugna, Evelyne Lebrun, and Wolfgang Nitschke

Simple and Complex Iron–Sulfur Proteins in Sulfate Reducing Bacteria
Isabel Moura, Alice S. Pereira, Pedro Tavares, and José J. G. Moura

Application of EPR Spectroscopy to the Structural and Functional Study of Iron–Sulfur Proteins
Bruno Guigliarelli and Patrick Bertrand

INDEX

VOLUME 48

Cumulative Index for Volumes 1–47

VOLUME 49

Inorganic and Bioinorganic Reaction Mechanisms: Application of High-Pressure Techniques
Rudi van Eldik, Carlos Dücker-Benfer, and Florian Thaler

Substitution Studies of Second- and Third-Row Transition Metal Oxo Complexes
Andreas Roodt, Amira Abou-Hamdan, Hendrik P. Engelbrecht, and Andre E. Merbach

Protonation, Oligomerization, and Condensation Reactions of Vanadate(V), Molybdate(VI), and Tungstate(VI)
J. J. Cruywagen

Medicinal Inorganic Chemistry
Zijian Guo and Peter J. Sadler

The Cobalt(III)-Promoted Synthesis of Small Peptides
Rebecca J. Browne, David A. Buckingham, Charles R. Clark, and Paul A. Sutton

Structures and Reactivities of Platinum-Blues and the Related Amidate-Bridged Platinum^{III} Compounds
Kazuko Matsumoto and Ken Sakai

INDEX

VOLUME 50

The Reactions of Stable Nucleophilic Carbenes with Main Group Compounds
Claire J. Carmalt and Alan H. Cowley

Group 1 Complexes of P- and As-Donor Ligands
Keith Izod

Aqueous Solution Chemistry of Beryllium
Lucia Alderighi, Peter Gans, Stefano Midollini, and Alberto Vacca

Group 2 Element Precursors for the Chemical Vapor Deposition of Electronic Materials
Jason S. Matthews and William S. Rees Jr.

Molecular, Complex Ionic, and Solid-State PON Compounds
Roger Marchand, Wolfgang Schnick, and Norbert Stock

Molecular Clusters of Dimetalated Primary Phosphanes and Arsanes
Matthias Driess

Coordination Complexes of Bismuth(III) Involving Organic Ligands with Pnictogen or Chalcogen Donors
Glen G. Briand and Neil Burford

Phanes Bridged by Group 14 Heavy Elements
Hideki Sakurai

INDEX

VOLUME 51

Clinical Reactivity of the Active Site of Myoglobin
Emma Lloyd Raven and A. Grant Mauk

Enzymology and Structure of Catalases
Peter Nicholls, Ignacio Fita, and Peter C. Loewen

Horseradish Peroxidase
Nigel C. Veitch and Andrew T. Smith

Structure and Enzymology of Diheme Enzymes: Cytochrome cd_1 Nitrate and Cytochrome *c* Peroxidase
Vilmos Fülöp, Nicholas J. Watmough, and Stuart J. Ferguson

Binding and Transport of Iron-Porphyrins by Hemopexin
William T. Morgan and Ann Smith

Structures of Gas-Generating Heme Enzymes: Nitric Oxide Synthase and Heme Oxygenase
Thomas L. Poulos, Huiying Li, C. S. Raman, and David J. Schuller

The Nitric Oxide-Releasing Heme Proteins from the Saliva of the Blood-Sucking Insect *Rhodnius prolixus*
F. Ann Walker and William R. Montfort

Heme Oxygenase Structure and Mechanism
Paul R. Ortiz de Montellano and Angela Wilks

De Novo Design and Synthesis of Heme Proteins
Brian R. Gibney and P. Leslie Dutton

INDEX

VOLUME 52

High-Nuclearity Paramagnetic 3*d*-Metal Complexes with Oxygen- and Nitrogen-Donor Ligands
Richard E. P. Winpenny

Transition Metal–Noble Gas Complexes
D. C. Grills and M. W. George

The Materials Chemistry of Alkoxystilbazoles and their Metal Complexes
Duncan W. Bruce

Tetra- and Trinuclear Platinum(II) Cluster Complexes
Tadashi Yamaguchi and Tasuku Ito

Complexes of Squaric Acid and Its Monosubstituted Derivatives
Lincoln A. Hall and David J. Williams

Applications for Polyaza Macrocycles with Nitrogen-Attached Pendant Arms
Kevin P. Wainwright

Perfluorinated Cyclic Phosphazenes
Anil J. Elias and Jean' ne M. Shreeve
INDEX

VOLUME 53

Wheel-Shaped Polyoxo and Polyoxothiometalates: From the Molecular Level to Nanostructures
Anne Dolbecq and Francis Sécheresse

Redox Chemistry and Functionalities of Conjugated Ferrocene Systems
Hiroshi Nishihara

New Aspects of Metal–Nucleobase Chemistry
Andrew Houlton

Advances in the Chemistry of Chlorocyclophosphazenes
Vadapalli Chandrasekhar and Venkatasubbaiah Krishnan

Self-Assembly of Porphyrin Arrays
Laura Baldini and Christopher A. Hunter
INDEX

VOLUME 54

Solvent Exchange on Metal Ions
Frank A. Dunand, Lothar Helm, and André E. Merbach

Ligand Substitution Reactions
John Burgess and Colin D. Hubbard

Oxygen Transfer Reactions: Catalysis by Rhenium Compounds
James H. Espenson

Reaction Mechanisms of Nitric Oxide with Biologically Relevant Metal Centers
Peter C. Ford, Leroy E. Laverman and Ivan M. Lorkovic

Homogeneous Hydrocarbon C–H Bond Activation and Functionalization with Platinum
Ulrich Fekl and Karen I. Goldberg

Density Functional Studies of Iridium Catalyzed Alkane Dehydrogenation
Michael B. Hall and Hua-Jun Fan

Recent Advances in Electron-Transfer Reactions
David M. Stanbury

Metal Ion Catalyzed Autoxidation Reactions: Kinetics and Mechanisms
István Fábián and Viktor Csordás
INDEX

This Page Intentionally Left Blank